JSCSEN 78(12)1837–2236(2013)

ISSN 1820-7421(Online)

Journal of the Serbian Chemical Society

Electronic Version

VOLUME 78

No 12

BELGRADE 2013

Available on line at

www.shd.org.rs/JSCS/

Journal of the Serbian Chemical Society

JSCS-info@shd.org.rs • www.shd.org.rs/JSCS

J. Serb. Chem. Soc. Vol. 78, No. 12 (2013)

CONTENTS

J. Serb. Chem. Soc. Vol. 78, No. 12 (2013)

ISSN 0352-5139

CONTENTS Continued

Published by the Serbian Chemical Society
Karnegijeva 4/III, 11000 Belgrade, Serbia
Printed by the Faculty of Technology and Metallurgy
Karnegijeva 4, P.O. Box 35-03, 11120 Belgrade, Serbia

Journal of the Serbian Chemical Society
JSCS-info@shd.org.rs • www.shd.org.rs/JSCS

EDITORIAL

This issue of the *Journal of the Serbian Chemical Society* is dedicated to Professor Branislav Ž. Nikolić on the occasion of his 70th birthday as the tribute to his accomplishments in the field of Electrochemistry and to his contributions to the advancement of Chemistry in Serbia. In parallel with his scientific work, Professor Nikolić was a dedicated teacher of Physical Chemistry and Electrochemistry for generations of students at the University of Belgrade.

The articles in this issue are contributions of Professor Nikolić's colleagues, friends and students from all over the world. In addition to articles from the area of Electrochemistry, there are a number from several fields of Chemistry illustrating Professor Nikolic's diverse interests. Technical limitations determined the size of this issue, and we are sorry that we could not invite more contributors.

It was a great pleasure and honor for us to be the Guest Editors of this special issue. We are indebted for the great help from several colleagues and to the Society's office and the *Journal*'s team for their support in the processing of this issue. The additional financial support of the Faculty of Technology and Metallurgy and Institute of Chemistry, Technology and Metallurgy is very much appreciated.

Belgrade, Serbia/Upton, New York, December 2013

Guest Editors

Radoslav Adžić
Bogdan Šolaja

Journal of the Serbian Chemical Society
JSCS-info@shd.org.rs • www.shd.org.rs/JSCS
J. Serb. Chem. Soc. 78 (12) 1839–1845 (2013) UDC 929 Branislav Ž. Nikolić

Professor Branislav Ž. Nikolić

On the occasion of his 70th Birthday

Branislav Nikolić was born on 22 September 1943, in the town of Knjaževac (Serbia). He attended secondary school in Podgorica (Montenegro), and graduated in 1966 from the Faculty of Technology and Metallurgy, University of Belgrade. In 1977, he obtained his PhD in Technical Sciences under the mentorship of Professor Aleksandar Despić, from the same school. After employment at the Institute of Chemistry, Technology and Metallurgy, University of Belgrade for three years, he became a permanent staff member at the Faculty of Technology and Metallurgy, University of Belgrade. He rose from the position of Teaching Assistant through all the ranks (Assistant Professor in 1978, Associate Professor in 1985), to Full Professor in Physical Chemistry and Electrochemical Engineering in 1992. He served two terms as Vice-Dean, and became Chair of Physical Chemistry and Electrochemistry (1999–2005). He taught Physical Chemistry, Electrochemistry, Electrochemical Engineering (basic and advanced courses), Electrometallurgy and Mass Transport in Electrochemical Systems, at the University and at the Centre for Multidisciplinary Studies. He was mentor for approximately twenty Diploma Dissertations, a well as fifteen MS, and ten PhD Theses. During his career, he authored two university textbooks on *Experimental Physical Chemistry* and *Electrochemical Engineering*. At Case Western Reserve University, Cleveland, OH, Professor Nikolić was a Postdoctoral Fellow under the mentorship of Professor Ernest Yeager (1977/78), Visiting Scientist (1979) and Visiting Professor (1990).

Professor Nikolić participated in numerous scientific research projects, and coordinated several complex projects sponsored by the Serbian Ministry of Science (2000/2008). He has published more than 120 scientific papers (approximately 70 in international journals and meeting proceedings) and 20 professional papers. He delivered 15 invited lectures and had some 130 contributed papers at international and national meetings with more than 650 citations.

Professor Nikolić's three main scientific interests are in the field of Electrochemistry. The first involves electrocatalysis of chlorine and chlorine compounds. He studied the kinetics and mechanisms of electrochemical reactions of chlorine and chlorine–oxygen compounds, including the effects of the composition and structure of anode materials, current density, current density distribution, pH value, hydrodynamic regime and temperature. The main outcome of this research included the formation and characterization of electrocatalytic oxide (such as $RuO_2/IrO_2/TiO_2$) coatings, and their optimization for chlorine and oxygen evolution, as well as the oxidation of organic compounds. He also contributed to the characterization of ruthenium oxide as a supercapacitor material.

Mass transfer in electrochemical systems is another area that was in the focus of his research. He studied mass transfer in electrochemical reactors (chlorate electrolysis) and rotating disc electrodes (disc, disc–ring, ring–ring and rectangular patch electrodes), which are successfully used as a measuring technique in electrochemical kinetics.

Electrocatalysis of the oxygen reduction reaction is the topic he embraced long ago by starting pioneering studies of the adsorption of macrocyclic complexes of transition metals, and their role in oxygen reduction. He also contributed to the understanding of the oxygen reduction reaction and the electrochemical behavior of Pt single crystal electrodes.

Professor Nikolić participated in projects sponsored by the chemical industry, involving electrolytic technologies for the production of chlorine, sodium hydroxide, sodium hypochlorite, chlorate, and perchlorate. His interest in applied electrochemistry finally resulted in his significant achievement in oxide electrodes: titanium electrodes with ruthenium–titanium oxide coatings as the result of his team's research were successfully used in industrial electrolyzers. He and his research team developed a sol–gel procedure for the production and application of RuO_2–TiO_2 anode coatings.

For his scientific achievements, Professor Nikolić received the Annual Award of the City of Belgrade (1974) in the field of Mathematics/Physics, the Medal of the Serbian Chemical Society for outstanding industrial application of science (1998), and the Serbian Chemical Society Award for long-lasting and outstanding contributions to science (2007).

Professor Nikolić has been a very active member of the Serbian Chemical Society. He was General Secretary (1984–1988), Vice-president (1996–2001), and President (2001–2005). Since 2012, he serves as Honorary President of the Society. He is a long-time member of the Editorial Board of the *Journal of the Serbian Chemical Society*. Moreover, he was the Secretary of the Union of the Chemical Societies of Yugoslavia. He is a member of the International Society of Electrochemistry, acting as the Yugoslav (Serbia and Montenegro) National Secretary, and a member of the European Federation of Chemical Engineers – Work-

ing Party on Electrochemical Engineering (used to be also National Representative). As an officer of the *Serbian Chemical Society*, he was a member of the General Assembly of the European Association for Chemical and Molecular Sciences.

In 2006, our dear colleague Prof. Nikolić became Editor-in-Chief of the *Journal of the Serbian Chemical Society*. With his enthusiasm and personal touch, he continues to improve the quality and diversity of the Serbian Chemical Society's flagship journal, for which all of us are enormously grateful. It is our privilege and great pleasure to give you this short biographical note on Professor Nikolić on the occasion of his jubilee. On behalf of his colleagues and friends, we wish him to stay with our Society and our Journal for many years to come.

Bogdan Šolaja
Radoslav Adžić

BRANISLAV Ž. NIKOLIĆ – SELECTED PAPERS

1. M. M. Jakšić, A. R. Despić, M. I. Csonka, **B. Ž. Nikolić**, Studies on chlorate cell process. V. Theory and practice of a modified technology for electrolytic chlorate production, *J. Electrochem. Soc.* **116** (1969) 1316
2. M. M. Jakšić, A. R. Despić, **B. Ž. Nikolić**, Noveišie tehnologišeskie aspekti elektrolitičkoeskogo proizvodstvo hloratov, *Elektrokhimiya* **8** (1972) 1573
3. A. R. Despić, M. M. Jakšić, **B. Ž. Nikolić**, Effect of kinetic and hydrodynamic factors on current efficiency in the chlorate cell process, *J.Appl. Electrochem.* **2** (1972) 337
4. V. Yu. Filinovsky, I. V. Kadija, **B. Ž. Nikolić**, M. V. Nakić, Mass transfer on the rotating double ring electrode. Reaction without gas evolution, *J. Electroanal. Chem.* **54** (1974) 39
5. I. V. Kadija, **B. Ž. Nikolić**, A. R. Despić, Mass transfer during gas evolution on rotating double ring electrodes, *J. Electroanal. Chem.* **57** (1974) 35
6. R. T. Atanasoski, **B. Ž. Nikolić**, M. M. Jakšić, A. R. Despić, Platinum-iridium catalysed titanium anode. i. properties and use in chlorate electrolysis, *J. Appl. Electrochem.* **5** (1975) 155
7. A. R. Despić, M. V. Mitrović, **B. Ž. Nikolić**, S. D. Cvijović, Mass transfer at a rotating disc with rectangular patch electrodes, *J. Electroanal. Chem.* **60** (1975) 141
8. M. M. Jakšić, **B. Ž. Nikolić**, Die Grundlagen der optimalen Auslegung von Chlorat-Zellen. I. Chlorate-Zellen mit intensiever rueckwartiger Elektrolytruehrung, *Chem. Tech*. **27** (1975) 158

9. M. M. Jakšić, **B. Ž. Nikolić**, M. D. Spasojević, Die Grundlagen der optimalen Auslegung von Chlorat-Zellen. II.Die Chlorat Zellen mit einfacher Durchstromung des Elektrolyten. Die Stromdichte, *Chem. Tech*. **27** (1975) 534
10. **B. Ž. Nikolić**, R. R. Adžić, A. R. Despić, Investigation of the anodic processes on platinum in perchlorate and chlorate solution by linerar sweep voltammetry using the rotating duble ring electrodes, *J. Electroanal. Chem.* **72** (1976) 251
11. **B. Ž. Nikolić**, R. R. Adžić, E. B. Yeager, Reflectance spectra of monolayers of tetrasulfonated transition metal phthalocyanines adsorbed on electrode surfaces, *J. Electroanal. Chem.* **103** (1979) 281
12. E. Yeager, J. Zagal, **B. Nikolić**, R. Adžić, Optical and electrochemical studies of adsorbed transition metal complexes and their o_2 electrolytic properties, in *Proceedings of Third Symposium on Electrode Processes*, Boston, MA, USA, 1979, S. Bruckenstein, J. D. E. McIntyre, B. Miller, E. Yeager, Eds., The Electrochemical Society, Inc., Princeton, NY, 1980, p. 436
13. **B. Ž. Nikolić**, H. Huang, D. Gervasio, A. C. Fierro, E. B. Yeager, R. R. Adžić, Electroreduction of carbon dioxide on platinum single crystal electrodes: Electrochemical and *in situ* FTIR studies, *J. Electroanal. Chem.* **295** (1990) 415
14. V. M. Jovanović, A. Dekanski, P. Despotov, **B. Ž. Nikolić**, R. T. Atanasoski, The roles of the ruthenium concentration profile, the stabilizing component and the substrate on the stability of oxide coatings, *J. Electroanal. Chem.* **339** (1992) 147
15. R. R. Adžić, F. Freddrix, **B. Ž. Nikolić**, E. B. Yeager, The elucidation of hydrogen and anion adsorption on Pt (111) through the co-adsorption of metal adatoms and carbon monoxide, *J. Electroanal. Chem.* **341** (1992) 287
16. **B. Nikolić**, R. Adžić, The electrosorption valence of adsorbed phosphoric acid anions on the Pt (111) surface, *J. Serb. Chem. Soc.* **62** (1997) 515
17. T. Vidaković, M. Avramov-Ivić, S. Zečević, **B. Nikolić**, Electrochemical study of metal––tetrasulfonated phthalocyanines adsorbed on gold, platinum and iron electrodes and their role in electrochemical oxygen reduction, *J. Serb. Chem. Soc.* **63** (1998) 41
18. V. V. Panić, A. B. Dekanski, S. K. Milonjić, R. T. Atanasoski, **B. Ž. Nikolić**, RuO_2–TiO_2 coated titanium anodes obtained by sol–gel procedure and their electrochemical behaviour in chlorine evolution reaction, *Colloids Surfaces, A* **157** (1999) 269
19. R. Adžić, J. Wang, S. Štrbac, **B. Nikolić**, The structure of active and inactive surfaces of gold and platinum for oxygen electroreduction, in *New Challenges in Catalysis II*, P. Putanov, Ed., ‚Serbian Academy of Science and Arts, Branch in Novi Sad, Novi Sad, 1999, p. 37
20. V. Panić, A. Dekanski, S. Milonjić, R. Atanasoski, **B. Nikolić**, The influence of the aging time of RuO_2 and TiO_2 sols on the electrochemical properties and behavior of activated titanium anodes obtained by sol–gel procedure for the chlorine evolution reaction, *Electrochim. Acta* **46** (2000) 415
21. A. Dekanski, J. Stevanović, R. Stevanović, **B. Nikolić**, V. Jovanović, Glassy carbon electrodes. I. Characterisation and electrochemical activation, *Carbon* **39** (2001) 1195
22. V. Panić, A. Dekanski, G. Wang, M. Fedoroff, S. Milonjić, **B. Nikolić**, The morphology of RuO_2–TiO_2 coatings and tem characterization of oxide sols used for the coating preparation *via* sol–gel route, *J. Colloid Interface Sci.* **263** (2003) 68
23. V. Panić, T. Vidaković, S. Gojković, A. Dekanski, S. Milonjić, **B. Nikolić**, The properties of carbon-supported hydrous ruthenium oxide obtained from RuO_xH_y sol, *Electrochim. Acta* **48** (2003) 3805

24. V. V. Panić, A. B. Dekanski, T. R. Vidaković, V. B. Mišković-Stanković, B. Ž. Jovanović, **B. Ž. Nikolić**, Oxidation of phenol on RuO_2–TiO_2/Ti anodes, *J. Solid State Electrochem.* **9** (2005) 43
25. V. Panić, A. Dekanski, V. B. Mišković-Stanković, S. Milonjić, **B. Nikolić**, On the deactivation mechanism of RuO_2-TiO_2/Ti anodes prepared by the sol–gel procedure, *J. Electroanal. Chem.* **579** (2005) 67
26. V. V. Panić, T. R. Vidaković, A. B. Dekanski, V. B. Mišković-Stanković, **B. Ž. Nikolić**, Capacitive properties of RuO_2-coated titanium electrodes prepared by the alkoxide ink procedure, *J. Electroanal. Chem.* **609** (2007) 120
27. V. V. Panić, **B. Ž. Nikolić**, Sol–gel prepared active ternary coating on titanium in cathodic protection, *J. Serb. Chem. Soc.* **72** (2007) 1393
28. V. V. Panić, **B. Ž. Nikolić**, Electrocatalytic properties and stability of titanium anodes activated by the inorganic sol–gel procedure, *J. Serb. Chem Soc.* **73** (2008) 1083.
29. V. V. Panić, A. B. Dekanski, V. B. Mišković-Stanković, **B. Ž. Nikolić**, The study of capacitance change during electrolyte penetration through carbon-supported hydrous ruthenium oxide prepared by the sol–gel procedure, *Chem. Biochem. Eng. Q.* **23** (2009) 23
30. **B. Nikolić**, Titan, oksidi, elektrokataliza i superkapacitivnost, *Chemical Review* **53** (2010) 58 (in Serbian)
31. V. V. Panić, A. B. Dekanski, M. Mitrić, S. K. Milonjić, V. B. Mišković-Stanković, **B. Ž. Nikolić**, The effect of the addition of colloidal iridium oxide into sol–gel obtained titanium and ruhenium oxide coatings on titanium on their electrochemical properties, *Phys. Chem. Chem. Phys.* **12** (2010) 7521
32. **B. Ž. Nikolić**, V. V. Panić, A. B. Dekanski, Intrinsic potential-depedent performances of a sol–gel prepared electrocatalytic IrO_2–TiO_2 coating of dimensionally stable anodes, *Electrocatalysis* **3** (2012) 360
33. Ž. Jovanović, A. Radosavljević, J. Stojkovska, **B. Nikolić**, B. Obradović, Z. Kačarević-Popović, V. Mišković-Stanković, Silver/poly(*n*-vinyl-pyrrolidone) hydrogel nanocomposites obtained by electrochemical synthesis of silver nanoparticles inside the polymer hydrogel aimed for biomedical applications, *Polymer Composites*, 2013, DOI 10.1002/pc.22653
34. **B. Ž. Nikolić**, V. V. Panić, Electrocatalysis of chlorine evolution, in *Encyclopedia of Applied Electrochemistry*, R. F. Savinell, K.-I. Ota, G. Kreysa, Eds., Springer, Berlin, 2013, DOI 10.1007/978-1-4419-6996-5.

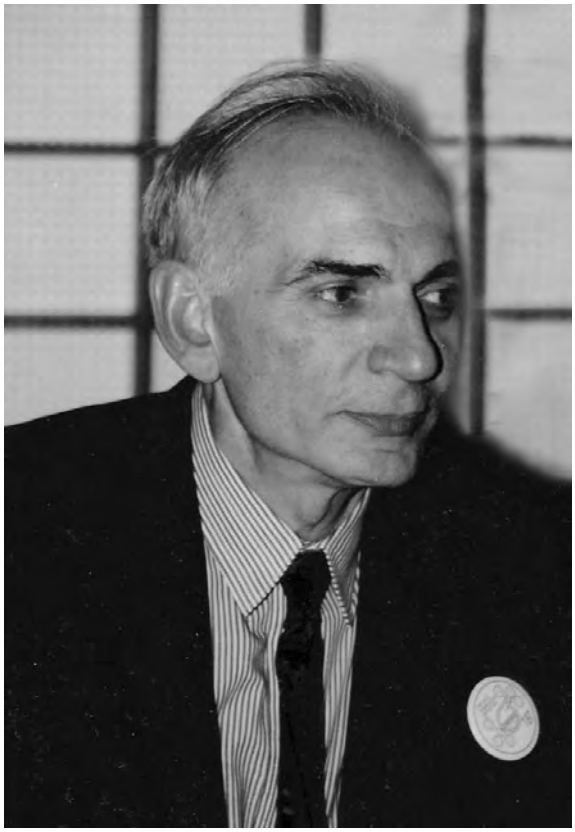

Journal of the Serbian Chemical Society
JSCS-info@shd.org.rs • www.shd.org.rs/JSCS

J. Serb. Chem. Soc. *78* (12) 1847–1864 (2013)
JSCS–4536

UDC **Clostridium botulinum*+547.583.5:
615.285:612.014.46+616.8+615.9+57
Original scientific paper

New 9-aminoacridine derivatives as inhibitors of botulinum neurotoxins and *P. falciparum* malaria•

MIKLOŠ TOT[1], DEJAN M. OPSENICA[2#], MILENA MITRIĆ[1], JAMES C. BURNETT[3], LAURA GOMBA[4], SINA BAVARI[5] and BOGDAN A. ŠOLAJA[1*#]

[1]Faculty of Chemistry, University of Belgrade, Studentski trg 16, P. O. Box 51, 11158, Belgrade, Serbia, [2]Institute of Chemistry, Technology, and Metallurgy, University of Belgrade, Njegoševa 12, 11000 Belgrade, Serbia, [3]SAIC-Frederick, Inc., Frederick National Laboratory for Cancer Research, P. O. Box B, Frederick, MD 21702, USA, [4]United States Army Medical Research Institute of Infectious Diseases, Department of Bacteriology, 1425 Porter Street, Frederick, MD 21702, USA and [5]United States Army Medical Research Institute of Infectious Diseases, Fort Detrick, 1425 Porter Street, Frederick, MD 21702, USA

(Received 24 September, revised 20 October 2013)

Abstract: Steroidal and adamantane aminoacridine derivatives were prepared and tested as both botulinum neurotoxin (BoNT) inhibitors and antimalarials. Steroid-bound acridines provided good potency against both the BoNT/A and BoNT/B light chains (LCs). The observed inhibition of the BoNT/B LC by *ca*. 50 % is the highest attained inhibitory activity against this serotype by acridine-based compounds to date. With respect to the antimalarial activity, the adamantane acridines were the most potent derivatives (IC_{50} = 6–9 nM, *SI* > 326), indicating that an adamantyl group is a better carrier than a steroidal motif for this indication.

Keywords: antiviral, BoNT/A; BoNT/B; antimalarial; aminoacridine.

INTRODUCTION

Botulinum neurotoxins (BoNTs),** secreted by the anaerobic, spore-forming bacterium *Clostridium botulinum*, are the most potent of known biological tox-

* Corresponding author. E-mail: bsolaja@chem.bg.ac.rs
# Serbian Chemical Society member.

• This manuscript is dedicated to our dear colleague and friend Prof. Branislav Nikolić on the occasion of his 70th birthday.

doi: 10.2298/JSC130924112T

** Abbreviations: BoNT, botulinum neurotoxin; SNARE, soluble *N*-ethylmaleimide-sensitive factor attachment protein receptor; BoNT/A, botulinum neurotoxin serotype A; BoNT/A LC, BoNT/A light chain; SMNPIs, small molecule non-peptidic inhibitors; ACR, 9-amino-2-metoxy-7-chloroacridine; ACR2, *N*-(6-chloro-2-methoxyacridin-9-yl)ethane-1,2-diamine; ACR3, *N*-(6-chloro-2-methoxy-9-anthryl)propane-1,3-diamine; ACR5,

ins.[1,2] The proteolytic activities of these enzymes are responsible for the potentially fatal disease botulism, which is commonly associated with food contamination, wound infection, and colonizing infection in infants. BoNTs can be easily produced and disseminated,[3] and therefore are listed as priority biological threat agents.[4] On the other hand, when dosed locally in minute concentrations, BoNTs are used for the effective treatment of severe diseases.[5]

There are seven known BoNT serotypes identified as A–G. Each cleaves a component of the SNARE complex, which mediates the transport of acetylcholine into neuromuscular junctions.[6,7] BoNTs are secreted as holotoxins composed of a heavy chain (HC) and light chain (LC), which are connected by a disulfide bridge.[8,9] The HC, which transports the LC into the neuronal cytosol *via* an acidic endosome, is comprised of two ≈50 kDa domains. The *C*-terminal domain (H_C), the ganglioside and protein receptor-binding domain, plays a role in binding to the cell membrane and internalization of a toxin into cholinergic neurons; the *N*-terminal domain (H_N) facilitates the release of the LC from endosomes into the cytosol. The LC is a zinc-dependent metalloprotease that cleaves SNARE proteins, thereby inhibiting the formation of the SNARE complex. BoNT serotypes A and E cleave SNAP-25 (synaptosomal-associated protein (25 kDa)),[10] serotypes B, D, F[11] and G cleave VAMP (vesicle-associated membrane protein),[12] and serotype C cleaves both SNAP-25 and syntaxin 1.[13] Serotype A (BoNT/A) is the most potent of the seven serotypes. For example, it is 10^6-fold more potent than cobra toxin and 10^{11}-fold more potent than cyanide,[6] and its lethal dose is estimated to be between 1 and 5 ng kg^{-1} for humans.[14] Moreover, the BoNT/A LC is longest acting of the LC serotypes in the neuronal cytosol.[15]

Currently, there are no therapies available for the treatment of BoNT LC-mediated paralysis post-neuronal intoxication, although several different approaches are currently under development. Two of these approaches include antibody-based therapeutics and small molecule-based therapeutics.[16] However, antibodies cannot reverse the proteolytic effects of the toxins after the LC component has entered the neuronal cytosol.[2] Hence, the development of small molecules that will effectively inhibit proteolytic activity of BoNT LC after post-neuronal intoxication is of special interest, with the BoNT/A LC being the main enzyme of study. At this time, one of the best known inhibitors of the BoNT/A LC is mpp-RATKML, which consists of the oligopeptide RATKML covalently bonded to 2-mercapto-3-phenylpropionyl (mpp) group (K_i = 330 nM).[17] However, peptides are readily hydrolyzed by proteases, thus limiting their application in the therapy.

N-(6-chloro-2-methoxyacridin-9-yl)pentane-1,5-diamine; ACR6, *N*-(6-chloro-2-methoxyacridin-9-yl)hexane-1,6-diamine; CQR, chloroquine resistant strain; CQS, chloroquine susceptible strain; MDR, multi-drug resistant strain; BS, binding site; QA, quinacrine; CQ, chloroquine; MFQ, mefloquine; ART, artemisinin; EA, ethyl acetate; DCM, dichloromethane; PCC, pyridinium chlorochromate; TFA, trifluoroacetic acid.

For this reason, the development of small molecule inhibitors is crucial. To this end, many inhibitors of the BoNT/A LC have been reported,[18] and are composed of compounds that competitively coordinate the catalytic zinc ion,[19] as well as allosteric inhibitors.[20] The most potent possess K_i values ranging from 0.1–10 μM and include zinc (Zn^{2+}) bidentate coordinating hydroxamic acid **1**,[21] 2,5-diphenyl-thiophene derivative **2**,[22] and diazachrysene **3**[23] (Chart 1).

In contrast to BoNT/A LC inhibitors, a paucity of small molecules that inhibit the BoNT/B LC has been reported. These include isocoumarine **4**,[24] aryl--phosphoramidic acid **ICD 2821**[25], bis-benzimidazole-5-carboximidamide **5**[26] (which bidentately coordinates the catalytic Zn ion of enzymes), and L-chicoric acid **6** (which is reported to bond to an exosite of the enzyme).[27] In addition, it has been reported that the reducing agent **TCEP** (tris(2-carboxyethyl)phosphine hydrochloride) reduces the disulfide bond connecting the HC–LC bond of the enzyme both *in vitro* and in neuronal cells, and that it works prophylactically with a maximum activity at 1 mM.[28] In this way, the LC cannot undergo endocytosis, and therefore cannot cleave VAMP.

It is well known that many 4-aminoquinoline antimalarials act as inhibitors of the BoNT/A LC.[29,30] In contrast, little has been reported about the efficacy of acridine-based (ACR) compounds as BoNT inhibitors. However, it was found that quinacrine (QA, Chart 2), effectively prolonged the time of BoNT/A blocking of nerve-elicited muscle twitch in isolated mouse diaphragms.[31] Furthermore, it was found that QA was four times more efficacious than CQ, with a muscle twitch protective index of 2.85 at 10 μM.

Malaria* is a devastating disease and a global health problem. It is estimated to cause 300–500 million clinical cases and *ca*. one million deaths *per annum*.[32] The most successive drugs appeared to kill the parasite either by producing toxic free radicals[33] or by blocking the polymerization of heme, as in the case of the 4-amino-7-chloroquinolines (ACQs).[34] The development of widespread drug-resistance to CQ has resulted in an urgent need for new drug modalities, for example, synthetic peroxide antimalarials,[35] as well as for the development of novel molecules that prevent heme polymerization.[36]

Quinacrine was the first synthetic antimalarial used clinically that acts as a blood schizonticide, but later it was replaced with the more efficient CQ.[37] However, due to the widespread development of CQ resistant (CQR) strains, there is renewed interest for evaluating acridine-based compounds as antimalarials. For example, *N*-sulfonamide derivatives, obtained from various simple 9-aminoacridines, show high antimalarial activity against both CQS and CQR strains.[38] They do not lose activity even when the amino group is stripped of its basic character, which is in contrast to most CQs or other quinoline or acridine derivatives.[39] Qui-

* Malaria is caused by five *Plasmodium* species, *P. falciparum*, *P. ovale*, *P. vivax*, *P. malariae* and *P. knowlesi*, of which *P. falciparum* causing cerebral malaria is the major death threat.

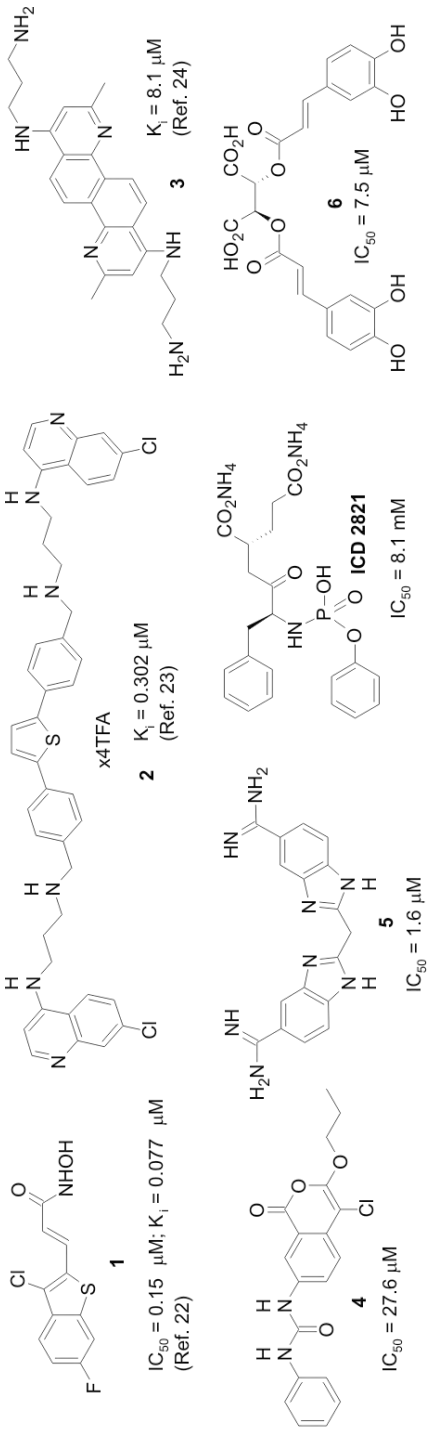

Chart 1. Structures of potent inhibitors of BoNT/A LC and BoNT/B LC.

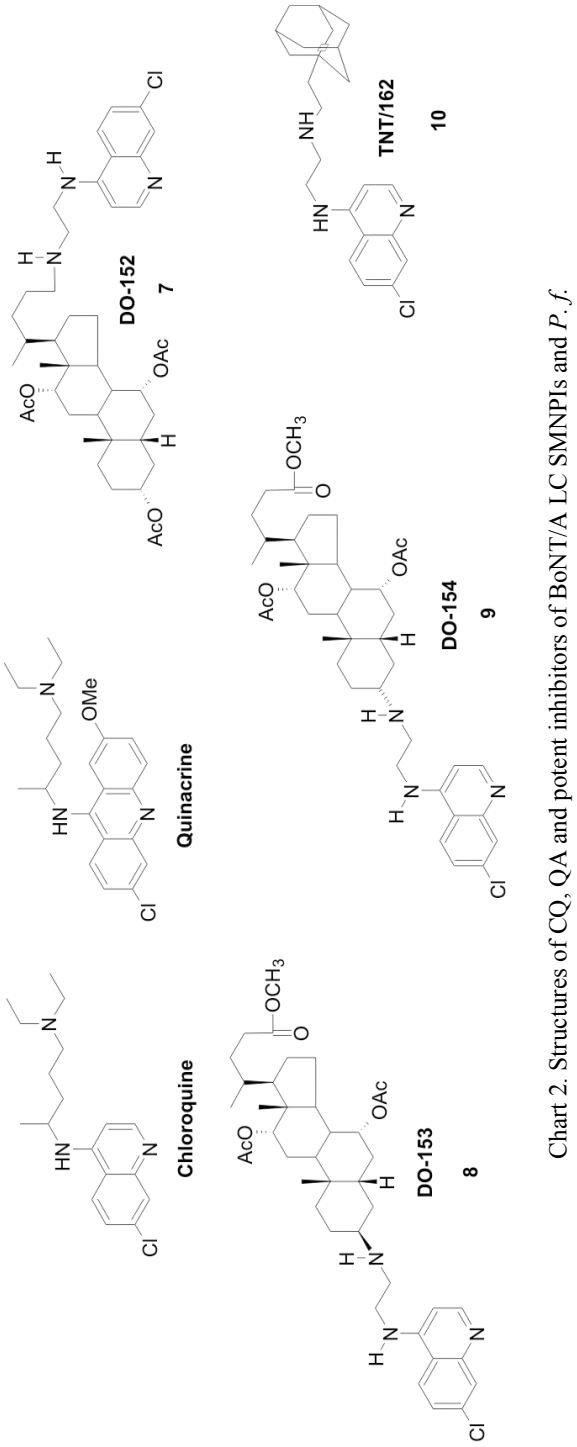

Chart 2. Structures of CQ, QA and potent inhibitors of BoNT/A LC SMNPIs and *P. f.*

nolizidinyl and quinolizidinyl-alkyl derivatives of 9-amino-6-chloro-2-methoxy-acridine were almost 10 times more active than CQ against CQR (W2) strain, and were as active as CQ against the CQS (D10) strain;[40] a series of 9-amino-acridines showed high inhibitory potency.[41] Most active derivatives have diamino-propylidene side chains and exert low nM activity (EC_{50} in range 1–4.1 nM).

Similar to AQ antimalarials, 9-aminoacridines inhibit polymerization of hemozoin. In a β-hematin inhibitory assay (BHIA), it was found that ACR derivatives formed complexes with hematin in a 3:2 molar ratio (hematin:drug).[42] It was shown that the presence of 2-methoxy, 6-chloro substituents and an ionizable terminal amino group are essential for good antimalarial activity. It was also discovered that ACRs inhibit DNA topoisomerase II,[39,43] parasite folate metabolism[44] and plasmepsin II.[45] However, chimeric derivatives with ART[46] or AQ,[47] as well as bis-ACR derivatives,[39,48] showed poor activities.

In addition to their significant antimalarial activity, ACR-based compounds exhibit other biological activities, including nuclear localization signal (NLS)--labeling agents for plasmid DNA,[49] photocleavage reagents for DNA,[50] anti-leishmania agents[51] and anti-prion compounds.[52]

Previously, we reported on the inhibitory activities of steroidal 4-amino-quinolines **7**–**9** and adamantyl-aminoquinolines (for example, **10**) against the BoNT/A LC[30] and as antimalarial agents[53] were reported (Chart 2). Specifically, these derivatives provided a high degree of inhibition of BoNT/A metallopro-tease, as well as significant inhibition of CQS and more important, CQR strains of *P. falciparum*. Herein, the synthesis and biological evaluation of new ACR derivatives possessing steroid and adamantane carrier component are presented.

RESULTS AND DISCUSSION

Synthesis

The syntheses of the ACR derivatives examined in this study are provided in Scheme 1, and the corresponding structures are given in Chart 3. First, aminoalk-

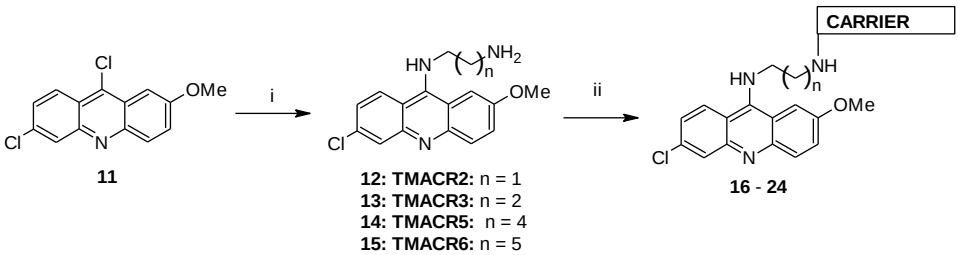

i) diamine, Δ;
ii) ketone, $NaBH_3CN$/ MeOH/CH_3CN, or $NaBH_4$ / MeOH or $NaBH_4$ / $Ti(OPr^i)_4$ / EtOH, or $NaB(OAc)_3H$ / DCM

Scheme 1. Synthesis of acridine derivatives **12**–**24**.

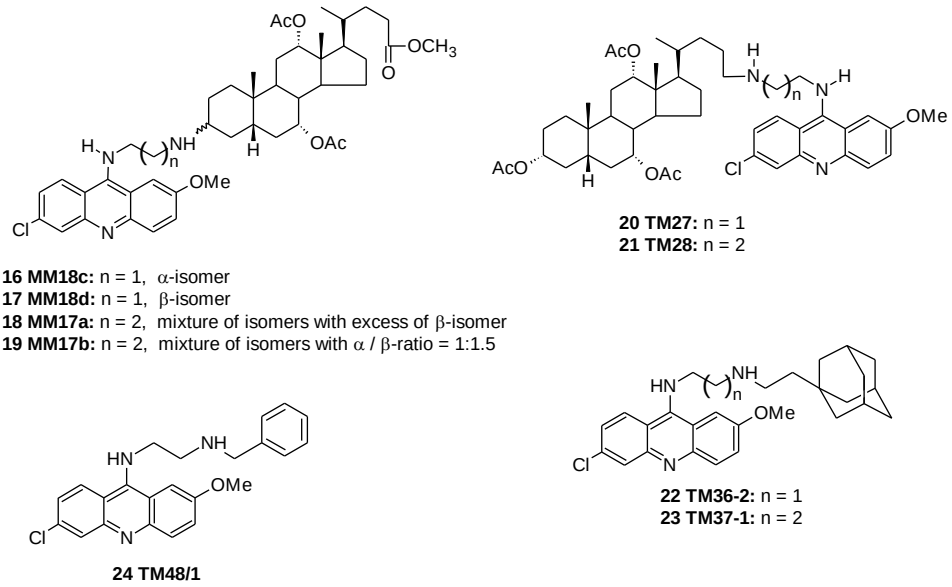

16 MM18c: n = 1, α-isomer
17 MM18d: n = 1, β-isomer
18 MM17a: n = 2, mixture of isomers with excess of β-isomer
19 MM17b: n = 2, mixture of isomers with α / β-ratio = 1:1.5

20 TM27: n = 1
21 TM28: n = 2

22 TM36-2: n = 1
23 TM37-1: n = 2

24 TM48/1

Chart 3. Structures of examined derivatives **16**–**24**.

ylamino acridines **12**–**15** were obtained by the heating of 6,9-dichloro-2-methoxyacridine **11** with neat diamines.[50] The spectra of the isolated products were in agreement with literature data, and the compounds were used in the next reaction step without additional purification. Derivatives **16**–**24** were synthesized using procedures described earlier.[30,53] The 3-keto steroidal derivative (7*α*,12*α*-diacetoxy-3-oxo-5*β*-cholan-24-oate)[54] was coupled with aminoalkylamino acridines **12** and **13** to afford the corresponding 3*α*-and 3*β*-diastereomers (**16**–**19**). The crude reaction product obtained from **12** afforded diastereomers **16** and **17** *via* chromatographic separation. However, derivatives obtained from **13** were only partially separated to afford **18** containing *ca*. 20 % of **19**, and the second fraction consisting of both isomers in a 1:1.5 ratio. The configuration at C(3) of the derivatives **16**–**19** was deduced from the respective ^{1}H-NMR spectra. The corresponding H–C(3) atom of derivative **16** had a broad multiplet at 2.50–2.34 ppm, while that of derivative **17** had a narrow signal at 2.93 ppm. Therefore, **16** has an axial H–C(3) (in the *β*-orientation) and acridine substituent in an *α*-orientation (*α*-isomer). Consequently, **17** is the *β*-isomer since it has H_α–C(3) and the acridine substituent in the *β*-orientation. Based on the above correlations, it was possible to establish the approximate composition of mixtures obtained from partially separated isomers **18** and **19**. Steroidal alcohol 3*α*,7*α*,12*α*-triacetoxy-5*β*--cholan-24-ol was oxidized to the corresponding aldehyde,[30] which was further coupled to **12** and **13** to give the corresponding steroidal acridine derivatives **20** and **21**. Following the general approach, 2-(adamantyl)ethanal[53] gave the ada-

mantyl–acridine derivatives **22** and **23**, and the benzaldehyde afforded *N*-benzyl acridine **24**. The structures of all synthesized compounds were confirmed by spectral and analytical techniques, with all details given in the Supplementary material to this paper.

Inhibition of BoNT/A LC

The inhibitory efficacies of synthesized derivatives **16**–**21** and **24** at 20 μM concentration were obtained using a well-established HPLC-based assay for BoNT/A LC inhibition.[55] These data are presented in Table I. The activities of corresponding aminoquinoline derivatives **7**–**9** were established previously,[30] and are provided for comparison. In this study, the inhibitory effects of CQ were also examined. It exhibited only marginal inhibition and thus clearly emphasized the necessity of the cholic acid component for superior inhibitory activity.

TABLE I. *In vitro* inhibitory activities (%, at 20 μM concentration) of the tested compounds against BoNT/A LC and BoNT/B LC; N.T. – not tested

Compound	BoNT/A-LC	BoNT/B-LC
NSC 240898	81.43	77.38
16	58.34	57.03
17	58.25	52.04
18	77.04	47.40
19	59.38	48.10
20	15.07	31.94
21	61.25	33.63
24	5.82	N.T.
12	42	N.T.
13	20	N.T.
14	8	N.T.
15	10	N.T.
7[a]	74	N.T.
8[a]	47.22	N.T.
9[a]	56.26	N.T.
CQ[b]	6.51	N.T.
MQ[c]	28.06	N.T.

[a]Results published earlier;[31] [b]tested as diphosphate salt; [c]tested as HCl salt

The results given in Table I indicate that 9-aminoacridine derivatives coupled to cholic acid derivative as the carrier exhibited moderate to good activities against the BoNT/A LC, with potencies ranging from 58 to 77 % inhibition. The exception is derivative **20,** which provided only 15 % inhibition. The most active derivative was compound **18,** which contains the acridine moiety in the *β*-orientation. However, the results obtained for derivatives **18** and **19** are not so easily interpretable, since both samples were mixtures of diastereomers: **18** contained ≈20 % of the *α*-isomer, and **19** was a mixture of both isomers in 1:1.5

α:β ratio. Nevertheless, from the obtained results, it is plausible to assume that the pure β-isomer would have higher activity *versus* the pure α-isomer (since the former sample showed 20 % higher potency – **18** 77.04 % inhibition *vs*. **19** 59.38 % inhibition).

The compounds incorporating acridine **12**, *i.e.*, **16** and **17,** were equally potent, suggesting that the configuration at position C(3), in this instance, is not crucial for BoNT/A LC inhibition. Comparison of the inhibitory activities for steroidal acridines with the corresponding data for steroidal aminoquinolines **7**–**9** indicates that these compounds expressed approximately the same level of inhibitory capacity. This suggests that both acridine and quinoline moieties within the small molecule inhibitors engage in similar types of interactions with the active site of the BoNT LC metalloprotease. However, more reliable correlations will be made on pure isomers after measuring the corresponding K_i values.

The simple 9-aminoacridines **12**–**15** exhibited poor inhibitory activity (8–20 % inhibition) with **12** being an exception (42 % inhibition). In addition, the results showed that elongation of the aminoalkyl chain leads to decreased activity for this class of inhibitor. The low activities of 9-aminoacridines **12**–**15** clearly indicate that for good inhibitory activity, a carrier is necessary in order to enable additional interactions within the active site of a metalloprotease. The poor activity of *N*-benzyl derivative **24** further supports this observation.

Derivatives **16**–**21** were also tested for inhibition of BoNT/B LC, giving rise to some of the most potent inhibitors of this serotype reported to date (Table I). The results indicate that steroidal C(3) derivatives are slightly more active in comparison to C(24) derivatives. Moreover, the results showed no differences between the stereoisomers, *i.e.*, the H_β–C(3) isomers exhibited the same level of activity as the H_α–C(3) isomers. The most active derivative was **16,** which provides 57 % inhibition at 20 μM concentration.

As steroidal 9-aminoacridines inhibited Zn proteases BoNT/A and B LCs, the next step was to examine the activity of synthesized derivatives against a sampling of human metalloprotease – to evaluate selectivity. The four derivatives **16**–**19** were tested at 20 μM concentration against human metalloprotease thermolysin, serine protease trypsin, and cysteine protease papain. The results are given in Table II. The data indicate that the compounds are poor inhibitors of generic human proteases. The exception was derivative **18**, which meaningfully inhibited papain. Nevertheless, in general, it could be concluded that these derivatives selectivity inhibit BoNT LC metalloproteases (as opposed to human proteases). In addition, the low activities of the compounds against the Zn-dependent protease thermolysin indicates the inhibitory potencies against BoNT LCs were not the result of general preferences for interaction with the Zn ion, but that additional specific interactions with the enzymes were involved.

TABLE II. Inhibitory activities (%,at 20 μM concentration) of ACR SMNPIs against human proteases; A: trypsin; B: thermolysin; C: papain

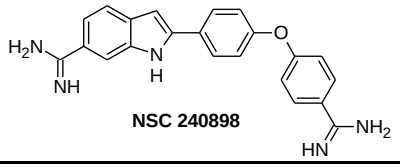

NSC 240898

Compound	A	B	C
NSC 240898	52.07	8.53	–11.78
16	12.36	13.98	5.19
17	17.24	15.42	20.76
18	22.94	22.37	78.54
19	7.48	12.68	–7.85

Antimalarial activity

It was previously shown that aminoquinoline SMNPIs exerted both BoNT inhibiting effects and were simultaneously excellent antimalarials.[30,53] Based on this observation, acridine derivatives were elected for screening against three *P. falciparum* strains: D6 (a CQ and MFQ susceptible strain), W2 (a CQ-resistant, susceptible to MFQ strain), and TM91C235 (Thailand), a multi-drug-resistant strain, using a well-established protocol.[55] The gathered *in vitro* antimalarial activities (Table III) show that all tested derivatives had significantly better activities than CQ against the CQR strain W2 (16–53 times) and the multi-drug resistant TM91C235 strain (2–24 times). Against the CQS strain D6, the steroidal derivatives were less active than CQ; however, the other derivatives were as active as CQ. The steroidal acridines **20** and **21** were less active in comparison to **7** against all the tested strains. However, at the same time, the adamantyl derivatives **22** and **23** were more active when compared to **10** against the CQR W2 and the multi-drug-resistant TM91C235 strains. Importantly, all the new derivatives were significantly more active than *N*-sulfonamides,[38] 9-amino-polyamide acridines,[39] aminoalkylamino acridines,[42] and had activities to those of quinolizidinyl and quinolizidinylalkyl derivatives, which are the second best known acridine antimalarials.[40] The most active of the derivatives was **22,** with IC_{50}(W2) = 8.6 nM, IC_{50}(D6) = 9.3 nM and IC_{50}(TM91C235) = 5.8 nM. Its *in vitro* activity is comparable to that of artemisinin (Table III). In addition, compound **22** had similar activity to those of the most potent diaminopropylidene-aminoacridine derivatives described in the literature.[41]

It should be emphasized that steroidal/adamantane carriers of the 9-aminoalkylamino acridine moiety had significantly improved antimalarial activities. Comparatively, simple acridines such as **12** and **15** showed much lower antimalarial activity against the CQR W2 strain versus new derivatives (**12** (IC_{50} = = 250 nM) and **15** (IC_{50} = 180 nM)).[42] Thus, the attachment of these simple

ACRs to either cholic acid or the adamantyl moiety significantly increased antimalarial activity against CQR strains. The same trend was observed against the CQS strain. The results reported herein indicate that steroidal and adamantyl acridines are highly effective antimalarials.

TABLE III. *In vitro* IC_{50} antimalarial activities (nM) and cytotoxicity of the compounds tested against *P. falciparum* strains; N.D. – not determined

Compd.	W2[a]	D6[b]	TM91C235[c]	*RI*[d]	HEPG2	*SI*[e]
20	23.8	41.5	51.8	1.25 / 0.57	4281	180 / 103 / 83
21	23.3	39.0	53.0	1.36 / 0.60	1030	44 / 26 / 19
22	8.6	9.3	5.8	0.62 / 0.92	>3030	>352 / >326 / >522
23	11.2	15.7	12.2	0.78 / 0.71	3261	291 / 208 / 267
24	28.0	17.9	15.6	0.56 / 1.56	1183	42 / 66 / 76
7[f]	11.4	16.9	27.7	1.64 / 0.67	N.D.	–
10[g]	15.66	8.59	17.76			
12	250[h]	N.D.	N.D.	–	N.D.	–
15	180[h]	N.D.	N.D.	–	N.D.	–
CQ	456.20	12.27	138.82	23.17 / 43.32	N.D.	–
MFQ	4.93	15.70	36.50	3.43 / 0.39	N.D.	–
ART[i]	6.70	9.00	13.40	1.36 / 0.90	N.D.	–

[a]*P. falciparum* Indochina W2 clone; [b]*P. falciparum* African D6 clone; [c]*P. falciparum* multi-drug resistant TM91C235 strain (Thailand); [d]resistance index, defined as the ratio of the IC_{50} for the resistant *versus* sensitive strain, TM91C235/D6 and W2/D6, respectively; [e]selectivity index, defined as the ratio of the IC_{50} for HepG2/W2, HepG2/D6 and HepG2/ TM91C235, respectively; [f]results published earlier;[30] [g]results published earlier;[53] [h]results taken from literature;[42] [i]average of more than eight replicates

The toxicities of the new derivatives were estimated using the human liver carcinoma cell line HEPG2, and the results are given in Table III. The HEPG2 cell line is frequently used for cytotoxicity examination of xenobiotics, since this cell line has low levels of CYP450 enzymatic activities and possible toxic effects are the result of particular molecules and not metabolites.[56] In addition, since all xenobiotics pass through the liver, it is essential to know if they provide heapto-toxic side effects. In this study, it was found that steroidal derivative **20,** containing aminoacridine part **12**, was the least cytotoxic of the series, possessing an IC_{50} = 4281 nM. However, the adamantyl derivatives had a much better selectivity index (*SI*) than the other antimalarials. Thus, **22** has *SI* values 352/326/522 *vs*. 180/103/83 for **20**, and thus have a higher therapeutic potential. It was also observed that elongation of aminoalkylamino chains by only one methylene group in **21** significantly increased cytotoxicity when compared to **20**.

EXPERIMENTAL

Melting points were determined on a Boetius PMHK or a Mel-Temp apparatus and were not corrected. IR spectra were recorded on a Perkin-Elmer spectrophotometer FT-IR 1725X. NMR spectra were recorded on Varian Gemini-200, Varian XL-300, and Bruker AM-250 spectrometers in the indicated solvent using TMS as an internal standard. Chemical shifts are

recorded in parts per million (ppm), and coupling constants *J* are expressed in Hz. ESI-MS spectra were recorded on an Agilent Technologies 6210 Time-Of-Flight LC-MS instrument in positive ion mode with CH_3CN/H_2O–0.2 % HCOOH as eluent. The samples were dissolved in CH_3CN or MeOH (HPLC grade purity). The elemental analysis was performed on the Vario EL III – C, H, N, S/O elemental analyzer (Elementar Analysensysteme GmbH, Hanau, Germany). Thin-layer chromatography (TLC) was performed on pre-coated Merck silica gel 60 F_{254} and RP-18 F_{254} plates. For column chromatography, Lobar LichroPrep Si 60 (40–63 μm), RP-18 (40–63 μm) columns coupled to a Waters RI 401 detector were used, Biotage SP1 system with UV detector.

*Methyl 7α,12α-diacetoxy-3α-{*N*-{2-[(6-chloro-2-methoxyacridin-9-yl)amino]ethyl}amino}--5β--cholan-24-oate (**16**) and methyl 7α,12α-diacetoxy-3β-(*N*-{2-[(6-chloro-2-methoxyacridin-9--yl)amino] ethyl}amino)-5β-cholan-24-oate (**17**)*

To a solution of methyl 7*α*,12*α*-diacetoxy-3-oxo-5*β*-cholan-24-oate (300 mg, 0.59 mmol) in CH_3CN (6.0 mL), **12** (357.9 mg, 1.19 mmol) in MeOH (3 mL) was added, and after stirring for 30 min at r.t., $NaBH_3CN$ (48.39 mg, 0.77 mmol) was added in one portion. The resulting mixture was further stirred for 2 h at r.t., followed by the addition of glac. AcOH (4 drops) and stirring was continued until TLC indicated the consumption of all starting ketone (*ca*. 1 h). The reaction was quenched with Et_3N, the solvents were evaporated to dryness, and after chromatographic purification (dry-flash, SiO_2, gradient EA → EA/MeOH/NH_3; Lobar RP-18, eluent MeOH/H_2O = 9:1; Biotage flash SP, gradient EA/Hex = 6:4 → EA/Hex = 9:1) **16** (45.0 mg) and **17** (40 mg) were isolated (9.6 and 8.5 % yield, respectively).

*Methyl 7α,12α-diacetoxy-3β-(*N*-{3-[(6-chloro-2-methoxyacridin-9-yl)amino]propyl}amino)--5β-cholan-24-oate (**18**) and methyl 7α,12α-diacetoxy-3α-(*N*-{3-[(6-chloro-2-methoxyacridin--9-yl)amino]propyl}amino)-5β-cholan-24-oate (**19**)*

To a solution of methyl 7*α*,12*α*-diacetoxy-3-oxo-5*β*-cholan-24-oate (500 mg, 0.99 mmol) in CH_3CN (9.5 mL), **13** (124.3 mg, 0.39 mmol) in MeOH (5 mL) was added, and after stirring for 30 min at r.t., $NaBH_3CN$ (82.8 mg, 1.32 mmol) was added in one portion. The resulting mixture was stirred for 2 h at r.t. followed by the addition of glac. AcOH (4 drops) and stirring was continued until TLC indicated the consumption of all starting ketone. The reaction was quenched with Et_3N, the solvents were evaporated to dryness and after chromatographic purification (dry-flash, SiO_2, gradient EA → EA/MeOH/NH_3; Lobar RP-18, eluent MeOH/ /H_2O = 9:1; Biotage flash SP, gradient EA/Hex = 6:4 → EA/Hex = 9:1) **18** and **19** were isolated (120.0 mg, 15 % and 90 mg, 11 %, respectively). **18** contained *ca*. 20 % of 3*α*-isomer **19** and **19** was a mixture of a *ca*. 1:1.5 ratio of the *β*- and *α*-isomers.

*3α,7α,12α-Triacetoxy-24-{*N*-{2-[(6-chloro-2-methoxyacridin-9-yl)amino]ethyl}amino}-5β--cholan (**20**)*

The alcohol 3*α*,7*α*,12*α*-triacetoxy-5*β*-cholan-24-ol (540 mg, 1.04 mmol) was dissolved in DCM (50 mL), PCC (185 mg, 1.56 mmol) was added and the mixture was stirred at r.t. for 3.5 h. The reaction mixture was filtered through a short SiO_2 column (eluent CH_2Cl_2/EA = = 95/5). Obtained crude aldehyde (500 mg) was dissolved in MeOH (10.0 mL), followed by **12** (290 mg, 0.96 mmol) and mixture was stirred at r.t. After 12 h, $NaBH_4$ (73 mg, 1.92 mmol) was added in one portion and stirring was continued at r.t. for 2 h. The solvent was evaporated to dryness and after chromatographic purification (dry-flash, SiO_2, eluent EA/MeOH = 8/2), the desired product was isolated as an orange solid. Yield: 325 mg (42 %).

*3α-7α,12α-Triacetoxy-24-{*N*-{3-[(6-chloro-2-methoxyacridin-9-yl)amino]propyl}amino}-5β--cholan (**21**)*

The alcohol 3*α*,7*α*,12*α*-triacetoxy-5*β*-cholan-24-ol (540 mg, 1.04 mmol) was dissolved in DCM (50 mL), PCC (185 mg, 1.56 mmol) was added and the mixture was stirred at r.t. for 3.5 h. The reaction mixture was filtered through a short SiO_2 column (eluent CH_2Cl_2/EA = = 95/5). The obtained crude aldehyde (500 mg) was dissolved in MeOH (10.0 mL) followed by **13** (303 mg, 0.96 mmol), and the mixture was stirred at r.t. After 12 h, $NaBH_4$ (73 mg, 1.92 mmol) was added in one portion and stirring was continued at r.t. for 2 h. The solvent was evaporated to dryness and after chromatographic purification (dry-flash, SiO_2, eluent EA/ /MeOH = 8/2), product was isolated as an orange solid. Yield 230 mg (29 %).

N-*[2-(1-Adamantyl)ethyl]*-N′-*(6-chloro-2-methoxyacridin-9-yl)ethane-1,2-diamine (**22**)*

Into stirred mixture of 2-(1-adamantyl)acetaldehyde (140 mg, 0.86 mmol) and **12** (260 mg, 0.86 mmol) in abs. EtOH (10 mL), $Ti(OPr^i)_4$ (381 μL, 1.29 mmol) was added dropwise. After stirring for 1 h at r.t., $NaBH_4$ (65 mg, 1.72 mmol) was added in one portion and when all the aldehyde had been consumed, the reaction was quenched with 0.1 M NaOH (10mL). The reaction mixture was extracted with CH_2Cl_2 (3×30 mL), the combined organic layers were washed with brine and dried over anh. Na_2SO_4. The solvent was removed under reduced pressure and the crude product was purified by dry-flash chromatography (SiO_2, eluent hexane/EA = = 1/1). Yield 40 mg (10 %).

N-*[2-(1-Adamantyl)ethyl]*-N′-*(6-chloro-2-methoxyacridin-9-yl)propane-1,3-diamine (**23**)*

According to the procedure described for **22**, 2-(1-adamantyl)acetaldehyde (140 mg, 0.86 mmol) was transformed into **23** using **13** (271 mg, 0.86 mmol). The product was isolated after dry-flash chromatography (SiO_2, eluent EA/MeOH = 8/2). Brown–orange amorphous solid. Yield: 190 mg (46 %).

N-*Benzyl*-N′-*(6-chloro-2-methoxyacridin-9-yl)ethane-1,2-diamine (**24**)*

To a stirred mixture of benzaldehyde (100 μL, 0.98 mmol) and **12** (312.0 mg, 1.03 mmol) in CH_2Cl_2 (15 mL), $NaB(OAc)_3H$ (313.0 mg, 1.47 mmol) was added. After stirring for 20 h at r.t., the reaction was quenched with 1 M NaOH (10 mL). The mixture was extracted with CH_2Cl_2 (3×30 mL), the combined organic layers were washed with brine and dried over anh. Na_2SO_4. The solvent was removed under reduced pressure and the crude product was purified by dry-flash chromatography (SiO_2, eluent EA/MeOH = 95/5). Yield 230.0 mg (60 %).

N-*(6-Chloro-2-methoxyacridin-9-yl)ethane-1,2-diamine (**12**)*[57]

A solution of 6,9-dichloro-2-methoxyacridine **11** (600 mg, 2.15 mmol) in 1,2-diaminoethane (10 mL, 140 mmol) was stirred at 70 °C under an Ar atmosphere. After 1 h, the mixture was poured into ice cold water, the powder was filtered and dried under reduce pressure. The product was obtained as a yellow powder and used in the next reaction step without further purification. Yield 580 mg (89 %).

N-*(6-Chloro-2-methoxy-acridin-9-yl)propane-1,3-diamine (**13**)*[57]

According to procedure described for **12,** 6,9-dichloro-2-methoxyacridine (1 g, 3.59 mmol) was transformed into **13** using 1,3-diaminopropane (20 mL, 232 mmol). The product was obtained as a yellow powder and used in the next reaction step without further purification. Yield 1.08 mg (95 %).

N-*(6-Chloro-2-methoxyacridin-9-yl)pentane-1,5-diamine (**14**)*[49]

According to procedure described for **12** 6,9-dichloro-2-methoxyacridine (500 mg, 1.79 mmol) was transformed into **14** using 1,5-diaminopentane (13 mL, 11.3 g) at 80 °C. The product was obtained as yellow powder and used in next reaction step without further purification.

N-*(6-Chloro-2-methoxyacridin-9-yl)hexane-1,6-diamine (**15**)*[39]

According to procedure described for **12** 6,9-dichloro-2-methoxyacridine (1g, 3.59 mmol) was transformed in **15** using 1,6-diaminohexane (23 g, 197.9 mmol) at 90 °C. Product was obtained as yellow powder and used in next reaction step without further purification.

In vitro *BoNT LC metalloprotease activity*

Determination of BoNT/A LC percent inhibition by SMNPIs was performed as previously described.[55]

For BoNT/B LC percent inhibition, the HTS-assay utilizes a commercially available fluorogenic substrate from List Biological Laboratories (Campbell, CA). Briefly, a multi-channel pipette was used to add fluorescent substrate (final concentration 20 μM) and small molecules (final concentration 20 μM) to a 96 well microplate. The reactions were initiated by adding recombinant BoNT/B LC (final concentration 40 nM) to each well. All reactions were conducted in a buffered solution consisting of 40 mM Hepes pH 7.2, 1 mM DTT and 100 μM $ZnCl_2$. The change in fluorescence intensity over time was continuously monitored in each well using a 96 well plate fluorimeter (Saphire 2, Tecan, Männedorf, Switzerland). The assays were run at 37 °C, quenched by the addition of TFA, and analyzed using reverse-phase HPLC. Potential SMNPIs of the BoNT B LC were identified by comparing the reaction velocities (change in fluorescence intensity over time) of samples assayed in the presence of compounds *versus* control samples.

In vitro *antimalarial activity and toxicity*

The *in vitro* antimalarial drug susceptibility and toxicity screening were realized at the Walter Reed Army Institute of Research.[23]

CONCLUSIONS

Aminoacridine derivatives possessing adamantane and steroid carriers were prepared and tested for BoNT/A LC, BoNT/B LC, and antimalarial activity. Acridines with the cholic acid-derived carrier showed good potency against both the BoNT/A LC and BoNT/B LC. The inhibition of the BoNT/B LC by *ca*. 50 % is the highest inhibitory activity of any acridine reported to date. The antimalarial potency of adamantane acridines (IC_{50} in range 6–9 nM), combined with their low potencies (IC_{50} *ca*. 3000 nM) is a good starting point for further research in this area.

SUPPLEMENTARY MATERIAL

Spectral and analytical data of all the synthesized compounds are available electronically at http://www.shd.org.rs/JSCS/, or from the corresponding author on request.

Acknowledgements. This research was supported by National Institute of Allergy and Infectious Diseases (USA) grant 5-U01AI082051-02, by the Ministry of Education, Science and Technological Development of the Republic of Serbia (Grant No. 172008) and the

Serbian Academy of Sciences and Arts. Furthermore, for J.C.B., in compliance with SAIC--Frederick, Inc. contractual requirements: this project was funded in whole or in part with federal funds from the National Cancer Institute, National Institutes of Health (USA), under Contract No. HHSN261200800001E. The content of this publication does not necessarily reflect the views or policies of the Department of Health and Human Services (USA), or the US Army, nor does the mention of trade names, commercial products, or organizations imply endorsement by the US Government, or the US Army. B.Š. is grateful to WRAIR for providing the *in vitro* antimalarial results.

ИЗВОД

НОВИ ДЕРИВАТИ 9-АМИНОАКРИДИНА КАО ИНХИБИТОРИ БОТУЛИНУМ НЕУРОТОКСИНА И *P. falciparum* ПАРАЗИТА МАЛАРИЈЕ

МИКЛОШ ТОТ[1], ДЕЈАН М. ОПСЕНИЦА[2], МИЛЕНА МИТРИЋ[1], JAMES C. BURNETT[3], LAURA GOMBA[4], SINA BAVARI[5] и БОГДАН А. ШОЛАЈА[1]

[1]Хемијски факултет, Универзитет у Београду, Студентски трг 16, п. пр. 51, 11158 Београд, [2]Институт за хемију, технологију и металургију, Његошева 12, 11000 Београд, [3]SAIC-Frederick, Inc., Frederick National Laboratory for Cancer Research, P. O. Box B, Frederick, MD 21702, USA, [4]United States Army Medical Research Institute of Infectious Diseases, Department of Bacteriology, 1425 Porter Street, Frederick, MD 21702, USA и [5]United States Army Medical Research Institute of Infectious Diseases, Fort Detrick, 1425 Porter Street, Frederick, MD 21702, USA

Синтетисани су деривати стероидних и адамантил-акридина и испитана је њихова инхибиторна активност према ботулинум неуротоксинима (BoNT) и паразиту маларије. Стероидни акридини показују добру инхибицију према кратком низу (LCs) BoNT/A и BoNT/B. Остварена инхибиција BoNT/B LC од око 50 % је највша постигнута вредност акридинских деривата према овом серотипу. Адамантил–акридински деривати су показали највећу антималаријску активност (IC_{50} у опсегу 6–9 nM, $SI > 326$), показујући да је адамантил-група бољи носач фармакофоре у поређењу са стероидним, према овој индикацији.

(Примљено 24. септембра, ревидирано 20. октобра 2013)

REFERENCES

1. J. C. Burnett, E. A. Henchal, A. L. Schmaljohn, S. Bavari, *Nat. Rev. Drug Discovery* **4** (2005) 281
2. B. Willis, L. M. Eubanks, T. J. Dickerson, K. D. Janda, *Angew. Chem. Int. Ed. Engl*. **47** (2008) 8360
3. B. M. Paddle, *J. Appl. Toxicol*. **23** (2003) 139
4. L. M. Wein, Y. Liu, *Proc. Natl. Acad. Sci. U.S.A*. **102** (2005) 9984
5. a) M.-C. Shin, M. Wakita, D.-J. Xie, T. Yamaga, S. Iwata, Y. Torii, T. Harakawa, A. Ginnaga, S. Kozaki, N. Akaike, *J. Pharmacol. Sci.* **118** (2012) 33; b) M. Ho, C.-H. Goh, M. C. Brothers, S. Wang, R. L. Young, Y. Ou, J. N.-M. Lui, M. Kalafatis, X. Lan, A. E. Wolf, C. M. Rienstra, B. A. Wilson, *Protein Sci.* **21** (2012) 318; c) J. Wang, T. H. Zurawski, M. O. Bodeker, J. Meng, S. Boddul, K. R. Aoki, J. O. Dolly, *Biochem. J.* **444** (2012) 59; d) J. O. Dolly, M. A. O'Connell, *Curr. Opin. Pharm.***12** (2012) 100
6. B. R. Singh, *Nat. Struct. Biol.* **7** (2000) 617
7. K. Turton, J. A. Chaddock, K. R. Acharya, *Trends Biochem. Sci*. **27** (2002) 552
8. D. B. Lacy, W. Tepp, A. C. Cohen, B. R. DasGupta, R. C. Stevens, *Nat. Struct. Biol.* **5** (1998) 898

9. S. Swaminathan, S. Eswaramoorthy, *Nat. Struct. Biol.* **7** (2000) 693
10. T. Binz, J. Blasi, S. Yamasaki, A. Baumeister, E. Link, T. C. Sudhof, R. Jahn, H. Niemann, *J. Biol. Chem.* **269** (1994) 1617
11. J. J. Schmidt, R. G. Stafford, *Biochemistry* **44** (2005) 4067
12. a) G. Schiavo, F. Benfenati, B. Poulain, O. Rossetto, P. Polverino de Laureto, B. R. DasGupta, C. Montecucco, *Nature* **359** (1992) 832; b) G. Schiavo, C. Malizio, W. S. Trimble, P. Polverino de Laureto, G. Milan, H. Sugiyama, E. A. Johnson, C. Montecucco, *J. Biol. Chem.* **269** (1994) 20213; c) G. Schiavo, O. Rossetto, S. Catsicas, P. Polverino de Laureto, B. R. DasGupta, F. Benfenati, C. Montecucco, *J. Biol. Chem.* **268** (1993) 23784; d) G. Schiavo, C. C. Shone, O. Rossetto, F. C. Alexander, C. Montecucco, *J. Biol. Chem.* **268** (1993) 11516
13. J. Blasi, E. R. Chapman, S. Yamasaki, T. Binz, H. Niemann, R. Jahn, *EMBO J.* **12** (1993) 4821
14. S. S. Arnon, R. Schechter, T. V. Inglesby, D. A. Henderson, J. G. Bartlett, M. S. Ascher, E. Eitzen, A. D. Fine, J. Hauer, M. Layton, S. Lillibridge, M. T. Osterholm, T. O'Toole, G. Parker, T. M. Perl, P. K. Russell, D. L. Swerdlow, K. Tonat, *JAMA* **285** (2001) 1059
15. a) P. G. Foran, B. Davletov, F. A. Meunier, *Trends Mol. Med*. **9** (2003) 291; b) P. G. Foran, N. Mohammed, G. O. Lisk, S. Nagwaney, G. W. Lawrence, E. Johnson, L. Smith, K. R. Aoki, J. O. Dolly, *J. Biol. Chem.* **278** (2003) 1363
16. J. C. Larsen, *Drug Develop. Res.* **70** (2009) 266
17. J. C. Burnett, G. Ruthel, C. M. Stegmann, R. G. Panchal, T. L. Nguyen, A. R. Hermone, R. G. Stafford, D. J. Lane, T. A. Kenny, C. F. McGrath, P. Wipf, A. M. Stahl, J. J. Schmidt, R. Gussio, A. T. Brunger, S. Bavari, *J. Biol. Chem.* **282** (2007) 5004
18. T. Eichhorn, B. Z. Dolimbek, K. Deeg, T. Efferth, M. Z. Atassi, *Toxicon* **60** (2012) 1180
19. a) S. Potavathri, A. Kantak, B. DeBoef, *Chem. Commun.* **47** (2011) 4679; b) G. E. Boldt, J. P. Kennedy, K. D. Janda, *Org. Lett.* **8** (2006) 1729
20. P. Šilhár, K. Čapková, N. T. Salzameda, J. T. Barbieri, M. S. Hixon, K. D. Janda, *J. Am. Chem. Soc.* **132** (2010) 2868
21. P. Čapek, Y. Zhang, D. J. Barlow, K. L. Houseknecht, G. R. Smith, T. J. Dickerson, *ACS Chem. Neurosci.* **2** (2011) 288
22. I. Opsenica, V. Filipović, J. E. Nuss, L. M. Gomba, D. Opsenica, J. C. Burnett, R. Gussio, B. A. Šolaja, S. Bavari, *Eur. J. Med. Chem.* **53** (2012) 374
23. I. Opsenica, J. C. Burnett, R. Gussio, D. Opsenica, N. Todorović, C. A. Lanteri, R. J. Sciotti, M. Gettayacamin, N. Basilico, D. Taramelli, J. E. Nuss, L. Wanner, R. G. Panchal, B. A. Šolaja, S. Bavari, *J. Med. Chem.* **54** (2011) 1157
24. M. Adler, J. D. Nicholson, B. E. Hackley Jr., *FEBS Lett.* **429** (1998) 234
25. M. Adler, J. D. Nicholson, D. F. Starks, C. T. Kane, F. Cornille, B. E. Hackley, Jr., *J. Appl. Toxicol.* **19** (1999) S5
26. M. A. Hanson, T. K. Oost, C. Sukonpan, D. H. Rich, R. C. Stevens, *J. Am. Chem. Soc.* **122** (2000) 11268
27. N. T. Salzameda, L. M. Eubanks, J. S. Zakhari, K. Tsuchikama, N. J. DeNunzio, K. N. Allen, M. S. Hixond, K. D. Janda, *Chem. Commun.* **47** (2011) 1713
28. X. Shi, G. E. Garcia, R. J. Neill, R. K. Gordon, *J. Cell. Biochem.* **107** (2009)1021
29. a) J. E. Nuss, Y. Dong, L. M. Wanner, G. Ruthel, P. Wipf, R. Gussio, J. L. Vennerstrom, S. Bavari, J. C. Burnett, *ACS Med. Chem. Lett.* **1** (2010) 301; b) J. C. Burnett, C. Wang, J. E. Nuss, T. L. Nguyen, A. R. Hermone, J. J. Schmidt, R. Gussio, P. Wipf, S. Bavari, *Bioorg. Med. Chem. Lett.* **19** (2009) 5811; c) J. C. Burnett, J. J. Schmidt, R. G. Stafford, R. G. Panchal, T. L. Nguyen, A. R. Hermone, J. L. Vennerstrom, C. F. McGrath, D. J.

Lane, E. A. Sausville, D. W. Zaharevitz, R. Gussio, S. Bavari, *Biochem. Biophys. Res. Commun.* **310** (2003) 84
30. J. C. Burnett, D. Opsenica, K. Sriraghavan, R. G. Panchal, G. Ruthel, A. R. Hermone, T. L. Nguyen, T. A. Kenny, D. J. Lane, C. F. McGrath, J. J. Schmidt, J. L. Vennerstrom, R. Gussio, B. A. Šolaja, S. Bavari, *J. Med. Chem.* **50** (2007) 2127
31. S. S. Deshpande, R. E. Sheridan, M. Adler, *Toxicon* **35** (1997) 433
32. http://www.malaria.org/, last accessed in September, 2013
33. a) D. M. Opsenica, B. A. Šolaja, *J. Serb. Chem. Soc.* **74** (2009) 1155, and references cited therein; b) I. Opsenica, N. Terzić, D. Opsenica, G. Angelovski, M. Lehnig, P. Eilbracht, B. Tinant, Z. Juranić, K. S. Smith, Z. S. Yang, D. S. Diaz, P. L. Smith, W. K. Milhous, D. Đoković, B. A. Šolaja, *J. Med. Chem.* **49** (2006) 3790
34. P. M. O'Neill, V. E. Barton, S. A. Ward, J. Chadwick, in *Treatment and Prevention of Malaria: Antimalarial Drug Chemistry, Action and Use*, H. M. Staines, S. Krishna, Eds., Series: *Milestones in Drug Therapy*, M. J. Parnham, J. Bruinvels, Series Eds., Springer, Basel, 2012, p. 19
35. a) D. M. Opsenica, B. A. Šolaja, in *Treatment and Prevention of Malaria: Antimalarial Drug Chemistry, Action and Use*, H. M. Staines, S. Krishna, Eds., Series: *Milestones in Drug Therapy*, M. J. Parnham, J. Bruinvels, Series Eds., Springer, Basel, 2012. p. 191; b) R. D. Slack, A. M. Jacobine, G. H. Posner, *Med. Chem. Commun.* **3** (2012) 281; c) N. Kumar, R. Singh, D. S. Rawat, *Med. Res. Rev.* **32** (2012) 581
36. a) K. Kaur, M. Jain, R. P. Reddy, R. Jain, *Eur. J. Med. Chem.* **45** (2010) 3245; b) E. Milner, W. McCalmont, J. Bhonsle, D. Caridha, J. Cobar, S. Gardner, L. Gerena, D. Goodine, C. Lanteri, V. Melendez, N. Roncal, J. Sousa, P. Wipf, G. S. Dow, *Malar. J.* **9** (2010) 51 doi:10.1186/1475-2875-9-51 c) C. A. Lanteri, J. D. Johnson, N. C. Waters, *Recent Pat. Antiinfect. Drug Discov*. **2** (2007) 95
37. E. I. Elueze, S. L. Croft, D. C. Warhurst, *J. Antimicrob. Chemother.* **37** (1996) 511
38. K. Chibale, H. Haupt, H. Kendrick, V. Yardley, A. Saravanamuthu, A. H. Fairlamb, S. L. Croft, *Bioorg. Med. Chem. Lett.* **11** (2001) 2655
39. L. Guetzoyan, F. Ramiandrasoa, H. Dorizon, C. Desprez, A. Bridoux, C. Rogier, B. Pradines, M. Perrée-Fauveta, *Bioorg. Med. Chem*. **15** (2007) 3278
40. A. Sparatore, N. Basilico, S. Parapini, S. Romeo, F. Novelli, F. Sparatorec, D. Taramelli, *Bioorg. Med. Chem*. **13** (2005) 5338
41. M. O. Anderson, J. Sherrill, P. B. Madrid, A. P. Liou, J. L. Weisman, J. L. DeRisi, R. K. Guy, *Bioorg. Med. Chem.* **14** (2006) 334
42. L. Guetzoyan, X.-M. Yu, F. Ramiandrasoa, S. Pethe, C. Rogier, B. Pradines, T. Cresteil, M. Perrée-Fauvet, J.-P. Mahy, *Bioorg. Med. Chem.* **17** (2009) 8032
43. a) X.-M. Yu, F. Ramiandrasoa, L. Guetzoyan, B. Pradines, E. Quintino, D. Gadelle, P. Forterre, T. Cresteil, J.-P. Mahy, S. Pethe, *ChemMedChem* **7** (2012) 587; b) S. A. Gamage, N. Tepsiri, P. Wilairat, S. J. Wojcik, D. P. Figgitt, R. K. Ralph, W. A. Denny, *J. Med. Chem.* **37** (1994) 1486
44. C. Santelli-Rouvier, B. Pradines, M. Berthelot, D. Parzy, J. Barbe, *Eur. J. Med. Chem.* **39** (2004) 735
45. M. K. Azim, W. Ahmed, I. A. Khan, N. A. Rao, K. M. Khan, *Bioorg. Med. Chem. Lett.* **18** (2008) 3011
46. M. Jones, A. E. Mercer, P. A. Stocks, L. J. I. La Pensée, R. Cosstick, B. K. Park, M. Rawe, J. Baird, T. Charidza, O. Janneh, P. M. O'Neill, *Bioorg. Med. Chem. Lett.* **19** (2009) 2033

47. A. Kumar, K. Srivastava, S. R. Kumar, S. K. Puri, P. M. S. Chauhan, *Bioorg. Med. Chem. Lett.* **20** (2010) 7059
48. C. R. Caffrey, D. Steverding, R. K. Swenerton, B. Kelly, D. Walshe, A. Debnath, Y.-M. Zhou, P. S. Doyle, A. T. Fafarman, J. A. Zorn, K. M. Land, J. Beauchene, K. Schreiber, H. Moll, A. Ponte-Sucre, T. Schirmeister, A. Saravanamuthu, A. H. Fairlamb, F. E. Cohen, J. H. McKerrow, J. L. Weisman, B. C. H. May, *Antimicrob. Agents Chemother.* **51** (2007) 2164
49. C. Boulanger, C. Di Giorgio, P.Vierling, *Eur. J. Med. Chem.* **40** (2005) 1295
50. Y. Ishikawa, A. Yamashita, T. Uno, *Chem. Pharm. Bull.* **49** (2001) 287
51. C. Di Giorgio, F. Delmas, N. Filloux, M. Robin, L. Seferian, N. Azas, M. Gasquet, M. Costa, P. Timon-David, J.-P. Galy, *Antimicrob. Agents Chemother.* **47** (2003) 174
52. S. Bongarzone, H. N. A. Tran, A. Cavalli, M. Roberti, P. Carloni, G. Legname, M. L. Bolognesi, *J. Med. Chem.* **53** (2010) 8197
53. B. A. Šolaja, D. Opsenica, K. S. Smith, W. K. Milhous, N. Terzić, I. Opsenica, J.C. Burnett, J. Nuss, R. Gussio, S. Bavari, *J. Med. Chem.* **51** (2008) 4388
54. D. Opsenica, G. Pocsfalvi, Z. Juranić, B. Tinant, J.-P. Declercq, D. E. Kyle, W. K. Milhous, B. A. Šolaja, *J. Med. Chem.* **43** (2000) 3274
55. I. M. Opsenica, M. Tot, L. Gomba, J. E. Nuss, R. J. Sciotti, S. Bavari, J. C. Burnett, B. A. Šolaja, *J. Med. Chem*. **56** (2013) 5860, and references cited therein
56. J. J. Xu, K. Hoffmaster, *Hepatic toxicity in ADMET, for Medicinal Chemists A Practical guide*, Wiley, New York, 2011, p. 353
57. S. Bongarzone, H. N. A. Tran, A. Cavalli, M. Roberti, P. Carloni, G. Legname, M. L. Bolognesi, *J. Med. Chem.* **53** (2010) 8197.

Journal of the Serbian Chemical Society
JSCS-info@shd.org.rs • www.shd.org.rs/JSCS

J. Serb. Chem. Soc. 78 (12) 1865–1874 (2013)
JSCS–4537

UDC 576.315:577.23:57.089:
547.857+537.872
Original scientific paper

Purinergic responses of chondrogenic stem cells to dynamic loading•

IVANA GADJANSKI[1,2] and GORDANA VUNJAK-NOVAKOVIC[1]*

[1]*Department of Biomedical Engineering, Columbia University, New York, NY, USA and*
[2]*R&D Center for Bioengineering, Metropolitan University, Belgrade, Serbia*

(Received 18 November, revised 21 November 2013)

Abstract: In habitually loaded tissues, dynamic loading can trigger ATP (adenosine-5′-triphosphate) release to the extracellular environment, and result in calcium signaling *via* ATP binding to purine P2 receptors.[1] In the current study, the purinergic responses (ATP release) of two types of cells: bovine chondrocytes (bCHs) and human mesenchymal stem cells (hMSCs) that were encapsulated in agarose and subjected to dynamic loading were compared. Both cell types were cultured under chondrogenic conditions, and their responses to loading were evaluated by an ATP release assay in combination with a connexin (Cx)-sensitive fluorescent dye (lucifer yellow – LY) and a Cx-hemichannel blocker (flufenamic acid – FFA). In response to dynamic loading, the chondrogenic hMSCs released significantly higher amounts of ATP (5-fold) in comparison to the bCHs early in culture (day 2). The triggering of LY uptake in the bCHs and hMSCs by dynamic loading implies opening of the Cx-hemichannels. However, the number of LY-positive cells in the hMSC-constructs was 2.5-fold lower compared to the loaded bCH-constructs, suggesting utilization of additional mechanisms of ATP release. Cx-reactive sites were detected in both the bCHs and hMSCs-constructs. FFA application led to reduced ATP release in both the bCHs and hMSCs, which confirmed the involvement of connexin hemichannels, with more prominent effects in the bCHs than in the hMSCs, further implying the existence of additional mechanisms of ATP release in chondrogenic hMSCs. Taken together, these results indicate a stronger purinergic response to dynamic loading of the chondrogenic hMSCs than that of primary chondrocytes, by activation of connexin hemichannels and additional mechanisms of ATP release.

Keywords: cartilage; loading; calcium signaling *via* ATP; ATP binding; Cx-hemichannels.

* Corresponding author. E-mail: gv2131@columbia.edu
• To Professor Branislav Nikolić, a great scientist, mentor and teacher, on the occasion of his 70th birthday.
doi: 10.2298/JSC131118141G

INTRODUCTION

Tissue engineering is a new discipline that has enormous potential to provide biological substitutes for damaged or dysfunctional human tissues. Tissues can be grown in the laboratory or regenerated in the body using a number of different strategies. In all cases, the presence of biosynthetically active cells is a fundamental requirement, as there is no way to grow a tissue except from cells, by mechanisms similar to those underlying normal development. In addition, biomaterial scaffolds are employed to provide cells with a structural and logistic template for tissue formation, and bioreactors are used to "instruct" the cells to form a specific tissue structure by providing molecular and physical regulatory factors. The designs of tissue engineering systems require guidance by biological requirements, which are in turn tissue-specific and "biomimetic" that is derived from the developmental principles.

One tissue of particularly high interest is articular cartilage, the lining of the surfaces of bones in human joints, due to the complete inability of this load-bearing tissue to regenerate itself following injury or disease. In the aging human population, the maintenance of healthy cartilage is an already significant and a constantly growing health concern. A number of new strategies for cartilage treatment and cartilage tissue engineering are being devised using different cell sources. Human mesenchymal stem cells (hMSCs) emerged as a clinically relevant cell source for regenerative medicine due to their multi-lineage differentiation potential and relative ease of isolation and expansion in culture.[2] Based on their ability to undergo chondrogenesis in a variety of natural and synthetic scaffold materials in the presence of the appropriate growth factors and mechanical loading, hMSCs are especially suitable for cartilage repair.[3] In addition, hMSCs are less likely to dedifferentiate when expanded *in vitro* in comparison to native chondrocytes.[4]

However, native chondrocytes (CHs) produce an extracellular matrix (ECM) with superior mechanical properties as compared to MSCs.[5] Achieving the physiological composition and functionality of hMSC-engineered cartilage remains a challenge. The focus of many current studies is set on the utilization of signaling molecules, scaffolds and mechanical stimulation towards achieving this goal.[6] In the context of mechanical stimulation and signaling molecules, it is crucial to identify and characterize the mechanotransduction pathways through which cells sense and respond to their mechanical environment. Potential mechanotransduction events include mechanical deformation of the nucleus,[7] changes in the membrane potential,[8] alterations in membrane transport and activation of ion channels.[9]

Several studies have shown that dynamic compression of native articular CHs activates intracellular calcium signaling.[10] This response is blocked by the addition of apyrase, which degrades extracellular adenosine-5′-triphosphate (ATP), or

by treatment with nonspecific blockers of purine P2 receptors.[11] Other studies report that in chondrocytes, ATP can induce calcium signaling,[12] which is released in response to compressive stress.[13] These results suggest that dynamic loading can trigger ATP release to the extracellular environment and induce calcium signaling in CHs *via* ATP binding to purine P2 receptors.[1]

At this time, the mechanisms of ATP release in CHs have not been defined. In other cell types, main physiological ATP release mechanisms have been elucidated: connexin and pannexin hemichannels, anion channels, and exocytosis of ATP-filled vesicles.[14] Recent studies report that native CHs release ATP *via* hemichannels composed of connexin 43 (Cx)[15,16] and/or pannexin 3.[17] However, the mechanisms of ATP release in chondrogenic hMSCs in response to dynamic loading remain largely unknown, despite being of great interest for the progression of cartilage formation in these cells. The purinergic responses to dynamic mechanical loading during chondrogenic differentiation of human mesenchymal stem cells were investigated in the present study, in order to better understand and potentially utilize this mechanism to enhance cartilage formation.

EXPERIMENTAL

Cell isolation and expansion

Two types of chondrogenic cells were studied: primary chondrocytes, and mesenchymal stem cells. For the primary chondrocytes, articular cartilage was harvested from fresh bovine carpometacarpal joints obtained from 4–6-month old calves. The cartilage was rinsed in phosphate buffered saline (PBS) and digested in Dulbecco Modified Eagle Medium (DMEM, Gibco, New York) with 0.5 mg mL^{-1} collagenase type IV (Sigma Chemicals, St. Louis, MO) for 10 h at 37 °C under stirring. The resulting cell suspension was filtered through a 70-μm pore size mesh to isolate the individual cells.[18] After rinsing the pellets, the chondrocytes were plated at high density (>1×10^5 cells cm^{-2}) in chondrocyte culture medium (high glucose DMEM – hgDMEM – supplemented with 10 % FBS, 100 U mL^{-1} penicillin, 100 μg mL^{-1} streptomycin). For the mesenchymal stem cells, commercially obtained human bone marrow aspirates were used to derive human mesenchymal stem cells (hMSCs). The cells were cultured to passage 3 in an expansion medium (hgDMEM supplemented with 10 % fetal bovine serum, 100 U ml^{-1} penicillin, 100 μg mL^{-1} streptomycin and 1 ng mL^{-1} basic fibroblast growth factor) and used in the experiments.

Cell seeding in hydrogel

To produce cell-ladened agarose gels, type VII agarose (AG) (Sigma Chemicals, St. Louis, MO) was dissolved in phosphate-buffered saline (PBS) at a concentration of 4 %, w/v, autoclaved and cooled to 40 °C. The AG was combined with the cell suspension (40×10^6 cells mL^{-1}) in a 1:1 ratio to result in a seeding density of 20×10^6 cells ml^{-1}. The suspension was cast between two glass plates separated by 2.5 mm spacers. After cooling, cylindrical disks (4 mm in diameter×2.5 mm thick) were cored out using a biopsy punch as in previous studies,[18,19] resulting in 6.2×10^5 cells per scaffold.

Mechanical loading

The cell–agarose constructs were pre-cultured under static conditions for 48 h and then subjected to controlled dynamic deformational loading within a well-characterized loading

system used in previous studies.[20-22] The constructs are placed at the bottom of a 35×10 mm Petri dish and 3mL of sterile PBS was added into the Petri dish. A loading platen was positioned on top of the constructs inducing a tare strain of less than 0.5 %. Cyclic compression was applied for 40 min at a frequency of 1 Hz and a nominal 10 % strain. Sinusoidal deformation was applied *via* revolution of an eccentric cam calibrated to produce a defined displacement of a spring-loaded linear stage follower connected to the loading platen.[22] Unloaded constructs served as controls (Fig. 1).

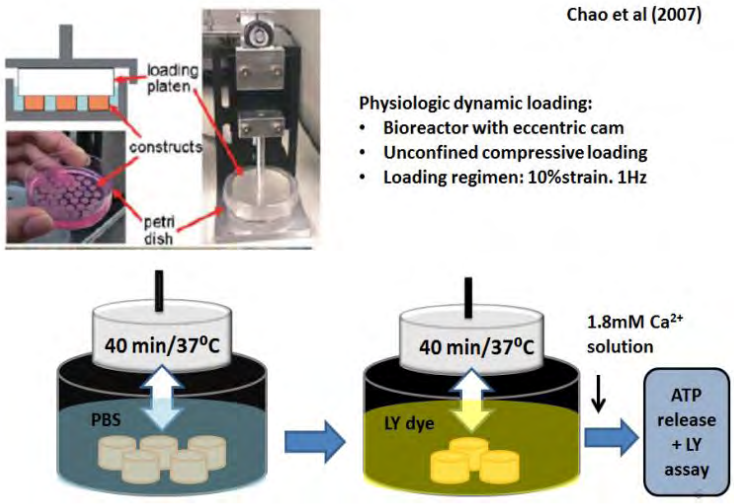

Fig. 1. Experimental setup. Cartilage constructs were prepared in the form of 4 mm in diameter×2.5 mm thick discs, as in previous studies[20] by encapsulation of primary chondrocytes and hMSCs in agarose. After 2 days of preculture, the constructs were subjected to 40 min of dynamic mechanical loading (with unloaded constructs serving as controls), and evaluated for ATP release and activation of connexin hemichannels.

ATP release

The effect of mechanical loading on the chondrogenic cells was first evaluated by measuring the release of ATP into the extracellular surrounding. The cell–agarose constructs were subjected to a 40-min period of mechanical loading or an equivalent unloaded period, after which the PBS bathing solution was removed and boiled for 1 min to deactivate any ATPases.[15] The solutions were kept individually frozen at –20 °C prior to determination of the ATP concentration, using a commercially available luciferin–luciferase assay kit (Sigma–Aldrich, St. Louis, MO) in conjunction with a standard luminescence plate reader.[1,15] For calibration purposes, ATP standards were freshly prepared using an ATP stock solution (Sigma–Aldrich, St. Louis, MO) in PBS. Additional cell–agarose constructs were treated prior to and during mechanical loading with flufenamic acid (500 μM FFA) – a widely used hemichannel blocker.[23] The ATP assay readout was in RLU (relative light units) proportional to the amount of ATP in the solution. The RLU values were used to calculate the ATP (as the RLU/DNA ratio).

Activation of hemichannels

To examine the influence of mechanical loading on the activation of connexin hemichannels, cell–agarose constructs were mechanically loaded as described above, in the presence of the hemichannel indicator lucifer yellow (LY). For the LY incorporation assay, a solution of 0.4 % LY, w/v (CH dilithium salt, Sigma–Aldrich, Poole, UK), was prepared in phosphate-buffered saline (PBS) with 5 mM ethidium homodimer-1 (Sigma–Aldrich, St. Louis, MO) to label the nuclei of dead cells. Control constructs remained unstrained in the presence of an identical LY solution. Separate groups of constructs were additionally treated with FFA, both prior to and during a 40-min period of mechanical loading. Unloaded control constructs were treated in the same manner.

The concentrations and incubation periods for each reagent were based on those used in previous studies.[15] Immediately after loading, the constructs were washed in normal DMEM supplemented with 20 % fetal calf serum (FCS, Gibco, New York) containing 1.8 mM Ca^{2+} to close any activated hemichannels, and then fixed in 3.7 % formaldehyde (37 °C, 15 min). The cell–agarose constructs were cut into 1-mm thick slices, perpendicular to the cylindrical axis, and the central section of each construct was mounted on a cover-slip. The samples were imaged using a color CCD camera mounted onto an inverted microscope (Olympus IX-81) and analyzed using MetaMorph (Molecular Devices, Sunnyvale, CA). Fluorescein isothiocyanate (FITC) and tetramethylrhodamine isothiocyanate (TRITC) filter blocks were used to visualize the lucifer yellow and ethidium homodimer-1, respectively. The number of LY-positive viable cells was determined in 10 adjacent fields of view that covered the whole diameter of the construct cross section. Each field of view contained approximately 70 individual cells. The number of TRITC-positive cells was deduced from the total number of fluorescent cells. The procedure was repeated on 3–5 separate constructs under each condition.

Biochemical composition

The tissue constructs were blotted dry, weighed and lyophilized overnight. Dry samples were digested with proteinase K overnight at 56 °C, as described previously.[24] For quantification of the DNA content, aliquots were analyzed using the PicoGreen assay (Invitrogen, Carlsbad, CA).

Immunochemistry

For immunochemical staining, tissue sections were first deparaffinized in Citrisolv (Fisher) and rehydrated in a series of descending concentrations of aqueous solutions of ethanol. Antigen retrieval was performed by heating in 0.01 M citrate buffer, pH 6.0, for 10 min. Slides were incubated for 5 min with 0.5 % Triton-X-100 in PBS for permeabilization and for 30 min at room temperature (RT) in 5% goat serum for blocking. Next, primary antibody (rabbit anti-connexin 43 antibody, C-terminus, cytosolic – AB1728 in 1:200 dilution from Chemicon – Millipore, Billerica, MA) was added overnight at 4 °C. The secondary goat anti-rabbit-FITC antibody (65-6111, Invitrogen) was applied to sections for 1 h at RT in the dark. Sections were mounted onto slides using Vectashield (Vector, Burlingame, CA) mounting medium. Construct samples without the applied primary antibody were used as a negative control. The samples were imaged using a color CCD camera mounted onto an inverted microscope (Olympus IX-81) and analyzed using MetaMorph (Molecular Devices, Downingtown, PA).

Statistical analysis

Statistics were performed with GraphPadPrism 5.01 software (http://graphpad-prism.software.informer.com/5.0/). Each data point represents the average±*SEM* of $n = 5$ samples for the chondrocyte-groups, and n of 3–5 samples for the hMSCs-groups. Each group was examined for significant differences by the one-way ANOVA, with the ATP/DNA ratio and number of LY-positive cells as the dependent variables using the Tukey honest significant difference test.

RESULTS

ATP release in response to dynamic loading. Bovine chondrocytes (bCHs)

Unconfined compressive loading (1 Hz, 10 % strain, 40 min) induced an approximately 5-fold increase of the normalized ATP/DNA ratio in comparison to both the unloaded control group and the group treated with the hemichannel blocker – FFA prior to loading (Fig. 2).

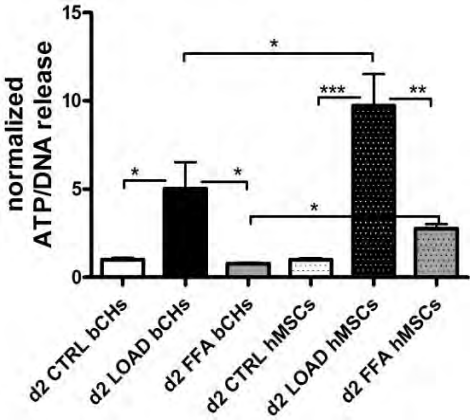

Fig. 2. ATP release in response to dynamic loading and connexin-blocking treatment. (d2: day two of culture; CTRL: unloaded; LOAD: loaded; bCHs: bovine chondrocytes; hMSCs: human mesenchymal stem cells; FFA: supplementation of flufenamic acid. Values indicate the mean ATP/DNA ratios normalized to the unloaded corresponding controls. ***$p < 0.001$, ** $p < 0.01$ and *$p < 0.05$.

Human MSCs (hMSCs). Notably, in the hMSC-ladened constructs, the ATP/DNA ratio was approximately 10-fold higher in the loaded group in comparison to unloaded control. FFA-treatment prior to loading induced a significant, 3-fold reduction of ATP release *vs*. the loaded group (Fig. 2). Moreover, the ATP/DNA ratio was 5-fold higher in the loaded group of hMSC-seeded constructs in comparison to the loaded bCHs constructs. In the FFA-treated hMSC-group, the normalized ATP/DNA ratio was also significantly higher than in the FFA-treated bCHs group (Fig. 2).

Hemichannel indicator (LY) uptake – bovine chondrocytes (bCHs). Fluorescence microscopy revealed a high number of LY-positive cells in the loaded group; about 3-fold higher than in the CTRL and FFA-treated groups (Fig. 3).

Human MSCs (hMSCs). The number of LY-positive cells was significantly higher in the loaded group than in both the CTRL and FFA groups (Fig. 3). The

loaded hMSC-constructs had about 2.5-fold lower number of LY-positive cells compared to the loaded bCH-constructs (Fig. 3).

Expression of connexin 43. Immunochemistry for connexin 43, the main hemichannel component, revealed positive reactive sites in both the bCHs- and hMSCs-constructs. The images in Fig. 4 show cross sections of paraffin-embedded bCHs- and hMSC-agarose constructs stained with primary anti-connexin 43 antibody and FITC-labeled secondary antibodies (green).

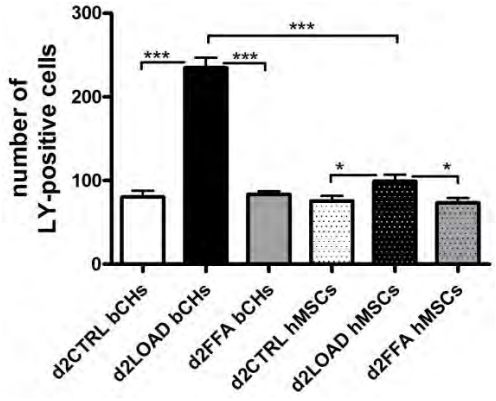

Fig. 3. Connexin indicator (LY) incurporation. Values indicate the average number of LY-positive cells in 10 fields-of-view that cover the whole diameter of the cross section. ***$p < 0.001$, **$p < 0.01$ and *$p < 0.05$. Abbreviations as in Fig. 2.

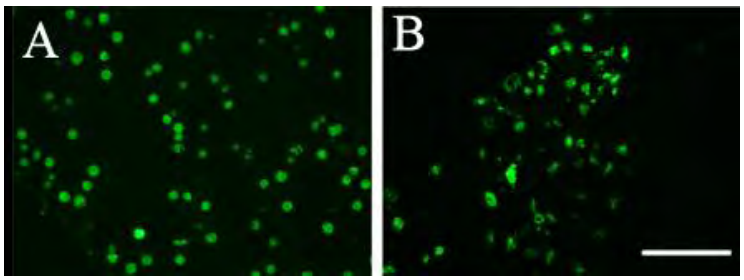

Fig. 4. Cross sections of paraffin-embedded bCHs- (A) and hMSC-agarose (B) constructs stained with primary anti-connexin 43 antibodies and FITC-labeled secondary antibodies (green).

DISCUSSION

The present study shows that chondrogenic cells, both primary chondrocytes and mesenchymal stem cells, respond to dynamic mechanical loading by purinergic signals that involve the activation of connexin hemichannels and additional mechanisms of ATP release. Under chondrogenic conditions, hMSCs released 5-fold higher amounts of ATP in response to dynamic loading than native bCHs. Dynamic loading triggered hemichannel-indicator (LY) uptake in both cell types, implying opening of the connexin hemichannels. However, the number of LY-positive cells in the hMSC-constructs was 2.5-fold lower com-

pared to the loaded bCH-constructs, suggesting that additional mechanisms of ATP release are utilized in the chondrogenic hMSCs.

Connexin-reactive sites were detected by immunochemistry in both the bCHs- and hMSCs-constructs. Hemichannel blocker (FFA) application led to reduced ATP release in both bCHs and hMSCs, which confirmed the involvement of connexin hemichannels, with more prominent effects in the bCHs than in the hMSCs, further implying additional mechanisms of ATP release in chondrogenic hMSCs.

Previous studies were mainly focused on undifferentiated bone-marrow derived hMSCs and detected expression of several subtypes of P2 receptors, which were activated by their natural ligand ATP, inducing fast changes in the intracellular ion homeostasis and modulating the molecular and functional properties of hMSCs.[25,26] Riddle *et al*. showed that exposure to fluid flow induced a flow rate--dependent release of ATP from undifferentiated hMSCs, and that ATP is unique, among nucleotides, in its ability to induce hMSC proliferation.[27] The same study reported a vesicular mechanism of ATP release. Hemichannels (connexin 43 and connexin 45) were also detected in MSCs,[28,29] which is consistent with the present results. In addition, shear stress modified the expression of connexin 43[30] in undifferentiated stromal hMSCs. However, there are no reports on the mechanisms of ATP secretion and expression of connexin 43 in chondrogenic MSCs. The study by Fodor *et al*. only reports that chondrifying micromass cultures of chicken mesenchymal cells secrete ATP as an autocrine factor,[31] but without identification of the ATP secretion mechanisms.

The present results indicate that the mechanism of purinergic response to dynamic loading of chondrogenic hMSCs is different to that reported for hMSCs subjected to fluid flow, and that this purinergic response involves activation of connexin hemichannels. Furthermore, chondrogenic hMSCs responded to dynamic loading more strongly than primary chondrocytes. The present study also implies that the hemichannel-mediated route is not the only mechanism of ATP release occurring in the chondrogenic hMSCs in response to dynamic loading. Further studies are necessary to identify other components of the purinergic signaling system in chondrogenic MSCs and to develop tissue-engineering strategies utilizing this important mechanism.

Acknowledgements. The authors gratefully acknowledge research funding by the Fulbright Foundation (Visiting Scholar grant to IG), the Ministry of Education, Science and Technological Development of the Republic of Serbia (Grant Nos. ON174028 and III41007 to IG) and NIH (Grant Nos. DE016525 and EB002520 to GVN).

ИЗВОД

ПУРИНЕРГИЧКИ ОДГОВОР ХОНДРОГЕНИХ МАТИЧНИХ ЋЕЛИЈА НА МЕХАНИЧКО ОПТЕРЕЋЕЊЕ

IVANA GADJANSKI[1,2] и GORDANA VUNJAK-NOVAKOVIC[1]

[1]*Department of Biomedical Engineering, Columbia University, New York, NY, USA и* [2]*R&D Center for Bioengineering, Metropolitan University, Belgrade, Serbia*

У многим типовима ћелија, механичко оптерећење изазива секрецију аденозин-трифосфата (ATP) у екстрацелуларну средину, што даље може активирати сигнализацију путем калцијума преко везивања ATP-а за пуринске П2 рецепторе.[1] У овом раду смо поредили пуринергички одговор, тј. ATP секрецију под утицајем динамичког оптерећења код говеђих хондроцита (bCHs) и хуманих мезенхималних матичних ћелија (hMSCs) у агарозном хидрогелу, коришћењем теста за ATP секрецију у комбинацији са флуоресцентном бојом (луцифер жуто – LY) специфичном за конексине у оквиру хемиканала, као и са блокером конексинских хемиканала, флуфенаминском киселином (енгл. *flufenamic acid* – FFA). Резултати показују да хондрогене hMSCs ослобађају ATP у одговору на динамичко оптерећење. Хондрогене hMSCs су ослободиле значајно веће количине ATP-а (5× веће) у поређењу са bCHs после истог времена у култури (2 дана). Динамичко оптерећење је довело и до преузимања LY боје и код bCHs и код hMSCs, што наводи на закључак да је дошло до отварања конексинских хемиканала. Међутим, број LY-позитивних ћелија у hMSC култури је био 2,5× нижи у поређењу са bCH-културом. Тај резултат указује на то да код хондрогених hMSCs постоји и други механизам ATP секреције поред оног који се одвија путем конексинских хемиканала. Имунохемијска анализа је показала позитивну реакцију за конексин 43 и у bCHs и у hMSCs култури. Такође, примена блокера FFA је довела до смањене ATP секреције у bCHs и hMSCs, али је смањење било израженије у bCHs култури што потврђује да су у секреције укључени хемиканали, али и да у hMSCs то није једини механизам за ослобађање ATP-а.

(Примљено 18. новембра, ревидирано 21. новембра 2013)

REFERENCES

1. A. K. Wann, N. Zuo, C. J. Haycraft, C. G. Jensen, C. A. Poole, S. R. McGlashan, M. M. Knight,. *FASEB J.* **26** (2012)1663
2. L. Bian, D. Y. Zhai, R. L. Mauck, J. A. Burdick, *Tissue Eng., A* **17** (2011) 1137
3. B. S. Dhinsa, A. B. Adesida, *Curr. Stem Cell Res. Ther*. **7** (2012)143
4. A. T. Hillel, J. M. Taube, T. C. Cornish, B. Sharma, M. Halushka, E. F. McCarthy, G. M. Hutchins, J. H. Elisseeff, *Cells Tissues Organs* **191** (2010) 12
5. I. E. Erickson, A. H. Huang, C. Chung, R. T. Li, J. A. Burdick, R. L. Mauck, *Tissue Eng., A* **15** (2009) 1041
6. L. Kock, C. C. van Donkelaar, K. Ito, *Cell Tissue Res*. **347** (2012) 613
7. M. M. Knight, J. van de Breevaart Bravenboer, D. A. Lee, G. J. van Osch, H. Weinans, D. L. Bader, *Biochim. Biophys. Acta* 1570 (2002) 1
8. S. J. Millward-Sadler, M. O. Wright, H.-S. Lee, H. Caldwell, G. Nuki, D. M. Salter, *Osteoarthr. Cartilage* **8** (2000) 272
9. A. Mobasheri, S. D. Carter, P. Martin-Vasallo, M. Shakibaei, *Cell Biol. Int* **26** (2002) 1
10. S. R. Roberts, M. M. Knight, D. A. Lee, D. L. Bader *J. Appl. Physiol*. **90** (2001) 1385
11. B. Pingguan-Murphy, M. El-Azzeh, D. L. Bader, M. M. Knight, *J. Cell Physiol*. **209** (2006) 389

12. M. K. Elfervig, R. D. Graff, G. M. Lee, S. S. Kelley, A. Sood, A. J. Banes, *Osteoarthr. Cartilage* **9** (2001) 518
13. R. D. Graff, E. R. Lazarowski, A. J. Banes, G. M. Lee, *Arthritis Rheum.* **43** (2000) 1571
14. R. Sabirov, Y. Okada, *Purinergic Signal.* **1** (2005) 311
15. M. Garcia, M. M. Knight, *J. Orthop. Res* **28** (2010) 510
16. M. M. Knight, S. R. McGlashan, M. Garcia, C. G. Jensen, C. A. Poole, *J. Anat*. **214** (2009) 275
17. T. Iwamoto, T. Nakamura, A. Doyle, M. Ishikawa, S. de Vega, S. Fukumoto, Y. Yamada, *J. Biol. Chem*. **285** (2010) 18948
18. R. L. Mauck, S. L. Seyhan, G. A. Ateshian, C. T. Hung, *Ann. Biomed. Eng.* **30** (2002) 1046
19. P. H. Chao, S. Yodmuang, X. Wang, L. Sun, D. L. Kaplan, G. Vunjak-Novakovic, *J. Biomed. Mater. Res., B* **95** (2010) 84
20. P. H. Chao, W. Grayson, G. Vunjak-Novakovic, *J. Orthop. Sci*. **12** (2007) 398
21. R. L. Mauck, M. A. Soltz, C. C. Wang, D. D. Wong, P. H. Chao, W. B. Valhmu, C. T. Hung, G. A. Ateshian, *J. Biomech. Eng*. **122** (2000) 252
22. C. T. Hung, R. L. Mauck, C. C. Wang, E. G. Lima G. A., Ateshian, *Ann. Biomed. Eng*. **32** (2004) 35
23. E. R. Lazarowski, *Purinergic Signal*. **8** (2012) 359
24. E. G. Lima, L. Bian, K. W. Ng, R. L. Mauck, B. A. Byers, R. S. Tuan, G. A. Ateshian, C. T. Hung, *Osteoarthr. Cartilage* **15** (2007) 1025
25. D. Ferrari, S. Gulinelli, V. Salvestrini, G. Lucchetti, R. Zini, R. Manfredini, L. Caione, W. Piacibello, M. Ciciarello, L. Rossi, M. Idzko, S. Ferrari, F. Di Virgilio, R. M. Lemoli, *Exp. Hematol*. **39** (2011) 360, 374 e361
26. E. Coppi, A. M. Pugliese, S. Urbani, A. Melani, E. Cerbai, B. Mazzanti, A. Bosi, R. Saccardi, F. Pedata *Stem Cells* **25** (2007) 1840
27. R. C. Riddle, A. F. Taylor, J. R. Rogers, H. J. Donahue, *J. Bone Miner. Res*. **22** (2007) 589
28. M. Kamijo, T. Haraguchi, M. Tonogi, G. Y. Yamane, *Biomed. Res*. **27** (2006) 289
29. A. Schajnovitz, T. Itkin, G. D'Uva, A. Kalinkovich, K. Golan, A. Ludin, D. Cohen, Z. Shulman, A. Avigdor, A. Nagler, O. Kollet, R. Seger, T. Lapidot, *Nat. Immunol*. **12** (2011) 391
30. M. Grellier, R. Bareille, C. Bourget, J. Amedee, *J. Tissue Eng. Regen. Med*. **3** (2009) 302
31. J. Fodor, C. Matta, T. Juhasz, T. Olah, M. Gonczi, Z. Szijgyarto, P. Gergely, L. Csernoch, R. Zakany, *Cell Calcium* **45** (2009) 421.

Journal of the Serbian Chemical Society
JSCS-info@shd.org.rs • www.shd.org.rs/JSCS

J. Serb. Chem. Soc. 78 (12) 1875–1892 (2013) UDC 638.165.8:58.087:581.9:913(497.11)
JSCS–4538 *Original scientific paper*

Quality parameters and pattern recognition methods as a tool in tracing the regional origin of multifloral honey

KRISTINA B. LAZAREVIĆ[1], JELENA Đ. TRIFKOVIĆ[2#], FILIP Lj. ANDRIĆ[2#], ŽIVOSLAV Lj. TEŠIĆ[2*#], IVAN B. ANĐELKOVIĆ[3#], DEJAN I. RADOVIĆ[4], NEBOJŠA M. NEDIĆ[5] and DUŠANKA M. MILOJKOVIĆ-OPSENICA[2**#]

[1]Center for Food Analysis, Zmaja od Noćaja 11, 11000 Belgrade, Serbia, [2]Faculty of Chemistry, University of Belgrade, P. O. Box 51, 11158 Belgrade, Serbia, [3]Innovation Center, Faculty of Chemistry Ltd., Studentski trg 12–16, 11000 Belgrade, Serbia, [4]Faculty of Biology, University of Belgrade, Studentski trg 16, 11000 Belgrade, Serbia and [5]Faculty of Agriculture, University of Belgrade, Nemanjina 6, 11080 Belgrade, Serbia

(Received 1 July, revised 19 September 2013)

Abstract: Multifloral honey was characterized in regards mineral to composition, sugar content and basic physicochemical properties. A total of 164 honey samples were collected from different regions of Serbia during the harvesting season 2009. Univariate data analysis (descriptive statistics and analysis of variance), geographic information system and pattern recognition methods (principal component analysis and cluster analysis) were utilized in order to identify the geographical origin of honey. The content of Mg, K, and Cu, electrical conductivity and optical rotation were established as useful indicators in tracing regional differences between honey samples. Samples originating from Zlatibor region were clearly distinguished from those from the rest of Serbia, showing higher K and Mg contents, as well as higher values of optical rotation, electrical conductivity, and free acidity. The influence of the soil composition, and climate conditions, as well as the presence of particular flora on the honey composition is emphasized. The modeling of the geographic origin of honey was attempted by means of linear discriminant analysis.

Keywords: multifloral honey; geographical origin; pattern recognition; Geographic Information System; Serbia.

INTRODUCTION

Honey is a complex mixture because its composition and properties depend not only on the nectar-providing plant species, but also on other factors such as bee species, geographic area, season, mode of storage, and even harvest technology and conditions. The European Council directive 2001/110/EC concerning

*,** Corresponding authors. E-mail: (*)ztesic@chem.bg.ac.rs; (**)dusankam@chem.bg.ac.rs
Serbian Chemical Society member.
doi: 10.2298/JSC130701099L

honey allows specific denominations of honey, where the name "honey" can be supplemented by information on the floral, vegetable, regional, territorial or topographical origin. The term "unifloral honey" is used to describe honey in which the major part of the nectar or honeydew is derived from a single plant species. The overwhelming majority of the honeys on the market contain nectar or honeydew from several botanical sources in the foraging area of the beehive and are, therefore, called multifloral or polyfloral honey.

Honey composition is tightly associated to its botanical origin, which is closely related to the geographical area from which the honey originated.[1] The volatile composition is very dependent on the geographical location even for the same plant species, as accumulation of phytochemicals depends on climatic conditions (sunlight and moisture), soil characteristics, and the presence of different minerals arising from soil. This suggests that the chemical composition of the honeys even of the same floral origin may be quite different.[2] Due to the botanical origin given by the particular flora and the ecosystem diversity conditioned by the given territory, honey may have unique characteristics. Indeed, the estimation of honey quality by consumers depends on its organoleptic characteristics, which are strongly dependent on botanical origin of the honey and to some extent on its geographical origin.[3,4]

Considering that honey is a complex natural product, produced by honeybees under relatively uncontrolled conditions, an appropriate characterization of honey samples requires the use of many variables. Thus, multivariate statistical analysis can be applied to find trends or associations among the analyzed data, or to establish a subset of measured parameters allowing honey characterization. Over the last few decades, there have been several reports on the use of multivariate chemometric analysis of the general physicochemical parameters, minerals, sugars, and other constituents, in order to differentiate types of unifloral honeys, honeydew and blossom honeys.[5–7]

Among the parameters tested to assess the provenance of honey, the polyphenolic profile, electric conductivity, acidity, amino acids composition, carbohydrate profile, and pollen proteins were found to be the most useful.[8,9] The mineral composition has also been employed to discriminate honey samples arising from different geographical areas.[10,11] Indeed, due to their stability, minerals seem to be a good criterion for honey classification. The mineral composition of honey is intrinsically connected to the territory of its production and it is closely tied to the flora visited by the bees. In addition, the mineral content of honey is tightly associated to geographical and climatic conditions.[12]

Serbia has very good prerequisites for the development of beekeeping (apiculture), distinguished by heterogeneous relief and climatic conditions and by the existence of various honeybee pastures. Considering the area of wild flora, it would be possible to breed up to 800,000-bee colonies.[13] However, disregarding

this possibility, the current utilization of capabilities is only 33.4 %, resulting in annual production of 4000–5000 tons of honey.[14] According to the annual honey production, Serbia would be in the middle of the list of EU member states.[15]

The main goal of this work was to characterize multifloral honeys from a hitherto relatively unexplored geographical area, by using methods easily available to a large number of analytical laboratories dealing in authenticity control of honey in order to establish possible relationships between corresponding chemical variables and the production zone of honey. Thus, the basic physicochemical parameters, minerals, and characteristic mono-, di- and tri-saccharides were evaluated. By the means of several pattern recognition methods, the variables that discriminate honey arising from different regions of Serbia were identified and successful models for further prediction were developed.

EXPERIMENTAL

Sample collection

The total numbers of 164 multifloral honey samples collected from different parts of Serbia (Fig. 1) during the harvesting season 2009, were provided from "The Association of the Beekeeping Organizations of Serbia" (SPOS).[16] The botanical origin of the samples was established by the SPOS based on information provided by the beekeepers and some sensory characteristics of the collected honeys. All samples were in their original packages and were transferred to the laboratory and kept in a refrigerator until analysis.

Physicochemical analysis

Physicochemical parameters (pH, electrical conductivity (*EC*), free acidity (*FA*), optical rotation (*OR*) and moisture) were analyzed using The Harmonized Methods of the International Honey Commission,[17] as described in a previous paper.[13]

Mineral composition

The mineral composition of honey was analyzed by inductively coupled plasm-optical emission spectrometry (ICP-OES). About 0.6–0.7 g of fresh honey was treated with 7 mL of 65 % HNO_3 (Merck, Darmstadt, Germany) and 1 mL of 35 % H_2O_2 (Merck) in polytetrafluoroethylene (PTFE) vessels. A microwave closed digestion system (ETHOS 1, Milestone, Italy) was used for the mineralization process. The final clear solution was made up to 50 mL with bidistilled water. All mineral elements in the digested solutions were determined using an ICP-OES (iCAP 6500 Duo ICP, Thermo Scientific, UK). A multi-element plasma standard solution 4, Specpure, containing 1 g dm^{-3} of each element was analyzed for reference purposes. The results are expressed as mg metal per kg honey (ppm) for the macro elements (K, Mg, Na and Ca) and the micro-elements (Fe, Zn, Cu and Co), or as μg metal per kg honey (ppb) for the trace elements (Cd, Cr and Ni).

Sugar content

The sugar content, *i.e.*, glucose, fructose, sucrose, trehalose, maltose, isomaltose, isomaltotriose, melezitose and turanose with gentiobiose (Gen + Tur), was determined by the means of ion chromatography with amperometric detection. Samples of homogenized honey were weighed (between 0.2 and 0.3 g) and diluted 10,000-fold with ultrapure water (Millipore Simplicity 185 S.A., 67120, Molsheim, France). The solution was filtered (Cronus syringe nylon filter 13 mm, 0.45 μm) and transferred to vials. The honeys were analyzed using an ISC

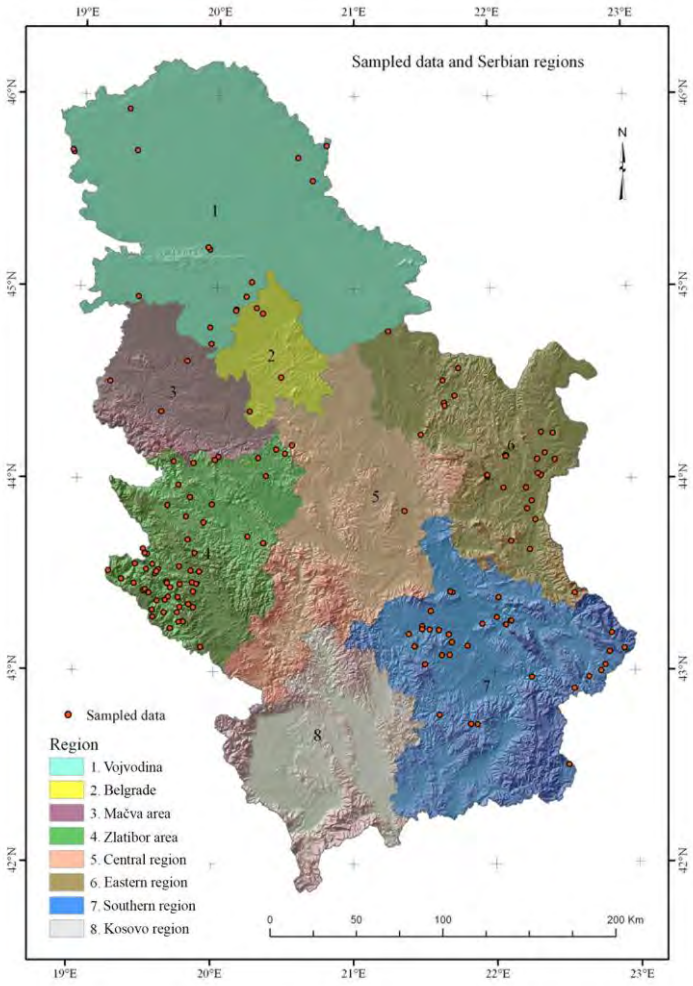

Fig. 1. The regional map of Serbia with marked locations of honey sampling.

3000 DP liquid chromatograph system (Dionex, Sunnyvale, CA, USA) equipped with a quaternary gradient pump (Dionex, Sunnyvale, CA, USA). The carbohydrates were separated on a Carbo Pac® PA10 pellicular anion-exchange column (4×250 mm) (Dionex, Sunnyvale, CA, USA) at 30 °C. Each sample (25 µL) was injected with an ICS AS-DV 50 autosampler (Dionex, Sunnyvale, CA, USA). Sodium hydroxide solution was used as the eluent. Analyses were performed under isocratic mode (52 mM NaOH) with the flow rate set to 1.0 mL min^{-1}. The calibration was performed with standard solutions (D-(+)-Treh, D-(+)-Mel, D-(+)-Tur, D-(–)-Fruc, D-(+)-Sach, D-(+)-Malt, and D-(+)-Glc (Tokyo Chemical Industry, TCI, Europe, Belgium); Gen, iMalt, and iMaltotri (Tokyo Chemical Industry, TCI, Tokyo, Japan)) obtained by the dilution of ten standard sugars in powder form. The evaluation of the sugar content of honey samples was obtained from calibration curves of each sugar contained in the standard

solutions. Under these chromatographic conditions, the last sugar was detected after approximately 35 min, and the analysis was ended at 40 min. Results are expressed as percentage of sugar content.

Data analysis

Principal component analysis (PCA) and cluster analysis (CA) were realized by the means of PLS ToolBox, v.6.2.1, for MATLAB 7.12.0.0635 (R2011a). All data were mean centered and scaled to the unit standard deviation prior to any multivariate analysis. For PCA, a singular value decomposition algorithm was employed and in the case of CA, the Ward method for calculating distances was used, since it usually gives clusters of optimal size and form.

Descriptive statistics, Kruskal–Wallis test and linear discriminant analysis (LDA) were performed by means of a demo version of NCSS statistical software (J. Hintze (2001), NCSS and PASS Number Cruncher Statistical Systems, Kaysville, Utah).

Microsoft Office Excel and Access were used to organize the Geographic Information System (GIS) database. Locations of data sampling are vector (point) data. Vector data and the database were integrated, analyzed and printed with GIS software (ArcGIS 9). Geostatistical analyst was used to create a predicted distribution of the attributive data. The Kriging method was used for interpolation.

RESULTS AND DISCUSSION

The results of analysis of physicochemical parameters, mineral and sugar content indicated that some of the honey samples show outlying effects. Regarding the basic physicochemical parameters, these samples met the criteria to be considered as honeydew honeys. According to descriptive sheets for main European unifloral honey,[18] the values of *EC*, pH, *OR* and *FA* for honeydew honeys are in the following ranges, respectively: 0.85–1.63 mS cm^{-1}, 4.4–5.7, $[\alpha]_D^{20}$ 25.2–5, 16.8–37.1 meq kg^{-1}. Several investigators found that honeydew honeys were generally characterized by higher electric conductivity, as well as a higher pH and acidity.[19] According to the Serbian regulations ("Sl. list SCG", No. 45/2003 and "Sl. glasnik RS", No. 43/2013) samples with EC > 1.0 mS cm^{-1}, should be declared as honeydew honey. Consequently, in order to determine the geographical origin of multifloral honey, the 30 samples of honeydew honeys were excluded from the further analysis.

The summarized parameters of descriptive statistics of 134 multifloral honey samples are presented in Table I.

The moisture level had similar values across the regions in the range from 15 to 17 %. In all samples, except of those originating from the Zlatibor region, the pH values agreed with those reported by Arvanitoyannis *et al*.[5] (pH 3.9). The higher pH value measured in the samples from the Zlatibor region (pH 4.31) was in agreement with the values reported for Slovenian multifloral honeys collected from three regions: Alpine, Pannonian and Mediterranean.[8] Furthermore, the electrical conductivity was higher in the honey collected from the Zlatibor area (0.74 mS cm^{-1}) compared to the samples from the rest of Serbia, as well as from

the values reported for multifloral honeys in other studies.[5,8,20,21] The free acidity did not show fluctuations among the studied regions and was in agreement with data reported for neighboring countries.[8,20,21] The optical rotation of the samples coming from Serbia was similar to the data reported for Slovenian multifloral honeys, except for the samples collected from the Zlatibor region, which had lower values.

TABLE I. Parameters of descriptive statistics for the investigated honey samples of different geographical origin

Parameter		Vojvodina (17)[a]	Belgrade region (3)	Central Serbia (15)	Eastern Serbia (27)	Southern Serbia (28)	Zlatibor area (38)	Western region (6)[b]
K, mg kg^{-1}	Mean	564.67	609.73	413.26	707.97	547.64	1352.83	597.59
LOQ = 25	*SD*	307.35	201.38	225.85	322.83	253.01	417.77	439.24
µg kg^{-1}	Median	472.40	652.83	336.51	706.14	531.29	1373.05	387.97
	Max.	1211.10	786.07	1058.19	1363.39	1255.74	2559.44	1360.23
	Min.	189.90	390.28	194.48	220.21	164.32	539.69	257.92
Ca, mg kg^{-1}	Mean	84.13	71.04	38.72	57.33	42.99	51.35	72.31
LOQ = 25	*SD*	27.03	32.42	18.17	20.52	14.61	16.20	43.33
µg kg^{-1}	Median	84.60	70.14	35.63	51.58	40.91	50.44	72.67
	Max.	126.84	103.89	85.89	106.40	76.14	100.10	133.13
	Min.	26.99	39.07	16.19	30.53	21.04	17.65	22.08
Mg, mg kg^{-1}	Mean	22.01	15.74	15.62	20.85	17.61	49.69	21.73
LOQ = 10	*SD*	7.69	5.04	8.05	12.50	12.04	19.31	15.68
µg kg^{-1}	Median	21.92	14.70	10.96	17.88	12.69	45.44	16.48
	Max.	44.99	21.22	31.19	66.81	63.01	88.22	46.42
	Min.	7.50	11.30	6.13	8.90	5.94	17.59	5.39
Na, mg kg^{-1}	Mean	19.64	30.00	17.30	18.41	18.36	23.98	16.96
LOQ = 25	*SD*	12.87	23.22	8.30	16.10	12.44	16.15	12.33
µg kg^{-1}	Median	16.76	23.69	16.66	14.80	15.01	20.70	15.55
	Max.	59.12	55.72	30.09	60.85	69.90	91.25	39.21
	Min.	2.59	10.58	1.39	1.74	0.97	7.34	2.90
Zn, mg kg^{-1}	Mean	4.12	0.82	1.65	6.12	2.69	3.71	2.77
LOQ = 2	*SD*	6.38	0.32	1.67	11.84	2.13	6.95	2.37
µg kg^{-1}	Median	1.78	0.76	1.26	2.49	1.83	2.09	1.98
	Max.	27.46	1.16	7.46	61.52	9.54	43.44	7.56
	Min.	0.82	0.53	0.46	0.82	0.71	0.91	1.22
Fe, mg kg^{-1}	Mean	3.49	0.94	1.59	1.97	1.87	2.33	2.40
LOQ = 10	*SD*	5.25	0.17	1.58	1.72	1.41	1.34	1.12
µg kg^{-1}	Median	2.11	0.98	1.18	1.54	1.54	1.96	2.21
	Max.	23.68	1.09	6.78	7.87	8.56	7.26	3.90
	Min.	1.18	0.76	0.38	0.75	0.78	0.79	1.09
Cu, mg kg^{-1}	Mean	0.32	0.27	0.23	0.36	0.27	0.54	0.27
LOQ = 2	*SD*	0.11	0.04	0.09	0.12	0.11	0.18	0.10
µg kg^{-1}	Median	0.28	0.28	0.20	0.34	0.25	0.54	0.24
	Max.	0.56	0.30	0.41	0.69	0.58	1.02	0.44
	Min.	0.18	0.22	0.09	0.18	0.14	0.23	0.17

TABLE I. Continued

Parameter		Vojvodina (17)[a]	Belgrade region (3)	Central Serbia (15)	Eastern Serbia (27)	Southern Serbia (28)	Zlatibor area (38)	Western region (6)[b]
Mn, mg kg^{-1}	Mean	1.51	1.58	2.31	2.05	1.73	4.25	3.97
LOQ = 5	*SD*	2.09	1.49	2.47	1.87	2.16	2.80	5.27
µg kg^{-1}	Median	0.51	1.01	1.21	1.41	0.76	3.64	1.68
	Max.	6.97	3.27	8.49	7.84	8.99	12.15	13.73
	Min.	0.22	0.46	0.20	0.11	0.12	0.78	0.33
Co, mg kg^{-1}	Mean	0.11	0.06	0.02	0.05	0.10	0.07	0.05
LOQ = 2	*SD*	0.16	0.07	0.01	0.05	0.17	0.10	0.07
µg kg^{-1}	Median	0.05	0.02	0.02	0.04	0.04	0.04	0.02
	Max.	0.71	0.15	0.05	0.25	0.83	0.49	0.18
	Min.	0.02	0.02	0.01	0.01	0.01	0.01	0.01
Cr, µg kg^{-1}	Mean	108.16	47.69	32.39	79.95	43.4	39.63	36.09
LOQ = 2	*SD*	105.92	30.34	12.11	91.99	48.9	22.70	49.82
µg kg^{-1}	Median	63.77	45.62	36.33	40.96	34.7	38.38	20.38
	Max.	455.33	79.02	44.24	375.10	222.5	123.22	132.30
	Min.	ND [c]	18.45	ND	ND	ND	ND	ND
Ni, µg kg^{-1}	Mean	71.45	55.95	100.08	77.92	94.3	235.51	60.05
LOQ = 2	*SD*	53.92	28.89	63.71	49.77	100.7	168.28	61.82
µg kg^{-1}	Median	56.14	68.53	81.60	62.18	64.0	173.94	54.30
	Max.	182.94	76.42	230.49	173.82	521.0	956.40	165.57
	Min.	ND	22.90	ND	ND	ND	23.38	ND
Cd, µg kg^{-1}	Mean	4.03	0.59	1.42	2.57	1.9	8.74	2.39
LOQ = 2	*SD*	6.19	0.32	2.45	4.56	2.5	8.90	3.70
µg kg^{-1}	Median	1.35	0.70	0.13	0.35	0.7	6.52	1.15
	Max.	18.55	0.83	8.66	18.07	7.4	42.15	9.70
	Min.	ND	0.23	ND	ND	ND	ND	ND
Moisture, %	Mean	16.79	15.55	16.30	16.46	16.67	17.24	17.80
	SD	1.28	0.25	0.96	1.54	1.24	1.45	1.49
	Median	16.75	15.61	15.99	16.39	16.46	17.12	17.78
	Max.	19.19	15.76	17.67	21.28	20.27	19.93	19.77
	Min.	14.75	15.28	14.72	14.01	14.92	14.01	15.47
EC	Mean	0.37	0.35	0.27	0.40	0.31	0.74	0.35
mS cm^{-1}	*SD*	0.12	0.11	0.12	0.15	0.10	0.14	0.18
	Median	0.34	0.34	0.24	0.35	0.30	0.73	0.28
	Max.	0.61	0.45	0.62	0.68	0.59	0.99	0.63
	Min.	0.19	0.24	0.17	0.18	0.17	0.44	0.18
pH	Mean	3.72	3.87	3.91	3.90	3.88	4.31	3.86
	SD	0.33	0.12	0.31	0.31	0.30	0.25	0.18
	Median	3.76	3.90	4.01	3.91	3.89	4.34	3.96
	Max.	4.22	3.98	4.48	4.58	4.32	4.66	4.00
	Min.	3.07	3.74	3.16	3.45	3.26	3.38	3.58

TABLE I. Continued

Parameter		Vojvodina (17)[a]	Belgrade region (3)	Central Serbia (15)	Eastern Serbia (27)	Southern Serbia (28)	Zlatibor area (38)	Western region (6)[b]
FA	Mean	27.84	25.57	19.33	25.23	23.7	30.88	20.4
meq kg^{-1}	SD	6.66	6.17	7.45	6.89	6.36	6.24	7.41
	Median	31.00	24.50	16.20	23.00	24.0	31.60	18.4
	Max.	37.20	32.20	34.20	38.70	34.2	45.20	30.2
	Min.	11.40	20.00	10.60	15.60	12.8	16.60	13.4
OR / $[\alpha]_D^{20}$	Mean	–14.38	–13.52	–13.48	–12.51	–13.2	–6.50	–14.2
	SD	2.89	1.59	2.52	2.12	2.09	4.84	1.64
	Median	–14.46	–13.04	–13.77	–12.19	–13.0	–6.28	–14.8
	Max.	–10.32	–12.22	–7.67	–8.81	–9.3	6.96	–11.3
	Min.	–20.10	–15.30	–17.22	–17.02	–17.8	–16.83	–15.5
Trehalose	Mean	0.24	0.19	0.14	0.36	0.28	0.30	0.08
%	*SD*	0.31	0.15	0.17	0.32	0.39	0.33	0.07
	Median	0.18	0.24	0.07	0.21	0.13	0.14	0.06
	Max.	1.32	0.32	0.67	1.12	1.76	1.34	0.17
	Min.	0.01	0.02	0.02	0.04	0.03	0.01	0.01
Glucose	Mean	26.41	24.03	24.68	23.29	24.79	24.54	21.52
%	*SD*	3.58	1.99	2.63	2.71	2.80	3.56	2.06
	Median	26.99	23.88	24.92	23.74	24.32	25.06	21.28
	Max.	32.03	26.09	28.37	28.95	29.63	33.56	24.70
	Min.	19.04	22.12	19.25	15.54	19.77	16.97	18.49
Fructose	Mean	36.10	35.89	37.98	34.35	36.81	35.58	31.87
%	*SD*	2.68	3.06	3.57	3.31	2.98	4.54	4.27
	Median	36.82	37.16	37.41	34.17	36.14	35.63	32.22
	Max.	40.71	38.11	43.48	41.11	42.87	44.67	38.09
	Min.	30.81	32.40	32.66	24.64	31.69	24.45	25.08
Sucrose	Mean	3.34	2.19	5.19	4.24	4.48	4.90	3.79
%	*SD*	2.48	1.78	1.36	3.09	3.25	1.36	1.43
	Median	2.46	1.92	5.11	3.10	3.82	5.08	3.90
	Max.	7.53	4.09	8.67	14.36	19.50	7.03	5.71
	Min.	0.12	0.56	2.92	0.31	1.65	1.52	2.18
Isomaltose	Mean	0.64	0.75	0.31	1.01	0.73	0.41	0.37
%	*SD*	0.75	0.65	0.40	0.72	0.58	0.74	0.44
	Median	0.30	1.02	0.07	0.92	0.78	0.16	0.11
	Max.	2.33	1.22	1.06	3.42	1.79	3.64	0.96
	Min.	0.01	ND	ND	0.01	0.03	0.01	0.05
Melezitose	Mean	0.22	0.33	0.31	0.22	0.21	0.36	0.37
%	*SD*	0.13	0.26	0.40	0.06	0.11	0.24	0.44
	Median	0.19	0.19	0.07	0.21	0.19	0.33	0.11
	Max.	0.59	0.63	1.06	0.37	0.58	0.97	0.96
	Min.	0.07	0.16	ND	0.10	0.08	0.01	0.05

TABLE I. Continued

Parameter		Vojvodina (17)[a]	Belgrade region (3)	Central Serbia (15)	Eastern Serbia (27)	Southern Serbia (28)	Zlatibor area (38)	Western region (6)[b]
Gentiobiose plus turanose, %	Mean	0.42	0.47	0.45	0.45	0.34	0.41	0.37
	SD	0.27	0.09	0.36	0.15	0.19	0.17	0.33
	Median	0.44	0.47	0.36	0.42	0.30	0.41	0.25
	Max.	0.91	0.56	1.39	0.77	0.75	0.87	0.97
	Min.	0.02	0.39	0.05	0.13	0.11	0.16	0.06
Isomalto-triose, %	Mean	0.13	0.18	0.13	0.30	0.25	0.18	0.32
	SD	0.13	0.17	0.13	0.16	0.19	0.13	0.09
	Median	0.07	0.19	0.07	0.34	0.24	0.16	0.35
	Max.	0.39	0.35	0.39	0.57	0.87	0.46	0.44
	Min.	ND	ND	ND	ND	0.03	0.01	0.17
Maltose, %	Mean	1.50	1.13	2.11	1.52	1.59	1.35	1.40
	SD	0.90	0.88	0.64	0.72	0.61	0.74	0.90
	Median	1.68	1.60	2.00	1.32	1.61	1.17	1.65
	Max.	3.24	1.68	3.68	3.07	3.45	4.07	2.31
	Min.	0.09	0.12	0.97	0.56	0.59	0.38	0.24

[a]Number of samples; [b]Western region without Zlatibor area; [c]not detected

Twelve minerals were quantified for each honey sample (K, Na, Ca, Mg, Fe, Zn, Mn, Cu, Ni, Cr, Co and Cd). Potassium was the most abundant mineral component, considering all the investigated samples, which agrees with other studies indicating that K is the most common element in honeys.[19,22] The average levels ranged from 400 to 700 mg kg^{-1} for all regions of Serbia, except foe the Zlatibor area, where this parameter reached a value of 1300 mg kg^{-1}. The relatively high contents of potassium reported in the case of Italian (731±397 mg kg^{-1}),[22] Slovenian (1090–1220 mg kg^{-1})[8] and Indian (932.56±0.15 mg kg^{-1})[23] honey did not exceed the values measured in the samples from the Zlatibor region. Calcium and magnesium were the next most common elements, followed by sodium, iron, and zinc. Sodium and magnesium were also present in significant amounts in all the studied samples, but several times lower than the potassium content and 2-time lower than the calcium content. Magnesium was present in higher amount in the samples coming from the Zlatibor mountain area (50 mg kg^{-1}) than in the samples coming from the rest of Serbia (15–22 mg kg^{-1}). The rest of the studied minerals (Zn, Fe, Cu, Mn, Co, Cr, Ni and Cd) were present in minor quantities and some of them could be detected in trace amounts (μg kg^{-1}).

In this study, ten sugars were identified and quantified, which included two monosaccharides, six disaccharides and two trisaccharides (Table I). Similar chromatograms were obtained for all the considered honey samples. The glucose and fructose were clearly the predominant sugars in all samples. A good resolution and separation of all quantified di- and trisaccharides were also observed.

Moreover, the chromatographic method used here was relatively fast (about 30 min) and an approximate sugar profile was obtained.

Fructose was found to be the most abundant sugar component in all samples, followed by glucose. The content of both compounds was in most cases within the limits established by EU legislation (Council Directive 2001/110/EC). Some observed lower values could correspond to mixtures of honeys and honeydew honeys, since many authors found significantly lower glucose and fructose content in honeydew honeys compared with blossom honeys.[22] The ratio of fructose to glucose was between 1.36 and 1.61, indicating that the honey would remain fluid for longer periods. Among the disaccharides, sucrose and maltose were the major components.

Data analysis

According to the D'Agostino *K*-squared, Kolmogorov–Smirnov and the Shapiro–Wilk test for normality of distribution, there was significant deviation from normal distribution for each of the studied variables. The modified Levene equality variance test showed significant heteroscedasticity among the different regions for each variable. Therefore, for statistical evaluation of differences in the results, the Kruskal–Wallis test was employed for each of the variables, taking the appropriate region as a single factor. The results are presented in Table S1 (Supplementary material this paper). In the cases of the observed statistically significant difference between the medians, the Kruskal–Wallis multiple-comparison *Z*-value test was performed. The separated regions are denoted in parentheses (Table S1). Based on the Kruskal–Wallis test, several factors, such as K, Mg, Cu, Ni, and Cd, as well as *EC*, pH and *OR*, were identified as parameters that separate the honey samples from the Zlatibor area from those originating from the rest of Serbia. The other factors are responsible for the differentiation of only limited numbers of regions while the Na, Co, trehalose and gentiobiose plus turanose level do not provide any significant difference among any of the considered regions of Serbia.

A Geographical Information System (GIS) was employed to build the area distribution of each of the studied parameters. A GIS is a system designed to capture, store, manipulate, analyze, manage and present all types of geographical data by merging of cartography, statistical analysis and database technology.[24] The GIS, unlike the other employed statistical methods, provides an estimated geographical distribution of a certain property over the map, therefore being more straightforward and a rather convenient approach. GIS has been introduced in addition to other statistical methods in order to improve the classification performance. The spatial distributions of all parameters are given in Figs. S1–S7 of the Supplementary material.

PCA and CA

Both PCA and CA were performed In order to obtain a basic insight into the data structure, detect possible outliers and identify similarities and specific grouping patterns among the studied samples. PCA resulted in a three-component model that explains 41.35 % of total variance. The first principal component, PC1, accounted for 24.12 % of the overall data variance, the second principal component, PC2, for 9.26 % and the third principal component for 7.97 %. Mutual projections of factor scores and their loadings for the first two PCs are presented in Fig. 2a and b, respectively. Score plot reveals two distinct groups of

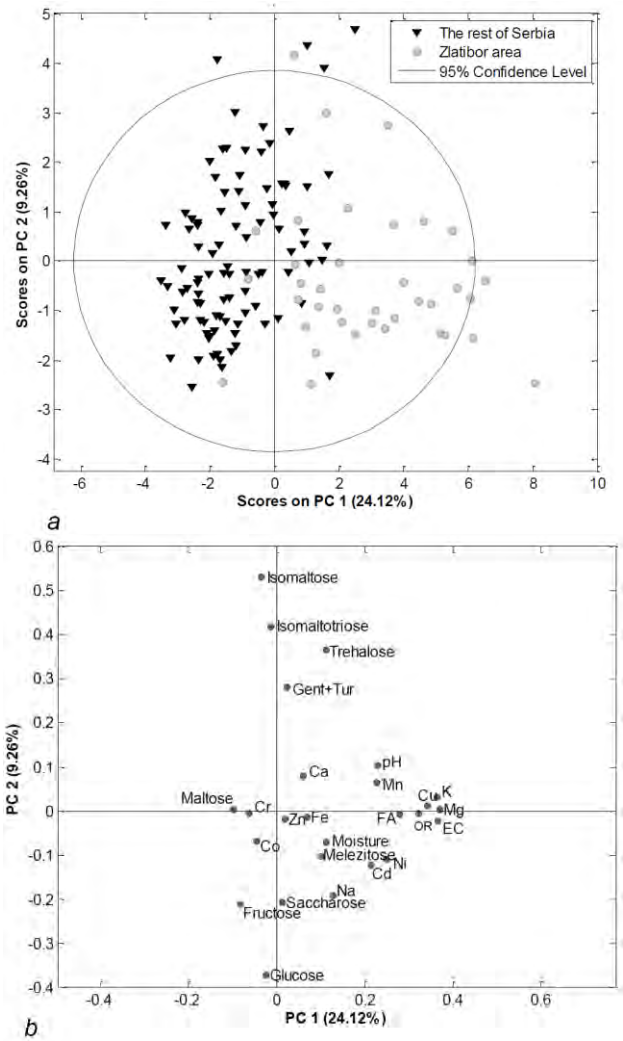

Fig. 2. Principal component analysis: a) score plot, b) loading plot.

samples, separated along the PC1 axis. The majority of the samples originating from Zlatibor region are grouped in the right side of the graph, while those collected from the rest of Serbia form a compact cluster mostly on the opposite side of the PC1 axis. There was no meaningful separation along the PC2 direction. The loading plot implies that the Mg, K, and Cu contents, as well as FA, *OR* and *EC*, are parameters that have the most positive impact on the PC1 direction. The isomaltose, isomaltotriose and glucose contents significantly affect the PC2 component.

Several samples exceeded the limits imposed by the Hotteling T^2 95 % probability ellipse, hence they could be considered as outliers. Among the samples coming from the rest of the Serbian regions, those that could be considered as outliers have higher levels of trehalose and isomaltose. The contents of K, Mg, Cu, and Cd, and the values for *EC* and pH were similar to those obtained for the samples from the Zlatibor region. The three samples from the Zlatibor region that exhibited an outlying effect had very high contents of K, Ca, Mg and Na.

Cluster analysis revealed five clusters at 17 variance weighted distance units (Fig. 3). One cluster consisted entirely of honey samples from the Zlatibor region, while the others accounted for all the samples from the rest of Serbia, as well as a small number of samples from the Zlatibor region. However, any further subclustering according to the proposed regional division of Serbia could not be evidenced.

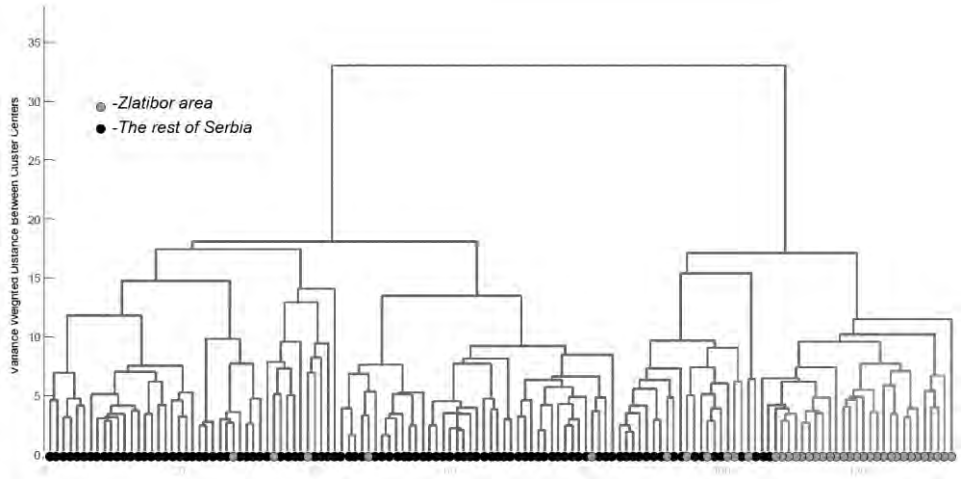

Fig. 3. Dendrogram obtained by the means of hierarchical cluster analysis.

All the employed statistical procedures (Kruskal–Wallis, PCA and CA) as well as GIS (Figs. 4 and S1–S7) confirmed a unique set of parameters (Mg, K, Cu, *EC* and *OR*) that differentiated the samples originating from the Zlatibor area

from the rest of the samples collected from Serbia. Different factors could influence a separation among the mentioned areas, such as climate, soil composition, or presence of regional endemic flora, which strongly influences the mineral content in honeys.[10]

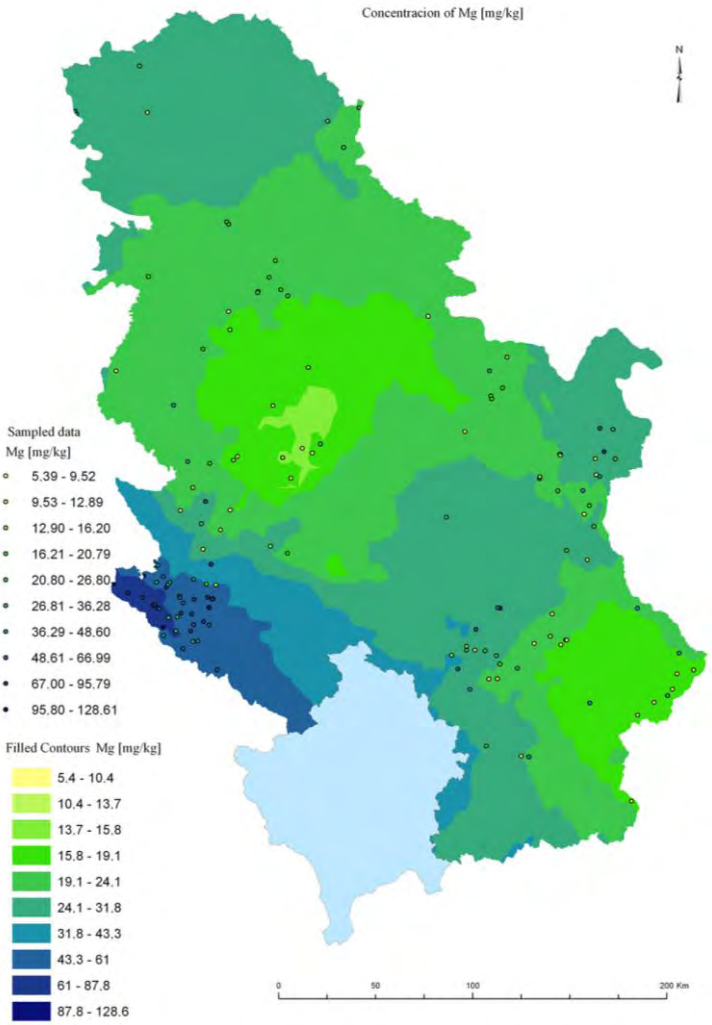

Fig. 4. GIS spatial distribution of Mg content in multifloral honey.

The main soil type of the northern part of Serbia (Vojvodina, the Belgrade region and the Western region, excluding the Zlatibor area) is chernozem, which is characterized by the presence of $CaCO_3$ and high quality calcium mull humus.[25] The two-times higher calcium levels measured in the honey samples obtained

from Vojvodina (84.13±27.03 mg kg^{-1}), Belgrade (71.04±32.42 mg kg^{-1}) and the Western region (72.31±43.33 mg kg^{-1}) are in accordance with the soil composition.

The Zlatibor region belongs to the largest serpentine block in the Balkans, which belongs to a group of siliceous rocks that are characterized by calcium deficiency and high concentrations of aluminum, iron, magnesium, nickel, cobalt and chromium and a few plant nutrients.[26] Probably the high amounts of Mg and Ni found in serpentine soils could be responsible for higher amounts of these elements found in honeys from the Zlatibor region.[25,27]

The regional endemics characteristic for the Zlatibor region are *Knautia pancicii*, *Verbascum bosnense*, *Thymus adamovicii* and *Potentilla mollis*. All mentioned plant species are blossom plants and could significantly contribute to distinguishing multifloral honeys originating from the Zlatibor region compared to the rest of Serbia.[26] Unlike other mountain regions of Serbia, Zlatibor area is rich in various coniferous species and other evergreen plants, of which the Serbian spruce (*Picea omorika*) stands out as an endemic one. They represent a reach source of honeydew, together with silver fir (*Abies alba*), European spruce (*P. abies*), Aleppo pine (*Pinus halepensis*) and European larch (*Larix decidua*).

Linear discriminant modeling

LDA was performed in order to establish the best possible mathematical models that would be able to sort unknown samples according to their geographic origin. The linear discriminant analysis was performed on a training set comprised of two types of samples: those from Zlatibor region and the others from the rest of Serbia. The model resulted in one canonical function, with *EC*, and K and Mg levels as the most significant variables that differentiate the two types of samples. Values of standardized canonical coefficients were, respectively: 1.681, –0.750, and 0.680. Two out of 38 (5.26 %) samples originating from Zlatibor region were misclassified, while all samples from the rest of Serbia were properly classified (Tables SII.I–SII.III of the Supplementary material).

In addition, discrimination among the entire set of the studied regions was attempted. The LDA model resulted in six statistically significant canonical functions. The score plot of the first two canonical functions and the first *vs*. the third (Figs. 5a and b) revealed that the samples from the Zlatibor area were completely separated from the other regions. Samples collected from Vojvodina were sufficiently separated from the other regions, with the exception of the samples from the East, which exhibited moderate overlapping. The other regions form well-shaped groups that are mutually overlapped to a certain degree. The factors that discriminate the Zlatibor region from the rest of Serbia are amounts of magnesium (in a positive manner), potassium, and calcium (in a negative manner), and electrical conductivity, with standardized canonical scores of respectively: –0.527,

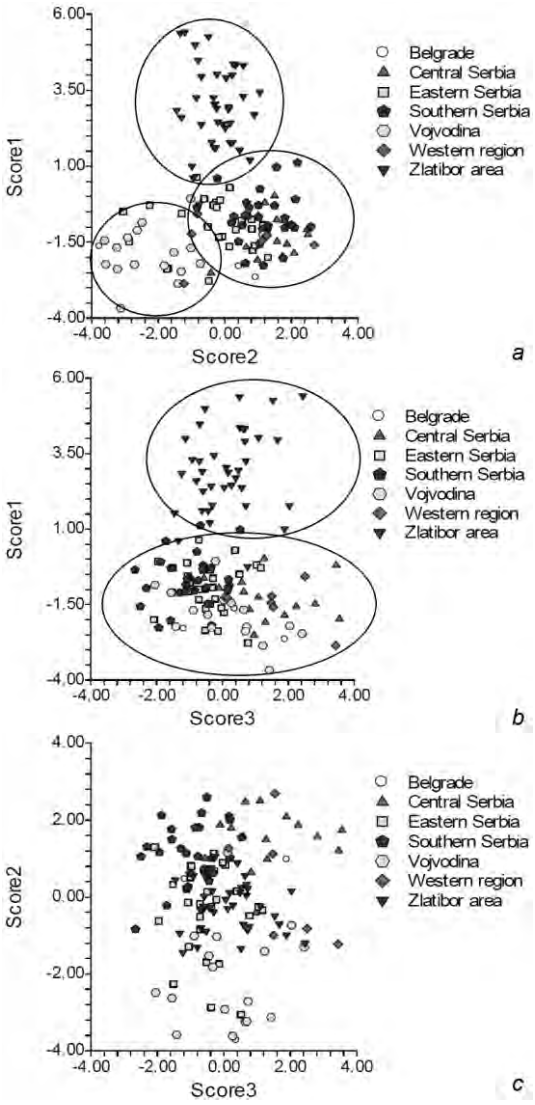

Fig. 5. Linear discriminant analysis, canonical score plots: a) score1/score2, b) score1/score3 and c) score2/score3.

–0.693, 0.643 and 1.602. In addition to the mentioned parameters, Vojvodina was separated from the other regions by the potassium and calcium contents. For these parameters, values of standardized canonical coefficients were respectively: 0.813 and –0.866. A total 36 (94.73 %) of 38 samples from Zlatibor are correctly assigned, 12 (70.58 %) of 17 samples from Vojvodina were also correctly assigned, with two samples being misclassified as Belgrade region, and three assigned to Eastern, Southern and Western region. The rest of the studied samples were misclassified with low to moderate rates (Tables SIII.I–SIII.III of the Supplementary

material). This implies that obtained LDA models have quite good predictive power, especially when the number of studied regions is considered.

CONCLUSIONS

The results of this comprehensive study, based on a vast number of genuine honey samples, represent the first attempt to classify multifloral honey over a relatively small area, *i.e.*, the territory of Serbia. Characterization of the studied samples was performed regarding the basic physicochemical properties, mineral composition and sugar content. Univariate (descriptive statistics and analysis of variance) and multivariate (principal component analysis, cluster analysis and linear discriminant analysis) data analyses were performed in order to identify the geographical origin of the honeys.

The following parameters: Mg, K, Cu, electrical conductivity and optical rotation were selected as useful indicators in tracing regional differences between the honey samples. Samples obtained from the Zlatibor region were clearly distinguished from the rest of Serbia, showing higher values of potassium and magnesium contents, as well as higher values of electrical conductivity, pH and free acidity. The influence of the soil composition, and climate conditions, as well as the presence of particular flora on the honey composition was highlighted. Taking into account that there are a small number of articles dealing with the determination of geographical origin of bee products, the presented study provides useful data that could be compared with similar results obtained in the other regions.

SUPPLEMENTARY MATERIAL

Tables S-I–SIII and Figs. S1–S7 are available electronically at http://www.shd.org.rs/ /JSCS/, or from the corresponding author on request.

Acknowledgements. This work was supported by the Ministry of Education, Science and Technological Development of the Republic of Serbia, Grant Nos. 172017 and 451-03-2372--IP Type 1/107. The authors acknowledge support of the FP7 RegPot project FCUB ERA GA No. 256716. The EC does not share responsibility for the content of this article. The authors wish to thank "The Association of the Beekeeping Organizations of Serbia" (SPOS) (www.spos.info) for providing the honey samples.

И З В О Д

ОДРЕЂИВАЊЕ ГЕОГРАФСКОГ ПОРЕКЛА ПОЛИФЛОРАЛНИХ МЕДОВА ПОМОЋУ ПАРАМЕТАРА КВАЛИТЕТА И МЕТОДА ПРЕПОЗНАВАЊА ОБРАЗАЦА

КРИСТИНА Б. ЛАЗАРЕВИЋ[1], ЈЕЛЕНА Ђ. ТРИФКОВИЋ[2], ФИЛИП Љ. АНДРИЋ[2], ЖИВОСЛАВ Љ. ТЕШИЋ[2], ИВАН Б. АНЂЕЛКОВИЋ[3], ДЕЈАН И. РАДОВИЋ[4], НЕБОЈША М. НЕДИЋ[5] и ДУШАНКА М. МИЛОЈКОВИЋ-ОПСЕНИЦА[2]

[1]Центар за испитивање намирница, Змаја од Ноћаја 11, 11000 Београд, [2]Хемијски факултет, Универзитет у Београду, п. пр. 51, 11158 Београд, [3]Иновациони центар Хемијског факултета у Београду д.о.о., Студентски трг 12–16, 11000 Београд, [4]Биолошки факултет, Универзитет у Београду, Студентски трг 16, 11000 Београд и [5]Пољопривредни факултет, Универзитет у Београду, Немањина 6, 11080 Београд-Земун

Карактеризација полифлоралних медова у погледу минералног састава, садржаја шећера и основних физичко-хемијских параметара извршена је на основу анализе 164

узорка из различитих региона Србије сакупљених током 2009. године. Униваријантна анализа података (дескриптивна статистика и анализа варијансе), заједно са географским информационим системом и мултиваријантном хемометријском анализом (анализа главних компонената и кластерска анализа) примењене су у циљу одређивања географског порекла меда. Утврђено је да су садржај Mg, K и Cu, електрична проводљивост и оптичка ротација параметри који указују на разлике у регионалном пореклу меда. Узорци који потичу из златиборског региона су се јасно раздвојили од узорака из осталих делова Србије на основу већег садржаја K и Mg, као и већих вредности оптичке ротације, електричне проводљивости и слободне киселости. Указано је на утицај састава земљишта, климатских услова и постојања ендемичних врста на састав меда. Моделовање географског порекла меда је урађено применом линеарне дискриминантне анализе.

(Примљено 1. јула, ревидирано 19. септембра 2013)

REFERENCES

1. V. Kaškoniene, P. R. Veskutonis, *Compr. Rev. Food Sci. Food Saf.* **9** (2010) 620
2. L. M. Castro-Várquez, M. C. Díaz-Maroto, C. De Tores, M. S. Pérez-Coello, *Food Res. Int.* **43** (2010) 2335
3. J. M. Camiña, R. G. Pellerano, E. J. Marchevsky, *Curr. Anal. Chem.* **8** (2012) 408
4. K. Ruoff, W. Luginbuhl, R. Kunzli, S. Bogdanov, J. O. Bosset, K. von der Ohe, W. von der Ohe, R. Amado, *J. Agric. Food Chem.* **54** (2006) 6858
5. I. S. Arvanitoyannis, C. Chalhoub, P. Gotsiou, N. Lydakis-Simantiris, P. Kefalas, *Crit. Rev. Food Sci. Nutr.* **45** (2005) 193
6. M. V. Baroni, C. Arrua, M. L. Nores, P. Fayé, M. D. PilarDíaz, G. A. Chiabrando, D. A. Wunderlin, *Food Chem.* **114** (2009) 727
7. M. J. Nozal Nalda, J. L. Bernal Yague, J. C. Diego Calva, M. T. Martýn Gomez, *Anal. Bioanal. Chem.* **382** (2005) 311
8. U. Kropf, J. Bertoncelj, M. Korošec, M. Nečemer, P. Kump, N. Ogrinc, T. Golob, *Apiacta* **44** (2009) 33
9. S. Kečkeš, U. Gašić, T. Ćirković Veličković, D. Milojković-Opsenica, M. Natić, Ž. Tešić, *Food Chem*. **138** (2013) 32
10. P. Pohl, *Trends Anal. Chem.* **28** (2009) 117
11. S. Bogdanov, M. Haldimann, W. Luginbühl, P. Gallmann, *J. Apic. Res. Bee World* **46** (2007) 269.
12. R. G. Pellerano, M. A. Uñates, M. A. Cantarelli, J. M. Camiña, E. J. Marchevsky, *Food Chem.* **13** (2012) 578
13. K. B. Lazarević, F. Andrić, J. Trifković, Ž. Tešić, D. Milojković-Opsenica, *Food Chem.* **132** (2012) 2060
14. Statistical Office of the Republic of Serbia, www.webrzs.stat.gov.rs (22.5.2013)
15. Agriculture in the European Union, Statistical and economic information, 2011, www.eurostat.ec.europa.eu (22.5.2013)
16. The Union of Beekeeping Organizations of Serbia, www.spos.info (22.5.2013) (in Serbian)
17. S. Bogdanov, *Harmonised methods of the international honey commission*. International Honey Commission, internet publication 2002, http://www.apiculturacluj.com/ApiculturaCluj/italiano/Documents/IHCmethods_e.pdf (22.5.2013)
18. L. Persano Oddo, R. Piro, *Apidologie* **35** (2004) S38
19. L. Vela, C. De Lorenzo, R. A. Pérez, *J. Sci. Food Agric.* **87** (2007) 1069
20. G. Šarić, D. Matković, M. Hruškar, N. Vahčić, *Food Technol. Biotechnol.* **46** (2008) 355

21. M. E. Conti, J. Stripeikis, L. Campanella, D. Cucina, M. B. Tudino, *Chem. Cent. J*. 2007, 1:14 http://journal.chemistrycentral.com/content/1/1/14 (22.5.2013)
22. A. Pisani, G. Protano, F. Riccobono, *Food Chem.* **107** (2008) 1553
23. V. Nanda, B. C. Sarkar, H. K. Sharma, A. S. Bawa, *J. Food Compos. Anal.* **16** (2003) 613
24. P. Longley, M. Goodchild, D. Maguire, D. Rhind, *Geographic Information Systems and Science,* Wiley, New York, 2005
25. B. Atanacković, in: *Socialistic Republic of Serbia, Tom I*, NIRO Književne novine, Belgrade, 1982 (in Serbian)
26. V. Stevanović, K. Tan, G. Iatrou, *Plant Syst. Evol.* **242** (2003) 149
27. N. Protić, Lj. Martinović, B. Miličić, D. Stevanović, M. Mojašević, *European Soil Bureau – Research Report No. 9*, 2005, p. 297.

Journal of the Serbian Chemical Society
JSCS-info@shd.org.rs • www.shd.org.rs/JSCS

J. Serb. Chem. Soc. 78 (12) 1893–1909 (2013)
JSCS–4539

UDC 547.416+542.913:678.86:
542.62'18:546.185–034.5
Original scientific paper

3-(Methylamino)propylamine as a templating agent in the synthesis of phosphate-based inorganic polymers

SANJA O. JEVTIĆ[1], NEVENKA Z. RAJIĆ[1] and VENČESLAV V. KAUČIČ[2]*

[1]*University of Belgrade, Faculty of Technology and Metallurgy, Karnegijeva 4, 11000 Belgrade, Serbia and* [2]*National Institute of Chemistry, Hajdrihova 19, 1000 Ljubljana, Slovenia*

(Received 9 October, revised 17 October 2013)

Abstract: 3-(Methylamino)propylamine (MPA) was studied as a structure-directing agent (template) in the synthesis of open-framework phosphate-based materials. The influence of temperature, mole ratio of reactants, crystallization time and presence of fluoride ions on the crystallization of aluminophosphate, transition metal-substituted aluminophosphate (transition metal – Mn(II), Cr(III) and Co(II)) and zincophosphate was also investigated. MPA exhibited a templating role and in all the as-synthesized crystalline products, it is entrapped in an inorganic lattice interacting with the framework *via* hydrogen or/and electrostatic interactions. According to detailed thermal analysis, the type of interactions seems to be crucial for the thermal behavior of MPA and for the thermal stability of the organic–inorganic crystal system. Structural analysis suggested that the formed crystalline structures had no mutual structural analogy. This indicates that the precise role of the organic (guest) component in nucleation process for the open-framework phosphates (host) is very complex as is the nucleation process itself.

Keywords: microporous; aluminophosphates; MAPO; zinc phosphate; open framework.

INTRODUCTION

Phosphate-based inorganic materials are mainly crystalline solids with well-defined crystal structures. The crystal structure is built from tetrahedral phosphate building units that are connected in 1-, 2- or 3-dimensions *via* oxygen atoms to metal oxide units possessing different geometries (tetrahedral, pyramidal or octahedral). The typical metal cation in these materials is aluminum, although zinc and gallium also readily form porous metallophosphates. Metallophoshates typically crystallize from a reactive gel containing inorganic reactants and an organic reactant that plays the role of a structure-directing agent (temp-

* Corresponding author. E-mail: venceslav.kaucic@ki.si
doi: 10.2298/JSC131009113J

late). Usually, different amines and/or quaternary ammonium cations exhibit template ability in the synthesis of metallophosphates.[1] It should be added that the relationship between the template and the crystal type of the formed metallophosphate has not yet been well established.[1] It is known that the organic template itself is not the sole factor involved in the structure-directing role. Namely, various other parameters also influence the crystallization process, such as the source of the inorganic components, pH, conditions of crystallization, *etc*. However, the presence of organic species in the crystallization process is crucial. Without the organics, a metallophosphate cannot be formed.

The template species remain after crystallization in the lattice pores and their removal from the channels and cages is necessary in order to achieve lattice porosity.[2] The removal of the template is performed by a thermal treatment (calcination), usually in an air atmosphere at about 500 °C. The calcined product usually possesses molecular sieving, catalytic and/or adsorptive properties.[3,4]

Moreover, in order to obtain novel materials with catalytic properties for specific reaction systems, as well as to obtain materials of desired selectivity, various investigations were directed towards transition metal substituted aluminophosphates.[5] Incorporation of transition metal cations in an aluminophosphate lattice at the aluminum or phosphorous crystallographic sites brings a charge into neutral aluminophosphate skeleton and greatly affects its catalytic and adsorptive properties. In addition, the use of fluoride ions in the synthesis of porous aluminophosphates led to the emergence of novel and zeolite-like aluminophosphate structures. As an example, an open-framework aluminophosphate with a chabazite structure can be obtained only if fluoride ions are present in the reactive gel.[6]

Different organic species were studied as templates in the synthesis of porous phosphates. For some of them (such as di-*n*-propylamine), a structural specifity is conspicuous: di-*n*-propylamine directs the crystallization of different framework structures by slightly changing the synthesis parameters. On the other hand, the formation of one structure type ($AlPO_4$–5) can be realized using more than twenty different amines and quaternary amine cations.[1]

In this work, the structure-directing role of one simple amine, 3-(methylamino)propylamine (MPA), which has not been studied so far in the synthesis of open-framework phosphates, was investigated. The influence of temperature, mole ratio of reactants, crystallization time and the presence of fluoride in the crystallization of several metallophosphate was examined using MPA as a template. Moreover, crystallization under two heating regimes, hydrothermal and microwave heating, was studied.

EXPERIMENTAL

Preparation of fluoride-free reaction mixtures

Aluminophosphates, zincophosphates and transition metal-substituted aluminophosphates were obtained under hydrothermal conditions using the mole ratio of the reactants

given in Table I. The sources of zinc, aluminum, cobalt(II) and chromium (III) were $Zn(CH_3COO)_2 \cdot 2H_2O$ (Fluka), $Al(OH)_3$ (Sigma-Aldrich), $Co(CH_3COO)_2 \cdot 4H_2O$ (Sigma-Aldrich), $Mn(CH_3COO)_2 \cdot 4H_2O$ (Sigma-Aldrich) and CrO_3 (Fluka), respectively. To enhance the chromium reactivity, chromium(III) was obtained *in situ* by reduction of CrO_3 using ethanol (Sigma-Aldrich).[7] Orthophosphoric acid, H_3PO_4 (85 wt. % Sigma-Aldrich), was used as the phosphorous source. MPA was used as a 98 wt. % solution (Sigma-Aldrich).

TABLE I. Composition of the reaction mixtures and the crystallization conditions

Product	Composition of the reaction mixture	Crystallization time, days	Crystallization temperature, °C	Crystalline phase
ZnPO-A	$ZnO:2.75P_2O_5:2MPA:100H_2O$	6–12	120	Hopeite
		6	160	Novel phase
ZnPO-B	$ZnO:1.5P_2O_5:2MPA:100H_2O$	6	120	Novel phase
		2–6	160	Novel phase
AlPO	$0.5Al_2O_3:0.5P_2O_5:0.5MPA:$ $:100H_2O$	7–10	160	$AlPO_4$-21
CoAPO	$0.4Al_2O_3:0.2CoO:0.5P_2O_5:$ $:0.5MPA:100H_2O$	6–10	160	CoAPO-21
CrAPO	$0.4Al_2O_3:0.1Cr_2O_3:0.5P_2O_5:$ $:0.5MPA:100H_2O$	7–10	190	CrAPO-21
MnAPO	$0.4Al_2O_3:0.2MnO:0.5P_2O_5:$ $:0.5MPA:100H_2O$	4–7	190	MnAPO-12

Reaction gels were prepared by intensive stirring of the reactants using an ULTRA--TURRAX®, IKA® T18 stirrer. The synthesis proceeds in several steps. First, an aqueous suspension of metal salts or $Al(OH)_3$ and 85 wt. % H_3PO_4 was prepared by vigorous stirring. The obtained mixture was stirred until homogeneity (about 30 min) and finally, MPA was added dropwise. The resulting gel was intensively stirred for another 30 min and then transferred into a Teflon-lined stainless steel autoclave and left to crystallize at 160–190 °C in an oven or under microwave radiation (Milestone, Ethos TC).

Preparation of fluoride-containing reaction mixtures

Fluoride-containing reactive mixtures were prepared in a manner similar to that described above. Hydrofluoric acid (40 wt. %, Fluka) was used as the source of fluoride and it was added in the first step of the reactive mixture preparation. The employed mole ratios of the reactants are given in Table II.

Characterization

The crystallinty of the products was studied by XRD analysis using a PANalytical X'Pert PRO diffractometer and CuK_α radiation. The data obtained at room temperature were collected in the 2θ range from 5 to 75° in steps of 0.017° with a total measurement time of 4 h. The high temperature X-ray diffraction (HTXRD) patterns were recorded at four different temperatures, *i.e.*, room temperature and at 573, 623 and 673 K.

The size and morphology of the crystals as well as the elemental analyses were studied by a scanning electron microscope Zeiss Supra 35VP. Carbon, hydrogen and nitrogen were determined using a standard C–H–N analyzer. Fourier transformed infrared (FTIR) spectra were recorded in the 4000 to 400 cm^{-1} range on a Digilab-FTS-80 spectrophotometer, using the KBr wafer technique. Thermal decomposition was performed using an SDT Q-600 simul-

taneous DSC–TGA instrument (TA Instruments). The samples (mass ≈10 mg) were heated in standard alumina 90-µl sample pans. All experiments were performed under synthetic air at a flow rate of 0.1 dm^3 min^{-1}.

TABLE II. Composition of the fluoride-containing reaction mixtures

Product	Composition of the reaction mixture	Crystallization time, days	Crystallization temperature, °C	Crystalline phase
APOF	$0.5Al_2O_3$:$0.5P_2O_5$:0.5MPA:1HF: :$100H_2O$	4–7	160	ULM-3
CoAPOF	$0.4Al_2O_3$:0.2CoO:$0.5P_2O_5$: :0.5MPA:1HF:$100H_2O$	4–7	160	ULM-3 and amorphous solids
CrAPOF	$0.4Al_2O_3$:$0.1Cr_2O_3$:$0.5P_2O_5$: :0.5MPA:1HF:$100H_2O$	4–7	160	ULM-3 and amorphous solids
MnAPOF	$0.4Al_2O_3$:0.2MnO:$0.5P_2O_5$: :0.5MPA:1HF:$100H_2O$	4–7	130	Mixture different crystalline phases
		4–7	160	Mixture different crystalline phases

RESULTS AND DISCUSSION

SEM analysis of the obtained products

The use of MPA yielded crystalline products with different morphologies depending on the crystallization conditions and composition of reactive mixtures. The SEM photographs of the products obtained by hydrothermal crystallization are shown in Fig. 1. The crystals appear as monocrystals or crystalline aggregates. Microwave-assisted heating yielded crystalline products mainly in the form of aggregates (not shown).

ZnPO, AlPO, CrAPO, CoAPO and CoAPOF were plate-like crystals of about 100–140 µm in length. APOF and MnAPOF crystallized as ball aggregates of about 50 µm in diameter. On closer inspection of the aggregates, it could be seen that they were in the form of plate conglomerates. CrAPOF appeared in the form of irregular aggregates of about 200 µm in length.

Structural analysis of the products obtained under hydrothermal conditions from fluoride-free reaction mixtures

Zincophosphates. For the preparation of the ZnPO products, two reaction mixtures (A and B) were found to be optimal in order to obtain crystalline products. Depending on the crystallization temperature, mixture A (with the Zn/P molar ratio of 1/5) yielded two crystalline phases: a dense $ZnPO_4$ phase – hopeite

(at 120 °C) and a novel crystalline product at 160 °C. From mixture B (with the Zn/P molar ratio of 1/3), the same novel phase was formed at both temperatures. Its XRD pattern is given in Fig. 2.

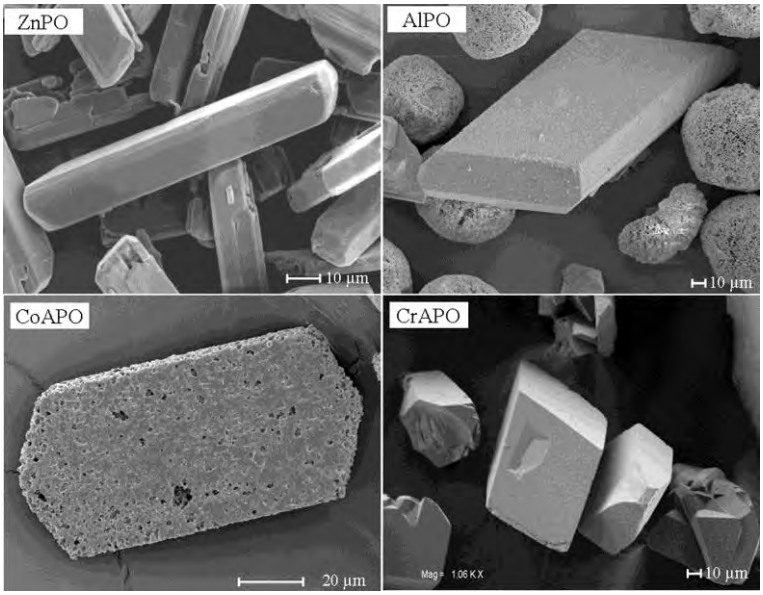

(a)

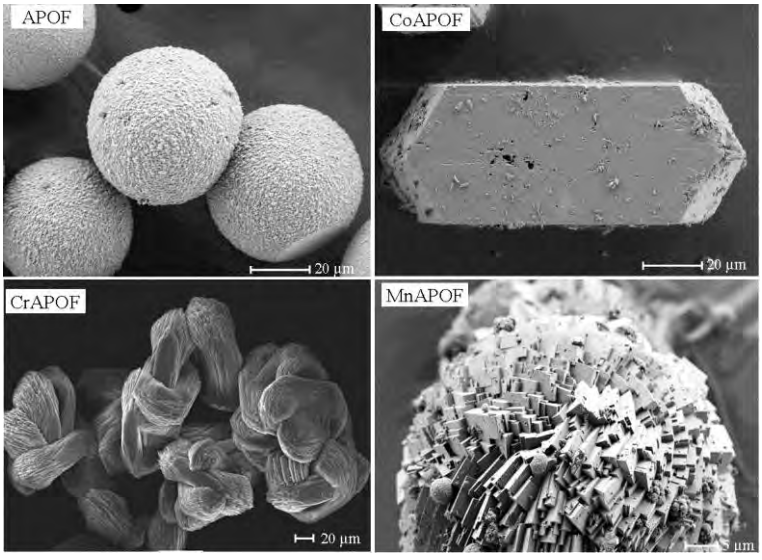

(b)

Fig. 1. SEM photograph of a) metallophosphates obtained under hydrothermal crystallization and b) the products obtained from fluoride-containing reactive mixtures.

Single crystal structure determination of the novel zincophosphate phase showed that the zincophosphate was built of macro-anionic $[Zn_2(PO_4)(HPO_4)(H_2PO_4)]^{2-}$ layers, which were intercalated by doubly protonated MPA cations (Fig. 3). The layers were built of ZnO_4 and $PO_4/HPO_4/H_2PO_4$ tetrahedra. Within the layers, small channels of an approximate diameter 3.7 Å were present. The inorganic framework and MPA interact *via* the template-to-framework N—H···O hydrogen bonds, which are important for stabilization of the structure.[8,9]

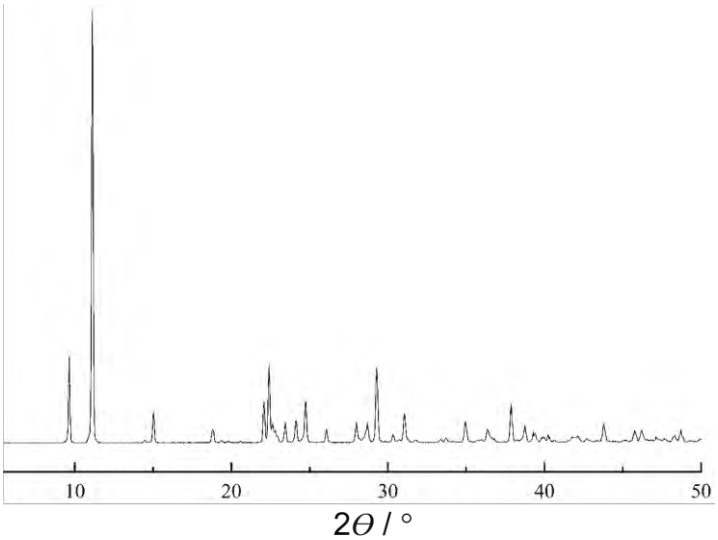

Fig. 2. XRD pattern of the novel zincophosphate phase.

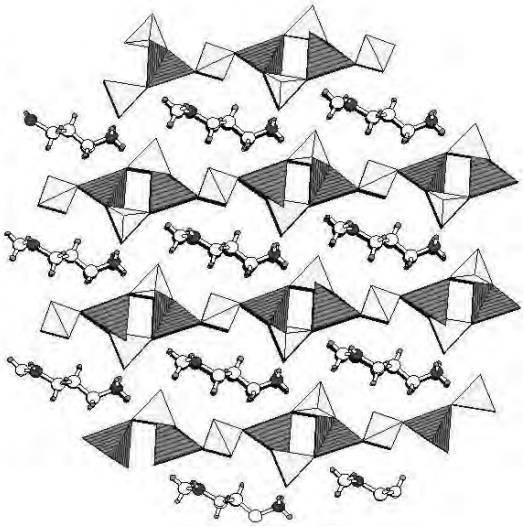

Fig. 3. A view of the novel zincophosphate, showing zincophosphate layers (dark gray tetrahedra – ZnO_4, light gray tetrahedra – phosphate building units) and intercalated doubly protonated MPA cations.

Aluminophosphates and metal-substituted aluminophosphates. Two types of reaction mixtures were studied: 1) the reaction mixture containing an alumino-phosphate and 2) the reaction mixture containing an aluminophosphate and some transition metal ions. Crystallization of both types of mixtures yielded crystalline products with the aluminophosphate topology denoted as the structure type 21.[10] Representative XRD patterns are given in Fig. 4. Hitherto, three different amines

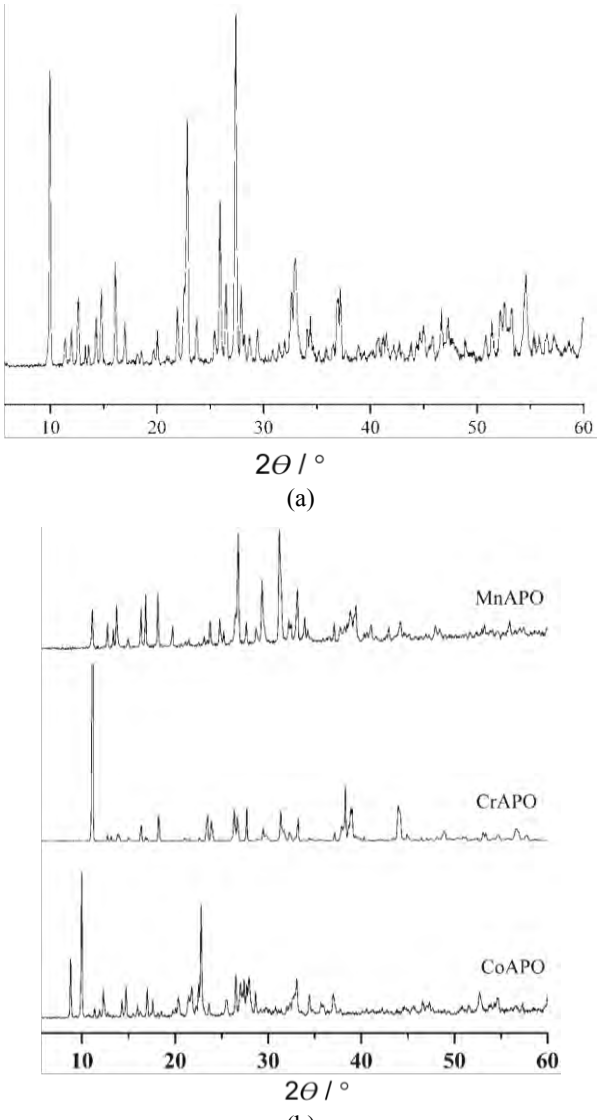

Fig. 4. XRD patterns of a) $AlPO_4$-21 and b) the metal-containing aluminophosphates [MAPO, M = Co(II), Cr(III), Mn(II)].

have been reported as templates for $AlPO_4$-21: 1,2-diaminopropane, pyrrolidine[11] and *N*,*N*,*N*′,*N*′-tetramethyl-1,3-diaminopropane.[10] X-ray single crystal structure analysis of the aluminophosphate product showed that the $AlPO_4$-21 framework was built of corrugated aluminophosphates sheets, which were cross-linked by Al–O–P chains to form a network of straight eight-membered-ring channels extending along the *c* crystallographic axis. The MPA appeared to be disordered and positioned in the eight-membered-ring channels. It was held within the channels through strong hydrogen bonds: MPA forms two such bonds, the N···O distances being 2.914 and 2.985 Å.[12]

From the transition metal-containing aluminophosphate reaction mixtures, different crystalline products (MAPO) were obtained depending on the type of the transition metal cation (Table I). The XRD patterns (Fig. 4) revealed that from the Co(II)- and Cr(III)-containing mixtures, CoAPO and CrAPO products belonging to the structure type 21 crystallized, whereas the MnAPO obtained from the Mn(II)-containing reaction mixture belonged to the structural type 12.[13] The lattice of $AlPO_4$-12 is rather complex and is based on an interrupted net in which one of the P atoms is linked to only 3 Al atoms and one of the Al atoms is linked to only 3 P atoms.

The results of elemental analysis of the obtained products are given in Table III. It is evident that the metal content depended on the metal type, indicating that not only MPA but also transition metal cations influence the crystallization process. Moreover, the preparation of the transition metal-substituted aluminophosphates (MAPOs) is important considering their catalytic application.[1] In a MAPO crystalline lattice, transition metal ions generally occupy aluminum crystallographic sites, thereby generating different types of acid sites (Brønsted or Lewis) important for catalytic activity. Based on the results of the elemental analyses, it could be concluded that Co(II), Cr(III) and Mn(II) substitute aluminum in the parent aluminophosphate lattice. The (Al+M)/P molar ratio is approximately one in all the prepared samples.

TABLE III. Results of the energy-dispersive x-ray spectroscopy (EDS) analysis

Sample	Zn	Al	P	Co	Cr	Mn
ZnPO	25.9	–	16.6	–	–	–
AlPO	–	16.8	19.3	–	–	–
CoAPO	–	15.8	20.6	3.1	–	–
CrAPO	–	22.1	26.4	–	1.0	–
MnAPO	–	18.1	24.2	–	–	6.8

Microwave-assisted heating. In order to study the influence of microwave radiation on the crystallization of the investigated reaction mixtures, microwave-assisted heating was also employed. Namely, it has been reported that the micro-

wave technique enables a more rapid crystallization than the conventional hydrothermal method and leads to an improved crystal quality.[14]

Microwave radiation showed differing effects on the studied reaction systems. Crystallization of the novel ZnPO and $AlPO_4$-21 proceeded more rapidly under microwave-assisted heating: the crystalline products formed in the course of 2 h. However, for the MAPO products, the microwave radiation had a negative effect on the crystallization. For all the studied transition metal-containing reaction mixtures, no crystalline products were obtained.

Structural analysis of the products obtained under hydrothermal conditions from fluoride-containing reaction mixtures

Taking into account that the presence of fluoride ions in an aluminophosphate reaction mixture could lead to novel structures,[15] experiments with MPA in a fluoride-containing medium were performed. It is known that aluminum ions readily form complex species with fluoride ions, which increases the solubility of the aluminum source and accordingly influences the crystallization process. In the fluorinated aluminophosphate structures, the fluorine atoms usually bridge the aluminum-building units and typically occupy one or two vertices of the aluminum octahedral.[16]

The presence of fluoride in the aluminophosphate reaction mixture led to the formation of a crystalline product (APOF), the diffractogram (given in Fig. 5a) of which corresponded to that of the open-framework gallophosphate ULM-3.[17,18]

The single crystal X-ray structure analysis revealed an open-framework built up of hexa-nuclear units formed by three PO_4 tetrahedra, two AlO_4F trigonal bipyramids and one AlO_4F_2 octahedron. The three-dimensional framework was negatively charged and had two interconnected channel systems: 10-membered-ring channels running along the [101] direction and 8-membered-ring channels running along the [10-1] direction. The negative charge is compensated by doubly protonated MPA located in the 10-membered-ring channels (Fig. 6).[19]

The XRD patterns of CoAPOF and CrAPOF also showed the presence of the ULM-3 crystalline phase (Fig. 5b). However, a detailed EDS analysis did not confirm the presence of Co(II)- or Cr(III)-substituted products in the crystals found in the obtained products. It seems that the transition metal cations only contribute to nucleation of single crystals of the fluorinated aluminophosphate and do not become a part of the framework. Namely, the fluorinated aluminophosphate obtained from the Co(II)- and Cr(III)-free mixture appeared in the form of ball aggregates, in contrast to the single crystals formed in the presence of the metals (Fig. 1). The MnAPOF product seems to have consisted of different crystalline phases for which no structural analogs have been found.

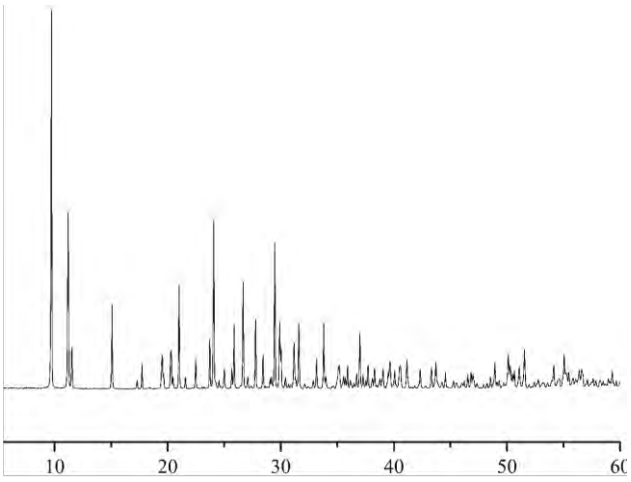

(a)

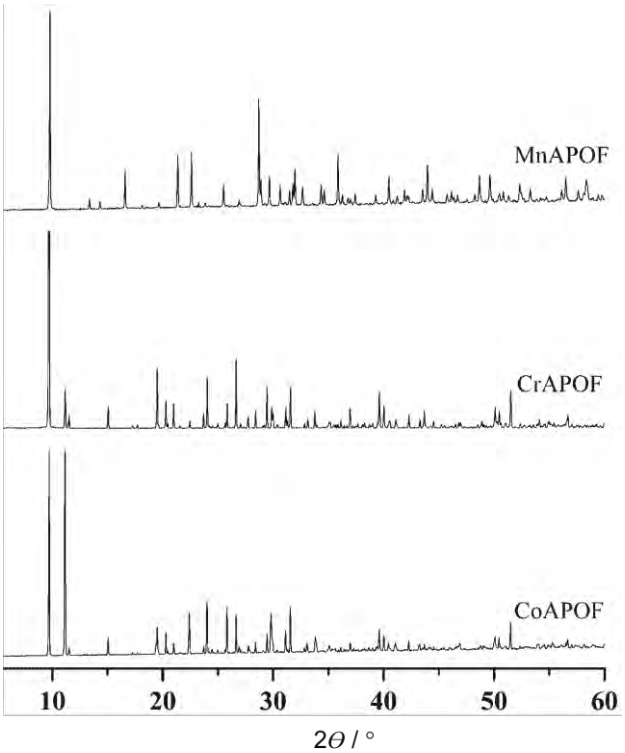

(b)

Fig. 5. XRD patterns of (a) the fluorinated aluminophosphate product (APOF) and (b) Co(II)-, Cr(III)- and Mn(II)-containing fluorinated aluminophosphates (CoAPOF, CrAPOF and MnAPOF, respectively).

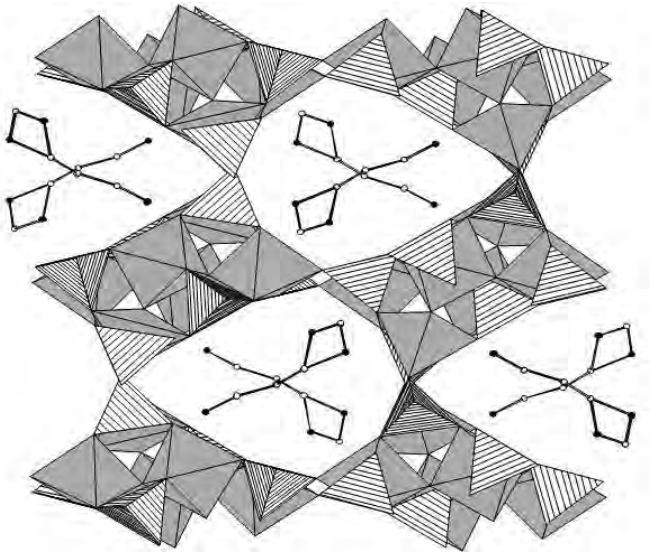

Fig. 6. Protonated MPA species in the 10-membered-ring channel of the fluorinated aluminophosphate framework.

Study of the organic/inorganic interactions

FTIR analysis. Figure 7 shows the FTIR spectra of the ZnPO, $AlPO_4$-21, CoAPO-21 and the fluorinated aluminophosphate (APOF). All the samples displayed vibrations that clearly show the vibrational features of the entrapped orga-

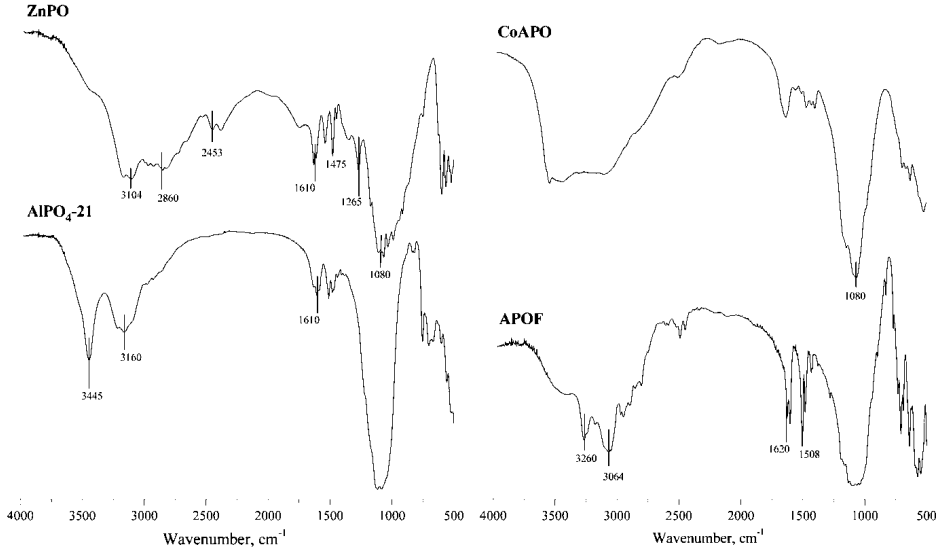

Fig. 7. FTIR spectra of the novel zincophosphate (ZnPO), $AlPO_4$-21, Co(II)-containing $AlPO_4$-21 (CoAPO-21) and the fluorinated aluminophosphate (APOF).

nic species. Vibrations displayed in the range 3200–2000 cm^{-1} correspond to amine groups,[20] and the bands appearing in the 1600–1350 cm^{-1} region are due to C–H bonds[21]. Strong bands at 3450 and 1620 cm^{-1} can be attributed to the water molecules present in the crystalline lattice.[22] All spectra except that of $AlPO_4$-21 display a strong band at about 1540 cm^{-1} which is attributed to NH_3^+, suggesting that the MPA species was protonated,[8] while the inorganic frameworks of ZnPO, CoAPO-21 and APOF were negatively charged.

TGA/DTG studies. To gain an insight into the strength of the organic/inorganic interactions, the thermal behavior of ZnPO, $AlPO_4$-21, MAPO-21 (M = Co(II), Cr(III), Mn(II)) and APOF were studied. The obtained results are shown in Fig. 8. All the samples exhibit a strong DTG maximum that could be attributed to the decomposition of MPA, according to the corresponding mass loss and the results of C–H–N analysis. The position of the maximum differs with the type of solid. This indicates that the entrapped MPA interacts in different ways with the inorganic frameworks. This was confirmed by detailed kinetics analyses.[8,12] Thus, MPA entrapped in ZnPO decomposes in a three-step process with the first step having the highest activation energy (343 kJ mol^{-1}). This is attributed to the strong hydrogen bonds and to electrostatic bonds, which hold the protonated MPA and zincophosphate layers together. The decomposition of MPA in $AlPO_4$--21 proceeded in a single-step reaction, with the activation energy lying in the range 173–151 kJ mol^{-1}.[12] In this solid, MPA interacts with the aluminophosphate framework only *via* hydrogen bonds. The MPA decomposition in APOF was a multi-step reaction with an average activation energy of 209 kJ mol^{-1}. In this solid, the anionic fluoro-aluminophosphate framework interacts with doubly protonated MPA *via* hydrogen and electrostatic bonds.[23]

The crystallinity of the calcined products was investigated by high temperature X-ray diffraction analysis. The patterns of $AlPO_4$-21 and APOF, being representative, are presented in Fig. 9. As can be seen, the decomposition of the MPA in $AlPO_4$-21 (as well as in MAPO-21) resulted in a crystal structure transformation. The XRD patterns of calcined $AlPO_4$-21 and MAPO-21 entirely corresponded to the aluminophosphate of structure type 25.[24] The decomposition of MPA in APOF resulted in a gradual loss of crystallinity and the formation of a dense trydimite aluminum phosphate. Similarly, ZnPO lost crystallinity during the decomposition of MPA and was converted into the dense hoppeite zinc phosphate (not shown).

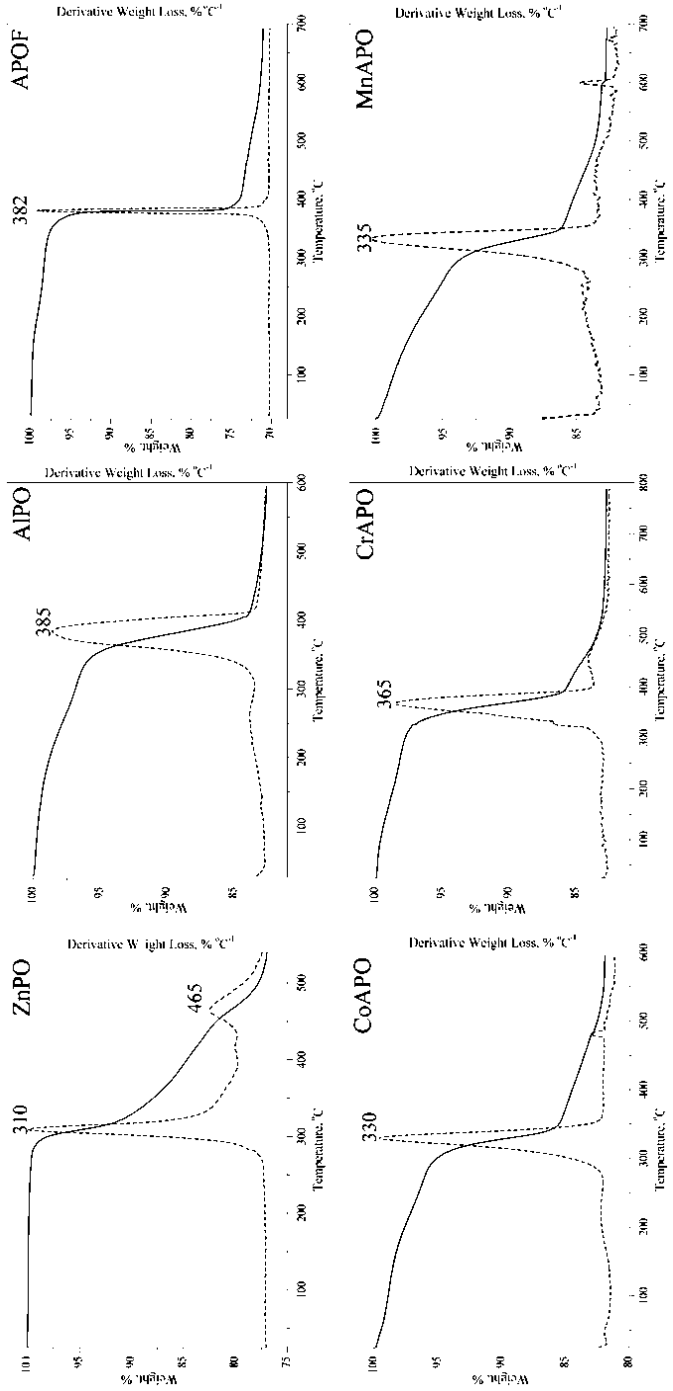

Fig. 8. TG and DTG curves of the novel zincophosphate (ZnPO), $AlPO_4$-21, the fluorinated aluminophosphate and Co(II)-, Cr(III)- and Mn(II)-containing aluminophosphates (CoAPO, CrAPO and MnAPO, respectively).

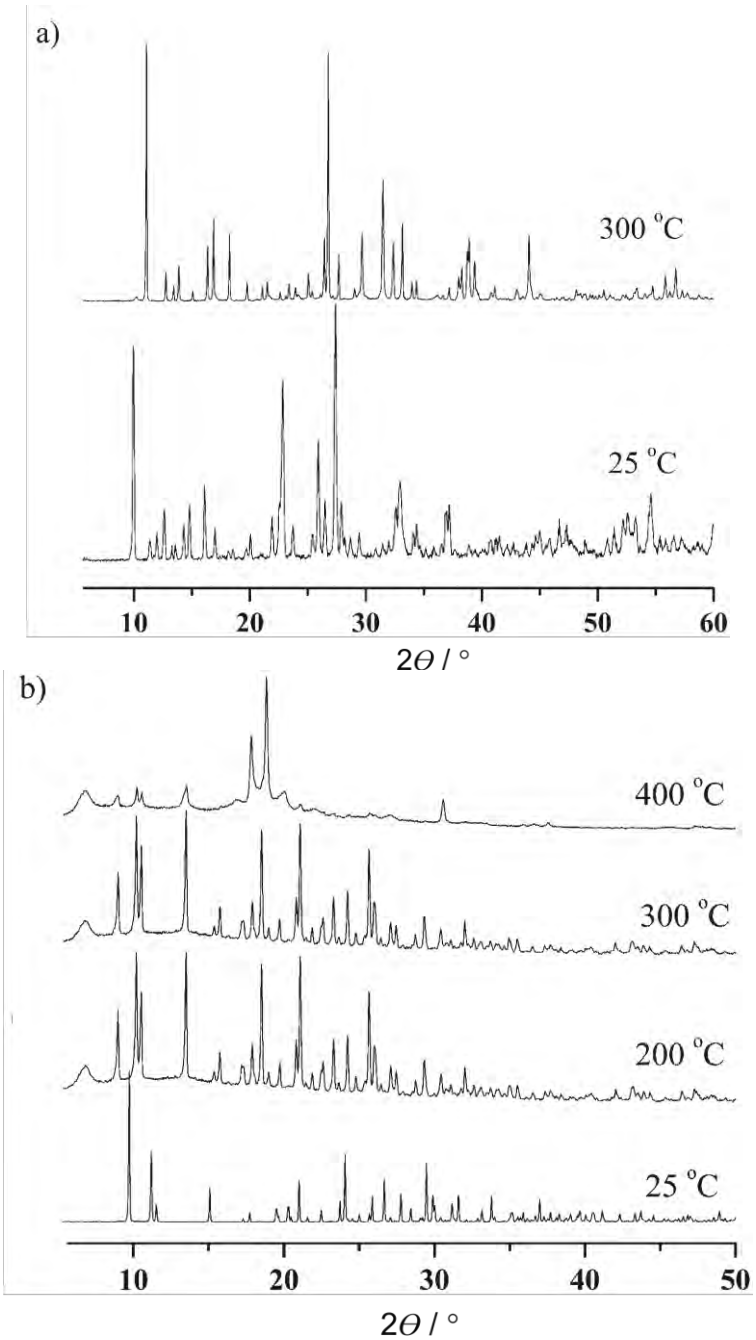

Fig. 9. The high temperature XRD patterns of a) $AlPO_4$-21 and b) the fluorinated aluminophosphate (APOF).

CONCLUSIONS

The results show that MPA, which has not been hitherto studied, as the structure-directing agent in the synthesis of open-framework phosphate-based materials played a structure-directing role. The presence of the diamine in a zinc phosphate reaction mixture led to crystallization of a layered zincophosphate with a novel structure. The layered zincophosphate crystallized not only under hydrothermal but also under microwave conditions. The microwave-assisted heating significantly decreases the crystallization time from 10 days to 2 h.

MPA has also the templating role in two types of reaction mixtures: 1) consisting of an aluminophosphate and 2) consisting of aluminophosphate and transition metal cations (Co(II), Cr(III) and Mn(II)). From mixture 1) and reaction mixture 2) containing Co and Cr, the same crystalline phase formed, corresponding to aluminophosphate of the structure type 21. From the Mn-containing mixture, a crystalline material of structure type 12 was obtained. This indicates that not only 3-(methylamino)propylamine, but also the type of the transition metal cation influenced the nucleation process. Microwave-assisted heating can also significantly decrease the crystallization time.

MPA exhibits the templating role in the fluoride-containing reaction mixtures. From an aluminophosphate reaction mixture, an open-framework aluminophosphate forms, having the structure of the gallophosphate ULM-3. The product from this reaction system is also a confirmation that not only the organic species but also the fluoride and transition metal ions affect the nucleation process. The presence of Co(II), Cr(III) and Mn(II) in fluoride-containing reaction mixtures resulted in either the formation of several unknown crystalline phases (Cr and Mn) or the fluorinated aluminophosphate with a ULM-3 structure.

In all obtained crystalline products, MPA was entrapped in the inorganic lattice interacting with the host framework *via* hydrogen and/or electrostatic interactions. The type of interactions affected not only its thermal stability but also the thermal stability of the organic–inorganic system. Finally, the formed structures have no mutual structural analogy, suggesting complexity of the nucleation process for the open-framework phosphates as well as complexity regarding the precise role of the organic (guest) component.

Acknowledgements. This work was supported by the Ministry of Education, Science and Technological Development of the Republic of Serbia (Project No. 172018) and by the Slovenian Research Agency (Program P1-0021).

ИЗВОД

3-(МЕТИЛАМИНО)ПРОПИЛАМИН КАО СТРУКТУРНИ АГЕНС У СИНТЕЗИ НЕОРГАНСКИХ ПОЛИМЕРА НА БАЗИ ФОСФАТА

САЊА О. ЈЕВТИЋ[1], НЕВЕНКА З. РАЈИЋ[1] и VENČESLAV V. KAUČIČ[2]

[1]*Универзитет у Београду, Технолошко–металуршки факултет, Карнегијева 4, 11000 Београд и* [2]*National Institute of Chemistry, Hajdrihova 19, 1000 Ljubljana, Slovenia*

3-(Метламино)пропиламин (МПА) изучаван је као структурни агенс (темплат) у синтези порозних материјала на бази фосфата. Утицај температуре, молског односа реактаната, времена и присуства флуорид-јона на кристализацију алумофосфата, алумофосфата који у решетки садрже јоне прелазних елемената (прелазни елемент – Mn(II), Cr(III) и Co(II)) такође су изучавани. МПА испољава својства темплата и у свим синтетисаним кристалним производима заробљен је у неорганској решетки са којом остварује водоничне и/или електростатичке интеракције. Према детаљној термичкој анализи врста интеракција је од пресудног значаја за термичка својства МПА као и термичку стабилност читавог органско-неорганског кристалног система. Структурна анализа је указала да међу насталим кристалним структурама нема сличности. Ово указује да је улога органске („гостујуће“) компоненте у процесу нуклеације порозних фосфата сложена као и сам процес нуклеације.

(Примљено 9. октобра, ревидирано 17. октобра 2013)

REFERENCES

1. N. Rajić, V. Kaučič, *Molecular sieves: Aluminophosphates*, in *Encyclopedia of Catalysis*, Vol. 5, I. T. Horvath, Ed., Wiley, Hoboken, NJ, 2003, p. 189
2. H. O. Pastore, S. Coluccia, L. Marchese, *Annu. Rev. Mater. Res.* **35** (2005) 351
3. N. Rajić, *J. Serb. Chem. Soc*. **70** (2005) 371
4. N. L. Rosi, J. Eckert, M. Eddaoudi, D. T. Vodak, J. Kim, M. O'Keeffe, O. M. Yaghi, *Science* **300** (2003) 1127
5. M. Hartmann, L. Kevan, *Chem. Rev.* **99** (1999) 635
6. J. L. Guth, H. Kessler, R. Wey, *Stud. Surf. Sci. Catal.* **28** (1986) 121
7. N. Rajić, Đ. Stojaković, S. Hočevar, V. Kaučić, *Zeolites* **13** (1993) 384
8. N. Rajić, N. Zabukovec-Logar, Đ. Stojaković, S. Šajić, A. Golobič, V. Kaučić, *J. Serb. Chem. Soc.* **70** (2005) 625
9. N. Zabukovec-Logar, G. Mali, N. Rajić, S. Jevtić, M. Rangus, A. Golobic, V. Kaučić, *Acta Crystallogr., E* **61** (2005) m1354
10. J. M. Bennett, J. M. Cohen, G. Artioli, J. J. Pluth, J. V. Smith, *Inorg. Chem*. **24** (1985) 188
11. J. B. Parise, C. S. Day, *Acta Crystallogr., C* **41** (1985) 515
12. Đ. Stojaković, N. Rajić, S. Šajić, N. Zabukovec-Logar, V. Kaučić, *J. Therm. Anal. Calorim.* **87** (2007) 337
13. J. M. Bennett, W. J. Dytrych, J. J. Pluth, J. W. Richardson Jr., J. V. Smith, *Zeolites* **6** (1986) 349
14. G. A. Tompsett, W. C. Conner, K. S. Yngvesson, *Chem. Phys. Chem*. **7** (2006) 296
15. W. Yan, J. Yu, Z. Shi, Y. Wang, Y. Zou, R. Xu, *J. Solid State Chem*. **161** (2001) 259
16. T. Loiseau, R. Walton, R. Francis, D. O'Hare, G. Ferey, *J. Fluorine Chem*. **101** (2000) 181
17. J. Renaudin, T. Loiseau, F. Taulelle, G. Ferey, *C. R. Acad. Sci. Paris Ser. IIb* **323** (1996) 545

18. T. Loiseau, R. Retoux, P. Lacorre, G. Ferey, *J. Solid State Chem.* **111** (1994) 427
19. N. Zabukovec-Logar, N. Rajić, Đ. Stojaković, S. Šajić, A. Golobič, V. Kaučič, *J. Solid State Chem.* **183** (2010) 1055
20. N. Rajic, N. Zabukovec-Logar, A. Golobic, V. Kaucic, *J. Phys. Chem. Solids* **64** (2003) 1097
21. A. John, D. Philip, K. R. Morgan, S. Devanarayanan, *Spectrochim. Acta, A* **56** (2000) 2715
22. T. L. Tarbuck, S. T. Ota, G. L. Richmond, *J. Am. Chem. Soc.* **128** (2006) 14519
23. N. Rajic, Đ. Stojakovic, S. Jevtic, N. Zabukovec-Logar, G. Mali, V. Kaucic, *J. Therm. Anal. Calorim.* **101** (2010) 919
24. R. Jelinek, B. F. Chmelka, Y. Wu, P. J. Grandinetti, A. Pines, P. J. Barrie, K. Klinowski, *J. Am. Chem. Soc.* **113** (1991) 4097.

Journal of the Serbian Chemical Society
JSCS-info@shd.org.rs • www.shd.org.rs/JSCS

J. Serb. Chem. Soc. *78* (12) 1911–1924 (2013)
JSCS–4540

UDC 546.593+547.78+547.466.1+
543.422.25+543.552:576+615.9
Original scientific paper

Solution study under physiological conditions and cytotoxic activity of gold(III) complexes with L-histidine-containing peptides

BILJANA Đ. GLIŠIĆ[1], ZORKA D. STANIĆ[1#], SNEŽANA RAJKOVIĆ[1], VESNA KOJIĆ[2], GORDANA BOGDANOVIĆ[2] and MILOŠ I. DJURAN[1]*

[1]*Department of Chemistry, Faculty of Science, University of Kragujevac, R. Domanovića 12, 34000 Kragujevac, Serbia and* [2]*Oncology Institute of Vojvodina, Institutski put 4, 21204 Sremska Kamenica, Serbia*

(Received 20 September 2013)

Abstract: Proton NMR spectroscopy and cyclic voltammetry were applied to study the stability of three gold(III) complexes with L-histidine-containing peptides, [Au(Gly–L-His–*N*,*N*′,*N*″)Cl]$NO_3 \cdot 1.25H_2O$ (**Au1**), [Au(L-Ala–L-His––*N*,*N*′,*N*″)Cl]$NO_3 \cdot 2.5H_2O$ (**Au2**) and [Au(Gly–Gly–L-His–*N*,*N*′,*N*″,*N*‴)]$Cl \cdot H_2O$ (**Au3**) under physiologically relevant conditions. It was found that tridentate coordination of Gly–L-His and L-Ala–L-His dipeptides, as well as tetradentate coordination of Gly–Gly–L-His tripeptide in **Au1**, **Au2** and **Au3** complexes, respectively, stabilized +3 oxidation state of gold and prevented its reduction to Au(I) and Au(0). No release of the coordinated peptides from Au(III) was observed under these experimental conditions. Considering the remarkable stability of the **Au1**, **Au2** and **Au3** complexes, their cytotoxic activity was evaluated by the MTT (3-(4,5-dimethylthiazol-2-yl)-2,5-diphenyltetrazolium bromide) assay toward five human tumor cell lines, MCF-7 (human breast adenocarcinoma), HT-29 (human colon adenocarcinoma), HeLa (human cervix carcinoma), HL-60 (human promyelocytic leukemia), Raji (human Burkitt's lymphoma) and one human normal cell line MRC-5 (human fetal lung fibroblasts). While the cytotoxic activity of **Au1**, **Au2** and **Au3** against investigated human malignant cell lines was strongly cell line dependent, none of these complexes was cytotoxic against normal MRC-5 cell line. This study can contribute to the future development of gold(III)–peptide complexes as potential antitumor agents.

Keywords: gold(III) complexes; L-histidine-containing peptides; ^{1}H-NMR spectroscopy; cyclic voltammetry; cytotoxic activity.

* Corresponding author. E-mail: djuran@kg.ac.rs
# Serbian Chemical Society member.
doi: 10.2298/JSC130920105G

INTRODUCTION

Platinum(II) complexes are the most widely used drugs for cancer treatment.[1] However, due to the cross-resistance and severe toxicity, ongoing efforts are aimed at finding novel metal-based drugs that would exhibit comparable or even greater antitumor activity and overcome toxic-side effects produced by platinum(II) complexes.[1] In this context, during the last decades, special attention was devoted to the synthesis and biological evaluation of gold(III) complexes as potential antitumor agents.[2] The initial interest for gold(III) complexes was based on their chemical features, very similar to those of clinically approved platinum(II) complexes, such as square-planar geometry and d^8 electronic configuration of the corresponding metal ion. However, the high reduction potential and fast rate of hydrolysis of Au(III) complexes under physiologically relevant conditions hindered their possible application in medicine.[3] Despite that, stability of the Au(III) ion has been achieved by an appropriate choice of the ligands, in most cases containing nitrogen donor atoms.[4–16] Thus, different polydentate ligands, such as polyamines, bipyridine, terpyridine, phenanthroline, macrocyclic ligands (cyclam), porphyrins and dithiocarbamates, have been used and a number of mononuclear and dinuclear gold(III) complexes have been synthesized that show remarkable stability under physiologically relevant conditions.[4–16] Some of these complexes displayed *in vitro* cytotoxicity comparable or even greater than that of cisplatin toward different human tumor cell lines, but only a few have been proved to be antitumor active *in vivo*.[17–19] Peptides containing the amino acid histidine in the side chain have also been shown to be good chelating agents, being able to coordinate and stabilize the Au(III) ion.[20–22] Although the reactions of gold(III) ion with L-histidine-containing peptides have been extensively investigated,[23] only a few gold(III)–peptide complexes were synthesized and characterized by application of X-ray crystallography: those of glycyl–L-histidine (Gly–L-His), [Au(Gly–L-His–*N*,*N*′,*N*″)Cl]Cl·3H_2O,[20] [Au(Gly–L-His–*N*,*N*′,*N*″)Cl]NO_3·1.25H_2O,[21] [Au(Gly–L-His–*N*,*N*′,*N*″)Cl)]NO_3[21] and [Au(Gly–L-His–*N*,*N*′,*N*″,*N*‴)]$_4$·10H_2O,[20] that of the dipeptide L-alanyl–L-histidine (L-Ala–L-His), [Au(L-Ala–L-His–*N*,*N*′,*N*″)Cl]NO_3·2.5H_2O[21] and of the tripeptide glycyl–glycyl–L-histidine (Gly–Gly–L-His), [Au(Gly–Gly–L-His–*N*,*N*′,*N*″,*N*‴)]Cl·H_2O.[22] However, data related to the biological evaluation of the above mentioned complexes are rather scarce. Hitherto, only the gold(III) complex with Gly–L-His dipeptide has been evaluated toward A2780 human ovarian carcinoma cell line.[24] The results from this investigation showed that the Gly–L-His–Au(III) complex manifested a far higher cytotoxic activity than its Zn(II), Pd(II), Pt(II) and Co(II) analogues, proving that the Au(III) center plays a crucial role in determining pharmacological effects.[24]

The promising cytotoxic activity of the Gly–L-His–Au(III) complex encouraged further investigation of the biological activity of gold(III) complexes

with different histidine-containing peptides. Hence, the present paper reports the synthesis, spectroscopic characterization, solution study and cytotoxic activity of three gold(III) complexes with L-histidine-containing peptides, [Au(Gly–L-His––*N*,*N*′,*N*″)Cl]NO_3·1.25H_2O (**Au1**), [Au(L-Ala–L-His–*N*,*N*′,*N*″)Cl]NO_3·2.5H_2O (**Au2**) and [Au(Gly–Gly–L-His–*N*,*N*′,*N*″,*N*‴)]Cl·H_2O (**Au3**).

EXPERIMENTAL

Reagents

Distilled water was demineralized and purified to a resistance of greater than 10 MΩ cm^{-1}. Potassium tetrachloridoaurate(III) (K[$AuCl_4$]) and deuterium oxide (99.8 %) were purchased from the Sigma–Aldrich Chemical Co. The peptides glycyl–L-histidine (Gly–L-His), L-alanyl–L-histidine (L-Ala–L-His) and glycyl–glycyl–L-histidine (Gly–Gly–L-His) were obtained from Bachem A.G. Nitric acid, sodium dihydrogen phosphate monohydrate, sodium hydrogen phosphate dihydrate and sodium chloride were obtained from Zorka Pharma. All the employed chemicals were of analytical reagent grade.

Synthesis of the gold(III) complexes

The gold(III) complexes with L-histidine-containing peptides were synthesized by modification of previously described methods.[20-22] A solution of 0.5 mmol of the corresponding peptide (106.1 mg of Gly–L-His, 113.1 mg of L-Ala–L-His and 134.6 mg of Gly–Gly–L-His) in 5.0 mL of water (pH had previously been adjusted to 2.00–2.50 by addition of 1 M HNO_3) was added slowly under stirring to the solution containing an equimolar amount of K[$AuCl_4$] (188.9 mg of K[$AuCl_4$] in 3.0 mL of water). The resulting solution was stirred in the dark in a water bath at 37 °C for at least 5 days. Any colloidal gold formed was removed by filtration and filtrate was left standing in the dark at ambient temperature to evaporate slowly. The yellow crystals of [Au(Gly–L-His–*N*,*N*′,*N*″)Cl]NO_3·1.25H_2O (**Au1**), [Au(L-Ala–L-His––*N*,*N*′,*N*″)Cl]NO_3·2.5H_2O (**Au2**) and [Au(Gly–Gly–L-His–*N*,*N*′,*N*″,*N*‴)]Cl·H_2O (**Au3**) that formed after 3–5 days were filtered off, washed with cold acetone, and dried in the dark at ambient temperature. The yield was 54 % for **Au1** (142.6 mg), 48 % for **Au2** (135.5 mg) and 44 % for **Au3** (113.9 mg). The purity of the complexes was checked by elemental microanalysis and ^{1}H-NMR spectroscopy. These data were all found to be in accordance with those reported previously for the corresponding Au(III) complexes.[21,22]

Measurements

Elemental microanalyses. Elemental microanalyses for carbon, hydrogen and nitrogen of the synthesized gold(III)–peptide complexes were performed by the Microanalytical Laboratory, Faculty of Chemistry, University of Belgrade.

*[Au(Gly–L-His–*N,N′,N″*)Cl]NO_3·1.25H_2O (**Au1**)*. Anal. Calcd. for $C_8H_{13.50}AuClN_5O_{7.25}$ (FW: 528.15): C, 18.19; H, 2.58; N, 13.26 %. Found: C, 18.45; H, 2.48; N, 13.09 %.

*[Au(L-Ala–L-His–*N,N′,N″*)Cl]NO_3·2.5H_2O (**Au2**)*. Anal. Calcd. for $C_9H_{18}AuClN_5O_{8.50}$ (FW: 564.70): C, 19.14; H, 3.21; N, 12.40 %. Found: C, 19.02; H, 3.29; N, 12.24 %.

*[Au(Gly–Gly–L-His–*N,N′,N″,N‴*)]Cl·H_2O (**Au3**)*. Anal. Calcd. for $C_{10}H_{15}AuClN_5O_5$ (FW: 517.68): C, 23.20; H, 2.92; N, 13.53 %. Found: C, 23.43; H, 2.58; N, 13.34 %.

^{1}H-NMR spectroscopy. The ^{1}H-NMR spectra of **Au1**, **Au2** and **Au3** were recorded on a Varian Gemini 2000 spectrometer (200 MHz) using 5-mm NMR tubes. Sodium trimethylsilylpropane-3-sulfonate (TSP, δ = 0.00 ppm) was used as an internal reference. All samples were prepared in 50 mM phosphate buffer at pH 7.40 in D_2O, containing 4 mM NaCl. The

concentration of the final solution was 10 mM in each complex and the total volume was 600 μL. The NMR spectra were processed using Varian VNMR software (version 6.1, revision C). The chemical shifts are reported in parts per million (ppm).

Cyclic voltammetry. Cyclic voltammetric (CV) measurements were performed with an Autolab potentiostat (PGSTAT 302N). The working electrode for the cyclic voltammetric measurements was glassy carbon (GC) with a 3 mm inner and 9 mm outer diameter PTFE sleeve. Prior to use, the GC electrode was wet-polished on an Alpha A polishing cloth (Mark V Lab) with small particles of alumina (0.05 μm diameter). The electrode was washed twice with doubly-distilled water and then with the background electrolyte solution. The washed electrode was then placed into the voltammetric cell with supporting electrolyte solution. The reference electrode was a saturated calomel electrode (SCE) type 401 (Radiometer, Copenhagen) and the counter electrode was a platinum wire.

The supporting electrolyte used to perform the cyclic voltammetric experiments was 50 mM phosphate buffer containing 4 mM NaCl at pH 7.40. Cyclic voltammograms of **Au1**, **Au2** and **Au3** were recorded immediately after dissolving of the corresponding complex in phosphate buffer, as well as after 24 and 48 h of incubation in a water bath at 37 °C. The concentration of the gold(III) complexes in the final solutions was 5×10^{-4} M. The conditions were the following: E_{begin} = –1.0 V and E_{end} = 1.5 V, as well as E_{begin} = 0.0 V and E_{end} = 1.5 V; E_{step} = = 0.003 V at a scan rate of 0.070 V s^{-1}. All experiments were repeated at least three times. The data were collected and analyzed using the Origin 8 program.

pH measurements. All pH measurements were made at ambient temperature (25 °C). The pH meter (Iskra MA 5704) was calibrated with a Fischer certified buffer solutions of pH 4.00 and 7.00. The results were not corrected for the deuterium isotope effect.

Cytotoxicity studies

Cell lines. The cell lines used in the study were MCF-7 (human breast adenocarcinoma, American Type Culture Collection, ATCC, HTB 22), HT-29 (human colon adenocarcinoma, ATCC, HTB 38), HeLa (human cervix carcinoma, ATCC, CCL 2), HL-60 (human promyelocytic leukemia, ATCC, CCL 240), Raji (human Burkitt's lymphoma, ATCC, CCL 86), and MRC-5 (human fetal lung fibroblasts, ATCC, CCL 171). The cells were grown in RPMI 1640 medium (HL-60 and Raji) or Dulbecco's modified Eagle's medium (DMEM) with 4.5 % of glucose (MCF-7, HeLa, HT-29 and MRC-5), supplemented with 10 % of fetal calf serum (FCS, NIVNS) and antibiotics: 100 IU mL^{-1} penicillin and 100 μg mL^{-1} streptomycin (ICN Galenika). All cell lines were cultured in flasks (Sarstedt, 25 cm^2) at 37 °C under a 100 % humidity atmosphere and 5 % of CO_2. The cells were sub-cultured twice a week and a single cell suspension of adherent cells was obtained using 0.25 % trypsin in EDTA (Serva). Exponentially growing cells were used throughout the assays. The cell density (number of cells per unit volume) and percentage of viable cells were determined using the dye exclusion test by trypan blue. The viability of cells used in the assay was over 95 %.

MTT assay. Cytotoxicity was evaluated by the tetrazolium colorimetric MTT assay (Sigma). The assay is based on the cleavage of the tetrazolium salt MTT (3-(4,5-dimethylthiazol-2-yl)-2,5-diphenyltetrazolium bromide) to formazan by mitochondrial dehydrogenases in viable cells. Gold(III) complexes, **Au1**, **Au2** and **Au3**, were dissolved in water at pH 7.00. Cells were plated into 96-well microtiter plates (Costar) in a volume of 90 μL per well, in the complete medium at the optimal seeding density of 10^4 (Raji and HL-60 cells) or 5×10^3 cells (adherent cells) per well to assure a logarithmic growth rate throughout the assay period. Tested substances at concentration ranging from 10^{-8} to 10^{-4} M were added to all wells except to the control ones. Plates were incubated at 37 °C for 48 h. Three hours before the end of

incubation period, 10 μL of MTT solution (5 mg mL^{-1}) was added to all wells and the plates were incubated for 3 h at 37 °C, after which, the medium and MTT were removed by suction. The formazan product was then solubilized in acidified 2-propanol (0.04 M HCl was added in 2-propanol). After a few minutes at room temperature, the plates were read on a spectrophotometer plate reader (Multiscan MCC340, Labsystems) at 540/690 nm. The wells without cells containing complete medium and MTT only acted as the blank.

The cytotoxicity was expressed as a percent and calculated according the formula:

$$\% C = (1 - A_{test}/A_{control}) \times 100$$

where A_{test} is the absorbance of the treated cells and $A_{control}$ is the absorbance of the control (untreated) cells.

Data analysis. Two independent experiments were set up with quadruplicate wells for each concentration of the complex. The IC_{50} value defines the dose of the complex that inhibits cell growth by 50 %. The IC_{50} of the complexes was determined by median effect analysis.[25]

RESULTS AND DISCUSSION

Three gold(III) complexes with L-histidine-containing peptides:
[Au(Gly–L-His–*N*,*N*′,*N*″)Cl]$NO_3 \cdot 1.25H_2O$ (**Au1**),
[Au(L-Ala–L-His–*N*,*N*′,*N*″)Cl]$NO_3 \cdot 2.5H_2O$ (**Au2**) and
[Au(Gly–Gly–L-His–*N*,*N*′,*N*″,*N*‴)]$Cl \cdot H_2O$ (**Au3**) (Fig. 1),
were synthesized by modification of the previously described methods.[20–22] The square-planar geometry of these complexes was confirmed by comparison of their ^{1}H-NMR data with those previously reported in the literature.[21,22] The obtained spectroscopic data of **Au1** and **Au2** complexes are in accordance with tridentate coordination of the Gly–L-His and L-Ala–L-His dipeptides to gold(III), respectively. This coordination occurred through the amino group of the glycyl/ /alanyl residue, the deprotonated peptide nitrogen, the imidazole N3 nitrogen and a chloride ion in the fourth coordination site. However, in **Au3** complex, the tripeptide Gly–Gly–L-His acts as a tetradentate ligand coordinating to the Au(III) ion through the terminal amino group, two deprotonated peptide nitrogens, and the N3 imidazole nitrogen. The solution behaviors of the **Au1**, **Au2** and **Au3** complexes were investigated under physiologically relevant conditions (50 mM phosphate buffer containing 4 mM NaCl at pH 7.40 and 37 °C) by ^{1}H-NMR spectroscopy and cyclic voltammetry (CV). The cytotoxic activity of these complexes was evaluated toward five human tumor cell lines, MCF-7 (human breast adenocarcinoma), HT-29 (human colon adenocarcinoma), HeLa (human cervix carcinoma), HL-60 (human promyelocytic leukemia), Raji (human Burkitt's lymphoma) and one human normal cell line MRC-5 (human fetal lung fibroblasts).

Solution study of the gold(III)–peptide complexes

An essential prerequisite for biological evaluation of metal complexes as cytotoxic agents is their sufficient stability in solution under physiologically relevant conditions. In order to investigate the stability of the gold(III)–peptide

complexes within a physiological environment, **Au1**, **Au2** and **Au3** were dissolved in 50 mM phosphate buffer containing 4 mM NaCl at pH 7.40, and their ^{1}H-NMR spectra and cyclic voltammograms were recorded after dissolution, as well as after 24 and 48 h of incubation in a water bath at 37 °C.

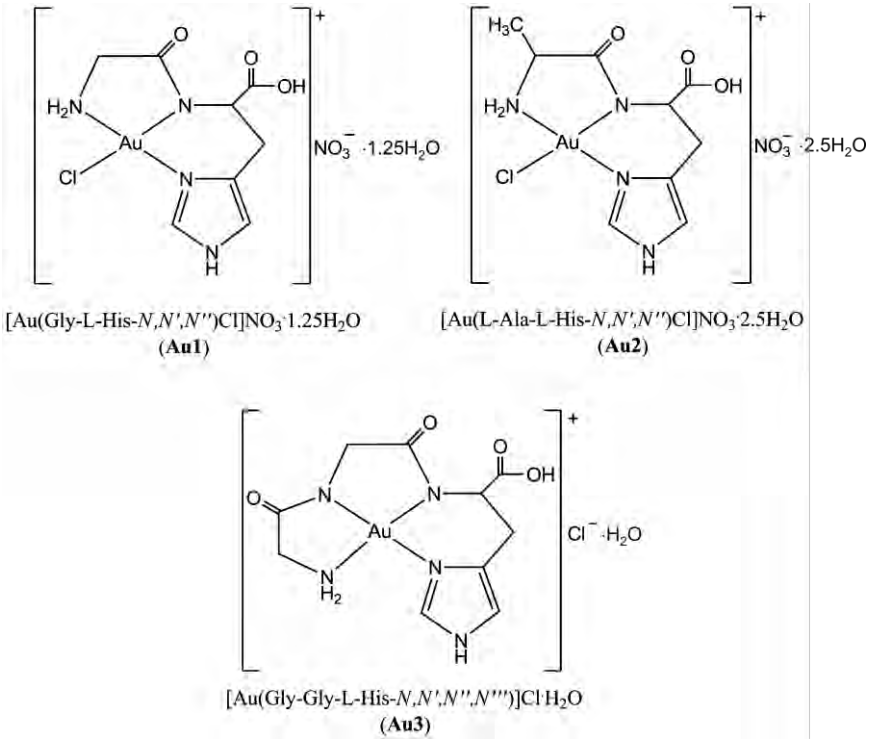

Fig. 1. Schematic drawings of the gold(III) complexes with L-histidine-containing peptides used in the present study.

^{1}H-NMR spectroscopy. When **Au1** and **Au2** complexes were dissolved in 50 mM phosphate buffer solution at pH 7.40, along with two singlets for the C2H and C5H imidazole protons of the corresponding monomeric gold(III)–peptide complex, four new resonances for these protons appeared in the ^{1}H-NMR spectrum (Table I and Fig. 2). This undoubtedly confirms that some changes in the structure of monomeric **Au1** and **Au2** complexes occurred under these experimental conditions. It is assumed that these changes resulted from the formation of the Au(III)–imidazole bridged terameric [Au(Gly–L-His–*N*,*N*′,*N*″,*N*‴)]$_4$ and [Au(L-Ala–L-His–*N*,*N*′,*N*″,*N*‴)]$_4$ complexes. The ^{1}H-NMR spectra over time showed that the intensities of the singlets due to the C2H and C5H imidazole protons of the monomeric **Au1** and **Au2** complexes decreased, while those for the observed imidazole protons of the corresponding tetrameric complexes

enhanced. The formation of the tetrameric [Au(Gly–L-His–*N*,*N*′,*N*″,*N*‴)]$_4$ and [Au(L-Ala–L-His–*N*,*N*′,*N*″,*N*‴)]$_4$ complexes is in accord with previous finding by Messori *et al.* for the solution behavior of the Gly–L-His–Au(III) complex with chloride as the counter-anion under physiologically relevant conditions.[24] Moreover, the tetrameric [Au(Gly–L-His–*N*,*N*′,*N*″,*N*‴)]$_4$·10H_2O complex was obtained by Lippert *et al.* by dissolving the monomeric [Au(Gly–L-His––*N*,*N*′,*N*″)Cl]Cl·3H_2O complex in water and then adjusting the pH to 6.00––7.00.[20] The crystallographic results for the latter tetrameric complex[20] showed that each Au(III) ion was coordinated by three nitrogen atoms as in the monomeric complex (amino, amidate and N3 imidazole nitrogens) and in addition to the N1 nitrogen of the deprotonated imidazole of the second monomeric unit. It was found that tetramerization of the **Au2** complex was slower in comparison to the same process of **Au1** (Fig. 2). Thus, after 24 h of incubation at 37 °C, the tetramerization of the **Au1** was complete, while the tetrameric [Au(L-Ala–L-His––*N*,*N*′,*N*″,*N*‴)]$_4$ complex was obtained in a yield of 55 % during this time. The difference in the rate of the tetramerization process of **Au1** and **Au2** complexes could be attributed to the effects of the electron donating methyl group of the L-alanyl residue, which decreased the acidity of the gold(III) center.

TABLE I. Proton NMR chemical shifts (δ / ppm) for the monomeric **Au1**, **Au2** and **Au3** and the corresponding tetrameric complexes in 50 mM phosphate buffer containing 4 mM NaCl at pH 7.40 and 37 °C (the chemical shifts are in accordance with those previously reported for gold(III) complexes with L-histidine-containing peptides characterized by X-ray analysis[20-22])

Gold(III)–peptide complex	Imidazole protons		Gly1-CH_2	Gly2-CH_2	Alaα-CH	Alaβ-CH_3	Hisα-CH	Hisβ-CH	Hisβ′-CH
	C2H	C5H							
[Au(Gly–L-His––*N*,*N*′,*N*″)Cl]NO_3·1.25H_2O (**Au1**)	8.55	7.27	4.00	–	–	–	4.45	3.02	3.50
[Au(Gly–L-His–*N*,*N*′,*N*″,*N*‴)]$_4$	7.39; 7.27	7.13; 6.71	4.01	–	–	–	4.39	3.10	3.56
[Au(L-Ala–L-His––*N*,*N*′,*N*″)Cl]NO_3·2.5H_2O (**Au2**)	8.52	7.24	–	–	4.13	1.55	4.43	3.04	3.50
[Au(L-Ala–L-His––*N*,*N*′,*N*″,*N*‴)]$_4$	7.39; 7.20	7.10; 6.75	–	–	4.14	1.54	4.37	3.11	3.55
[Au(Gly–Gly–L-His––*N*,*N*′,*N*″,*N*‴)]Cl·H_2O (**Au3**)[a]	8.26	7.25	4.15	4.29	–	–	4.52	3.00	3.50

[a]No terameric species was observed in solution

On the other hand, only one monomeric species was observed in the buffered solution of the **Au3** complex (Table I). The singlets at 8.26 and 7.25 ppm were assigned to the C2H and C5H imidazole protons of the tetradentate coordinated Gly–Gly–L-His tripeptide, respectively. The absence of formation of Au(III)––imidazole bridged species in the case of **Au3** complex is in accordance with the

fact that this complex has no monodentate coordinated ligand (H_2O, Cl^- or NO_3^-), like **Au1** and **Au2**, which could be replaced by the deprotonated N1 imidazole nitrogen atom of the second monomeric unit.

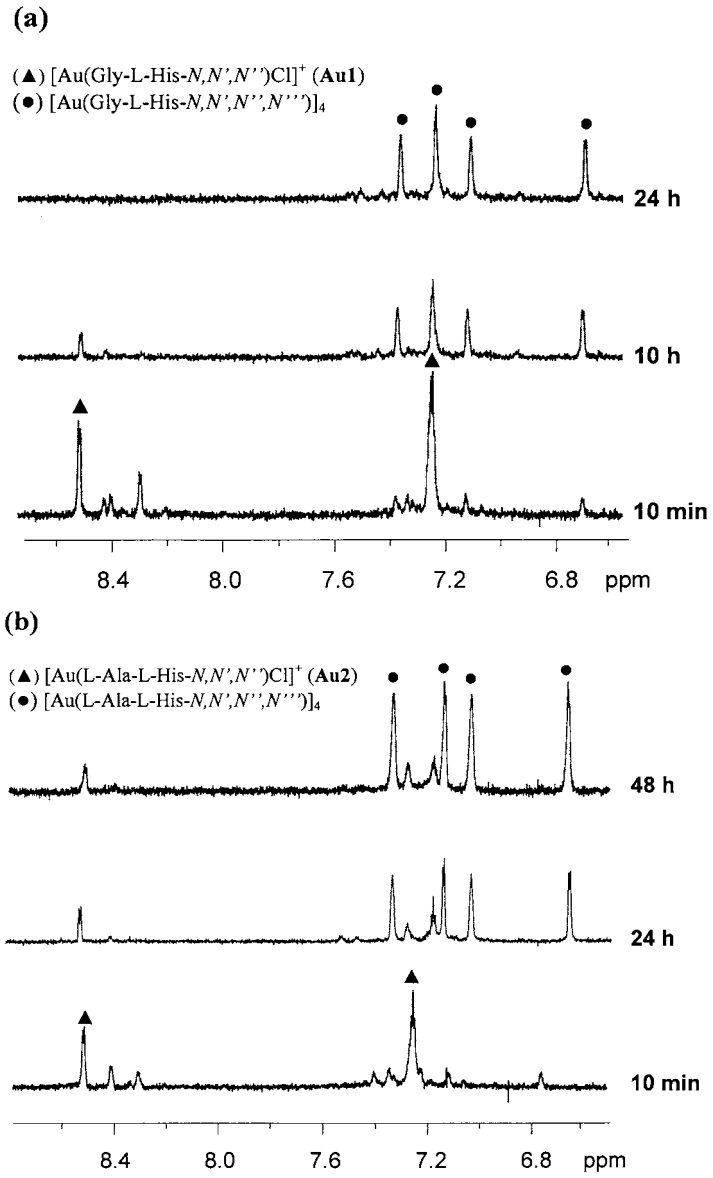

Fig. 2. Proton NMR spectra in the imidazole region (C2H and C5H protons) showing the changes in concentration of monomeric **Au1** (a) and **Au2** (b) and corresponding tetrameric complexes during time. All spectra were recorded in 50 mM phosphate buffer containing 4 mM NaCl at pH 7.40 and 37 °C.

Finally, from the above ^{1}H-NMR investigation, it could be concluded that **Au1, Au2** and **Au3** complexes are quite stable in solution with no release of the coordinated peptide from Au(III) under physiological conditions.

Cyclic voltammetry. When the cyclic voltammograms of **Au1**, **Au2** and **Au3** complexes were recorded at a GC electrode in 50 mM phosphate buffer containing 4 mM NaCl at pH 7.40, in potential region 0.0–1.5 V, no characteristic voltammetric peaks were observed (Fig. 3). These measurements were repeated every 2 h and no change in the cyclic voltammograms for the investigated gold(III) complexes were observed during 48 h. The cyclic voltammograms of these three gold(III)–peptide complexes were completely identical and, consequently, only the cyclic voltammogram of the **Au1** complex is shown in Fig. 3. For comparison, the cyclic voltammogram of the $[AuCl_4]^-$ complex is given in the same figure. In contrast to the investigated gold(III)–peptide complexes, the $[AuCl_4]^-$ complex displayed a distinct cathodic peak at 0.32 V, corresponding to gold(III) reduction ($[AuCl_4]^- + 3e^- \rightarrow Au(0) + 4Cl^-$).[26] On the reverse sweep, a definite oxidation wave at 1.02 V corresponding to metallic gold oxidation was observed: $Au(0) + 4Cl^- \rightarrow [AuCl_4]^- + 3e^-$.[26] The inactive nature of gold(III) metal center was also previously found for [Au(*para*-Y-TPP)]Cl complexes (TPP is *meso*-tetraphenylporphyrin and Y = Cl, Br, H, Me, MeO)[27] and gold(III)

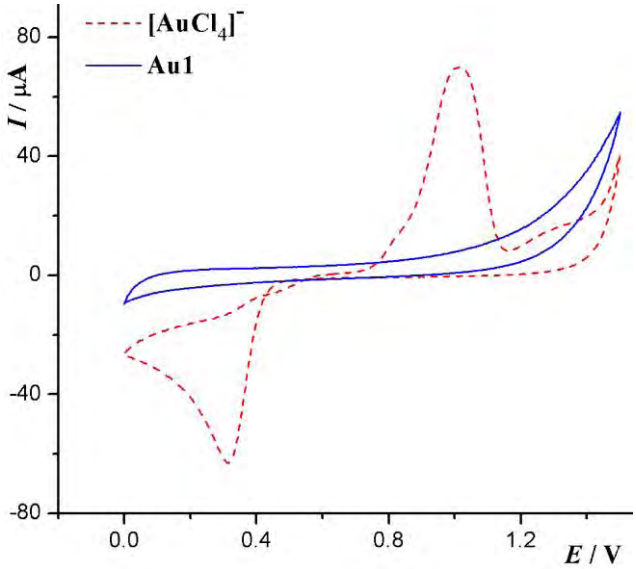

Fig. 3. Cyclic voltammogram of the [Au(Gly–L-His–*N*,*N*′,*N*″)Cl]$^+$ (**Au1**) complex recorded at a GC electrode in 50 mM phosphate buffer containing 4 mM NaCl as background electrolyte at pH 7.40 and 37 °C, E_{begin} = 0.0 V, E_{end} = 1.5 V, E_{step} = 0.003 V at a scan rate of 0.070 V s^{-1}. For comparison, the cyclic voltammogram of the $[AuCl_4]^-$ complex recorded at a GC electrode in 10 mM HCl containing 40 mM NaCl is shown.[26]

complexes containing various tridentate cyclometalating ligands derived from 6-phenyl-2,2′-bipyridine and alkynyl ligands.[28]

Based on the obtained results, it could be concluded that the gold remained in the +3-oxidation state in the **Au1**, **Au2** and **Au3** complexes under physiologically relevant conditions. Owing to the electron-donating ability and the chelate effect of the peptide moiety,[29] tridentate coordination of Gly–L-His and L-Ala–L-His dipeptides, as well as tetradentate coordination of Gly–Gly–L-His tripeptide contributed to the complete stabilization of the +3-oxidation state of gold against reduction.

Cytotoxic activity of the gold(III)–peptide complexes

In the second part of this study, the cytotoxic activity of the **Au1, Au2** and **Au3** complexes was evaluated against human leukemia (HL-60), lymphoma (Raji), three different human carcinoma cell lines (MCF-7, breast adenocarcinoma, HT-29, colon adenocarcinoma, and HeLa, cervix carcinoma) and one human normal cell line (MRC-5, human fetal lung fibroblasts). The experiments were performed by the tetrazolium MTT assay and cells were exposed for 48 h. The IC_{50} values (μM) of the **Au1**, **Au2** and **Au3** complexes are given in Table II, while the cytotoxic curves from MTT assay showing sensitivity of HeLa and HL-60 cells as percentage of cytotoxicity for 48 h in the presence of increasing concentrations of gold(III)–peptide complexes are presented in Fig. 4.

None of the presently investigated gold(III)–peptide complexes was cytotoxic against normal fetal lung fibroblasts (MRC-5), whereas cisplatin (*cis*-$[PtCl_2(NH_3)_2]$) was very toxic to these cells (Table II). Breast (MCF-7) and colon (HT-29) adenocarcinoma cells were moderately sensitive only to the **Au1** complex (Table II). In comparison with previously reported literature data,[6] the **Au1** complex (IC_{50} = 19.68±0.23 μM) was found to be more active toward the MCF-7 cell line than $[Au(bipy^{dmb}\text{-}H)(OH)][PF_6]$ (IC_{50} = 35.30±8.80 μM) and $K[Au(pz^{Ph}\text{-}H)Cl_3]$ (IC_{50} = 33.70±2.15 μM), but less active than $[Au(bipy^{dmb}\text{-}H)(2,6\text{-xylidine-}H)][PF_6]$ (IC_{50} = 5.20±0.40 μM), where $bipy^{dmb}$ is 6-(1,1-dimethylbenzyl)-2,2′-bipyridine and pz^{Ph} is 1-phenylpyrazole. Furthermore, the **Au1** complex (IC_{50} = 14.70±1.36 μM) was more active toward HT-29 cells than $[AuX_2(damp)]$ (damp is 2-[(dimethylamino)methyl]phenyl, and X = = chloride, thiocyanate, acetate, oxalate and malonate).[30]

All the investigated gold(III)–peptide complexes displayed cytotoxic activity toward cervix carcinoma (HeLa) cells (Table II and Fig. 4a). The HeLa cells were highly sensitive to the **Au3** complex, and moderately sensitive to the **Au1** and **Au2**. Thus, the **Au3** complex (IC_{50} = 0.0045±0.0002 μM) was found to be 3.5×10^4, 7.8×10^4 and 4.5×10^2-fold more active than **Au1** (IC_{50} = 15.90±1.69 μM), **Au2** (IC_{50} = 35.14±1.08 μM) and cisplatin (IC_{50} = 2.02±0.12 μM), respectively. Moreover, the **Au3** complex manifested a far higher cytotoxic activity toward HeLa cell line than previously reported gold(III) complexes con-

taining dithiocarbamate ligands, [Au(dmdt)X_2] and [Au(esdt)]X_2] (dmdt is *N*,*N*--dimethyldithiocarbamate, esdt is ethyl *N*-(dithiacarboxy)-*N*-methylglycinate, and X is chloride or bromide), with IC_{50} values falling in the range from 2.10 to 8.20 μM.[9]

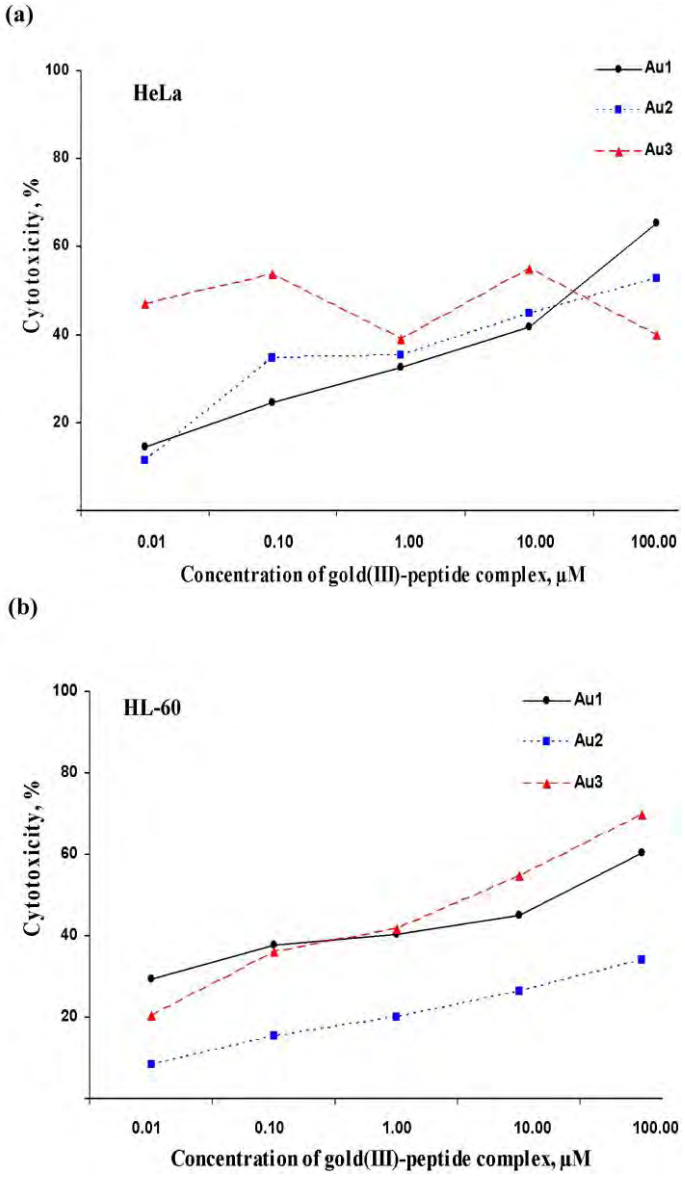

Fig. 4. Sensitivity of HeLa (a) and HL-60 (b) cells to the **Au1**, **Au2** and **Au3** complexes in the MTT assay; the results are presented as percentage of cytotoxicity and represent mean values of two independent assays, each performed in quadruplicate.

TABLE II. *In vitro* growth inhibition (IC_{50} / μM) of human normal (MRC-5) and human tumor cell lines (MCF-7, HT-29, HeLa, HL-60 and Raji) by **Au1**, **Au2** and **Au3** after a 48 h complex exposure. Cisplatin (*cis*-$[PtCl_2(NH_3)_2]$) is reported as a reference complex

Complex	IC_{50}±*SD* / μM					
	MRC-5[a]	MCF-7	HT-29	HeLa	HL-60	Raji
Au1	>100.0	19.68±0.23	14.70±1.36	15.90±1.69	11.93±1.02	3.30±0.02
Au2	>100.0	>100.0	>100.0	35.14±1.08	>100.0	>100.0
Au3	>100.0	92.31±7.78	>100.0	0.0045±0.0002	2.98±0.12	12.04±1.35
Cisplatin	0.48±0.02	1.56±0.26	18.6±2.32	2.02±0.12	10.31±2.54	2.25±0.10

[a]MRC-5 is human fetal lung fibroblasts, MCF-7 is human breast adenocarcinoma; HT-29 is human colon adenocarcinoma; HeLa is human cervix carcinoma; HL-60 is human promyelocytic leukemia; Raji is human Burkitt's lymphoma

The **Au1** and **Au3** complexes produced strong inhibition of the *in vitro* growth of hematopoietic cell lines, HL-60 and Raji (Table II and Fig. 4b). The **Au3** complex was 4-fold more active against HL-60 (IC_{50} = 2.98±0.12 μM) in comparison to the Raji cells (IC_{50} = 12.04±1.35 μM), while **Au1** was 3.6-fold more active against Raji cells (IC_{50} = 3.30±0.02 μM) in comparison to HL-60 cells (IC_{50} = 11.93±1.02 μM) (Table II). However, the gold(III)–peptide complexes were less active toward HL-60 cells than $[Au(dmdt)X_2]$ and $[Au(esdt)]X_2$].[9]

CONCLUSIONS

Based on the above results, it could be concluded that the tridentate coordination of Gly–L-His and L-Ala–L-His dipeptides, as well as the tetradentate coordination of the Gly–Gly–L-His tripeptide in the **Au1, Au2** and **Au3** complexes, respectively, stabilized Au(III) ion and prevented its reduction to Au(I) and Au(0) under physiologically relevant conditions. Moreover, no release of the coordinated peptides from Au(III) was observed under these experimental conditions. Given the appreciable stability of **Au1, Au2** and **Au3** complexes under physiological conditions, their cytotoxic activity toward one human normal and five human tumor cell lines was evaluated. The obtained results show that the cytotoxic activity of the gold(III)–peptide complexes is strongly cell line dependent. None of the gold(III)–peptide complexes was cytotoxic against normal fetal lung fibroblasts (MRC-5). The **Au1** complex was active against all the investigated human malignant cell lines. On the other hand, **Au2** and **Au3** complexes show different cytotoxic activity regarding the type of cell line. The **Au3** complex manifested a far higher cytotoxic activity toward the HeLa cell line than cisplatin, making this complex a good candidate for further pharmacological evaluation and *in vivo* testing. The results presented in this article could contribute to the development of new gold(III) complexes as potential antitumor agents and could be important in relation to the severe toxicity of gold-based drugs.

Acknowledgement. This work was funded in part by the Ministry of Education, Science and Technological Development of the Republic of Serbia (Project No. 172036).

ИЗВОД

ИСПИТИВАЊЕ ПОНАШАЊА У РАСТВОРУ ПРИ ФИЗИОЛОШКИМ УСЛОВИМА И ЦИТОТОКСИЧНА АКТИВНОСТ КОМПЛЕКСА ЗЛАТА(III) СА ПЕПТИДИМА КОЈИ САДРЖЕ L-ХИСТИДИН

БИЉАНА Ђ. ГЛИШИЋ[1], ЗОРКА Д. СТАНИЋ[1], СНЕЖАНА РАЈКОВИЋ[1], ВЕСНА КОЈИЋ[2], ГОРДАНА БОГДАНОВИЋ[2] и МИЛОШ И. ЂУРАН[1,*]

[1]*Природно–математички факултет, Универзитет у Крагујевцу, Р. Домановића 12, 34000 Крагујевац и* [2]*Институт за онкологију Војводине, Институтски пут 4, Сремска Каменица*

Применом ^{1}H-NMR спектроскопије и цикличне волтаметрије испитивано је понашање у раствору при физиолошким условима комплекса злата(III) са пептидима који садрже аминокиселину L-хистидин, [Au(Gly–L-His–*N*,*N*′,*N*″)Cl]$NO_3 \cdot 1.25H_2O$ (**Au1**), [Au(L-Ala–L-His–*N*,*N*′,*N*″)Cl]$NO_3 \cdot 2.5H_2O$ (**Au2**) и [Au(Gly–Gly–L-His–*N*,*N*′,*N*″,*N*‴)]$Cl \cdot H_2O$ (**Au3**). На основу добијених спектроскопских и електрохемијских података, закључено је да тридентатна координација Gly–L-His и L-Ala–L-His дипептида у **Au1** и **Au2** комплексима, као и тетрадентатна координација Gly–Gly–L-His трипептида у **Au3** комплексу, стабилизује +3 оксидационо стање злата и спречава његову редукцију до Au(I) и елементарног злата, Au(0). Имајући у виду значајну стабилност **Au1**, **Au2** и **Au3** комплекса у раствору при физиолошким условима, применом MTT теста, испитивана је њихова цитотоксична активност на пет туморских ћелијских линија, MCF-7 (хумани карцином дојке), HT-29 (хумани карцином колона), HeLa (хумани карцином грлића материце), HL-60 (хумана промијелоцитна леукемија), Raji (хумани Беркитов лимфом) и на једној здравој ћелијској линији MRC-5 (хумани фибропласти плућа). Нађено је да цитотоксична активност **Au1**, **Au2** и **Au3** комплекса зависи од врсте туморске ћелијске линије и да ниједан комплекс злата(III) није активан према здравој MRC-5 ћелијској линији. Ови резултати су од значаја за синтезу нових комплекса злата(III) који се потенцијално могу применити као антитуморски агенси.

(Примљено 20. септембра 2013)

REFERENCES

1. B. Lippert, *Cisplatin: Chemistry and Biochemistry of a Leading Anticancer Drug*, Wiley, New York, 1999
2. S. Nobili, E. Mini, I. Landini, C. Gabbiani, A. Casini, L. Messori, *Med. Res. Rev.* **30** (2010) 550
3. S. J. Berners-Price, *Gold-Based Therapeutic Agents: A New Perspective*, in *Bioinorganic Medicinal Chemistry*, E. Alessio, Ed., Wiley–VCH Verlag, Wienheim, Germany, 2011, p. 197
4. L. Messori, F. Abbate, G. Marcon, P. Orioli, M. Fontani, E. Mini, T. Mazzei, S. Carotti, T. O'Connell, P. Zanello, *J. Med. Chem.* **43** (2000) 3541
5. G. Marcon, S. Carotti, M. Coronnello, L. Messori, E. Mini, P. Orioli, T. Mazzei, M. A. Cinellu, G. Minghetti, *J. Med. Chem.* **45** (2002) 1672
6. L. Messori, G. Marcon, M. A. Cinellu, M. Coronnello, E. Mini, C. Gabbiani, P. Orioli, *Bioorg. Med. Chem.* **12** (2004) 6039
7. A. Casini, M. A. Cinellu, G. Minghetti, C. Gabbiani, M. Coronnello, E. Mini, L. Messori, *J. Med. Chem*. **49** (2006) 5524
8. C. Gabbiani, A. Casini, L. Messori, A. Guerri, M. A. Cinellu, G. Minghetti, M. Corsini, C. Rosani, P. Zanello, M. Arca, *Inorg. Chem.* **47** (2008) 2368

9. L. Ronconi, L. Giovagnini, C. Marzano, F. Bettìo, R. Graziani, G. Pilloni, D. Fregona, *Inorg. Chem.* **44** (2005) 1867
10. R. W.-Y. Sun, C.-M. Che, *Coord. Chem. Rev*. **253** (2009) 1682
11. A. N. Wein, A. T. Stockhausen, K. I. Hardcastle, M. Reza Saadein, S. Peng, D. Wang, D. M. Shin, Z. Chen, J. F. Eichler, *J. Inorg. Biochem*. **105** (2011) 663
12. K. Palanichamy, N. Sreejayan, A. C. Ontko, *J. Inorg. Biochem.* **106** (2012) 32
13. L. R. Gouvea, L. S. Garcia, D. R. Lachter, P. R. Nunes, F. de Castro Pereira, E. P. Silveira-Lacerda, S. R. W. Louro, P. J. S. Barbeira, L. R. Teixeira, *Eur. J. Med. Chem.* **55** (2012) 67
14. M. N. Kouodom, G. Boscutti, M. Celegato, M. Crisma, S. Sitran, D. Aldinucci, F. Formaggio, L. Ronconi, D. Fregona*, J. Inorg. Biochem*. **117** (2012) 248
15. M. Milovanović, A. Djeković, V. Volarević, B. Petrović, N. Arsenijević, Ž. D. Bugarčić, *J. Inorg. Biochem.* **104** (2010) 944
16. M. Arsenijević, M. Milovanović, V. Volarević, A. Djeković, T. Kanjevac, N. Arsenijević, S. Dukić, Ž. D. Bugarčić, *Med. Chem.* **8** (2012) 2
17. V. Milacic, D. Chen, L. Ronconi, K. R. Landis-Piwowar, D. Fregona, Q. P. Dou, *Cancer Res*. **66** (2006) 10478
18. C. T. Lum, Z. F. Yang, H. Y. Li, R. W.-Y. Sun, S. T. Fan, R. T. P. Poon, M. C. M. Lin, C.-M. Che, H. F. Kung, *Int. J. Cancer* **118** (2006) 1527
19. Y. F. To, R. W.-Y. Sun, Y. Chen, V. S.-F. Chan, W.-Y. Yu, P. K.-H. Tam, C.-M. Che, C.-L. S. Lin, *Int. J. Cancer* **124** (2009) 1971
20. M. Wienken, B. Lippert, E. Zangrando, L. Randaccio, *Inorg. Chem*. **31** (1992) 1983
21. U. Rychlewska, B. Warżajtis, B. Đ. Glišić, M. D. Živković, S. Rajković, M. I. Djuran, *Dalton Trans.* **39** (2010) 8906
22. S. L. Best, T. K. Chattopadhyay, M. I. Djuran, R. A. Palmer, P. J. Sadler, I. Sóvágó, K. Varnagy, *J. Chem. Soc. Dalton Trans*. (1997) 2587
23. B. Đ. Glišić, U. Rychlewska, M. I. Djuran, *Dalton Trans.* **41** (2012) 6887
24. S. Carotti, G. Marcon, M. Marussich, T. Mazzei, L. Messori, E. Mini, P. Orioli, *Chem. Biol. Interact.* **125** (2000) 29
25. T. Mosmann, *J. Immunol. Methods* **65** (1983) 55
26. B. Đ. Glišić, S. Rajković, Z. D. Stanić, M. I. Djuran, *Gold Bull*. **44** (2011) 91
27. C.-M. Che, R. W.-Y. Sun, W.-Y. Yu, C.-B. Ko, N. Zhu, H. Sun, *Chem. Commun.* (2003) 1718
28. V. K.-M. Au, W. H. Lam, W.-T. Wong, V. W.-W. Yam, *Inorg. Chem*. **51** (2012) 7537
29. L. Ronconi, C. Marzano, P. Zanello, M. Corsini, G. Miolo, C. Maccà, A. Trevisan, D. Fregona, *J. Med. Chem*. **49** (2006) 1648
30. R. G. Buckley, A. M. Elsome, S. P. Fricker, G. R. Henderson, B. R. C. Theobald, R. V. Parish, B. P. Howe, L. R. Kelland, *J. Med. Chem*. **39** (1996) 5208.

Journal of the Serbian Chemical Society
JSCS-info@shd.org.rs • www.shd.org.rs/JSCS
J. Serb. Chem. Soc. 78 (12) 1925–1933 (2013)
JSCS–4541
UDC 537.12+537.872+519.17:535.566
Original scientific paper

Estimating the total π-electron energy

IVAN GUTMAN[1,2*#] and KINKAR CH. DAS[3]

[1]*Faculty of Science, University of Kragujevac, P. O. Box 60, 34000 Kragujevac, Serbia,* [2]*Department of Chemistry, Faculty of Science, King Abdulaziz University, Jeddah 21589, Saudi Arabia and* [3]*Department of Mathematics, Sungkyunkwan University, Suwon 440–746, Republic of Korea, E-mail: kinkardas2003@googlemail.com*

(Received 5 September 2013)

Abstract: The paper gives a short survey of the most important lower and upper bounds for the total π-electron energy, *i.e*., the graph energy (*E*). In addition, a new lower and a new upper bound for *E* are deduced, valid for general molecular graphs. The strengthened versions of these estimates, valid for alternant conjugated hydrocarbons, are also reported.

Keywords: total π-electron energy; graph energy; HMO theory.

INTRODUCTION

The total π-electron energy (E_π), as calculated within the simple tight-binding Hückel molecular orbital (HMO) approximation, is one of the most precious pieces of information that can be directly related with molecular structure, by means of spectral graph theory.[1–4] In the case of the chemically most relevant conjugated π-electron systems (in particular, benzenoids,[5] phenylenes,[6] fluoranthenes,[7] *etc*), E_π can be expressed as:

$$E_\pi = \alpha n + \beta E$$

where α and β are the standard HMO parameters (constants), n is the number of carbon atoms (number of vertices of the underlying molecular graph G), whereas:

$$E = E(G) = \sum_{i=1}^{n} |\lambda_i| \qquad (1)$$

is the structure-sensitive term, depending on the eigenvalues $\lambda_1, \lambda_2, \ldots, \lambda_n$ of the molecular graph G. The non-trivial part of the theory of total π-electron energy is just the study of the structure-dependency of the quantity E, which nowadays is referred to[8] as the *energy* of the (molecular) graph G. The energy of chemically

* Corresponding author. E-mail: gutman@kg.ac.rs
# Serbian Chemical Society member.
doi: 10.2298/JSC130905092G

relevant molecular graphs was shown to be quantitatively related with the experimentally determined heats of formation and other measures of thermodynamic stability of the underlying conjugated compounds.[2,5,9]

In the last 10–15 years, graph energy became a popular topic of mathematical research, resulting in hundreds of published papers. Details on graph energy can be found in a book,[8] the references cited therein, and recent papers.[10–15]

One of the earliest results in the theory of total π-electron energy are the estimates obtained by McClelland,[16] namely:

$$\sqrt{2m + n(n-1)\,|\det A|^{2/n}} \le E(G) \le \sqrt{2mn} \tag{2}$$

where n is the number of vertices of the molecular graph G (equal to the number of carbon atoms of the underlying conjugated hydrocarbon), m is the number of edges of G (equal to the number of carbon–carbon bonds), and $A = A(G)$ is the adjacency matrix of the graph G.

McClelland's upper bound $\sqrt{2mn}$ played a significant role in the theory of the total π-electron energy, because it was demonstrated[16] that $a\sqrt{2mn}$, for $a \approx 0.9$, provides an excellent approximation for E. Comparative testings[5,17–19] of the numerous existing (n,m)-type approximate formulas for E revealed that not one was better than that of McClelland. This somewhat puzzling result found an explanation after the discovery of McClelland-type lower bounds for energy.[20–23] It was first shown[20] that for $g = \sqrt{16/27} = 0.77$, the expression $g\sqrt{2mn}$ is a lower bound for the energy of benzenoid hydrocarbons. Türker obtained $g = 0.5$ for all alternant conjugated hydrocarbons,[21] which was further improved[22,23] as $g = \sqrt{32/81} = 0.63$.

Eventually, several other estimates of E were obtained, of which here only those depending solely on the number of edges of the molecular graph are mentioned:[24]

$$2\sqrt{m} \le E(G) \le 2m \tag{3}$$

and those depending solely on the number of its vertices:[24,25]

$$2\sqrt{n-1} \le E(G) \le \frac{n}{2}\left(\sqrt{n}+1\right) \tag{4}$$

At this point, also an (n,m)-type improvement of McClelland's upper bound should be mentioned:

$$E(G) \le \frac{2m}{n} + \sqrt{(n-1)\left[2m - \left(\frac{2m}{n}\right)^2\right]}, \tag{5}$$

discovered 30 years later[25,26] than the estimates (2).

By means of the bounds (2)–(5) and McClelland's approximate expression for E, the two most important structural parameters, determining the gross part of total π-electron energy were established: these are n and m. The evident next step was to find estimates and approximate expressions for E possessing more than two structural parameters.

Although there is no general agreement about which the third-important structural parameter should be, most attention was paid to the number of Kekulé structures, $K = K(G)$, and to the closely related determinant of the adjacency matrix.[27] In particular:
if B is the molecular graph of a benzenoid hydrocarbon, then:[28,29]

$$\det A(B) = (-1)^{n/2} K(B)^2;$$

if F is the molecular graph of a fluoranthene, then:[30,31]

$$\det A(F) = (-1)^{n/2} [K(F_1) K(F_2)]^2;$$

where F_1 and F_2 are the „male" and „female" fragments of F; if P is the molecular graph of a phenylene, then:[32]

$$\det A(P) = (-1)^{n/2} K(HS)^2$$

where HS stands for the hexagonal squeeze of P.

The dependence of the total π-electron energy on the number of Kekulé structures was much investigated, especially for benzenoids,[33–40] fluoranthenes,[41] and phenylenes.[6] In view of the above stated relations between the determinant of the adjacency matrix and the number of Kekulé structures, every lower and upper bound for E contains information on the K-dependence of the total π-electron energy. Hitherto, the best such estimates were:[42]

$$\sqrt{2m + n(n-1)\,|\det A|^{2/n}} \le E(G) \le \sqrt{2m(n-1) + n\,|\det A|^{2/n}}, \qquad (6)$$

valid for general molecular graphs, and

$$\sqrt{4m + n(n-2)\,|\det A|^{2/n}} \le E(G) \le \sqrt{2m(n-2) + 2n\,|\det A|^{2/n}}, \qquad (7)$$

valid for alternant conjugated hydrocarbons. Recently a further upper bound for E was established:[43]

$$E(G) \ge \frac{2m}{n} + n - 1 + \ln\left(\frac{n\,|\det A|}{2m}\right), \qquad (8)$$

valid under the condition that $\det A \neq 0$, *i.e.*, that no eigenvalue of the molecular graph is equal to zero, *i.e.*, that the respective conjugated molecule has no non-bonding molecular orbitals.[1]

In what follows, two novel $(n, m, \det A)$-type estimates of graph energy were obtained. To realize this, some preparations were required.

PRELIMINARIES

In this section, some previously known results that will be needed in the next two sections are listed.

Lemma 1.[44] Let $x_1, x_2, \ldots, x_N$ be non-negative numbers, and let:

$$\alpha = \frac{1}{N}\sum_{i=1}^{N} x_i \text{ and } \gamma = \left(\prod_{i-1}^{N} x_i\right)^{1/N}$$

be their arithmetic and geometric means. Then:

$$\frac{1}{N(N-1)}\sum_{i<j}\left(\sqrt{x_i}-\sqrt{x_j}\right)^2 \le \alpha - \gamma \le \frac{1}{N}\sum_{i<j}\left(\sqrt{x_i}-\sqrt{x_j}\right)^2$$

Moreover, equality holds if and only if $x_1 = x_2 = \cdots = x_N$.

Lemma 2.[45] For a graph G with n vertices and m edges, eigenvalues $\lambda_1, \lambda_2, \ldots, \lambda_n$, and for $1 \le j \le n$:

$$-\sqrt{\frac{2m(j-1)}{n(n-j+1)}} \le \lambda_j \le \sqrt{\frac{2m(n-j)}{n\,j}}$$

Lemma 3.[46] Let G be a connected graph of order n. Then $\lambda_1 \ge 2m/n$, with equality if and only if G is regular.

LOWER BOUND FOR GRAPH ENERGY

Theorem 1. The lower bound in (6) can be improved as:

$$E(G) \ge \sqrt{2m + n(n-1)\,|\det A|^{2/n} + \frac{4}{(n+1)(n-2)}\left[\sqrt{\frac{2m}{n}} - \left(\frac{2m}{n}\right)^{1/4}\right]^2} \qquad (9)$$

Proof. From Lemma 1, one obtains:

$$\sum_{i=1}^{N} x_i \ge N\left(\prod_{i=1}^{N} x_i\right)^{1/N} + \frac{1}{N-1}\sum_{i<j}\left(\sqrt{x_i}-\sqrt{x_j}\right)^2 \qquad (10)$$

Substituting in (10) $N = n(n-1)/2$ and $x_i = |\lambda_j| \cdot |\lambda_k|$ for $i = 1,2,\ldots,n(n-1)/2$, $j = 1,2,\ldots,n-1$ and $k = j+1, j+2, \ldots, n$, one arrives at:

$$\sum_{j<k} |\lambda_j|\,|\lambda_k| \ge \frac{n(n-1)}{2}\left(\prod_{i=1}^{n} |\lambda_i|\right)^{2/n} + \frac{2}{n^2-n-2}\sum_{j<k<r<s}\left(\sqrt{|\lambda_j|\,|\lambda_k|} - \sqrt{|\lambda_r|\,|\lambda_s|}\right)^2$$

which is the same as:

$$2\sum_{j<k}|\lambda_j||\lambda_k| \geq n(n-1)|\det A|^{2/n} + \frac{4}{n^2-n-2}\sum_{j<k<r<s}\left(\sqrt{|\lambda_j||\lambda_k|}-\sqrt{|\lambda_r||\lambda_s|}\right)^2$$

By Lemma 2:

$$\lambda_{n/2} \leq \sqrt{\frac{2m}{n}}$$

whereas by Lemma 3:

$$\lambda_1 \geq \frac{2m}{n}$$

If, in addition, one takes into account that:[44] $\lambda_n \leq -1$, *i.e.*, $|\lambda_n| \geq 1$, one obtains:

$$\sum_{j<k<r<s}\left(\sqrt{|\lambda_j||\lambda_k|}-\sqrt{|\lambda_r||\lambda_s|}\right)^2 \geq \left(\sqrt{|\lambda_1||\lambda_n|}-\sqrt{|\lambda_{n/2}||\lambda_n|}\right)^2 =$$

$$=|\lambda_n|\left(\sqrt{|\lambda_1|}-\sqrt{|\lambda_{n/2}|}\right)^2 \geq \left(\sqrt{\frac{2m}{n}}-\left(\frac{2m}{n}\right)^{1/4}\right)^2 \tag{11}$$

which combined with:

$$2\sum_{j<k}|\lambda_j||\lambda_k| + \sum_{j=1}^{n}|\lambda_j|^2 = \sum_{j=1}^{n}\sum_{k=1}^{n}|\lambda_j||\lambda_k| = \left(\sum_{j=1}^{n}|\lambda_j|\right)\left(\sum_{k=1}^{n}|\lambda_k|\right) = E^2$$

and bearing in mind that:

$$\sum|\lambda_j|^2 = 2m$$

results in a $(n, m, \det A)$-type lower bound (9).

For alternant conjugated hydrocarbons[1,2] (*i.e.*, for bipartite molecular graphs[46]), $\lambda_j = -\lambda_{n-j+1}$ holds for all $j = 1,2,\ldots,n$. In particular, $\lambda_1 = -\lambda_n$ and $\lambda_{n/2} = -\lambda_{n/2+1}$. Bearing this in mind, the inequalities in (11) can be strengthened as:

$$\sum_{j<k<r<s}\left(\sqrt{|\lambda_j||\lambda_k|}-\sqrt{|\lambda_r||\lambda_s|}\right)^2 \geq \left(\sqrt{|\lambda_1||\lambda_n|}-\sqrt{|\lambda_{n/2}||\lambda_{n/2+1}|}\right)^2 =$$

$$=\left(\lambda_1-\lambda_{n/2}\right)^2 \geq \left(\frac{2m}{n}-\sqrt{\frac{2m}{n}}\right)^2$$

resulting in the following $(n, m, \det A)$-type lower bound for total π-electron energy of alternant conjugated hydrocarbons:

$$E(G) \geq \sqrt{2m + n(n-1)\,|\det A|^{2/n} + \frac{4}{(n+1)(n-2)}\left(\frac{2m}{n} - \sqrt{\frac{2m}{n}}\right)^2} \qquad (12)$$

Recall that benzenoids and phenylenes are alternant conjugated hydrocarbons, whereas fluoranthenes are not. It is easy to show that the estimate (12) is better than (9).

UPPER BOUND FOR GRAPH ENERGY

Theorem 2. Under the condition that $\det A \neq 0$, the upper bound in (3) can be improved as:

$$E(G) \leq 2m - \frac{2m}{n}\left(\frac{2m}{n} - 1\right) - \ln\left(\frac{n\,|\det A|}{2m}\right) \qquad (13)$$

One should compare this result with the lower bound (8).

Proof. Consider the function $f(x) = x^2 - x - \ln x$, which is increasing for $x \geq 1$ and decreasing for $0 < x \leq 1$. Thus, for $x \geq 1$,

$$f(x) \geq f(1) = 0, \; i.e., \; x \leq x^2 - \ln x$$

with equality holding if and only if $x = 1$. Using this result and the definition of graph energy, Eq. (1), one obtains:

$$E = \lambda_1 + \sum_{j=2}^{n} |\lambda_j| \leq \lambda_1 + \sum_{j=2}^{n} (\lambda_j^2 - \ln|\lambda_j|) = \lambda_1 + 2m - \lambda_1^2 - \ln \prod_{j=1}^{n} |\lambda_j| + \ln \lambda_1$$

that is:

$$E \leq \lambda_1 + 2m - \lambda_1^2 - \ln|\det A| + \ln \lambda_1 = 2m - \ln|\det A| - f(\lambda_1) \qquad (14)$$

Inequality (13) is now obtained by replacing in (14) λ_1 by:

$$\frac{2m}{n}$$

This is legitimate since by Lemma 3:

$$\lambda_1 \geq \frac{2m}{n}$$

and since:

$$\frac{2m}{n}$$

is the average vertex degree, which in molecular graphs is necessarily greater than unity.

By means of arguments analogous to those used for deducing the lower bound (12), in particular, using $\lambda_1 = -\lambda_n$, for alternant conjugated hydrocarbons without zero graph eigenvalues, the estimate (13) can also be improved as:

$$E(G) \le 2m - \frac{4m}{n}\left(\frac{2m}{n} - 1\right) - \ln\left(\frac{n^2 \,|\det A|}{4m^2}\right) \tag{15}$$

DISCUSSION AND CONCLUDING REMARKS

In this paper, our attention was focused on bounds for the HMO total π-electron energy (E_π) of conjugated hydrocarbons, which depend on the number of carbon atoms (n), the number of carbon–carbon bonds (m), and the Kekulé structure count (K). For algebraic reasons, instead of dependence on K, expressions were found in which the determinant of the adjacency matrix ($\det A$) is one of the parameters. As explained in the Introduction, for the most important polycyclic conjugated π-electron systems, there are simple relations between $\det A$ and the Kekulé structure count. Thus, the new estimates reported in this paper, namely (9), (12), (13) and (15), may be viewed as contributions towards a better understanding of the structure-dependency of E_π, in particular of its (n, m, K)--dependence.

If E_L and E_D is a pair of lower and upper bounds for E, then an approximate expression for E could be obtained by taking their arithmetic mean: $1/2(E_\mathrm{L} + E_\mathrm{D})$. However, in view of the algebraic forms of the estimates discussed in this paper, it is better to construct these approximate expressions as $\sqrt{1/2(E_\mathrm{L}^2 + E_\mathrm{D}^2)}$. If so, then from the estimates (6), one obtains:

$$E \approx \sqrt{\frac{1}{2}\left(2mn + n^2 \,|\det A|^{2/n}\right)} \approx \frac{\sqrt{2}}{2}\sqrt{2mn} + \frac{n\,|\det A|^{2/n}}{\sqrt{8}m}$$

which, recalling that $\sqrt{2}/2 = 0.707$, is evidently a modification of the original McClelland's formula $a\sqrt{2mn}$. It is interesting that exactly the same expression was obtained from the improved estimates (7). Equally interesting (and somewhat surprising) is the approximate formula obtained from the estimates (8) and (13):

$$E \approx \sqrt{m + \frac{n-1}{2} + \frac{2m}{n} - \frac{2m^2}{n^2}}$$

which is of the (n, m)-type, not containing the logarithm of the determinant of the adjacency matrix, and thus – in contrast to the estimates (8) and (13) – applicable to all molecular graphs.

Acknowledgement. The second author was supported by the Faculty research Fund, Sungkyunkwan University, 2012, and the National Research Foundation funded by the Korean government through Grant No. 2013R1A1A2009341.

И З В О Д

ГРАНИЦЕ ЗА УКУПНУ ЕНЕРГИЈУ π-ЕЛЕКТРОНА

ИВАН ГУТМАН[1,2] и KINKAR CH. DAS[3]

[1]Природно–математички факултет Универзитета у Крагујевцу, [2]Department of Chemistry, Faculty of Science, King Abdulaziz University, Jeddah 21589, Saudi Arabia и [3]Sungkyunkwan University, Suwon, Republic of Korea

Дат је кратак преглед најважнијих доњих и горњих граница за укупну енергију π-електрона, тј. енергију графа (E). У наставку су добијене по једна нова доња и горња граница за E, које важе за све молекулске графове. Такође су наведене побољшане верзије тих граница, које важе за алтернантне конјуговане угљоводонике.

(Примљено 5. септембра 2013)

REFERENCES

1. A. Graovac, I. Gutman, N. Trinajstić, *Topological Approach to the Theory of Conjugated Molecules,* Springer, Berlin, 1977
2. I. Gutman, O. E. Polansky, *Mathematical Concepts in Organic Chemistry*, Springer, Berlin, 1986
3. I. Gutman, *J. Serb. Chem. Soc.* **70** (2005) 441
4. M. Perić, I. Gutman, J. Radić-Perić, *J. Serb. Chem. Soc.* **71** (2006) 771
5. I. Gutman, *Topics Curr. Chem.* **162** (1992) 29
6. I. Gutman, A. Stajković, S. Marković, P. Petković, *J. Serb. Chem. Soc.* **59** (1994) 367
7. I. Gutman, J. Đurđević, S. Radenković, A. Burmudžija, *Indian J. Chem*., *A* **48** (2009) 194
8. X. Li, Y. Shi, I. Gutman, *Graph Energy*, Springer, New York, 2012
9. L. J. Schaad, B. A. Hess, *J. Am. Chem. Soc.* **94** (1972) 3068
10. X. Hu, H. Liu, *MATCH Commun. Math. Comput. Chem.* **66** (2011) 863
11. S. Wagner, *MATCH Commun. Math. Comput. Chem.* **68** (2012) 661
12. E. O. D. Andriantiana, *MATCH Commun. Math. Comput. Chem.* **68** (2012) 675
13. H. Y. Shan, J. Y. Shao, L. Zhang, C. X. He, *MATCH Commun. Math. Comput. Chem.* **68** (2012) 703
14. M. P. Stanić, I. Gutman, *MATCH Commun. Math. Comput. Chem.* **70** (2013) 681
15. K. C. Das, S. A. Mojallal, *MATCH Commun. Math. Comput. Chem.* **70** (2013) 657
16. B. J. McClelland, *J. Chem. Phys.* **54** (1971) 640
17. I. Gutman, S. Marković, A. V. Teodorović, Ž. Bugarčić, *J. Serb. Chem. Soc*. **51** (1986) 145
18. I. Gutman, A. Graovac, S. Vuković, S. Marković, *J. Serb. Chem. Soc*. **54** (1989) 189
19. I. Gutman, T. Soldatović, *MATCH Commun. Math. Comput. Chem*. **44** (2001) 169
20. I. Gutman, *J. Chem. Soc. Faraday Trans.* **86** (1990) 3373
21. L. Türker, *MATCH Commun. Math. Comput. Chem.* **30** (1994) 243
22. I. Gutman, *Croat. Chem. Acta* **68** (1995) 187
23. D. Babić, I. Gutman, *MATCH Commun. Math. Comput. Chem.* **32** (1995) 7
24. G. Caporossi, D. Cvetković, I. Gutman, P. Hansen, *J. Chem. Inf. Comput. Sci.* **39** (1999) 984
25. J. H. Koolen, V. Moulton, *Adv. Appl. Math*. **26** (2001) 47
26. J. H. Koolen, V. Moulton, I. Gutman, *Chem. Phys. Lett*. **320** (2000) 213
27. A. Graovac, I. Gutman, *MATCH Commun. Math. Comput. Chem*. **6** (1979) 49
28. M. J. S. Dewar, H. C. Longuet-Higgins, *Proc. R. Soc. London, Ser. A* **214** (1952) 482

29. I. Gutman, S. J. Cyvin, *Introduction to the Theory of Benzenoid Hydrocarbons,* Springer, Berlin, 1989
30. I. Gutman, *Z. Naturforsch., A* **65** (2010) 473
31. D. Vukičević, J. Đurđević, I. Gutman, *J. Serb. Chem. Soc*. **75** (2010) 1093
32. I. Gutman, *J. Chem. Soc. Faraday Trans.* **89** (1993) 2413
33. G. G. Hall, *Int. J. Math. Educ. Sci. Technol.* **4** (1973) 233
34. I. Gutman, *Chem. Phys. Lett*. **156** (1989) 119
35. I. Gutman, G. G. Hall, *Int. J. Quantum Chem*. **41** (1992) 667
36. I. Gutman, S. Marković, G. G. Hall, *Chem. Phys. Lett*. **234** (1995) 21
37. I. Gutman, S. Marković, D. Vukičević, A. Stajković, *J. Serb. Chem. Soc.* **60** (1995) 93
38. I. Gutman, *Int. J. Quantum Chem*. **74** (1999) 627
39. I. Gutman, S. Radenković, *Chem. Phys. Lett*. **423** (2006) 382
40. S. Radenković, I. Gutman, *J. Serb. Chem. Soc.* **74** (2009) 155
41. J. Đurđević, S. Radenković, I. Gutman, *J. Serb. Chem. Soc.* **73** (2008) 989
42. I. Gutman, *Chem. Phys. Lett*. **24** (1974) 283
43. K. C. Das, S. A. Mojallal, I. Gutman, *MATCH Commun. Math. Comput. Chem.* **70** (2013) 663
44. H. Kober, *Proc. Am. Math. Soc.* **59** (1958) 452
45. R. C. Brigham, R. D. Dutton, *J. Comb. Theory Ser. B* **37** (1984) 228
46. D. M. Cvetković, M. Doob, H. Sachs, *Spectra of Graphs - Theory and Application*, Academic Press, New York, 1980.

Journal of the Serbian Chemical Society
JSCS-info@shd.org.rs • www.shd.org.rs/JSCS
J. Serb. Chem. Soc. *78* (12) 1935–1962 (2013)
JSCS–4542
UDC 531.314:537.872:531.3:539.193
Original scientific paper

An alternative derivation of (almost-) Watson's Hamiltonian•

MILJENKO PERIĆ*#

Faculty of Physical Chemistry, University of Belgrade, Studentski trg 12–16, P. O. Box 47, 11158 Belgrade, Serbia

(Received 9 October 2013)

Abstract: A derivation of the general wave-mechanical Hamiltonian for non-linear molecules is presented. It is based on the transformation of proper classical (Hamilton) momenta into their wave-mechanical counterparts by means of the Podolsky Transformation in its original form. The result is essentially identical to that obtained by Watson in his milestone paper (J. K. G. Watson, *Mol. Phys.* **15** (1968) 479). While not so elegant as that of the original reference, the way proposed in the present study is conceptually much simpler. This procedure could also be applied to other types of molecular Hamiltonians.

Keywords: Watson's molecular Hamiltonian; classical kinetic energy; Podolsky transformation.

INTRODUCTION

Among the papers I have been forced to understand, there is hardly one I found so difficult as Watson's milestone study[1] in which he simplified the vibration–rotation Hamiltonian for polyatomic molecules, originally derived by Wilson and Howard.[2,3] Just to reproduce five pages of this paper, I needed a whole month, and in order to decipher the extremely complicated formulae in condensed Levi-Civita form, I penned several hundreds of leaves. It seems that other people also had similar problems. I found once in a very serious paper the sentence: "If the Watson's Hamiltonian is correct …". Even Watson himself wrote in his paper, "The simplicity of the final result suggests that it should be obtainable by a less complicated calculation than that described here, I have, however, been unable to find a more direct derivation." As another illustration of the complexity of this study can serve the fact that as Watson needed two years to apply the same procedure for deriving the Hamiltonian for linear polyatomic molecules,[4] some researchers questioned his results,[5] and that Watson's answer to this

* Correspondence on E-mail: peric@ffh.bg.ac.rs
# Serbian Chemical Society member.
• Dedicated to Professor Branislav Nikolić on the occasion of his 70th birthday.
doi: 10.2298/JSC131109107P

criticism came only seven years later.[6] Thus, the goal of the present study was to attempt to derive Watson's Hamiltonian in a less elegant but simpler, or at least more straightforward, way.

Separation of variables represents an unavoidable step that precedes every practical *ab initio* handling of the molecular Schrödinger equation, and/or a treatment of the dynamics of molecules. Experimental spectroscopy indicates that molecular spectra can be understood in a good approximation if the existence of several more or less loosely coupled motion modes is supposed. This concept is supported by theoretical considerations. A „normal" molecule has a relatively rigid nuclear skeleton, *i.e*. the nuclei are held at nearly constant mutual distances. More precisely, the changes of these distances (molecular vibrations) are small compared to the average values of the distances. These average distances determine the equilibrium structure of the molecule. The electrons can be imagined as the constituents of an electron cloud tied to the nuclear skeleton. As a whole, the molecule translates and rotates in space.

There are two main approaches for construction of the wave-mechanical Hamiltonian.[7] In the "first" one (a), the wave-mechanical operator is first derived in terms of Cartesian derivatives and subsequently, these derivatives are replaced by the derivatives with respect to appropriately chosen (typically curvilinear) coordinates, or by some impulses (momenta) not conjugate to any coordinates. This can be represented schematically as

$$E\left(\dot{X}\right) \rightarrow H\left(P_X\right) \rightarrow \hat{H}\left(\hat{P}_X\right) \rightarrow \hat{H}\left(\hat{P}_q\right) \tag{1}$$

where $\hat{P}_X = -i\hbar\partial / \partial X$, but in general, $\hat{P}_q \neq -i\hbar\partial / \partial q$. In the "second" approach (b), one derives first the classical Hamiltonian in terms of (classical) impulses conjugate to chosen non-Cartesian coordinates and only after that are these impulses replaced by the corresponding wave-mechanical operators:

$$E\left(\dot{X}\right) \rightarrow E\left(\dot{q}\right) \rightarrow H\left(P_q\right) \rightarrow \hat{H}\left(\hat{P}_q\right) \tag{2}$$

This alternate way was invented by Podolsky and it is called the Podolsky transformation.[8] Sometimes, Hamiltonians are even derived in terms of momenta not conjugate to any coordinates (such momenta are not "true momenta" in the sense of the Hamilton formalism).[1,3,4]

WILSON–WATSON'S HAMILTONIAN

Only the construction of the kinetic energy part of the Hamiltonian will be considered. The transformation of the potential energy is trivial since it only depends on the distances between the particles (electrons and nuclei) and these are invariant to changes in coordinate frames.

An isolated polyatomic molecule composed of S (>2) nuclei $A, B, ..., S$, and N electrons, $1, ...\mu, ..., N$, with non-linear equilibrium geometry, is consi-

dered and handled in the non-relativistic approximation. When summing over electrons, Greek letters, $\mu,\nu,...$ will be used. The nuclear masses will be denoted by $m_A,...,m_S$, and the electron mass by m_e. The total mass of the nuclei is denoted by M_n, and the mass of the molecule by M ($M = M_n + Nm_e$). One starts with a space-fixed coordinate system (*SFS*). A disadvantage of this is that all the molecular motion modes are mixed in it. For this reason, the Hamiltonian is transformed to the coordinate system with the axes parallel to those of the *SFS* and the origin coinciding with the center of mass of the molecule (including both the nuclei and electrons, *MCMS*). This transformation serves to separate off the translational motions of the molecule. A consequence of the introduction of three center of mass coordinates is that one remains with $3(S+N)-3$ linearly independent particle coordinates in the *MCMS*. Thus a set of redundant coordinates, say those of the nucleus A, is eliminated, and they are expressed as linear combinations of the coordinates of the other nuclei ($B,...,S$).

The *MCMS* has two drawbacks: First, in the *MCMS*, the coordinates of the nuclei and electrons are (indeed weakly, $\sim m_e / M_n$) coupled. Secondly, contrary to the situation with the nuclear skeleton, which has at any moment a definite structure (it determines the „geometry" of the molecule), the „electron cloud" cannot be associated with any simple geometric structure. For these reasons, the positions of all particles are related to the center of mass of the nuclei (*NCMS*). Since the axes of all three mentioned coordinate systems are mutually parallel, the transformation of the kinetic energy expressions is relatively simple and can be realized separately for X, Y and Z coordinates. The position vectors of the nuclei in the *NCMS* will be denoted by $\left(\vec{R}_A\right), \vec{R}_B, ..., \vec{R}_S$ and that of the μ^{th} electron by $\vec{R}_\mu$ ($\mu = 1,2,...,N$).

The classical kinetic energy in the velocity form in the *NCMS* is:[7]

$$T = T_n + T_e = \frac{1}{2}\sum_{K=B}^{S} m_K\left(\dot{X}_K^2 + \dot{Y}_K^2 + \dot{Z}_K^2\right) + \\ + \frac{1}{2m_A}\sum_{K=B}^{S}\sum_{L=B}^{S} m_K m_L\left(\dot{X}_K\dot{X}_L + \dot{Y}_K\dot{Y}_L + \dot{Z}_K\dot{Z}_L\right) + \\ + \frac{1}{2}m_e\sum_{\mu=1}^{N}\left(\dot{X}_\mu^2 + \dot{Y}_\mu^2 + \dot{Z}_\mu^2\right) - \frac{m_e^2}{2M}\sum_{\mu=1}^{N}\sum_{\nu=1}^{N}\left(\dot{X}_\mu\dot{X}_\nu + \dot{Y}_\mu\dot{Y}_\nu + \dot{Z}_\mu\dot{Z}_\nu\right) \quad (3)$$

where $\dot{X}_K \equiv \mathrm{d}X_K / \mathrm{d}t$ *etc*. are time derivatives of the coordinates. The corresponding wave-mechanical operator is:

$$\hat{T}=\hat{T}_n+\hat{T}_e=-\frac{\hbar^2}{2}\sum_{K=B}^{S}\frac{1}{m_K}\left(\frac{\partial^2}{\partial X_K^2}+\frac{\partial^2}{\partial Y_K^2}+\frac{\partial^2}{\partial Z_K^2}\right)+$$
$$+\frac{\hbar^2}{2M_n}\sum_{K=B}^{S}\sum_{L=B}^{S}\left(\frac{\partial^2}{\partial X_K\partial X_L}+\frac{\partial^2}{\partial Y_K\partial Y_L}+\frac{\partial^2}{\partial Z_K\partial Z_L}\right)- \quad (4)$$
$$-\frac{\hbar^2}{2m_e}\sum_{\mu=1}^{N}\left(\frac{\partial^2}{\partial X_\mu^2}+\frac{\partial^2}{\partial Y_\mu^2}+\frac{\partial^2}{\partial Z_\mu^2}\right)-\frac{\hbar^2}{2M_n}\sum_{\mu=1}^{N}\sum_{\nu=1}^{N}\left(\frac{\partial^2}{\partial X_\mu\partial X_\nu}+\frac{\partial^2}{\partial Y_\mu\partial Y_\nu}+\frac{\partial^2}{\partial Z_\mu\partial Z_\nu}\right)$$

Since the translational motion is of no interest, from now on, as a rule, the terms „space-fixed coordinate system“ and „nuclear center of mass system“ will be used as synonyms. In this way, the distinction between these two systems (having parallel corresponding axes), on the one hand, and the molecule-fixed coordinate system (*MFS*) that follows the rotation of the molecule (this is just going to be introduced), on the other hand, will be more clearly expressed.

The form of the kinetic energy operator (4) is not yet optimal because in it, the vibrational and rotational coordinates of the nuclei are completely mixed (they are hidden in Cartesian coordinates). Thus, the rotational motion of the molecule will now be separated, as well as possible, from vibrations of the nuclei. In order to accomplish this, a coordinate system is introduced with the origin in the *NCMS* but with the axes $x, y,$ and z differently oriented than those of the *SFS* / *NCMS*. The unit vectors along the *x*-, *y*- and *z*-axes are denoted by $\vec{i}, \vec{j}$ and $\vec{k}$, and the unit vectors along the space-fixed axes X, Y and Z by $\vec{I}, \vec{J}$ and $\vec{K}$. The position vector of the i^{th} particle in the *SFS* will be denoted in the general case (nucleus or electron) by $\vec{R}_k$. Its components are X_k, Y_k and Z_k. For the same position vector in the *MFS*, the symbol $\vec{r}_k$ will be used. The components of $\vec{r}_k$ are x_k, y_k and z_k. Since both the coordinate frames have the same origin, $\vec{R}_k = \vec{r}_k$, that is:

$$\vec{R}_k \equiv X_k\vec{I}+Y_k\vec{J}+Z_k\vec{K}=x_k\vec{i}+y_k\vec{j}+z_k\vec{k}\equiv\vec{r}_k \quad (5)$$

For derivation of the classical Hamiltonian and the angular momentum, the time derivative of this (these) vector(s) is (are) required. One can differentiate both in the *SFS* and *MFS*. When the differentiation is realized by an observer in the *SFS*, symbols like $\dot{\vec{R}}_k, \dot{\vec{r}}_k$ will be used and for differentiation within the *MFS*, $\vec{R}_k, \vec{r}_k$. Differentiating in the *SFS*, $\vec{R}_k$, *i.e.*, the radius-vector with the components along the *SFS* -axes, one obtains:

$$\dot{\vec{R}}_k=\left(\dot{X}_k\vec{I}+\dot{Y}_k\vec{J}+\dot{Z}_k\vec{K}\right)+\left(X_k\dot{\vec{I}}+Y_k\dot{\vec{J}}+Z_k\dot{\vec{K}}\right)=\dot{X}_k\vec{I}+\dot{Y}_k\vec{J}+\dot{Z}_k\vec{K} \quad (6)$$

because the unit vectors $\vec{I}, \vec{J}, \vec{K}$ do not change in time ($\dot{\vec{I}}=0, \dot{\vec{J}}=0, \dot{\vec{K}}=0$). However, if the same vector is differentiated in the *SFS*, but expressed in terms of the components along the *MFS* -axes, it has to be taken into account that for

the observer in the *SFS* not only do the components of the vector (x_k, y_k, z_k) change, but also the unit vectors $\vec{i}, \vec{j}, \vec{k}$. Thus:

$$\dot{\vec{r}}_k = \left(\dot{x}_k\vec{i} + \dot{y}_k\vec{j} + \dot{z}_k\vec{k}\right) + \left(x_k\dot{\vec{i}} + y_k\dot{\vec{j}} + z_k\dot{\vec{k}}\right) \tag{7}$$

On the other hand, if the same vector is differentiated within the *MFS*, one obtains:

$$\mathring{\vec{r}}_k = \left(\mathring{x}_k\,\vec{i} + \mathring{y}_k\,\vec{j} + \mathring{z}_k\,\vec{k}\right) + \left(x_k\,\mathring{\vec{i}} + y_k\,\mathring{\vec{j}} + z_k\,\mathring{\vec{k}}\right) = \dot{x}_k\vec{i} + \dot{y}_k\vec{j} + \dot{z}_k\vec{k} \tag{8}$$

The expression on the right-hand side follows from the fact that for the observer in the MFS, the unit vectors $\vec{i}, \vec{j}, \vec{k}$ are at rest ($\mathring{\vec{i}} = \mathring{\vec{j}} = \mathring{\vec{k}} = 0$), and in the non-relativistic approximation, time is the same in all coordinate frames, *i.e.*, $\mathring{x}_k = \dot{x}_k$ *etc*., as for all scalar quantities.

The *MFS* is chosen so that it rotates together with the nuclear skeleton of the molecule, *i.e*., the coordinate system itself takes over (as completely as possible) the molecular rotations, while (ideally) the only kind of motion of the nuclei within it represent vibrations. The orientation of the *MFS*-axes with respect to the axes of the *SFS* is usually defined by means of Euler angles φ, θ, χ. They are certain functions of the nuclear coordinates. In this way, the number of linearly independent nuclear coordinates in the *MFS* will be reduced to $3S-6$. Let us assume that the coordinates of nucleus *B* are eliminated by the relations $\xi_B = f_{\xi_B}(x_C, ..., z_S)$, where $\xi = x, y, z$. Besides, there are $3N$ electronic coordinates, $x_\alpha, y_\alpha, z_\alpha$, ..., x_N, y_N, z_N. Thus, there are the following two sets of $3(S+N)-3$ coordinates: a) *NCMS*: $\vec{R}_B, ..., \vec{R}_S$, $\vec{R}_1, ..., \vec{R}_\mu, ..., \vec{R}_N$ and b) *MFS*: $\varphi, \theta, \chi, \vec{r}_C, ..., \vec{r}_S, \vec{r}_1, ..., \vec{r}_\mu, ..., \vec{r}_N$. They are related by:

$$\varphi = f_\varphi(X_B, ..., Z_S), \quad \theta = f_\theta(X_B, ..., Z_S), \quad \chi = f_\chi(X_B, ..., Z_S),$$

$$\begin{pmatrix} x_n \\ y_n \\ z_n \end{pmatrix} = \begin{pmatrix} \lambda_{xX}(X_B, ..., Z_S) & \lambda_{xY}(X_B, ..., Z_S) & \lambda_{xZ}(X_B, ..., Z_S) \\ \lambda_{yX}(X_B, ..., Z_S) & \lambda_{yY}(X_B, ..., Z_S) & \lambda_{yZ}(X_B, ..., Z_S) \\ \lambda_{zX}(X_B, ..., Z_S) & \lambda_{zY}(X_B, ..., Z_S) & \lambda_{zZ}(X_B, ..., Z_S) \end{pmatrix} \begin{pmatrix} X_n \\ Y_n \\ Z_n \end{pmatrix} \tag{9}$$

$$n = C, ..., S, 1, ..., N$$

and, reversely,

$$\begin{pmatrix} X_n \\ Y_n \\ Z_n \end{pmatrix} = \begin{pmatrix} \lambda_{Xx}(\varphi,\theta,\chi) & \lambda_{Xy}(\varphi,\theta,\chi) & \lambda_{Xz}(\varphi,\theta,\chi) \\ \lambda_{Yx}(\varphi,\theta,\chi) & \lambda_{Yy}(\varphi,\theta,\chi) & \lambda_{Yz}(\varphi,\theta,\chi) \\ \lambda_{Zx}(\varphi,\theta,\chi) & \lambda_{Zy}(\varphi,\theta,\chi) & \lambda_{Zz}(\varphi,\theta,\chi) \end{pmatrix} \begin{pmatrix} x_n \\ y_n \\ z_n \end{pmatrix}$$

$$n = B,...,S,1,...,N \tag{10}$$

$$\left\{ x_B = f_{x_B}(x_C,...,z_S), \quad y_B = f_{y_B}(x_C,...,z_S), \quad z_B = f_{z_B}(x_C,...,z_S) \right\},$$

where the coefficients $\lambda_{Xx}=[\lambda_{xX}=\vec{i}\cdot\vec{I}=\cos(x,X)]$, $\lambda_{Xy}=[\lambda_{yX}=\vec{j}\cdot\vec{I}=\cos(y,X)]$ expressed in terms of the Euler angles φ,θ,χ are:

$$\begin{aligned} &\lambda_{xX} = \cos\varphi\cos\theta\cos\chi - \sin\varphi\sin\chi,\ \lambda_{xY} = \sin\varphi\cos\theta\cos\chi + \cos\varphi\sin\chi, \\ &\lambda_{xZ} = -\sin\theta\cos\chi \\ &\lambda_{yX} = -\cos\varphi\cos\theta\sin\chi - \sin\varphi\cos\chi,\ \lambda_{yY} = -\sin\varphi\cos\theta\sin\chi + \cos\varphi\cos\chi, \\ &\lambda_{yZ} = \sin\theta\sin\chi \\ &\lambda_{zX} = \cos\varphi\sin\theta,\ \lambda_{zY} = \sin\varphi\sin\theta,\ \lambda_{zZ} = \cos\theta \end{aligned} \tag{11}$$

The transformations (10) look completely symmetric with respect to the nuclei and electrons, but in fact, they are not. Since the coefficients $\lambda_{xX},...,\lambda_{zZ}$ (*via* the Euler angles φ,θ,χ) are determined (solely) by the positions of the nuclei, the relationship between electronic coordinates in the *SFS* and *MFS* is just an orthogonal linear transformation involving constant coefficients. On the other hand, the transformation of the coordinates of the nuclei is not linear.

The number of linearly independent nuclear coordinates in the *MFS*, $3S-6$, is just necessary and sufficient to define unambiguously the form of the nuclear skeleton. In praxis, the Cartesian coordinates $x_C,y_C,z_C,...,x_S,y_S,z_S$ of the nuclei will not be used but rather some "internal coordinates", which determine the positions of the nuclei with respect to one another. These can be chosen in a pure geometric way, such that they represent the bond lengths, the angles between bonds, *etc*. In this paper, however, instead of them, appropriate linear combinations of the displacements of the Cartesian coordinates of the nuclei from their equilibrium positions measured in the *MFS*, the "normal coordinates" $Q_1,Q_2,...,Q_{3S-6}$, will be used.

It is easy to show that the form of the electronic part of the kinetic energy operator (4), when carried out *via* the "first way" is not changed during the transition to the *MFS*, *i.e*., that it becomes:

$$\begin{aligned} \hat{T}_e = &-\frac{\hbar^2}{2m_e}\sum_{\mu=1}^{N}\left(\frac{\partial^2}{\partial x_\mu^2}+\frac{\partial^2}{\partial y_\mu^2}+\frac{\partial^2}{\partial z_\mu^2}\right)- \\ &-\frac{\hbar^2}{2M_n}\sum_{\mu=1}^{N}\sum_{\nu=1}^{N}\left(\frac{\partial^2}{\partial x_\mu\partial x_\nu}+\frac{\partial^2}{\partial y_\mu\partial y_\nu}+\frac{\partial^2}{\partial z_\mu\partial z_\nu}\right) \end{aligned} \tag{12}$$

The invariance of the electronic kinetic energy operator is a consequence of the fact that the transformation matrix (9) is only a function of the nuclear coordinates. The transformation of the nuclear kinetic energy operator is much more complex. For example, the first derivative with respect to the coordinate X_K transforms into:

$$\frac{\partial}{\partial X_K} \rightarrow \frac{\partial \varphi}{\partial X_K}\frac{\partial}{\partial \varphi} + \frac{\partial \theta}{\partial X_K}\frac{\partial}{\partial \theta} + \frac{\partial \chi}{\partial X_K}\frac{\partial}{\partial \chi} + \sum_{i=1}^{3S-6}\frac{\partial Q_I}{\partial X_K}\frac{\partial}{\partial Q_I} + \\ + \sum_{\mu=1}^{N}\left(\frac{\partial x_\mu}{\partial X_K}\frac{\partial}{\partial x_\mu} + \frac{\partial y_\mu}{\partial X_K}\frac{\partial}{\partial y_\mu} + \frac{\partial z_\mu}{\partial X_K}\frac{\partial}{\partial z_\mu}\right) \tag{13}$$

Nothing on the right-hand side vanishes automatically. Not only the Euler angles and normal coordinates, but even the electronic coordinates x_μ, y_μ, z_μ, *via* the elements λ_{xX} ,... of the transformation matrix in Eq. (9) are functions (moreover, very complicated) of the coordinate X_K . The last sum on the right-hand side of Eq. (13) will introduce into the expression for $\partial / \partial X_K$ also derivatives of the electronic coordinates in the *MFS*. The same conclusions hold for the second derivatives. This means that the transformation whose role was to separate the rotations from vibrations introduces a coupling between nuclear and electronic coordinates in the kinetic energy operator. The above analysis of the structure of Eq. (13) shows that a derivation of the expression for $\hat{T}_n$ in the MFS in the way applied for transformation of $\hat{T}_e$ into (12) would be very difficult. For this reason, it is more convenient to use instead the "second way" (b).

From now on, the derivation presented in Wilson's book[3] is closely followed It is easy to show that the classical expression for the kinetic energy of the nuclei from Eq. (3) equals:

$$T_n = \frac{1}{2}\sum_{K=A}^{S} m_K\left(\dot{\vec{R}}_K \cdot \dot{\vec{R}}_K\right) = \frac{1}{2}\sum_{K=A}^{S} m_K\left(\dot{X}_K^2 + \dot{Y}_K^2 + \dot{Z}_K^2\right) \tag{14}$$

under the condition:

$$\sum_{K=A}^{S} m_K \vec{R}_K = 0 \tag{15}$$

The following notations are used: $\vec{R}_K$ is the position vector and $\dot{\vec{R}}_K$ the velocity vector of the nucleus K in the *SFS* (more precisely, in the *NCMS*) *i.e.*, the vector whose components are measured along the axes of the *SFS*; $\vec{r}_K$ is the position vector, and $\vec{r}_K^0$ the equilibrium position vector in the *MFS*; $\Delta\vec{r}_K$ represents the (vibrational) displacement of the nucleus *K* with respect to its equilibrium value and $\dot{\vec{r}}_K$ is the velocity of the nucleus measured in the *MFS*. The time

derivatives of the radius-vector $\vec{r}_K$ as measured in the *SFS* and in the *MFS* rotating with an angular velocity $\vec{\omega}$, respectively, are connected by the relation:

$$\dot{\vec{r}}_K = \overset{\circ}{\vec{r}}_K + \vec{\omega} \times \vec{r}_K \tag{16}$$

The first term on the right-hand side describes the change in time of the vector $\vec{r}_K$ within the *MFS*, and the second term the effect of rotation of this system on the change of $\vec{r}_K$ as measured in the *SFS*. As stated above, the orientation of the *MFS* is determined by the values of the Euler angles φ, θ and χ, chosen in such a way that the relative displacements of the nuclei with respect to one another (vibrations) be minimally coupled with the rotations of the nuclear skeleton. Note that the components of the angular velocity, $\omega_x, \omega_y, \omega_z$, are not „true“ velocities in the sense that they do not represent time derivatives of the corresponding coordinates – they can be expressed as linear combinations of time derivatives of the Euler angles.

Complete separation of the vibrational from the rotational coordinates would be possible if the “vibrational angular momentum”:

$$\vec{J}_v = \sum_{K=A}^{S} m_K \left(\vec{r}_K \times \overset{\circ}{\vec{r}}_K \right) \tag{17}$$

in the *MFS* were vanishing. It turns out, however, that the three scalar equations, $\vec{J}_{vx} = 0, \vec{J}_{vy} = 0,$ and $\vec{J}_{vz} = 0$ do not enable the determination of the values of φ, θ, and χ such that the corresponding vectors $\{\vec{r}_K\}$ and $\{\overset{\circ}{\vec{r}}_K\}$ fulfill the condition $\vec{J}_v = 0$. The best that can be done in trying to separate vibrations from rotations is to replace the condition $\vec{J}_v = 0$ by:

$$\sum_{K=A}^{S} m_K (\vec{r}_K^{\,0} \times \overset{\circ}{\vec{r}}_K) = 0 \tag{18}$$

The quantity on the left-hand side of (18) differs from (17) in that the instantaneous position vectors $\vec{r}_K$ (which appear in $\vec{J}_v$) are replaced by their equilibrium counterparts, $\vec{r}_K^{\,0}$ – the difference between them tends to zero when the nuclei undergo small-amplitude (“infinitesimal”) vibrations. Since the vibrations are commonly characterized by small amplitudes, the condition (18) ensures, as a rule, good separation of the rotations from the vibrational degrees of freedom. It is easy to show that expression (18) can be obtained by differentiating the Eckart condition:[9]

$$\sum_{K=A}^{S} m_K (\vec{r}_K^{\,0} \times \vec{r}_K) = 0 \tag{19}$$

Inserting the expression (16) for the nuclear velocity in (14), replacing $\vec{r}_K$ by $\vec{r}_K^{\,0} + \Delta\vec{r}_K$, taking into account (19), and expanding the vector quantities into their

scalar components, one obtains for the classical kinetic energy of the nuclei the expression:

$$T_n = \frac{1}{2}\sum_{K=A}^{S} m_K \left(\dot{\vec{R}}_K \cdot \dot{\vec{R}}_K\right) =$$
$$= \frac{1}{2}I_{xx}\omega_x^2 + \frac{1}{2}I_{yy}\omega_y^2 + \frac{1}{2}I_{zz}\omega_z^2 + I_{xy}\omega_x\omega_y + I_{yz}\omega_y\omega_z + I_{zx}\omega_z\omega_x +$$
$$+\omega_x \sum_{K=A}^{S} m_K (\Delta\vec{r}_K \times \mathring{\vec{r}}_K)_x + \omega_y \sum_{K=A}^{S} m_K (\Delta\vec{r}_K \times \mathring{\vec{r}}_K)_y + \tag{20}$$
$$+\omega_z \sum_{K=A}^{S} m_K (\Delta\vec{r}_K \times \mathring{\vec{r}}_K)_z + \frac{1}{2}\sum_{K=A}^{S} m_K \left(\mathring{\vec{r}}_K\right)$$

where:

$$I_{xx} \equiv \sum_{K=A}^{S} m_K \left(y_K^2 + z_K^2\right), \quad I_{yy} \equiv \sum_{K=A}^{S} m_K \left(z_K^2 + x_K^2\right), \quad I_{zz} \equiv \sum_{K=A}^{S} m_K \left(x_K^2 + y_K^2\right),$$
$$I_{xy} = I_{yx} = -\sum_{K=A}^{S} m_K x_K y_K, \quad I_{yz} = I_{zy} = -\sum_{K=A}^{S} m_K y_K z_K, \quad I_{zx} = I_{xz} = -\sum_{K=A}^{S} m_K z_K x_K \tag{21}$$

are the instantaneous moments and products of inertia. Note that these quantities are not constant but are functions of the nuclear positions, which change in the course of vibrations.

The expression (20) for the kinetic energy of the nuclei consists of three parts. In the first one appear the moments and products of inertia and the components of the angular velocity vector $\vec{\omega}$, and this part describes the rotational motion of the molecule as a whole. The last term on the right-hand side of (20) involves (besides the nuclear masses) only the velocities of the nuclei moving in the *MFS*, and thus represents the vibrational kinetic energy. In the middle term appear both the angular velocity and velocities within the *MFS*; it describes the coupling between the rotations and vibrations. The appearance of this term is a consequence of defining the orientation of the *MFS* axes by means of the conditions (18), instead of equating (17) to zero.

The most convenient way to describe the molecular vibrations is based on the use of the normal coordinates, $Q_1,...,Q_i,...,Q_{3S-6}$. Actually, their form is not known at this stage, because they can be determined only after the introduction of the Born–Oppenheimer approximation[10] and solving the electronic Schrödinger equation at various nuclear arrangements around the equilibrium molecular geometry. Only the fact that these coordinate do exist can be used at this moment. By summing, the normal coordinates are denoted by lowercase Latin

subscripts i, j. They are connected with the Cartesian displacement coordinates, $\Delta x_K, \Delta y_K, \Delta z_K$, by the linear relations:

$$\begin{aligned}\sqrt{m_K}\Delta x_K &= \sum_{i=1}^{3S-6} l_{xK,i}Q_i, \sqrt{m_K}\Delta y_K = \sum_{i=1}^{3S-6} l_{yK,i}Q_i, \\ \sqrt{m_K}\Delta z_K &= \sum_{I=1}^{3S-6} l_{zK,i}Q_i, \quad K=1,...,S\end{aligned} \tag{22}$$

where the (constant) coefficients $l_{xK,i}, l_{yK,i}, l_{zK,i}$ are chosen such that the normal coordinates simultaneously reduce the expressions for the kinetic energy and the quadratic part of the potential energy of vibrations to the sums of quadratic terms:

$$T_v = \frac{1}{2}\sum_{i=1}^{3S-6}\dot{Q}_i^2, \quad V = \frac{1}{2}\sum_{i=1}^{3S-6}\lambda_i Q_i^2 \tag{23}$$

Expressed in terms of the normal coordinates, the terms coupling vibrations with rotations are:

$$\begin{aligned}\sum_{K=A}^{S} m_K(\Delta\vec{r}_K \times \mathring{\vec{r}}_K)_x &= \sum_{i=1}^{3S-6}\mathfrak{I}_i\dot{Q}_i \\ \sum_{K=A}^{S} m_K(\Delta\vec{r}_K \times \mathring{\vec{r}}_K)_y &= \sum_{i=1}^{3S-6}\mathfrak{R}_i\dot{Q}_i \\ \sum_{K=A}^{S} m_K(\Delta\vec{r}_K \times \mathring{\vec{r}}_K)_z &= \sum_{i=1}^{3S-6}\aleph_i\dot{Q}_i\end{aligned} \tag{24}$$

where:

$$\begin{aligned}\mathfrak{I}_i &= \sum_{j=1}^{3S-6}\left[\sum_{K=A}^{S}\left(l_{yK,j}l_{zK,i} - l_{zK,j}l_{yK,i}\right)\right]Q_j \equiv \sum_{j=1}^{3S-6}\zeta_{ji}^{x}Q_j, \\ \mathfrak{R}_i &= \sum_{j=1}^{3S-6}\left[\sum_{K=A}^{S}\left(l_{zK,j}l_{xK,i} - l_{xK,j}l_{zK,i}\right)\right]Q_j \equiv \sum_{j=1}^{3S-6}\zeta_{ji}^{y}Q_j, \\ \aleph_i &= \sum_{j=1}^{3S-6}\left[\sum_{K=A}^{S}\left(l_{xK,j}l_{zK,i} - l_{yK,j}l_{xK,i}\right)\right]Q_j \equiv \sum_{j=1}^{3S-6}\zeta_{ji}^{z}Q_j\end{aligned} \tag{25}$$

are linear combinations of the normal coordinates. Inserting (24) into (20), one obtains:

$$T_n = \frac{1}{2}I_{xx}\omega_x^2 + \frac{1}{2}I_{yy}\omega_y^2 + \frac{1}{2}I_{zz}\omega_z^2 + I_{xy}\omega_x\omega_y + I_{yz}\omega_y\omega_z + I_{zx}\omega_z\omega_x + \omega_x\sum_{i=1}^{3S-6}\Im_i\dot{Q}_i + \omega_y\sum_{i=1}^{3S-6}\Re_i\dot{Q}_i + \omega_z\sum_{i=1}^{3S-6}\aleph_i\dot{Q}_i + \frac{1}{2}\sum_{i=1}^{3S-6}\dot{Q}_i^2 \quad (26)$$

Equation (26) is the kinetic energy of the nuclei in terms of the coordinates and velocities.

In order to obtain the Hamiltonian, the velocities $\omega_x, \omega_y, \omega_z$ and $\dot{Q}_i = \mathring{Q}_i$ have to be replaced by impulses. The impulse, P_i, canonically conjugate to the normal coordinate Q_i, is:

$$P_i = \frac{\partial T_n}{\partial \dot{Q}_i} = \dot{Q}_i + \Im_i\omega_x + \Re_i\omega_y + \aleph_i\omega_z \quad (27)$$

First, in expression (26), the components of the angular velocity $\vec{\omega}$ are replaced by the components of the nuclear angular momentum $\vec{R}$:

$$\vec{R} = \sum_{K=A}^{S} m_K(\vec{r}_K \times \dot{\vec{r}}_K) = \sum_{K=A}^{S} m_K(\vec{r}_K \times \mathring{\vec{r}}_K) + \sum_{K=A}^{S} m_K\left[\vec{r}_K \times (\vec{\omega} \times \vec{r}_K)\right] \quad (28)$$

along the axes of the *MFS*:

$$\begin{aligned} R_x &= I_{xx}\omega_x + I_{xy}\omega_y + I_{xz}\omega_z + \sum_{i=1}^{3S-6}\Im_i\dot{Q}_i = \frac{\partial T_n}{\partial \omega_x}, \\ R_y &= I_{yx}\omega_x + I_{yy}\omega_y + I_{yz}\omega_z + \sum_{i=1}^{3S-6}\Re_i\dot{Q}_i = \frac{\partial T_n}{\partial \omega_y}, \\ R_z &= I_{zx}\omega_x + I_{zy}\omega_y + I_{zz}\omega_z + \sum_{i=1}^{3S-6}\aleph_i\dot{Q}_i = \frac{\partial T_n}{\partial \omega_z}. \end{aligned} \quad (29)$$

When dealing only with the nuclei, as now, these quantities equal the components J_x, J_y, J_z of the total angular momentum (also involving electronic contributions). Using Eq. (27), one derives

$$\begin{aligned} R_x - p_x &= I'_{xx}\omega_x + I'_{xy}\omega_y + I'_{xz}\omega_z, \\ R_y - p_y &= I'_{yx}\omega_x + I'_{yy}\omega_y + I'_{yz}\omega_z, \\ R_z - p_z &= I'_{zx}\omega_x + I'_{zy}\omega_y + I'_{zz}\omega_z. \end{aligned} \quad (30)$$

where:

$$p_x = \sum_{i=1}^{3S-6}\Im_i P_i, \quad p_y = \sum_{i=1}^{3S-6}\Re_i P_i, \quad p_z = \sum_{i=1}^{3S-6}\aleph_i P_i \quad (31)$$

are "vibrational angular momenta", and the quantities, defined as:

$$I'_{xx} \equiv I_{xx} - \sum_{i=1}^{3S-6} \mathfrak{I}_i^2, \quad I'_{yy} \equiv I_{yy} - \sum_{i=1}^{3S-6} \mathfrak{R}_i^2, \quad I'_{zz} \equiv I_{zz} - \sum_{i=1}^{3S-6} \aleph_i^2,$$
$$I'_{xy} \equiv I_{xy} - \sum_{i=1}^{3S-6} \mathfrak{I}_i \mathfrak{R}_i, \quad I'_{yz} \equiv I_{yz} - \sum_{i=1}^{3S-6} \mathfrak{R}_i \aleph_i, \quad I'_{zx} \equiv I_{zx} - \sum_{i=1}^{3S-6} \aleph_i \mathfrak{I}_i, \tag{32}$$

reduce, in the case of small-amplitude vibrations, to the instantaneous moments and products of inertia. To eliminate from the expressions (26) and (28) the components of the angular velocity, the transformation inverse to (30) is required:

$$\begin{aligned} \omega_x &= \mu_{xx}(R_x - p_x) + \mu_{xy}(R_y - p_y) + \mu_{xz}(R_z - p_z), \\ \omega_y &= \mu_{yx}(R_x - p_x) + \mu_{yy}(R_y - p_y) + \mu_{yz}(R_z - p_z), \\ \omega_z &= \mu_{zx}(R_x - p_x) + \mu_{zy}(R_y - p_y) + \mu_{zz}(R_z - p_z). \end{aligned} \tag{33}$$

The coefficients $\mu_{\alpha\beta} = \mu_{\beta\alpha}$ ($\alpha, \beta = x, y$ or z) are elements of the matrix inverse to the matrix with elements $I'_{\alpha\beta}$. $\mu_{\alpha\beta}$ are only the functions of the normal coordinates. Using the relations (27)–(33), expression (26) can be transformed into:

$$T_n = \frac{1}{2} \sum_{\gamma=x}^{z} \sum_{\delta=x}^{z} \mu_{\gamma\delta}(R_\gamma - p_\gamma)(R_\delta - p_\delta) + \frac{1}{2} \sum_{i=1}^{3S-6} P_i^2 \tag{34}$$

PODOLSKY TRANSFORMATION

Equation (34) represents the classical expression for the kinetic energy of nuclei in terms of the momenta P_i conjugate to the normal coordinates, the vibrational angular momenta, p_x, p_y, p_z, and the nuclear angular momenta R_x, R_y, R_z. The construction of the corresponding wave-mechanical operator is, however, not trivial for two reasons. First, curvilinear coordinates (Euler angles) are being dealt with, and secondly, the momenta R_x, R_y, R_z are (in general) not conjugate to any concrete coordinates. The first problem was solved by Podolsky.[8]

Suppose that one has M generalized (in the general case non-Cartesian) coordinates, $q_1, q_2, ..., q_M$. In all cases of present interest, the classical kinetic energy will be homogeneous quadratic functions of generalized velocities:

$$T = \frac{1}{2} \sum_{m=1}^{M} \sum_{n=1}^{M} T_{mn}(q_1, q_2, ..., q_M) \dot{q}_m \dot{q}_n \tag{35}$$

The coefficients T_{mn} ($= T_{nm}$) depend, in general, on generalized coordinates. The relationship between the generalized velocities and the impulses conjugate to the coordinates $q_1, q_2, ..., q_M$ are:

$$p_n = \frac{\partial T}{\partial \dot{q}_n} = \sum_{m=1}^{M} T_{mn}(q_1, q_2, ..., q_M)\dot{q}_m, \qquad n = 1, ..., M \tag{36}$$

The relations inverse to (36) are:

$$\dot{q}_n = \sum_{m=1}^{n} g_{mn}(q_1, q_2, ..., q_M)p_m, \qquad n = 1, ..., M \tag{37}$$

where $g_{mn} = g_{nm}$ are elements of the matrix inverse to the matrix $\{T_{mn}\}$, $g_{mn} = (T^{-1})_{mn}$. Inserting the expressions (37) for $\dot{q}_n$ into (35), one obtains the classical kinetic energy in impulse form:

$$T = \frac{1}{2}\sum_{m=1}^{M}\sum_{n=1}^{M} g_{mn}\left(q_1, q_2, ..., q_M\right)p_m p_n \tag{38}$$

If an attempt is made to construct the corresponding wave-mechanical operator by replacing the impulses in expression (38) with the corresponding operators, problems are encountered. Since the impulse operators do not in general commute with the coefficients g_{mn} (because these depend on the coordinates), it is not possible based on (38) to conclude which is the correct ordering of the quantities on the right-hand side. If one worked instead with Cartesian coordinates (or any other „rectilinear“ coordinates as, *e.g.*, the normal coordinates), the expansion coefficients would be constant, and since the impulse operators associated with different coordinates or particles commute, one would directly obtain the wave-mechanical kinetic energy operator as:

$$\hat{T} = \frac{1}{2}\sum_{m=1}^{M}\sum_{n=1}^{M} g_{mn}\hat{p}_m\hat{p}_n = -\frac{\hbar^2}{2}\sum_{m=1}^{M}\sum_{n=1}^{M} g_{mn}\frac{\partial^2}{\partial q_m \partial q_n} \tag{39}$$

Podolsky showed that it is nevertheless possible, without intermediate use of Cartesian coordinates, to construct the wave-mechanical Hamiltonian that corresponds to the classical expression (38) if this classical expression is first appropriately symmetrized:

$$T \equiv \frac{1}{2}g^{1/4}\sum_{m=1}^{M}\sum_{n=1}^{M} p_m g^{-1/2} g_{mn} p_n g^{1/4} \tag{40}$$

This leads to the operator in the form:

$$\hat{T} = \frac{1}{2} s_q^{-1/2} g^{1/4} \left\{ \sum_{m=1}^{M} \sum_{n=1}^{M} \hat{p}_m g^{-1/2} g_{mn} \hat{p}_n \right\} g^{1/4} s_q^{1/2} = \\ = -\frac{\hbar^2}{2} s_q^{-1/2} g^{1/4} \left\{ \sum_{m=1}^{M} \sum_{n=1}^{M} \frac{\partial}{\partial q_m} g^{-1/2} g_{mn} \frac{\partial}{\partial q_n} \right\} g^{1/4} s_q^{1/2} \tag{41}$$

By g is denoted the determinant with elements g_{mn}, and s_q is a conveniently chosen weight factor (in general a function of the coordinates) of the volume (integration) element, $dV = dq_1 dq_2 ... dq_M \equiv s_q \Pi_{n=1}^{M} dq_n$. In the expression (41), the operators act onto everything on their right-hand sides (including, of course, the wave function). The operator (41) can be transformed so that the differential operators only act on the wave function:

$$\hat{T} \equiv \hat{T}^{(2)} + \hat{T}^{(1)} + \hat{T}^{(0)} = -\frac{\hbar^2}{2} \sum_{m=1}^{M} \sum_{n=1}^{M} g_{mn} \frac{\partial^2}{\partial q_m \partial q_n} - \\ -\frac{\hbar^2}{2} \sum_{m=1}^{M} \left[\sum_{n=1}^{M} \left(\frac{\partial g_{mn}}{\partial q_n} + \frac{g_{mn}}{s_q} \frac{\partial s_q}{\partial q_n} \right) \right] \frac{\partial}{\partial q_m} - \\ -\frac{\hbar^2}{8} \sum_{m=1}^{M} \sum_{n=1}^{M} \{ \frac{1}{g} \left(\frac{\partial g_{mn}}{\partial q_n} \frac{\partial g}{\partial q_n} + g_{mn} \frac{\partial^2 g}{\partial q_m \partial q_n} \right) + \\ + \frac{2}{s_q} \left(\frac{\partial g_{mn}}{\partial q_n} \frac{\partial s_q}{\partial q_m} + g_{mn} \frac{\partial^2 s_q}{\partial q_m \partial q_n} \right) - \frac{g_{mn}}{s_q^2} \frac{\partial s_q}{\partial q_m} \frac{\partial s_q}{\partial q_n} \} \tag{42}$$

Note that the kinetic energy operator in curvilinear coordinates (unlike the operator in Cartesian coordinates, which is a homogenous quadratic form of derivatives) also involves terms linear in derivatives and a constant (*i.e.*, not containing any derivatives) term. Both the linear and constant terms are completely determined by the expansion coefficients of the quadratic part. In a special, but quite common case, when $g = J^{-2}$ and $s_q = J$, where J is the Jacobian of the transformation from Cartesian into non-Cartesian coordinates, $\hat{T}^{(0)} = 0$.

The Podolsky transformation in its original version covers the cases when all momenta are conjugate to the corresponding, in general curvilinear, coordinates. However, sometimes it is more convenient to use the momenta, such as the components of the angular momentum, which are not conjugate to any coordinates. These quantities are called quasi-momenta. This topic was investigated by Wilson and Howard[2,3] and later more generally by Watson;[1,4] they showed that the wave-mechanical Hamiltonian could be expressed in terms of the operators corresponding to quasi-momenta, provided that some special conditions are fulfilled.

In the present case, the quasi-momenta are the quantities $\left(R_\gamma - p_\gamma\right)$. It can be shown that the components of the total angular momentum, J_x, J_y, J_z, along the *MFS* axes, being in the present case equal to the components of the angular momentum of the nuclei, R_x, R_y, R_z, are related to the impulses $p_\varphi, p_\theta, p_\chi$, conjugate to the Euler angles:

$$p_\varphi = \frac{\partial T}{\partial \dot{\varphi}}, \quad p_\theta = \frac{\partial T}{\partial \dot{\theta}}, \quad p_\chi = \frac{\partial T}{\partial \dot{\chi}} \tag{43}$$

by:[7,11]

$$\begin{aligned} J_x &= -\frac{\cos\chi}{\sin\theta}\cdot p_\varphi + \sin\chi\cdot p_\theta + \cot\theta\cos\chi\cdot p_\chi, \\ J_y &= \frac{\sin\chi}{\sin\theta}\cdot p_\varphi + \cos\chi\cdot p_\theta - \cot\theta\sin\chi\cdot p_\chi, \\ J_z &= p_\chi \end{aligned} \tag{44}$$

Note that the relations (44) are valid independently of whether the electronic coordinates are related to the *SFS* or *MFS*, whereas the expressions on the right-hand side equal to R_x, R_y, R_z, respectively, are only valid when the electronic coordinates are left in the *SFS*. There were some reasons to prefer up to now the symbols R_x, R_y, R_z; but from now on, we skip to J_x, J_y, J_z. It turns out that the transformations (43/44) fulfill the conditions required for application of the generalized Podolsky transformation. The volume element at the integration of the wave functions will be $dV = \sin\theta\cdot d\varphi\cdot d\theta\cdot d\chi\cdot dQ_1 ... dQ_{3S-6}$. Therefore, the wave-mechanical operator for the kinetic energy of nuclei, analogous to the general expression (41), is:

$$\begin{aligned} \hat{T}_n = \frac{1}{2}\mu^{\frac{1}{4}}\left\{\sum_{\gamma=x}^{z}\sum_{\delta=x}^{z}\left(\hat{J}_\gamma - \hat{p}_\gamma\right)\mu_{\gamma\delta}\mu^{-\frac{1}{2}}\left(\hat{J}_\delta - \hat{p}_\delta\right)\right\}\mu^{\frac{1}{4}} + \\ + \frac{1}{2}\mu^{\frac{1}{4}}\left\{\sum_{i=1}^{3S-6}\hat{P}_i\mu^{-\frac{1}{2}}\hat{P}_i\right\}\mu^{\frac{1}{4}} \end{aligned} \tag{45}$$

where the wave-mechanical operators $\hat{J}_\gamma$ and $\hat{p}_\gamma$ ($\gamma = x, y, z$) are obtained by replacing in the expressions (44) and (31), the classical impulses $\hat{p}_q$ ($q = \varphi, \theta, \chi, P_i$) by the operators $-i\hbar\partial/\partial q$. (Watson[4] claimed that this did not in general hold and that in the present case the correct result was obtained thanks to "a more-or-less fortuitous cancellation" of some terms. I find this statement a little bit severe; the mentioned fortuitous cancellation is actually a direct consequence of the proper choice of the volume element $\mathrm{d}V$).

Watson[1] showed that the expression (45) could be simplified. He derived certain commutation relations, such as:

$$\sum_{\alpha=x}^{z}\left[\hat{p}_\alpha,\mu_{\alpha\beta}\right]=0 \tag{46}$$

which enabled Eq. (45) to be rearranged into:

$$\begin{aligned}\hat{T}_n &= \frac{1}{2}\left\{\sum_{\gamma=x}^{z}\sum_{\delta=x}^{z}\left(\hat{J}_\gamma-\hat{p}_\gamma\right)\mu_{\gamma\delta}\left(\hat{J}_\delta-\hat{p}_\delta\right)\right\}+\frac{1}{2}\sum_{i=1}^{3S-6}\hat{P}_i^2-\frac{\hbar^2}{8}\sum_{\gamma=x}^{z}\mu_{\gamma\gamma}= \\ &= \frac{1}{2}\left\{\sum_{\gamma=x}^{z}\sum_{\delta=x}^{z}\mu_{\gamma\delta}\left(\hat{J}_\gamma-\hat{p}_\gamma\right)\left(\hat{J}_\delta-\hat{p}_\delta\right)\right\}+\frac{1}{2}\sum_{i=1}^{3S-6}\hat{P}_i^2-\frac{\hbar^2}{8}\sum_{\gamma=x}^{z}\mu_{\gamma\gamma}\end{aligned} \tag{47}$$

The term $-\left(\hbar^2/8\right)\sum_\gamma\mu_{\gamma\gamma}$ can be handled as an additional part of the potential; however, unlike the common potential terms, it depends on the nuclear masses and thus, it is not isotopically invariant.

TRANSFER OF ELECTRONIC COORDINATES INTO A MOLECULE FIXED SYSTEM

Now both the electronic (Eq. (12)) and the nuclear kinetic energy (Eq. (47)) operators, expressed in terms of the desired impulses/momenta, are available. Let us return, however, to Eq. (13) and the text following it: It was concluded that the transformed nuclear kinetic energy operator would be spoiled by electron variables but the operator (47) does not contain them. What has happened? The explanation is the following: the full classical kinetic energy was separated into two parts, which were handled in different ways. The electronic kinetic energy operator was constructed by method (a) (as defined in Introduction), and the kinetic energy operator by method (b). These two methods give identical results when applied to the full kinetic energy, but not always when the classical kinetic energy is separated into its constituent part. Thus, although we started with the classical kinetic energy for nuclei being equivalent to the corresponding quantum mechanical operator in terms of the *NCMS* variables, results identical to those that would have been derived if the problem had been handled using method (a) were not obtained. Since good reasons existed to avoid scheme (a) in the construction of the nuclear kinetic energy operator, now the electronic kinetic energy will be transformed also by method (b). Note that neither Wilson[2,3] nor Watson[1] considered the transfer of the electronic variables into the *MFS*. This topic was handled in the classical paper by Van Vleck,[12] nowadays very difficult to read due to the old-fashioned notation and definition of the Euler angles. A modern presentation can be found in the book by Brown and Carrington.[13] The non-appearance of the electronic coordinates in the operator (47) is explained as being a consequence of the tacit assumption that the angular momentum operator with the components J_x, J_y, J_z, depending only on the Euler angles, does not act on the electron coordinates. However, if the electronic coordinates are defined with

respect to the *MFS*-axes, the indirect effect of the operators J_x, J_y, J_z on them (*via* the transformation coefficients expressed in terms of the Euler angles) has to be taken into account. The way chosen herein is more straightforward.

Starting with the classical electronic kinetic energy in velocity form, defined in the *NCMS* (see Eq. (3)):

$$T_e = \frac{1}{2} m_e \sum_{\mu=1}^{N} \left(\dot{\vec{R}}_\mu \cdot \dot{\vec{R}}_\mu \right) - \frac{m_e^2}{2M} \sum_{\mu=1}^{N} \sum_{\nu=1}^{N} \left(\dot{\vec{R}}_\mu \cdot \dot{\vec{R}}_\nu \right) \tag{48}$$

and substituting $\dot{\vec{R}}_K$ by the expressions analogous to (16), $\dot{\vec{r}}_\mu = \mathring{\vec{r}}_\mu + \vec{\omega} \times \vec{r}_\mu$, one obtains:

$$\begin{aligned} T_e = {} & \frac{1}{2} I_{xx}^e \omega_x^2 + \frac{1}{2} I_{yy}^e \omega_y^2 + \frac{1}{2} I_{zz}^e \omega_z^2 + I_{xy}^e \omega_x \omega_y + I_{yz}^e \omega_y \omega_z + I_{zx}^e \omega_z \omega_x + \\ & + \omega_x \left[\sum_{\mu=1}^{N} m_e \left(y_\mu - \frac{m_e}{M} \sum_{\nu=1}^{N} y_\nu \right) \dot{z}_\mu - \sum_{\mu=1}^{N} m_e \left(z_\mu - \frac{m_e}{M} \sum_{\nu=1}^{N} z_\nu \right) \dot{y}_\mu \right] + \\ & + \omega_y \left[\sum_{\mu=1}^{N} m_e \left(z_\mu - \frac{m_e}{M} \sum_{\nu=1}^{N} z_\nu \right) \dot{x}_\mu - \sum_{\mu=1}^{N} m_e \left(x_\mu - \frac{m_e}{M} \sum_{\nu=1}^{N} x_\nu \right) \dot{z}_\mu \right] + \\ & + \omega_z \left[\sum_{\mu=1}^{N} m_e \left(x_\mu - \frac{m_e}{M} \sum_{\nu=1}^{N} x_\nu \right) \dot{y}_\mu - \sum_{\mu=1}^{N} m_e \left(y_\mu - \frac{m_e}{M} \sum_{\nu=1}^{N} y_\nu \right) \dot{x}_\mu \right] + \\ & + \frac{1}{2} \sum_{\mu=1}^{N} m_e \dot{x}_\mu \left(\dot{x}_\mu - \frac{m_e}{M} \sum_{\nu=1}^{N} \dot{x}_\nu \right) + \frac{1}{2} \sum_{\mu=1}^{N} m_e \dot{y}_\mu \left(\dot{y}_\mu - \frac{m_e}{M} \sum_{\nu=1}^{N} \dot{y}_\nu \right) + \\ & + \frac{1}{2} \sum_{\mu=1}^{N} m_e \dot{z}_\mu \left(\dot{z}_\mu - \frac{m_e}{M} \sum_{\nu=1}^{N} \dot{z}_\nu \right) \end{aligned} \tag{49}$$

where:

$$\begin{aligned} I_{xx}^e &= m_e \sum_{\mu=1}^{N} \left[\left(y_\mu^2 + z_\mu^2 \right) - \frac{m_e}{M} \sum_{\nu=1}^{N} \left(y_\mu y_\nu + z_\mu z_\nu \right) \right], \ldots, \\ I_{zx}^e &= -m_e \sum_{\mu=1}^{N} \left[z_\mu x_\mu - \frac{m_e}{M} \sum_{\nu=1}^{N} z_\mu x_\nu \right] \end{aligned} \tag{50}$$

are the electronic moments and products of inertia. (The physical sense of these quantities is less sound than that of their nuclear counterparts but they will not appear in any final result). Adding (49) to (26), one obtains the total classical kinetic energy of the molecule.

The momenta conjugate to the electronic velocities have the form:

$$
\begin{aligned}
P_{\mu x} \equiv \frac{\partial T}{\partial \dot{x}_\mu} = \frac{\partial T_e}{\partial \dot{x}_\mu} &= m_e\left(\dot{x}_\mu - \frac{m_e}{M}\sum_{\nu=1}^{N}\dot{x}_\nu\right) + m_e\omega_y\left(z_\mu - \frac{m_e}{M}\sum_{\nu=1}^{N} z_\nu\right) - \\
&- m_e\omega_z\left(y_\mu - \frac{m_e}{M}\sum_{\nu=1}^{N} y_\nu\right), \\
P_{\mu y} \equiv \frac{\partial T}{\partial \dot{y}_\mu} = \frac{\partial T_e}{\partial \dot{y}_\mu} &= m_e\left(\dot{y}_\mu - \frac{m_e}{M}\sum_{\nu=1}^{N}\dot{y}_\nu\right) + m_e\omega_z\left(x_\mu - \frac{m_e}{M}\sum_{\nu=1}^{N} x_\nu\right) - \\
&- m_e\omega_x\left(z_\mu - \frac{m_e}{M}\sum_{\nu=1}^{N} z_\nu\right), \\
P_{\mu z} \equiv \frac{\partial T}{\partial \dot{z}_\mu} = \frac{\partial T_e}{\partial \dot{z}_\mu} &= m_e\left(\dot{z}_\mu - \frac{m_e}{M}\sum_{\nu=1}^{N}\dot{z}_\mu\right) + m_e\omega_x\left(y_\mu - \frac{m_e}{M}\sum_{\nu=1}^{N} y_\nu\right) - \\
&- m_e\omega_y\left(x_\mu - \frac{m_e}{M}\sum_{\nu=1}^{N} x_\nu\right)
\end{aligned}
\tag{51}
$$

The electronic momenta associated with the components of the angular velocity are:

$$
\begin{aligned}
\frac{\partial T_e}{\partial \omega_x} \equiv L_x = I^e_{xx}\omega_x + I^e_{xy}\omega_y + I^e_{xz}\omega_z &+ m_e\sum_{\mu=1}^{N} y_\mu\left(\dot{z}_\mu - \frac{m_e}{M}\sum_{\nu=1}^{N}\dot{z}_\nu\right) - \\
&- m_e\sum_{\mu=1}^{N} z_\mu\left(\dot{y}_\mu - \frac{m_e}{M}\sum_{\nu=1}^{N}\dot{y}_\nu\right), \\
\frac{\partial T_e}{\partial \omega_y} \equiv L_y = I^e_{yx}\omega_x + I^e_{yy}\omega_y + I^e_{yz}\omega_z &+ m_e\sum_{\mu=1}^{N} z_\mu\left(\dot{x}_\mu - \frac{m_e}{M}\sum_{\nu=1}^{N}\dot{x}_\nu\right) - \\
&- m_e\sum_{\mu=1}^{N} x_\mu\left(\dot{z}_\mu - \frac{m_e}{M}\sum_{\nu=1}^{N}\dot{z}_\nu\right), \\
\frac{\partial T_e}{\partial \omega_z} \equiv L_z = I^e_{zx}\omega_x + I^e_{zy}\omega_y + I^e_{zz}\omega_z &+ m_e\sum_{\mu=1}^{N} x_\mu\left(\dot{y}_\mu - \frac{m_e}{M}\sum_{\nu=1}^{N}\dot{y}_\nu\right) - \\
&- m_e\sum_{\mu=1}^{N} y_\mu\left(\dot{x}_\mu - \frac{m_e}{M}\sum_{\nu=1}^{N}\dot{x}_\nu\right).
\end{aligned}
\tag{52}
$$

Taking into account (50) and (51), Eqs. (52) can be transformed into:

$$\frac{\partial T_e}{\partial \omega_x} = \sum_{\mu=1}^{N} \left(y_\mu P_{\mu z} - z_\mu P_{\mu y} \right) = L_x \,, \quad \frac{\partial T_e}{\partial \omega_y} = \sum_{\mu=1}^{N} \left(z_\mu P_{\mu x} - x_\mu P_{\mu z} \right) = L_y \,, \\ \frac{\partial T_e}{\partial \omega_z} = \sum_{\mu=1}^{N} \left(x_\mu P_{\mu y} - y_\mu P_{\mu x} \right) = L_z \tag{53}$$

Thus, by summing R_x, R_y, R_z and L_x, L_y, L_z, one has, based on Eq. (30):

$$J_x = \frac{\partial T}{\partial \omega_x} = \frac{\partial T_n}{\partial \omega_x} + \frac{\partial T_e}{\partial \omega_x} = R_x + L_x = \\ = I'_{xx}\,\omega_x + I'_{xy}\,\omega_y + I'_{zx}\,\omega_z + p_x + L_x \,, \\ J_y = \frac{\partial T}{\partial \omega_y} = \frac{\partial T_n}{\partial \omega_y} + \frac{\partial T_e}{\partial \omega_y} = R_y + L_y = \\ = I'_{xy}\,\omega_x + I'_{yy}\,\omega_y + I'_{yz}\,\omega_z + p_y + L_y \,, \\ J_z = \frac{\partial T}{\partial \omega_z} = \frac{\partial T_n}{\partial \omega_z} + \frac{\partial T_e}{\partial \omega_z} = R_z + L_z = \\ = I'_{zx}\,\omega_x + I'_{yz}\,\omega_y + I'_{zz}\,\omega_z + p_z + L_z \tag{54}$$

Using the above relations and Eqs. (26), (27), (31) and (32), one obtains for the total kinetic energy:

$$T_n + T_e = \frac{1}{2} I'_{xx}\,\omega_x^2 + \frac{1}{2} I'_{yy}\,\omega_y^2 + \frac{1}{2} I'_{zz}\,\omega_z^2 + I'_{xy}\,\omega_x\omega_y + I'_{yz}\,\omega_y\omega_z + \\ + I'_{zx}\,\omega_z\omega_x + \frac{1}{2}\sum_{i=1}^{2S-6} P_i^2 + \frac{1}{2m_e}\sum_{\mu=1}^{N}\left(P_{\mu x}^2 + P_{\mu y}^2 + P_{\mu z}^2 \right) + \\ + \frac{1}{2M_n}\sum_{\mu=1}^{N}\sum_{\nu=1}^{N}\left(P_{\mu x}P_{\nu x} + P_{\mu y}P_{\nu y} + P_{\mu z}P_{\nu z} \right) \tag{55}$$

Note that the electronic moments of inertia have disappeared. From Eq. (54), one has:

$$J_x - p_x - L_x = I'_{xx}\,\omega_x + I'_{xy}\,\omega_y + I'_{zx}\,\omega_z \,, \\ J_y - p_y - L_y = I'_{xy}\,\omega_x + I'_{yy}\,\omega_y + I'_{yz}\,\omega_z \,, \\ J_z - p_z - L_z = I'_{zx}\,\omega_x + I'_{zy}\,\omega_y + I'_{zz}\,\omega_z \tag{56}$$

It follows:

$$T_n + T_e = \frac{1}{2}\left(J_x - p_x - L_x\right)\omega_x + \frac{1}{2}\left(J_y - p_y - L_y\right)\omega_y +$$
$$+\frac{1}{2}\left(J_z - p_z - L_z\right)\omega_z + \frac{1}{2}\sum_{i=1}^{2S-6} P_i^2 + \frac{1}{2m_e}\sum_{\mu=1}^{N}\left(P_{\mu x}^2 + P_{\mu y}^2 + P_{\mu z}^2\right) + \quad (57)$$
$$+\frac{1}{2M_n}\sum_{\mu=1}^{N}\sum_{\nu=1}^{N}\left(P_{\mu x}P_{\nu x} + P_{\mu y}P_{\nu y} + P_{\mu z}P_{\nu z}\right)$$

The transformation inverse to (56) is:

$$\begin{aligned}
\omega_x &= \mu_{xx}\left(J_x - p_x - L_x\right) + \mu_{xy}\left(J_y - p_y - L_y\right) + \mu_{zx}\left(J_z - p_z - L_z\right), \\
\omega_y &= \mu_{xy}\left(J_x - p_x - L_x\right) + \mu_{yy}\left(J_y - p_y - L_y\right) + \mu_{yz}\left(J_z - p_z - L_z\right), \quad (58) \\
\omega_z &= \mu_{zx}\left(J_x - p_x - L_x\right) + \mu_{yz}\left(J_y - p_y - L_y\right) + \mu_{zz}\left(J_z - p_z - L_z\right)
\end{aligned}$$

Inserting the expressions (58) for $\omega_x, \omega_y, \omega_z$ into Eq. (57), one obtains:

$$T_n + T_e = \frac{1}{2}\sum_{\gamma=x}^{z}\sum_{\delta=x}^{z}\mu_{\gamma\delta}\left(J_\gamma - p_\gamma - L_\gamma\right)\left(J_\delta - p_\delta - L_\delta\right) +$$
$$+\frac{1}{2}\sum_{i=1}^{2S-6} P_i^2 + \frac{1}{2m_e}\sum_{\mu=1}^{N}\left(P_{\mu x}^2 + P_{\mu y}^2 + P_{\mu z}^2\right) + \quad (59)$$
$$+\frac{1}{2M_n}\sum_{\mu=1}^{N}\sum_{\nu=1}^{N}\left(P_{\mu x}P_{\nu x} + P_{\mu y}P_{\nu y} + P_{\mu z}P_{\nu z}\right)$$

Thus, as predicted, the electronic coordinates (*via* the electronic angular momentum) have crept into the nuclear kinetic energy (first sum on the right-hand side). This expression differs from the Wilson one, Eq. (34), due to presence of the last two terms representing the electronic kinetic energy, and by the substitution:

$$\begin{aligned}
R_x - p_x &\rightarrow J_x - L_x - p_x, \\
R_y - p_y &\rightarrow J_y - L_y - p_y, \quad (60) \\
R_z - p_z &\rightarrow J_z - L_z - p_z
\end{aligned}$$

in the rotation part of the kinetic energy. If the electron spin variables were also defined in the *MFS*, the expression on the right-hand side of Eq. (60) would be replaced by $J_\xi - L_\xi - p_\xi - S_\xi$ ($\xi = x, y, z$). Since L_x, L_y, L_z only involve the electronic variables, and the coefficients $\mu_{\gamma\delta}$ only depend on the normal coordinates, one could now proceed in the same way as Watson.[1] The final result for the total kinetic energy operator would be analogous to (47):

$$\hat{T} = \hat{T}_n + \hat{T}_e = \frac{1}{2}\left\{\sum_{\gamma=x}^{z}\sum_{\delta=x}^{z}\mu_{\gamma\delta}\left(\hat{J}_\gamma - \hat{L}_\gamma - \hat{p}_\gamma\right)\left(\hat{J}_\delta - \hat{L}_\delta - \hat{p}_\delta\right)\right\} + \\ + \frac{1}{2}\sum_{i=1}^{3S-6}\hat{P}_i^2 - \frac{\hbar^2}{8}\sum_{\gamma=x}^{z}\mu_{\gamma\gamma} + \frac{1}{2m_e}\sum_{\mu=1}^{N}\left(\hat{P}_{\mu x}^2 + \hat{P}_{\mu y}^2 + \hat{P}_{\mu z}^2\right) - \\ - \frac{1}{2m_e}\sum_{\mu=1}^{N}\sum_{\nu=1}^{N}\left(\hat{P}_{\mu x}\hat{P}_{\nu x} + \hat{P}_{\mu y}\hat{P}_{\nu y} + \hat{P}_{\mu z}\hat{P}_{\nu z}\right) \tag{61}$$

The last two terms (sums) on the right-hand side of Eq. (61) represent the kinetic energy operator of electrons. The result (60) will be used to simplify the derivation of the total kinetic energy operator. Only T_n, will be explicitly transformed and later the fact that the components of the electronic angular momentum, L_x, L_y, L_z, enter the kinetic energy operator in the same way as those of the vibrational (p_x, p_y, p_z) one will be used.

DERIVATION OF THE HAMILTONIAN WITHOUT USE OF QUASI-MOMENTA

Now several relations will be derived that will be required later. First, the time derivatives of the elements λ_{xX} ,… can be expressed in terms of these elements and the time derivatives of the Euler angles:

$$\dot{\lambda}_{xX} = -\lambda_{xY}\dot{\varphi} - \lambda_{zX}\cos\chi\cdot\dot{\theta} + \lambda_{yX}\dot{\chi},..., \quad \dot{\lambda}_{zZ} = -\sin\theta\cdot\dot{\theta} \tag{62}$$

The time derivatives $\dot{\vec{i}}, \dot{\vec{j}}, \dot{\vec{k}}$ are expressible in terms of the unit vectors $\vec{i}, \vec{j}, \vec{k}$ themselves:

$$\dot{\vec{i}} = \left(\lambda_{zZ}\dot{\varphi} + \dot{\chi}\right)\vec{j} + \left(-\lambda_{yZ}\dot{\varphi} - \cos\chi\cdot\dot{\theta}\right)\vec{k}, \\ \dot{\vec{j}} = \left(-\lambda_{zZ}\cdot\dot{\varphi} - \dot{\chi}\right)\vec{i} + \left(\lambda_{xZ}\dot{\varphi} + \sin\chi\cdot\dot{\theta}\right)\vec{k}, \\ \dot{\vec{k}} = \left(\lambda_{yZ}\dot{\varphi} + \cos\chi\cdot\dot{\theta}\right)\vec{i} + \left(-\lambda_{xZ}\dot{\varphi} - \sin\chi\cdot\dot{\theta}\right)\vec{j} \tag{63}$$

Using (62) and (63), one can rewrite Eqs. (6) and (7) in the form:

$$\dot{\vec{R}}_i = \dot{\vec{r}}_i = \left[\dot{x}_i + \left(-\lambda_{zZ}\dot{\varphi} - \dot{\chi}\right)y_i + \left(\lambda_{yZ}\dot{\varphi} + \cos\chi\cdot\dot{\theta}\right)z_i\right]\vec{i} + \\ + \left[\dot{y}_i + \left(\lambda_{zZ}\dot{\varphi} + \dot{\chi}\right)x_i + \left(-\lambda_{xZ}\dot{\varphi} - \sin\chi\cdot\dot{\theta}\right)z_i\right]\vec{j} + \\ + \left[\dot{z}_i + \left(-\lambda_{yZ}\dot{\varphi} - \cos\chi\cdot\dot{\theta}\right)x_i + \left(\lambda_{xZ}\dot{\varphi} + \sin\chi\cdot\dot{\theta}\right)y_i\right]\vec{k} \tag{64}$$

Based on Eq. (64), for the classical nuclear energy, the following expression was derived:

$$T_n = \frac{1}{2}\sum_{K=A}^{S} m_K\left(\dot{\vec{R}}_K\cdot\dot{\vec{R}}_K\right) = \frac{1}{2}\sum_{K=A}^{S} m_K\left(\dot{\vec{r}}_K\cdot\dot{\vec{r}}_K\right) = \frac{1}{2}\sum_{i=1}^{3S-6}\dot{Q}_i^2 +$$
$$+\sum_{i=1}^{3S-6}\left(\lambda_{xZ}\Im_i+\lambda_{yZ}\Re_i+\lambda_{zZ}\aleph_i\right)\dot{Q}_i\dot{\varphi}+\sum_{i=1}^{3S-6}\left(\Im_i\sin\chi+\Re_i\cos\chi\right)\dot{Q}_i\dot{\theta}+$$
$$+\sum_{i=1}^{3S-6}\aleph_i\dot{Q}_i\dot{\chi}+\frac{1}{2}[\lambda_{xZ}^2 I_{yy}+\lambda_{yZ}^2 I_{xx}+\lambda_{zZ}^2 I_{zz}+2\lambda_{xZ}\lambda_{yZ}I_{xy}+$$
$$+2\lambda_{yZ}\lambda_{zZ}I_{yz}+2\lambda_{xZ}\lambda_{zZ}I_{zx}]\dot{\varphi}^2+\frac{1}{2}[I_{xx}\sin^2\chi+I_{yy}\cos^2\chi+ \qquad (65)$$
$$+2I_{xy}\sin\chi\cos\chi]\dot{\theta}^2+\frac{1}{2}I_{zz}\dot{\chi}^2+[\left(\lambda_{xZ}I_{xx}+\lambda_{yZ}I_{xy}+\lambda_{zZ}I_{xz}\right)\sin\chi+$$
$$+\left(\lambda_{xZ}I_{yx}+\lambda_{yZ}I_{yy}+\lambda_{zZ}I_{yZ}\right)\cos\chi]\dot{\varphi}\dot{\theta}+[\lambda_{xZ}I_{zx}+\lambda_{yZ}I_{zy}+$$
$$+\lambda_{zZ}I_{zz}]\dot{\varphi}\dot{\chi}+\left[I_{yz}\cos\chi+I_{zx}\sin\chi\right]\dot{\theta}\dot{\chi}$$

where by means of the relations (22), the Cartesian coordinates and their time derivatives are replaced by the normal coordinates and their derivatives:

$$\sum_{K=A}^{S} m_K\left(y_K\dot{z}_K-z_K\dot{y}_K\right)=\sum_{i=1}^{3S-6}\Im_i\dot{Q}_i,$$
$$\sum_{K=A}^{S} m_K\left(z_K\dot{x}_K-x_K\dot{z}_K\right)=\sum_{i=1}^{3S-6}\Re_i\dot{Q}_i, \qquad (66)$$
$$\sum_{K=A}^{S} m_K\left(x_K\dot{y}_K-y_K\dot{x}_K\right)=\sum_{i=1}^{3S-6}\aleph_i\dot{Q}_i$$

These relations, when accompanied by the Eckart condition (17), are equivalent to (24). The momenta conjugate to the coordinates are:

$$P_i\equiv\frac{\partial T}{\partial\dot{Q}_i}=\dot{Q}_i+\left[\lambda_{xZ}\Im_i+\lambda_{yZ}\Re_i+\lambda_{zZ}\aleph_i\right]\dot{\varphi}+\left[\Im_i\sin\chi+\Re_i\cos\chi\right]\dot{\theta}+\aleph_i\cdot\dot{\chi}$$
$$p_\varphi\equiv\frac{\partial T}{\partial\dot{\varphi}}=\sum_{i=1}^{3S-6}\left(\lambda_{xZ}\Im_i+\lambda_{yZ}\Re_i+\lambda_{zZ}\aleph_i\right)\dot{Q}_i$$
$$\left[\lambda_{xZ}^2 I_{yy}+\lambda_{yZ}^2 I_{xx}+\lambda_{zZ}^2 I_{zz}+2\lambda_{xZ}\lambda_{yZ}I_{xy}+2\lambda_{yZ}\lambda_{zZ}I_{yz}+2\lambda_{xZ}\lambda_{zZ}I_{zx}\right]\dot{\varphi}+ \qquad (67)$$
$$+\left[\left(\lambda_{xZ}I_{xx}+\lambda_{yZ}I_{xy}+\lambda_{zZ}I_{xz}\right)\sin\chi+\left(\lambda_{xZ}I_{yx}+\lambda_{yZ}I_{yy}+\lambda_{zZ}I_{yZ}\right)\cos\chi\right]\dot{\theta}+$$
$$+\left[\lambda_{xZ}I_{zx}+\lambda_{yZ}I_{zy}+\lambda_{zZ}I_{zz}\right]\dot{\chi},$$

$$p_\theta \equiv \frac{\partial T}{\partial \dot{\theta}} = \sum_{i=1}^{3S-6} \left(\Im_i \sin\chi + \Re_i \cos\chi\right)\dot{Q}_i +$$
$$+\left[\left(\lambda_{xZ} I_{xx} + \lambda_{yZ} I_{xy} + \lambda_{zZ} I_{xz}\right)\sin\chi + \left(\lambda_{xZ} I_{xy} + \lambda_{yZ} I_{yy} + \lambda_{zZ} I_{yz}\right)\cos\chi\right]\dot{\varphi} +$$
$$+\left[I_{xx}\sin^2\chi + I_{yy}\cos^2\chi + 2I_{xy}\sin\chi\cos\chi\right]\dot{\theta} + \left[I_{xz}\sin\chi + I_{yz}\cos\chi\right]\dot{\chi},$$
$$p_\chi \equiv \frac{\partial T}{\partial \dot{\chi}} = \sum_{i=1}^{3S-6} \aleph_i \dot{Q}_i + \left[\lambda_{xZ} I_{xz} + \lambda_{yZ} I_{yz} + \lambda_{zZ} I_{zz}\right]\dot{\varphi} +$$
$$+\left[I_{yz}\cos\chi + I_{zx}\sin\chi\right]\dot{\theta} + I_{zz}\dot{\chi}$$

The transformation inverse to (67) is a concrete case of the relations (37) with $\dot{q}_n = \dot{Q}_1,\ldots,\dot{Q}_{3S-6},\dot{\varphi},\dot{\theta},\dot{\chi}$, and $p_m = P_1,\ldots,P_{3S-6},p_\varphi,p_\theta,p_\chi$, where the coefficients g_{mn} are:

$$g_{Q_iQ_j} = \delta_{ij} + \Xi_{ix}\Im_j + \Xi_{iy}\Re_j + \Xi_{iz}\aleph_j$$
$$g_{Q_i\varphi} = \Xi_{ix}\frac{\cos\chi}{\sin\theta} - \Xi_{iy}\frac{\sin\chi}{\sin\theta}$$
$$g_{Q_i\theta} = -\Xi_{ix}\sin\chi - \Xi_{iy}\cos\chi$$
$$g_{Q_i\chi} = -\Xi_{ix}\cot\theta\cos\chi + \Xi_{iy}\cot\theta\sin\chi - \Xi_{iz}$$
$$g_{\varphi\varphi} = \mu_{xx}\frac{\cos^2\chi}{\sin^2\theta} + \mu_{yy}\frac{\sin^2\chi}{\sin^2\theta} - 2\mu_{xy}\frac{\sin\chi\cos\chi}{\sin^2\theta}$$
$$g_{\theta\theta} = \mu_{xx}\sin^2\chi + \mu_{yy}\cos^2\chi + 2\mu_{xy}\sin\chi\cos\chi$$
$$g_{\chi\chi} = \left(\mu_{xx}\cos^2\chi + \mu_{yy}\sin^2\chi - 2\mu_{xy}\sin\chi\cos\chi\right)\cot^2\theta +$$
$$+2\left(\mu_{zx}\cos\chi - \mu_{yz}\sin\chi\right)\cot\theta + \mu_{zz}$$
$$g_{\varphi\theta} = \left(\mu_{yy} - \mu_{xx}\right)\frac{\sin\chi\cos\chi}{\sin\theta} - \mu_{xy}\frac{\cos^2\chi - \sin^2\chi}{\sin\theta}$$
$$g_{\varphi\chi} = -\mu_{xx}\frac{\cos\theta\cos^2\chi}{\sin^2\theta} - \mu_{yy}\frac{\cos\theta\sin^2\chi}{\sin^2\theta} +$$
$$+2\mu_{xy}\frac{\cos\theta\sin\chi\cos\chi}{\sin^2\theta} + \mu_{yz}\frac{\sin\chi}{\sin\theta} - \mu_{zx}\frac{\cos\chi}{\sin\theta}$$
$$g_{\theta\chi} = \left(\mu_{xx} - \mu_{yy}\right)\cot\theta\sin\chi\cos\chi +$$
$$+\mu_{xy}\cot\theta\left(\cos^2\chi - \sin^2\chi\right) + \mu_{yz}\cos\chi + \mu_{zx}\sin\chi \qquad (68)$$

with:

$$\Xi_{ix} \equiv \mu_{xx}\Im_i + \mu_{xy}\Re_i + \mu_{xz}\aleph_i, \quad \Xi_{iy} \equiv \mu_{yx}\Im_i + \mu_{yy}\Re_i + \mu_{yz}\aleph_i, \quad \Xi_{iz} \equiv \mu_{zx}\Im_i + \mu_{zy}\Re_i + \mu_{zz}\aleph_i \qquad (69)$$

The determinant of the matrix with elements g_{mn} is:

$$g = \frac{\mu_{xx}\mu_{yy}\mu_{zz} - \mu_{xx}\mu_{yz}^2 - \mu_{yy}\mu_{zx}^2 - \mu_{zz}\mu_{xy}^2 + 2\mu_{xy}\mu_{yz}\mu_{zx}}{\sin^2\theta} g = \\ = \mu(Q_1, Q_2, Q_3)\sin^{-2}\theta \tag{70}$$

The coefficients (68) determine the classical kinetic energy of the nuclei and at the same time the quadratic part of the corresponding wave-mechanical operator (42):

$$\hat{T}_n^{(2)} = -\frac{\hbar^2}{2}\sum_{m=1}^{3S-3}\sum_{n=1}^{3S-3} g_{mn}\frac{\partial^2}{\partial q_m \partial q_n}, \qquad m,n = Q_1,...,Q_{3S-6},\varphi,\theta,\chi \tag{71}$$

The linear (in derivatives) part of the wave-mechanical operator (42) corresponding to the choice:

$$g \propto \mu(Q_1, Q_2, Q_3)\sin^{-2}\theta, \quad s_q = \sin\theta \tag{72}$$

where the symbol $\propto$ stands for irrelevant constant factors, is determined by the second term on the right-hand side of Eq. (42), having in the present case the form:

$$\hat{T}^{(1)} = -\frac{\hbar^2}{2}\left\{\sum_{i=1}^{3S-6}\left[\sum_{j=1}^{3S-6}\frac{\partial g_{Q_iQ_j}}{\partial Q_j}\right]\frac{\partial}{\partial Q_i} + \right. \\ +[\sum_{j=1}^{3S-6}\frac{\partial g_{Q_j\varphi}}{\partial Q_j} + \frac{\partial g_{\varphi\theta}}{\partial\theta} + g_{\varphi\theta}\cot\theta + \frac{\partial g_{\varphi\chi}}{\partial\chi}]\frac{\partial}{\partial\varphi} + \\ +[\sum_{j=1}^{3S-6}\frac{\partial g_{Q_j\theta}}{\partial Q_j} + g_{\theta\theta}\cot\theta + \frac{\partial g_{\theta\chi}}{\partial\chi}]\frac{\partial}{\partial\theta} \\ \left. +[\sum_{j=1}^{3S-6}\frac{\partial g_{Q_j\chi}}{\partial Q_j} + \frac{\partial g_{\chi\varphi}}{\partial\varphi} + \frac{\partial g_{\chi\theta}}{\partial\theta} + g_{\chi\theta}\cot\theta + \frac{\partial g_{\chi\chi}}{\partial\chi}]\frac{\partial}{\partial\chi}\right\} \tag{73}$$

The constant term (with respect to derivatives) from Eq. (42) reduces in the present case to:

$$\hat{T}^{(0)} = -\frac{\hbar^2}{8}\sum_{i=1}^{3S-6}\sum_{j=1}^{3S-6}\{\frac{1}{\mu}\left(\frac{\partial g_{Q_iQ_j}}{\partial Q_i}\frac{\partial u}{\partial Q_j} + g_{Q_iQ_j}\frac{\partial^2 u}{\partial Q_i\partial Q_j}\right) - \\ -\frac{5}{4\mu^2}g_{Q_iQ_j}\frac{\partial\mu}{\partial Q_i}\frac{\partial\mu}{\partial Q_j}\} \tag{74}$$

Using the formulae (68), (31), (44), those for the quantities $\hat{J}_x^2 = \hat{J}_x\hat{J}_x$, $\hat{J}_x\hat{J}_y$, $\hat{J}_y\hat{J}_x$,..., which can be derived starting with Eqs. (44), and rearranging,

one obtains for the wave-mechanical kinetic energy operator of the nuclei the expression:

$$\hat{T}_n = \frac{1}{2}\left\{\sum_{\gamma=x}^{z}\sum_{\delta=x}^{z}\left(\hat{J}_\gamma - \hat{p}_\gamma\right)\mu_{\gamma\delta}\left(\hat{J}_\delta - \hat{p}_\delta\right)\right\} + \frac{1}{2}\sum_{i=1}^{3S-6}\hat{P}_i^2 + \hat{T}^{(0)} \tag{75}$$

The explicit form of $\hat{T}^{(0)}$ is:

$$\begin{aligned}\hat{T}^{(0)} = -\frac{\hbar^2}{8}\Bigg\{&\left[\frac{1}{(I'')^2}\sum_{i=1}^{3S-6}\left(\frac{\partial I''}{\partial Q_i}\right)^2 - \frac{2}{I''}\sum_{i=1}^{3S-6}\frac{\partial^2 I''}{\partial Q_i^2}\right] + \\ &+\left[\frac{1}{(I'')^2}\sum_{i=1}^{3S-6}\sum_{j=1}^{3S-6}\frac{\partial I''}{\partial Q_i}\frac{\partial I''}{\partial Q_j} - \frac{2}{I''}\sum_{i=1}^{3S-6}\sum_{j=1}^{3S-6}\frac{\partial^2 I''}{\partial Q_i \partial Q_j}\right]\sum_{\gamma=x}^{z}\sum_{\delta=x}^{z}\mu_{\gamma\delta} \\ &\sum_{k=1}^{3S-6}\zeta_{ki}^{\gamma}Q_k\sum_{l=1}^{3S-6}\zeta_{lj}^{\delta}Q_l - \\ &-\frac{2}{I''}\sum_{j=1}^{3S-6}\frac{\partial I''}{\partial Q_j}\sum_{i=1}^{3S-6}\sum_{\alpha=x}^{z}\sum_{\beta=x}^{z}\frac{\partial \mu_{\alpha\beta}}{\partial Q_i}\sum_{k=1}^{3S-6}\zeta_{ki}^{\alpha}Q_k\sum_{l=1}^{3S-6}\zeta_{lj}^{\beta}Q_l - \\ &-\frac{2}{I''}\sum_{j=1}^{3S-6}\frac{\partial I''}{\partial Q_j}\sum_{i=1}^{3S-6}\sum_{\alpha=x}^{z}\sum_{\beta=x}^{z}\mu_{\alpha\beta}\zeta_{ij}^{\beta}\sum_{k=1}^{3S-6}\zeta_{ki}^{\alpha}Q_k\end{aligned} \tag{76}$$

where:

$$\begin{aligned}&\mu_{\alpha\beta} = \sum_{\varepsilon=x}^{z}\left(I''^{-1}\right)_{\alpha\varepsilon} I^0_{\varepsilon\varepsilon}\left(I''^{-1}\right)_{\varepsilon\beta}, \quad I''_{\alpha\beta} = I^0_{\alpha\beta}\delta_{\alpha\beta} + \frac{1}{2}\sum_{i=1}^{3S-6}a_i^{\alpha\beta}Q_i, \\ &a_i^{\alpha\beta} = \left(\frac{\partial I_{\alpha\beta}}{\partial Q_i}\right)_0, \quad \alpha,\beta,\varepsilon = x,y,z\end{aligned} \tag{77}$$

are the quantities introduced by Watson. After some algebra, one finds that:

$$\hat{T}^{(0)} = U_1 + U_2 + U_3 + U_4 \tag{78}$$

where U_1, U_2, U_3, U_4 are the quantities defined by Eqs. (45), (48), (50) and (52) in Watson's paper.[1]

CONCLUSIONS

In the present study, I derived the kinetic energy operator for molecules with non-linear equilibrium geometry in the form (when the electron variables are included *via* Scheme (60)):

$$\hat{T}_n = \frac{1}{2}\left\{\sum_{\gamma=x}^{z}\sum_{\delta=x}^{z}\left(\hat{J}_\gamma - \hat{p}_\gamma - \hat{L}_\gamma\right)\mu_{\gamma\delta}\left(\hat{J}_\delta - \hat{p}_\delta - \hat{L}_\delta\right)\right\} + \\ + \frac{1}{2}\sum_{i=1}^{3S-6}\hat{P}_i^2 + U_1 + U_2 + U_3 + U_4 + \\ + \frac{1}{2m_e}\sum_{\mu=1}^{N}\left(\hat{P}_{\mu x}^2 + \hat{P}_{\mu y}^2 + \hat{P}_{\mu z}^2\right) - \\ - \frac{1}{2m_e}\sum_{\mu=1}^{N}\sum_{\nu=1}^{N}\left(\hat{P}_{\mu x}\hat{P}_{\nu x} + \hat{P}_{\mu y}\hat{P}_{\nu y} + \hat{P}_{\mu z}\hat{P}_{\nu z}\right) \tag{79}$$

It is almost equal to the Watson's one. "Almost" because I was not able to show in a simple way two things: a) that the coefficients $\mu_{\gamma\delta}$ can also be put before the term $\left(\hat{J}_\gamma - \hat{p}_\gamma - \hat{L}_\gamma\right)$ in the first sum on the right-hand side of Eq. (79), as in the last link of the chain of Eqs. (47) – for doing that, I needed the commutation relations (46) derived by Watson; b) I have not proven that:

$$U_1 + U_2 + U_3 + U_4 = -\left(\hbar^2/8\right)\sum_\gamma \mu_{\gamma\gamma}$$

However, I find the expression (79) indeed essentially equal to Watson's one. If one compares it with Wilson's expression (45), it can be seen that the determinant μ, appearing in Eq. (45), is not present in Eq. (79), which is the most important simplification made by Watson. Furthermore, although I did not show that the free term in Eq. (79) is simply:

$$-\left(\hbar^2/8\right)\sum_\gamma \mu_{\gamma\gamma}$$

I showed that it represents a small correction of the potential, because according to Eqs. (76) and (77), it involves derivatives (of second and higher order) of the instantaneous moments of inertia. From the point of view of a computer (and *it* solves nowadays every Schrödinger equation), the difference between $U_1 + U_2 + U_3 + U_4$ and $-\left(\hbar^2/8\right)\sum_\gamma \mu_{\gamma\gamma}$ is only of esthetical significance. When already speaking about esthetics, let me mention that (not attempting to diminish the achievement of Watson) the middle expression in Eq. (47), being obviously Hermitean, looks nicer than the last one. Thus, I hope that I have shown in a sense that also in the present case "*Omnes viae Romam ducunt*", or, more modestly, when not directly to Rome, than at least "*Romam ad/ante portas*".

A great part of the present study represents in fact compilation of already derived results. I think, however, that the approach applied in Section "Derivation of the Hamiltonian without use of quasi-momenta" has some advantages when compared with that used by Wilson and Watson. The fulfillment of the conditions that allowed the application of the generalized Podolsky trans-

formation to quasi-momenta such as J_x, J_y, J_z might look accidental. As mentioned in the Introduction, the algebraic efforts connected with the application of this approach are tremendous. On the other hand, the only real difficulty in using the approach of the present study consists in inverting the matrix of coefficients appearing in the transformation (67) to obtain the coefficients g_{mn} given in Eq. (68). This looks difficult, because the transformation matrix is of the order $3S-3$ (when only dealing with the nuclei), but in fact it is not so. The final result could be obtained quite easily stepwise: One inverts first the 3×3 matrix involving solely the time derivatives of the Euler angles and the corresponding impulses and, bearing in mind the structure of this transformation, it is not difficult to invert the matrix additionally involving one and two normal coordinates. The jump to the real $(3S-3)\times(3S-3)$ problem is then straightforward. The present procedure becomes very appealing in some other cases, *e.g.*, in the construction of the Hamiltonian for triatomic molecules in terms of a set of internal coordinates (*e.g.*, two bonds and the valence angle, or Jacobi coordinates) and the Euler angles, at various definitions of the *MFS* (*e.g.*, with the axes coinciding with the instantaneous principal moments of inertia). Due to the fact that the nuclear skeleton of triatomic molecules is always planar (or linear), it is even possible to reduce the Podolsky transformation to a 4×4 matrix problem.[14,15]

Acknowledgements. I thank Prof. Nikolić for a great, forty years lasting friendship, and say: "Srećan ti rođendan, dragi Bane". The financial support provided by the Ministry of Education, Science and Technological Development of the Republic of Serbia (Contract No. 172040) is acknowledged.

И З В О Д

АЛТЕРНАТИВНО ИЗВОЂЕЊЕ (СКОРО-) ВОТСОНОВОГ ХАМИЛТОНИЈАНА

МИЉЕНКО ПЕРИЋ

Факултет за физичку хемију Универзитета у Београду

Приказано је извођење општег таласномеханичког хамилтонијана за нелинеарне молекуле. Оно се базира на трансформацији Хамилтонових импулса у одговарајуће таласномеханичке операторе помоћу трасформације Подолског. Резултат је суштински идентичан ономе који је извео Вотсон у свом епохалном раду (J. K. G. Watson, *Mol. Phys.* **15** (1968) 479). Мада не тако елегантан као онај из оригиналне референце, пут предложен у овом раду је концептуално много једноставнији. Овај поступак може се примијенити и на извођење других типова хамилтонијана.

(Примљено 9. октобра 2013)

REFERENCES

1. J. K. G. Watson, *Mol. Phys.* **15** (1968) 479
2. E. B. Wilson Jr., J. B. Howard, *J. Chem. Phys*. **4** (1936) 260
3. E. B. Wilson Jr., J. C. Decius, P. C. Cross, *Molecular Vibrations*, McGraw-Hill New York, 1955, pp. 273–284

4. J. K. G. Watson, *Mol. Phys.* **19** (1970) 465
5. D. Estes, D. Secrest, *Mol. Phys.* **59** (1986) 569
6. J. K. G. Watson, *Mol. Phys.* **79** (1993) 943
7. P. R. Bunker, *Molecular Symmetry and Spectroscopy*, Academic Press, New York, 1979, pp. 116–125
8. B. Podolsky, *Phys. Rev.* **32** (1928) 812
9. C. Eckart, *Phys. Rev*. **47** (1935) 552
10. M. Born, J. R. Oppenheimer, *Ann. Phys*. **84** (1927) 457
11. R. N. Zare, *Angular Momentum*, Wiley, New York, Chichester, Brisbane, Toronto, Singapore, 1988, pp. 81–85
12. J. H. Van Vleck, *Phys. Rev*. **33** (1929) 46
13. J. M. Brown, A. Carrington, *Rotational Spectroscopy of Diatomic Molecules*, Cambridge University Press, Cambridge, 2003, pp. 51–58
14. M. Perić, M. Mladenović, S. D. Peyerimhoff, R. J. Buenker, *Chem. Phys.* **82** (1983) 317
15. M. Perić, M. Mladenović, S. D. Peyerimhoff, R. J. Buenker, *Chem. Phys.* **86** (1984) 85.

Journal of the Serbian Chemical Society
JSCS-info@shd.org.rs • www.shd.org.rs/JSCS
J. Serb. Chem. Soc. *78* (12) 1963–1973 (2013) UDC 547.828+544.022+542.913+544.4:51–3
JSCS–4543 *Original scientific paper*

Structure–reactivity correlation for the kinetics of the formation reaction of 4-(substituted phenyl)-1,4-dihydropyridines•

JOVICA V. UROŠEVIĆ[1]**, SAŠA Ž. DRMANIĆ[1#], JASMINA B. NIKOLIĆ[1#], IVAN O. JURANIĆ[2#] and BRATISLAV Ž. JOVANOVIĆ[1*#]

[1]*Department of Organic Chemistry, Faculty of Technology and Metallurgy, University of Belgrade, Karnegijeva 4, 11120 Belgrade, Serbia and* [2]*Institute of Chemistry, Technology and Metallurgy, University of Belgrade, Njegoševa 12, 11000 Belgrade, Serbia*

(Received 20 November, revised 28 November 2013)

Abstract: Quantitative structure–reactivity correlations for the kinetics of the Hantzsch synthesis of 4-(substituted phenyl)-1,4-dihydropyridines in the reaction between ethyl *m*- and *p*-substituted 2-benzylideneacetoacetate and the enamine (ethyl 3-aminocrotonate) was studied. The reaction kinetics was followed spectrophotometrically. It was found that the reaction correspond to second-order kinetics. Quantitative structure–reactivity correlations of log *k* were obtained with the corresponding substituent constants (σ, σ^+, σ_I and σ_R^+) using the Hammett and extended Hammett equation (dual substituent parameter, DSP, equation). They showed linear relationships with positive values of reaction constants (ρ). The obtained data were processed by linear regression analysis. It was confirmed that Michael addition of the enamine to benzylidene represented the slow step of the reaction with a high positive charge at the benzylidene molecule. MO calculations were performed and they were in agreement with the conclusions derived from the structure–reactivity correlations.

Keywords: 1,4-dihydropyridines; Hantzsch synthesis; Michael addition; Hammet equation; extended Hammett equation; MO calculations.

INTRODUCTION

The derivatives of 4-phenyl-1,4-dihydropyridine are often synthesized because of their importance due to their pharmaceutical properties (*e.g.*, the commercial drug nifedipine).[1,2] Derivatives of 1,4-dihydropyridines are used in the treatment

* Corresponding author. E-mail: bataj@tmf.bg.ac.rs
** Present address: School of Chemistry and Technology, "B. Đ. Kukar", Vlajkova 96, Leskovac, Serbia.
# Serbian Chemical Society member.
• Dedicated to Branislav Nikolić, a great scientist, a great professor, and above all, a great friend.
doi: 10.2298/JSC131120139U

of cardiac insufficiency, by increasing cardiac muscle contractions and decreasing blood pressure. Substituted 1,4-dihydropyridines are also known to be vasodilators, bronchodilators and anti-diabetic agents.[3]

The most common method for the synthesis of this group of compounds is the Hantzsch synthesis, which has often been studied in terms of the reactants, reaction conditions and the pharmacological effects of the products.[1,2]

The original Hantzsch synthesis starts from ethyl acetoacetate, ammonia and the appropriate aldehyde, depending on the required product (Scheme 1).[4,5]

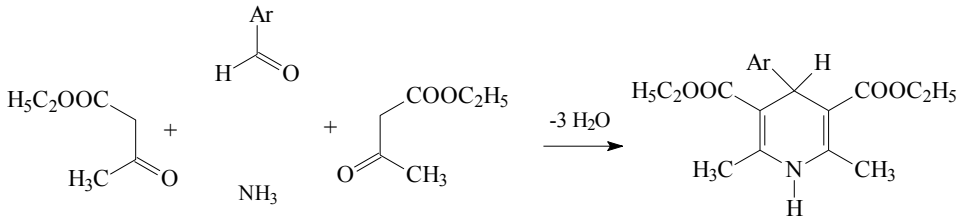

Scheme 1. The Hantzsch synthesis.

The aldehyde could be aliphatic, heteroaromatic or aromatic. 1,3-Diketones could be used as the active methylene compound instead of ethylacetoacetate, whereby the corresponding 3,5-diacyl-1,4-dihydropyridines are formed.[6,7] Ammonium salts, formamide or hexamethylenetetramine are often applied as the source of nitrogen instead of ammonia.[8,9]

One modification of this synthesis can be realized by the use of a specific enamine (ethyl 3-aminocrotonate) instead of ethyl acetoacetate[10,11] in the presence of various aldehydes.

The second possible modification consists of the reaction of the enamine with aldehydes and esters (or nitriles) or *β*-keto carboxylic acids, which enable the synthesis of asymmetric 1,4-dihydropyridines.[12]

A significant modification of the Hantzsch synthesis is also the reaction of the enamine and ethyl arylideneacetoacetate,[6,11,13] the kinetics of which are discussed in this paper.

The influence of the properties and positions of the substituents on the benzaldehyde ring on the product yield in the examined reaction showed that electron-accepting substituents considerably increase the yield. The yield is the lowest for *o*-substituted benzaldehydes because of steric hindrance to the reaction. In the case of *m*-substituted benzaldehydes, it was registered that the yields were somewhat higher than those for the corresponding *p*-substituted benzaldehydes.[14]

The mechanism of the Hantzsch synthesis[5] is given in Scheme 2.

The active methylene compound (ethyl acetoacetate) reacts with the aldehyde to give the corresponding ethyl arylideneacetoacetate (**I**), while with ammonia, it gives the enamine (**II**). In the subsequent step, **I** and **II** react by a so-called

Michael addition to yield the tautomeric keto–enamine (**III**), which is converted by cyclization to hydroxytetrahydropyridine (**IV**). The 1,4-dihydropyridine (**V**) is formed from (**IV**) by elimination of water.

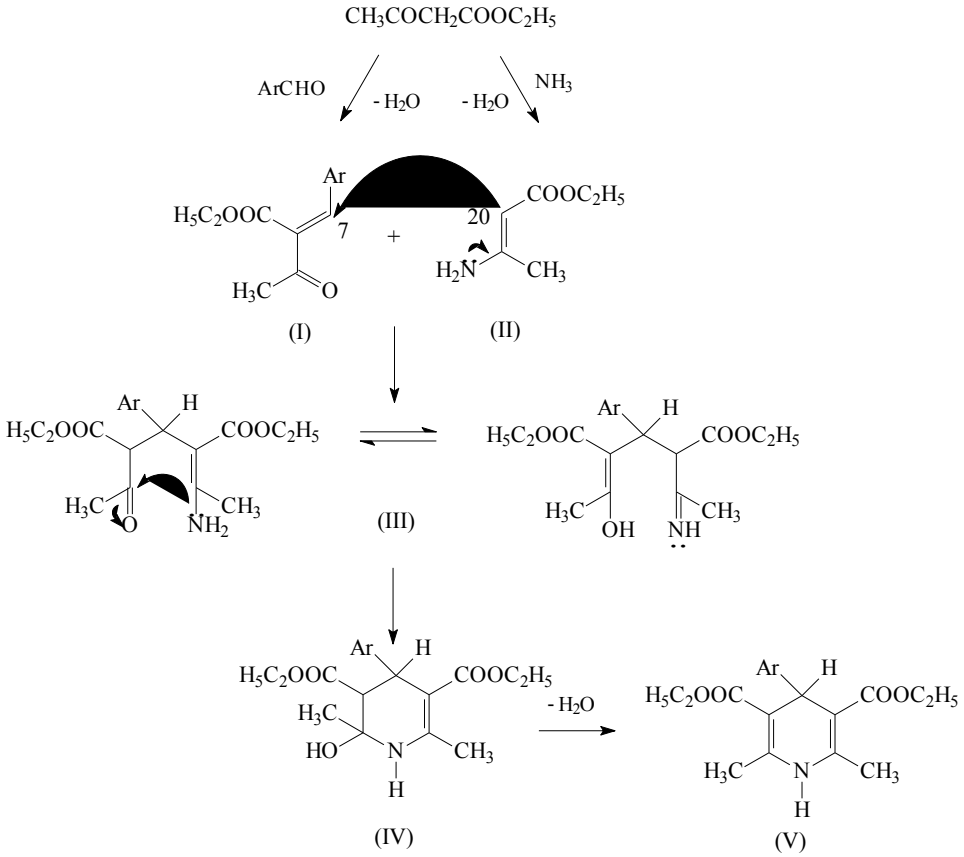

Scheme 2. The mechanism of the Hantzsch synthesis.

The aim of this study was to analyze the kinetics of this reaction using *m*- and *p*-substituted derivatives of ethyl benzylideneacetoacetate (Scheme 2, Ar = *m*- and *p*-substituted benzaldehydes, where the substituents (X) were: H (**Ia**); *p*-NO_2 (**Ib**), *p*-Cl (**Ic**), *m*-OCH_3 (**Id**), *p*-OCH_3 (**Ie**) and the enamine (ethyl 3-aminocrotonate) (**II**) in ethanol as solvent. The described kinetic data have not hitherto been mentioned in the literature.

The analysis of the obtained kinetic data was realized by correlation with the Hammet equation and the extended Hammett equation (dual substituent parameter, DSP, equation) in order to explain the reaction mechanism.[15]

EXPERIMENTAL

Synthesis

*All substituted 4-phenyl-1,4-dihydropridines (Scheme 2: **Va**–**Ve**)*. All compounds were obtained by mixing equimolar amounts (0.05 mol) of 25 % ammonia and the required benzaldehyde, 0.1 mol of ethyl acetoacetate and 25 cm^3 of methanol. The reaction mixture was mixed, refluxed for 6 h at 65 °C and then cooled in to crystallize the products. The raw crystals were drained and recrystallized from methanol. The following compounds were synthesized: diethyl 2,6-dimethyl-4-phenyl-1,4-dihydropyridine-3,5-dicarboxylate (**Va**); diethyl 2,6-dimethyl-4-*p*-nitrophenyl-1,4-dihydropyridine-3,5-dicarboxylate (**Vb**); diethyl 2,6--dimethyl-4-*p*-chlorophenyl-1,4-dihydropyridine-3,5-dicarboxylate (**Vc**); diethyl 2,6-dimethyl-4-*m*-methoxyphenyl-1,4-dihydropyridine-3,5-dicarboxylate (**Vd**); diethyl 2,6-dimethyl-4--*p*-methoxyphenyl-1,4-dihydropyridine-3,5-dicarboxylate (**Ve**). The melting points of the obtained compounds were in agreement with literature data.[6,16,17]

*Enamine (ethyl 3-aminocrotonate) (Scheme 2: **II**)*. A current of ammonia was passed through 250 cm^3 of ethyl acetoacetate at 35 °C for 5 h. The reaction mixture divided into two layers: the top layer (water and ammonia) was removed and the bottom layer extracted with diethyl ether, then dried and the solvent was evaporated and the enamine distilled under vacuum.[18]

*Substituted ethyl benzylideneacetoacetates (Scheme 2: **Ia**–**Ie**)*. Equimolar quantities of ethyl acetoacetate and the required benzaldehyde were mixed at –5 °C with piperidine in ethanol (1:2). The reaction mixture was left in a freezer for a few days, until crystals of the raw ester were formed. Subsequently, they were recrystallized from diethyl ether. The following compounds were synthesized: ethyl 2-benzylideneacetoacetate (**Ia**); ethyl 2-(*p*-nitrobenzylidene)acetoacetate (**Ib**); ethyl 2-(*p*-chlorobenzylidene)acetoacetate (**Ic**); ethyl 2-(*m*--methoxybenzylidene)acetoacetate (**Id**) and ethyl 2(*p*-methoxybenzylidene)acetoacetate (**Ie**). The melting points of the obtained compounds were in agreement with the literature data.[19]

All the employed chemicals were of *p.a*. quality (Fluka, Subsidiary of the Sigma–Aldrich Company, St. Louis, MO, USA).

The structures of all compounds were confirmed by their UV and FTIR spectra (Shimadzu 1700A and Bomem MB-Series, respectively).

Kinetic measurements

Reaction rates of the modified Hantzsch syntheses (Scheme 2) between enamine (**II**) and the ethyl *m*- and *p*-substituted benzylideneacetoacetates (**Ia**–**Ie**) were followed by UV spectrophotometry. The UV spectra of the examined compounds were recorded using a Shimadzu 1700A spectrophotometer.

The kinetic experiments were realized at a concentration of 0.03 M for both reactants in absolute ethanol at temperature 78 °C, with mixing for 6 h. Aliquots of 0.1 cm^3 were taken every hour, diluted to 25 cm^3 with absolute ethanol and their absorbances at the specific wavelength were measured.

The increases in the absorbance of the synthesized 4-phenyl-1,4-dihydropyridines were followed at wavelengths of about 355 nm (marked by arrow in Fig. 1), which originates from the 1,4-dihydropyridine ring. The wavelengths used in kinetics measurements are given in Table I. The concentrations of reaction products were determined from the recorded absorbances using a calibration diagram according the Lambert–Beer law ($A = slope \times c$, where A is the measured absorbance and c is the concentration of the reaction product).

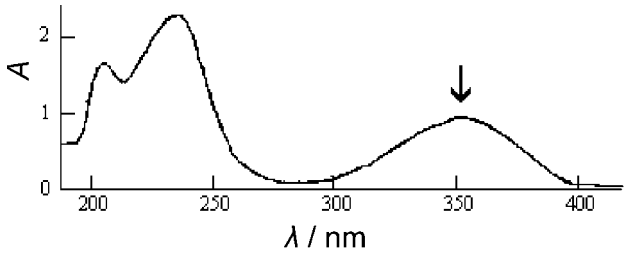

Fig. 1. The UV spectra of 4-phenyl-1,4-dihydropyridine.

TABLE I. The wavelengths used for the kinetic measurements

Compd.	Substituent	λ / nm
1	H	355.0
2	*p*-NO_2	355.0
3	*p*-Cl	355.6
4	*m*-OCH_3	354.6
5	*p*-OCH_3	354.2

The corresponding linear dependences of the concentrations of the reaction products on time confirmed the assumption that the reaction obeyed second order kinetics ($kt = (c_0 - x)^{-1} - - c_0^{-1}$, where k is reaction rate constant, t is time, c_0 is initial reactant concentration and x reaction variable). Using linear regression analysis, k values were calculated.

RESULTS AND DISCUSSION

A typical absorbance spectrum of 4-phenyl-1,4-dihydropyridine is shown in Fig. 1. The absorbance spectra of the reactants, as well as the FTIR spectra of the investigated compounds are in accordance with literature data.[20]

The obtained values of the rate constants for the reaction between the ethyl *m*- and *p*-substituted benzylideneacetoacetates (**Ia**–**Ie**) and the enamine (**II**) in ethanol under reflux (78 °C), shown in Scheme 2, are given in Table II.

TABLE II. The calculated reaction rate constants for the examined Hantzsch syntheses in ethanol at 78 °C and the corresponding Hammett substituent constants σ and the Brown electrophilic σ^+ constants[21]

Compd.	Substituent	k / 10^{-6} dm^3 mol^{-1} s^{-1}	log (k / dm^3 mol^{-1} s^{-1})	$\sigma_{m/p}$	$\sigma^+_{m/p}$
1	H	2.96	–5.53	0	0
2	*p*-NO_2	13.8	–4.86	0.81	0.79
3	*p*-Cl	2.42	–5.62	0.24	0.11
4	*m*-OCH_3	1.64	–5.78	0.10	0.05
5	*p* -OCH_3	0.347	–6.46	–0.28	–0.78

The basic form of the Hammett equation, the classic Hammett equation, is:

$$\log k = \rho\sigma + \log k_0 \quad (1)$$

where the logarithm of the reaction rate constant, k, represented as a function of the electronic effects of substituents (expressed by the substituent constant, σ) and the parameter ρ (reaction constant), displays the sensitivity of the reaction rate constant of the unsubstituted compound to substituent effects. It is a well-known and reliable method to determine quantitatively a structure–reactivity relationship.[15]

The established Hammett correlation with the data given in Table II is as follows:

$$\log k = (1.32 \pm 0.13)\ \sigma_{m/p} - (5.88 \pm 0.11) \qquad (2)$$
$$r = 0.931,\ s = 0.24,\ F = 20,\ n = 5$$

where, r – correlation coefficient, s – standard deviation, F – Fisher's test, n – number of points included in the correlation.

Although the correlation coefficient is not optimal ($r < 0.95$), the positive value of the reaction constant ($\rho = 1.32$) points to the conclusion that the electron-acceptor substituents are accelerating the reaction, which could be confirmed by the values of the reaction rate constants. The Hammett equation gives a less reliable correlation of log k and the σ^- values (nucleophilic substituent constants) with an unsatisfactory correlation coefficient ($r < 0.90$).

On the other hand, when the Hammett correlation with the corresponding electrophilic Brown constants was determined, Eq. (3) was obtained:

$$\log k = (1.01 \pm 0.11)\sigma^+_{m,p} - (5.68 \pm 0.06) \qquad (3)$$
$$r = 0.981,\ s = 0.13,\ F = 76,\ n = 5$$

More successful correlation with electrophilic (σ^+) constants, as well as the observed fact that the electron-accepting substituents increased the reaction rate, suggests that the kinetic data should be treated by the Taft equation[22] of the dual substituent parameter (DSP), which belongs to the extended Hammett equations. It is of the form:

$$\log k = \rho_I \sigma_I + \rho_R \sigma_R + \log k_0 \qquad (4)$$

By application of Eq. (4), the electronic substituent effects can be divided into inductive (σ_I) and resonance (σ_R). The corresponding reaction constants are ρ_I and ρ_R.

The inductive substituent constants and the various scales of the resonance substituent constants are given in Table III.

The different scales for the σ_R substituent constants describe the different ranges of the interactions of the present substituents and the reaction center, which enables a better insight into reaction mechanism. The unreliable correlations of DSP equation with σ_I and σ_R^- indicates to the conclusion that no negative charge develops at the reaction center, which would be delocalized by electron-accepting groups.

TABLE III. Inductive (σ_I) and various resonance (σ_R) subsitutent constants[23]

Substituent	σ_I	$\sigma_{R\ (BA)}$	σ_R^+	σ_R^-
H	0	0	0	0
p-NO_2	0.65	0.16	0.16	0.47
p-Cl	0.46	–0.23	–0.36	–0.23
m-OCH_3[a]	0.27	–0.214	–0.357	–0.157
p-OCH_3	0.27	–0.61	–1.02	–0.45

[a]The values were obtained from the expression $0.35\sigma_R$ for *p*-OCH_3

An excellent DSP correlation was obtained with the σ_R^+ and σ_I values:

$$\log k = (0.75 \pm 0.08)\sigma_I + (1.12 \pm 0.04)\sigma_R^+ - (5.54 \pm 0.04) \quad (5)$$
$$r = 0.999,\ s = 0.04,\ F = 406,\ n = 5$$

From Eq. (5), the conclusion could be drawn that the reaction center is a strong electron-acceptor with a high positive charge, which can be stabilized by electron-donating groups.

In order to explain the given structure–reactivity correlation analysis (LFER), MO calculations of this reaction were undertaken.

The calculation was realized by MOPAC semi-empirical quantum-chemical program package, using the PM6 Hamiltonian.[24] The geometric variable that was used to mimic the reaction coordinates was the distance between atoms (7) and (20), which are connected by an arrow in Scheme 2. The distance between these atoms was systematically diminished without any other geometric constraint. A shallow energy minimum, Fig. 2, was found at 3.2 Å (the structure is shown in Fig. 3). Further approach of reactants goes through a transition state (Fig. 2) at 2.006 Å (the structure is shown in Fig. 4). This structure was confirmed by vibration analysis, showing only one negative vibration. Further approach is accompanied by a lowering of the potential energy.

This approach does not go smoothly. At a distance of 2.58 Å, a hydrogen atom transfer occurs from the amine nitrogen to the acetyl oxygen of other moiety. At 1.549 Å, the structure of the primary product is achieved (Fig. 5).

Simple reasoning suggests that the electron density shifts from the enamine to the benzylic moiety during the reaction. The partial atomic charges were calculated according to the Mulliken method and their variation on the atoms involved in the formation of a new C–C bond are presented in Fig. 6. Upper line shows the variation of electronic charge on the benzylic carbon as the function of distance. It shows a continuously increasing positive charge until the transition state is achieved. Then, at shorter distances, the electron density from the enamine goes to form new C–C bond.

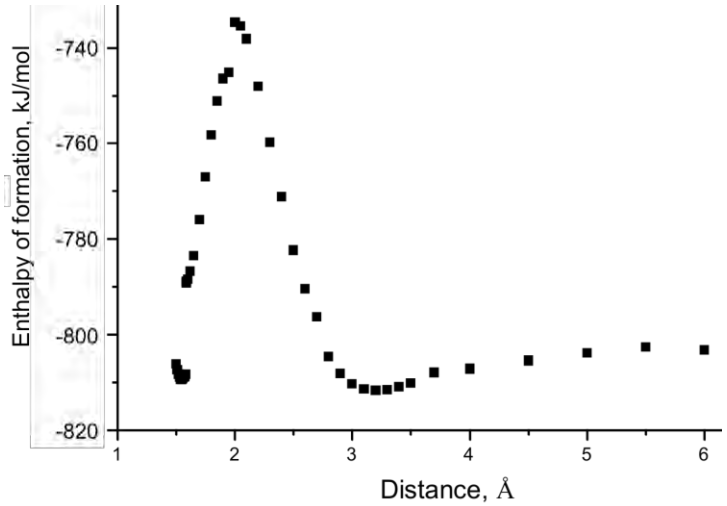

Fig. 2. Energy profile along the reaction coordinate.

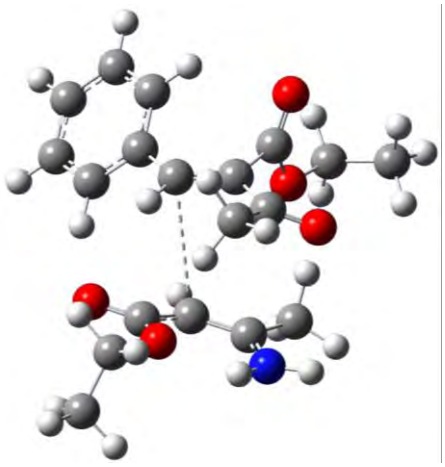

Fig. 3. (Meta)stable arrangement of reactants at distance 3.2 Å.

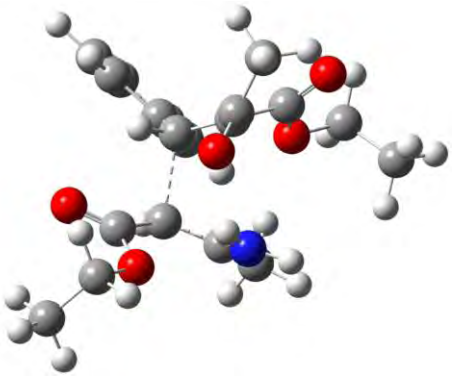

Fig. 4. Transition state for the reaction outlined in Scheme 2.

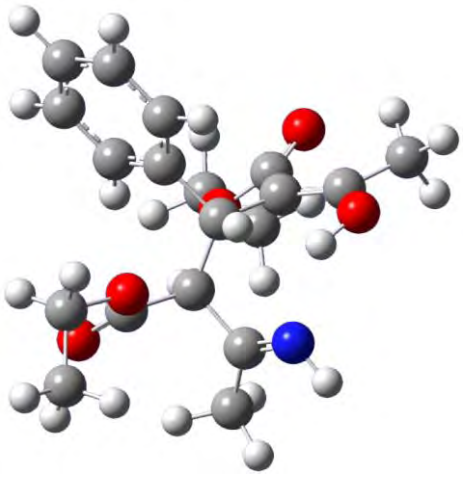

Fig. 5. Structure of the adduct at 1.549 Å.

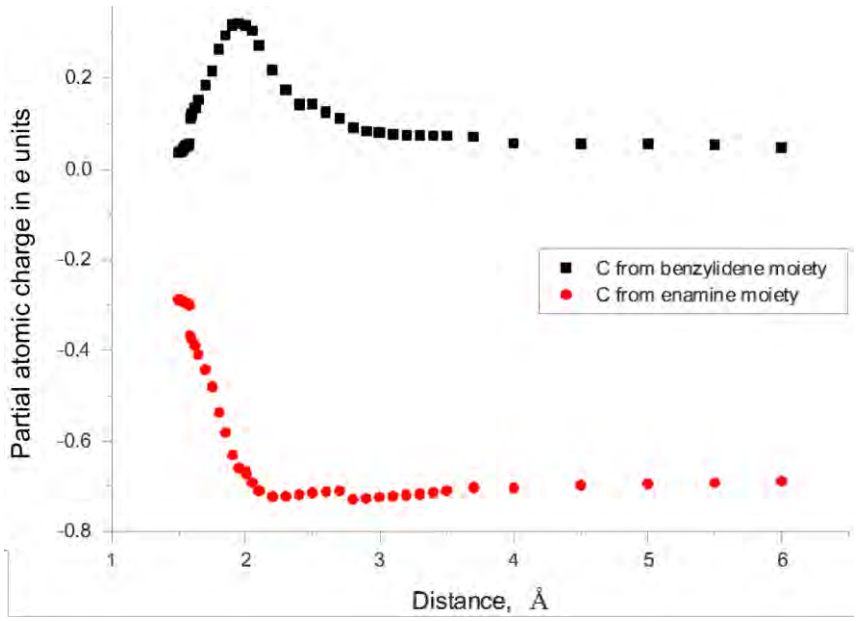

Fig. 6. Partial atomic charges on carbons directly involved in metathesis.

Therefore, the increasing electron demand at the benzylic reaction center is stabilized by electron-donor substituents on the aromatic ring, which should correlate with the σ^+ substituent constants (as was found by LFER analysis).

CONCLUSIONS

The study of the kinetics of the Hantzsch synthesis of substituted 1,4-dihydropyridines, with the *m*- and *p*-substituted benzylideneacetoacetates and an ena-

mine as reactants was presented. It was established that this reaction follows second order kinetics.

The reaction rate constants were analyzed by the Hammett equation and an extended Hammett equation (the DSP equation) using various substituent constants. It was concluded that a nucleophilic attack of the enamine on benzylideneacetoacetate causes an increase in the positive charge on the benzylic atom of benzylidene in the transition state, which enabled the stabilization by the electron-donating substituents. This conclusion established by the structure–reactivity relationships was explained and confirmed by MO calculations.

Acknowledgement. Our gratitude goes to the Ministry Education, Science and Technological Development of the Republic of Serbia (Grants 172013 and 172035) for financial support.

И З В О Д

КОРЕЛАЦИЈЕ СТРУКТУРЕ И РЕАКТИВНОСТИ ЗА КИНЕТИКУ РЕАКЦИЈЕ СИНТЕЗЕ СУПСТИТУИСАНИХ 4-ФЕНИЛ-1,4-ДИХИДРОПИРИДИНА

ЈОВИЦА В. УРОШЕВИЋ[1], САША Ж. ДРМАНИЋ[1], ЈАСМИНА Б. НИКОЛИЋ[1], ИВАН О. ЈУРАНИЋ[2] и БРАТИСЛАВ Ж. ЈОВАНОВИЋ[1]

[1]Катедра за органску хемију, Технолошко–металуршки факултет, Универзитета у Београду, Карнегијева 4, 11120 Београд и [2]Институт за хемију, технологију и металургију Универзитета у Београду, Његошева 12, 11000 Београд

Проучаван је квантитативан однос структуре и реактивности за кинетику Ханчове синтезе супституисаних 4-фенил-1,4-дихидропиридина у реакцији етил-*m*- и *p*-супституисаних 2-бензилиден-ацетоацетата и енамина. Кинетика испитиване реакције је праћена спектрофотометријским методом. Запажено је да је реч о реакцији другог реда. Квантитативне корелације структуре и реактивности које изражавају логаритам одређене константе брзине реакције (log *k*) у зависности од одговарајућих константи супституената (σ, σ^+,σ_I и $\sigma_R{}^+$) одређене су за Хаметову (Hammett) и проширену Хаметову једначину (DSP-једначину). Показале су линеарну зависност са позитивним вредностима нагиба, односно реакционе константе (ρ). Тиме је потврђено да Мајклова (Michael) адиција енамина на бензилиден представља спори ступањ у реакцији са израженим позитивним наелектрисањем на молекулу бензилидена. МО прорачуни су такође урађени и њихови резултати су били у складу са закључцима изведеним из корелација структуре и реактивности.

(Примљено 20. новембра, ревидирано 28. новембра 2013)

REFERENCES

1. H. R. Roodsari, A. M Sadeghipour, Z. N. Harat, P. Daneshgar, M. Vosooghi, A. Shafiee, *J. App. Sci.* **8** (2008) 158
2. S. Patra, *Int. J. Pharm., Chem. Biol. Sci.* **2** (2012) 482
3. H. Lullman. K. Mohr, A. Ziegler, D. Bieger, *Color Atlas of Pharmacology*, Thieme Verlag, New York, 2000, p. 118
4. A. Hantzsch, *Liebigs Ann.* **215** (1882) 1
5. U. Eisner, J. Kuthan, *Chem. Rev.* **72** (1972) 1
6. J. A. Berson, E. Brown, *J. Am. Chem. Soc* **77** (1955) 444

7. C. A. C. Hailey, P. Maitland, *J. Chem. Soc.* (1951) 3155
8. N. Sugimoto, *J. Pharm. Soc. Jpn.* **64** (1944) 192
9. M. Jonescu, V. N. Georgescu, *Bull. Soc. Chim. Fr.* **41** (1927) 627
10. A. H. Cook, I. M. Heilbronn, L. J. Steger, *J. Chem. Soc.* (1943) 413
11. A. P. Phillips, *J. Am. Chem. Soc.* **72** (1950) 2780
12. H. J. Kahn, V. Petrow, R. Rewald, B. Sturgeon, *J. Chem. Soc.* (1949) 2128
13. A. Courts, V. Petrow, *J. Chem. Soc.* (1952) 1
14. *Pyridine and Its Derivatives,* Part I, E. Klinsberg, Ed., Interscience, New York, 1961, p. 66
15. L. P. Hammett, *J. Am. Chem. Soc.* **59** (1937) 96
16. L. E. Hinkel, E. E. Ayling, W. H. Morgan, *J. Chem. Soc.* (1931) 1835
17. A. R. Katritzky, D. L. Osterkamp, T. I. Yousaf, *Tetrahedron* **42** (1986) 5729
18. A. Gomez-Sanchez, A. M. Walle, J. Bellanato, *J. Chem. Soc., B* (1971) 2330
19. P. D. Gardner, R. L. Brandon, *J. Org. Chem.* **22** (1957) 1704
20. J. V. Uroševic, *MS Thesis*, Faculty of Technology and Metallurgy, Belgrade, 2009 (in Serbian), and references therein
21. M. B. Smith, J. March, *Advanced Organic Chemistry,* 6th ed. Wiley, New York, 2007, p. 404
22. R. W. Taft, *J. Am. Chem. Soc.* **79** (1957) 1045
23. R. A. Y. Jones, *Physical and Mechanistic Organic Chemistry,* Cambridge University Press, Cambridge, UK, 1979, p. 56
24. J. P. Stewart, *J. Mol. Model*. **13** (2007) 1173.

Journal of the Serbian Chemical Society
JSCS-info@shd.org.rs • www.shd.org.rs/JSCS

J. Serb. Chem. Soc. 78 (12) 1975–1982 (2013)
JSCS–4544

UDC 546.831+541.182:544.032.1:
541.135–039.6:543.24
Original scientific paper

Stability of zirconia sol in the presence of various inorganic electrolytes

JELENA P. MARKOVIĆ[1], SLOBODAN K. MILONJIĆ[1]*# and VUKADIN M. LEOVAC[2#]

[1]*The Vinča Institute of Nuclear Sciences, University of Belgrade, Serbia and* [2]*Chemistry Department, Faculty of Sciences, University of Novi Sad, Serbia*

(Received 21 October 2013)

Abstract: The zirconia sol was prepared from a zirconium oxychloride solution by forced hydrolysis at 102 °C. The prepared sol consisted of almost spherical, monoclinic, hydrated zirconia particles of 61 nm in diameter. The stability of zirconia sol in the presence of various inorganic electrolytes (LiCl, NaCl, KCl, CsCl, KBr, KI, KNO_3 and K_2SO_4) was studied by the potentiometric titration method. The dependence of the critical concentration of coagulation (*ccc*) on the dispersion pH was determined for all studied electrolytes. The critical coagulation concentration values for all investigated electrolytes were lower at higher pH values. These values for all 1:1 electrolytes were the same within the range of experimental error. For a given pH value, the *ccc*s of K_2SO_4 are 3–4 orders of magnitude lower than the corresponding values for the 1:1 electrolytes.

Keywords: zirconia sol; stability; electrolytes; critical coagulation concentration; potentiometric titration.

INTRODUCTION

For further development of nanostructured materials, new technologies that yield physically and chemically stable nanoparticles are required. Zirconia (ZrO_2) is an important ceramic material with an increasing range of applications, *e.g.*, for thin-film coatings and catalysis. An understanding of the surface charge characteristics as a function of pH and ionic strength is important in optimizing the processing conditions for high technology ceramics applications.[1] A colloidal dispersion is said to be stable when there is no significant agglomeration, *i.e.*, when the potential barrier is sufficiently high to prevent particles from contacting one another. Whether or not a dispersion is stable depends on both the surface

* Corresponding author. E-mail: smiloni@vinca.rs
# Serbian Chemical Society member.
doi: 10.2298/JSC131021118M

electrostatic potential (dependent on dispersion pH) of the solid particles and the ion concentration in the solution.[2]

Coagulation of a colloidal dispersion may be affected by numerous factors, such as dispersion aging, change in the amount of the dispersion phase, mechanical and light action, change in temperature, *etc*. However, the coagulation caused by the addition of an electrolyte into a sol is of the greatest theoretical and practical importance. The interaction between a colloid and an electrolyte depends on the nature of the solid phase, especially on its surface composition, as well as on the type and concentration of ion species in the solution.[2] A fair amount of interest has also been shown in the stability of colloidal dispersions.[3–10]

Charged colloidal particles lead to the formation of a layer of opposite charge in the fluid adjacent to a particle – the so-called diffuse electrical double layer – that partly screens the charge on the particle. At low ionic strengths, the double layer extends beyond the range of the van der Waals force. The resulting electrical repulsion between the particles prevents agglomeration, unless the particles are nearly electrically neutral (which depends on the pH). At high ionic strengths, the double layer shrinks in size and the net force is always attractive. Hence, at high ionic strengths, agglomeration always occurs.

Surface charge at the metal oxide–electrolyte interface is formed by protonation or deprotonation of surface hydroxyl groups as well as the formation of other surface species from the background electrolyte ions (ion pairs or surface complexes). The structure of the inner region of the electrical double layer (edl) for such systems is very often described by the site-binding model.[11]

Most colloidal particles are electrically charged, *e.g*., most metal oxides have surface layers formed by/made of hydroxyl groups which are amphoteric and can become either positively or negatively charged, by proton association or proton dissociation, depending on the pH:[12]

$$\geq Zr–OH + H^+ \rightarrow \geq ZrOH_2^+,\ pH < pH_{pzc} \quad (1)$$

$$\geq Zr–OH + OH^- \rightarrow \geq Zr–O^- + H_2O,\ pH > pH_{pzc} \quad (2)$$

Reaction (1) is favored by a low pH, while reaction (2) occurs at a high pH. pH_{pzc} represents the pH value at which the solid surface charge is equal to zero. For oxide systems, and many other colloids, H^+ and OH^- ions are the potential-determining ions. In such systems, the surface charge and potential are determined largely by the balance between H^+ and OH^- in the solution, *i.e*., by the pH.

This paper presents a continuation of studies devoted to the study of inorganic sol stability. To the best of our knowledge, there are no literature data on the stability of colloidal zirconia in the presence of inorganic electrolytes; such a study is thus the aim of the present work.

EXPERIMENTAL

The corresponding author's group has been successful in synthesizing different stable and monodisperse metal oxide sols using the forced hydrolysis method.

Zirconia sol was prepared from aqueous solution by the forced hydrolysis method, according to the procedure described in a previous paper,[13] using zirconium oxychloride octahydrate (Merck, *p.a*. grade) as the precursor and hydrochloric acid (35 % HCl, Lachema, *p.a*. grade). Doubly distilled water was used to prepare the acid solution. A solution of 0.01 M HCl was stirred in a reactor up to the boiling point (102 °C). The required amount of premixed $ZrOCl_2$ in 0.01M HCl solution was added to this solution under vigorous stirring and kept boiling under reflux for 24 h. This procedure was followed in order to avoid the local precipitation effect. The important parameters in direct synthesis are the choice of the type and concentration of precursors, solution pH, temperature and mixing.

In order to increase the stability of the prepared zirconia sol, it was ultrafiltered using an Amicon YCO5 membrane and an Amicon ultrafiltration cell (model 8200), until the permeate was free of chloride ions (negative $AgNO_3$ test). The ultrafiltered zirconia sol was stable (no precipitation) over 6 years. The zirconia particle size distribution was determined by the DLS (Dynamic Light Scattering) method using a Zetasizer Nano ZS with a 633 nm He–Ne laser (Malvern, UK). The Zetasizer Nano system is the latest generation of light scattering instruments, containing both the hardware and the software for combined static, dynamic, and electrophoretic light scattering measurements. A wide range of sample properties available for measurement with the system includes particle size, molecular weight and zeta potential. The instrument can measure particle sizes from 0.6 nm to 6 μm.

The stability of colloidal systems can be determined in various ways. One of them is the use of a classical and rather qualitative method consisting of a series of test tubes containing solutions with equal amounts of dispersed material, but with gradually increasing electrolyte concentrations. After a certain period, usually several hours, the point at which electrolyte concentration sedimentation or creaming had just occurred is visually established.[8,9,14,15] These experiments give better results than turbidity measurements.[14,15]

The coagulation of the zirconia sol containing different concentrations of electrolytes was monitored/examined. Eight different inorganic salts (LiCl, NaCl, KCl, CsCl, KBr, KI, KNO_3 and K_2SO_4) were used as electrolytes. These cations and anions were chosen with the aim of studying the relationship between the diameter size and the valence of ions and the pH of coagulation.

The employed experimental technique was potentiometric titration of separate samples.[2,4,5,16-18] PVC vessels containing the samples were equilibrated (with intensive mechanical stirring) for 4 h at room temperature. Then, each sample was visually examined; coagulation and phase separation, whenever it occurred, was noted.

RESULTS AND DISCUSSION

The particle size distribution of the zirconia sol, registered as the intensity during several successive DLS runs, is shown in Fig. 1. The experimental data are the average of at least six runs. Each curve/run presents a mean value of 14 measurements. The obtained average particle diameter represents the hydrodynamic diameter of a sphere (*i.e*., diameter of a particle with a hydration shell), having the same volume as the particle. It is evident that the size distribution is monomodal and monodisperse. The polydispersity index (*PDI*) was 0.071, and

the average zirconia particle diameter, d_{av}, 61 nm. As shown earlier,[13] the apparent crystallite size of the zirconia powder, calculated from XRD patterns according to the Scherrer equation, was about 6 nm. This means that zirconia particles in the prepared sol consist of several (up to ten) crystallites.

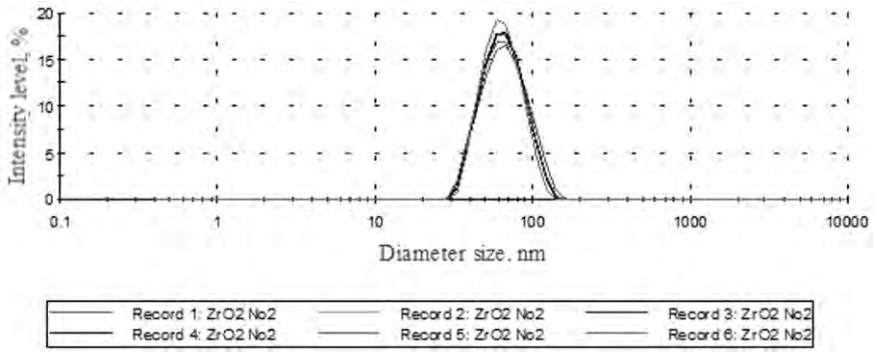

Fig. 1. Particle size distribution of the zirconia sol.

Before performing the coagulation measurements in the presence of selected inorganic cations and anions, the pH of coagulation (pH_c) of the zirconia colloid without electrolyte was found to be 7.75 (close to pH_{pzc} – point of zero charge of zirconia), by potentiometric titration with 0.1 mol dm^{-3} KOH. The stable, ultrafiltered zirconia dispersion (zirconia sol) used in this study had a pH value of 3.54.

Profiles of the logarithms of critical coagulation concentrations (log *ccc*, *ccc* is given in mol dm^{-3}) of the selected electrolytes (influence of anions and cations) as a function of pH_c show linear dependences (Figs. 2 and 3). The stability region for a given anion or cation is below and to the left side of the corresponding curve. For any point (pH_c, log *ccc*) chosen in this region, the stability of the system is preserved. On the other hand, the area above each curve and to its right side represents the coagulation region, *i.e.*, for any log *ccc* value at the corresponding pH_c, the coagulation is inevitable. For all the investigated electrolytes, the higher the critical coagulation concentration, the lower was the pH_c value.

For positively charged zirconia surface ($pH < pH_{pzc}$), near to pH_{pzc}, the critical coagulation concentration for monovalent anions increases in the following order: $NO_3^- \leq Cl^- < I^- \leq Br^-$. There is a slight difference in the pH_c values between the various monovalent anions at high salt concentrations.

The higher the $\Delta pH = pH_c - pH_{pzc}$ value, the more electrolyte is required to attain the critical coagulation concentration. Increasing ΔpH also causes an increase in surface charge of zirconia, which results in a more stable sol.

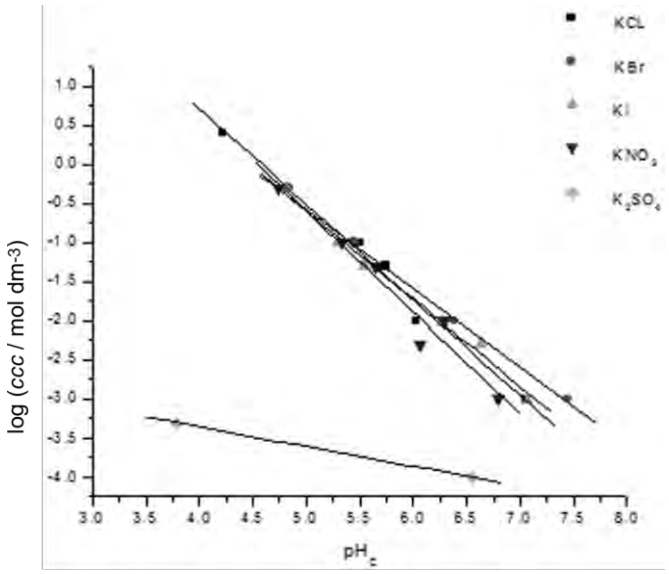

Fig. 2. Profiles of the logarithm of the critical concentrations of the selected anions as a function of pH_c.

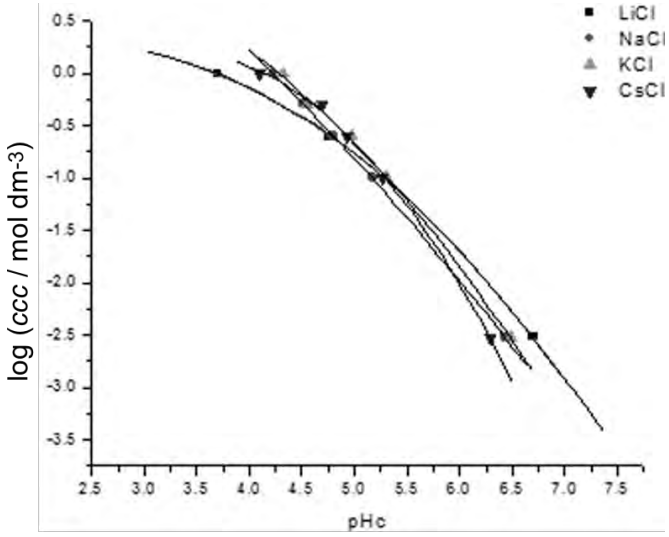

Fig. 3. Profiles of logarithm of the critical concentrations of the selected cations as a function of pH_c.

It can be seen from Fig. 2 that the critical coagulation concentrations of bivalent anion (SO_4^{2-}) for a given pH_c value were 3–4 orders of magnitude lower with respects to the corresponding values for monovalent anions.

Pérez-Maqueda and Matijević[19] investigated the stability of a dispersion of zirconium (hydrous) oxide in the presence of $NaNO_3$, Na_2SO_4 and $H_4SiW_{12}O_{40}$. They obtained the following *ccc* values 3.5×10^{-3}, 7×10^{-5} and 2×10^{-4} mol dm^{-3} at pH 4 for NO_3^-, SO_4^{2-} and $SiW_{12}O_{40}^{4-}$, respectively. Comparing these values with the present results, it is evident that the herein studied sol was much more stable toward NO_3^-, SO_4^{2-} ions at this pH value. The following *ccc* values, at pH 4, for NO_3^- and SO_4^{2-} were 5.6 and 4×10^{-4} mol dm^{-3}, respectively (see Fig. 2). To obtain zirconium (hydrous) oxide particles, Pérez-Maqueda and Matijević[19] applied the precipitation procedure. They used solutions of zirconium chloride and triethanolamine (TEA). According to the XRD pattern, the zirconium hydrous oxide sample was amorphous. In addition, their procedure yielded stable dispersions at low temperatures and short reaction times.

A possible reason for SO_4^{2-} coagulation behavior lies in the specific character of the sulfate anion. The specific ion sorption changes the electrical properties of the electrical layer in different ways with respect to the simple attractive electrostatic interaction between non-specifically sorbed ions and the particle surface. For this reason, the Schultze–Hardy rule cannot be fully obeyed by the specifically sorbed anions. Besides, the critical coagulation concentration values for multi-charged ions are characteristic of a given system and cannot be generalized.

The minimum electrolyte concentration required to cause coagulation, known as the critical concentration of coagulation, for a divalent ion should be two-time lower than that for a monovalent ion, and for a trivalent ion, three times lower than that for a monovalent ion. This is the basis of the Schultze–Hardy rule: cZ^6 = constant, where c is the concentration of electrolyte and Z is the ion charge. The Schultze–Hardy rule is an empirical rule, stating that coagulation concentration of hydrophobic sols decreases very strongly with increasing valency Z of the counter-ion.[20]

For monovalent and divalent ions, the critical concentration of coagulation according to the Schultze–Hardy rule exhibited the proportion 1:0.016. The monovalent/divalent (SO_4^{2-}) anion ratio varied in the experiments from 0.0002 to 0.0129 for pH from 4.5 to 6.5. In practice, there was often evidence of deviations from this rule, mainly due to specific ion adsorption. Multivalent ions tend to adsorb on solid particles by specific binding. The interpretation of the Schultze–Hardy rule implies that the coagulation concentration is determined by a combination of specific ion adsorption and diffuse double layer overlap. The higher the ion valency, the higher is the contribution of the specific adsorption.[20]

CONCLUSIONS

Measurement of the particle size distribution proved the zirconia sol to be monomodal and monodisperse (with a polydispersity index 0.071). The obtained

average zirconia particle diameter was 61 nm. Particles of initial zirconia sol were positively charged. The ultrafiltered zirconia sol was stable (no precipitation) for over 6 years. Eight inorganic electrolytes (LiCl, NaCl, KCl, CsCl, KBr, KI, KNO_3 and K_2SO_4) were added to the zirconia sol and potentiometric titration was performed in order to determine the stability of the sol in the presence of these cations and anions. The coagulation pH (pH_c), determined by potentiometric titration, varied from 4 to 7.5. The 1:1 electrolytes for cations of the same periodic group showed similar behavior. K_2SO_4 behaved differently showing much lower *ccc* values (3–4 times lower than for the 1:1 electrolytes).

Acknowledgement. This work was partially supported by the Ministry of Education, Science and Technological Development of the Republic of Serbia (Project No. III 45012).

ИЗВОД

СТАБИЛНОСТ СОЛА ЦИРКОНИЈУМ(IV)-ОКСИДА У ПРИСУСТВУ РАЗЛИЧИТИХ НЕОРГАНСКИХ ЕЛЕКТРОЛИТА

ЈЕЛЕНА П. МАРКОВИЋ[1], СЛОБОДАН К. МИЛОЊИЋ[1] и ВУКАДИН М. ЛЕОВАЦ[2]

[1]Институт за нуклеарне науке "Винча", Универзитет у Београду, Београд и [2]Департман за хемију, Природно–математички факултет, Универзитет у Новом Саду, Нови Сад

Извршена је синтеза мономодалног и монодисперзног цирконијум(IV)-оксида. Индекс полидисперзности добијеног сола је 0,071 а средњи пречник честица износи 61 nm. Честице припремљеног сола су позитивно наелектрисане. Полазни сол је стабилан у дужем временском периоду (дуже од шест година). Одређивана је стабилност синтетизованог сола у присуству осам одабраних неорганских електролита (LiCl, NaCl, KCl, CsCl, KBr, KI, KNO_3 и K_2SO_4). Вредности pH коагулације, у присуству наведених електролита, варирају у опсегу од 4 до 7,5. Електролити са једновалентним јонима имају слично понашање. Вредности критичних концентрација коагулације добијеног сола у присуству калијум-сулфата су 3–4 пута ниже у односу на оне за 1:1 електролите.

(Примљено 21. октобра 2013)

REFERENCES

1. R. J. Xie, M. Mitomo, K. Uheda, F. F. Xu, Y. Akimune, *J. Am. Ceram. Soc*. **85** (2002) 1127
2. S. K. Milonjić, N. B. Vučić, *Mater. Sci. Forum* **282–283** (1998) 189
3. E. J. W. Verwey, J. Th. G. Overbeek, *Theory of the Stability of Lyophobic Colloids*, Elsevier, Amsterdam, 1948.
4. S. K. Milonjić, *Colloids Surf.* **63** (1992) 113
5. M. Petković, S. K. Milonjić, V. Dondur, *Bull. Chem. Soc. Jpn*. **68** (1995) 2133
6. J. D. F. Ramsay, S. R. Daish, *Discuss. Faraday Soc*. **66** (1978) 65
7. L. H. Allen, E. Matijević, *J. Colloid Interface Sci*. **33** (1970) 420
8. D. R. Harding, *J. Colloid Interface Sci*. **35** (1971) 172
9. M. Tschapek, R. M. Tores Sanchez, *J. Colloid Interface Sci*. **54** (1976) 460
10. R. Brace, E. Matijević, *Colloid Polym. Sci*. **255** (1977) 153
11. D. E. Yates, S. Levine, T. W. Healy, *J. Chem. Soc., Faraday Trans. 1* **70** (1974) 1807
12. J. Davis, R. O. James, J. O. Leckie, *J. Colloid Interface Sci*. **63** (1978) 480

13. J. Marković, S. K. Milonjić, *J. Serb. Chem. Soc*. **71** (2006) 613
14. B. H. Bijsterbosch, *Stability of solid/ liquid dispersions,* in: *Solid/Liquid Dispersions*, Th. F. Tadros, Ed., Acad. Press, London, 1987, p. 91
15. E. Frey, G. Lagaly, *J. Colloid Interface Sci*. **70** (1979) 46
16. S. K. Milonjić, V. L. Razin, Yu. G. Frolov, *Kolloidn. Zh*. **42** (1980) 147
17. S. K. Milonjić, M. M Kopečni, Z. E. Ilić, *Bull. Soc. Chim. Beograd* **48** (1983) 351
18. A. Onjia, S. K. Milonjić, *Mater. Sci. Forum* **352** (2000) 111
19. L. A. Pérez-Maqueda, E. Matijević, *J. Mater. Res*. **12** (1997) 3286
20. J. Lyklema, *J. Colloid Interface Sci*. **392** (2013) 102.

Journal of the Serbian Chemical Society
JSCS-info@shd.org.rs • www.shd.org.rs/JSCS
J. Serb. Chem. Soc. 78 (12) 1983–1992 (2013)
JSCS–4545
UDC 546.92+546.98+621.039.51:
544.478–44+66.094.2+546.21
Original scientific paper

Pt monolayer shell on hollow Pd core electrocatalysts: scale up synthesis, structure, and activity for the oxygen reduction reaction•

MIOMIR B. VUKMIROVIC[1], YU ZHANG[1], JIA X. WANG[1], DAVID BUCETA[1#], LIJUN WU[2] and RADOSLAV R. ADZIC[1]*

[1]*Chemistry Department, Brookhaven National Laboratory, Upton, NY 11973, USA and* [2]*Condensed Matter Physics & Materials Science Department, Brookhaven National Laboratory, Upton, NY 11973, USA*

(Received 24 October 2013)

Abstract: The synthesis, characterization and kinetics of the oxygen reduction reaction (ORR) of a Pt monolayer shell on Pd(hollow), or Pd–Au(hollow) core electrocatalysts are reported. Comparisons between the ORR catalytic activity of the electrocatalysts with hollow cores and those of Pt solid and Pt hollow nanoparticles were obtained using the rotating disk electrode technique. Hollow nanoparticles were made using Ni or Cu nanoparticles as sacrificial templates. The Pt ORR specific and mass activities of the electrocatalysts with hollow cores were found to be considerably higher than those of the electrocatalysts with solid cores. This enhanced Pt activity is attributed to the smooth surface morphology and hollow-induced lattice contraction. In addition, the hollow particles have a mass-saving geometry.

Keywords: platinum overlayer, electrocatalysis, fuel cells, surface strain.

INTRODUCTION

The rapidly increasing demand for fossil fuels used in transportation and power generation, and their detrimental environmental effects, have resulted in a wide-spread challenge for the development of renewable energy technologies. Fuel cells are one of the most promising clean energy technologies, particularly attractive for automobile applications, due to their high efficiency, high energy density, and low or zero emissions. The most challenging problem of their application is the slow kinetics of oxygen reduction reaction (ORR) at fuel cell

* Corresponding author. E-mail: adzic@bnl.gov
# Current address: Department of Physical Chemistry, University of Santiago de Compostela, E-15782 Santiago de Compostela, Spain.
• Dedicated to Professor Branislav Nikolić on the occasion of his 70th birthday.
doi: 10.2298/JSC131024117V

cathodes, even on Pt - the best single element electrocatalyst, which causes a large loss of the cell voltage, resulting in significant efficiency loss. In addition, Pt dissolves under certain operating condition of fuel cells. To mitigate these two drawbacks, catalysts containing large amounts of expensive Pt are required. This is one of the main reasons for the slow commercialization of fuel cells.

The ORR is a complex multi-step reaction involving the exchange of four electrons and four protons, the detailed mechanism of which still defies formulation.[1,2] Irrespective of the microscopic mechanism, a four electron process must involve the breakage of O–O bonds and the formation of O–H bonds.[1,2] According to the Sabatier principle,[3] the optimal catalyst should have moderate binding properties, such that both hydrogenation of O/OH and O–O scission are active. Density functional theory (DFT) calculations showed[4,5] that pure Pt is active for O–O scission, but hydrogenation of O/OH is slow. Therefore, weakening O and OH binding will improve ORR activity of Pt.

To address these drawbacks, the use of Pt monolayer (Pt_{ML}) electrocatalysts was proposed to reduce the cost of Pt while attempting to enhance their ORR activity and stability.[6,7] Such catalysts, consisting of a monolayer of Pt on a substrate of another material, minimize the amount of Pt while ensuring that all Pt atoms are available at the surface for catalytic activity.[6,7] Additionally, through geometric and electronic interactions with the substrate,[8,9] a Pt_{ML} can change its electronic properties and be more active and durable than pure Pt electrocatalysts.

The role of substrate (core) in determining the activity of a Pt_{ML}(shell), as a way to fine tune the balance between breaking of O–O bonds and the formation of O–H bonds, was first demonstrated in studies of the ORR, in both acid and alkaline media, on Pt_{ML} deposited on five different single-crystal surfaces (Au, Ir, Rh, Pd and Ru) and confirmed with nanoparticle supports.[7,10–12] Variations in ORR activity could be accounted for by the oxygen binding energy, which must be tuned to intermediate strength. This leads to a classic catalysis 'volcano plot' of ORR activity *vs*. oxygen binding energy, with Pt_{ML} on Pd(111) at the top of the volcano plot, having a higher ORR activity than Pt(111).[10] In addition, a fuel cell test showed that Pt_{ML} on Pd electrocatalysts was more durable than a pure Pt electrocatalyst.[13] However, further improvements in activity and durability are desirable.

Since oxygen binding energy appears to be the major descriptor of the ORR kinetics, DFT calculations suggests that further enhancement in ORR activity of Pt_{ML} on Pd could be accomplished by weakening the O and OH binding energies.[10] This could be achieved by additional contraction of the Pt_{ML} shell. A hollow core is an interesting structure to investigate geometric interaction between the Pt_{ML} shell and the core because a hollow core may induce a desirable lattice contraction of a Pt_{ML}, leading to improved ORR activity by reducing the oxygen

binding energy. In this paper, how the oxygen binding energy could be modified using a Pd hollow core is explored. The results are compared with those obtained with hollow Pt nanoparticles in order to elucidate the geometric and electronic interactions between the Pt_{ML} shell and the Pd core.

EXPERIMENTAL

Pt and Pd–Au hollow nanoparticles were obtained using Ni as a sacrificial template. First, a thin-film carbon electrode was prepared by pipetting a 15-μL aliquot of a 1 mg mL^{-1} aqueous suspension of carbon powder (Vulcan 72C) onto a polished glassy carbon surface of a rotating disk electrode (5 mm diameter, 0.196 cm^2, Pine Instrument). Then, the as-prepared thin-film electrode was immersed in a deaerated solution of 0.1 M $NiSO_4$ and 0.5 M H_3BO_3, and Ni nanoparticles were created on the carbon support by application of a double potential pulse, typically about 0.4 s at –1.4 V and 20 s at –0.8 V (*vs*. Ag/AgCl, 3 M NaCl). Once the open-circuit potential of the electrode had stabilized, it was transferred into deaerated (0.05–1 mM) K_2PtCl_4 (for Pt hollow) or 0.5 mM $Pd(NH_3)_4Cl_2$ + *x*$HAuCl_4$ (for Pd–Au hollow) solutions without exposure to air, whereby the galvanic replacement of Ni by Pt or Pd and Au occurred. After 3–30 min, electrode was rinsed with water, to eliminate residual metal ions, and cycled (for about 20 cycles) from 0.05 to 1.2 V *vs*. the reversible hydrogen electrode (RHE) in a deaerated 0.1 M $HClO_4$ solution to facilitate the complete removal of the Ni atoms. The hollow Pd–Au nanoparticles were prepared with Pd-to-Au concentration ratios of 20:1 and 10:1 in the precursor solutions. They are denoted as $Pd_{20}Au(h)/C$ and $Pd_{10}Au(h)/C$, respectively. The hollow Pt nanoparticles are denoted as Pt(h)/C. The Pt_{ML} was placed on the hollow Pd–Au nanoparticles using galvanic replacement of an underpotentially deposited Cu monolayer, as previously reported.[7,14] The experimental set-up was described elsewhere.[15] These samples are designated as $Pt_{ML}/Pd_{20}Au(h)/C$ and $Pt_{ML}/Pd_{10}Au(h)/C$ respectively. The solid Pt (Pt(s)/C) and Pd (Pd(s)/C) nanoparticle samples were carbon-supported Pt (45 wt. %) and Pd (10 wt. %), respectively.

For large-scale synthesis, the carbon-supported hollow Pd nanoparticles (Pd(h)/C) were prepared by a two-step synthesis method. In the first step, Cu nanoparticles were prepared by slowly adding $NaBH_4$ into the mixture of carbon (Vulcan X72), $CuCl_2$, and Na-citrate. In the second step, $Pd(NH_3)_4Cl_2$ was added, thus forming Pd hollow nanoparticles by galvanic displacement of Cu with Pd. The procedure for one batch-synthesis of 650 mg of the Pt_{ML}/ /Pd(h)/C catalyst was described elsewhere.[16]

All the electrochemical treatments and measurements were performed with a Voltalab PGZ402 potentiostat (Radiometer Analytical) at room temperature. The electrolyte was 0.1 M $HClO_4$ solution. An Ag/AgCl (3 M NaCl) electrode was used as the reference electrode and a Pt flag was used as the counter electrode. All the potentials are given with respect to a RHE. The electrochemical surface area (*ESA*) was calculated using the integrated hydrogen desorption charges from cyclic voltammetry (CV) curves assuming 0.21 mC cm^{-2}.[17] Kinetic currents at 0.9 V were calculated from the ORR polarization curves using $j_k = j/(1–j/j_L)$, where j is the measured current at 0.9 V and j_L is the diffusion-limited current below 0.5 V. The obtained kinetic current was further normalized to *ESA* and Pt mass to calculate Pt specific (*SA*) and mass activities (*MA*), respectively. The currents in the voltamograms were normalized to the geometric electrode surface area.

Transmission electron microscope (TEM) imaging was realized using a JEOL 3000F TEM operating at 300 kV equipped with Gatan image filter system. The mass contents of Pd and Pt were determined using inductively coupled plasma mass spectrometry (ICP–MS)

measurements. The very small amount of Au could not be reliably determined by ICP–MS and was estimated using the measured Pd mass and the atomic ratio in the mixed Pd–Au solutions. Scanning TEM (STEM) measurements were performed using a Hitachi HD2700C microscope equipped with a cold field emission electron source and a probe aberration corrector. X-Ray diffraction (XRD) experiments were performed on a Beamline X7B (λ = = 0.3196 Å) of the National Synchrotron Light Source at Brookhaven National Laboratory. Two dimensional powder patterns were collected with a Perkin Elmer image plate detector, and the diffraction rings were integrated using the FIT2D code. The fitted parameters (lattice constant and particle size) were obtained through a Rietveld refinement. Lanthanum hexaboride (LaB_6) was used as the instrumental reference.

RESULTS AND DISCUSSION

As discussed above, hollow Pt, Pd, and Pd–Au nanoparticles were prepared by exposing Ni or Cu nanoparticles to Pt, Pd, or Pd–Au containing solutions. The formation of voids in these nanoparticles was governed by both galvanic replacement and the Kirkendall Effect (vacancy-mediated diffusion mechanism). While galvanic replacement is responsible for displacing Ni (or Cu) with Pt, Pd or Pd–Au and thus creating core–shell structure, due to Kirkendall effect, Ni (Cu) from the core can diffuse through the shell to its surface where it will be replaced with Pt, Pd, or Pd–Au. Due to the different diffusion rates of Ni (Cu) and Pt, Pd, or Pd–Au, vacancies will be generated inside the core–shell nanostructures, and they may coalesce into a single void (hollow) or multiple voids (porous).

Ni nanoparticles were found suitable as templates to facilitate the formation of single-void particles with complete Pt shells.[18] Pt hollow nanoparticle in high-resolution STEM images for the samples after electrochemical measurements are displayed in Fig. 1a. The synthetic parameters were varied in order to optimize the ORR activity and durability. The best catalytic activity was found with 3–9 nm hollow spheres with a 1–2 nm thick shell.

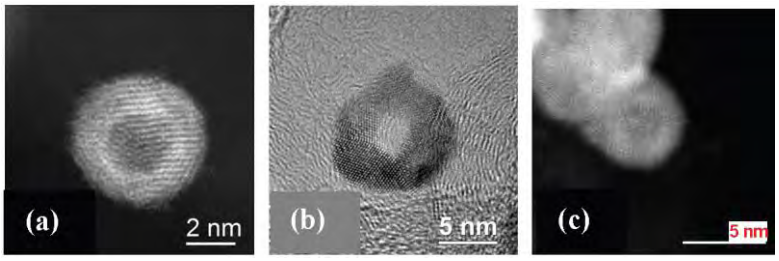

Fig. 1. a) High-resolution STEM image of a Pt(h)/C nanoparticle, b) TEM image of $Pt_{ML}/Pd_{20}Au(h)/C$ nanoparticle and c) TEM image of $Pt_{ML}/Pd(h)/C$ nanoparticle.

However, hollow structures were more difficult to form with Pd or Au ions alone when using Ni nanoparticles as sacrificial templates. Lower melting temperature of Au compared to Ni suggests that Ni diffuses slower than Au. Consequently, the voids generated by Ni atoms slowly diffusing out through the Au

shell will be filled by inward faster-diffusing Au atoms before they coalesce into a single void, thus resulting in solid Au particles. In Ni–Pd case, the difference in diffusivity between Ni and Pd is not large enough (the small difference in melting temperatures) to create sufficient vacancies to form Pd hollow nanoparticles.

The addition of Au ions in Pd solutions may mediate the diffusion process and promote the formation of hollow particles.[19] In the Pd–Au mixed solution, since the standard reduction potential of the $AuCl_4^-$/Au redox couple (1.002 V *vs*. SHE) is higher than that of the $Pd(NH_3)_4^{2+}$/Pd couple (0.902 V *vs*. SHE),[20] Au ions will be preferentially reduced instead of Pd ions and deposited on the surface of the Ni templates as a thin shell. The imbalance between the outward flux of faster-diffusing Ni–Au atoms and the inward flux of the slower-diffusing Pd atoms will be compensated for by an inward flux of vacancies. The vacancies will then supersaturate and coalesce into a single void. On the shell surface, the Ni atoms that flowed out will spontaneously dissolve because of their lower reduction potential, while the Au atoms will remain intact because of their higher reduction potential. Typical TEM images of a $Pt_{ML}/Pd_{20}Au(h)/C$ sample with hollow cores are shown in Fig. 1b. The adding of a small amount of Au to the Pd core only improved the stability of Pd while its interaction with Pt_{ML} was not influenced.[13] Therefore, as long as only the core–Pt_{ML} interaction is considered, Pd–Au can be treated as Pd.

The TEM images confirmed the hollow structure of the Pd nanoparticles prepared by the large-scale synthesis method. They had a narrow size distribution with an average diameter of 5 nm and shell thickness of 1.5 nm (Fig. 1c).

The effect of the voids in nanoparticles on the ORR activity of the top Pt layer was investigated by recording the ORR polarization curves in oxygenated 0.1 M $HClO_4$ using the rotating disk electrode technique. The ORR polarization curves for Pt(h) and Pt(s) nanoparticles are shown in Fig. 2a, while the ORR polarization curves for $Pt_{ML}/Pd_{20}Au(h)/C$ and $Pt_{ML}/Pd(s)/C$ nanoparticles are presented in Fig. 2b. In both cases, solid and hollow nanoparticles show similar onset and kinetic part of the ORR polarization curve. However, the onset and half-wave potentials are not true measures of ORR activity but only qualitative indicators since they are sensitive to catalyst loading. This could be clearly seen if the respective voltammetry curves of the samples in deaerated 0.1 M $HClO_4$ are examined, Fig. 3a and b. The H adsorption–desorption charge at low potentials and the OH adsorption–desorption charge at high potentials are both smaller on the hollow than on the solid samples because the catalyst loading of the hollow samples is lower than that of the solid ones. Additionally, the hollow samples have smaller *ESA* values compared to those of the solid samples, due to their larger average particle size (Table I).

The correct way to compare the ORR activity of these catalysts is to use the Pt mass and specific activities, which compare the ORR activity of the catalysts

to the same reference point, as shown in Table I. The *SA* and *MA* values of the hollow samples were higher than those for the solid ones. The *ESA* per Pt mass (ESA_{Pt}) is similar for the solid and hollow samples. This means that the enhancement in *MA* (where $MA = SA \times ESA_{Pt}$) for hollow samples mainly results from increased *SA* values.

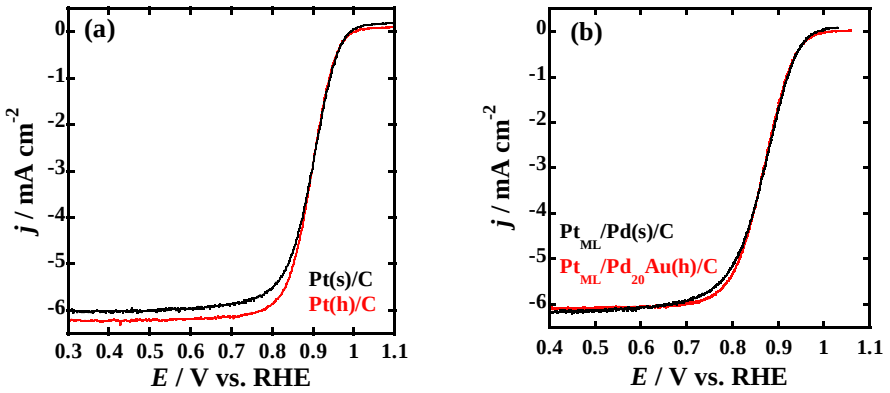

Fig. 2. ORR polarization curves in oxygen-saturated 0.1 M $HClO_4$ solutions, in the forward potential sweep at 10 mV s^{-1} with a 1600 rpm rotation rate for a) Pt(s)/C and Pt(h)/C and b) $Pt_{ML}/Pd_{20}Au$(h)/C and Pt_{ML}/Pd(s)/C nanoparticles.

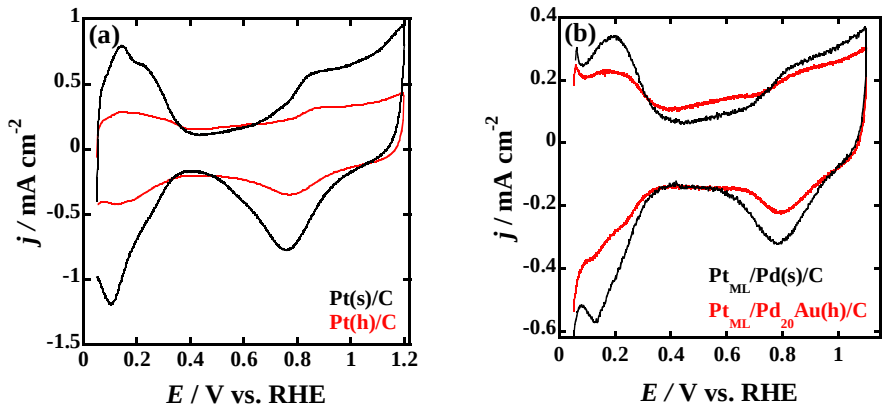

Fig. 3. Voltammetry curves in deareated 0.1 M $HClO_4$ solutions for a) Pt(s)/C and Pt(h)/C and b) $Pt_{ML}/Pd_{20}Au$(h)/C and Pt_{ML}/Pd(s)/C nanoparticles.

The oxidation of hollow samples was shifted to more positive potentials compared to those of the solid samples (Fig. 3). This indicates that the Pt–OH interaction became weaker for the hollow particles, causing an increase in their *SA*. The reduction in the coverage of the oxygen-containing species could be attributed to the smooth (Fig. 1) and void-induced contracted surface of the hollow samples. The binding energy of oxygen was decreased for the hollow samples

because the smooth surface possessed high-coordination sites that are less reactive than the low-coordination sites at the edges and defects while the hollow-induced surface contraction down-shifted the d-band center of the Pt top layer, thus making it less reactive.[8,9]

TABLE I. Particle diameter, loading, and Pt specific and mass activities for the ORR at 0.9 V in oxygen-saturated 0.1 M $HClO_4$ solutions for Pt(h)/C, Pt(s)/C, $Pt_{ML}/Pd_{20}Au$(h)/C and Pt_{ML}/Pd(s)/C nanoparticles; h = hollow, s = solid, d = particle diameter, L = loading, R_{SA} = enhancement in SA between hollow and solid nanoparticles, $cm^2_{geo.}$ = geometric area, cm^2_r = real area

Nanoparticle	D nm	L μg $cm^{-2}_{geo.}$	ESA_{Pt} cm^2_r μg^{-1}	SA mA cm^{-2}_r	R_{SA}	MA mA μg^{-1}
Pt(h)/C	6.5	5	0.64	1.71	4.275	1.1
Pt(s)/C	3.2	22	0.62	0.4		0.25
$Pt_{ML}/Pd_{20}Au$(h)/C	9	1.4 Pt 3.9 total metal	1.9	0.85	1.71	1.62
Pt_{ML}/Pd(s)/C	4	7 Pd	1.92	0.5		0.96

To examine the hollow-induced lattice contraction, X-ray diffraction measurements on hollow and solid nanoparticles were performed. As shown in Fig. 4, the diffraction peaks shifted to higher angles for the hollow samples compared to those of the solid ones, indicating that a smaller lattice spacing was induced by the hollow cores.

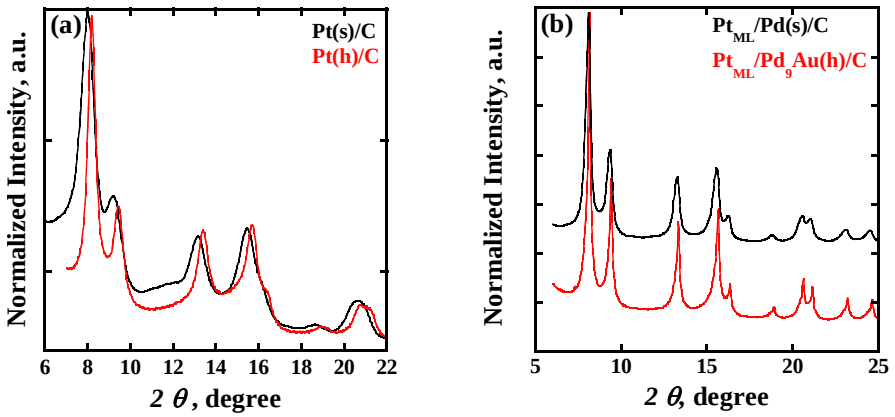

Fig. 4. X-Ray powder diffraction intensity for a) Pt(s)/C and Pt(h)/C and b) Pt_{ML}/Pd_9Au(h)/C and Pt_{ML}/Pd(s)/C nanoparticles.

As discussed above, in both systems, the enhancement in MA for hollow samples mainly stems from their increased SA. However, the improvement of SA for pure Pt samples is 2.5 times larger than for Pt–Pd samples (Table I). This could be explained taking into account the mechanical stress state of the top Pt

layer on Pt(s)/C and the Pt_{ML} on Pd(s)/C, and that *SA* enhancement, in these cases, is only due to geometric effects. While top Pt layer on Pt(s) is neither compressed nor expanded (neglecting the effect of the small particles), the Pt_{ML} on Pd(s) is compressed due to the difference in lattice constants between Pt and Pd. Therefore, the top Pt layer on Pt(h) could be compressed more than Pt_{ML} on $Pd_{20}Au$(h)/C. As a result, a larger enhancement in *SA* for the pure Pt than for the Pt–Pd samples was achieved.

The durability of the Pt_{ML}/Pd(h)/C catalyst was tested under half-cell conditions. The potential was cycled from 0.6 to 1.0 V in naturally aerated 0.1 M $HClO_4$. A comparison of the ORR polarization curves before and after 5,000 cycles is shown in Fig. 5. The small negative shift of ORR polarization curve after 5,000 cycles indicates good stability.

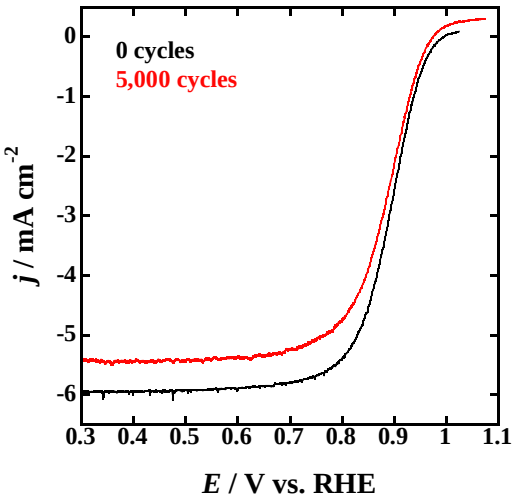

Fig. 5. ORR polarization curves in oxygen-saturated 0.1 M $HClO_4$ solutions for Pt_{ML}/Pd(h)/C before and after 5,000 cycles.

CONCLUSIONS

Pt_{ML} on Pd(s) and Pd–Au(h) cores electrocatalysts were synthesized and characterized. Their ORR activities were examined and compared with the ORR activity of Pt(s) and Pt(h) nanoparticles. Hollow nanoparticles were made using Ni or Cu as sacrificial templates. The hollow architecture of Pt and Pd–Au nanoparticles was achieved by the delicate balance between galvanic displacement and the Kirkendall Effect in controlling the reaction kinetics. Since the *ESA* per Pt mass was similar for the solid and hollow samples, the enhancement in *MA* for the hollow samples mainly resulted from increased *SA* values. The increase in *SA* could be mainly attributed to the void-induced contracted surface of the hollow samples and partially due to the smooth surface morphology of the hollow nanoparticles. The binding energy of oxygen was decreased for the hollow samples because their smooth surface posses high-coordination sites, which are less reac-

tive than the low-coordination sites at edges and defects. Additionally, the hollow-induced surface contraction downshifted the d-band center of the Pt top layer, thus making it less reactive. The Pt_{ML}/Pd(h)/C catalyst showed good durability after 5,000 potential cycles from 0.6 to 1.0 V. The hollow-induced lattice contraction provides an alternative route to fine tune the oxygen binding characteristics of surface of the catalysts toward better ORR activities.

Acknowledgments. Work at Brookhaven National Laboratory was supported by the US Department of Energy, Division of Chemical Sciences, Geosciences and Biosciences Division, under Contract No. DE-AC02-98CH10886. LW was supported by the US Department of Energy, Office of Basic Energy Science, Division of Materials Science and Engineering, under Contract No. DE-AC02-98CH10886. DB thanks the MICINN, Spain (MAT2010-20442 and MAT2011-28673-C02-01) for an FPU grant.

ИЗВОД

ЕЛЕКТРОКАТАЛИЗАТОРИ СА МОНОСЛОЈНОМ Pt ЉУСКОМ НА ШУПЉЕМ ЈЕЗГРУ Pd: СИНТЕЗА, СТРУКТУРА И АКТИВНОСТ ЗА РЕАКЦИЈУ РЕДУКЦИЈЕ КИСЕОНИКА

MIOMIR B. VUKMIROVIC[1], YU ZHANG[1], JIA X. WANG[1], DAVID BUCETA[1], LIJUN WU[2] и RADOSLAV R. ADZIC[1]

[1]*Chemistry Department, Brookhaven National Laboratory, Upton, NY 11973, USA и* [2]*Condensed Matter Physics & Materials Science Department, Brookhaven National Laboratory, Upton, NY 11973, USA*

Приказана је синтеза, карактеризација и електрокаталитичка активност за реакцију редукције кисеоника (РРК) катализатора који се састоји од монослојне Pt љуске на шупљем језгру Pd или Pd–Au. За упоређење каталитичке активности катализатора са шупљим језгром и Pt катализатора (пуна Pt и шупље Pt наночестице) за РРК, коришћена је техника ротирајућег диска. Шупље наночестице добијене су коришћењем Ni или Cu наночестица као „жртвујућих“ матрица. Нађено је да је специфична и масена активност Pt катализатора са шупљим језгром за РРК знатно већа него за пуно језгро. Увећана активност Pt приписана је глаткој површинској морфологији и контракцији решетке која је изазвана шупљом структуром језгра, што је додатни ефекат уз уштеду масе метала код честица са шупљином.

(Примљено 24. октобра 2013)

REFERENCES

1. R. R. Adzic, *Recent Advances in the Kinetics of Oxygen Reduction* in *Electrocatalysis*, J. Lipkowski, P. N. Ross, Eds., Wiley–VCH, New York, 1998, p. 197
2. M. R. Tarasevich, A. Sadkowsky, E. Yeager, *Oxygen Electrochemistry*, in *Comprehensive Treatise of Electrochemistry*, Vol. 7, B. E. Conway, J. O'M. Bockris, E. Yeager, S. U. M. Khan, R. E. White, Eds., Plenum Press, New York, 1983, p. 301
3. R. I. Masel, *Principles of Adsorption and Reaction on Solid Surfaces*, Wiley, New York, 1996, p. 702
4. J. K. Nørskov, J. Rossmeisl, A. Logadottir, L. Lindqvist, J. R. Kitchin, T. Bligaard, H. Jonsson, *J. Phys. Chem., B* **108** (2004) 17886
5. J. A. Herron, J. Jiao, K. Hahn, G. Peng, R. R. Adzic, M. Mavrikakis, *Electrocatalysis* **3** (2012) 192

6. R. R. Adzic, J. Zhang, K. Sasaki, M. B. Vukmirovic, M. Shao, J. X. Wang, A. U. Nilekar, M. Mavrikakis, J. A. Valerio, F. Uribe, *Top. Catal.* **46** (2007) 249
7. J. Zhang, Y. Mo, M. B. Vukmirovic, R. Klie, K. Sasaki, R. R. Adzic, *J. Phys. Chem., B* **108** (2004) 10955
8. B. Hammer, J. K. Nørskov, *Adv. Catal.* **45** (2000) 71
9. J. Greeley, J. K. Nørskov, M. Mavrikakis, *Annu. Rev. Phys. Chem.* **53** (2002) 319
10. J. Zhang, M. B. Vukmirovic, Y. Xu, M. Mavrikakis, R. R. Adzic, *Angew. Chem. Int. Ed.* **44** (2005) 2132
11. F. H. B. Lima, J. Zhang, M. H. Shao, K. Sasaki, M. B. Vukmirovic, E. A. Ticianelli, R. R. Adzic, *J. Phys. Chem., C* **111** (2007) 404
12. F. H. B. Lima, J. Zhang, M. H. Shao, K. Sasaki, M. B. Vukmirovic, E. A. Ticianelli, R. R. Adzic, *J. Solid State Electrochem.* **12** (2008) 399
13. K. Sasaki, H. Naohara, Y. Cai, Y. M. Choi, P. Liu, M. B. Vukmirovic, J. X. Wang, R. R. Adzic, *Angew. Chem. Int. Ed.* **49** (2010) 8602
14. S. R. Brankovic, J. X. Wang, R. R. Adzic, *Surf. Sci.* **474** (2001) L173
15. M. B. Vukmirovic, S. T. Bliznakov, K. Sasaki, J. X. Wang, R. R. Adzic, *Electrochem. Soc. Interface* **Summer** (2011) 33
16. K. Sasaki, J. X. Wang, H. Naohara, N. Marinkovic, K. More, H. Inada, R. R. Adzic, *Electrochim. Acta* **55** (2010) 2645
17. T. J. Schmidt, H. A. Gasteiger, G. D. Stab, P. M. Urban, D. M. Kolb, R. J. Behm, *J. Electrochem. Soc.* **145** (1998) 2354
18. J. X. Wang, C. Ma, Y. M. Choi, D. Su, Y. Zhu, P. Liu, R. Si, M. B. Vukmirovic, Y. Zhang, R. R. Adzic, *J. Am. Chem. Soc.* **133** (2011)13551
19. Y. Zhang, C. Ma, Y. Zhu, R. Si, Y. Cai, J. X. Wang, R. R. Adzic, *Catal. Today* **202** (2013) 50
20. A. J. Bard, R. Parsons, J. Jordan, *Standard Potentials in Aqueous Solution*, M. Dekker, New York, 1985.

Journal of the Serbian Chemical Society
JSCS-info@shd.org.rs • www.shd.org.rs/JSCS

J. Serb. Chem. Soc. 78 (12) 1993–2005 (2013)
JSCS–4546

UDC 546.96+546.93+544.478+
621.352:539.196:541.574
Original scientific paper

XPS and STEM study of the interface formation between ultra-thin Ru and Ir OER catalyst layers and Perylene Red support whiskers•

LJILJANA L. ATANASOSKA[1]*, DAVID A. CULLEN[2] and RADOSLAV T. ATANASOSKI[1]*

[1]3M Co., 3M Center, St. Paul, MN, 55144-1000 USA and [2]Materials Science and Technology Division, Oak Ridge National Laboratory, Oak Ridge TN 37831 USA

(Received 27 September 2013)

Abstract: The interface formation between nano-structured Perylene Red (PR) whiskers and the oxygen evolution reaction (OER) catalysts ruthenium and iridium was studied systematically by XPS and STEM. The OER catalyst over-layers with thicknesses ranging from ≈0.1 to ≈50 nm were vapor deposited onto PR *ex situ*. STEM images demonstrated that, with increasing thickness, Ru and Ir transform from amorphous clusters to crystalline nanoparticles, which agglomerate with increased over-layer thickness. XPS data showed a strong interaction between Ru and PR. Ir also interacts with PR although not to the extent seen for Ru. At low coverages, the entire Ru deposit was in the reacted state while a small portion of the deposited Ir remained metallic. Ru and Ir bonding occur at the PR carbonyl sites as evidenced by the attenuation of carbonyl photoemission and the emergence of new peak assigned to C–O single bonds. Curve fitting analysis and the derived stoichiometry indicated the formation of metallo–organic bonds. The co-existence of oxide bonds was also apparent.

Keywords: fuel cell; catalyst; surface properties; deposition.

INTRODUCTION

Highly active oxygen evolution reaction (OER) catalysts based on deposited Ru and Ir onto Pt-coated nano-structured Perylene Red whiskers (3M Pt–NSTF) are currently being investigated for polymer electrolyte membrane fuel cell (PEMFC) applications. A key issue for the successful transition of PEMFC technology from the development to the pre-commercial phase is failure of the catal-

* Corresponding author. E-mail: rtatanasoski@mmm.com

• To Prof. Branislav Nikolić, our long time friend and colleague, for his many contributions in the area of fundamental and applied electrochemistry.

doi: 10.2298/JSC130927111A

yst and the other thermodynamically unstable membrane electrode assembly (MEA) components during the so-called transient conditions, start-up/shutdown (SU/SD) and cell reversal (CR). If left unchecked, during these periods, the electrodes can attain potentials of up to 2 V,[1–3] leading to rapid carbon corrosion and Pt dissolution. To improve the durability of the fuel cell catalyst and support, minute loadings of Ru/Ir OER catalysts (2 and 10 μg cm^{-2}) were incorporated into the electrode to favor water electrolysis over carbon corrosion. This has resulted in vastly improved fuel cell robustness and durability during transient conditions due to a reduction in the peak cell voltages.[1,2]

During the course of a study of OER catalysts sputter-coated on Pt–NSTF, it was discovered that the Ru/Ir catalyst had unusually high activity and stability when grown on Pt–NSTF.[4,5] Furthermore, a distinct difference in the C 1s–Ru 3d line shape between 2 and 10 μg cm^{-2} OER catalyst loadings was observed, despite the fact that the OER catalysts were sputter-coated over a relatively thick Pt film. The reacted Ru $3d_{5/2}$ shoulder, shifted to a higher binding energy (BE) with respect to the BE location of the un-reacted Ru $3d_{5/2}$ peak, which was more pronounced for the 2 μg cm^{-2} loading than for the 10 μg cm^{-2} loading. Curve fitting analysis and the obtained O, C and Ru stoichiometry balance suggested a chemical interaction of Ru with the underlying Perylene Red support and the formation of organo–metallic type bonds, such as $Ru(OC)_x$ or $Ru(CO)_x$. The STEM images confirmed the existence of discontinuities in the Pt coating, indicating of the availability of exposed bare Perylene Red sites for interaction with Ru.

In order to confirm that the existence and the anchoring action of Ru–O–C bonds at the interface with Perylene Red (PR) was potentially the cause of the Ru-containing OER catalyst stability, a systematic study of the interfaces between Ru, Ir and PR was conducted. The Ru and Ir over-layers with thicknesses ranging from 0.2 to 48 nm and 0.1 to 34.8 nm, respectively, were formed onto PR whiskers *ex situ* by physical vapor deposition. Scanning transmission electron microscopy (STEM) was used to study the growth of Ru and Ir on the Perylene Red support. The XPS core level spectra and curve fitting analysis revealed a strong interaction between Ru and PR. Ir was also found to interact with PR although not to the extent seen for Ru. At low coverages, the entire Ru deposit was in the reacted state, while a small portion (≈10 at. %) of the deposited Ir remains metallic. Ru and Ir bonding occurred at the PR carbonyl sites, as evidenced by the preferential attenuation of carbonyl carbon photoemission and the emergence of new carbon peak assigned to C–O single bonds. Curve fitting analysis and the derived stoichiometry indicated the formation of $Ru(OC)_x$ or $Ru(CO)_x$ metallo–organic bonds. The co-existence of oxide bonds was also apparent.

EXPERIMENTAL

Materials and sample preparation

Ru and Ir over-layers were deposited on a Perylene Red whiskers (3M NSTF) substrate by a DC-magnetron sputtering process. A Mills-Lane vacuum deposition system was equipped with 4 CTI cryo-pumps, a Pfeiffer 450 turbo-pump and specially designed sputtering target assemblies from the Sierra Applied Science Company. High purity Ru and Ir (99.99+ %) from Sophisticated Alloys (Butler, PA) were used for the sputtering targets. Ultra high purity Ar was used as the sputtering gas with magnetron power range from 30–300 Watts. A pre-sputter of each target was performed to clean the surface. Before deposition, the PVD chamber was evacuated to a base pressure of 7×10^{-7} Torr.

XPS Surface analysis

Chemical states and elemental compositions of the OER catalyst over-layers on Perylene Red NSTF were analyzed by X-ray photoelectron spectroscopy, using a Kratos Axis Ultra™ XPS system at a base pressure below 10^{-9} Torr. The monochromatic AlKα (1486.6 eV) X-ray source was operated at 140 W (14 kV, 10 mA). A hemispherical electron energy analyzer was operated at constant pass energy of 160 eV for survey and 20 eV for the high-resolution spectra. The binding energy (BE) scale was calibrated relative to the BE of the C 1s peak. The spectra were acquired at a 90° take-off angle with respect to the sample surface. The data processing was realized with PHI MultiPak V8.2B, 2006 and Casa XPS V 2.3.16 Dev41 software. The curve fitting analysis of the core level spectra was based on summed Gaussian/Lorentzian GL functions, with a PHI line-shape to represent the asymmetric nature of the peaks and Shirley-type background subtraction. The Ru $3d_{5/2}$–Ru $3d_{3/2}$ spin orbital doublet branching ratio was constrained to 3:2 and their binding energy separation to 4.17 eV. The branching ratio and BE splitting of the Ir $4f_{7/2}$–Ir $4f_{5/2}$ spin orbital doublet were constrained for the fitting at their theoretical values 4:3 and 2.98 eV, respectively. The FWHM of resolved peaks was not constrained but was kept consistent with the allowed variations of ≈15 %.

STEM Characterization

As-received OER catalyst-coated whiskers were prepared for STEM analysis by sonicating the material in methanol, then placing a small amount of the solution onto lacy carbon films supported on standard Cu-mesh TEM grids. A JEOL 2200FS probe-corrected STEM was used for complementary high-angle annular dark-field (HAADF).

RESULTS AND DISCUSSION

XPS and STEM characterization of the evolving ruthenium–Perylene Red interface

The C 1s core level spectra of the bare PR substrate (0 nm Ru thickness) and the C 1s–Ru 3d core level photoemission for Ru deposits from 0.2 to 48 nm are plotted together in Fig. 1. The bare PR C 1s core level spectra consisted of two distinct peaks, the main, more intense peak at ≈285 eV from the PR aliphatic and aromatic carbons and the less intense peak at ≈288 eV from the PR carbonyl carbon. The intensity ratio of the two PR carbon peaks is in agreement with the chemical structure.[6] The C 1s–Ru 3d core level spectra for Ru deposits are more complex because the PR aliphatic and aromatic carbon peak overlap with the Ru $3d_{3/2}$ photoemission. However, in spite of the complexity of the C 1s–Ru 3d line-

shape, its change with increasing Ru coverage clearly demonstrated that chemical interaction occurred at the Ru–PR interface. At the ultra low Ru coverages of 0.2 and 0.4 nm, a notable broadening of the Ru $3d_{5/2}$ peak and a visible BE shift of ≈2 eV, with respect to the metallic Ru $3d_{5/2}$ BE observed for the higher coverages of 12 and 48 nm, suggested the formation of multiple Ru oxidation states.[7] Moreover, the preferential attenuation of the PR carbonyl carbon peak and the emergence of a new carbon peak at 287 eV, associated with ether like C–O single bonds, indicated that the Ru chemical attack occurred preferentially at the PR carbonyl group sites.

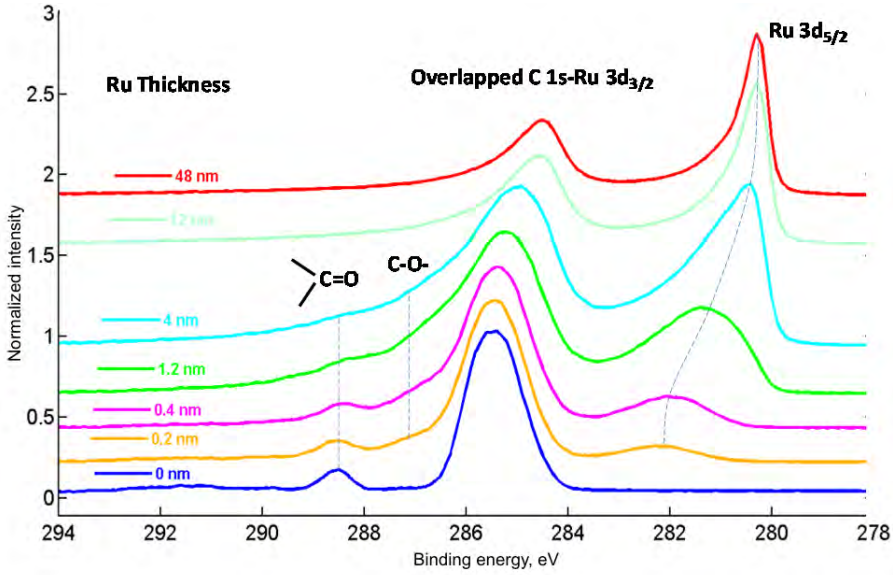

Fig. 1. C 1s core level spectra for bare PR substrate and C 1s–Ru 3d core level photoemission for Ru deposits from 0.2 to 48 nm in thickness.

The O 1s core level spectra of the evolving Ru–PR interface, shown in Fig. 2, further confirm the interaction at the interface. The Ru deposition on PR resulted in a striking increase in the intensity of the oxygen peak associated with ether like O–C bonds. In addition, with further ruthenium deposition, the appearance of an oxide oxygen peak was obvious.

Curve fitting analysis was realized in order to resolve the multiple Ru oxidation states and to quantify the chemical changes occurring at the growing interface. As seen in Fig. 3, from the curve fitting analysis example of C 1s–Ru 3d core level spectra for 1.2 nm Ru coverage, three different ruthenium chemical states were resolved. The resolved Ru $3d_{5/2}$ peaks I–III at a BE of ≈280.5, ≈281.5 and ≈282.5 eV came from un-reacted/metallic Ru^0, reacted Ru^{x+} and reacted Ru^{y+} states, respectively.

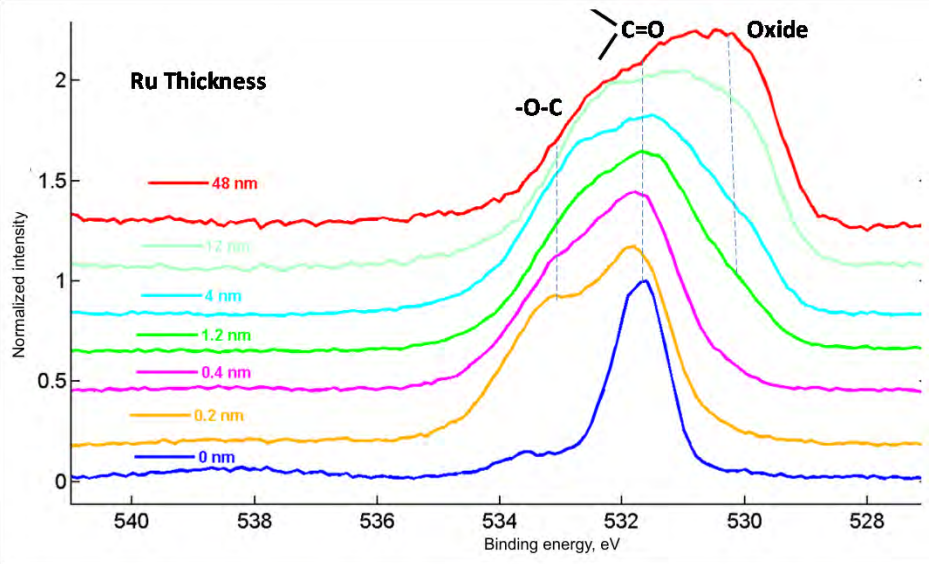

Fig. 2. O 1s core level spectra for bare PR substrate and O 1s core level photoemission for Ru deposits from 0.2 to 48 nm in thickness.

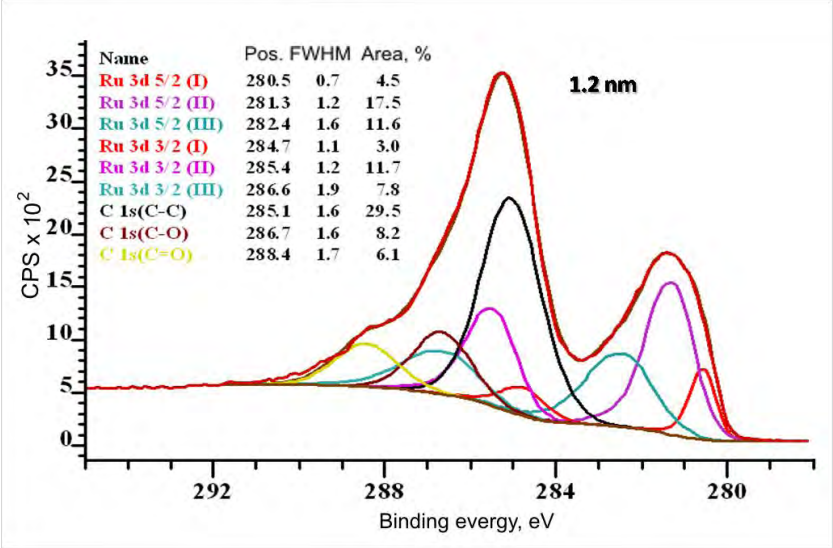

Fig. 3. Curve fitting analysis of the C 1s–Ru 3d core level spectra for 1.2 nm Ru coverage.

The results of C 1s–Ru 3d curve fitting analysis are plotted in Fig. 4 as a function of Ru deposit thickness. No un-reacted metallic Ru was present at the interface for ultra low Ru coverage, up to 1 nm. As expected, the increase in the contribution of metallic Ru resulted in an attenuation of the PR C–C photo-

emission. The attenuation behavior of the resolved Ru^{x+} and Ru^{y+} species suggested that organo–metallic Ru–O–C bonds contributed to their photoemission for Ru coverages up to 2–4 nm. Final state screening effects may also be involved in the photoemission of the resolved Ru^{y+} species.[7] As seen from Fig. 4, there was an initial sharp increase in the contribution of both resolved Ru reacted states. Then, Ru^{y+} species became attenuated by metallic Ru over-layers, while Ru^{x+} remained flat due to its conversion into RuO_x forms.

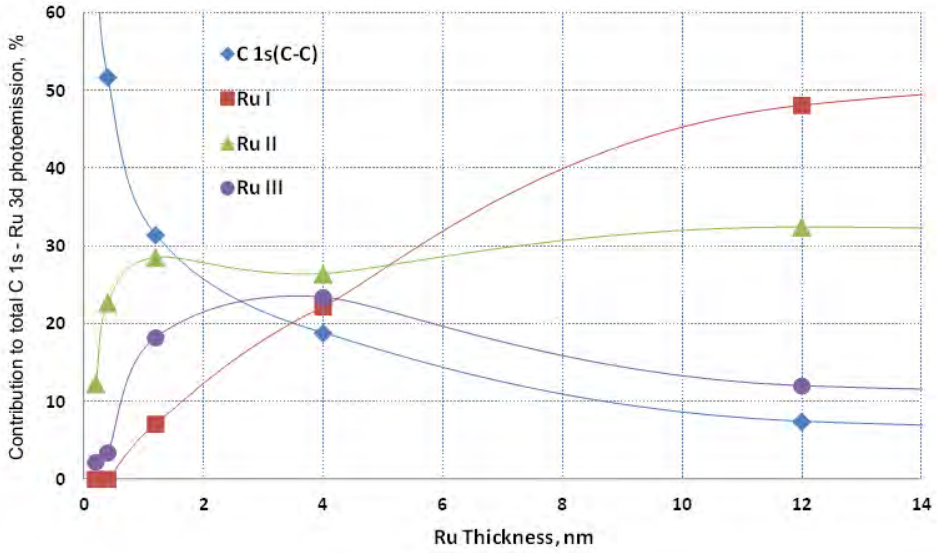

Fig. 4. Contribution of metallic and reacted Ru as a function of Ru thickness: Ru-I is unreacted/metallic Ru^0, Ru-II is reacted Ru^{x+} and Ru-III is reacted Ru^{y+}.

The curve fitting analysis of both C 1s–Ru 3d and O 1s core level spectra along with the stoichiometry balance confirmed the chemical interaction of Ru with PR and formation of $Ru(OC)_x$ or $Ru(CO)_x$ metallo–organic bonds. The co-existence of oxide bonds was also apparent. The formation of Ru complexes with PR may result in multiple resonance hybrid states, such as those shown in Fig. 5. The metal–carbonyl group interaction is likely to occur and it was previously observed for molecules that have comparable structures to that of PR.[8,9]

High-angle annular dark-field (HAADF) STEM images of whiskers with Ru layer thicknesses of 0.2, 0.4, 1.2 and 4 nm are shown in Fig. 6. At the lowest loading, Ru was present in atomic clusters. As the loading increased, the Ru formed into crystalline nanoparticles, which further developed into an interconnected network. Even at 4.0 nm thickness, regions of bare PR were observed and mobile Ru atoms were visible in these exposed regions.

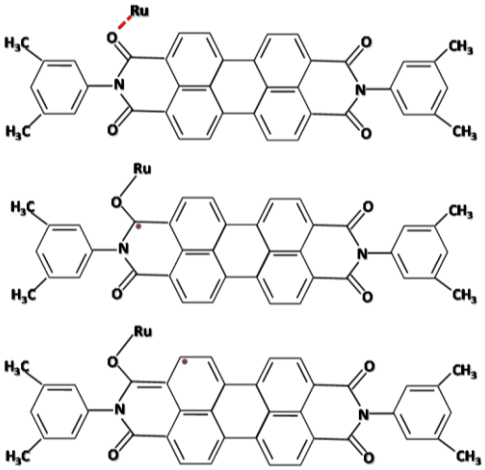

Fig. 5. Perylene Red–ruthenium interaction: Ru–O–C complex formation and possible resonance hybrid structures.

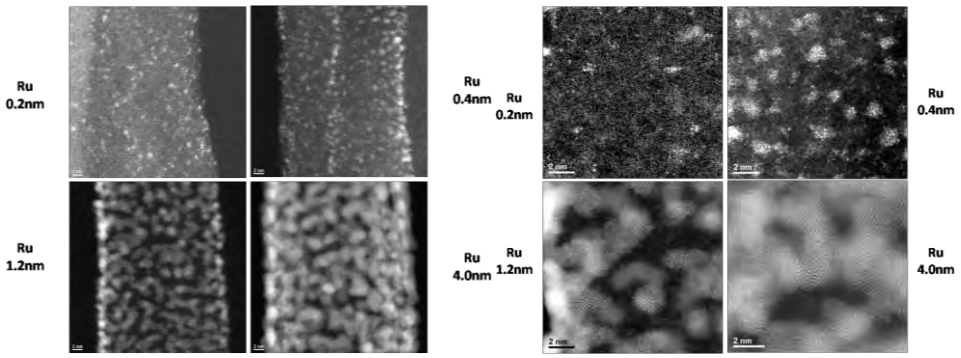

(a) (b)

Fig. 6. High-angle annular dark-field (HAADF) images of whiskers with Ru layers of thicknesses 0.2, 0.4, 1.2 and 4 nm taken at a) 4 M× and b) 10M× magnification.

XPS and STEM characterization of an evolving iridium–Perylene Red interface

The Ir 4f, C 1s and O 1s core level spectra in Figs. 7–9 demonstrate that interaction also occurred at the Ir–PR interface. At low Ir coverages, the Ir 4f peaks exhibit a line-shape broadening and a BE shift of ≈2 eV with respect to the BE location of metallic Ir. A preferential attenuation of the carbonyl carbon peak and the emergence of the ether carbon peak are also apparent from the C 1s core level spectra. The sharp increase in the oxygen peak associated with the ether oxygen bonds could also be seen from the O 1s core level spectra, although it was not so striking as in the case of Ru, which indicates a weaker interaction at the Ir–PR interface. The appearance of the oxide oxygen peak at higher Ir coverages also occurred at the Ir–PR interface.

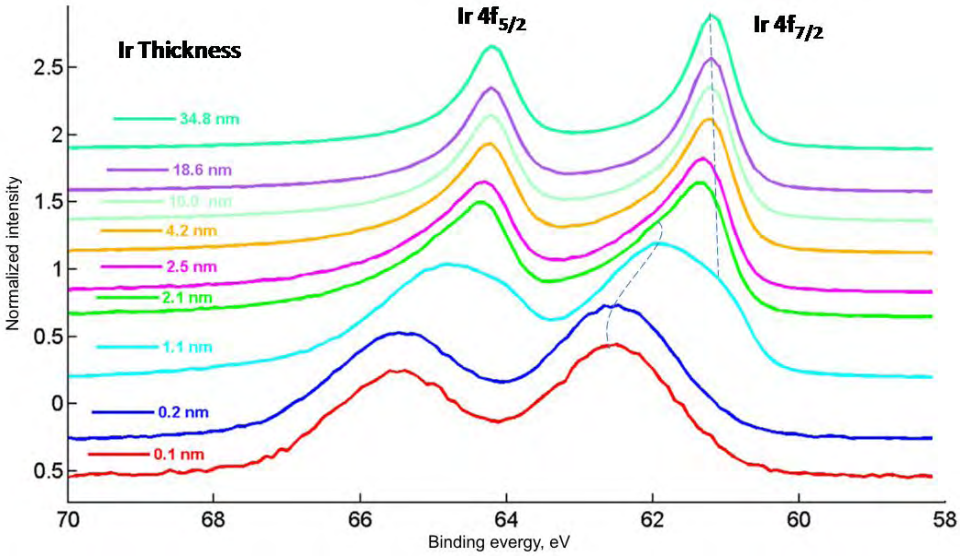

Fig. 7. Ir 4f core level photoemission for Ir deposits from 0.1 to 34.8 nm in thickness.

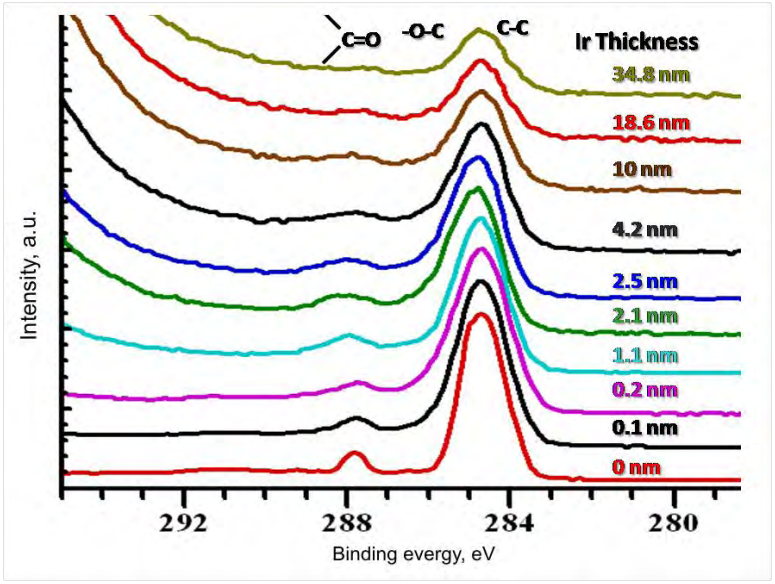

Fig. 8. C 1s core level photoemission for Ir deposits from 0.1 to 34.8 nm in thickness.

The curve fitting analysis of Ir 4f core level spectra resolved three different Ir chemical states. The Ir $4f_{7/2}$ peaks at BE of ≈ 61, ≈62 and 63 eV correspond to un-reacted/metallic Ir, reacted Ir^{x+} and reacted Ir^{y+} states, respectively.[8] The examples of curve fitting analysis of Ir 4f core level spectra realized for Ir thicknesses of 1.1 and 2.1 nm are presented in Fig. 10.

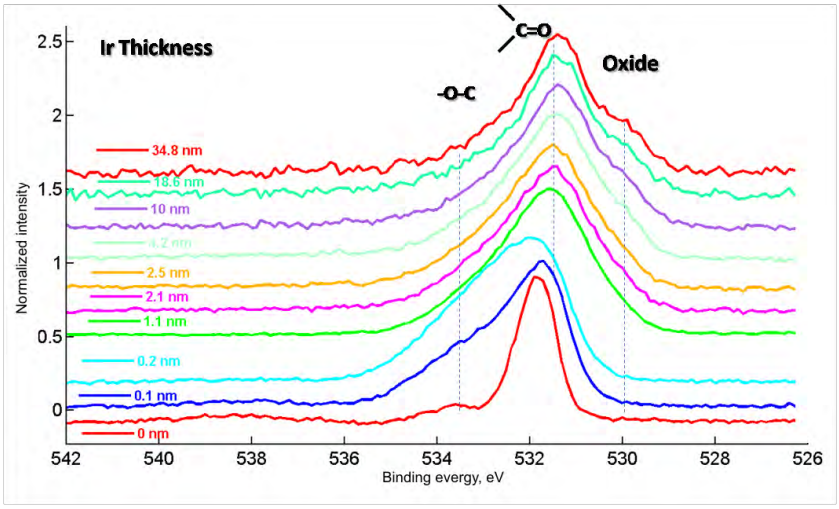

Fig. 9. O 1s core level photoemission for Ir deposits from 0.1 to 34.8 nm in thickness.

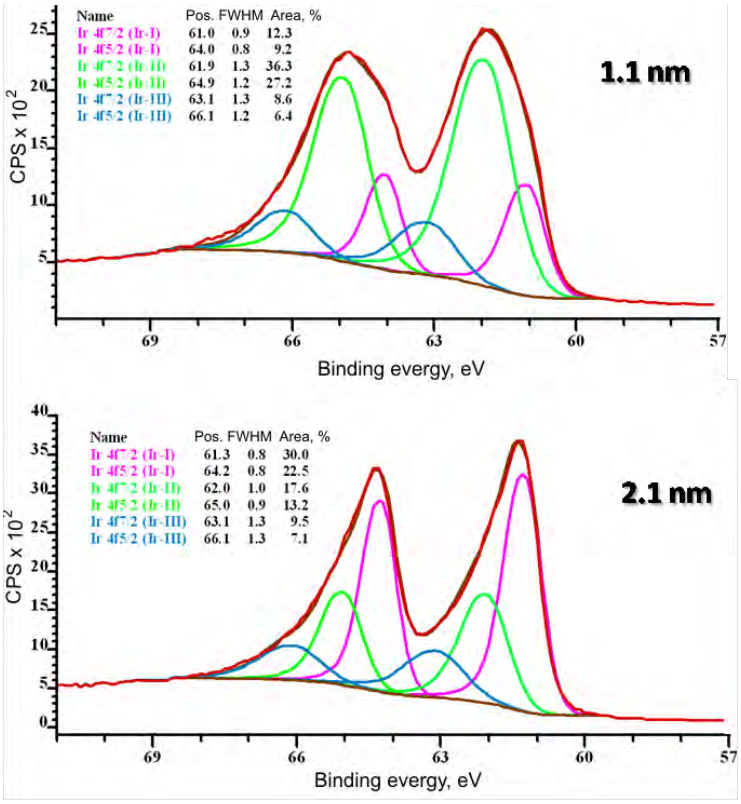

Fig. 10. Examples of Ir 4f core level curve fitting analysis realized for 1.1 and 2.2 nm thick Ir deposits on a PR substrate.

The results of Ir 4f curve fitting analysis are plotted in Fig. 11 as a function of the thickness of the Ir deposit. Fig. 11 shows that un-reacted metallic Ir was present at the interface for the lowest Ir coverages of 0.1 and 0.2 nm, which further confirmed the weaker interactions at the Ir/PR interface compared to those at the Ru–PR interface. The attenuation behavior of the resolved Ir^{x+} and Ir^{y+} species suggested that organo–metallic Ir–O–C bonds (Ir^{y+}) were formed only at the lowest Ir coverage of 0.1 nm and that they were immediately substantially attenuated by the growing contribution of Ir oxide bonds (Ir^{x+}). As in the case of Ru, final state screening effects may also participate in the photoemission of the resolved Ir^{y+} species.[10] The attenuation of IrO_x (Ir^{x+}) by the growing metallic Ir occurred sharply at ≈1 nm.

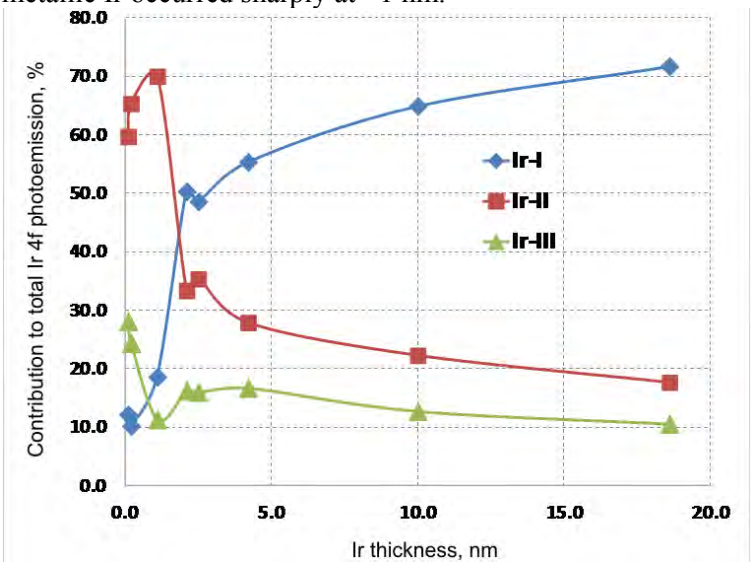

Fig. 11. Contribution of metallic and reacted Ir as a function of Ir thickness: Ir-I is un-reacted/metallic Ir^0, Ir-II is reacted Ir^{x+} and Ir-III is reacted Ir^{y+}.

As in the case of the Ru–PR interface, the formation of organo–metallic iridium bonds along with the Ir oxide was confirmed by the curve fitting analysis of both Ir 4f and O 1s core level spectra along with the stoichiometry balance.

The contribution of resolved un-reacted and reacted species for both interfaces are plotted together in Fig. 12 to illustrate how much stronger the interaction of Ru with PR is relative to that of Ir with PR.

HAADF-STEM images of PR whiskers with Ru and Ir layer thicknesses of approximately 1.2 and 0.2 nm are compared in Fig. 13. The Ir layer appears to deposit in the same manner observed previously for Ru, with the initial formation of small clusters at the lowest loading followed by the formation of crystalline nanoparticles with increased deposition.

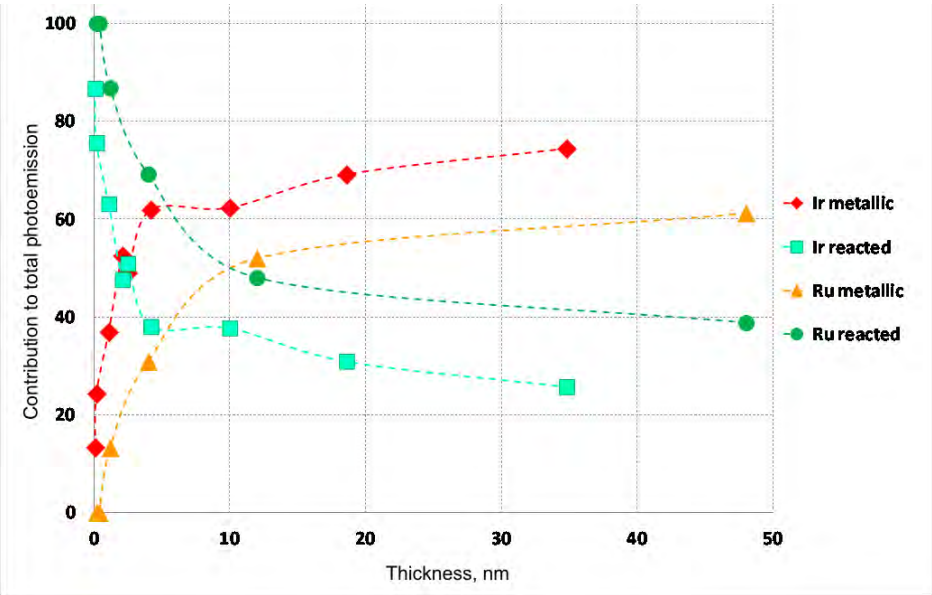

Fig. 12. Comparison of the evolving interface behavior of Ir and Ru with PR: Contribution of metallic and reacted states as a function of deposit thickness.

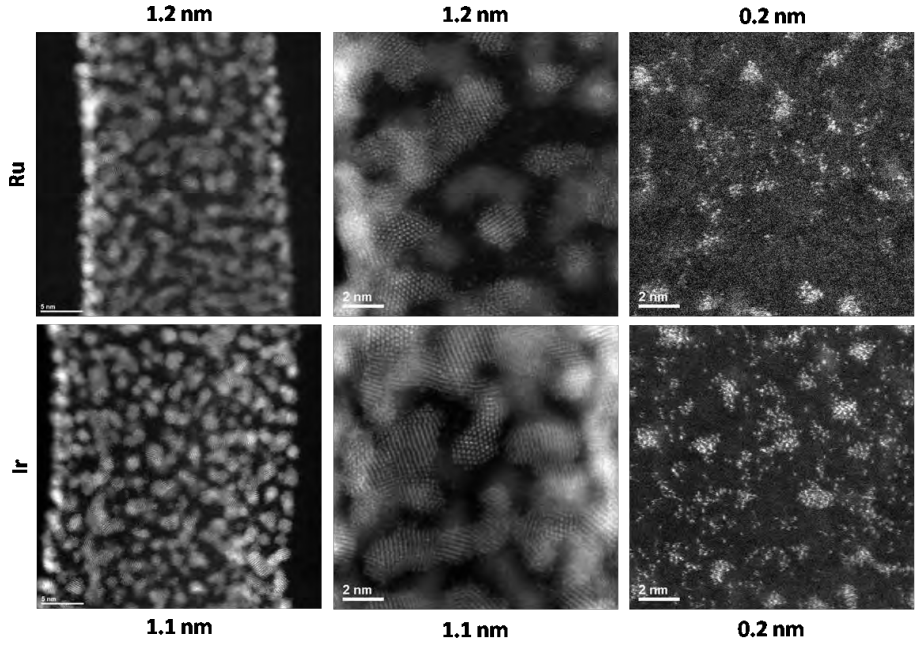

Fig. 13. Comparison of Ru–PR and Ir–PR interface nano-morphology for two different Ru and Ir thicknesses.

CONCLUSIONS

A systematic study of evolving Ru–PR and Ir–PR interfaces was conducted. A strong interaction of ruthenium with Perylene Red whiskers was found to the extent that no metallic ruthenium was present at low Ru coverage. Curve fitting analysis and the stoichiometry balance confirmed the presence of metallo––organic bonds, such as $Ru(OC)_x$ and $Ru(CO)_x$. A co-existence of oxide bonds was also apparent. Interaction of iridium with Perylene Red whiskers was also found, although not to the extent seen for ruthenium, as evidenced by the presence of metallic iridium at low iridium coverage. STEM imaging revealed a similar growth behavior for both iridium and ruthenium, starting from small clusters at low loadings to an interconnected network of crystalline nanoparticles at higher loadings.

The existence of Ru–O–C bonds could indicate to the root cause of the improved Ru OER catalyst stability on Pt–NSTF: the strong bonding of Ru to Perylene Red could increase the surface area of the deposited OER nanoparticles by preventing coalescence and reduce the rate of dissolution in an electrochemical environment. Thus, these findings revealed a fundamental relationship that provides a basis for understanding the electrochemical behavior of these materials.

Acknowledgements. This work was supported by the DOE Fuel Cell Technology Office, Award No. DE-EE0000456 and the Oak Ridge National Laboratory's Shared Research Equipment (ShaRE) User Program, sponsored by the Office of Basic Energy Sciences, U.S. DOE.

И З В О Д

XPS И STEM ПРОУЧАВАЊЕ ФОРМИРАЊА МЕЂУСЛОЈА ИЗМЕЂУ УЛТРА-ТАНКОГ Ru И Ir КАТАЛИТИЧКОГ СЛОЈА ЗА РЕАКЦИЈУ ИЗДВАЈАЊА КИСЕОНИКА И ПОДЛОГЕ ОД ВИСКЕРА ПЕРИЛЕН-ЦРВЕНОГ

LJILJANA L. ATANASOSKA[1], DAVID A. CULLEN[2] и RADOSLAV T. ATANASOSKI[1]

[1]3M Co., 3M Center, St. Paul, MN, 55144-1000 USA и [2]Materials Science and Technology Division, Oak Ridge National Laboratory, Oak Ridge TN 37831 USA

(Received 27 September 2013)

Проучавано је формирање међуслоја између нано-структурних вискера перилен--црвеног (PR) и рутенијум и иридијум катализатора за реакцију издвајања кисеоника (OER) коришћењем XPS и STEM техника. Површински слојеви катализатора за OER дебљине ≈0,1 до ≈50 nm су *ex situ* депоновани из гасовите фазе на PR. STEM фотографије су показале да се, са повећањем дебљине, Ru и Ir трансформишу од аморфних кластера у кристалиничне нано-честице, са агломератима који превазилазе дебљине површинског слоја. XPS подаци показују јаку интеракцију између Ru и PR. Ir такође реагује са PR, мада не у степену регистрованом за Ru. При ниским степенима покривености целокупни Ru је прореаговао, док је мала количина Ir остала у металном облику. Ru и Ir се везују на PR карбонилним местима, што показује смањење фотоемисије са карбонилних места и преклапање нових пикова који се приписују једнострукој вези C–O. Анализа

фитоване криве и изведена стехиометрија указују на формирање метало–органских веза. Очигледно је и паралелно постојање оксидних веза.

(Примљено 27. септембра 2013)

REFERENCES

1. R. T. Atanasoski, L. L. Atanasoska, D. A. Cullen, G. M. Haugen, K. L. More, G. D. Vernstrom, *Electrocatalysis* **3** (2012) 284
2. M. Shao, *Electrocatalysis in Fuel Cells: A Non and Low Platinum Approach,* Springer, New York, 2013, p. 637
3. R. T. Atanasoski, D. A. Cullen, G. D. Vernstrom, G. M. Haugen, L. L. Atanasoska, *ECS Electrochem. Lett.* **2** (2013) F25
4. 2010 DOE Hydrogen Program Review, http://www.hydrogen.energy.gov/pdfs/ review10/ /fc006_atanasoski_2010_o_web.pdf (accessed in September 2013)
5. D. A. Cullen, K. L. More, K. S. Reeves, G. D. Vernstrom, L. L. Atanasoska, G. M. Haugen, R. T. Atanasoski, *ECS Trans.* **41** (2011) 1099
6. L. L. Atanasoska, D. A. Cullen, A. Hester, R. T. Atanasoski, *ECS Trans.* **50** (2013) 19
7. L. Atanasoska, W. O'Grady, R. Atanasoski, F. Pollak, *Surface Sci.* **202** (1988) 192
8. L. Atanasoska, S. Anderson, H. M. Meyer III, Z. Lin, J. H. Weaver, *J. Vac. Sci. Technol., A* **5** (1987) 3325
9. L. Atanasoska, H. M. Meyer III, S. Anderson, J. H. Weaver, *J. Vac. Sci. Technol*., *A* **6** (1988) 2175
10. L. Atanasoska, R. Atanasoski, S. Trasatti, *Vacuum* **40** (1990) 91.

Journal of the Serbian Chemical Society
JSCS-info@shd.org.rs • www.shd.org.rs/JSCS
J. Serb. Chem. Soc. *78* (12) 2007–2015 (2013)
JSCS–4547
UDC 544.351–145.82+66.097.3–034+
546.212–124+546.74–36:66.097
Original scientific paper

Electrocatalysis of the HER in acid and alkaline media

NEMANJA DANILOVIC, RAM SUBBARAMAN, DUSAN STRMCNIK, VOJISLAV R. STAMENKOVIC and NENAD M. MARKOVIC*

Materials Science Division, Argonne National Laboratory, Argonne, Illinois 60439, USA

(Received 18 November 2013)

Abstract: Trends in the HER were studied on selected metals (M = Cu, Ag, Au, Pt, Ru, Ir and Ti) in acid and alkaline environments. It was found that with the exception of Pt, Ir and Au, due to high coverage by spectator species on non-noble metal catalysts, the experimentally established positions of Cu, Ag, Ru and Ti in the observed volcano relations are still uncertain. It was also found that while the M–H_{upd} binding energy most likely controls the activity trends in acidic solutions, the trends in activity in alkaline solutions are controlled by a delicate balance between two descriptors: the M–H_{ad} interaction and the energetics required to dissociate water molecules. The importance of the second descriptor was confirmed by introducing bifunctional catalysts such as M modified by Ni(OH); *e.g.*, while the latter serves to enhance the catalytic decomposition of water, the metal sites are required for collecting and recombining the produced hydrogen intermediates.

Keywords: volcano plot; HER; hydrogen evolution reaction; acid; alkaline.

INTRODUCTION

Electrocatalysis lies at the heart of a spectrum of chemical transformations that occur at electrochemical interfaces. In the near future, it will be the key driving force for technological innovations that are urgently needed to address the delivery of reliable, affordable, and environmentally friendly energy. There is no rigorous definition of the term “electrocatalysis”, but in the broadest sense, it is the study of electrode reactions where the kinetics have a strong dependence on the nature of the electrode material.[1] Not surprisingly, virtually every electrochemical reaction in which chemical bonds are made or formed is electrocatalytic, and the kinetics varies by many orders of magnitude for different electrode materials. This is true even for the simplest electrochemical reaction in which chemical bonds are broken,[2] such as the hydrogen evolution reaction (HER), which, for decades, has served as a model reaction for probing how the

* Corresponding author. E-mail: nmmarkovic@anl.gov
doi: 10.2298/JSC131118136D

nature of the electrode material (and/or structure of the double layer[3–6]) may affect electrochemical transformation of protons (acid electrolytes) or water (basic electrolytes) into molecular hydrogen ($2H^+$ $[2H_2O]$ + $2e^-$ ⇆ H_2 + $[2OH^-]$).[7–9] Traditionally, the mechanism of the HER is assumed to proceed by an initial formation of hydrogen intermediates (denoted hereafter as H_{ad}) which, depending on the pH of solution, are formed *via* charge-induced discharge of protons or water (H^+ $[H_2O]$ + e^- ⇆ H_{ad} $[+ OH^-]$). This, so-called Volmer step, is then followed either by either a Tafel chemical recombination step ($2H_{ad}$ ⇆ H_2) or by the transfer of a second electron in a Heyrovsky step (H^+ $[H_2O]$ + H_{ad} + e^- ⇆ H_2 + + $[+ OH^-]$).[8]

Analytical, experimental, and computation analyses of this reaction have, for the most part, been closely tied to the concept of the volcano plot. In electrocatalysis, such plots, which generally express the rate of an electrocatalytic reaction as a function of more fundamental properties of the catalyst, known as descriptors, date to the early HER rate expressions derived by Parsons[10] and Gerischer.[11] Parsons and Gerischer used of the hydrogen adsorption free energy (determined by the strength of adsorption of H_{ad} on the catalyst surface) as a descriptor for the trends in HER rates on different catalysts. This early analytical volcano was followed by experimentally derived volcanoes, developed by Trasatti[9] and extending the earlier work of Krishtalik,[12] in which the measured rates were correlated with measurements of the surface work function and the bulk heats of hydride formation. More recently, a combination of fundamental surface rate modeling, similar to the techniques employed by Parsons, with atom-specific free energy data obtained from Density Functional Theory calculations, have permitted the development of HER volcanoes in terms of descriptors (metal–hydrogen bonding) that may be rapidly calculated on both metals and metal alloys.[13–19] It should be noted that some authors, however, have identified some challenges in generating such volcano plots from experimental results, particularly when dealing with metals that are likely to form oxides or hydrides under HER conditions.[15] Given that the intrinsic activity of metal catalysts in alkaline medium are ≈2–3 orders of magnitude lower than in acid solutions, the question arises as to what type of relationships between activity in the HER and the nature of electrode material might be expect at high pH values. This has been addressed recently in several published papers[3,20,21] and will be summarized in the remaining part of this paper.

EXPERIMENTAL

The Pt, Ru, Ir, Au, Ag and Cu electrodes were prepared by radio frequency (RF) annealing at ≈800–1100 °C in a 3 % H_2–Ar gas mixture, while the Ti electrode was polished and chemically cleaned. The samples were transferred into an electrochemical cell (made from Teflon) with the surface protected with a drop of DI water and immersed under potential control at 0.05 V *vs*. the reversible hydrogen electrode (RHE) in 0.1 M KOH and 0.1 M

$HClO_4$. $Ni(OH)_2$-modified metal electrodes (*ca*. 30–40 % coverage) were prepared by chemical deposition, wherein, the pristine metal electrodes were immersed and equilibrated in 0.01–0.1 M $NiCl_2$ solutions for 2–12 h. For assessing the HER activity, a sweep rate of 50 mV s^{-1} was employed, while the rotation rate was 1600 rpm. Only the first negative going HER scan was used for activity determination, where the current densities were obtained based on the geometric surface area. Experiments were controlled using an Autolab PGSTAT 302N potentiostat with IR compensation. The used gases were of research grade (5N) Ar.

RESULTS AND DISCUSSIONS

HER activities in acid electrolytes

As in the past, Fig. 1 shows that if activities for the HER of the coinage metals (IB metals: Au, Cu, Ag), the platinum group (or PGM: Pt, Ir, Ru) metals and the valve metal (Ti) in 0.1M $HClO_4$, are plotted as a function of the $M–H_{ad}$ binding energy (the $M–H_{ad}$ binding energy values were taken from the literature[9]), a volcano relationship is established with Ir and Pt at the apex of the volcano curve. Further analysis of Fig. 1 reveals that the IB group elements are positioned on the ascending slope of the volcano with order in activity increasing from Au < Cu < Ag, which is different from the order predicted by DFT (Cu > > Au > Ag). The exact cause of this discrepancy is currently unknown, but considering that Cu is "less noble" than Au and Ag, it is reasonable to assume that the experimentally measured activity of Cu could be influenced by adsorbed spectator species, which may affect the availability of active sites required for adsorption of the hydrogen active intermediates. Fig. 1 also shows that the ele-

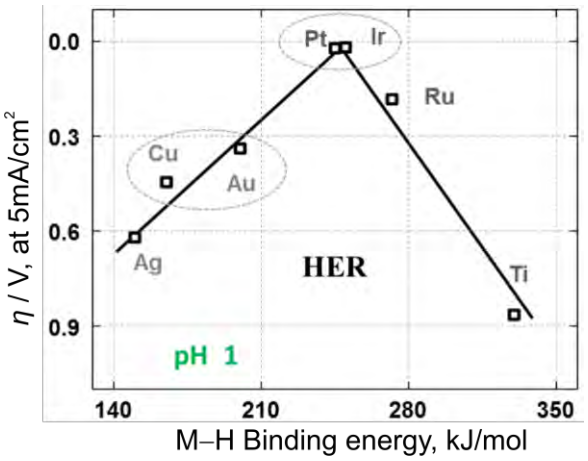

Fig. 1. A volcano plot, measured in 0.1 M $HClO_4$ (pH 1), of several metals denoting their HER activity, overpotential (η) at 5 mA cm^{-2}, as a function of their calculated M–H binding energy. At the apex of the plot are the noble metals Pt and Ir, which have nearly identical activities, while on either side are metals that either bind hydrogen too weakly (Ag) or too strongly (Ti). Note that the order of activity of the coinage metals is Au > Cu > Ag, which follows the trend in the M–H binding energies.

ments that interact strongly with H_{ad} (such as Ru and Ti) are positioned on the descending slope of the volcano, supporting previous suggestions that the M–H_{ad} binding energy can be used as a descriptor for the HER. Not in passing, given that recent analysis has demonstrated that neither Ru nor Ti are bare metals in the HER region, it is suggested that, in fact, experimentally it is very difficult (impossible) to determine unambiguously solely based on the metal–H_{ad} energetics what would be the correct position of these two elements in the observed volcano relationship. This is most likely also true for the HER in alkaline solutions, when the rates of the reaction are much slower than in acidic environments. Interestingly, with one recent exception,[20] there are no fundamental studies that have focused on deriving relationships between the nature of metals and activity of the HER at high pH values. Furthermore, there are still debates as to why the rate of the HER is 2 to 3 orders of magnitude lower at pH 13 than at pH 1 and why the reaction is sensitive to the structure of surface atoms in alkaline media but largely insensitive in acidic environments.[22–24] Finally, the question arises as to whether the HER on metal surfaces in alkaline solutions can approach the activity at low pH values. In the next two sections, focus is first directed on the differences and similarities between the volcano-type relationships in alkaline and acidic environments and, then, this knowledge is used to demonstrate that it is indeed possible to improve the activities of the HER at high pH values, simply by controlling the rates of the water dissociation step, *i.e.*, the Volmer step.

HER activities in alkaline electrolytes

Although the HER exhibits a volcano-like behavior in alkaline solutions (Fig. 2), there are three notable differences with change in pH: *i*) the activities in alkaline solutions are lower than in acid solutions (in line with previous observation that intrinsic activity of metal catalysts in alkaline medium are ≈2–3 orders of magnitude lower than in acid solutions); *ii*) significantly, in contrast to acid solutions, in alkaline solution Ir is more active than Pt (>55 mV), indicating that there might be substantial difference in the reaction mechanisms between the HER at low and high pH values; *iii*) the trend in the activity between IB group metals in alkaline solution increases from Ag < Au < Cu, an order of activity that is different from the one observed in acidic environments (Ag < Cu < Au). Clearly, these features cannot be explained solely based on the free energy of hydrogen adsorption since this descriptor should be independent of the pH of the solution. In previous reports,[3,20,21] it was argued that the main difference between the HER in acid and alkaline electrolytes lies in the source of the hydrogen; while in acid solution, active intermediates are formed from protons, in alkaline solutions an additional activation process involving the dissociation of water is required to generate the H_{ad}. It was recently shown that this is an important difference and that evolution of H_2 from H_2O in alkaline solutions requires

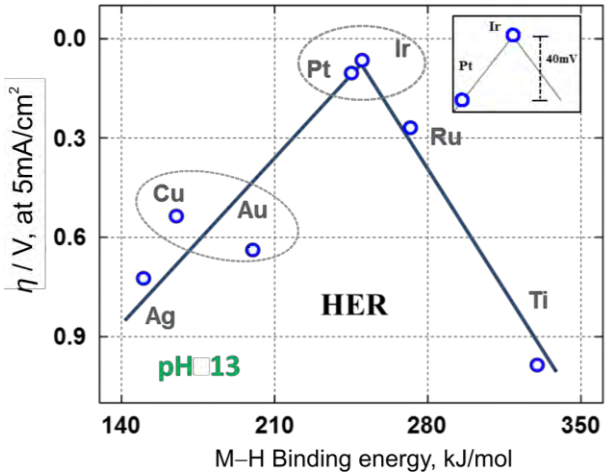

Fig. 2. A volcano plot, measured in 0.1 M KOH (pH 13), of several metals denoting their HER activity, overpotential (η) at 5 mA cm^{-2}, as a function of their calculated M–H binding energy. At the apex of the plot are noble metals Pt and Ir, while on either side are metals that either bind hydrogen too weakly (Ag) or too strongly (Ti). Note the distinctions between the volcano plot in acid electrolytes. The order of activity of the coinage metals is Cu > Au > Ag, which no longer follows the trend in their M–H binding energy and the difference in overpotential between Ir and Pt is significantly larger (≈55–60 mV) compared to acid electrolyte values (≈1–5 mV).

materials that are equally effective for water dissociation as well as H_{ad} recombination steps. In line with literature data,[20] it was concluded that Cu is more active for the HER in alkaline solution than Au because the former is a more effective water dissociation catalyst; hence, in alkaline solutions, Cu provides a higher rate for generation of hydrogen intermediates from water. The differences observed between Pt and Ir surfaces could be explained in a similar way. Considering that there is no difference in the energetics for the Tafel step on Pt and Ir (the same activities are observed in acid solutions), the higher activity of Ir compared to Pt in alkaline solution can only be due to improved dissociation of water on the Ir surface. Therefore, in order to construct the activity trends of the HER in alkaline solutions, two rather than one descriptor has to be taken into account; namely, synergy between the energy required to dissociate the water molecules (M–water energetics) and adsorption/recombination of hydrogen intermediates (M–H_{ad} energetics).

HER activities on metals modified with a "water dissociation catalyst" in alkaline electrolytes

In order to confirm the importance of both the descriptors in a complex transformation of H_2O to H_2 in alkaline solution, the metal electrodes were modi-

fied by $Ni(OH)_2$ clusters, which are known to be extremely active in the water dissociation step.[3] Thus, the activity curves in Fig. 3a and b for such modified systems were compared with the activities for the bare (unmodified) surfaces in the corresponding alkaline and acid environments. A close inspection of Fig. 3 unambiguously reveals that the activities for the $Ni(OH)_2$–M surfaces in alkaline

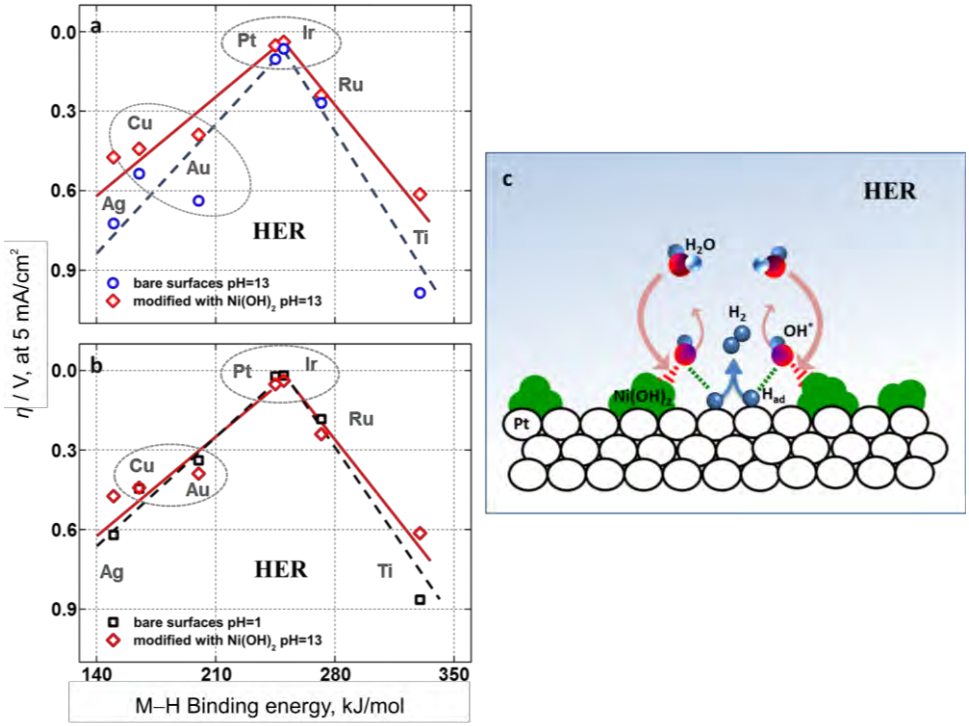

Fig. 3. a) Two volcano plots are overlaid, both measured in 0.1 M KOH (pH 13). One shows the HER activity of bare unmodified metals, while the second was measured on $Ni(OH)_2$--modified metal surfaces. Note that the HER is activated by the presence of $Ni(OH)_2$ on all of the bare metal surfaces. Furthermore, on the $Ni(OH)_2$-modified surfaces, the activities for Pt and Ir are nearly identical, and the trend of the coinage metals follows the trend in their M–H binding energies, Au > Cu > Ag. b) Two volcano plots are overlaid, in one the HER was measured in 0.1 M $HClO_4$ (pH 1) on bare metal surfaces while the other is constructed from HER activities measured in 0.1 M KOH (pH 13) on $Ni(OH)_2$-modified metal surfaces. The activities and positions of the elements are nearly identical suggesting that the elimination of the role of the water dissociation step in alkaline HER is the only way to validate the use of M–H binding energies as alkaline HER catalyst descriptors. c) A 2-D representation of the proposed model for the metal solution interface within the HER potential region of the metal surface covered by amorphous $Ni(OH)_2$ clusters. The HER is promoted by the presence of the $Ni(OH)_2$ clusters as they act as the "active" sites for water dissociation (OH* product removal and re-adsorption of H_2O), the resulting H_{ad} species originating from the clusters recombine on metal sites to form H_2 (Tafel step).

solutions approach the activities in acid solution for the pure metals, *i.e.*, Pt = Ir and Au > Cu > Ag. Based on these result, it is proposed that the rate of proton production from water is significantly enhanced on the Ni(OH)–M surfaces in alkaline environments so that the rate of the overall reaction is again affected predominantly by the M–H_{ad} binding energy, as is the case for acidic solutions. It should be remembered, however, that the M–H_{ad} energies alone cannot serve as the physicochemical descriptor for the HER on metal surfaces in alkaline environments. In other words, the *sine qua non* for the HER in alkaline medium is clearly a synergy between the effectiveness of the catalyst to break water molecules (predominantly on more oxophilic sites, such as defects or hydroxyoxides) and to efficiently collect and recombine hydrogen intermediates on more noble metal sites. Based on this supposition, it is reasonable to suggest that in alkaline solutions, the more defected Pt(110) is more active than the more "perfect" Pt(111) simply because the rate of the HER is proportional to the density of surface defect sites. Along the same lines, metals covered by $Ni(OH)_2$ are more active than bare M surfaces because in a bifunctional mechanism, the edges of $Ni(OH)_2$ clusters promote the dissociation of water while the produced intermediates are adsorbed and recombined on M sites (Fig. 3).

CONCLUSIONS

It is proposed that: *i*) due to coverage by spectator species, even in the HER potential region, it is still questionable if it would be possible to establish experimentally a true relationships between M–H_{ad} energetics and catalytic activity – therefore, with the exception of Pt, Ir and Au, the experimentally established positions of the other metal catalysts in the observed volcano relations are uncertain over the entire pH range; *ii*) while in acidic solutions the M–H_{upd} binding energy controls the activity trends (supported by DFT calculations), the trends in activity in alkaline solutions are controlled by a delicate balance between two descriptors: the M–H_{ad} interaction as well as the energetics required to dissociate water molecules; *iii*) the importance of the second descriptor was confirmed by the introduction of bifunctional catalysts, such as M modified by Ni(OH); *e.g.*, while the latter serves to enhance catalytic decomposition of water, the metal sites are required for the collection and recombination of the produced hydrogen intermediates.

Acknowledgments. This work was supported by the Office of Science, Office of Basic Energy Sciences, Division of Materials Science, U.S. Department of Energy, under contract DE-AC0-06CH11357.

И З В О Д

ЕЛЕКТРОКАТАЛИЗА РЕАКЦИЈЕ ИЗДВАЈАЊА ВОДОНИКА У КИСЕЛОЈ И АЛКАЛНОЈ СРЕДИНИ

NEMANJA DANILOVIC, RAM SUBBARAMAN, DUSAN STRMCNIK, VOJISLAV R. STAMENKOVIC и NENAD M. MARKOVIC

Materials Science Division, Argonne National Laboratory, Argonne, Illinois 60439, USA

Проучавани су трендови реакције издвајања водоника (HER) у киселој и алкалној срединини на одабраним металима (M: Cu, Ag, Au, Pt, Ru, Ir и Ti). Нађено је да су, са изузетком Pt, Ir и Au због високог степена покривености неактивним адсорбованим врстама позиције Cu, Ag, Ru и Ti на експериментално одређеним "вулканским" кривама још увек непоуздане. Такође је утврђено да су трендови активности у алкалној средини одређени осетљивим билансом два дескриптора: интеракције M–H_{ad} и енергије потребне за дисоцијацију молекула воде, док у киселој средини трендове активности највероватније одређује енергија везе M–H_{upd}. Значај енергије дисоцијације воде је потврђен уводјењем би-функционалног катализатора као што је *M* модификован Ni(OH). Док Ni(OH) каталитички убрзава декомпозицију воде, метал је неопходан за груписање и рекомбинацију насталих водоничних интермедијара.

(Примљено 18. новембра 2013)

REFERENCES

1. N. M. Markovic, P. N. Ross, *Surf. Sci. Rep.* **45** (2002) 117
2. R. R. Adzic, F. Feddrix, B. Z. Nikolic, E. Yeager, *J. Electroanal. Chem.* **341** (1992) 287
3. R. Subbaraman, D. Tripkovic, D. Strmcnik, K.-C. Chang, M. Uchimura, A. P. Paulikas, V. Stamenkovic, N. M. Markovic, *Science* **334** (2011) 1256
4. D. Strmcnik, M. Escudero-Escribano, K. Kodama, V. R. Stamenkovic, A. Cuesta, N. M. Marković, *Nat. Chem.* **2** (2010) 880
5. D. Strmcnik, K. Kodama, D. van der Vliet, J. Greeley, V. R. Stamenkovic, N. M. Marković, *Nat. Chem.* **1** (2009) 466
6. D. Strmcnik, D. F. van der Vliet, K.-C. Chang, V. Komanicky, K. Kodama, H. You, V. R. Stamenkovic, N. M. Marković, *J. Phys. Chem. Lett.* **2** (2011) 2733
7. J. O' M. Bockris, E. C. Potter, *J. Electrochem. Soc.* **99** (1952) 169
8. A. Lasia, in *Fuel Cell Electrocatalysis*, W. Vielstich, A. Lamm, H. A. Gasteiger, Eds., Wiley, Chichester, 2003, pp. 416–440
9. S. Trasatti, *J. Electroanal. Chem. Interf. Electrochem*. **39** (1972) 163
10. R. Parsons, *Trans. Faraday Soc.* **54** (1958) 1053
11. H. Gerischer, *Bull. Soc. Chim. Belg*. **67** (1958) 506
12. L. I. Krishtalik, *Electrokhimiya* **2** (1966) 616
13. J. Greeley, T. F. Jaramillo, J. Bonde, I. B. Chorkendorff, J. K. Norskov, *Nat. Mat.* **5** (2006) 909
14. J. Greeley, J. K. Norskov, L. A. Kibler, A. M. El-Aziz, D. M. Kolb, *ChemPhysChem* **7** (2006) 1032
15. W. Schmickler, S. Trasatti, *J. Electrochem. Soc.* **153** (2006) L31.
16. E. Skúlason, G. S. Karlberg, J. Rossmeisl, T. Bligaard, J. Greeley, H. Jónsson, J. K. Nørskov, *Phys. Chem. Chem. Phys.* **9** (2007) 3241
17. E. Skúlason, V. Tripkovic, M. E. Björketun, S. Gudmundsdóttir, G. Karlberg, J. Rossmeisl, T. Bligaard, H. Jónsson, J. K. Nørskov, *J. Phys. Chem., C* **114** (2010) 18182
18. M. M. Jaksic, *Electrochim. Acta* **29** (1984) 1539

19. J. Greeley N. M., Markovic, *Energy Environ. Sci*. **5** (2012) 9246
20. N. Danilovic, R. S. D. Strmcnik, K. C. Chang, A. P. Paulikas, V. R Stamenkovic, N.M. Markovic, *Angew. Chem.* **124** (2012) 12663
21. R. Subbaraman, D. Tripkovic, K.-C. Chang, D. Strmcnik, A. P. Paulikas, P. Hirunsit, M. Chan, J. Greeley, V. Stamenkovic, N. M. Markovic, *Nat. Mat.* **11** (2012) 550
22. N. M. Markovic, B. N. Grgur, P. N. Ross, *J. Phys. Chem., B* **101** (1997) 5405
23. N. M. Markovic, S. T. Sarraf, H. A. Gasteiger, P. N. Ross, *J. Chem. Soc., Faraday Trans.* **92** (1996) 3719
24. D. Strmcnik, M. Uchimura, C. Wang, R. Subbaraman, N. Danilovic, D. van der Vliet, A. P. Paulikas, V. R. Stamenkovic, N. M. Markovic, *Nat. Chem.* **5** (2013) 300.

Journal of the Serbian Chemical Society
JSCS-info@shd.org.rs • www.shd.org.rs/JSCS
J. Serb. Chem. Soc. *78* (12) 2017–2037 (2013)
JSCS–4548
UDC 546.98+667.287:539.24:66.094.1
Original scientific paper

Electrochemical and nanogravimetric studies of palladium phthalocyanine microcrystals•

ÁKOS NEMES, COLIN E. MOORE and GYÖRGY INZELT*

Department of Physical Chemistry, Institute of Chemistry, Eötvös Loránd University, Pázmány Péter sétány 1/A, 1117 Budapest, Hungary

(Received 9 September, revised 19 September 2013)

Abstract: An electrochemical quartz crystal nanobalance was used to study the redox behavior of palladium phthalocyanine microcrystals attached to gold and platinum in aqueous solutions at different pH values. In order to investigate the substrate effect, paraffin impregnated graphite electrodes were also applied. It was found that the redox transformations of palladium phthalocyanine are accompanied with deprotonation–protonation as well as the sorption and desorption of counter-ions, the extent of which depend on the pH. Based on the results of the nanogravimetric measurements, a redox mechanism describing the pH dependence is suggested. Simultaneously with charge transfer processes, solid–solid phase transitions and water transport occur.

Keywords: palladium phthalocyanine; microcrystals; electrochemical quartz crystal nanobalance (EQCN); redox transformations; solid–solid phase transition.

INTRODUCTION

The first phthalocyanine (iron phthalocyanine) was discovered by chance in 1928 during the industrial production of phthalimide, and it was first studied in detail by Linstead. Linstead published a series of papers devoted to the preparation and characterization of several phthalocyanines, and he also proposed the structure of this class of compounds.[1] Investigations of the electrochemical behavior of phthalocyanines have been in the foreground of research during the last 30 years,[2–46(and citations therein)] especially as a catalyst of the oxygen reduction reaction, since it is of utmost importance to find a suitable and cheap catalyst that could replace the expensive platinum. A wide range of other applications

* Corresponding author. E-mail: inzeltgy@chem.elte.hu
doi: 10.2298/JSC130909094N
• This paper is dedicated to Professor Branislav Nikolić on the occasion of his 70th birthday with the acknowledgement of his outstanding contributions to the development of electrochemistry.

beside catalysis, such as in electrochromic display devices, in electrochemical power sources including solar cells and in sensors has been put forward. However, elucidation of the electrochemical processes occurring during the redox transformations of phthalocyanines is an interesting and challenging task in itself. A survey of the literature revealed that there are not two similar cyclic voltammograms on a given phthalocyanine in papers devoted to the study of this group of compounds. The main reason is that the voltammetric and other (*e.g.*, spectroscopic) responses of the phthalocyanine ring (Pc) strongly depend on metal ions in the centre of the ring, the substituents on the periphery of the macrocyclic ring, the solvent and the electrolyte used (especially when complex forming agents are present), the presence of oxygen, temperature and even the morphology of the surface layer (adsorbed or deposited by different methods). A further difficulty in the comparison of the results is that in the majority of the cases, substituted phthalocyanines were used to make the compound soluble. Many diverse processes, including irreversible ones, can occur, such as the formation of peroxy and oxo-bridged species in contact with oxygen in solution or even in solid form, or nucleation-growth-like phase transition in the solid layer during redox processes. The variety of the shapes of the voltammograms is due to thermodynamic reasons and to kinetic effects.

According to theoretical considerations, if the *d* orbitals of a metal are positioned between HOMO and LUMO gap of the phthalocyanine (Pc^{2-}) ligand, *e.g.*, this is the case for Co and Fe, the redox transformation of the central metal ion can be observed, especially if suitable coordinating species are present in the solution. For other metal phthalocyanines, such as Cu, Ni, Zn, Pt and Pd, the metal ions do not participate in redox processes, only the Pc ring will be oxidized or reduced.[14,15,29,30] A wide arsenal of non-electrochemical methods have been used to characterize the different phthalocyanines, however, the electrochemical quartz crystal nanobalance (EQCN) has not yet been exploited, only platinum phthalocyanine microcrystals in contact with aqueous sulfuric acid and sodium sulfate solutions[33] and palladium phthalocyanine films in non-aqueous solutions[29] have been studied by this technique. While FePc, CoPc, MnPc, MgPc, *etc*., have been thoroughly investigated, only few of studies have been devoted to PtPc[19–23,28,33] and PdPc.[29–31]

In the present study, our attention was focused on an EQCN study of palladium phthalocyanine (PdPc) microcrystals attached to different substrates and investigated under different conditions.

EXPERIMENTAL

Palladium phthalocyanine (PdPc) (Merck) was used without further purification. Analytical grade chemicals such as H_2SO_4 (Merck), Na_2SO_4 (Merck) and NaOH (Sigma–Aldrich) were used as received. Doubly distilled water was used (Millipore water). A sodium chloride saturated calomel electrode (SCE) was used as the reference electrode, which was carefully

separated from the main compartment by a double frit. A platinum or a gold wire served as the counter electrode. Cycling of the potential as a pretreatment of the electrode was performed before each experiment in the supporting electrolyte, until a voltammogram characteristic of a clean Au, Pt or PIGE electrode was obtained. Phthalocyanine microcrystals were attached to the gold, platinum or paraffin impregnated graphite (PIGE) surface (surface area, A = 0.196 cm^2) either by mechanical abrasion or from a sonicated phthalocyanine–2-propanol sol *via* dropping an adequate amount of the suspension and drying it. The sonification was realized using a Realsonic 57, Korea.

Five-MHz AT-cut crystals of 2.54 cm diameter coated with gold or platinum (Stanford Research Systems, SRS, U.S.A.) were used in the EQCN measurements. The electrochemically and the piezoelectrically active areas were 1.37 and 0.4 cm^2, respectively. The integral sensitivity of the crystals (C_f) was found to be 56.6×10^6 Hz g^{-1} cm^2, *i.e.*, 1 Hz corresponded to 17.7 ng cm^{-2}. The integral sensitivity was calculated from the frequency change measured during silver deposition / dissolution or from the electroreduction of gold oxide using the "effective" charge related to the piezoelectrically active area, *i.e.*, the total charge consumed during the calibration was multiplied by the ratio of the piezoelectrically active and the electrochemically active areas. The experimental setup and conditions were the same as those previously reported.[47,48] The apparent molar mass of the deposited or the exchanged species (M) was calculated from the slope of the Δf *vs.* Q curve using the following formula: $M = (nFA/C_f)\, \mathrm{d}\Delta f/\mathrm{d}Q$, where n is the number of electrons involved in the electrochemical reaction, F is the Faraday constant, Δf is the frequency change, Q is the charge consumed and A is the electrode surface area. Although the requirements (uniform and homogeneous surface layer) for the application of the Sauerbrey Equation[49] were not strictly met, based on the measured frequency values, a rough estimation could be performed. The relative values of Δf obtained for the incorporation of different ions and solvent molecules, however, should be approximately correct. The crystals were mounted in a holder made from Kynar® (poly(vinilidene flouride)) and connected to a SRS QCM 200 unit. Either an Elektroflex 453 potentiostat or a Biologic VSP potentiostat and a Universal Frequency Counter PM6685 (Fluke) connected to an IBM personal computer were used for the control of the measurements and for data acquisition.

Simultaneously with the frequency, the surface resistance (loss) was also monitored. As it remained constant, the behavior of the surface layer consisting of microcrystals remained elastic during the electrochemical transformations, *i.e.*, no viscoelastic effect appeared.

RESULTS AND DISCUSSION

Cyclic voltammetric and EQCN responses for freshly prepared layers

Figure 1 shows a series of consecutive cyclic voltammograms obtained for PdPc microcrystals deposited on PIGE in contact with deaerated sulfuric acid solution. During cycling, four anodic waves and three cathodic waves developed; waves II_a, II_c and IV_c continuously increased, as can be seen in Fig. 1. However, this pattern depended on several factors: potential limits, presence or absence of oxygen, the type of the substrate, the nature and concentration of the electrolyte, the layer thickness and the deposition method.

This type of voltammogram developed only if the positive potential limit was higher than 1 V *vs.* SCE, *i.e.*, if the region of the oxidation at peak I_a was achieved in acidic solutions. For the re-reduction of the PdPc, relatively high

negative potential, higher than *ca*. –0.35 V had to be applied. The irreversible nature of the voltammetric wave indicates that a chemical reaction was coupled to electron transfer steps. The big difference between the anodic and cathodic peaks could be related to a phase transition in the solid layer of microcrystals. The peaks were named in series according to the order of their potential. Peak IV_c obviously belonged to the anodic waves I_a and II_a, since the charge injected (electrons removed) was regained in the potential region of IV_c.

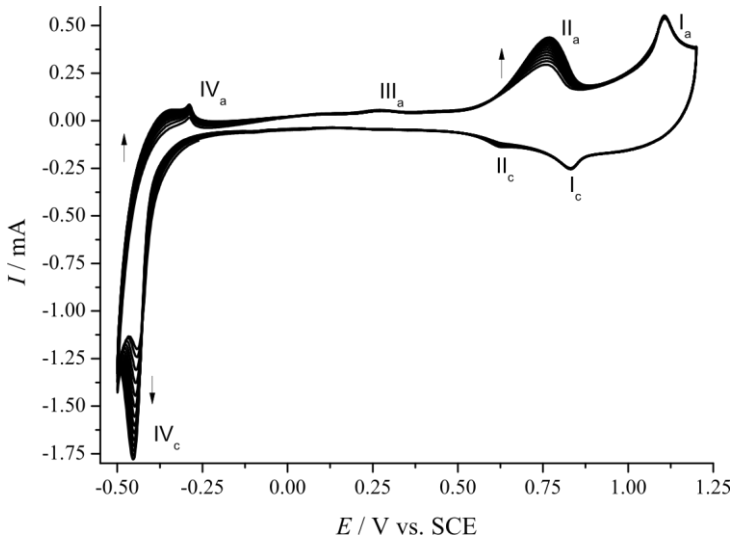

Fig. 1. Consecutive cyclic voltammograms (14 cycles) obtained for PdPc microcrystals deposited on PIGE. Electrolyte: 1 mol dm^{-3} deaerated sulfuric acid. Scan rate: 100 mV s^{-1}.

The very first cycle always differs from the subsequent ones, as can be seen in Fig. 2. Figure 2 also shows the effect of the positive potential limit since during the first cycle when the switching potential was set to 1 V, only a small current increase commenced at *ca*. 0.8 V but when 1.4 V was chosen as the positive potential limit, peak I_a became a well-developed peak and the I_c wave also appeared. The third cycle was started from –0.5 V, and while the reduction currents remained practically the same, three oxidation waves (I_a, II_a, III_a and IV_a) could be seen; peak I_a became smaller and shifted in the direction of less positive potentials.

The EQCN results revealed that a mass increase occurred simultaneously with the charge injection, which could be related to the incorporation of counter ions and water molecules in the layer of microcrystals (Fig. 3). The average molar mass derived for the interval between 0.9 and 1 V was $M = 126\pm15$ g mol^{-1}, which somewhat increased in the course of consecutive cycles. However, at the beginning of the oxidation, a much smaller value, $M = 28\pm3$ g mol^{-1} was

obtained, while close to the 1 V limit, this value increased to $M = 259 \pm 25$ g mol^{-1}, which indicated that the very first process was deprotonation, and the anions entered the layer in a later phase of the oxidation.

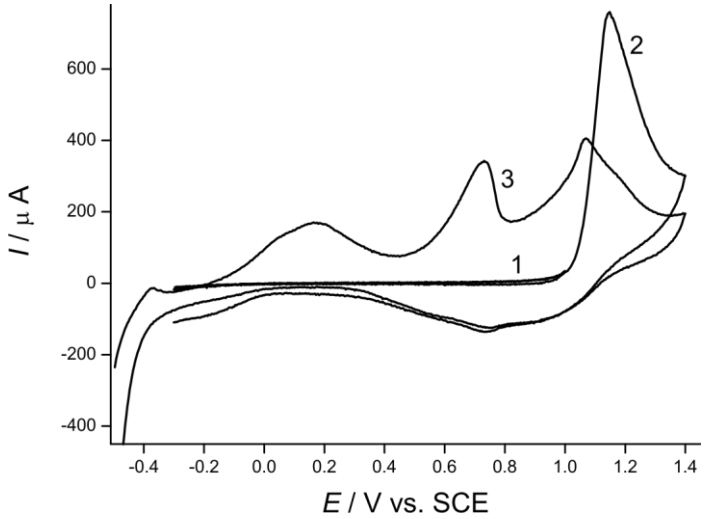

Fig. 2. Cyclic voltammograms obtained for a freshly prepared PdPc layer of microcrystals deposited on PIGE. Electrolyte: 0.5 mol dm^{-3} non-deaerated sulfuric acid. Scan rate: 100 mV s^{-1}. Potential limits were as follows: 1) first cycle from –0.3 to 1 V, 2) second cycle from –0.3 to 1.4 V and 3) third cycle from –0.5 to 1.4 V.

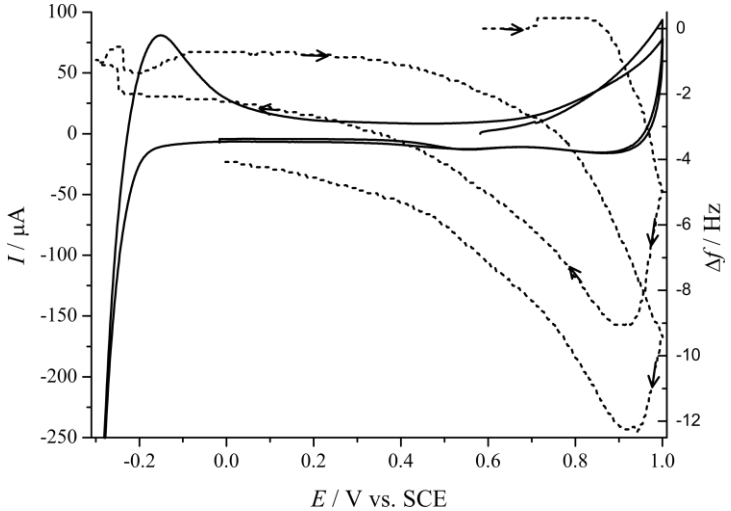

Fig. 3. Cyclic voltammograms (solid line) and the simultaneously obtained EQCN frequency changes (dotted line) for a freshly deposited PdPc layer of microcrystals on Au. Cycling was started from the open-circuit potential. Electrolyte: 1 mol dm^{-3} deaerated sulfuric acid. Scan rate: 20 mV s^{-1}.

However, this effect was observed only during the conditioning period. If the positive potential limit was set above 1 V, a mass decrease was observed, which was due to the dissolution of the microcrystals (Fig. 4). This dissolution or delamination of a portion of PdPc ceased after several cycles and both the cyclic voltammogram and the EQCN curve remained stable thereafter, providing that the experimental conditions, *e.g.*, the potential limit of cycling, remained the same.

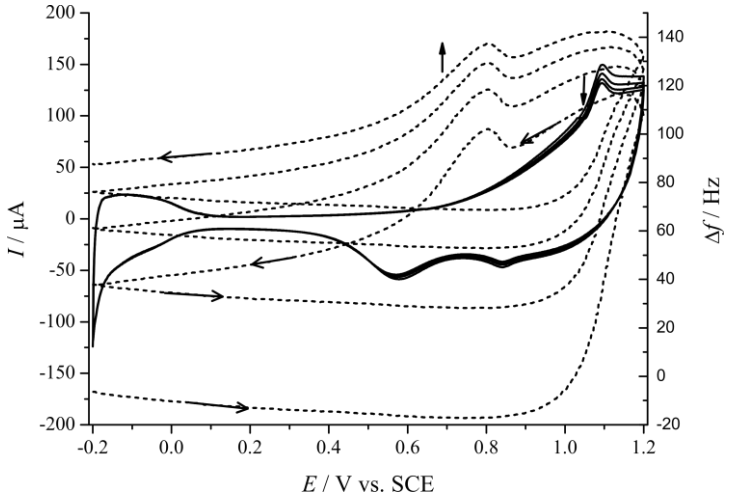

Fig. 4. Consecutive cyclic voltammograms (solid line) and the simultaneously obtained EQCN frequency changes (dotted line) for PdPc microcrystals on Au. Electrolyte: 1 mol dm^{-3} deaerated sulfuric acid. Scan rate: 20 mV s^{-1}.

Effect of the positive potential limit

The importance of the potential limits has already been emphasized. However, a closer look at this effect revealed an interesting phenomenon. While – as expected – the development of peak I_a and the respective peak I_c occurred gradually if the potential exceeds *ca*. 1 V, wave II_c appeared even when the positive potential did not reach this region. The EQCN frequency changes, however, evidenced that a different process started at lower potentials. Below *ca*. 1 V, a frequency increase occurred, while above it, a frequency decrease started. It follows that in the first phase of oxidation, the oxidation was accompanied by deprotonation, and anions entered the layer only at higher positive potentials. The latter process continued even during the cathodic half-cycle (Fig. 5).

Effect of the presence of oxygen

As seen in Fig. 6, in the presence oxygen the pair of waves II_a and II_c does not appear, I_a and I_c increase, and oxygen reduction starts at ca. 0.1 V. However, it is true only of layers after many cycles. (Voltammograms displayed on Figs. 1 and 6 were obtained for the same layer of microcrystals.) For a virgin layer, even

in the presence of oxygen, wave II_a appears and wave III_a, which is usually only a very small one, presents itself as a well-developed peak (Fig. 2).

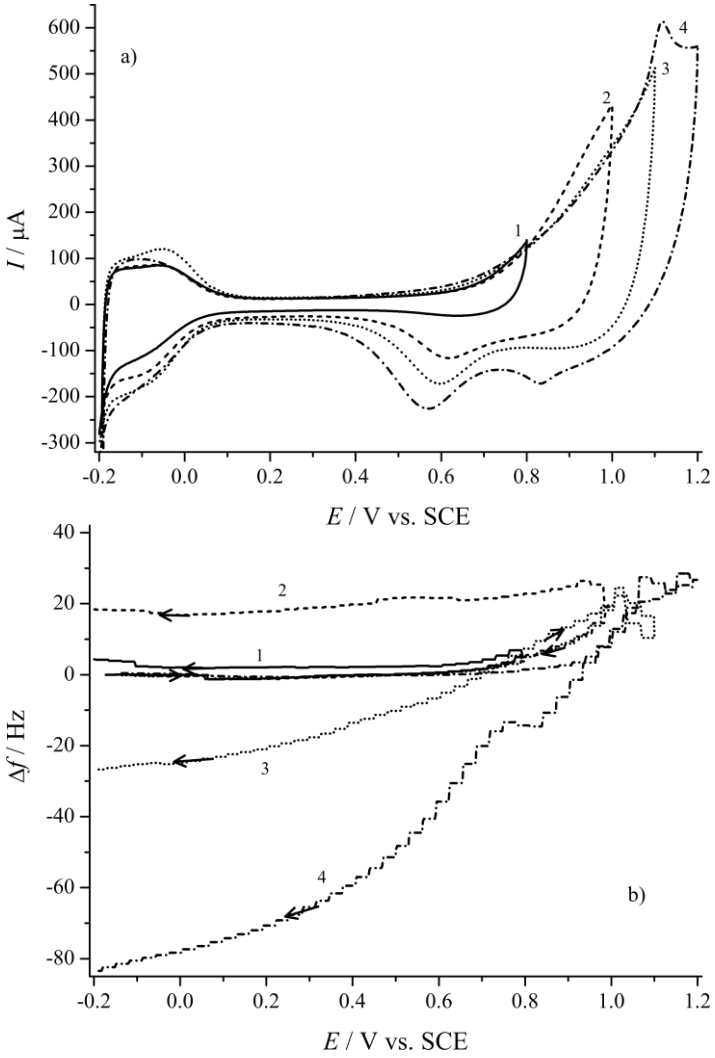

Fig. 5. a) Cyclic voltammograms and b) the simultaneously obtained EQCN frequency changes for PdPc microcrystals on Pt at different positive potential limits. Electrolyte: 1 mol dm^{-3} deaerated sulfuric acid. Scan rate: 20 mV s^{-1}.

In the case of PtPc, it is claimed that peak II_a is associated with the oxidation of the phthalocyanine at, or near to the Au | PtPc interface, and develops during repetitive cycling.[23,33] However, this statement is somewhat contradictory since it is to be expected that this wave would appear at the early phase of oxidation and would increase continuously. However, as it does not develop in the presence

of oxygen when PIGE and Au were substrates or when a Pt electrode was used, it could be concluded that it is rather due to the absence of interaction with oxygen. In the case of the Pt substrate, it could be explained by the interaction with PtO, which already appears in this potential range. Therefore, it is more likely that peak II_a does not appear if oxo or peroxy-bridged compounds are present (peroxy species are formed at low potentials).

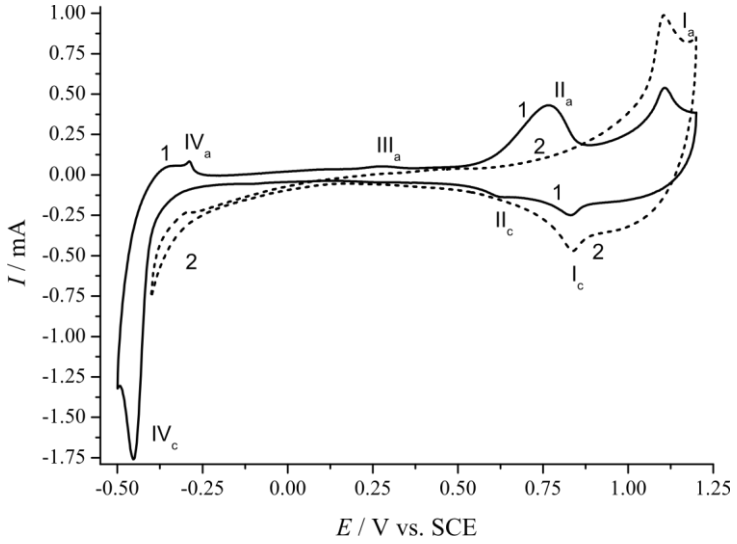

Fig. 6. Cyclic voltammograms obtained for PdPc microcrystals deposited on PIGE. Electrolyte: 1) 1 mol dm^{-3} deaerated and 2) oxygen saturated sulfuric acid. Scan rate: 100 mV s^{-1}.

Effect of scan rate

The scan rate dependence for a PIGE–PdPc system under an argon atmosphere is shown in Fig. 7. From the current (I) *vs*. scan rate (v) plots, it could be concluded that both I_a–I_c and II_a–II_c are surface waves since the function is linear, and the peak potential does not shift substantially with scan rate. In the potential region of wave IV_c, hydrogen evolution overlaps with the reduction of PdPc, which renders such analysis meaningless.

However, in the case of thick layers of microcrystals at higher scan rates, the cyclic voltammetric response becomes diffusional (Fig. 8).

It is even more noteworthy that at higher scan rates, the incorporation of the ionic species and especially of water, which is probably the slowest process, are incomplete. The shape of the cyclic voltammograms remain practically unaltered, *i.e*., the relative slowness of the anion incorporation is responsible for the diffusional behavior at high scan rates, while the lag of the water sorption is responsible for the incomplete mass change during the positive-going scan.

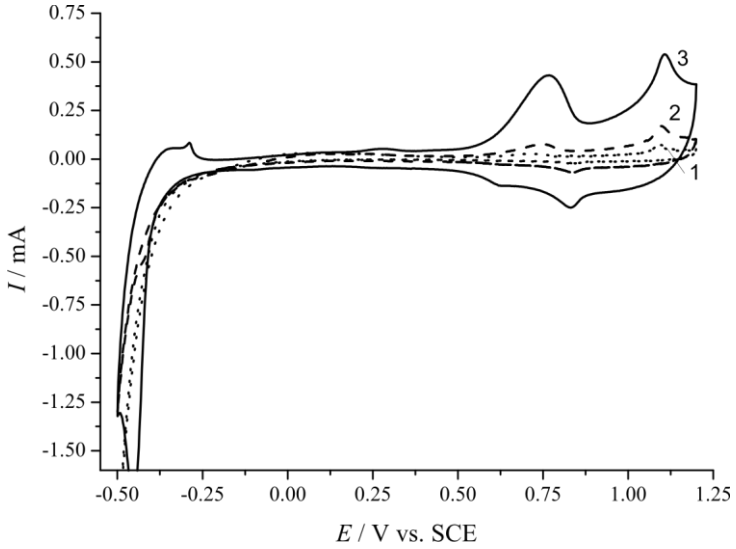

Fig. 7. Cyclic voltammograms obtained for PdPc microcrystals deposited on PIGE. Electrolyte: 1 mol dm^{-3} deaerated sulfuric acid. Scan rates: 1) 5, 2) 20 and 3) 100 mV s^{-1}.

Base line corrections

In the case of PIGE and gold, very low anodic current flows in the potential region of interest, and the oxide-reduction current, which might be substantial, is also small if the positive potential limit applied is less than 1.25 V. On the other hand, for platinum in both the hydrogen underpotential deposition (H-UPD) region and the oxide region substantial anodic and cathodic currents, respectively, arise. In the case of the calculation of the apparent molar mass value for the exchanged species, the charge and the frequency change should be corrected. The comparison when a gold substrate was used is shown in Fig. 9.

The cyclic voltammogram of PdPc shown in Fig. 9a does not show any contribution from the reduction of gold oxide. Furthermore, the EQCN frequency response (Fig. 9b) obtained for Au–PdPc was orders of magnitude higher than that of the gold electrode, *i.e.*, the surface of the gold electrode was covered by PdPc and the contribution from the gold substrate was negligible. It was also observed that even at high positive potential limits, the formation of gold oxide was hindered in the presence of PdPc.

As seen in Fig 10, in the case of platinum, the background current should be taken into account, even though both hydrogen adsorption in the H-UPD region and oxide formation are somewhat hindered by the surface PdPc layer of microcrystals. On the other hand, the EQCN response originating from the platinum oxide formation and reduction are negligibly small compared with the frequency change due to the PdPc crystals.

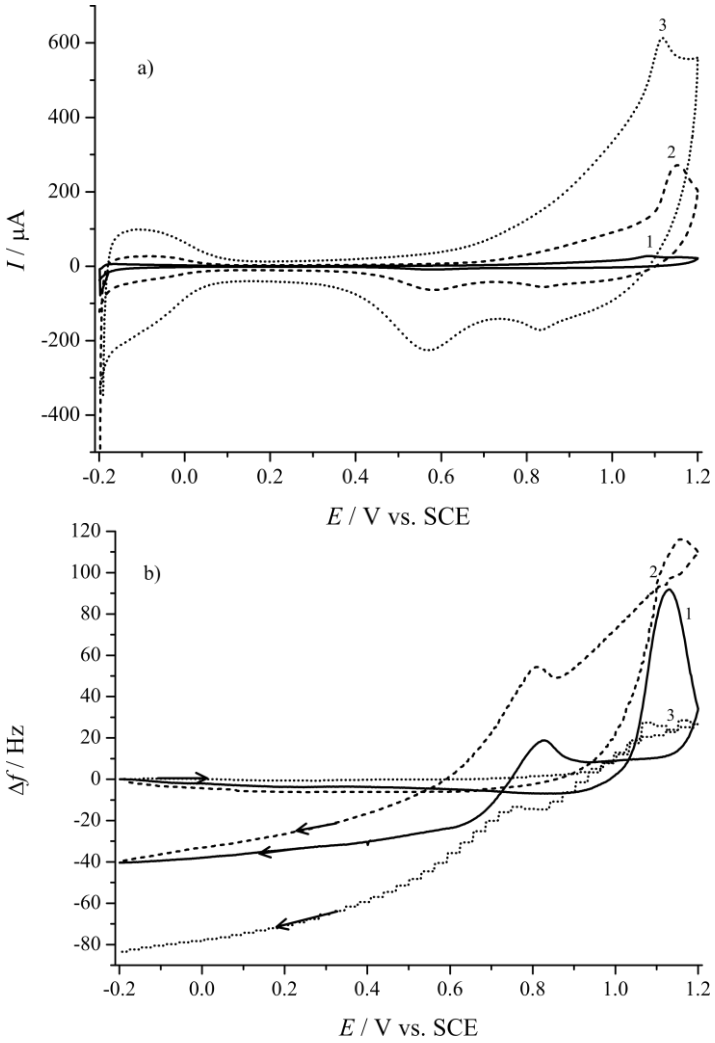

Fig. 8. a) Cyclic voltammograms and b) EQCN curves for PdPc microcrystals deposited on Pt. Electrolyte: 1 mol dm^{-3} deaerated sulfuric acid. Scan rates: 1) 5, 2) 20 and 3) 100 mV s^{-1}.

It could be concluded that the substrate–phthalocyanine interaction only slightly affected the voltammetric response at least compared to the behaviors of the layers on PIGE, Au and Pt, respectively. Under the same conditions (electrolyte composition, scan rate, potential region), the shift of the characteristic peak potentials was less than *ca*. 30 mV.

Effect of pH

On replacing sulfuric acid with a Na_2SO_4 solution, the respective waves appeared; however, as expected for any pH-dependent process, they were shifted

in the direction of more negative potentials (Fig. 11). This pH effect will be analyzed later because the Na_2SO_4 solution is an unbuffered system, *i.e.*, a pH change could occur near the electrode surface when protons are released or consumed. Experiments in the presence of phosphate buffers were also performed. However, a decreased electrochemical activity was observed when phosphate ions were present.

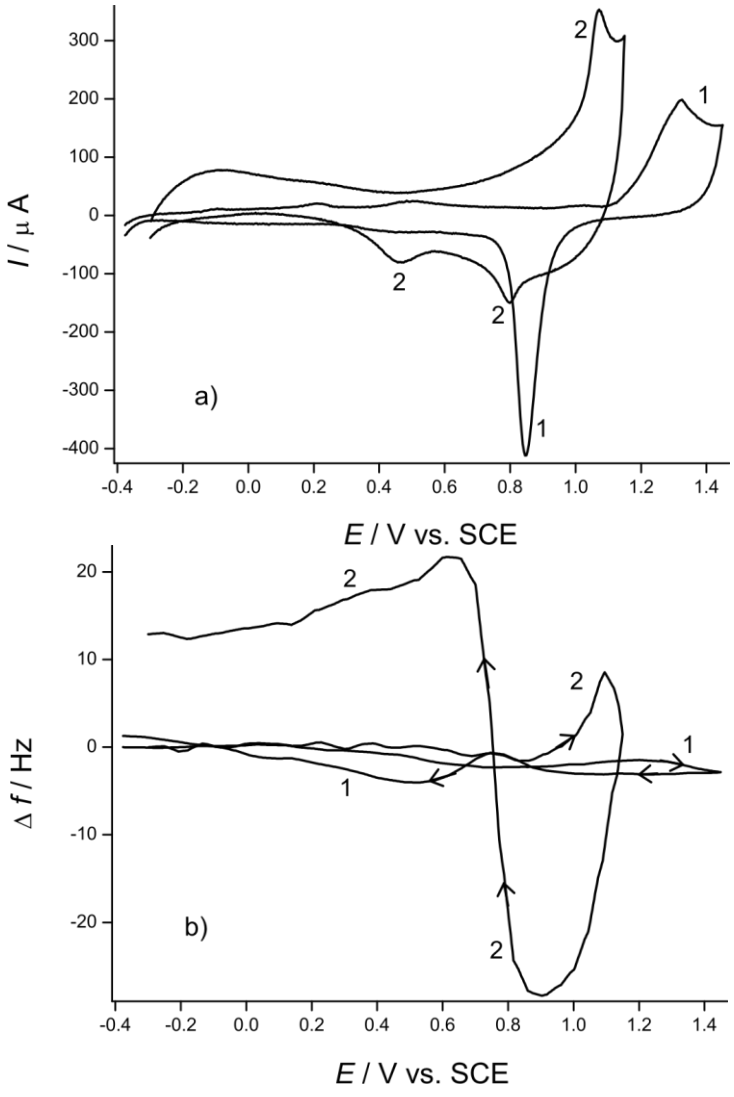

Fig. 9. a) Cyclic voltammograms and b) the simultaneously obtained EQCN frequency changes for 1) a gold electrode and 2) an Au|PdPc layer. Electrolyte: 0.5 mol dm^{-3} deaerated sulfuric acid. Scan rate: 100 mV s^{-1}.

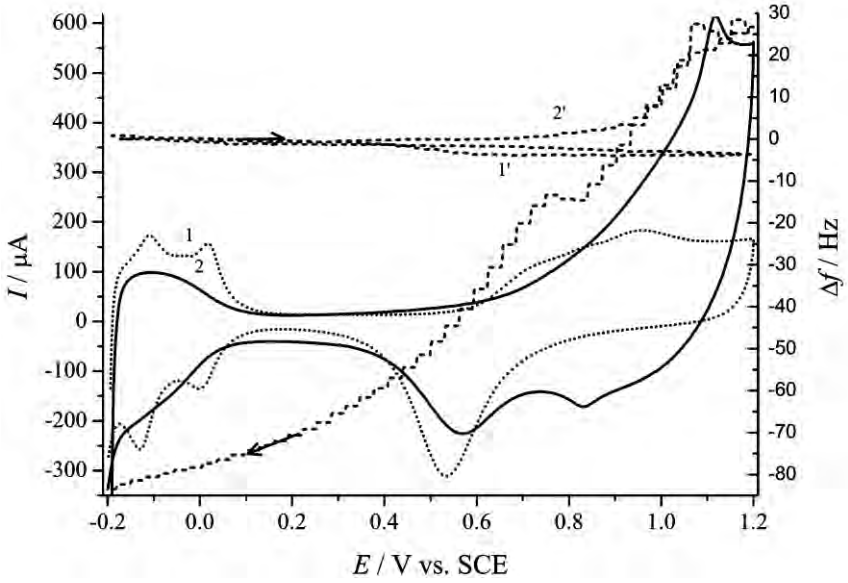

Fig. 10. Cyclic voltammograms (dotted line 1 Pt, continuous line 2 Pt|PdPc) and the simultaneously obtained EQCN frequency changes (dashed line 1′ Pt, dashed line 2′ Pt|PdPc) for 1) a platinum electrode and 2) a Pt|PdPc electrode. Electrolyte: 1 mol dm^{-3} deaerated sulfuric acid. Scan rate: 100 mV s^{-1}.

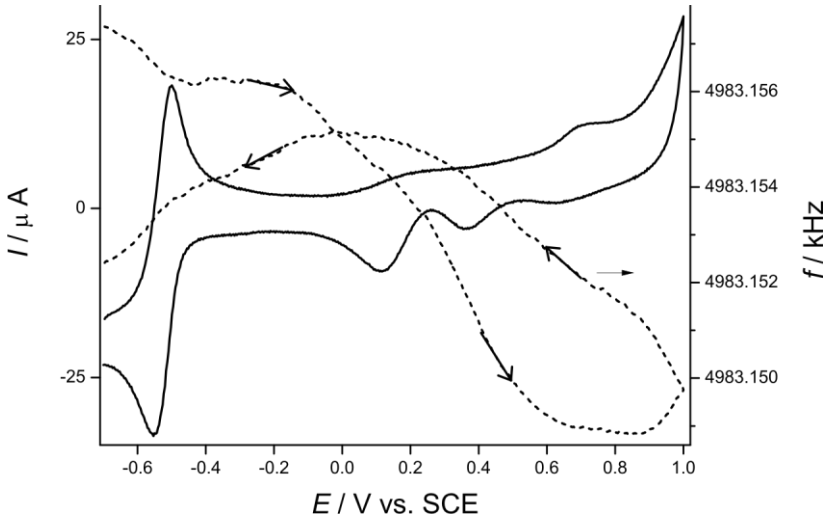

Fig. 11. Cyclic voltammogram (solid line) and the simultaneously obtained EQCN frequency curve (dashed line) obtained for PdPc microcrystals attached to Au. Electrolyte: 0.5 mol dm^{-3} deaerated Na_2SO_4 solution. Scan rate: 5 mV s^{-1}.

At *ca*. –0.5 V, a reversible pair of waves developed, which could be assigned to the hydrogen redox reaction since further reduction and re-oxidation of Pc ring

would involve a higher mass change due to the ionic exchange process. Nevertheless, it cannot be excluded that the redox reaction of PdPc contributes to this pair of waves, if protonation and deprotonation, respectively, occur. The EQCN curve is also of interest. Instead of the almost constant mass observed in acidic solutions, a frequency decrease (mass increase) was observed that commenced at wave II_a. In the region of wave I_a, the measured surface mass decreased again, as was also observed in acidic solution. Passing the reduction wave (II_c), the mass increased again. At the end of the cycle, the mass of the electrode was higher than its initial value. After several cycles at higher scan rates, the frequency returned to its starting value. This means that anions were incorporated and that a certain number of these ions remained permanently in the layer. Such an effect was previously observed *e.g.*, for PtPc layers in organic media.[21] As the peak potentials depend on the pH, the deprotonation accompanying the redox processes still prevails and positive charges appear in the PdPc layer that are compensated by the negatively charged counter-ions. In neutral media, the participation of the cations, in this case Na^+ cannot be excluded, either, since it was detected in the course of voltammetric studies of CoPc.[18]

In NaOH solution, all the waves appeared although the anodic waves were rather stretched while the cathodic peaks were well developed (Fig. 12). The EQCN response was substantially different from those measured in acidic or neutral solutions. At high negative potentials, a rather large, reversible frequency change was observed. During the anodic scan, this frequency increase was followed by a frequency decrease in the potential region of wave II_a. Reaching

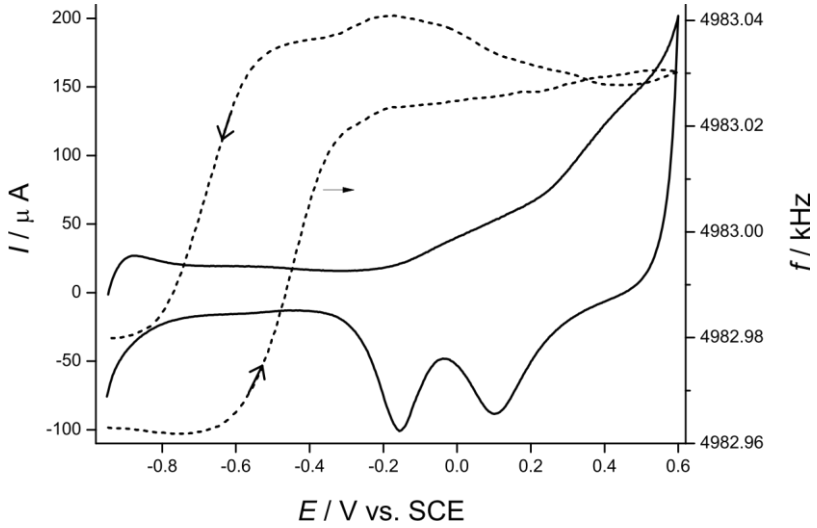

Fig. 12. Cyclic voltammogram (solid line) and the simultaneously obtained EQCN frequency curve (dashed line) obtained for PdPc microcrystals attached to Au. Electrolyte: 0.1 mol dm^{-3} NaOH + 0.4 mol dm^{-3} deaerated Na_2SO_4 solution. Scan rate: 50 mV s^{-1}.

the region of wave I_a, a small frequency increase again occurred. After potential reversal, slight mass increases occurred in two steps at the two cathodic waves, and eventually below *ca*. –0.4 V, the mass increased steeply until *ca*. –0.7 V. The apparent molar mass that could be calculated in this potential region was M = = 1025±75 g mol^{-1} for both the oxidation and the reduction processes.

A comparison of the pH dependence of the voltammetric and EQCN responses can be found in Fig. 13.

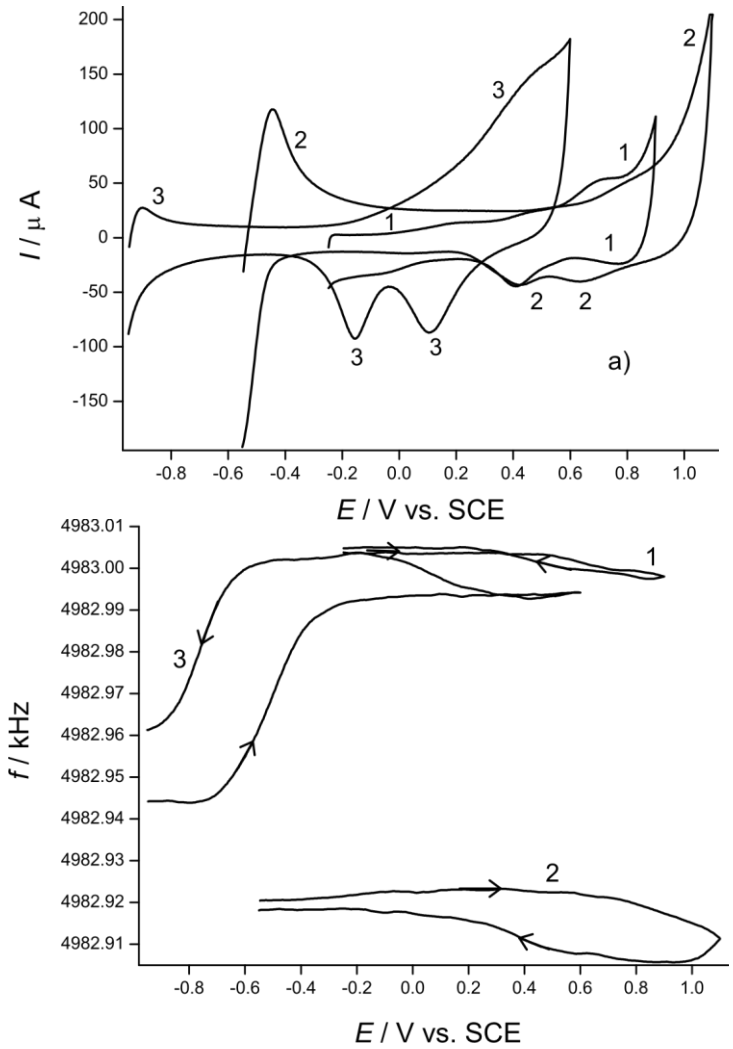

Fig. 13. a) Cyclic voltammograms and b) the simultaneously obtained EQCN frequency curve obtained for PdPc microcrystals attached to Au. Electrolyte: 1) 0.5 mol dm^{-3} sulfuric acid, 2) 0.5 mol dm^{-3} Na_2SO_4 and 3) 0.1 mol dm^{-3} NaOH + 0.4 mol dm^{-3} deaerated Na_2SO_4 solution. All solutions were deaerated with argon. Scan rate: 50 mV s^{-1}.

It is difficult to compare the peak potentials for the anodic peak. However, the potential shifts in the cases of waves I_c and II_c were found to be 700 and 600 mV, respectively, which was similar to the value of –780 mV expected for a H^+/e^- process. Therefore, H^+ ions certainly participate in the electrochemical transformations of PdPc. The changes of shape and magnitude of the EQCN responses show an increasing participation of species heavier than protons, which are obviously anions.

Usually, a rather simple scheme for the electrochemical transformations has been suggested when the central ion (*e.g.*, Me = Mg, Pt or Pd) does not undergo a redox process:

$$Me^{2+}Pc^{2-} + A^- \rightleftharpoons Me^{2+}Pc^-A^- + e^- \quad (1)$$

which, in the case of solid phase electrochemistry, necessarily involves the incurporation of an anion (A^-) in the layer. The removal of an electron from the ring renders the phthalocyanine conductive.

However, it was also suggested[10] that water molecules and/or OH^- could participate in the redox process as follows:

$$MePc \cdot H_2O \rightleftharpoons MePc^+OH^- + H^+ + e^- \quad (2)$$

which may explain the observed pH dependence.

From the obtained EQCN results taking into account also the shift of the peak potentials, it can be assumed that PdPc is protonated in its reduced form in aqueous acidic media and counter-ions compensate the positive charge, which are already present in the surface layer of microcrystals. During oxidation, H_3O^+ leaves the layer, and the exchange of anions is a minor process (see Scheme 1).

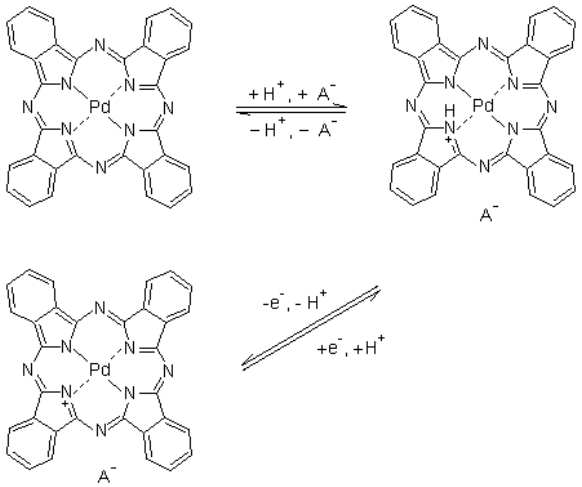

Scheme 1. The protonation equilibrium and the ionic exchange process during the electrochemical transformation of PdPc.

Surprisingly, the shift of the peak potentials as a function of concentration of sulfuric acid was previously assigned to the concentration changes of the anions,[33] albeit the shift observed was just the opposite to that expected based on the Nernst Law. However, an influx of protons was also assumed at short time scales. In sodium sulfate solutions, sorption and desorption of cations were also considered. With increasing pH and high positive potentials, the incorporation and expulsion of anions during the oxidation and reduction processes, respectively, would become the dominant process. In different non-aqueous solutions, only anion exchange was observed for conditioned PdPc layers,[29] which is understandable since no protonation could occur.

Of course, this is a rather simplified scheme since PdPc, as other metallic phthalocyanines, exists in different forms (monomeric and dimeric[29]), it has different degrees of crystallinity that change during electrochemical treatments.[30] Phase transitions can also occur during electrochemical transformation, which manifest themselves in a large separation of the respective pairs of waves, since additional energy is required to create a solid–solid interface between the reduced and non-reduced forms.[51–53] The phase transitions also influence the EQCN response because surface structural changes cause strain in the surface layer that can lead to anomalously large frequency changes (M values),[53–58] *i.e.*, the M values that are calculated from the frequency change and the charge will not be the same as the molar masses of the exchanged, charged species, counter-ions or hydrated protons that enter the layer consisting of microcrystals to maintain electroneutrality. Solvent sorption–desorption accompanying the charging–discharging processes and the phase transition may also affect the M values that can be derived from the EQCN data. Phase transition and dehydration–hydration are the only explanation for the very high but reversible frequency change observed in alkaline media during the initial oxidation and re-reduction (Curve 3, Fig. 10), where $M = 1025\pm75$ g mol^{-1} was calculated. Other factors that should be considered for the elucidation of the rather complex mass change pattern as a function of potential are the spontaneous binding and removal of O_2 (especially when an oxygen-saturated solution is used), H_2O_2 (formed during the reduction of oxygen molecules) and OH^- in alkaline media, the effects of which depend on the nature of the central metal ion and are therefore responsible for the different catalytic activities.[41]

Detailed analysis of the EQCN responses

In order to emphasize the important features, two characteristic cyclic EQCN curves obtained after several cycles are discussed below.

When wave II_a appears, a mass decrease could be detected in this region in acidic solutions (Fig. 14). The calculated molar mass was $M = 20\pm2$ g mol^{-1}, which may be interpreted as the loss of a H_3O^+ per electron. Although, some

detachment (dissolution) of the oxidized PdPc cannot be excluded, the observed effect is certainly due to the exchange of one or more species between the surface layer and the solution. (In the case of detachment, the mass loss would be permanent and higher, while here the original frequency value was more or less regained, albeit slowly.)

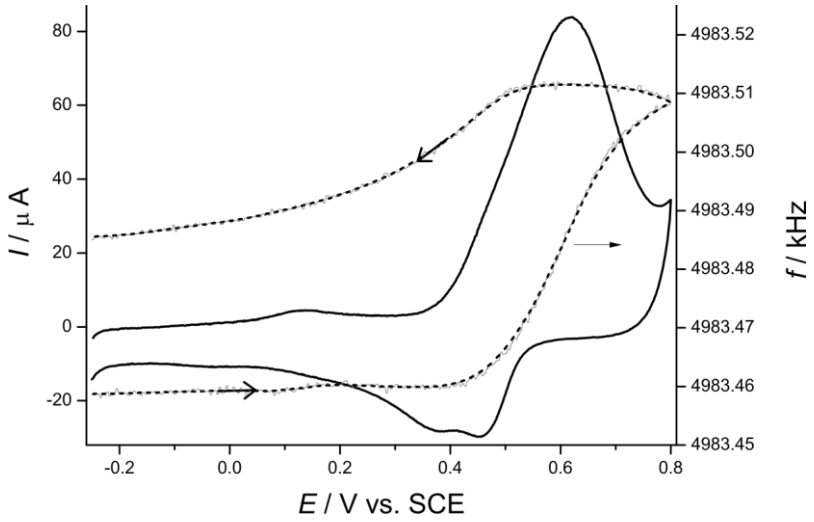

Fig. 14. Cyclic voltammogram (solid line) and the simultaneously obtained EQCN frequency curve (dashed line) obtained for PdPc microcrystals attached to Au. Electrolyte: 0.5 mol dm^{-3} deaerated sulfuric acid. Scan rate: 10 mV s^{-1}.

Even more instructive is the analysis of the EQCN curves obtained for a Pt–PdPc electrode at a slow scan rate (Fig. 15).

A slight mass increase could be observed in the region where no redox process occurs, *i.e.*, it is due to double layer charging. On reaching the region of peak I_a, a substantial frequency increase occurred. However, it became evident that wave I_a, in fact, consisted of two waves. At the second peak at more positive potentials, a large frequency decrease occurred that continued until positive current flowed during the reverse scan. No frequency change was observed until the reduction commenced at wave I_c, where a frequency increase occurred. However, this relatively small frequency increase was followed by a more intense frequency decrease that continued after wave II_c, with a lower slope until the end of the cathodic cycle. It is evident that no dissolution processes occurred in the regions of intense frequency increase, since at the end of the cycle, an overall mass gain was obtained. From the Δf *vs*. Q plots, the following values for the apparent molar masses were calculated. In the region of peak I_a, M = 230.6±20 g mol^{-1} was calculated for the "mass decrease" (the error is estimated herein since it was calculated from this, single measurement), while for the "mass increase" at

the wave at the more positive potential M = 213±20 g mol^{-1} was found. There are two possible explanations. First, at low scan rates, there is enough time for the solvent transport to be completed, and the deprotonation was accompanied by intense dehydration of the PdPc layer. This was followed by the incorporation of hydrated anions. However, it is likely that a phase transition also occurred in this region, which was partially responsible for the dehydration–hydration processes. This is supported by the analysis of the cathodic scan where, at peak I_c, a frequency increase–decrease pattern was observed that is characteristic of phase transition processes and the respective stress generated in the surface layer as well as of dehydration–hydration phenomena.[54–58] Here M = 156±20 g mol^{-1} and 258±20 g mol^{-1} were calculated for the regions of frequency increase and decrease, respectively. For the potential region less positive than the peak potential of II_a, a value of M = 18±2 g mol^{-1} was obtained, which might be due to slow rehydration of the layer.

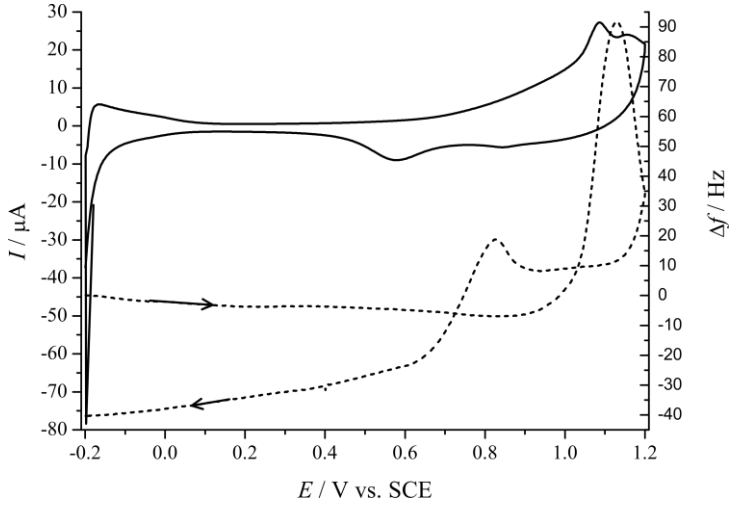

Fig. 15. Cyclic voltammograms (solid line) and the simultaneously obtained EQCN frequency changes (dashed line) for a Pt|PdPc electrode. Cycling was started from the open-circuit potential. Electrolyte: 1 mol dm^{-3} deaerated sulfuric acid. Scan rate: 2 mV s^{-1}.

CONCLUSIONS

The shape of the cyclic voltammograms, *i.e.*, the number of oxidation and reduction peaks and their relative ratios depend on several factors, such as the potential limits, presence and absence of oxygen, the type of the substrate, the nature and the concentration of the electrolyte, as well as the layer thickness and the method of the deposition.

In aqueous acidic media, PdPc is protonated in its reduced form and counter-ions compensate the positive charge; therefore, they are already present in the

surface layer. During oxidation, H_3O^+ leave the layer of microcrystals and the exchange of anions is a minor process in acid media except at high positive potentials. With increasing pH, the incorporation and expulsion of anions during the oxidation and reduction processes, respectively, becomes the dominant process.

Phase transitions also occur during the electrochemical transformations, which manifest themselves in the large separation of the respective pair of waves. The phase transition also influences the EQCN response because the surface structural changes cause strain in the surface layer, which leads to anomalously large frequency changes. Solvent sorption–desorption accompanies the charging––discharging processes and the phase transitions.

It was also observed that even at high positive potential limits, the presence of PdPc hinders the formation of gold or platinum oxide, respectively, as well as the hydrogen adsorption on Pt in the hydrogen UPD region.

Acknowledgements. Financial support of the National Scientific Research Fund (OTKA K100149) and TÁMOP-4.2.2/B-10/1-2010-0030 is gratefully acknowledged. One of the authors (Á. Nemes) is grateful for the support of the European Union and the State of Hungary, co-financed by the European Social Fund within the framework of TÁMOP 4.2.4. A/-11-1-2012-0001 "National Excellence Program".

ИЗВОД

ЕЛЕКТРОХЕМИЈСКО И НАНОГРАВИМЕТРИЈСКО ИСПИТИВАЊЕ МИКРОКРИСТАЛА ПАЛАДИЈУМ-ФТАЛОЦИЈАНИНА

ÁKOS NEMES, COLIN E. MOORE и GYÖRGY INZELT

Department of Physical Chemistry, Institute of Chemistry, Eötvös Loránd University, Pázmány Péter sétány 1/A, 1117 Budapest, Hungary

Електрохемијска кварцна нановага је коришћена за испитивање редокс трансформација микрокристала паладијум-фталоцијанина који су били депоновани на злато и платину у растворима различитих вредности pH. Да би се испитао ефекат супстрата, коришћена је и графитна електрода импрегнирана парафином. Показано је да су редокс трансформације паладијум-фталоцијанина праћене процесима депротонације–протонације као и сорпције и десорпције јона супротног наелектрисања, респективно, при чему њихов степен зависи од вредности pH раствора. На основу резултата наногравиметријских мерења предложен је механизам који објашњава зависност поменутих процеса од pH. Такође је утврђено да се истовремено са процесима прелаза наелектрисања одигравају и фазни прелази чврсто–чврсто и транспорт воде.

(Примљено 9. ссептембра, ревидирано 19. септембра 2013)

REFERENCES

1. R. P. Linstead, *J. Chem. Soc*. (1934) 1016, 1017, 1022, 1027, 1031, 1033
2. A. B. P. Lever, J. P. Wilshire, *Can. J. Chem.* **54** (1976) 2514
3. J. Zagal, P. Bindra, E. Yeager, *J. Electrochem. Soc.* **78** (1978) 1345
4. B. Z. Nikolić, R. R. Adzić, E. B. Yeager, *J. Electroanal. Chem.* **103** (1979) 281
5. J. Zagal, P. Bindra, E. Yeager, *J. Electrochem. Soc.* **127** (1982) 1506

6. D. A. Scherson, S. B. Yao, E. B. Yeager, J. Eldridge, M. E. Kordesch, R. W. Hoffman, *J. Phys. Chem.* **87** (1983) 932
7. B. Simic-Glavaski, S. Zecevic, E. Yeager, *J. Electroanal. Chem.* **150** (1983) 469
8. G. C. S. Collins, D. J. Schiffrin, *J. Electrochem. Soc.* **132** (1983) 1835
9. O. Contamin, E. Levart, G. Mangner, R. Parsons, M. Savy, *J. Electroanal. Chem.* **179** (1984) 41
10. J. L. Kahl, L. R. Faulkner, K. Dwarakanath, H. Tachikawa, *J. Am. Chem. Soc.* **108** (1986) 5434
11. A. Elzing, A. Van der Putten, W. Visscher, E. Barendrecht, *J. Electroanal. Chem.* **233** (1987) 99
12. F. Castaneda, V. Plichon, *J. Electroanal. Chem.* **233** (1987) 77
13. F. Castaneda, V. Plichon, *J. Electroanal. Chem.* **236** (1987) 163
14. C. Paliteiro, A. Hamnett, J. B. Goodenough, *J. Electroanal. Chem.* **239** (1988) 273
15. P. He, J. Lu, C. Cha, *J. Electroanal. Chem.* **290** (1990) 203
16. P. He, P. Crouigneau, B. Beden, C. Lamy, *J. Electroanal. Chem.* **290** (1990) 215
17. R. Jansen, F. Beck, *Electrochim. Acta* **39** (1994) 921
18. S. Komorsky-Lovric, *J. Electroanal. Chem.* **397** (1995) 211
19. I. L. Kogan, K. Yakushi, *Electrochim. Acta* **43** (1998) 2053
20. J. Jiang, A. Kucernak, *J. Electroanal. Chem.* **490** (2000) 17
21. J. Jiang, A. Kucernak, *Electrochim. Acta* **45** (2000) 2227
22. J. Jiang, A. R. Kucernak, *Electrochim. Acta* **46** (2001) 3445
23. R. J. C. Brown, A. R. Kucernak, *Electrochim. Acta* **46** (2001) 2573
24. D. Geraldo, C. Linares, Y. Y. Chen, S. Ureta-Zanartu, J. H. Zagal, *Electrochem. Comm.* **4** (2002) 182
25. C. Linares, D. Geraldo, M. Paez, J. H. Zagal, *J. Solid State Electrochem.* **7** (2003) 626
26. C. A. Caro, J. H. Zagal, F. Bedioui, *J. Electrochem. Soc.* **150** (2003) E95
27. J. Mi, L. Guo, Y. Liu, W. Liu, G. You, S. Qian, *Phys. Lett., A* **310** (2003) 486
28. R. J. C. Brown, A. R. Kucernak, *J. Solid State Electrochem.* **9** (2005) 459
29. L. Gaffo, D. Goncalves, R. C. Faria, W. C. Moreira, O. N. Oliveira Jr., *J. Porphyrins Phthalocyanines* **9** (2005) 16
30. L. Gaffo, M. J. S. P. Brasil, F. Cerdeira, C. Giles, W. C. Moreira, *J. Porphyrins Phthalocyanines* **9** (2005) 89
31. P. A. Koca, H. A. Dincer, M. B. Kocak, A. Gül, *Russ. J. Electrochem*. **42** (2006) 31
32. M. Arıcı, D. Arıcan, A. Lütfi Ugur, A. Erdogmus, A. Koca, *Electrochim. Acta* **87** (2013) 554
33. R. J. C. Brown, D. J. L. Brett, A. R. J. Kucernak, *J. Electroanal. Chem.* **633** (2009) 339
34. K. Sakamoto, E. Ohno-Okumura, *Materials* **2** (2009) 1127
35. S. Yamazaki, N. Fujiwara, K. Yasuda, *Electrochim. Acta* **55** (2010) 753
36. Y. Yuan, B. Zhao, Y. Jeon, S. Zhong, S. Zhou, S. Kim, *Bioresour. Technol.* **102** (2011) 5849
37. I. A. Akinbulu, K. I. Ozoemena, T. Nyokong, *J. Solid State Electrochem.* **15** (2011) 2239
38. I. Ponce, J. F. Silva, R. Onate, M. C. Rezende, M. A. Páez, J. Pavez, J. H. Zagal, *Electrochem. Comm.* **13** (2011) 1182
39. C. Selvaraj, N. Munichandraiah, L. G. Scanlon, *J. Porphyrins Phthalocyanines* **16** (2012) 255
40. A. O. Ogunsipe, M. A. Idowu, T. B. Ogunbayo, I. A. Akinbulu, *J. Porphyrins Phthalocyanines* **16** (2012) 885
41. J. Guo, H. He, D. Chu, R. Chen, *Electrocatalysis* **3** (2012) 252

42. J. H. Zagal, I. Ponce, D. Baez, R. Venegas, J. Pavez, M. Paez, M. Gulppi, *Electrochem. Solid-State Lett*. **15** (2012) B90
43. *Phthalocyanines: Properties and Applications*, Vols. 1–4, C. C. Leznoff, A. P. B. Lever, Eds., VCH Publ., New York, 1989–1996,
44. G. de la Torre, M. Nicolau, T. Torre, in *Phthalocyanines: Properties and Applications and Electroactive Materials*, H. S. Nalwa, Ed., Academic Press, New York, 2001, pp. 1––111
45. N. M. Alpatova, E. V. Ovsyannikova, in *Electropolymerization*, S. Cosnier, A. Karyakin, Eds., Wiley–VCH, Weinheim, Germany, 2010, p. 111
46. F. Scholz, U. Schröder, R. Gulaboski, *Electrochemistry of Immobilized Particles and Droplets*, Springer, Berlin, 2005, p. 114
47. B. B. Berkes, A. Székely, G. Inzelt, *Electrochem. Commun*. **12** (2010) 1095
48. G. Inzelt, B. B. Berkes, Á. Kriston, *Electrochim. Acta* **55** (2010) 4742
49. G. Sauerbrey, *Z. Phys*. **155** (1959) 206
50. F. Scholz, B. Meyer, in *Electroanalytical Chemistry, A Series of Advances*, Vol. 20, A. J. Bard, I. Rubinstein, Eds., Marcel Dekker, New York, 1998, p. 1
51. R. Ramaray, C. Kabbe, F. Scholz F, *Electrochem. Commun.* **2** (2000) 190
52. F. Scholz, M. Lovric, Z. Stojek, *J. Solid State Electrochem*. **1** (1997) 134
53. M. F. Suárez, A. M. Bond, R. G. Compton, *J. Solid State Electrochem*. **4** (1999) 24
54. C. D. Evans, J. Q. Chambers, *Chem. Mater.* **6** (1994) 454
55. M. Hepel, W. Janusz, *Electrochim Acta* **45** (2000) 3785
56. J. Wang, L. M. Frostman, M. D. Ward, *J. Phys. Chem*. **96** (1992) 5224
57. G. Inzelt, Z. Puskas, *Electrochem. Commun*. **6** (2004) 805
58. G. Inzelt, A. Róka, *Israel J. Chem*. **48** (2008) 185.

Journal of the Serbian Chemical Society
JSCS-info@shd.org.rs • www.shd.org.rs/JSCS

J. Serb. Chem. Soc. 78 (12) 2039–2052 (2013)
JSCS–4549

UDC 546.732+547.584.463.1'052.1+
547.288.3:66.094.3:544.4–44
Original scientific paper

Unusual behaviour of perfluorinated cobalt phthalocyanine compared to unsubstituted cobalt phthalocyanine for the electrocatalytic oxidation of hydrazine. Effect of the surface concentration of the catalyst on a graphite surface

JOSÉ H. ZAGAL[1]*, DANIELA A. GERALDO[2], MAMIE SANCY[3] and MARITZA A. PAEZ[1]

[1]*Facultad de Química y Biología, Departamento de Química de los Materiales Universidad de Santiago de Chile, Casilla 40, Correo 33, Sucursal Matucana, Santiago 9170022, Chile,* [2]*Departamento de Ciencias Químicas, Facultad de Ciencias Exactas, Universidad Andrés Bello. República 275, Santiago, Chile and* [3]*Fuerza Aérea de Chile, Academia Politécnica Aeronáutica, José Miguel Carrera 11085, El Bosque, Santiago, Chile*

(Received 24 October 2013)

Abstract: It was found that CoPc and 16(F)CoPc when adsorbed on a graphite electrode exhibited voltammograms in alkaline solution (0.2 M NaOH) that show the typical redox peaks attributable to the reversible Co(II)/(I) redox process. The peak potential for CoPc was independent of the surface concentration of the catalyst. In contrast, for 16(F)CoPc, the Co(II)/(I) redox process shifted to more negative potentials with increasing surface concentration of the catalyst. In a volcano correlation of log $(i/\Gamma)_E$ (activity per active site) *versus* the Co(II)/(I) formal potential of the catalyst (using several CoN4 chelates), CoPc appeared in the ascending portion (the activity increased with the Co (II)/(I) redox potential), whereas 16(F)CoPc appeared in the region where the activity decreases with the redox potential. In a plot of log $(i/\Gamma)_E$ *versus* the Co(II)/(I) formal potential of 16(F)CoPc, the declining portion of the volcano was reproduced for one single complex. Thus, 16(F)CoPc at different surface concentrations behaved as Co complexes, having different redox potential in the declining portion of the volcano plot, when the activity is normalized to the surface concentration. This was not observed for CoPc.

Keywords: cobalt phthalocyanine; cobalt-hexadecafluoro-phthalocyanine; surface concentration-dependent redox potential; hydrazine oxidation; electrocatalysis.

* Corresponding author. E-mail: jose.zagal@usach.cl
doi: 10.2298/JSC131024123Z

INTRODUCTION

Hydrazine (N_2H_4) is a powerful reducing agent, which can be employed in the anode in fuel cells.[1–5] Hydrazine and its derivatives are frequently found in the environment and are used as essential raw materials and/or intermediates in some industrial preparations, such as in the production of pesticides, but they are also suspected of being carcinogenic and mutagenic.[6] However, in spite of its high reactivity, hydrazine presents a rather large oxidization overpotential on most electrode materials.[7] One approach for minimizing the overpotential of the reaction is the use of chemically modified electrodes (CMEs), which contain specifically selected redox mediators immobilized on conventional materials, such as glassy carbon and graphite. Metallophthalocyanine-modified electrodes have been extensively studied due to their electrocatalytic activity for numerous reactions.[8–20] In the past years, various chemically modified electrodes have been prepared and employed in the determination of hydrazine, including cobalt phthalocyanine-modified carbon paste electrodes, ruthenium cyanide film-coated electrodes, cobalt tetraphenylporphyrin-modified electrodes, an inorganic mixed-valent Prussian Blue film-coated electrode, an oxymanganese film-modified electrode and an adsorbed vitamin B_{12} electrode.[21–38] However, in spite of the great variety of modified electrode systems studied for the oxidation of hydrazine, there are only a few systematic studies on the parameters that control the activity of these electrodes,[29–32,38,39] including theoretical calculations.[40–43] In particular, one reactivity parameter that has been studied in some detail is the effect of M(II)/(I) or M(III)/(II) formal potential of MN4 catalysts on their electrocatalytic activity, with the employed formal potential depending on the reaction.[22–24,29–32,38,39] For example, when comparing catalytic activities as currents at a constant potential, normalized to the surface concentration of the catalyst, Γ (mol cm^{-2}), nonlinear correlations of log $(i/\Gamma)_E$ *vs.* $E^{\circ\prime}$ (the formal potential of the M(II)/(I) catalyst) were obtained,[29–32,38,39] and this was not only true for hydrazine oxidation, but for other reactions as well.[11,16,17,18,32] The correlations have the shape of a volcano, indicating that the formal potential of the catalysts need to be "tuned" to a given value for the highest catalytic activity to be obtained. For hydrazine oxidation, this was corroborated for Fe and Co MN4 macrocyclic complexes.[29–32,38,39] For typical volcano correlations, the activity is plotted *versus* a parameter that accounts for the degree of interaction of the reacting molecule with the active site. Thus, the "ascending" portion of the volcano corresponds to catalysts where the binding energy of the reacting molecule is weak but increases gradually until the optimal condition (not too weak, not too strong according to the Sabatier principle) is achieved. For gradually stronger binding energies, the catalytic activity decreases since the active sites become gradually blocked by adsorbed intermediates. Hence, it is of interest to compare catalysts that are in different branches of the volcano correlation. As shown in previous studies for

the oxidation of hydrazine, Co phthalocyanine (CoPc) is located on the ascending portion of the volcano correlation (see Fig. 1), whereas perfluorinated Co phthalocyanine 16(F)CoPc, which exhibits the most positive Co(II)/(I) formal potential of the studied phthalocyanines, appears on the extreme side of the "falling region" of the volcano correlation.[29,32,39] In this work, it was found that the redox properties of 16(F)CoPc were dependent on the surface concentration of the catalysts and this affects the intrinsic activity of this complex. For this reason, there are two data points for 16(F)CoPc in Fig. 1 and reported in different publications.[29,32]

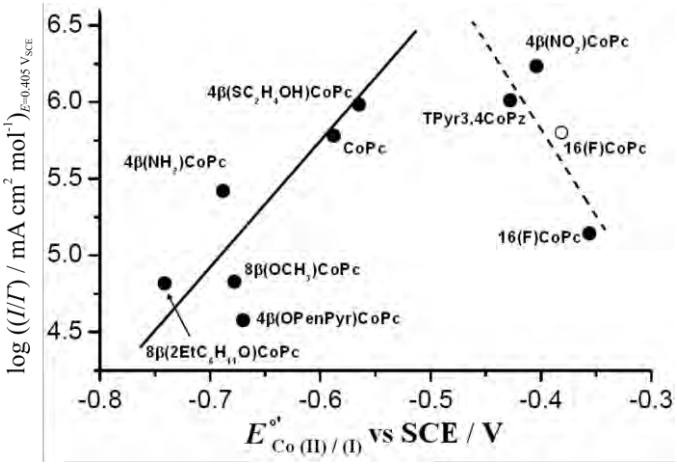

Fig. 1. Volcano correlation for the oxidation of hydrazine in 0.05 M [N_2H_4] N_2 saturated 0.1 M NaOH solutions (data ●[32] and data ○[29]). Reproduced by permission of the Electrochemical Society.

EXPERIMENTAL

Cobalt phthalocyanine (CoPc) and cobalt-hexadecafluoro-phthalocyanine (16(F)CoPc) were obtained from Aldrich and used as provided. All other products were of analytical reagent grade and used as received. The working electrode was an ordinary pyrolytic graphite (OPG) disk electrode from Pine Instruments (USA) with a geometrical area of 0.44 cm^2. The electrodes were polished before each experiment with 800 and 2400 grit emery paper followed by an extensive ultrasonic rinsing with ultra-pure Milli-Q water to remove solid particles. The electrochemical experiments were performed with a conventional three-electrode cell and a BAS-100 potentiostat (USA) or Autolab PGST30 potentiostat/galvanostat (The Netherlands). A spiral platinum wire of 2 cm^2 geometric area was used as the counter electrode and a saturated calomel electrode, SCE, as the reference electrode. Electrolytic solutions were routinely deoxygenated with pure nitrogen. All the potential values are given *versus* the saturated calomel electrode SCE. The electrolyte was aqueous 0.2 M NaOH, solution prepared in double-distilled water and deaerated with ultra pure N_2. CoPc and 16(F) $CoF_{16}Pc$ were adsorbed onto the OPG electrode by, respectively, placing a drop of 0.1 mM solution of the CoPc and 16(F)CoPc complexes in dimethylformamide (DMF) for various time intervals,

ranging from 10 to 1200 s on the graphite surface. After this procedure, the electrodes were rinsed with DMF, ethanol and double-distilled water, in order to remove any excess of the metal complexes. This procedure avoids the presence of microcrystals on the graphite surface, so the electrochemical response of the electrode can be attributed solely to molecules that are adsorbed on the electrode. Adsorption of all complexes was verified by the appearance of typical current peaks in the cyclic voltammograms of the modified electrodes.[21-25,29,31,32,38,39] Hydrazine was obtained from Riedel-de Haën and used as provided. NaOH was A.R. grade from Merck.

RESULTS AND DISCUSSION

The structure of Co phthalocyanine and perfluorinated Co phthalocyanine and also the Fukui profiles, obtained from theoretical calculations[44] to graphically illustrate the effect of electron-withdrawing groups located on the ligand on the charge distribution on the Co central metal, are illustrated in Fig. 2. The blue colour indicates high electron density and the red colour indicates low electron density on the Co centre. As a result of substitution of H atoms by F in the Co phthalocyanine ligand, the electron-withdrawing substituents cause a large increase in the ionization potential (IP) of 16(F)CoPc and a lowering of the energy of the frontier orbitals,[40,45] compared to CoPc, which could be written as 16(H)PcCo, to indicate that the –H groups have been replaced by –F groups on the phthalocyanine ligand. This effect causes the Co(II)/(I) formal potential to shift to more positive values, as it becomes more difficult to oxidize the Co(II) centre in 16(F)CoPc compared to CoPc. This is clearly illustrated in Fig. 3, which shows the cyclic voltammograms obtained with an OPG electrode modified with adsorbed

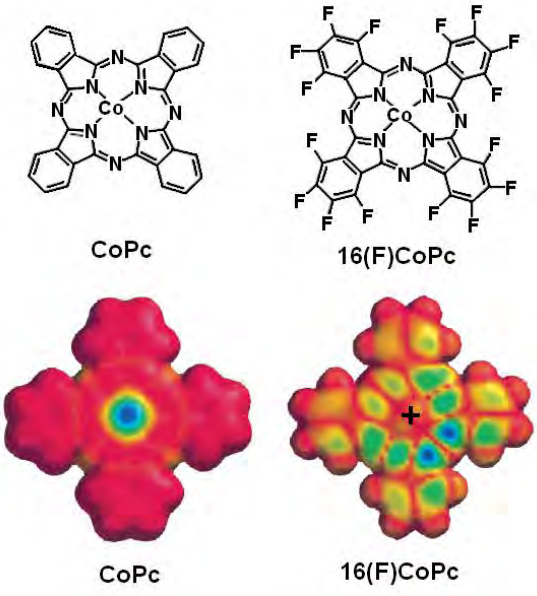

Fig. 2. Structures of CoPc (that can be written as 16(H)CoPc) and 16(F)CoPc) and the calculated Fukui profiles that illustrate the electron donating effect of the fluoro groups located on the ligand that shift electron density from the Co centre to the macrocycle ligand.[44] Reproduced by permission of the American Chemical Society.

layers of the examined cobalt phthalocyanines in a 0.2 M NaOH oxygen-free solution. CoPc exhibited a reversible peak at –0.59 V assigned to the reversible Co(II)/Co(I) couple.[9,21–24,29,39] For 16(F)CoPc, this process is shifted to more positive potentials (–0.33 V) by the effect of the electron-withdrawing groups, as discussed above. Indeed, it was shown in previous studies[9,11,17,18,21–24] that it is possible to "tune" the Co(II)/(I) formal potential of the catalyst by preparing CoPc phthalocyanines with groups on the ligand with different electron-withdrawing properties. Furthermore, a plot of Co(II)/(I) formal potential *versus* the sum of the Hammett parameters of the groups located on the ligand gave a linear correlation; hence, the redox properties of these complexes can be "tailored" to desired values, as discussed by Lever,[9] depending of the reaction and this is clearly demonstrated in the volcano correlation of Fig. 1.

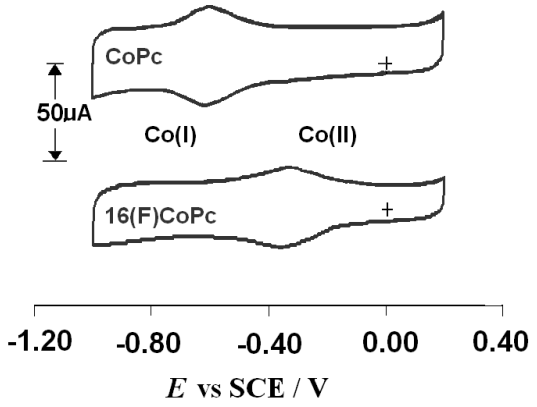

Fig. 3. Cyclic voltammograms of CoPc and 16(F)CoPc pre-adsorbed on an ordinary pyrolytic graphite electrode. Scan rate 0.1 V s^{-1}, N_2 saturated 0.2 M NaOH solution.

The surface concentration of the catalysts in Fig. 3 corresponded to the conditions where the OPG surface was saturated with phthalocyanine molecules, and this could be controlled by using different contact times between the solution of the complexes and the graphite surface during the modification procedure. For example, from the charge under the peaks in Fig. 3, it can be calculated that CoPc saturation was achieved at a surface concentration of 10×10^{-10} mol cm^{-2}, whereas for CoPc, surface saturation corresponded to a surface concentration of 6.8×10^{-10} mol cm^{-2}. This is not surprising since the size of the 16(F)CoPc molecule is larger than that of CoPc; hence, a lower surface concentration is expected for this particular complex, as 16(F)CoPc takes more room on the graphite than CoPc, assuming that they adsorb flat on the electrode surface.[46] The gradual increase in the surface concentration with modification time is illustrated in Fig. 4. For both complexes, the surface concentration exhibits an asymptotic behaviour with modification time, illustrating that the surface becomes saturated with the complexes after 800 s.

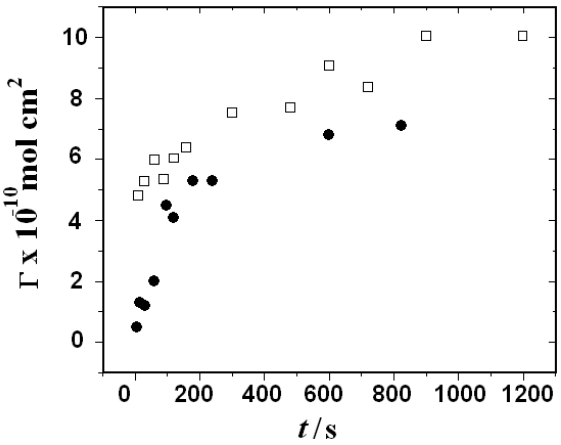

Fig. 4. Variation of the surface concentration for (□) CoPc and (●) 16(F)CoPc as a function of immersion time in 10^{-4} M solutions of the complexes at 20 °C, in the presence of air.

The cyclic voltammograms of the OPG electrode coated with different surface concentrations of 16(F)CoPc are shown in Fig. 5. The surface concentrations were estimated from the different electrical charges under the current peak, subtracting the capacitive currents. One interesting feature about the data in Fig. 5 is that, in contrast to that observed with CoPc, the peak potential shifts to more negative values with increasing concentration of the perfluorinated phthalocya-

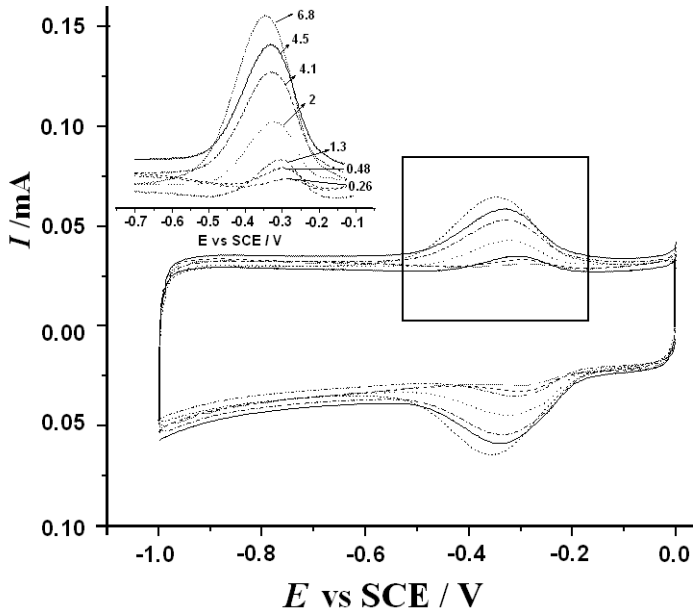

Fig. 5. Cyclic voltammograms of an OPG electrode modified with different surface concentrations of 16(F)CoPc. Potential scan rate: 0.2 V s^{-1}, electrolyte: 0.2 M NaOH, N_2 saturated.

nine. This effect is better illustrated in Fig. 6, in which the logarithm of surface molar concentration, Γ, is plotted *versus* the Co(II)/(I) formal potential found for the different concentrations.

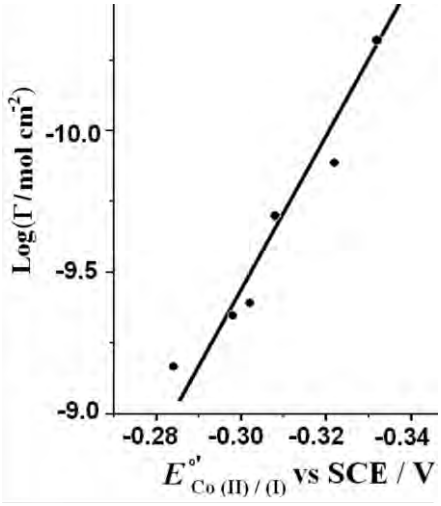

Fig. 6. Effect of the surface concentration of 16(F)CoPc on the Co(II)/(I) formal potential.

The slope of the linear correlation in Fig. 6 is –0.036 V per decade of log Γ. If there were no interactions between the l6(F)CoPc molecules, there would be no shift in the $E^{\circ\prime}$ Co(II)/(I) formal potential with variation of complex surface concentration, as was observed with CoPc.[29] The negative slope indicates that when Γ decreases, it is harder to oxidize the Co centre, *i.e.*, higher concentrations of l6(F)CoPc facilitate the reduction of Co(II); thus neighbouring molecules act as electron-withdrawing agents on the Co centre in one single molecule. The manner in which l6(F)CoPc is adsorbed on the graphite is unknown, but if they were to form stacks,[47] then only the molecules at the outermost should be active for a catalytic reaction, such as hydrazine oxidation. The catalytic activity of l6(F)CoPc should be independent of the surface coverage, at least in certain region of surface concentrations but, as it will be shown further on, this was not the case. From previous studies,[29,32,38] as illustrated in Fig. 1 (data taken from the literature,[30,32] shifting the formal potential to more negative values increases the catalytic activity of CoN4 macrocyclics when comparing to different complexes in one region of the volcano correlation. Thus, the activity per l6(F)CoPc molecule should decrease with dilution of the catalysts on the surface. To check this, the activity of OPG electrodes coated with different surface concentrations of 16(F)CoPc was examined and the same was realized with CoPc for comparison. This is illustrated in the polarization curves in Fig. 7. This data was further analysed in the Tafel correlations of Fig. 8. Correlations between $(\log i)_E$, current

densities at a constant potential taken from Fig. 8, and the logarithm of the surface concentration of the catalyst Γ are presented in Fig. 9.

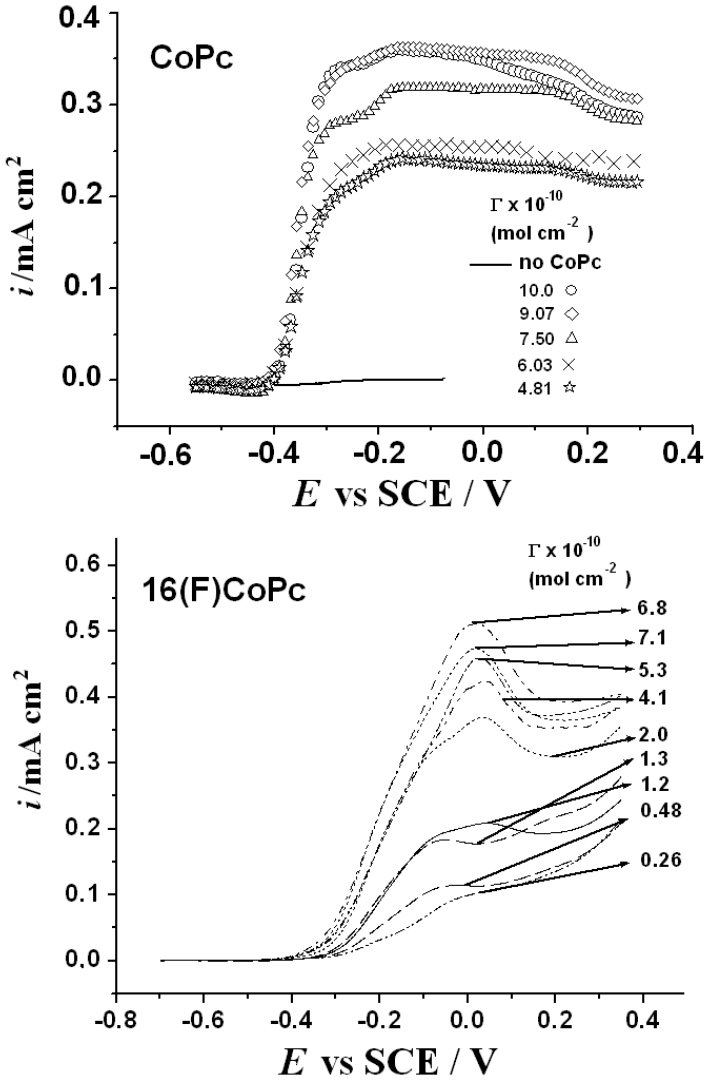

Fig. 7. Polarization curves of the chemically modified OPG electrode with different surface concentration of CoPc and 16(F)CoPc, in the presence of 5×10^{-4} M of hydrazine in 0.2 M NaOH solution saturated with N_2. Scan rate: 0.005 V s^{-1}.

Further analysis of the electrocatalytic process to assess the reaction order in surface concentration of the catalysts CoPc and 16(F)CoPc was performed by plotting log i at constant potential ($E = -0.35$ V) *versus* log Γ (shown in Fig. 9).

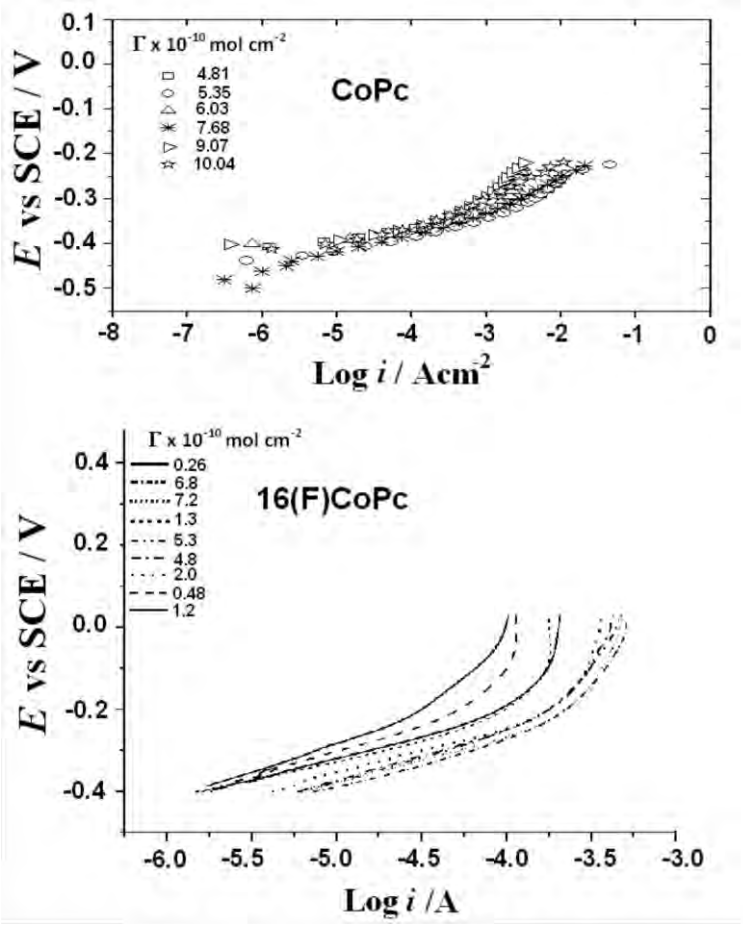

Fig. 8. Tafel plots for the oxidation of hydrazine on OPG modified with CoPc and 16(F)CoPc. Effect of surface concentration of the catalyst on the oxidation currents. Data obtained from Fig. 7.

In both cases, a linear correlation was observed, indicating that the catalytic currents increase linearly with the surface concentration of the catalyst. The order of the reaction in catalyst surface concentrations is $(\mathrm{d}(\log I)/\mathrm{d}\Gamma)_E$ and can be obtained from the slopes of the linear correlations in Fig. 9. For CoPc the slope was 1.2, so the reaction order could be considered to be one. However, for 16(F)CoPc, a fractional order of 0.58 was obtained. It might be difficult to explain an order close to 1/2 for this particular catalyst. However, further information could be obtained from kinetic data for this particular catalyst by plotting log (i/Γ) at constant potential *versus* the Co(II)/(I) redox potential for each particular surface concentration Γ of 16(F)CoPc. An interesting result was obtained that is illustrated in Fig. 10A. The activity normalized per surface concentration of the

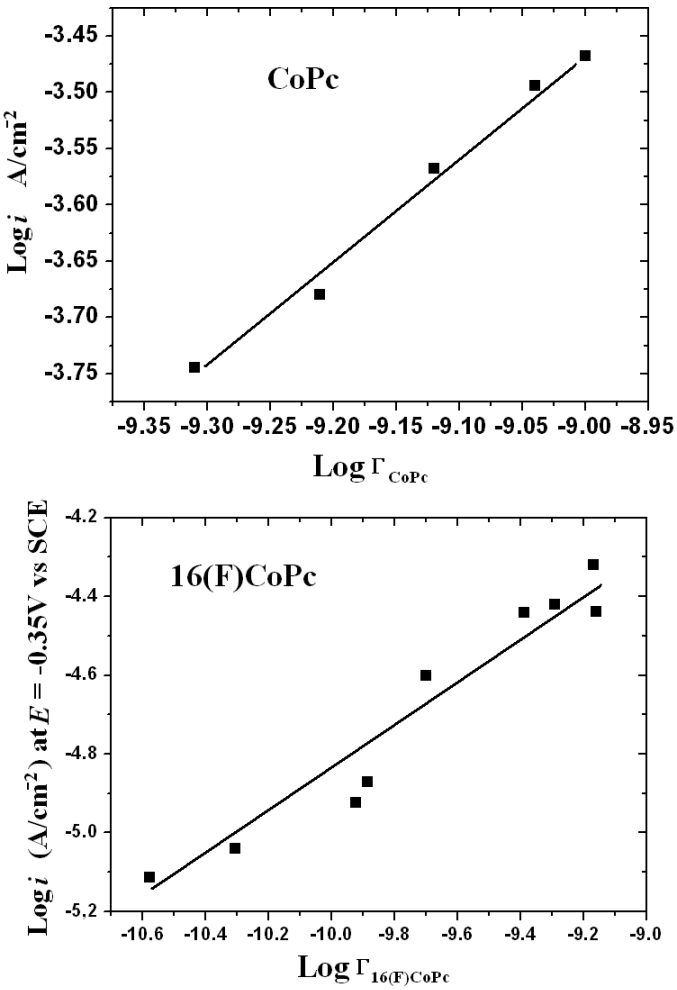

Fig. 9. Effect of catalyst surface concentration on the currents (as log *i* at constant potential) for the oxidation of hydrazine for CoPc and 16(F)CoPc. Data taken from Tafel plots in Fig. 8.

catalyst decreased with the formal potential, in a similar fashion to that observed in one of the branches of the volcano correlation of Fig. 1. Thus 16(F)CoPc at different surface concentrations behaves as if it were different Co complexes, so essentially it agrees with that observed in Fig. 1, *i.e.*, with one single complex, 16(F)CoPc, it is possible to reproduce the falling region of the volcano correlation. Since the activities were compared at –0.35 V, which is close to the Co(II)/(I) formal potentials observed for different surface concentration of 16(F)CoPc, it could be of interest to plot log $(i/\Gamma_{\mathrm{Co(II)}})_E$, *i.e.*, current divided by the surface concentrations of Co(II) calculated form the Nernst equation, assum-

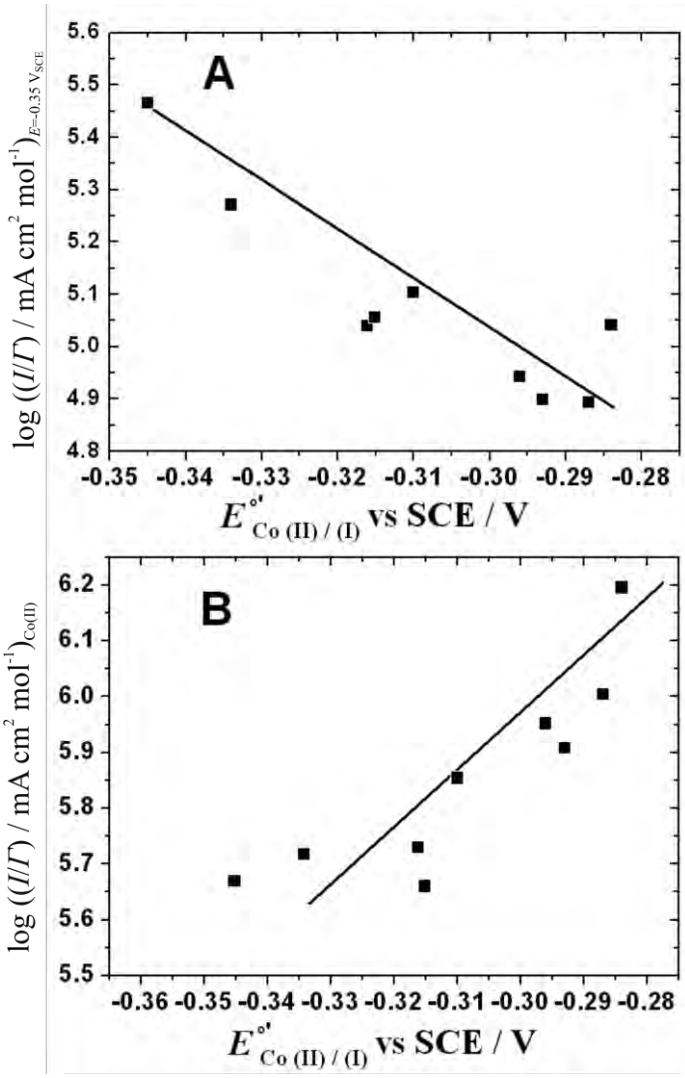

Fig. 10. A) Plot of log (i/Γ) at E = –0.35 V *vs*. the formal potential of the catalyst for a given Γ, the total surface concentration of 16(F)CoPc. Currents taken from the region of Tafel plots of Fig. 7 under kinetic control. B) The same as in (A) but currents are divided by the surface concentration of 16(F)Co(II)Pc, *i.e*., the real surface molar concentrations of the Co(II) active sites.

ing that the active sites are Co(II). Such a plot is illustrated in Fig. 10B. A linear correlation was again obtained but with a positive slope, *i.e*., the catalytic activity per Co(II) active site increased with increasing Co(II)/(I) redox potential of the catalyst. Fig. 10B is a free energy correlation since $i/\Gamma_{Co(II)}$ is proportional to the rate constant k at that electrode potential and the redox potential is proportional

to the driving force of the system. This type of behaviour was also observed for the catalytic oxidation of Fe phthalocyanines,[38] by comparing different Fe macrocyclics in a volcano correlation, when the currents in the falling regions were divided by the surface concentration of Fe(II) active sites, and the volcano becomes a linear correlation. The slope of the linear correlation in Fig. 10B is close to 0.120 V decade^{-1}, which is the same slope as that observed for the "linearized" volcano correlation for Fe complexes reported previously.[38] Furthermore, the linear correlation shown in Fig. 10B is similar to a linear Tafel correlation when the applied potential is the driving force of the reaction. In Fig. 10B, where the activities are compared at constant electrode potential, the "extra" driving force is provided by the M(II)/(I) redox potential of the catalyst.

CONCLUSIONS

It was found that the Co(II)/(I) formal potential of 16(F)CoPc adsorbed on graphite shifted to more negative values with increasing surface concentration of this catalyst. This was not observed for the unsubstituted CoPc. It is not clear why this phenomenon was observed for 16(F)CoPc since the exact orientation of these molecules on the graphite surface is unknown. If they formed stacks, instead of monolayers, it would be expect that only the molecules located at the outermost position in a stack would exhibit activity, since hydrazine molecules would not have access to 16(F)CoPc molecules located below. In this case, the correlations between $(\log i)_E$ might not be linear or should show linear behaviour only at low concentrations of 16(F)CoPc. This was not observed. However, some interaction between neighbouring 16(F)CoPc molecules could occur to affect the Co(II)/(I) formal potential, which does not occur with CoPc. When comparing the catalytic activities of electrodes coated with different surface concentrations of 16(F)CoPc, as $\log(i/\Gamma)$ (Γ is the total surface concentration of 16(F)CoPc) *versus* the Co(II)/(I) formal potential, it was possible to reproduce the falling region of a volcano correlation obtained by comparing the activity of several CoN4 macrocyclics and reported previously.[11,29,32,39] If the same plot is repeated using the surface concentration of Co(II) active sites at the potential used for the comparisons, *i.e.*, $\Gamma_{Co(II)}$, the activity per active site increases with the driving force of the catalyst, producing what could be considered a linear free energy correlation, with a slope close to 0.120 V decade^{-1}.

Acknowledgement. This work was supported by Fondecyt Project 1100773 and by Núcleo Milenio de Ingeniería Molecular P07-006-F.

ИЗВОД

НЕУОБИЧАЈЕНО ПОНАШАЊЕ ПЕРФЛУОРОВАНОГ КОБАЛТ-ФТАЛОЦИЈАНИНА У ПОРЕЂЕЊУ СА НЕСУПСТИТУИСАНИМ КОБАЛТ-ФТАЛОЦИЈАНИНОМ У ЕЛЕКТРОКАТАЛИТИЧКОЈ ОКСИДАЦИЈИ ХИДРАЗИНА. ЕФЕКАТ ПОВРШИНСКЕ КОНЦЕНТРАЦИЈЕ КАТАЛИЗАТОРА НА ПОВРШИНИ ГРАФИТА

JOSÉ H. ZAGAL[1], DANIELA A. GERALDO[2], MAMIE SANCY[3] и MARITZA A. PAEZ[1]

[1]Facultad de Química y Biología, Departamento de Química de los Materiales, Universidad de Santiago de Chile, Casilla 40, Correo 33, Sucursal Matucana, Santiago 9170022, Chile, [2]Departamento de Ciencias Químicas, Facultad de Ciencias Exactas, Universidad Andrés Bello, República 275, Santiago, Chile и [3]Fuerza Aérea de Chile, Academia Politécnica Aeronáutica, José Miguel Carrera 11085, El Bosque, Santiago, Chile

Циклични волтамограми CoPc и 16(F)CoPc адсорбованих на графитној електроди у алкалној средини (0,2 M NaOH) показују типичне реверзибилне редокс пикове који потичу од Co(II)/(I) реакције. Потенцијал пика за CoPc не зависи од површинске концентрације катализатора, али се за 16(F)CoPc са повећањем површинске концентрације катализатора помера ка негативнијим вредностима. У делу „вулканске“ корелације log $(i/\Gamma)_E$ (активност по активном месту) према Co(II)/(I) формалном потенцијалу катализатора, понашање CoPc (у неколико CoN4 хелата) показује тенденцију раста (активност се повећава са Co(II)/(I) редокс потенцијалом), док се 16(F)CoPc појављује у области у којој активност опада са редокс потенцијалом. Област опадања активности 16(F)CoPc репродукована је само за један појединачни комплекс. Отуда се 16(F)CoPc различитих површинских концентрација понаша као Co комплекси који имају различите редокс потенцијале у опадајућој области „вулканске“ криве, ако се активност нормализује по површинској концентрацији. Ово није опажено за CoPc.

(Примљено 24. октобра 2013)

REFERENCES

1. G. E. Evans, K. V. Kordesch, *Science* **158** (1967) 1148
2. S. G. Meibuhr, *J. Electrochem. Soc.* **121** (1974) 1264
3. K. Yamada, K. Yasuda, H. Tanaka, Y. Miyazaki, T. Kobayashi, *J. Power Sources* **122** (2003) 132
4. A. Serov, C. Kwak, *Appl. Catal., B* **98** (2010) 1
5. K. Asazawa, K. Yamada, H. Tanaka, A. Oka, M. Taniguchi, T. Kobayashi, *Angew. Chem. Int. Ed.* **46** (2007) 8024
6. K. I. Ozoemena, T. Nyokong, *Talanta* **67** (2005) 162
7. V. Rosca, T. M. M. Koper, *Electrochim. Acta* **53** (2008) 5199
8. J. H. Zagal, *Coord. Chem. Rev*. **119** (1992) 89
9. A. B. P. Lever, *J. Porphyrins Phthalocyanines* **3** (1999) 488
10. P. Vasudevan, S. N. Mann, S. Tyagi, *Transition Met. Chem.* **15** (1990) 81
11. J. H. Zagal, S. Griveau, J. F. Silva, T. Nyokong, F. Bedioui, *Coord. Chem. Rev*. **254** (2010) 2755
12. T. Nyokong, in *N_4-Macrocyclic Metal Complexes*, J. H. Zagal, F. Bedioui, J. P. Dodelet, Eds., Springer, Berlin, 2006, p. 315
13. A. Pailleret, F. Bedioui, in *N_4-Macrocyclic Metal Complexes*, J. H. Zagal, F. Bedioui, J. P. Dodelet, Eds., Springer, Berlin, 2006, p. 363
14. M. S. Ureta-Zañartu, A. Alarcón, C. Berríos, G. I. Cárdenas-Jirón, J. Zagal, C. Gutiérrez, *J. Electroanal. Chem.* **580** (2005) 94

15. T. V. Magdesieva, I. V. Zhukov, D. N. Kraavchuk, O. A. Semeninkhin, L. G. Tomilova, K. P. Butin, *Russ. Chem. Bull. Int. Ed.* **51** (2002) 805
16. C. A. Caro, F. Bedioui, M. A. Páez, G. I. Cárdenas-Jiron, J. H. Zagal, *J. Electrochem. Soc.* **151** (2004) E-32
17. C. Barrera, I. Zhukov, E. Villagra, F. Bedioui, M. A. Páez, J. Costamagna, J. H. Zagal, *J. Electroanal. Chem*. **589** (2006) 212
18. S. Griveau, M. Gulppi, F. Bedioui, J. H. Zagal, *Solid State Ionics* **169** (2004) 59
19. M. Gulppi, S. Griveau, J. Pavez, J. H. Zagal, F. Bedioui, *Electroanalysis* **15** (2003) 779
20. N. Sehlotho, T. Nyokong, J. H Zagal, F. Bedioui, *Electrochim. Acta* **51** (2006) 5125
21. J. H. Zagal, *J. Electroanal Chem*. **109** (1980) 389
22. J. H. Zagal, M. S. Ureta-Zañartu, *J. Electrochem. Soc*. **129** (1982) 2249
23. J. Zagal, S. Lira, M. S Ureta-Zañartu, *J. Electroanal. Chem*. **210** (1986) 95
24. J. Zagal, E. Muñoz, S. Ureta-Zañartu, *Electrochim. Acta* **27** (1982) 1373
25. M. Isaacs, M. J. Aguirre, A. Toro-Labbé, J. Costamagna, M. Páez, J. H. Zagal, *Electrochim. Acta* **43** (1998) 1821
26. J. Zhang, Y.-H. Tse, W. J. Pietro, A. B. P. Lever, *J. Electroanal. Chem*. **406** (1996) 203
27. E. Trollund, P. Ardiles, M. J. Aguirre, S. R. Biaggio, R. C. Rocha-Filho, *Polyhedron* **19** (2000) 2303
28. X. Li, S. Zhang, C. Sun, *J. Electroanal. Chem*. **553** (2003) 139
29. D. Geraldo, C. Linares, Y. Y. Chen, S. Ureta-Zañartu, *Electrochem. Commun*. **4** (2002) 182
30. C. Linares, D. Geraldo, M. Páez, J. H. Zagal, *J. Solid State Electrochem.* 7 (2003) 626
31. L. M. F. Dantas, A. P. dos Reis, S. M. C. N. Tanaka, J. H. Zagal, Y.-Y. Chen, A. A. Tanaka, *J. Braz. Chem. Soc.* **19** (2008) 720
32. G. Ochoa, D. Geraldo, C. Linares, T. Nyokong, F. Bedioui, J. H. Zagal, *ECS Trans*. **19** (2009) 97
33. D. A. Geraldo, C. A. Togo, J. Limson, T. Nyokong, *Electrochim. Acta* **53** (2008) 8051
34. S. V. Guerra, L. T. Kubota, C. R. Xavier, S. Nakagaki, *Anal. Sci.* **15** (1999) 1231
35. S. Antoniadou, A. D. Jannakoudakis, E. Theodoridou, *Synth. Met.* **30** (1989) 295
36. J. Jiang, Y. Bian, F. Furuya, W. Liu, M. Choi, M. Kobayashi, H. W. Li, Q. Yang, T. Ng, D. K. P. Mak, *Chem. Eur. J*. **7** (2001) 5059
37. J. H. Zagal, M. A. Paez, *Electrochim. Acta* **42** (1996) 3477
38. J. H. Zagal, P. Cañete, J. Recio, F. Tasca, C. Linares-Flores, *Electrochem. Commun*. **30** (2013) 34
39. F. J. Recio, D. Geraldo, P. Cañete, J. H. Zagal, *ECS Electrochem. Lett.* **2** (2013) H16
40. G. I. Cárdenas-Jirón, J. H. Zagal, *J. Electroanal. Chem.* **497** (2001) 55
41. D. Venegas, G. I. Cárdenas, J. H. Zagal, *J. Coord. Chem*. **56** (2003) 1269
42. D. Venegas-Yazigi, G. I. Cárdenas-Jirón, J. H. Zagal, *J. Coord. Chem.* **56** (2003) 1269
43. V. Paredes-García, G. I. Cárdenas-Jirón, D. Venegas-Yazigi, J. H. Zagal, M. Páez, J. Costamagna *J .Phys. Chem., A* **109** (2005) 1196
44. G. I. Cárdenas-Jiron, *J. Phys. Chem., A* **106** (2002) 3202
45. Z. Shi, J. Zhang, *J. Phys. Chem., C* **111** (2007) 7097
46. C. Song, L. Zhang, J. Zhang, D. P. Wilkinson, R. Baker, *Fuel Cells* **07** (2007) 9
47. J. Ouyang, K. Shigehara, A. Yamada, F. C. Anson, *J. Electroanal. Chem.* **297** (1991) 489.

Journal of the Serbian Chemical Society
JSCS-info@shd.org.rs • www.shd.org.rs/JSCS
J. Serb. Chem. Soc. 78 (12) 2053–2067 (2013)
JSCS–4550
UDC 669.14.018.8+546.3–31:
621.315.59+620.193:539.216
Original scientific paper

Change of *n*-type to *p*-type conductivity of the semiconductor passive film on N-steel: Enhancement of the pitting corrosion resistance

MIRJANA METIKOŠ-HUKOVIĆ[1]*, ZORAN GRUBAČ[2] and SASHA OMANOVIC[3]

[1]Department of Electrochemistry, Faculty of Chemical Engineering and Technology, University of Zagreb, P. O. Box 177, 10000 Zagreb, Croatia, [2]Department of General and Inorganic Chemistry, Faculty of Chemistry and Technology, University of Split, N. Tesle 10, 21000 Split, Croatia and [3]Department of Chemical Engineering, McGill University, 3610 University Street, Montreal, Quebec, Canada H3A 2B2

(Received 21 November, revised 24 November 2013)

Abstract: Electrochemically-assisted modification of the surface of N-austenitic stainless steel (ASS N25) was successfully employed to improve the barrier properties of the passive film in a chloride-containing solution. The chemical composition, electronic and barrier properties of the surface film before and after the electrochemical treatment were examined using X-ray photoelectron spectroscopy (XPS) and electrochemical impedance spectroscopy (EIS). The electrochemical measurements were performed in a corrosion testing solution. The excellent corrosion resistance (both pitting and general) of the modified surface of the N-steel was discussed according to a Mott–Schottky analysis of the interfacial capacitance of the space charge layer and EIS results. The conductivity change of the surface film from an *n*- to a *p*-type in the pitting susceptible region was explained using the XPS analysis and the semiconducting properties of the film.

Keywords: stainless steel; corrosion; passive films; metal oxide semiconductors.

INTRODUCTION

It was reported that the favourable effect of nitrogen on the electrochemical and mechanical properties of austenitic stainless steels (ASS) is a consequence of the electronic exchange between the iron and nitrogen atoms in austenitic fcc lattice, in which nitrogen contributes to the electronic states just at the Fermi level.[1] According to these authors, the increase in the free electron density due to

* Corresponding author. E-mail: mmetik@fkit.hr
doi: 10.2298/JSC131121144M

the nitrogen atoms in the iron lattice favours short-range ordering and enhances the metallic character of the interatomic bonds. Bonding between atoms of non-identical elements results in an enhanced thermodynamic stability of a solid solution, and thus much better corrosion and mechanical properties. Austenitic stainless steels (SSs) with nitrogen (ASS N25) offer acceptable resistance against general corrosion in a variety of corrosive environments.[2–4] Nitrogen is believed to play a major role pertaining to the corrosion properties of austenitic stainless steels, as it promotes passivity, and enhances the re-passivation properties of the stainless steel, in addition to its contribution to the mechanical strength.[5,6]

Although the improved corrosion resistance of nitrogen-containing SSs justifies their employment in many applications, the related literature indicates that vigorous pitting attacks still prevail when these SSs are exposed to chloride-containing solutions.[6] This evidences insufficiency in the improvement of the corrosion protection brought about by nitrogen addition to the stainless steel. Pitting attacks are not only responsible, to a large extent, for the mechanical failure of SSs, mainly in industrial applications, but also cause the release of bio-hazardous species into the surrounding environments, which are of particular concerns in food, pharmaceutical and biomedical applications.[7,8]

The pitting resistance of SSs is directly linked to the stability of the surface passive film, and is thus dictated by its physico-chemical properties. Oxide passive films grown on metal and alloy surfaces have recently been reviewed[9–11] and recent insights into the mechanism of passivity breakdown and localized (pitting) corrosion were given.[12,13] It was established that during passive film formation/growth on an ASS N25 electrode, Fe^{3+} species migrate outward through the cation vacancies ($V_{Cr^{3-}}$, are the main charge carriers) in the Cr_2O_3 layer.[14] Thus, the passive film on ASS N25 is believed to be comprised of an inner Cr_2O_3 barrier layer and an outer iron-rich sublayer,[15] whereby the point defect model (PDM) best explains the kinetics of passive film growth.[16,17]

Numerous efforts have been made to modify the structure of passive films and thus enhance the pitting and general corrosion resistance of stainless steels. The outcome ranged from very poor success to remarkable improvements in the properties of the passive films.[18–22]

Cyclic potentiodynamic polarization, as a surface treatment method, has been reported as an efficient method that could be employed to modify the physicochemical and electronic properties of the passive films on 316LVM stainless steel.[23,24]

In this paper, the effect of cyclic potentiodynamic polarization on the corrosion resistance of ASS N25 surface is presented. The pitting and barrier properties of an unmodified and a modified ASS N25 surface are also comparatively discussed based on the semiconducting properties of naturally and electrochemically grown passive films.

EXPERIMENTAL

A single compartment standard electrochemical cell was used in all electrochemical/corrosion measurements. The reference electrode (RE) was a saturated calomel electrode (SCE), and a platinum plate was used as the counter electrode (CE). A working electrode (WE) was made of ASS N25 samples with the chemical composition given in Table I. The WE was prepared by cutting ASS N25 into disc-shaped samples suitable for the EG&G PAR flat specimen holder, model K105. The sample area exposed to an electrolyte was 0.785 cm^2. All current density values reported in this work were normalized with respect to this geometrical surface area. Electrochemical passivation of the electrode surface was performed in a 0.1 M $NaNO_3$ solution. Corrosion tests were realized in a 0.16 M NaCl solution.

TABLE I. Chemical composition (mass %) of ASS N25 steel (the balance is Fe)

C	Mn	Si	Cr	Ni	Mo	N	Nb
0.030	4.60	0.29	21.15	12.72	2.22	0.247	0.170

The composition of the passive films was determined by X-ray photoelectron spectroscopy (XPS). The XPS spectra were recorded in a UHV chamber of a SPECS system with a Phoibos MCD 100 electron analyzer and monochromatised Al K_λ X-rays of 1486.74 eV. For the pass energy of 10 eV used in the present study, the total energy resolution was around 0.8 eV. The photoemission spectra were simulated with several sets of mixed Gaussian–Lorentzian functions with Shirley background subtraction.

In order to measure the surface corrosion resistance, electrode stabilization at the open circuit potential (OCP) was first performed in the corrosion testing solution for one hour. Next, electrochemical impedance spectroscopy (EIS) measurement was performed at the OCP in a frequency range between 100 kHz and 30 mHz with an *ac* amplitude (rms) of ±10 mV. Pitting polarization experiments were conducted by anodically polarizing the working electrode (WE) from 50 mV negative of the OCP to the potential at which the current density of 1 mA cm^{-2} was reached. Chronoamperometry measurements were performed following electrode stabilization at the OCP in a corrosion testing solution by potentiostatically (constant potential) polarizing the WE and measuring the resulting current density.

To investigate the semiconducting properties of naturally-grown (unmodified surface) and electrochemically formed passive films, capacitance measurements were performed in a borate buffer solution, pH 8.4 under a cathodic bias, starting from 1.0 V down to –0.9 V. The imaginary part of the impedance (Z_{imag}) measured at the frequency of 1.6 kHz was recorded as a function of the potential. The applied *ac* amplitude was ±10 mV. The experimental setup consisted of a PAR 273A potentiostat/galvanostat for voltammetric measurements, and a Solartron SI 1287 potentiostat/galvanostat and a Solartron SI 1255 HF frequency response analyzer for the electrochemical impedance spectroscopy measurements.

RESULTS AND DISCUSSION

Electrochemical formation of passive films on an ASS N25 surface

The cyclic voltammograms (CV) of an ASS N25 electrode recorded in a 0.1 M $NaNO_3$ in the potential region between –0.8 V and 0.9 V, representing the 1st (solid line) and the 300th (dashed line) sweeps, are shown in Fig. 1. It is evident that the shape of the CV changed significantly with the number of polarization sweeps. The anodic and cathodic shoulders/peaks observed on the voltammo-

grams and their corresponding redox reactions have already been explained in the literature,[25–29] and will not be elaborated in detail here. Briefly, in each sweep two oxidation reactions, Fe → Fe(II)/Fe(III) and Cr(III) → Cr(VI) in the anodic sweep, and their corresponding reduction reactions in the cathodic sweep, occur.[23] The first anodic shoulder/peak (at *ca.* –0.7 V) is related to the formation of a Fe(II)/Fe(III)-oxide layer (*i.e.*, Fe_2O_3) on the top of the Cr(III) oxide layer, followed by oxidation of the Cr(III) species to soluble Cr(VI) species (at *ca.* –0.1 V). The corresponding reduction reactions in the reverse sweep occur at potentials negative of *ca.* –0.4 V.

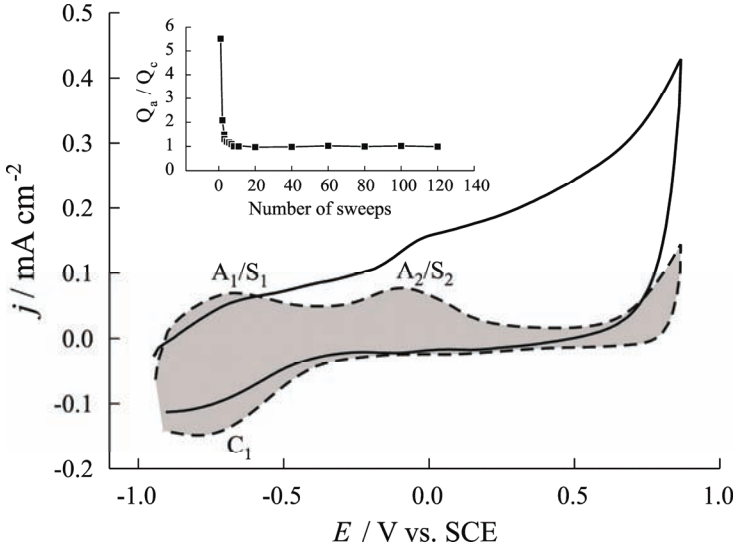

Fig. 1. Cyclic voltammograms of the freshly polished ASS N25 surface recorded in a 0.1 M $NaNO_3$ solution at a scan rate of 0.167 mV s^{-1}. The solid line represents the 1st sweep, and the broken line represents the 300th sweep. Inset: dependence of the anodic to cathodic total charge ratio on the number of sweeps.

On the freshly polished ASS N25 surface (1st sweep), the anodically formed Cr(VI)-species are mainly dissolved in the solution by diffusion through a very thin and non-compact pre-formed passive film. This explains the absence of a passive transition associated with the oxidation of Cr(III) to Cr(VI) in the anodic scan (shoulder S_2). On the other hand, the 300th sweep in Fig. 1 shows that the charge associated with the Cr(III)-to-Cr(VI) transition in the potential region of Cr(III) oxidation (positive of *ca.* –0.4 V) is negligible compared to that recorded in the first sweep. This demonstrates that the Cr(VI) species formed in the anodic sweep remain "locked" in the surface passive film. The results in Fig. 1 suggest that the passive film formed during prolonged cyclization of the electrode is more

compact or thicker than the film formed in the 1st sweep; thus effectively preventing the dissolution of Cr(VI) species into the electrolyte.

In order to obtain a better quantitative insight into changes during the cyclization of the ASS N25 electrode, the ratio of the total anodic-to-cathodic charge is presented as an inset to Fig. 1. The curve shows that the anodic reactions in the 1st sweep are quite irreversible ($Q_a/Q_c \approx 5.5$) and that only *ca.* 18 % of the charge related to these anodic processes is used to form species that do not dissolve into the solution but form the surface passive oxide film. However, on cyclization of the surface, the reversibility of the anodic processes rapidly increases, and after *ca.* 10 sweeps it approaches almost 100 %. This indicates that the cyclic polarization of the working electrode surface under the given conditions significantly enhances passivity of the surface oxide film, preventing the dissolution of the underlying metals into the solution, even at high anodic potentials. Similar behaviour was shown in the case of 316LVM stainless steel, when a considerable improvement in the corrosion resistance was observed.[24,25]

Chemical composition of passive films formed on an ASS N25 electrode – XPS characterization

The chemical composition of the electrochemically modified passive film and the naturally grown passive film (unmodified surface) was analyzed by XPS. The photoemission spectra (open circles) around the Cr $2p_{3/2}$ and Fe $2p_{3/2}$ energy levels recorded on an a) unmodified and b) electrochemically modified sample are shown in Fig. 2, together with the numerical fits (solid lines) obtained using Voigt profiles. The agreement between the modelled and experimental data is very good.

A comparison of the corresponding spectra revealed that Cr(VI) species were detected only in the electrochemically formed passive film. Chromium in both passive films was found as Cr(III) in $Cr(OH)_3$ and in Cr_2O_3. Both passive films contain Fe(II) and Fe(III), mostly in Fe_3O_4, with some contribution of Fe(II) in FeO. The peaks at 715.3 and 713.4 eV are well-known shake-up satellite peaks. Iron oxide satellite structures are frequently used as fingerprints to identify the iron oxide phases. The shake-up satellite in Fig. 2 at 715.3 eV can be assigned to Fe(II) in FeO, while the other satellite peak at 713.4 eV is attributed to Fe(II) in chromite ($FeCr_2O_7$). No shake-up satellite structures are visible on the chromium spectra.

Corrosion resistance of passive films formed on ASS N25 surfaces

Polarization voltammograms of the unmodified ASS N25 surface (solid line) and surfaces modified electrochemically (broken lines), recorded in 0.16 M NaCl solution, are shown in Fig. 3. The polarization curve of the unmodified surface

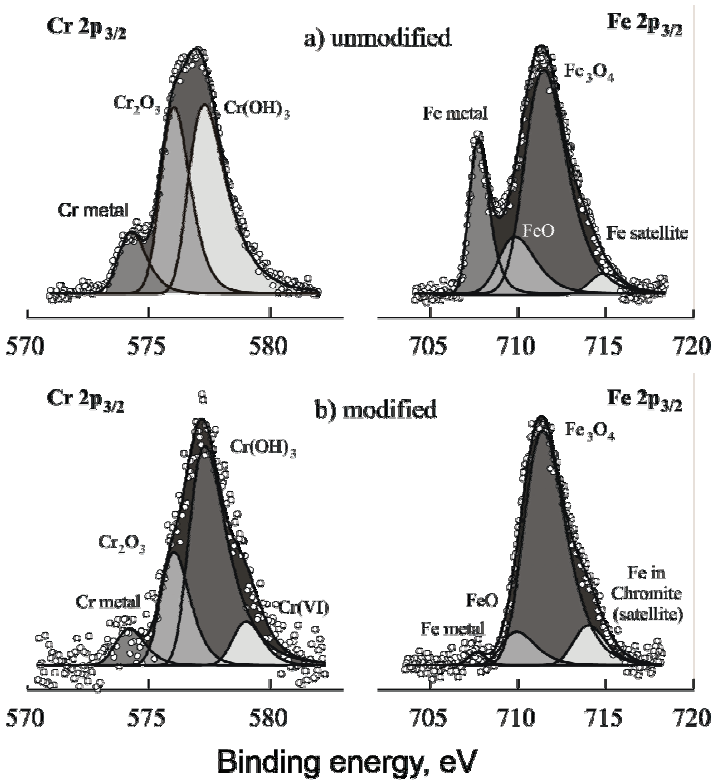

Fig. 2. The deconvoluted XPS spectra of Cr $2p_{3/2}$ and Fe $2p_{3/2}$ energy levels obtained for: a) an unmodified and b) an electrochemically modified ASS N25 surface.

exhibits a number of current spikes at potentials below 0.4 V, indicating the formation of metastable pits in this potential region. However, the formation of stable pits occurs at potentials positive of 0.4 V, which is in agreement with the results for austenitic types of stainless steels.[26,27] However, at potentials higher than *ca.* 0.5 V, the current density starts to rise more steeply and finally at more noble potentials, a breakdown of the film occurs. In the reverse scan, a pitting loop appears. On the other hand, the response of the electrochemically modified surfaces shows the absence of current spikes. An abrupt increase in anodic current at *ca*. 1.2 V could be connected with the oxygen evolution reaction. Moreover, the passive current density of these surfaces is significantly lower than that of the unmodified surface. With increasing number of passivation sweeps (from 50 to 200 scans), the passive current decreases, thus confirming that a more compact and the corrosion resistant surface film had been formed after a higher number of passivation scans. In summary, the results in Fig. 3 evidence that the electrochemical passivation of the ASS N25 surface improves its pitting corrosion resistance and passivity in a 0.16 M NaCl solution.

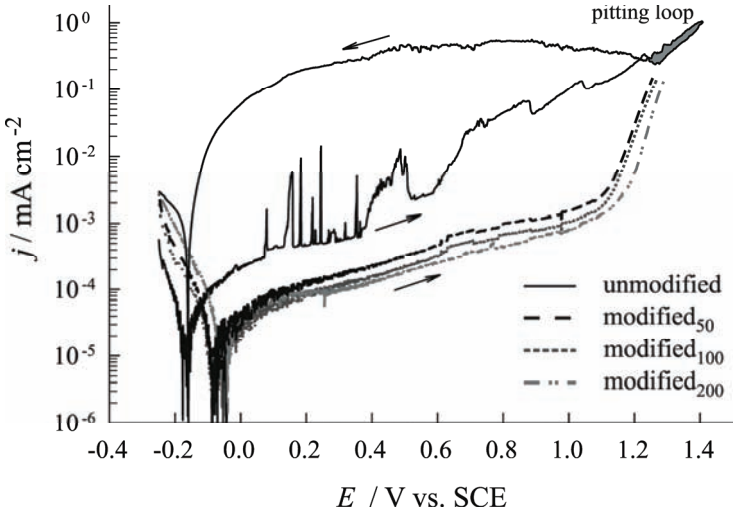

Fig. 3. Tafel plots of the polarization curves of the unmodified (solid line) and the electrochemically modified ASS N25 surface recorded in a 0.16 M NaCl solution at a scan rate of 0.167 mV s^{-1}. Modification of the surface was realised by applying 50 sweeps (broken line), 100 sweeps (dotted line) and 200 sweeps (dash dot dot dash line).

Investigation of the frequency of the formation of metastable pits under potentiostatic polarization, in the pitting susceptible region, is another criterion used to evaluate surface resistance against pitting corrosion. In other words, the higher the density of pitting-active spots on the surface, the higher is the susceptibility of the surface to pitting corrosion. On a current–time curve, recorded at a selected potential in the pitting-susceptible region, this is manifested as the appearance of current spikes. The chronoamperometry (CA) plots of the unmodified (1), and electrochemically modified (2) surfaces are comparatively shown in Fig. 4. The CA plot of the unmodified surface clearly shows the incidence of pitting corrosion, evidenced by the continuous and "rough" increase in current with time. On the other hand, the response of the electrochemically passivated surface is characterized by a “zero” line. Hence, the results presented in Fig. 4 clearly support the conclusions made from the results presented in Fig. 3, suggesting that the electrochemical passivation of ASS N25 yielded a passive film with excellent corrosion protection properties.

Semiconducting properties of the passive films formed on an ASS N25 surface

Correlation between the semiconducting properties of passive oxide films and their resistance against pitting corrosion was reported in the literature.[28–30] The semiconducting (electronic) properties of passive films have generally been studied using capacitance measurements, employing the Mott–Schottky analysis:[31]

$$\frac{1}{C_{SC}^2} = \frac{-2}{\varepsilon\varepsilon_0 e N_A}\left(E - E_{fb} - \frac{kT}{e}\right) \quad (1)$$

$$\frac{1}{C_{SC}^2} = \frac{2}{\varepsilon\varepsilon_0 e N_D}\left(E - E_{fb} - \frac{kT}{e}\right) \quad (2)$$

where ε is the relative permittivity (dielectric constant) of the oxide film, ε_0 is the vacuum permittivity (F cm^{-1}), e is the elementary charge of an electron (C), N_A is the acceptor density (cm^{-3}) and N_D is the donor density (cm^{-3}) in the non-stoichiometric passive film, E_{fb} is the flat-band potential (V), k is the Boltzmann constant (J K^{-1}) and T is the temperature (K).

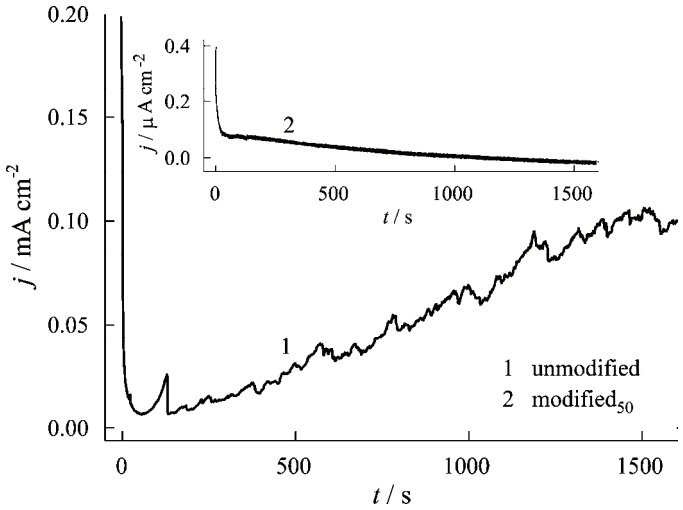

Fig. 4. Potentiostatic curves of the unmodified (1) and the electrochemically modified (2) ASS N25 surfaces recorded in a 0.16 M NaCl solution at a potential 0.45 V. Modification of the surface was realised by applying 200 sweeps.

The passive film/electrolyte interface is, in this analysis, treated as the space charge depletion zone, which behaves as a Schottky barrier. Thus, the measured capacitance, after correction for the electrochemical double layer capacitance, is attributed to the space charge capacitance, C_{SC}, inside the oxide film. If an oxide film behaves as a semiconductor that can be described by the Mott–Schottky model, the dependence between $1/C_{SC}^2$ *vs.* E should give a straight line. For an *n*-type semiconductor, the equation has a negative slope, while for a *p*-type semiconductor, the equation has a positive slope.

The Mott–Schottky response of a naturally grown passive film (unmodified surface) and of the passive film formed by applying a specific number of polarization (modification) cycles (Fig. 5) shows the existence of several potential regions characterizing the semiconducting behaviour of the corresponding sur-

face films. In the potential region between –0.9 and –0.6 V (Region I), the passive films behave as *p*-type semiconductors, while in the potential range between –0.3 and 0 V or 0.2 V for the unmodified and modified surface, respectively, (Region II), *n*-type behaviour is clearly visible. An *n*-type behaviour has been correlated with the response of iron oxides in the passive film, which are characterized by a non-stoichiometric composition resulting in oxygen vacancies that contribute to the *n*-type conductivity.[4,15,32,33] On the other hand *p*-type behaviour has been attributed to the response of chromium oxides, and is characterrized by the non-stoichiometry resulting in metal vacancies that contribute to the *p*-type semiconductivity.[4,15,34–36] Taking this into account, it could be concluded that in Region I, the space charge depletion zone is situated in the part of the passive film that is reach by chromium(III) oxide and behaves as a Schottky barrier, while the remaining Fe oxide rich part of the oxide is in a condition of accumulation. On the other hand, at potentials in Region II, the semiconducting property of the passive film is determined by the space charge depletion zone located in the iron oxide rich layer, while the chromium(III) oxide rich layer is in the accumulation condition.[32] In Region IV (at $E > 0.8$ V and $E > 1.2$ V), due to ionic (pitting corrosion) and electronic (oxygen evolution) transfer reactions on the solid/electrolyte interface, the main potential drop is no longer in the space charge layer but in the Helmholtz layer.

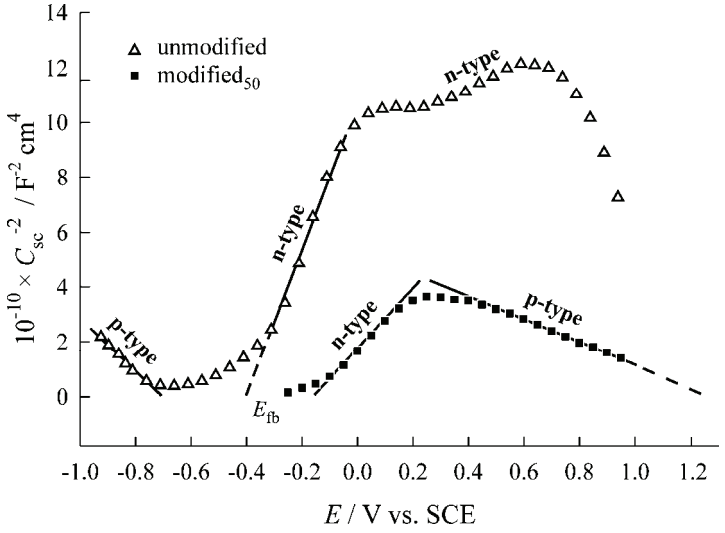

Fig, 5. Mott–Schottky plot of the unmodified (Δ) and the electrochemically modified (■) ASS N25 surfaces by applying 50 sweeps.

The main difference in $1/C_{SC}^2$ *vs.* E behaviour between the unmodified and the electrochemically modified surface is in Region III (0.2–0.7 V), in which the two surfaces display different types of semiconductivity. Here, focus will be

directed only to this region since it coincides with the pitting potential region of the unmodified surface (Fig. 3). Figure 5 shows that the unmodified surface behaves as an *n*-type semiconductor in Region III. There is general agreement that surfaces presenting *n*-type semiconductivity are more prone to pitting compared to surfaces exhibiting *p*-type semiconductivity.[28]

If the Mott–Schottky plot (Fig. 5) and the polarization curve (Fig. 3) of the unmodified sample are compared, it will be seen that the pitting potential coincides well with the *n*-type behaviour in Region III. This is quite in agreement with the point defect theory (PDM),[16,17] which states that the initial pitting reaction that occurs at a film/solution interface involves the adsorption of chloride ions into oxygen vacancies according to relation:

$$V_{O}^{\bullet\bullet}(\text{ox}) + \text{Cl}^- \cdot \text{n H}_2\text{O} \rightarrow V_{\text{Cl}}^{\bullet}(\text{ox}) + \text{n H}_2\text{O} \quad (3)$$

where $V_{O}^{\bullet\bullet}(\text{ox})$ is the positively charged oxygen vacancy, Cl^- is the chloride ion in an aqueous electrolyte and $V_{\text{Cl}}^{\bullet}(\text{ox})$ is the chloride vacancy occupying an oxygen lattice site (Kröger–Vink notation). To preserve electroneutrality, an equivalent number of cation vacancies, V_{M}^{3-}, must be formed through a corrosion process of metal dissolution.

Taking into account the PDM, it is assumed that an increase in the pitting corrosion resistance of a material could be achieved by increasing the concentration of metal vacancies in the passive film. This process occurs by the cyclic potentiodynamic formation of the passive film under the conditions presented in Fig. 1. Namely, by polarizing the ASS N25 surface (between the potentials of hydrogen and oxygen evolution) at high anodic potentials, Cr(VI) species are formed (see XPS results presented in Fig. 2). With cyclization, progressively more of these species remain "arrested" in the growing passive film. The formation of Cr(VI) species increases the oxygen content in the passive film (so-called secondary passivity), producing an increase in the density of metal vacancies, V_{M}^{3-}, according to the equation:[14]

$$\text{Cr(III)} \rightarrow \text{Cr(VI)} + V_{M}^{3-} + 3e^- \quad (4)$$

Electrochemical modification, in turn, leads to the changes in the electronic properties of the surface film and to the increased pitting resistance (Figs. 3 and 4). On the Mott–Schottky plot (Fig. 5), in the pitting susceptible Region III, a transition from *n*- to *p*-type conductivity occurs. Mott–Schottky results for the flat band potentials and charge carrier densities of the unmodified and modified film are summarized as follows:

i) unmodified surface of the steel: $E_{\text{fb}} = -0.405$ V, $N_{\text{D}}(\text{Fe}_2\text{O}_3) = 3.95\times10^{19}$ cm^{-3};

ii) modified surface of the steel: $E_{\text{fb}} = -0.179$ V, $N_{\text{D}}(\text{Fe}_2\text{O}_3) = 1.30\times10^{20}$ cm^{-3} and $E_{\text{fb}} = 1.250$V, $N_{\text{A}}(\text{CrO}_3) = 3.54\times10^{20}$ cm^{-3}.

The values obtained for the donor and acceptor densities were of the same order of magnitude as those reported previously for ASSs, without nitrogen.[32,35,37,38]

Barrier properties of the passive films formed on ASS N25 surfaces

In order to investigate the general corrosion resistance of the electrochemically modified ASS N25 surfaces, EIS measurements were performed and presented as the Nyquist plots in Fig. 6. To better investigate the frequency-dependent processes occurring at the surface/electrolyte interface and inside the passive oxide films, the EIS data were modelled using nonlinear least-squares fit analysis.[39] An equivalent electrical circuit (EEC) presented in the inset to Fig. 6 was used to model the experimental data presented in Fig. 6. R_{el} represents the electrolyte resistance, CPE is a constant phase element representing a double-layer capacitance, R_1 is the corrosion resistance and C_0 can be attributed to the faradaic pseudocapacitance corresponding to the film thickness/potential variation.[40–42] The values obtained by fitting the experimental EIS data using the presented EEC are given in Table II. It should be noted that the values presented in Table II were recorded for ASS N25 surfaces prior to the pitting polarization tests.

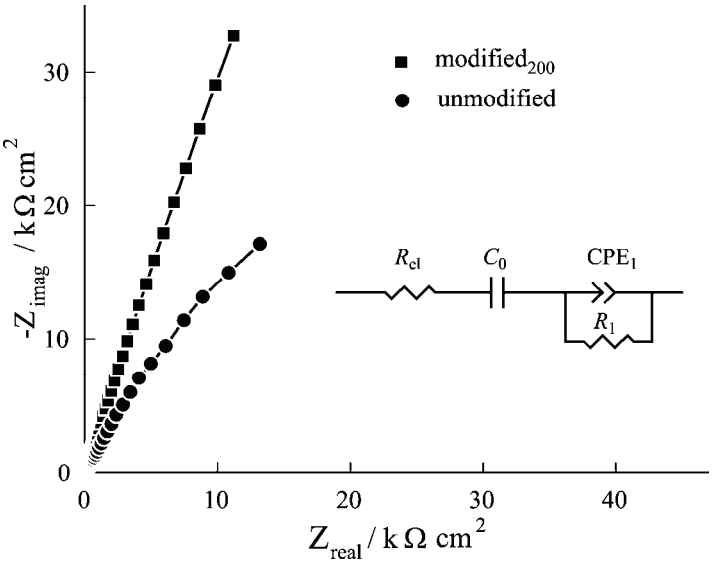

Fig. 6. Nyquist plots of the unmodified (●) and the modified (■) ASS N25 surfaces by applying 200 sweeps, recorded in a 0.16 M NaCl solution. Inset: Electric equivalent circuit used to fit experimental data.

Cyclic polarization of the surface of the steel results in an increase in the surface roughness, and thus in the real surface area exposed to the electrolyte. In order to eliminate the effect of surface area and determine the real general corrosion resistance, a true surface area was calculated for each sample. First, using

the Brug Equation[43] and CPE_1, the corresponding capacitance was calculated and presented in Table II. Taking into account that a double-layer capacitance of a smooth electrode surface is 25 μF cm^{-2},[44] the true surface area of each investigated ASS N25 sample was calculated as a ratio, $A_{true} = C_{DL}/25$ (cm^2), Table II. As can be seen, the electrochemical passivation of the surface resulted in a significant increase in the surface area, which is consistent with previous observations.[25] The numerical values of R_{true} were used to calculate the protection efficiency of the surface film according to the expression:

$$PE / \% = 100(R_{true,mod} - R_{true,unmod})/R_{true,mod} \quad (5)$$

where $R_{true,mod}$ and $R_{true,unmod}$ are the polarization resistance values of modified and unmodified samples, respectively. Table II shows that the electrochemical modification of the ASS N25 surface resulted in an increase in the general corrosion resistance, yielding a corrosion protection efficiency of *ca*. 90 %.

TABLE II. Impedance parameters for the ASS N25 electrode in a 0.16 M NaCl solution at the open circuit potential

Treatment	$Q_1 \times 10^6$ Ω^{-1} cm^{-2} s^n	n	R_1 kΩ cm^2	C_0 μF cm^{-2}	C_{dl} μF cm^{-2}	R_{true} kΩ cm^2
Unmodified	33.7	0.81	283	–	57	638
$Modified_{100}$	162.1	0.89	342	170	201	3491
$Modified_{200}$	144.0	0.90	356	780	234	4248

CONCLUSIONS

This work proves the applicability of the electrochemical cyclic polarization method for increasing the corrosion resistance of the surface film of ASS N25 steel.

The superior pitting resistance of the modified surface compared to the control surface was attributed to the modification of the electronic properties of the passive film, though conversion of the type of semiconductivity (from *n*- to *p*-type) in the pitting-susceptible region. This is due to the enrichment of the electrochemically formed passive film with Cr(VI) species (XPS), which results in a "replacement" of pitting-initiating oxygen vacancies by metal vacancies. The resulting oxide layer is a semiconductor of *p*-type and thus more corrosion resistant against pitting attack. The other beneficial consequence of the electrochemical passivity was an improvement in the general corrosion resistance of the surface.

LIST OF SYMBOLS

A area, cm^2
C capacitance, F cm^{-2}
C_0 faradaic pseudocapacitance, F cm^{-2}
CPE constant phase element
E potential, V
e charge of electron, 1.602×10^{-19} C

j current density, A cm^{-2}
k Boltzmann constant, 1.23 × 10^{-23} J K^{-1}
M metal
N charge carrier density, cm^{-3}
n exponent of the constant phase element
ox oxygen lattice site
PE protection efficiency, %
Q frequency-independent constant, (Ω^{-1} cm^{-2} s^n)
R resistance, Ω cm^2
T temperature, K
V vacancy
Z impedance, Ω cm^2.

Greek letters

ε relative permittivity
ε_o vacuum permittivity, ε_o = 8.85×10^{-14} F cm^{-1}
$\bullet$ positive charge.

Sub/superscripts

A acceptor
a anodic
c cathodic
D donor
DL double layer
fb flat band
el electrolyte
im imaginary
M metal site
mod modified
O oxygen
OCP open circuit potential
real real
SC space charge
true true
unmod unmodified.

ИЗВОД

ПРОМЕНА *n*-ТИПА У *p*-ТИП ПРОВОДЉИВОСТИ ПОЛУПРОВОДНИЧКОГ ПАСИВНОГ ФИЛМА ФОРМИРАНОГ НА N-АУСТЕНИТНОМ ЧЕЛИКУ: ПОВЕЋАЊЕ ОТПОРНОСТИ ПРЕМА ПИТИНГ КОРОЗИЈИ

MIRJANA METIKOŠ-HUKOVIĆ[1], ZORAN GRUBAČ[2] и SASHA OMANOVIC[3]

[1]Department of Electrochemistry, Faculty of Chemical Engineering and Technology, University of Zagreb, P. O. Box 177, 10000 Zagreb, Croatia, [2]Department of General and Inorganic Chemistry, Faculty of Chemistry and Technology, University of Split, N. Tesle 10, 21000 Split, Croatia and [3]Department of Chemical Engineering, McGill University, 3610 University Street, Montreal, Quebec, Canada H3A 2B2

Електрохемијска модификација површине N-легираног аустенитног нерђајућег челика (ASS N25) успешно је изведена како би се побољшала баријерна својства пасивног филма у растворима које садрже хлоридне јоне. Хемијски састав, електронске и

баријерне особине површинског филма, пре и после електрохемијског третмана (пасивације), испитивани су користећи фотоелектронску спектроскопију X-зрака (XPS), спектроскопију електрохемијске импеданције (EIS) и Mott–Schottky анализу. Резултирајућа супериорна отпорност модификоване ASS N25 површине према питинг корозији приписана је променама електронских (полупроводничких) својстава површинског филма. Проводљивост пасивног филма у подручју потенцијала осетљивом на питинг мења се из *n*- у *p*-тип током цикличне потенциодинамичке поларизације.

(Примљено 21. новембра, ревидирано 24. новембра 2013)

REFERENCES

1. V. G. Gavriljuk, H. Berns, *High Nitrogen Steels Structure Properties, Manufacture, Application*, Springer-Verlag, Berlin, 1999
2. U. Kamachi Mudali, S. Ningshen, *Trans. Indian Inst. Met.* **55** (2002) 461
3. S. Ningshen, U. Kamachi Mudali, V. K. Mittal, H. S. Khatak, *Corros. Sci.* **49** (2007) 481
4. M. Metikoš-Huković, R. Babić, Z. Grubač, Ž. Petrović, N. Lajçi, *Corros. Sci.* **53** (2011) 2176
5. H. Baba, T. Kodama, Y. Katada, *Corros. Sci.* **44** (2002) 2393
6. F. M. Bayoumi, W. A. Ghanem, *Mater. Lett.* **59** (2005) 3311
7. D. Gopi, V. C. A. Prakash, L. Kavitha, S. Kannan, P. R. Bhalaji, E. Shinyjoy, J. M. F. Ferreira, *Corros. Sci.* **53** (2011) 2328
8. D. Gopi, J. Indira, L. Kavitha, *Surf. Coat. Tech.* **206** (2012) 2859
9. V. Maurice, P. Marcus, *Electrochim. Acta* **84** (2012) 129
10. H.-H. Strehblow, V. Maurice, P. Marcus, in: *Corrosion Mechanisms in Theory and Practice*, 3rd ed., P. Marcus, Ed., CRC Press, Taylor and Francis, Boca Raton, FL, 2011, p. 235
11. P. Marcus, V. Maurice, in: *Oxide Ultrathin Films, Science and Technology*, G. Pacchioni, S. Valeri, Eds., Wiley–VCH Verlag, Weinheim, Germany, 2012, p. 119
12. P. Marcus, H.-H. Strehblow, V. Maurice, *Corros. Sci.* **50** (2008) 2698
13. A. Seyeux, V. Maurice, P. Marcus, *Electrochem. Solid State Lett.* **12** (2009) C25
14. M. Bojinov, G. Fabricius, T. Laitinen, K. Mäkelä, T. Saario, G. Sundholm, *Electrochim. Acta* **45** (2000) 2029
15. S. Martinez, M. Metikoš-Huković, N. Lajci, *Passivity of Nitrogen-Bearing Stainless Steel in Acidic Solution*, in *Passivation of metals and semiconductors, and properties of thin oxide layers*, P. Marcus, V. Maurice, Eds., Elsevier, Amsterdam, 2006, p. 35
16. D. D. MacDonald, *J. Electrochem. Soc.* **139** (1992) 3434
17. D. D. MacDonald, S. R. Biaggio, H. Song, *J. Electrochem. Soc.* **139** (1992) 170
18. J. S. Noh, N. J. Laycock, W. Gao, D. B. Wells, *Corros. Sci.* **42** (2000) 2069
19. C.-C. Shih, C.-M. Shih, Y.-Y. Su, L. H. J. Su, M.-S. Chang, S.-J. Lin, *Corros. Sci.* **46** (2004) 427
20. G. T. Burstein, R. M. Souto, *J. Electrochem. Soc.* **151** (2004) B537
21. S. Fujimoto, T. Yamada, T. Shibata, *J. Electrochem. Soc.* **145** (1998) L79
22. T. M. Yue, J. K. Yu, H. C. Man, *Surf. Coat. Technol.* **137** (2001) 65
23. Z. Bou-Saleh, A. Shahryari, S. Omanovic, *Thin Solid Films* **515** (2007) 4727
24. A. Shahryari, S. Omanovic, J. A. Szpunar, *Mater. Sci. Eng., C* **28** (2008) 94
25. A. Shahryari, S. Omanovic, J. A. Szpunar, *J. Biomed. Mater. Res., A* **89** (2009) 1049
26. M. P. Ryan, D. E. Williams, R. J. Chater, B. M. Hutton, D. S. McPhail, *Nature* **415** (2002) 770

27. M. F. Montemor, A. M. P. Simões, M. G. S. Ferreira, M. Da Cunha Belo, *Corros. Sci.* **41** (1999) 17
28. M. Da Cunha Belo, B. Rondot, C. Compere, M. F. Montemor, A. M. P. Simões, M. G. S. Ferreira, *Corros. Sci.* **40** (1998) 481
29. M. Z. Yang, J. L. Luo, Q. Yang, L. J. Qiao, Z. Q. Qin, P. R. Norton, *J. Electrochem. Soc.* **146** (1999) 2107
30. Y. F. Cheng, J. L. Lou, *Electrochim. Acta* **44** (1999) 2947
31. S. R. Morrison, *Electrochemistry at Semiconductor and Oxidised Metal Electrodes*, Plenum Press, New York, 1980
32. R. Babić, M. Metikoš-Huković, *J. Electroanal. Chem.* **358** (1993) 143
33. M. Bojinov, G. Fabricius, T. Laitinen, K. Makela, T. Saario, G. Sundholm, *Electrochim. Acta* **46** (2001) 1339
34. T. L. Sudesh, L. Wijesinghe, D. J. Blackwood, *Corros. Sci.* **50** (2008) 23
35. F. Gaben, B. Vuillemin, R. Oltra, *J. Electrochem. Soc.* **151** (2004) B595
36. Y. X. Qiao, Y. G. Zheng, W. Ke, P. C. Okafor, *Corros. Sci*. **51** (2009) 979
37. A. Fattah-Alhosseini, M. A. Golozar, A. Saatchi, K. Raeissi, *Corros. Sci.* **52** (2010) 205
38. K. S. Raja, D. A. Jones, *Corros. Sci*. **48** (2006) 1623
39. B. A. Boukamp, *Equivalent circuit users manual*; report CT88/265/128, University of Twente, Twente, 1989, p. 13
40. M. Metikoš-Huković, Z. Grubač, R. Babić, N. Radić, *Corros. Sci.* **52** (2010) 352
41. M. Bojinov, I. Kanazirski, A. Girginov, *Electrochim. Acta*, **41** (1996) 2695
42. M. Metikoš-Huković, Z. Grubač, *J. Electranal. Chem*. **556** (2003) 167
43. G. J. Brug, A. L. G. van der Eeden, M. Sluyters-Rehbach, J. H. Sluyters, *J. Electroanal. Chem.* **176** (1984) 275
44. L. Chen, A. Lasia, *J. Electrochem. Soc.* **139** (1992) 3214.

Journal of the Serbian Chemical Society
JSCS-info@shd.org.rs • www.shd.org.rs/JSCS

J. Serb. Chem. Soc. 78 (12) 2069–2086 (2013)
JSCS–4551

UDC 547.466+546.56:66.097.8:
546.131:620.193
Original scientific paper

Amino acids as corrosion inhibitors for copper in acidic medium: Experimental and theoretical study•

INGRID MILOŠEV[1]*, JASMINKA PAVLINAC[1]**, MILAN HODOŠČEK[2] and ANTONIJA LESAR[1]

[1]*Jožef Stefan Institute, Department of Physical and Organic Chemistry, Jamova 39, SI-1000, Ljubljana, Slovenia and* [2]*National Institute of Chemistry, Laboratory for Molecular Modeling, Hajdrihova 19, SI-1000 Ljubljana, Slovenia*

(Received 26 November 2013)

Abstract: Experimental electrochemical methods combined with quantum chemical calculations and molecular dynamics simulations were emplyed to investigate the possibility for the use of various amino acids as "green" corrosion inhibitors for copper in 0.5 M HCl solution. Among the eleven studied amino acids, cysteine achieved the highest inhibitor effectiveness, reaching 52 % at a concentration of 10 mM. The other amino acids achieved an effectiveness of less than 25 %; some of them even acted as corrosion accelerators. Based on the experimental results, the theoretical calculations and simulations were focused on cysteine and alanine. The electronic and reactivity parameters of their protonated forms in an electrical double layer were evaluated by density functional calculations. In addition, molecular dynamic simulations were introduced to follow the adsorption behaviour of these two amino acids at the Cu(111) surface in the electrolyte solution. The results indicate that the orientation of both molecules was nearly parallel to the surface except for the ammonium group, which was directed away from the surface. Therefore, as the orientation of the cysteine and alanine molecules at the surface were similar, the thiol functional group is responsible for the superior inhibition efficiency of cysteine.

Keywords: amino acids; copper; hydrochloric acid; green inhibitors; quantum chemical calculations; molecular dynamics.

INTRODUCTION

Due to their importance in industry and wide range of applications, copper and its alloys have been the subject of numerous investigations since the 1920s.

* Corresponding author. E-mail: ingrid.milosev@ijs.si
** Present address: Lek d.d.,Verovškova 57, SI-1526 Ljubljana, Slovenia.
• Paper dedicated to Professor Branislav Nikolić.
doi: 10.2298/JSC131126146M

These studies aimed at preventing or reducing the corrosion process in aggressive media.[1–10] As corrosion inhibitors, various substances, both inorganic and organic, can be used. While inorganic inhibitors reduce the corrosion through film formation, organic compounds act mostly *via* adsorption processes on the metal surface and complex formation. As most efficient organic corrosion inhibitors could be toxic and thus unacceptable for the environment, contemporary studies are directed towards the search for alternative inhibitors that would be ecologically acceptable, stable, non-toxic and available at a relatively low cost. These compounds, referred to as "green", "eco-friendly", or "environmentally-friendly", comprise both organic and inorganic inhibitors.[9,11–13] Among the organic inhibitors, natural plant extracts are used – from *Aloae vera* to radish leaves; most of them contain hetero-atoms such as N, S, P and O and can thus form protective films.[11–13] Among green inhibitors, studies on lanthanide salts, natural polymers, such as guar gum and starch, and bio-mimicking green inhibitors, such as amino acids, were conducted.[13] Amino acids are completely soluble in aqueous media and can be produced with high purity at low costs.

The majority of the investigations on copper were performed in acidic chloride media (HCl),[14–21] but also in HNO_3,[22,23] H_2SO_4,[24,25] H_3PO_4,[26] and even non-aqueous mineral oil[27] (Table I). Some copper alloys were also investigated, including Cu-5Ni and Cu-65Ni in 0.25 M Na_2SO_4 + 0.05 M H_2SO_4,[28] Cu-30Ni in 0.5 M H_2SO_4,[29] and bronze Cu-3Sn in 0.2 g L^{-1} Na_2SO_4 + 0.2 g L^{-1} $NaHCO_3$.[30,31] Among various amino acids, cysteine is the most extensively studied (Table I). This is related to the fact that it contains sulphur, which is expected to beneficially affect the inhibition mechanism, as reported for various organic inhibitors.[4] In HCl solution, cysteine achieved the highest inhibition efficiency (*IE*) of 93 % at 15 mM.[21] Other amino acids were also reported to perform well: alanine 94 % at 1 mM,[14] threonine 83 % and glutamic acid 90 % at 1 mM concentration.[17] Cysteine was also effective in nitric acid.[22,23] Furthermore, cysteine was also effective as a corrosion inhibitor for bronze. It reached an *IE* of 95 % at 10 mM for Cu-3Sn bronze in 0.2 g L^{-1} Na_2SO_4 + 0.2 g L^{-1} $NaHCO_3$.[30] For pre-corroded Cu-6Sn samples with bronze disease, a cysteine solution might be a better choice than benzotriazole for long-term exposure in an atmosphere of high relative humidity.[31] In contrast, cysteine was poorly effective as inhibitor for Cu-5Ni and Cu-65Ni alloys in 0.25 M Na_2SO_4 + 0.05 M H_2SO_4.[28] In non-aqueous medium cysteine and histidine were not efficient corrosion inhibitors for Cu.[27]

When comparing various amino acids, their inhibition effect in HCl depended on the type of amino acid and its concentration (Table I). Alanine outperformed aspartic acid and glutamine,[14] glutamic acid was better than serine and threonine,[17] cysteine was better than glycine and glutamic acid,[21] and glutamine was better than glutamic acid, asparagine and aspartic acid.[18] In nitric acid, cysteine

TABLE I. Literature data for the values of the inhibition efficiency (*IE*) for various amino acids as inhibitors of the corrosion of Cu and Cu alloys in different media

Reference	Material, medium	Amino acid	*IE*
14	Cu, 1 M HCl, 25 °C	Alanine	94 % at 1 mM
		Aspartic acid	52 % at 1 mM
		Glutamine	55 % at 1mM
16	Cu, 0.6 M HCl	Cysteine	84 % at 18 mM
		Cysteine + Cu^{2+}	88 % at 18 mM
15	Cu, 0.5 M HCl	Alanine	43 % at 0.01 mM
		Cysteine	59 % at 0.01 mM
17	Cu, 0.5 M HCl	Serine	55 % at 1 mM
		Threonine	83 % at 1mM
		Glutamic acid	90 % at 1mM
20	Cu, 0.5 M HCl	Arginine	63 % at 1 mM
		Arginine + KI	87 % at 1 mM + 5 mM KI
19	Cu, 0.5 M HCl	Methionine	77 % at 12 mM
		Methionine + Zn^{2+}	92 % at 12 mM + 0.5 mM Zn^{2+}
21	Cu, 0.5 M HCl	Glycine	60 % at 15 mM
		Glutamic acid	62 % at 15 mM
		GLY+GLU+CYS	91 % at 15 mM
		Cysteine	93 % at 15 mM
		Glutathione	95 % at 15 mM
18	Cu, 0.5 M HCl	Aspartic acid	57 % at 0.1 M
		Glutamic acid	60 % at 0.1 M
		Asparagine	65 % at 0.1 M
		Glutamine	73 % at 0.1 M
		Glutamine	67 % at 10 mM
		Glutamine + KI	94 % at 10 mM + 5 mM KI
25	Cu, 0.5 M H_2SO_4, 20 °C	Tryptophan	87 % at 10 mM
23	Cu, 1M HNO_3	Cysteine	88 % at 0.1 mM
22	Cu, 0.5 M HNO_3	Valine	–15 % at 1 mM
		Glycine	–4 % at 1 mM
		Arginine	38 % at 1 mM
		Lysine	54 % at 1 mM
		Cysteine	61 % at 1 mM
29	Cu-30Ni, 0.5 M H_2SO_4	Cysteine	91 % at 1mM
30	Cu-3Sn,	Cysteine	95 % at 10 mM
	Na_2SO_4+$NaHCO_3$	Alanine	82 % at 1 M
		Phenyl alanine	56 % at 10 mM
28	Cu-5Ni, 0.25 M	Glycine	12 % at 0.05 mM
	Na_2SO_4+0.05 M H_2SO_4	Alanine	25 % at 0.1 mM
		Leucine	39 % at 0.01 mM
		Lysine	38 % at 0.2 mM
		Histidine	–3 % at 0.01 mM
		Glutamic acid	38 % at 0.01 mM
		Cysteine	22 % at 0.01 mM

outperformed lysine and arginine.[22] As a corrosion inhibitor for bronze in acidic medium, cysteine was slightly more efficient than alanine and much more efficient than phenyl alanine.[30]

The inhibition efficiency of amino acids was improved by the addition of anions, such as iodide, and cations, such as Zn^{2+} and Cu^{2+}.[19,20] The synergistic effect of iodide ions was ascribed to a strong chemisorption of the ions on the metal surface. The columbic attraction between the chemisorbed anion and the cation of an amino acid leads to greater surface coverage and hence, greater inhibition efficiency.[19,20] The synergistic effect of Cu^{2+} was ascribed to the formation of a copper cysteinate complex (Cu(I) cysteine).[16] The Cu^{+} formed by the reduction of Cu^{2+} react with cysteine to form the Cu(I) cysteine complex which deposit at the surface and inhibits the cathodic partial reaction. A similar effect was reported for methionine in the presence of Zn^{2+}.[19]

In order to reveal the adsorption mechanism, different adsorption isotherms were tested.[14,16,17,19,25,26] Taking into account a commonly accepted value of –40 kJ mol^{-1} as a threshold between chemisorption and physisorption, the collected data indicated that the operative mechanism of adsorption of amino acids to a copper surface is physisorption.

Amino acids generally act as cathodic inhibitors, *i.e.*, they inhibit the cathodic partial reaction to a larger extent than the anodic partial reaction.[14–16,18,22,24,29,30] With increasing concentration of amino acid, the inhibition efficiency generally increased,[18,21,29] although deviations from this behaviour have been observed.[16,28,30] At a given concentration, the degree of protection decreased with temperature in the range from 25 to 55 °C.[14] The value of *IE* was noticed to increase with time of immersion.[20] An accelerating effect of some amino acids (glycine, alanine, leucine, lysine, histidine, glutamic acid and cysteine) on the corrosion was observed for the Cu–5Ni alloy in HCl solution,[28] and valine and glycine for Cu in nitric acid.[22]

The aim of the present work was to study several amino acids as corrosion inhibitors of copper corrosion in hydrochloric acid. The experimental electrochemical studies were supplemented with a theoretical investigation based on quantum chemical methods to characterize the electronic and reactivity parameters, while molecular dynamics simulations were applied to describe the adsorption behaviour of amino acid inhibitors in the electrolyte solutions at the molecular level. In this work, the investigations were focused on cysteine (CYS) and alanine (ALA) amino acids. Cysteine could be considered as alanine derivative in which one of the hydrogen atom of the terminal $–CH_3$ group of alanine is substituted by a –SH functional group.

EXPERIMENTAL

Amino acids

Eleven of the standard twenty α-amino acids were tested. The Lewis structures, names and abbreviations of the amino acids used in this study are summarized in Fig. 1. Amino acids can be generally sorted into six main groups based on their structure and the chemical characteristics of their functional (R) groups: aliphatic, hydroxyl- or sulphur-containing, cyclic, aromatic, basic and acidic. In the present work the following groups were tested regarding the functional group, polarity, charge and sulphur-containing group (Fig. 1):

Group I: aliphatic, non-polar, neutral amino acids: glycine (GLY), alanine (ALA), leucine (LEU) and methionine (MET); among these, methionine is S-containing;

Group II: uncharged group, non-polar, neutral amino acids: threonine (THR), asparagine (ASN) and cysteine (CYS); among these the cysteine is S-containing;

Group III: charged group, polar and basic amino acids: histidine (HIS) and arginine (ARG);

Group IV: aromatic, non-polar, neutral amino acids: tryptophan (TRP) and tyrosine (TYR).

All tested amino acids are L-enantiomers, except for glycine which is without a centre of chirality. Methionine and cysteine are the only ones to contain sulphur. Histidine and arginine

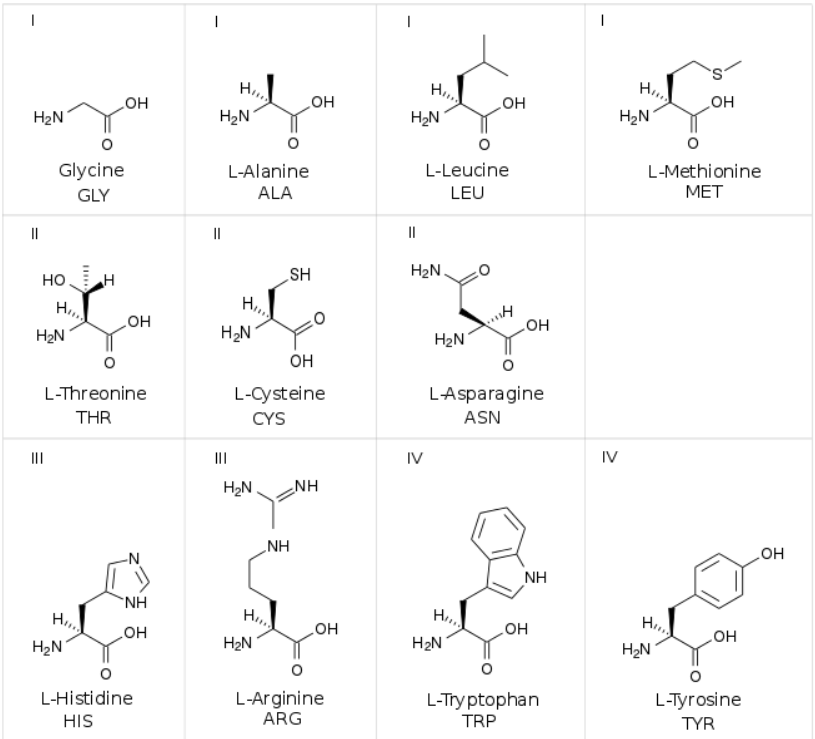

Fig. 1. Lewis structures, names and abbreviations of the amino acids. Roman number in the left corner denotes the group of the amino acids: I) aliphatic group, non-polar, neutral, II) uncharged group, polar, neutral, III) charged group, polar, basic and IV) aromatic group, non-polar, neutral.

are charged polar basic acids, whilst tryptophan and tyrosine belong to aromatic acids. Among these eleven amino acids, four are classified as essential: leucine, methionine, threonine and tryptophan.

The structure of the amino acids are sensitive to the phase, the different forms of the amino acids depending on the medium are displayed in Fig. 2. At pH between 2.2 and 9.4 (mean values for 20 common amino acids), the predominant form adopted by α-amino acid contains a negative carboxylate and a positive ammonium group, so has net zero charge (zwitterion form). Since amino acids have slightly different acid dissociation constants, (pK_a values), their iso-electric points, pI, are different ($pI = 1/2(pK_{a1} + pK_{a2})$.[32] Below 2.2 and above 9.4, the net charge is positive and negative, respectively. In acidic medium, they result from –the protonation of NH_2 group ($–NH_3^+$), while in alkaline medium, the –COOH group is deprotonated ($–CO_2^-$).

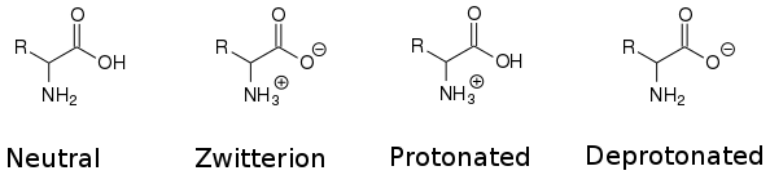

Fig. 2. The scheme of the amino acid forms depending on the medium.

Electrochemical measurements

Copper (99.9 %) was supplied by Goodfellow (Cambridge Ltd., UK) as 2-mm thick foil Samples were cut in the shape of discs of 15 mm in diameter. Prior to the measurements, the samples were mechanically ground under water using SiC paper successively up to 4,000-grit to achieve a surface with a uniform pattern of scratches. The samples were cleaned with ethanol in an ultrasonic bath for two minutes, double-rinsed with double-distilled water, and finally dried in a stream of nitrogen.

Electrochemical measurements were realised in a three-electrode corrosion cell (volume 350 mL) at room temperature. A specimen embedded in a Teflon holder, with an area of 0.785 cm^2 exposed to the solution, served as the working electrode. A saturated calomel electrode (SCE, 0.2415 V *vs*. saturated hydrogen electrode, SHE) was used as the reference electrode and carbon rods as the counter-electrode. Electrochemical experiments were realised using a PAR & EGG 263A potentiostat/galvanostat and controlled by Powersuite software. The measurements were performed in an aerated 0.5 M HCl (37 %) solution (Carlo Erba Reagents, Rodano, Italy). The amino acids were added to the HCl solution at a concentration of 10 mM.

Prior to the measurements, the samples were allowed to stabilize for 1 h under the conditions of the open circuit potential, E_{oc}. Potentiodynamic measurements were performed using a 1 mV s^{-1} potential scan rate, starting at 250 mV negative to the stabilized E_{oc} and then increased in the anodic direction. The values of E_{corr} and j_{corr} were determined from Tafel analysis. For each sample, measurements were performed at least in duplicate. Representative polarization curves were selected for graphical presentations. The inhibition effectiveness, *IE*, was calculated according to the formula:

$$IE = 100\frac{j_{corr,inh} - j_{corr}}{j_{corr,inh}} \quad (1)$$

where $j_{corr,inh}$ and j_{corr} are the corrosion current density in the inhibited and uninhibited solution, respectively.

Quantum chemical calculations

The molecular behaviour of cysteine (CYS) and alanine (ALA) as corrosion inhibitors for copper metal in acidic medium was studied by the quantum electrochemical approach. Density functional theory, specifically the B3LYP functional[33-35] using flexible 6-311G** basis set[36] containing polarization and diffuse functions, was used for the calculations of the electronic structure and reactivity parameter. Frequency calculations for species were calculated to verify the minimum-energy structures. Special care was devoted to setting up a reliable model that accounted for the experiment conditions. The corrosion process occurs in the liquid phase, thus, the self-consistent reaction field (SCRF) theory,[37] with the Tomasi polarized continuum model (PCM),[38] was used to perform the calculations in solution. These methods model the solvent as a continuum of uniform dielectric constant (ε = 78.5) and define the cavity where the solute is placed as a uniform series of interlocking atomic spheres. While the inhibitory action does not occur in the bulk solution but is related to the electrical double layer (EDL) interface, *i.e.*, the molecule–solution interface, a dielectric constant of 6.0 is more appropriate.[39] While an electric field is present in the EDL, it seems reasonable to check the effect of the EDF electric field, which was considered as a finite electric field (10^7 V cm^{-1}) along the dipole moment of molecule included in the Hamiltonian. Under these conditions, the electronic parameters, such as HOMO–LUMO energy gap and dipole moment, were calculated for CYS and ALA inhibitor molecules. Furthermore, the following global reactivity parameters: electronic chemical potential, global chemical hardness and the fraction of transferred electron were evaluated. The local reactivity parameters were analysed by means of Fukui indices,[40] calculated by the finite difference approximation approach.[41] The details of these calculations are widely available elsewhere.[42] The Gaussian 09 program package[43] was used for all quantum chemical calculations.

Molecular dynamics studies

Molecular dynamic simulations were applied to evaluate the interaction of the amino acid molecules with the cooper surface in acid solutions. The surface of Cu(111) was chosen to investigate the orientation and dynamics of CYS and ALA in electrolyte solutions. Cu atoms were restrained with a force constant of 50 kcal mol^{-1} $Å^{-3}$ throughout the simulation. The model of the solution was set up in a way to correspond a solution of 10 mM CYS (ALA) in an aqueous 0.5 M HCl solution. Two all-atom models were generated to summarize the experimental conditions. The model related to CYS in HCl medium illustrates the protonated form (CYS-PH), and also for ALA in HCl media, the protonated form (ALA-PH) is operative. Setting up the corresponding concentrations of experimental HCl electrolyte solution, 5000 water molecules were included in the orthorhombic box with the sizes 56.1, 53.1, 52.0 Å and then one molecule of amino acid was randomly added into the box. Furthermore, 45 protons randomly coupled with H_2O molecules to form H_3O^+ were added and the same number of chlorine anions. At constant pressure (1 atm) and temperature (300 K), the molecular dynamics protocol was applied in the equilibration phase of 100 ps. Then 20 ns long trajectory of the system with step-size of 1 fs and 3D periodic boundary conditions were pursued. The CHARMM program package[44] was employed for the molecular dynamics simulations using CHARMM version 36 parameter set[45] for the amino acids and ions. Parameters for copper atoms were produced according to the CHARMM parameter set development standard using *ab initio* results from a water molecule on a Cu(111) surface.[46]

RESULTS AND DISCUSSION

Potentiodynamic curves in hydrochloric acid with and without the addition of amino acids

The electrochemical behaviour of copper in 0.5 M HCl has been extensively studied.[1] A polarization curve is presented in Fig. 3. In HCl solution, the mechanism of cathodic reaction in the vicinity of the corrosion potential involves the reduction of dissolved oxygen:[1]

$$O_2 + 4H^+ + 4e^- \leftrightarrows 2H_2O \quad (2)$$

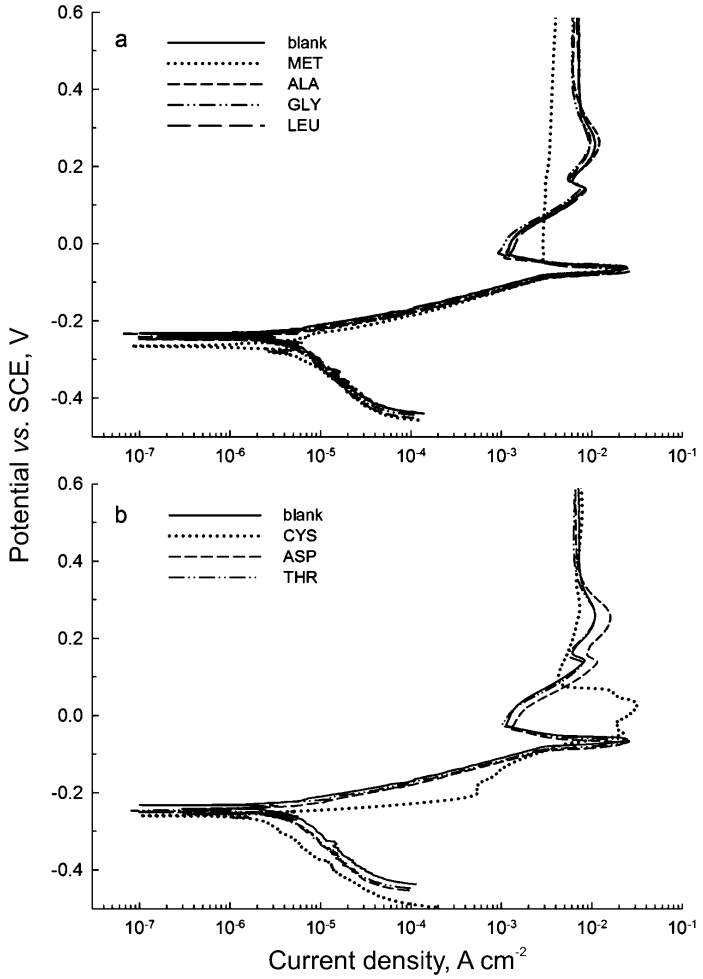

Fig. 3. Potentiodynamic polarization curves recorded for Cu in blank 0.5 M HCl and in 0.5 M HCl containing 10 mM of amino acids from a) group I: glycine (GLY), alanine (ALA), leucine (LEU) and methionine (MET) and b) group II; threonine (THR), asparagine (ASP) and cysteine (CYS). dE/dt = 1 mV s^{-1}.

The anodic curve shows three distinct regions: active dissolution in the apparent Tafel region, a transition region with the maximum current density and the limiting current region. It was proposed that $CuCl_2^-$ complex may be formed either through direct formation from the metal:

$$Cu + 2Cl^- \leftrightarrows CuCl_2^- + e^- \quad (3)$$

or

$$Cu + Cl^- \leftrightarrows CuCl + e^- \quad (4)$$

$$CuCl + Cl^- \leftrightarrows CuCl_2^- \quad (5)$$

The dissolution may also include dissolution of copper as the Cu^+ in the first instance:[1]

$$Cu \leftrightarrows Cu^+ + e^- \quad (6)$$

$$Cu^+ + 2Cl^- \leftrightarrows CuCl_2^- \quad (7)$$

In the apparent Tafel region, mixed charged transfer and mass transport are usually assumed.[1] The reaction is controlled by both electro-dissolution of copper and diffusion of $CuCl_2^-$ to the bulk solution.[1] The linear slope close to 60 mV denotes a one-electron transfer reaction. Film formation is reflected in the peak at –0.07 V followed by a decrease in the current density (Fig. 1). At the current minimum, the surface CuCl coverage reached its maximum. However, CuCl species do not attain sufficient protection since, due to film dissolution, reaction (5), or metal dissolution, reaction (7), the current density progressively increases. The cuprous chloride complex can further dissolve according to:

$$CuCl_{2,ads}^- \leftrightarrows Cu^{2+} + 2Cl^- + e^- \quad (8)$$

This process denotes the establishment of the limiting current region at approximately 0.4 V and continues at more positive potentials. Thus, the overall reaction for copper corrosion can be represented by:

$$2Cu + 4H^+ + 4Cl^- + O_2 \rightarrow 2Cu^{2+} + 4Cl^- + 2H_2O \quad (9)$$

Polarization curves recorded in the presence of amino acids are generally similar to blank curve (Figs. 3 and 4). Depending on the type of amino acid, its effect on the corrosion process of Cu can be accelerating (increasing the j_{corr} value) or inhibitory (decreasing the j_{corr} value), accompanied by the corresponding shift of the E_{oc} and E_{corr} values. The resulting inhibition effectiveness, *IE*, and values of E_{oc} and E_{corr} are presented in Fig. 5. Among the aliphatic amino acids, alanine and leucine modestly accelerated the corrosion process (*IE* of –12 and –2 %, respectively), whilst glycine had an almost negligible inhibitory effect. A slightly higher effect, but still modest, was achieved by methionine which exhibited a shift in E_{corr} to 30 mV more negative values and the smallest current

density of the cathodic branch (Fig. 3a). In the anodic part, the differences were almost negligible compared to the blank curve. At potentials more positive than the anodic peak, the curve for methionine differed from those of the other amino acids; it formed a current density plateau over a broad potential range.

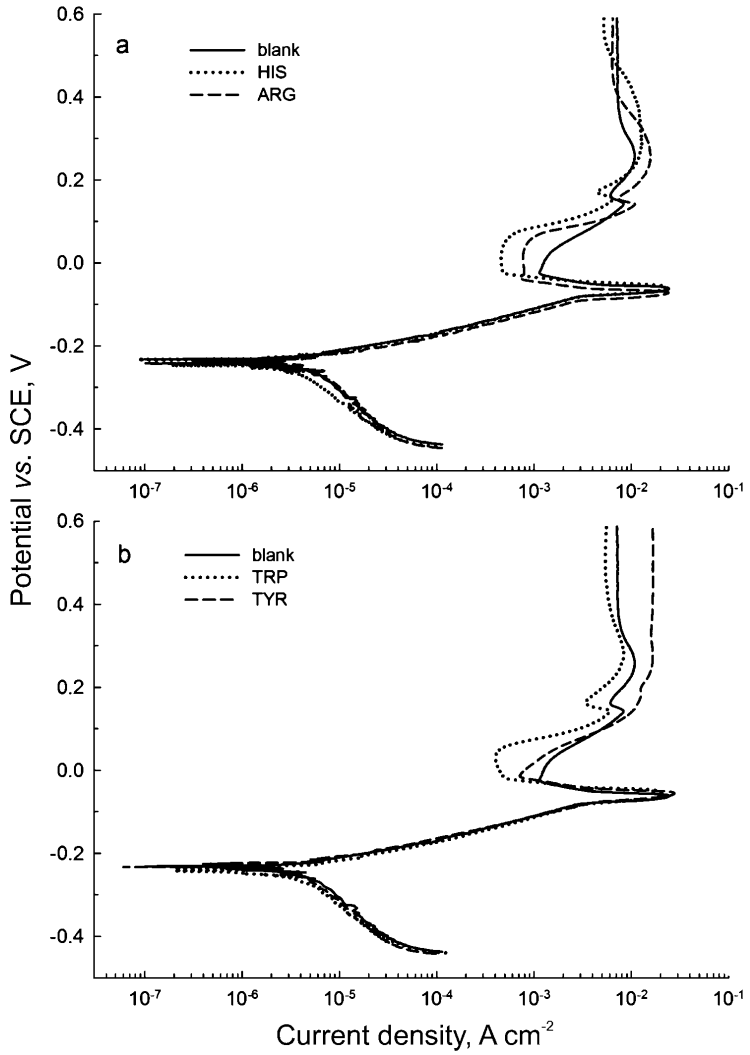

Fig. 4. Potentiodynamic polarization curves recorded for Cu in blank 0.5 M HCl and in 0.5 M HCl containing 10 mM of amino acids from a) group III: histidine (HIS) and arginine (ARG), and b) group (IV): tryptophan (TRP) and tyrosine (TYR). dE/dt = 1 mV s^{-1}.

Polar, neutral amino acids exhibited the most distinguished differences compared to the blank curve in the cathodic part (Fig. 3b): the cathodic current den-

sity decreased by approximately half a decade and the corrosion potential shifted in negative direction by 10–30 mV. In terms of *IE*, asparagine produced no effect, threonine achieved a value similar to that of methionine, 12 %, whilst the *IE* for cysteine was 52 % (Fig. 5a). In the anodic branch, the current densities for asparagine and threonine were slightly higher compared to the blank, whilst for cysteine, a small peak was formed at around –0.2 V. At more positive potentials, in addition to the peak at –0.07 V, ascribed to CuCl formation, another peak formed at 0.01 V, followed by a decrease in the current density and a limiting plateau region. Among the examined amino acids, the formation of two additional anodic peaks, at –0.2 and 0.01 V, was unique for cysteine.

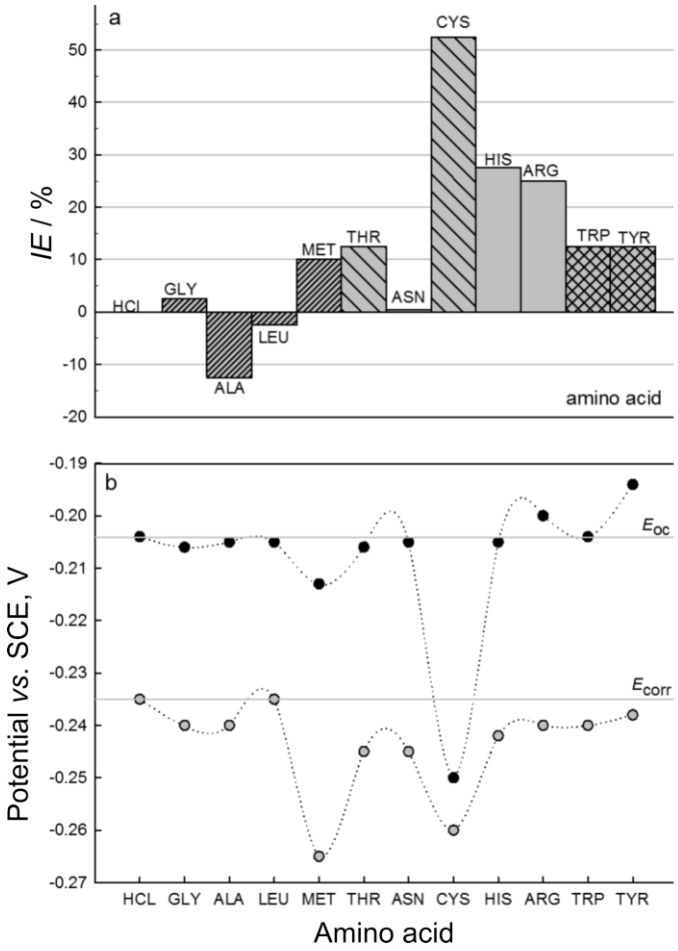

Fig. 5. a) Inhibition effectiveness, *IE*, deduced for copper from the values of the corrosion current density measured in 0.5 M HCl solution inhibited by various amino acids. b) Values of the open circuit potential, E_{oc}, and corrosion potential, E_{corr}, measured for copper in 0.5 M HCl solution inhibited by various amino acids.

Among the basic, non-polar amino acids, histidine and arginine with imidazole and guanidinium functional groups, histidine exhibited smaller current densities in the cathodic part (Fig. 4a). The *IE* values of 27 and 25 % were larger than those for aliphatic amino acids, but smaller than that for cysteine (Fig. 5a). In the region following the anodic peak, both amino acids caused a decrease in the current density. A plateau of ≈50 mV was established, which was not the case in the blank solution or in the presence of aliphatic and polar, neutral amino acids. The aromatic amino acids tryptophane and tyrosine showed similar behaviour: at potentials less negative than the anodic peak, only slight differences occurred compared to the blank curve (Fig. 4b). The resulting *IE* value for both was 12 % (Fig. 5a). In the region following the anodic peak, at ≈0 V, the related current density was smaller in the presence of tyrosine and, especially, of tryptophan, which formed a plateau of 40 mV.

Inhibition effectiveness of the amino acids

Two amino acids, alanine and leucine, slightly accelerated the corrosion process (Fig. 5a). No effect was observed for asparagine. All other amino acids acted as corrosion inhibitors, with cysteine being the most effective with an *IE* value of 52 %. The following order was observed: CYS > HIS ≈ ARG > THR ≈ TYR ≈ ≈ TRP > MET > GLY.

It is noteworthy that the difference in the effect of cysteine and methionine was quite large (Fig. 5a) although both contain sulphur which is believed to be mainly responsible for the strong adsorption of organic molecules. The adsorption achieved through thiol (S–H) group of cysteine was obviously stronger than through the methylthio ($S–CH_3$) group of methionine (Fig. 1). Furthermore, cysteine acted as an inhibitor and alanine as an accelerator although they differ only in the presence of the thiol group.

The values of open circuit potential, E_{oc}, measured after 1 h immersion and corrosion potential, E_{corr}, determined by Tafel analysis for the blank HCl solution and in the presence of various amino acids, are presented in Fig. 5b. Cysteine showed the most negative shift of E_{oc} followed by methionine, while the other amino acids showed very similar values to the blank. Among the E_{corr} values, methionine and cysteine again shifted them to the most negative values, compared to the blank.

Quantum chemical results

Two amino acids, cysteine and alanine, were considered. Cysteine achieved best inhibition effectiveness; on the other hand, alanine acted as corrosion accelerator; these two amino acids differ only in the presence of a thiol group (Fig. 1). The calculations have been adjusted to the experimental conditions as much as possible, *i.e.*, amino acids were considered in the protonated forms denoted as

CYS-PH and ALA-PH. The electronic data have been calculated with the model of inhibitors in EDL and with the model of inhibitors in EDL applying a finite electric field in the *z*-direction. The EDL has been simulated with solvent dielectric constant of 6.0 and the electric field of 10^7 V cm^{-1} has been applied. The B3LYP/6-311G** fully optimized structures of protonated forms of CYS and ALA molecules calculated for the EDL model are displayed in Fig. 6, where the most relevant bond distances are also stated. The bond distances calculated for the model with external field are insignificantly different from those given in the figure. The inhibitor performance was analysed by quantum chemical parameters responsible for the inhibitory action and was further addressed by evaluating the global reactivity parameters. Table II presents the HOMO–LUMO energy gap (ΔE) and dipole moment as electronic parameters and the following reactivity parameters: electronic chemical potential (μ), global chemical hardness (η) and the fraction of transferred electron (ΔN). The calculated values for both models employed are quite similar implying that the external field has small influence on the electronic as well as on the reactivity parameters of studied amino acids. Low values of energy gap are associated with effective inhibition. The ΔE results support the better inhibition effectiveness of cysteine in acid media compared to alanine. Further, similar conclusions are confirmed by the results on electronic chemical potential and global chemical hardness.

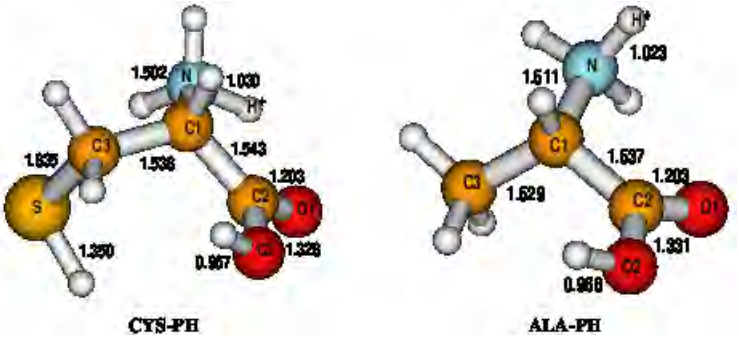

Fig. 6. The equilibrium structures (selected B3LYP/6-311G** bond distances in Å) of the protonated forms of cysteine and alanine molecules in the EDL molecule–aqueous solution interface.

To examine the local reactivity behaviour we have calculated the Fukui indices, which are summarised in Table III. The atomic sites with the maximum value of f_i^- are the preferred sites to which the amino acid molecule will donate charge when attacked by an electrophilic reagent. On the other hand, a large value of f_i^+ is assigned to the atomic sites where the amino acid molecule will receive charge, when attacked by a nucleophilic reagent. In the acid medium, the S atom of cysteine molecule is the most favourable site for an electrophilic

attack. For CYS-PH C2 and O1 are the preferred sites for nucleophilic attack. On the other hand, O2 and O1 atoms of ALA-PH are the most reactive centres for an electrophilic attack. C2 and O1 atoms participate in the nucleophilic attack of ALA-PH. From Fukui analysis it can be concluded that more centres are involved in the adsorption process of the both amino acid molecules.

TABLE II. Electronic parameters (HOMO–LUMO energy gap (ΔE), dipole moment) and global reactivity parameters (electronic chemical potential (μ), global chemical hardness (η), the fraction of transferred electron (ΔN)) of protonated cysteine and alanine forms in acidic medium; a: $\varepsilon = 6.0$; b: $\varepsilon = 6.0$, with an electric field of 10^7 V cm^{-1}

Species	Model	ΔE / eV	Dipole moment, Debye	μ	η	ΔN
CYS-PH	a	6.44	7.40	–5.04	3.22	–0.01
	b	6.40	6.89	–5.04	3.22	–0.01
ALA-PH	a	7.85	8.70	–5.48	3.93	–0.06
	b	7.81	8.97	–5.52	3.91	–0.07

TABLE III. Condensed Fukui functions (f^-, f^+) of protonated cysteine and alanine forms in acidic medium. The most favourable sites for electrophilic and nucleophilic attacks are bold; a: $\varepsilon = 6.0$; b: $\varepsilon = 6.0$, with an electric field of 10^7 V cm^{-1}

Species		Model	C1	C2	N	O1	O2	C3	S
	f^-	a	0.00	0.02	–0.01	–0.04	–0.02	0.04	**–0.80**
		b	0.00	0.01	–0.01	–0.04	–0.02	0.04	**–0.80**
CYS-PH	f^+	a	0.00	**–0.19**	–0.01	**–0.14**	–0.06	0.00	–0.10
		b	–0.01	**–0.17**	–0.02	**–0.13**	–0.06	0.00	–0.08
	f^-	a	–0.06	0.00	0.00	**–0.54**	**–0.13**	–0.01	–
		b	–0.06	0.00	0.00	**–0.54**	**–0.13**	–0.01	–
ALA-PH	f^+	a	0.00	**–0.16**	–0.02	**–0.13**	–0.06	0.00	–
		b	–0.03	**–0.22**	–0.06	**–0.14**	–0.07	0.01	–

Molecular dynamics results

The adsorption structures of CYS and ALA amino acids at the Cu(111) surface in the acid medium provided by molecular dynamics simulations were analysed through graphical visualization of the adsorption configurations in the electrolyte solution. The result of simulations of both models are shown in Fig. 7, where on left panel snapshot configurations of corresponding form of CYS or ALA after 20 ns dynamic simulations are displayed, while on right panel normalized histograms of the atomic positions perpendicular to the Cu(111) surface (Cu atoms being at 0 position) for the selected atoms of amino acid molecule forms are summarized. From top right panel in Fig. 7, it can be easily seen that the distances of the S, O1, O2 and C3 atoms of CYS-HP from the Cu surface are nearly the same; for the S atom the distance amounts to 2.3 Å. The distance of N atom from the Cu surface is in the range 3.7–4.1 Å, implying that the protonated cysteine molecule is absorbed nearly parallel to the copper surface, but with $–NH_3^+$ group oriented away from the surface into the solution. Furthermore, it

could be concluded from the figure that the protons are distributed throughout the solution and approach not less than 2.0 Å to the surface. Moreover, chlorine anions are distributed throughout the solution with minimum distance to the surface of 2.7 Å.

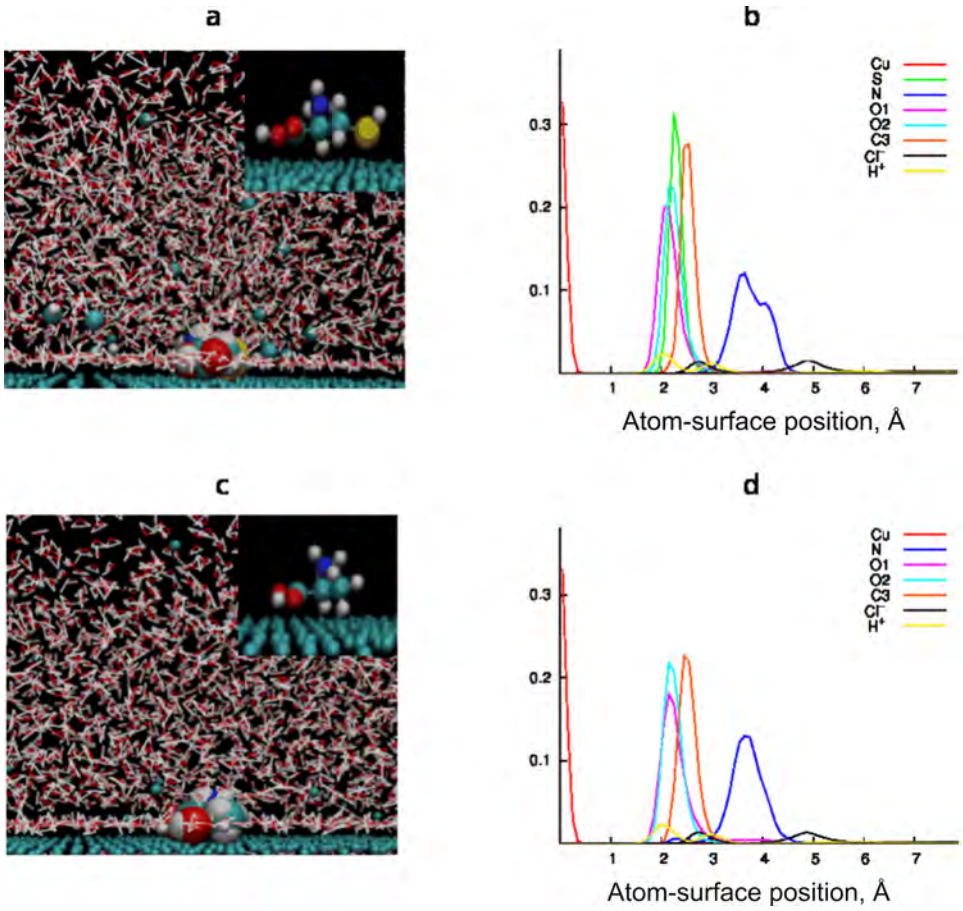

Fig. 7. Adsorption configurations (a and c panel) and normalized histograms of atomic positions relative to Cu(111) surface (b and d panel) for cysteine and alanine molecules in acid medium. In insets the medium is excluded to present more clearly the adsorption configurations of molecules at the Cu(111) surface (green). Legend: amino acid: O (red), N (blue), S (yellow), C (green), H (grey); medium: H_2O (white), H_3O^+ (red), Cl (green).

The ALA molecule in HCl electrolyte solution is shown in panels c and d of Fig. 7. Compared to the protonated form of cysteine, similar conclusions were drawn for orientation of protonated alanine molecule in acid solution. The only noticeable small difference is more sharp position of N atom with the maximum

at 3.7 Å above the Cu surface. It should be mentioned that an S atom is not involved in this amino acid.

CONCLUSIONS

An experimental electrochemical and a theoretical study were performed to investigate the possibility of employing various amino acids as corrosion inhibitors for copper in 0.5 M HCl solution. Eleven tested amino acids were divided into four groups based on the type of functional group, polarity, charge and presence of sulphur. No clear relationship between the groups was noticed in terms of the inhibition effectiveness in hydrochloric acid, *i.e.*, amino acids from the same group may act as corrosion inhibitor or corrosion accelerator. The experimental results confirmed that cysteine exhibited the largest inhibition effectiveness reaching about 50 % at a concentration of 10 mM. Histidine and arginine reached *IE* values of about 25 %, while the other amino acids yielded only moderate effects, not important for practical use. Alanine and leucine acted as corrosion accelerators.

The reasons for diametrically opposed behaviour of cysteine and alanine, differing only in the presence of a thiol group, were investigated further using quantum chemical calculations and molecular dynamics simulations. The better inhibition effectiveness of cysteine compared to alanine was confirmed by the results of the HOMO–LUMO energy gap, electronic chemical potential and global chemical hardness. The calculated local reactivity parameters indicated that several atomic centres are involved in the adsorption process of both amino acid molecules. The electrophilic attack of cysteine molecule is strongly related to the S atom, while in alanine molecule, both the O1 and O2 atoms are the favourable sites. On the other hand, C2 and O1 are preferred sites for nucleophilic attack, in other words, the –C=O carbonyl group is operative in a back donation process. The molecular dynamics simulations provided a relative comparison of the orientation of cysteine and alanine inhibitors in 0.5 M HCl solutions at the Cu(111) surface. No significant difference could be observed for the absorption of these amino acids regarding their orientation at the metal surface. Yet, cysteine achieved high inhibition effectiveness which can be ascribed to adsorption through the thiol group. Finally, the results of global reactivity parameters and those of molecular dynamic simulations do not support the participation of N atom of ammonium group in the adsorption process.

*Acknowledgement*s. The financial support of this work provided by the Slovenian Research Agency within the research grant P2-0148 is greatly appreciated. The authors thank Dr. A. Kokalj for fruitful discussions about the *ab initio* parameters for the Cu surface.

ИЗВОД

АМИНОКИСЕЛИНЕ КАО КОРОЗИОНИ ИНХИБИТОРИ ЗА БАКАР У КИСЕЛОЈ СРЕДИНИ: ЕКСПЕРИМЕНТАЛНА И ТЕОРИЈСКА СТУДИЈА

INGRID MILOŠEV[1], JASMINKA PAVLINAC[1], MILAN HODOŠČEK[2] и ANTONIJA LESAR[1]

[1]*Jožef Stefan Institute, Department of Physical and Organic Chemistry, Jamova 39, SI-1000, Ljubljana, Slovenia* и [2]*National Institute of Chemistry, Laboratory for Molecular Modeling, Hajdrihova 19, SI-1000 Ljubljana, Slovenia*

Коришћењем експерименталних електрохемијских метода у комбинацији са квантно-хемијским израчунавањем и симулацијама молекуларне динамике проучаване су могућности употребе различитих аминокиселина као "зелених" корозионих инхибитора за бакар у 0,5 M раствору HCl. Између једанаест тестираних аминокиселина цистеин је показао најбољу корозиону заштиту (52 % при концентрацији 10 mM). Остале аминокиселине су постигле заштиту мању од 25 %; неке међу њима чак делују као акцелератори корозије. На основу добијених експерименталних резултата за теоријска израчунавања и симулације изабрани су цистеин и аланин. Електронски и реактивни параметри електрохемијског двослоја одређени су за протоноване облике аминокиселина помоћу рачунања на основу теорије функционала густине. Симулацијом молекуларне динамике праћена је адсорпција ових аминокиселина на Cu(111) равни у раствору електролита. Оријентација обе аминокиселине је скоро паралелна са површином са изузетком амонијум групе која је усмерена од површине. Будући да је оријентација цистеина и аланина на површини слична, може да се закључи да је тиолска група у цистеину одговорна за његову супериорну корозиону заштиту у односу на друге аминокиселине.

(Примљено 26. новембра 2013)

REFERENCES

1. G. Kaer, B. D. Barker, F. C. Walsh, *Corros. Sci.* **46** (2004) 109
2. C. A. C. Sequeira, in *Uhlig's Corrosion Handbook*, 2nd ed., R. Winston Revie, Ed., Electrochemical Society Series, Wiley-Interscience, John Wiley & Sons, Inc., Hoboken, NJ, 2006, p. 729
3. E. Rocca, F. Mirambet, in "*Corrosion of metallic heritage artefacts*", P. Dillmann, G. Béranger, P. Piccardo, H. Matthieses, Eds., Woodhead Publishing in Materials, European Federation of Corrosion Publications, No. 48, Cambridge, 2007, p. 308
4. M. M. Antonijević, M. B. Petrović, *Int. J. Electrochem. Sci.* **3** (2008) 1
5. M. M. Antonijević, M. B. Radovanović, *Zaštita materijala* **51** (2010) 111
6. M. Finšgar, I. Milošev, *Corros. Sci.* **52** (2010) 2737
7. N. K. Allam, A. A. Nazeer, E. A. Ashour, *J. Appl. Electrochem.* **39** (2009) 961
8. J. Mathiyarasu, S. S. Pathak, V. Yegnaraman, *Corros. Rev.***24** (2011) 307
9. D. M. Bastidas, M. Criado, S. Fajardo, V. M. La Iglesia, E. Cano, J. M. Bastidas, *Inter. Mater Rev.*, **55** (2010) 99
10. V. S. Saji, *Recent Patents Corros. Sci.* **2** (2010) 6
11. M. Sangeetha, S. Rajendran, T. S. Muthumegala, A. Krishnaveni, *Zaštita materijala* **52** (2011) 3
12. P. B. Raja, M. G. Sathuraman, *Mater. Lett.* **62** (2009) 113
13. D. Kesavan, M. Gopiraman, N. Sulochana, *Chem. Sci. Rev. Lett.* **1** (2012) 1
14. G. K. Gomma, M. H. Wahdan, *Mater. Chem. Phys.* **39** (1994) 142
15. D.-Q. Zhang, L.-X. Gao, G.-D. Zhou, *J. Appl. Electrochem.* **35** (2005) 1081
16. K. M. Ismail, *Electrochim. Acta* **52** (2007) 7811

17. D.-Q. Zhang, Q.-R. Cai, L.-X. Gao, K. Y. Lee, *Corros. Sci.* **50** (2008) 3615
18. D.-Q. Zhang, Q.-R. Cai, X.-M. He, L.-X. Gao, G.-D. Zhou, *Mater. Chem. Phys.* **112** (2008) 353
19. D.-Q. Zhang, Q.-R. Cai, X.-M. He, L.-X. Gao, G. S. Kim, *Mater. Chem. Phys*. **114** (2009) 612
20. D.-Q. Zhang, X.-M. He, Q.-R. Cai, L.-X. Gao, G. S. Kim, *J. Appl. Electrochem.* **39** (2009) 1193
21. D.-Q. Zhang, B. Xie, L.-X. Gao, Q.-R. Cai, H. G. Joo, K. Y. Lee, *Thin Solid Films* **520** (2011) 356
22. K. Barouni, L. Bazzi, R. Salghi, M. Mihit, B. Hammouti, A. Albourine, S. El Issami, *Mater. Lett.* **62** (2008) 3325
23. A. Sedik, S. Abderrahmane, A. Himour, *Sensor Lett.* **9** (2011) 2219
24. J. B. Matos, L. P. Pereira, S. M. L. Agostinho, O. E. Barcia, G. G. O. Cordeiro, E. D'Elia, *J. Electrochem. Soc.* **570** (2004) 91
25. G. Moretti, F. Guidi, *Corros. Sci.* **44** (2002) 1995
26. H. H. Abdel Rahman, A. H. E. Moustafa, M. K. Awad, *Int. J. Electrochem. Soc.* **7** (2012) 1266
27. M. Levin, P. Wiklund, C. Leygraf, *Corros. Sci*. **58** (2012) 104
28. W. A. Badawy, K. M. Ismail, A. M. Fathi, *J. Appl. Electrochem.* **35** (2005) 879
29. H. Saifi, M. C. Bernard, S. Joiret, K. Rahmouni, H. Takenuti, B. Talhi, *Mater. Chem. Phys*. **120** (2010) 661
30. S. Varvara, I. Roratu, M. Popa, L. M. Muresan, *Rev. Roum. Chim.* **56** (2011) 793
31. M. Gravgaard, J. van Lanschot, *J. Inst. Conserv*. **35** (2012) 14
32. *CRC Handbook of Chemistry and Physics*, 58th ed., R. C. Weast, Ed., Section C: *Organic Compounds*, CRC Press, Inc., Palm Beach, FL, 1977/78, p. C-767
33. A. D. Becke, *J. Chem. Phys.* 98 (**1993**) 5648
34. C. Lee, W. Yang, R. G. Parr, *Phys. Rev., B.* **37** (1988) 785
35. B. Miehlich, A. Savin, H. Stoll, H. Preuss, *Chem. Phys. Lett.* **157** (1989) 200
36. A. D. McLean, G. S. Chandler, *J. Chem. Phys.* **72** (1980) 5639
37. M. W. Wong, M. J. Rrish, K. B. Wieberg, *J. Am. Chem. Soc.* **113** (1991) 4776
38. M. Cossi, V. Barone, R. Cammi, J. Tomasi, *Chem. Phys. Lett.* **225** (1996) 327
39. J. O'M. Bockris, S. U. M. Khan, *Quantum Electrochemistry,* Plenum Press, New York, 1979, p. 22
40. R. G. Parr, W. Yang, *J. Am. Chem. Soc.* **106** (1984) 4049
41. W. Yang, W. J. Mortier, *J. Am. Chem. Soc.* **108** (1986) 5708
42. A. Lesar, I. Milošev, *Chem. Phys. Lett.* **483** (2009) 198
43. Gaussian 09 Revision A.1, Gaussian Inc., Wallingford, CT, 2009
44. B. R. Brooks, C. L. Brooks III, A. D. Mackerell, L. Nilsson, R. J. Petrella, B. Roux, Y. Won, G. Archontis, C. Bartels, S. Boresch A. Caflisch, L. Caves, Q. Cui, A. R. Dinner, M. Feig, S. Fischer, J. Gao, M. Hodoscek, W. Im, K. Kuczera, T. Lazaridis, J. Ma, V. Ovchinnikov, E. Paci, R. W. Pastor, C. B. Post, J. Z. Pu, M. Schaefer, B. Tidor, R. M. Venable, H. L. Woodcock, X. Wu, W. Yang, D. M. York, M. Karplus, *J. Comp. Chem.* **30** (2009) 1545
45. A. D. MacKerell Jr., D. Bashford, M. Bellott, R. L. Dunbrack Jr., J. D. Evanseck, M. J. Field, S. Fischer, J. Gao, H. Guo, S. Ha, D. Joseph-McCarthy, L. Kuchnir, K. Kuczera, F. T. K. Lau, C. Mattos, S. Michnick, T. Ngo, D. T. Nguyen, B. Prodhom, W. E. Reiher, III, B. Roux, M. Schlenkrich, J. C. Smith, R. Stote, J. Straub, M. Watanabe, J. Wiorkiewicz-Kuczera, D. Yin, M. Karplus, *J. Phys. Chem., B* **102** (1998) 3586
46. P. Tereshchuk, J. L. F. Da Silva, *J. Phys. Chem., C* **116** (2012) 24695.

Journal of the Serbian Chemical Society
JSCS-info@shd.org.rs • www.shd.org.rs/JSCS

J. Serb. Chem. Soc. 78 (12) 2087–2098 (2013)
JSCS–4552

UDC 66.091+544.6:546.57:539.12:
678.744+544.35
Original scientific paper

Electrochemical synthesis of silver nanoparticles in poly(vinyl alcohol) solution

RADE SURUDŽIĆ[1#], ŽELJKA JOVANOVIĆ[1#], NATAŠA BIBIĆ[2], BRANISLAV NIKOLIĆ[1#] and VESNA MIŠKOVIĆ-STANKOVIĆ[1#*]

[1]*Faculty of Technology and Metallurgy, University of Belgrade, Karnegijeva 4, 11000 Belgrade, Serbia and* [2]*Vinča Institute of Nuclear Sciences, University of Belgrade, Mike Petrovića Alasa 12–14, 11000 Belgrade, Serbia*

(Received 17 October, revised 4 November 2013)

Abstract: In this work, silver/poly(vinyl alcohol), Ag/PVA, colloidal dispersions were obtained by electrochemical reduction of Ag^+. The electrochemical synthesis of silver nanoparticles in aqueous solutions of 5 and 10 wt. % PVA, containing 0.1 M KNO_3 and 3.9 mM $AgNO_3$, was performed at a constant current density of 25 mA cm^{-2} for a synthesis time of 10 min. The presence of silver nanoparticles was confirmed by UV–Vis spectroscopy. Cyclic voltammetry analysis and FT-IR spectroscopy indicated interactions between the silver nanoparticles and the PVA molecules. TEM analysis confirmed the spherical shape of the obtained silver nanoparticles, with a mean diameter of 15±9 nm.

Keywords: electrochemical synthesis; PVA; silver nanoparticles.

INTRODUCTION

Poly(vinyl alcohol) (PVA) is a widely used synthetic polymer. The benefits of its use lie in its properties: non-toxicity, water-solubility, biocompatibility, biodegradability and excellent mechanical properties.[1–6] In addition, its low price and wide availability makes PVA a polymer of choice in a large number of applications.[6] The regular linear structure of PVA with a large number of side hydroxyl groups on the main chain suggests excellent hydrophilicity and reactivity. Solubility of PVA in water permits the formation of transparent films by evaporating the water from the aqueous solution. PVA in the form of flexible water-soluble films is used, mostly for its oxygen barrier effect, *e.g.* in paper coatings, textile sizing and in packaging.[4] The functional modification of PVA molecule widened its use by making different adsorbents, such as ion-exchange films, hydrogels and metal-complexion membranes.[2] Different processing technologies

* Corresponding author. E-mail: vesna@tmf.bg.ac.rs
# Serbian Chemical Society member.
doi: 10.2298/JSC131017124S

are used for the enhancement of the chemical stability, biodegradation resistance and mechanical strength by chemical and physical crosslinking, and hardening modifications.[4,7–9] Hydrogels made of PVA have recently become attractive as matrices for the repair and regeneration of several types of tissues and organs in the fields of tissue engineering and regenerative medicine.[7–16] The significant swelling capacity of PVA hydrogels, that enables the absorption of exudates generated during the process of wound healing, makes them adequate biomaterials for wound dressings.[12,17–20]

Nanosized structures of silver, ranging from 1 to 100 nm, have been in the focus of investigations over several decades. Due to the maximization of the total surface area of the nanoparticles that leads to the highest values of the activity to weight ratio, the properties of silver nanoparticles (AgNPs) are significantly different from those of the bulk metal. As a result, AgNPs have found applications in various fields, first in medicine.[21–26] For years, silver products have been used as antimicrobials on different wounds, such as burns, traumas and diabetic ulcers. Silver toxicity implies complex activity against multiple components of bacterial cell metabolism, including damage to the bacterial cell wall (membrane permeability leads to changes in the cellular structure), blockage of systems responsible for transport and enzymatic activity (*e.g.* respiratory cytochromes), alteration of proteins as well as binding of microbial DNA and RNA, thus preventing transcription and division of bacteria.[27,28] This combined effect makes bacteria unable to become immune to the silver antimicrobial function, which is not the case with antibiotics.

High purity of the metal particles as well as the possibility of precise particle size control can be obtained by electrochemical synthesis, by adjusting the current density or applied potential.[26,29] Without the necessity of a large number of different chemical as used in conventional chemical methods, this approach is especially attractive for biomedical applications.

In this work, silver nanoparticles were electrochemically synthesized by reduction of silver ions, for the first time using PVA as a capping agent. The effect of the PVA concentration on the amount and size of AgNPs was investigated, as well as the interaction between the silver nanoparticles and PVA. The advantages of this procedure are especially attractive for biomedical applications: all steps of synthesis are clean, few chemicals are used, and the obtained Ag/PVA colloid solution is biocompatible and biodegradable.

EXPERIMENTAL

Materials

The following chemicals were utilized in this work: fully hydrolyzed PVA powder ("hot soluble", M_w = 70000–100000 g mol^{-1}, Sigma, St. Louis, MO, USA), $AgNO_3$ (M. P. Hemija, Belgrade, Serbia), KNO_3 (Centrohem, Stara Pazova, Serbia) and $Ca(NO_3)_2 \cdot 2H_2O$ (Alkaloid, Skopje, FYR Macedonia). In all experiments, ultra pure water from a Milli-Q system

(Millipore, Billerica, MA, USA) was used as well as N_2 gas of high purity (99.5 %, Messer Tehnogas a.d., Belgrade, Serbia).

Synthesis of Ag/PVA colloid dispersions

Ag/PVA colloid dispersions were obtained by electrochemical reduction of silver ions in PVA solutions. PVA powder was first dissolved in hot water and, after cooling to room temperature, mixed with KNO_3 and $AgNO_3$ solutions to obtain final concentrations of 5 and 10 wt. % PVA, 0.1 M KNO_3 and 3.9 mM $AgNO_3$. The electrochemical synthesis was performed galvanostatically in an electrochemical cell containing 50 cm^3 of the solution using a Reference 600 Potentiostat/Galvanostat/ZRA (Gamry Instruments, Warminster, PA, USA). Two Pt plates (9 mm×10 mm) were employed as the working and counter electrodes, and a saturated calomel electrode (SCE) was used as a reference electrode. The applied current density was 25 mA cm^{-2} and the synthesis time was 10 min. The synthesis was performed under continuous stirring; N_2 was introduced into the solution for 20 min prior to the synthesis, followed by continuous N_2 flow over the solution during the synthesis.

Characterization of Ag/PVA colloidal dispersions

UV–Vis spectroscopy. UV–Vis spectroscopy was employed to confirm the presence of AgNPs in the Ag/PVA colloidal dispersions (UV-3100 spectrophotometer, Mapada, Japan). The wavelength was scanned between 200 and 1000 nm.

Cyclic voltammetry. Cyclic voltammetry investigations of a Pt electrode were performed in 10 wt. % PVA solution and in the Ag/PVA colloidal dispersion (10 wt. % PVA) using two platinum electrodes (9 mm×10 mm) as the working and counter electrodes, and a saturated calomel electrode (SCE) as the reference. Cyclic voltammetry was performed using Reference 600 potentiostat/galvanostat/ZRA (Gamry Instruments, Warminster, PA, USA). The measurements were recorded at a scan rate of 50 mV s^{-1}, in the potential region from −1 to 1 V *vs.* SCE, starting from the open circuit potential, E_{ocp}. All potentials are given *versus* the SCE, and the plotted voltammograms are stationary ones.

Fourier transform infrared (FT-IR) spectroscopy. The IR spectra were recorded on PVA and Ag/PVA thin films that were obtained by evaporating the solvent from 10 wt. % PVA solution and the Ag/PVA colloid dispersion (10 wt. % PVA). A Thermoelectron Corporation Nicolet 380 FT-IR spectrophotometer, operating in ATR mode, was used.

Transmission electron microscopy. Transmission electron microscopy of the Ag/PVA colloid dispersion (10 wt. % PVA) was performed using a 100 CX Electron Microscope (JEOL Ltd., Tokyo, Japan) operated at 100 kV, in order to examine the size and shape of the Ag nanoparticles. Samples for TEM analysis were prepared by deposition of a diluted Ag/PVA colloidal dispersion (1:4) on C-coated Cu grids (SPI Supplies/Structure Probe Inc., West Chester, PA, USA).

RESULTS AND DISCUSSION

UV–Vis spectroscopy

UV–Vis spectroscopy was employed to monitor the formation of the silver nanoparticles. Nano-sized silver exhibits a strong absorption due to the collective oscillation of the conduction electrons, after appropriate excitation by suitable radiation. This phenomenon is known as localized surface plasmon resonance (LSPR), which is highly dependent on the size and shape of the nanoparticles.[30]

The absorption spectra of pure 10 wt. % PVA solution and Ag/PVA colloid dispersions with 5 and 10 wt. % of PVA in the initial solution are shown in Fig. 1. The PVA spectrum did not exhibit an absorbance peak in the examined range of wavelengths. Both Ag/PVA colloidal dispersions exhibited absorption spectra with two bands peaking at around 400 and around 650 nm.

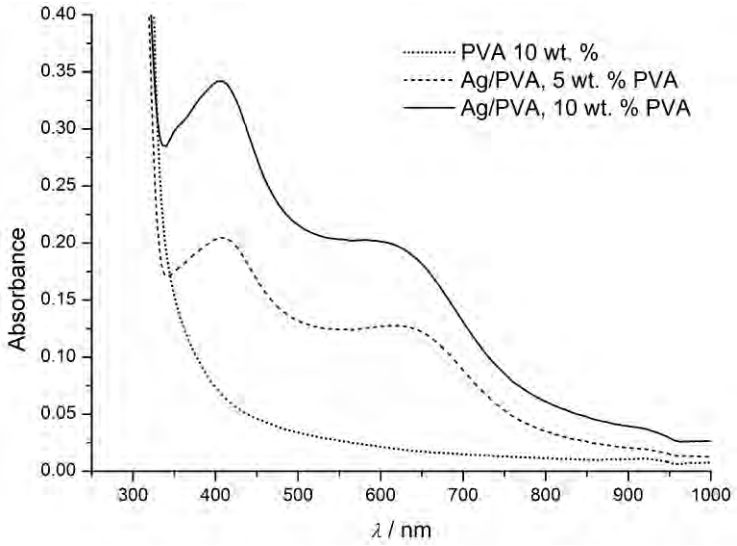

Fig. 1. Absorption spectra of 10 wt. % PVA solution and Ag/PVA colloidal dispersions with 5 and 10 wt. % PVA.

The first absorption peak at ≈400 nm confirms the formation of silver nanoparticles.[31,32] The second absorption band peaking at nearly 650 nm can be explained by aggregation or agglomeration of the silver nanoparticles present in the colloidal dispersion.[33,34] The size and shape of the obtained silver nanoparticles will be further discussed in the next section where the results of TEM analysis are presented. The only difference between the spectra of Ag/PVA colloid dispersions obtained from initial solutions containing 5 and 10 wt. % PVA was in the absorbance intensity, where a higher absorbance was exhibited by the solution with the higher PVA concentration. This suggests that a higher concentration of silver nanoparticles was obtained with a higher concentration of PVA in the initial solution, since the concentration of the silver nanoparticles is proportional to the absorbance intensity.[34]

UV–Vis analysis was also used to determine the effect of PVA concentration on the amount and relative size of silver nanoparticles. The time dependences of the absorbance maximum, A_{max}, and the wavelength of the absorbance maximum, λ_{max}, are presented in Figs. 2 and 3, respectively. It can be seen in Fig. 2 that an increase in the PVA concentration increased the absorbance maximum,

indicating the greater amount of silver nanoparticles in Ag/PVA colloid dispersion. For both Ag/PVA colloid solutions, A_{max} increases up to the 20th day and then remained almost constant up to the 30th day, while a further increase in A_{max} is the consequence of gelation. It could be stated that the absorbance maximum was attained 20 days after the synthesis, when the growth of the silver nanoparticles terminated.

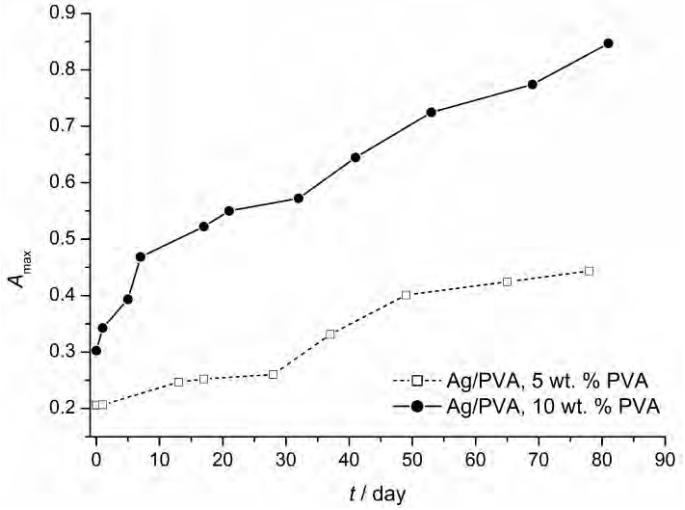

Fig. 2. Absorbance maximum, A_{max}, of Ag/PVA colloidal dispersions with 5 and 10 wt. % PVA as a function of time.

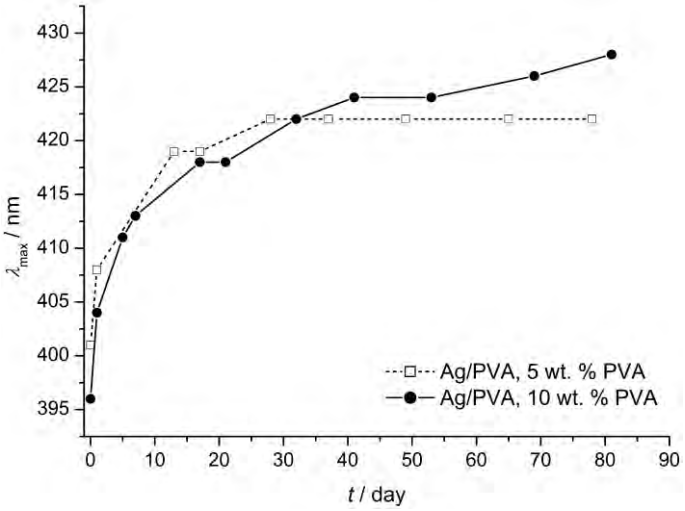

Fig. 3. Absorbance maximum wavelength, λ_{max}, of Ag/PVA colloid dispersions with 5 and 10 wt. % PVA as a function of time.

The time dependence of the wavelength of the absorbance maximum, λ_{max}, is presented in Fig. 3. It could be noticed that for both Ag/PVA dispersions, λ_{max} increased up to the 20th day, and then remained almost constant, and that the concentration of the PVA solution had no effect the size of the synthesized silver nanoparticles. This is in accordance with the previous assumption that the growth of silver nanoparticles terminated around 20 days after their synthesis.

Cyclic voltammetry

The cyclic voltammetry analysis of the Pt electrode was performed in 10 wt. % PVA solution and in Ag/PVA colloidal dispersion obtained from the initial solutions containing 5 and 10 wt. % PVA (Fig. 4). A better insight into the oxidation/reduction processes occurring in aqueous solutions of silver was obtained by comparison these cyclic voltammogram with those of the Pt electrode obtained in solutions containing 3.9 mM $AgNO_3$ and 0.1 M KNO_3.

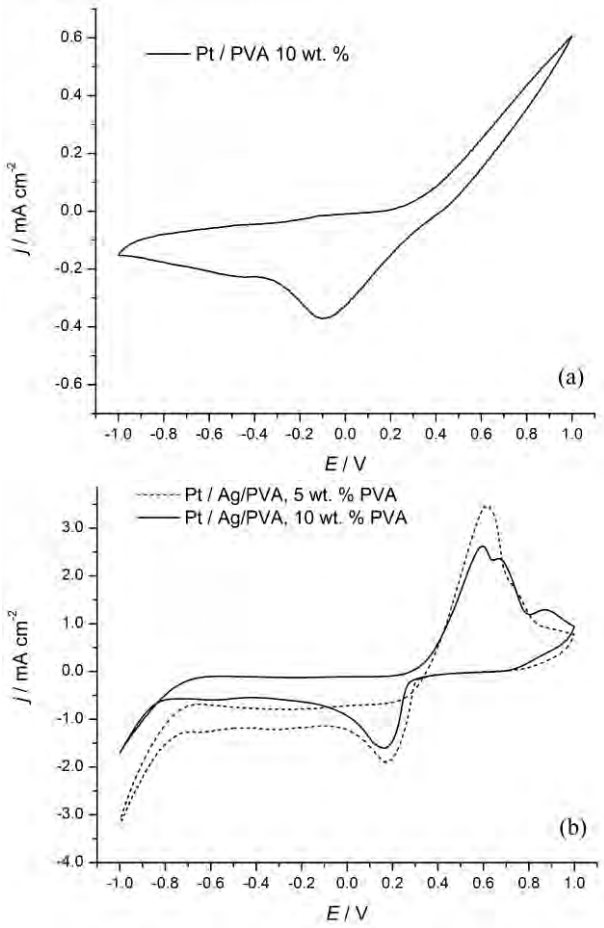

Fig. 4. Stationary cyclic voltammograms of a Pt electrode in a) 10 wt. % PVA solution and b) Ag/PVA colloidal dispersions with 5 and 10 wt. % PVA.

Cyclic voltammogram of the Pt electrode in 10 wt. % PVA solution (Fig. 4a) exhibited a broad cathodic peak at –100 mV, originating from reduction the Pt oxide formed during the anodic sweep. The anodic counterpart of this peak was not visible due to overlapping with the oxidation current at potentials more positive than 400 mV.

The stationary cyclic voltammograms of the Pt electrode in Ag/PVA colloid dispersions obtained from the initial solutions containing 5 and 10 wt. % PVA are shown in Fig 4b. In the Ag/PVA colloid solution obtained from the initial solution containing 5 wt. % PVA, the Pt electrode exhibited an anodic peak at around 611 mV, which originated from the oxidation of the Ag particles. This is connected with the oxidation/reduction processes of silver in the solution[24] where the appropriate pair of peaks appeared at 600 and 160 mV, respectively, and the minimal shifts towards more positive potentials (611 and 165 mV) could be the effect of the influence of the polymer molecules present in the solution. A small broad anodic peak appeared at around 870 mV, probably due to the oxidation of free Pt surface. The cathodic counterpart for the Pt oxide formation was not seen. However, considering the intensities of the cathodic currents in the potential region –200–200 mV, the cathodic counterpart for the Pt oxide formation could be overlapped with the Ag^+ reduction peak.

In the case of the Ag/PVA colloid dispersion obtained from the initial solution containing 10 wt. % PVA (Fig. 4b), three anodic peaks are obvious, at around 595, 667 and 871 mV. The first two could be related to the different oxidation processes of the silver nanoparticles in the Ag/PVA colloidal dispersion, while the peak at around 871 mV is related with the Pt oxide, as mentioned earlier. Only one cathodic peak was observed, at 160 mV. The two anodic peaks suggest differences between silver species; one was even less susceptible for oxidation.[35] This could be explained bearing in mind the entrapment of silver nanoparticles by PVA molecules, which implies silver nanoparticles with enhanced stability were obtained. Moreover, the coordination between Ag nanoparticles and hydroxyl groups of PVA was confirmed by FT-IR measurements, which will be discussed in the next section. The results indicated two types of AgNPs in the Ag/PVA colloidal dispersion, *i.e.*, relatively free ones that are susceptible to oxidation, and those already bonded to PVA molecules, that are hence less reactive.

Since it was proved that a higher concentration of silver nanoparticles in Ag/PVP solution were synthesized from the initial 10 wt. % PVA solution (UV––Vis measurements) as well as more stable silver nanoparticles were formed (CV measurements), all further characterizations were performed on Ag/PVA solution synthesized using the 10 wt. % PVA solution.

Transmission electron microscopy

Ag/PVA colloid dispersion obtained under the chosen experimental conditions (10 wt. % PVA, $c(AgNO_3)$ = 3.9 mM, j = 25 mA cm^{-2}, t = 10 min) was

analyzed using transmission electron microscopy. The TEM microphotograph confirmed the spherical shape of the synthesized silver nanoparticles (Fig. 5a). The average diameter of the obtained silver nanoparticles was 15±9 nm (Fig. 5b). It is known from the literature[36,27] that nanoparticles of the obtained dimensions exhibit antimicrobial characteristics.

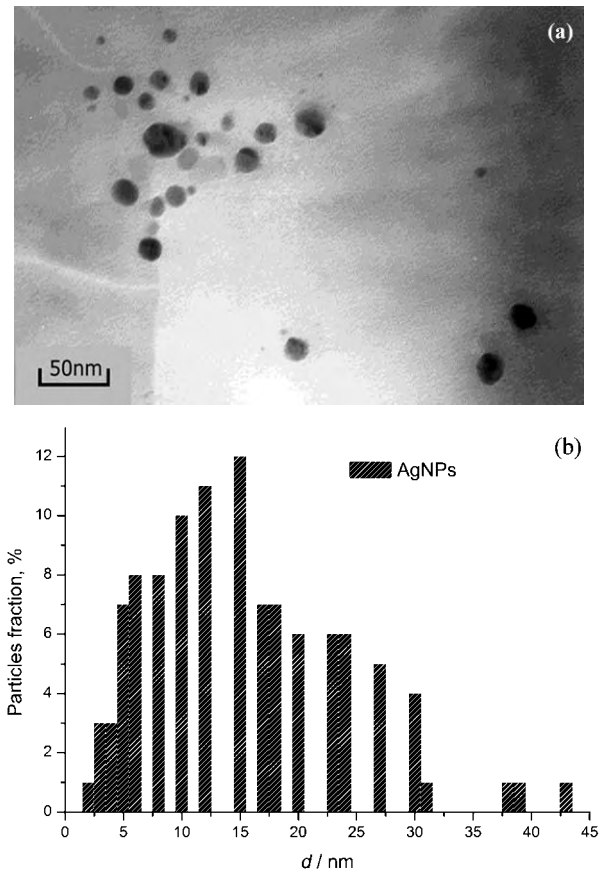

Fig. 5. a) TEM microphotograph of electrochemically synthesized silver nanoparticles in an Ag/PVA colloidal dispersion with 10 wt. % PVA and b) histogram of AgNPs particle size distribution.

Fourier transform infrared (FT-IR) spectroscopy

FT-IR measurements were performed on pure PVA and Ag/PVA thin films in order to determine the type of interactions between the PVA molecules and the silver nanoparticles. Thin PVA and Ag/PVA films were obtained by solvent evaporation from 10 wt. % PVA solution and Ag/PVA colloid dispersion obtained from the initial solution containing 10 wt. % of PVA, respectively (Fig. 6, Table I). The spectrum of the pure PVA exhibited characteristic peaks associated with poly(vinyl alcohol). A typical strong hydroxyl band for the –OH stretching vibration was observed at 3251 cm^{-1};[38] a band originating from C–H alkyl stretch-

ing was observed at a wavenumber of 2985 cm^{-1}.[39] Absorption peak originating from carboxyl stretching band (C–O) was verified at a wavenumber of 1141 cm^{-1}. The vibration band in the region between 1090 and 1150 cm^{-1} was attributed to the crystallinity of the PVA,[39] considering that PVA is a semi-crystalline synthetic polymer.[40]

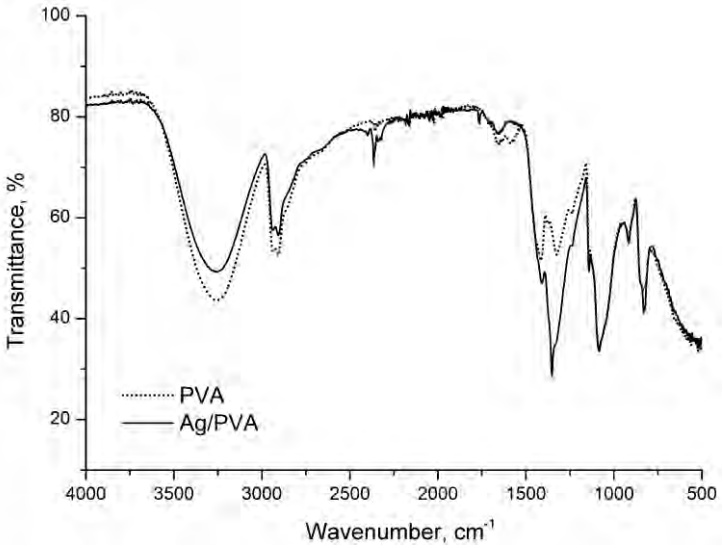

Fig. 6. IR Spectra of PVA and Ag/PVA thin films (PVA content in the initial solutions: 10 wt. %).

TABLE I. Wavenumbers of the characteristic bands and corresponding assignments for PVA and Ag/PVA thin films

Wavenumber (cm^{-1})		Assignment[38-46]
PVA	Ag/PVA	
3251	3253	–OH Stretching vibration
2937	2939	Asymmetric CH_2 stretching and aliphatic C–H stretching vibrations
–	1763	C=O Stretching of acetyl groups
1658	1650	Asymmetric and symmetric stretching vibration of –COO
1581	–	C=C Stretching vibration band
1414	1408	Weak –OH band vibration
1377	1352	–OH In plane coupling with C–H wagging
1325	–	
1238	1238	C–C Stretching vibration
1142	1142	Symmetric C–C stretching
1082	1084	C–O Stretching vibration of secondary alcohols
916	916	Symmetric C–C stretching
833	831	C–H rocking vibration

The IR spectrum of the Ag/PVA thin film exhibited a few differences compared to that of the pure PVA. Important changes were observed for the bands peaking at 1377 and 1325 cm^{-1} (in the PVA spectrum) and 1352 cm^{-1} (the in Ag/PVA spectrum). The strong band peaking at 1377 cm^{-1} is the result of the coupling of the –OH in-plane vibration with the C–H wagging vibrations. The increase in the intensity of the band at 1377 cm^{-1}, along with a slight shift of the band position (to 1352 cm^{-1} in the Ag/PVA spectrum), and the disappearance of the band peaking at 1325 cm^{-1} upon incorporation of Ag nanoparticles, suggests interaction between the AgNPs and the –OH groups of the PVA molecules through the decoupling between the corresponding vibrations. These results are in accordance with the results obtained from cyclic voltammetry, which indicated that PVA interacts with silver nanoparticles. As noted, there are two types of nanoparticles bonded with the PVA molecules, one which is more reactive, peaking at more negative values of the potential, and the other one, peaking at more positive values of the potential and thus more stable. Similar results were reported for alginate[26] and PVP.[24]

CONCLUSIONS

In this work, an electrochemical procedure was employed for the production of Ag/PVA colloidal dispersions with different concentrations of PVA. It was found using UV–Vis spectroscopy, that increasing PVA concentration in the initial solution increased the concentration of electrochemically synthesized AgNPs. Growth of the silver nanoparticles terminated around 20 days after the synthesis and their size remained almost constant up to the 30th day. The possibility of the use of PVA for the electrochemical synthesis of silver nanoparticles, as an adequate capping agent, was confirmed by cyclic voltammetry and IR spectroscopy, since the hydroxyl groups from PVA molecules coordinated with the Ag nanoparticles, making them more stable during a prolonged period. The obtained AgNPs were spherical, with a mean diameter of 15±9 nm, determined by TEM analysis. Thanks to the clean and simple procedure, electrochemically synthesized Ag/PVA colloidal dispersions could be utilized for the production of Ag/PVA hydrogels in different forms (thin films, discs and sheets), which could be used for antimicrobial treatments in biomedicine due to the release of AgNPs.

Acknowledgements. This work was financed by the Ministry of Education, Science and Technological Development of the Republic of Serbia, Grants No. III 45019 and Eureka E!6749.

ИЗВОД

ЕЛЕКТРОХЕМИЈСКА СИНТЕЗА НАНОЧЕСТИЦА СРЕБРА У РАСТВОРУ ПОЛИ(ВИНИЛ АЛКОХОЛА)

РАДЕ СУРУЦИЋ[1], ЖЕЉКА ЈОВАНОВИЋ[1], НАТАША БИБИЋ[2], БРАНИСЛАВ НИКОЛИЋ[1] и ВЕСНА МИШКОВИЋ-СТАНКОВИЋ[1]

[1]Технолошко-металуршки факултет, Универзитет у Београду, Карнегијева 4, Београд и [2]Institut za nuklearne nauke „Vinča“, Универзитет у Београду, Мике Петровића Аласа 12–14, Београд

У овом раду показано је добијање колоидних дисперзија сребро/поли(винил алкохол), Ag/PVA, електрохемијском редукцијом Ag^+. Електрохемијска синтеза наночестица сребра у воденим растворима поли(винил алкохола) са 5 и 10 мас. % PVA, који су садржали 0,1 M KNO_3 и 3,9 mM $AgNO_3$, вршена је при константној густини струје од 25 $mA{\cdot}cm^{-2}$ у трајању од 10 min. Присуство наночестица сребра потврђено је ултраљубичастом и видљивом спектроскопијом. Цикличном волтаметријом и инфрацрвеном спектроскопијом показана је интеракција између наночестица сребра и молекула поли(винил алкохола). Анализом трансмисионе електронске микроскопије је потврђено да су добијене наночестице сребра сферног облика, пречника 15±9 nm.

(Примљено 17. октобра, ревидирано 4. новембра 2013)

REFERENCES

1. M. Han, J. Yun, H. Kim, Y. Lee, *J. Ind. Eng. Chem.* **18** (2012) 752
2. L. Yang, Y. Li, H. Hu, X. Jin, Z. Ye, Y. Ma, S. Zhang, *Chem. Eng. J.* **173** (2011) 446
3. M. T. S. Alcântara, A. J. C. Brant, D. R. Giannini, J. O. C. P. Pessoa, A. B. Andrade, H. G. Riella, A. B. Lugão, *Radiat. Phys. Chem.* **81** (2012) 1465
4. J. Gaume, A. Rivaton, S. Thérias, J.-L. Gardette, *Polym. Degrad. Stabil.* **97** (2012) 488
5. I. M. Jipa, M. Stroescu, A. Stoica-Guzun, T. Dobre, S. Jinga, T. Zaharescu, *Nucl. Instrum. Meth., B* **278** (2012) 82
6. M. Constantina, G. Fundueanua, F. Bortolotti, R. Cortesi, P. Ascenzi, E. Menegatti, *Int. J. Pharmaceut.* **285** (2004) 87
7. N. Georgieva, R. Bryaskova, R. Tzoneva, *Mater. Lett.* **88** (2012) 19
8. A. Islam, T. Yasin, *Carbohyd. Polym.* **88** (2012) 1055
9. J. S. Gonzalez, A. S. Maiolo, C. E. Hoppe, V. A. Alvarez, *Procedia. Mater. Sci.* **1** (2012) 483
10. A. S. Maiolo, M. N. Amado, J. S. Gonzalez, V. A. Alvarez, *Mat. Sci. Eng., C* **32** (2012) 1490
11. D. Killeen, M. Frydrych, B. Chen, *Mat. Sci. Eng., C* **32** (2012) 749
12. S. Jiang, S. Liu, W. Feng, *J. Mech. Behav. Biomed.* **4** (2011) 1228
13. N. A. M. Zaina, M. S. Suhaimi, A. Idris, *Process. Biochem.* **46** (2011) 2122
14. A. N. Khodja, M. Mahlous, D. Tahtat, S. Benamer, S. L. Youcef, H. Chader, L. Mouhoub, M. Sedgelmaci, N. Ammi, M. B. Mansouri, S. Mameri, *Burns* **39** (2013) 98
15. B. Singh, L. Pal, *Int. J. Biol. Macromol.* **48** (2011) 501
16. M.-H. Huang, M.-C. Yang, *Int. J. Pharmaceut.* **346** (2008) 38
17. B. Singh, L. Pal, *J. Mech. Behav. Biomed.* **9** (2012) 9
18. O. M. Păduraru, D. Ciolacu, R. N. Darie, C. Vasile, *Mat. Sci. Eng., C* **32** (2012) 2508
19. P. Salarizadeh, M. Javanbakht, M. Abdollahi, L. Naji, *Int. J. Hydrogen Energ.* **38** (2013) 5473
20. A. L. Ahmad, N. M. Yusuf, B. S. Ooi, *Desalination* **287** (2012) 35

21. R. R. Khaydarov, R. A. Khaydarov, Y. Estrin, S. Evgrafova, T. Scheper, C. Endres, *Nanomaterials: Risks and Benefits*, NATO Science for Peace and Security Series C: Environmental Security, 2009, p. 287
22. S. Era ovi , A. Jan ovi , D . Vel ovi , E. Palcevs is, M. Mitri , T. Stevanovi , D . Jana ovi , V. Mi ovi -Stan ovi , *J. Phys. Chem., B* **117** (2013) 1633
23. S. Era ovi , A. Jan ovi , I. Z. Mati , Z. D. Jurani , M. Vu a inovi -Se uli , T. Stevanovi , V. Mi ovi -Stan ovi , *Mater. Chem. Phys.* **142** (2013) 521
24. Ž. Jovanovi , A. Radosavl evi , J. Sto ovs a, B. Ni oli , B. Obradovic, Z. Kačarevi -Popovi , V. Mi ovi -Stan ovi , *Polym. Composites* (2013), DOI 10.1002/pc.22653
25. Z. Jovanovi , A. Radosavl evi , Z. Kačarevi -Popovi , J. Sto ovs a, A. Peri -Gru i , M. Risti , I. Z. Mati , Z. D. Jurani , B. Obradovic, V. Mi ovi -Stan ovi , *Colloids Surfaces, B* **105** (2013) 230
26. Ž. Jovanovi , J. Sto ovs a, B. Obradovi , V. Mi ovi -Stan ovi , *Mater. Chem. Phys.* **133** (2012) 182
27. C. Cencettia, D. Bellini, A. Pavesio, D. Senigaglia, C. Passariello, A. Virga, P. Matricardi, *Carbohyd. Polym.* **90** (2012) 1362
28. R. Bryaskova, N. Georgieva, T. Andreeva, R. Tzoneva, *Surf. Coat. Tech.* **235** (2013) 186
29. L. Rodrıguez-Sanchez, M. C. Blanco, M. A. Lopez-Quintela, *J. Phys. Chem., B* **104** (2000) 9683
30. M. R. Guascito, D. Chirizzi, R. A. Picca, E. Mazzotta, C. Malitesta, *Mat. Sci. Eng., C* **31** (2011) 606
31. A. M. Abdelgawad, S. M. Hudson, O. J. Rojas, *Carbohyd. Polym.* **100** (2014) 166
32. S. Mahendia, A. K. Tomar, S. Kumar, *Mater. Sci. Eng., B* **176** (2011) 530
33. L. Lu, A. Kobayashi, K. Tawa, Y. Ozaki, *Chem. Mater.* **18** (2006) 4894
34. S. Kundu, K. Wang, H. Liang, *J. Phys. Chem. C* **113** (2009) 134
35. X. Li, A. Xu, H. Xie, W. Yu, W. Xie, X. Ma, *Carbohydr. Polym.* **79** (2010) 660
36. Y. M. Mohan, K. Lee, T. Premkumar, K. E. Geckeler, *Polymer* **48** (2007) 158
37. V. Sambhy, M. M. MacBride, B. R. Peterson, A. Sen, *J. Am. Chem. Soc.* **128** (2006) 9798
38. M. H. Buraidah, A. K. Arof, *J. Non-Cryst. Solids.* **357** (2011) 3261
39. H. S. Mansur, R. L. Oréfice, A. A. P. Mansur, *Polymer* **45** (2004) 7193
40. W. E. Hennink, C. F. van Nostrum , *Adv. Drug Deliver. Rev.* **54** (2002) 13
41. S. Rajendran, M. Sivakumar, R. Subadevi, *Mater. Lett.* **5** (2004) 641
42. Z. I. Ali, F. A. Ali, A. M. Hosam, *Spectrochim. Acta, A* **72** (2009) 868
43. B. Hui, Y. Zhang, L. Ye, *Chem. Eng. J.* (2013) **235** (2014) 207
44. S. Rajendran, M. Sivakumar, R. Subadevi, *Solid State Ionics* **167** (2004) 335
45. A. N. Kr l e , M. T. Marinovi -Cincovi , Z. M. Kacarevi -Popovi , J. M. Nedel ovi , *Eur. Polym. J.* **43** (2007) 2171
46. A. Radosavl evi , D. Božani , N. Bibi , M. Mitri , Z. Kačarevi -Popovi , J. Nedel ovi , *J. Appl. Polym. Sci.* **125** (2012) 1244.

Journal of the Serbian Chemical Society
JSCS-info@shd.org.rs • www.shd.org.rs/JSCS

J. Serb. Chem. Soc. *78* (12) 2099–2114 (2013)
JSCS–4553

UDC 544.6.001.5:546.815–31:66.087+
546.11.027*3:544.032.4
Original scientific paper

An electrochemical and radiotracer investigation on lead dioxide: influence of the deposition current and temperature

ROSSANO AMADELLI[1]*, LUCA SAMIOLO[1] and ALEKSANDR B. VELICHENKO[2]

[1]CNR-ISOF u.o.s. Ferrara c/o Dipartimento di Scienze Chimiche e Farmaceutiche, via Fossato di Mortara, 17, 44121 Ferrara, Italy and [2]Ukrainian State University of Chemical Technology, Gagarin ave. 8, 49005 Dnipropetrovsk, Ukraine

(Received 22 October 2013)

Abstract: The properties of electrodeposited PbO_2 are sensibly influenced by the deposition current and temperature. In particular, tritium radiotracer measurements demonstrated that protons were incorporated into the bulk of an oxide film and on its surface. The degree of hydration increased with increasing current and decreased with temperature, and was related to the morphological characteristics of the oxide, such as roughness measured by changes in the double layer capacity. Conversely, the amount of hydrogen had negligible effects on the number of free carriers as evaluated from Mott–Schottky plots. The hydration degree of the surface seems to be an important factor influencing electrocatalytic processes at high potentials, such as O_2 evolution and O_3 formation. On less hydrated, more crystalline PbO_2 surfaces, the first process was inhibited and accordingly, the second was favored.

Keywords: lead dioxide, tritium, electrodeposition, electrocatalysis.

INTRODUCTION

Lead dioxide electrodes have been studied for several years and continue to attract considerable interest from both practical and theoretical points of view. In the field of battery applications, research in lead-acid batteries is still very active,[1] and in particular, recent developments of new soluble lead-acid flow devices appear rather attractive.[2] A recent review by Li *et al.*[3] presents very informative state of the art studies on PbO_2. Despite the enormous amount of work, there is still a considerable debate on some issues, such as the stoichiometry of the oxide (sometimes described as PbO_x) and its influence on electrochemical properties.

The reason of this non-stoichiometry has been attributed to oxygen vacancies, interstitial protons or quasi-free electrons. In the model proposed by Rue-

* Corresponding author. E-mail: amr@unife.it
doi: 10.2298/JSC131022122A

tschi and Giovanoli,[4] vacancies are arranged to form layers (named "internal surfaces") between crystallographically ordered areas, and the charge due to missing Pb^{4+} would be compensated only by OH^- or by Pb^{2+} and OH^-. Thus, the formula proposed to describe better the composition of PbO_2 is:

$$Pb^{4+}_{(1-x-y)}Pb^{2+}_{y}OH^{2-}_{(2-4x-2y)}OH^{-}_{(4x+2y)}\ Pb^{4+}{}_{(1-x-y)}$$

The model accounts for the fact that experimental studies report evidence for the presence of Pb(II) and structural water in the PbO_2 lattice. On the one hand, earlier studies remained inconclusive in regards to whether it is fully stoichiometric with respect to oxygen[3–5] or not; on the other hand, according to recent studies based on theoretical calculation,[6–8] the conductivity is due to oxygen vacancies.

Different studies agree that electrochemically prepared PbO_2 contains structural water (hydrogen)[4] and that there is a correlation between the hydrogen content and its electrochemical activity.[9] The electrochemical behavior of electrodeposited PbO_2 is very sensitive to the preparation method, and the choice of the electrodeposition parameters of play an important role in the control of the morphological characteristics of PbO_2.[10–15] It seems, however, that there has been insufficient systematic investigations on how the control of different parameters in the electrodeposition of PbO_2 can affect the amount of structural water in the resulting oxide.

In this work, the influence of parameters such as the deposition temperature on the inclusion of tritium into electrodeposited PbO_2 films I discussed. Generally, radiochemical studies can provide useful complementary information in the study of electrochemical reactions.[16–20] In addition, the electrochemical behaviors of the obtained films are examined. The starting point was the question raised by Hill several years ago[21] on a possible connection between structural hydrogen and electrochemical reactions at PbO_2.

EXPERIMENTAL

Chemicals

Ultrapure acids were obtained from Merck and all other chemicals from Sigma–Aldrich

Equipment

The electrochemical experiments were performed employing an EG&G model 273A potentiostat–galvanostat using EG&G software. Additionally, for impedance measurements, an EG&G model 5210 lock-in amplifier was used. Simulation calculations of the impedance data were realized using the B. A. Boukamp Equivalent Circuit simulation program. Measurements were performed in a conventional three-compartment cell. The counter electrode was a large Pt flag, or a cylindrical Pt gauze surrounding the working electrode in the case of impedance measurements. A saturated calomel electrode (SCE) was used as the reference. This was in contact with the working electrode compartment through a Luggin tip. X-Ray diffraction experiments were performed with an Advance Bruker D8 diffractometer.

Methods

Cyclic voltammetry and impedance measurements were performed with PbO_2 electrodeposited on a Pt wire (geometrical area 0.18 cm^2). For the radiochemical experiments, PbO_2 was galvanostatically deposited onto platinized titanium (geometric area 2 cm^2). The experimental conditions were adjusted so that the weight of the deposit was constant, and thickness was estimated using the reported density of PbO_2.[4] Both the activity due to tritium incurporated in the whole films (A_t) and that due to exchange of tritium at the surface (A_s) were measured as described below.

i) For the measurement of A_t, PbO_2 films of different thickness were prepared by electrodeposition at a constant current from solutions of 1 M HNO_3 + 1 M $Pb(NO_3)_2$. [^{3}H]water (tritium water) was added to the solution to give a radiochemical activity of 5×10^7 d.p.m. (disintegrations per min). After preparation, the electrodes were washed with dry acetone, dried in an argon flow, weighed and dissolved in H_2O_2/aqueous acetate buffer at pH 5.5. A fixed amount of this solution was added to the scintillating liquid (Insta-gel, Packard), and the radiochemical activity was counted.

ii) For the determination of A_s, the amount of tritium exchanged at the oxide surface, the following procedure was adopted: lead dioxide films having a fixed thickness were prepared in the absence of [^{3}H]water. They were then immersed in solutions containing [^{3}H]water (5×10^7 d.p.m.) for 60 h; this conditioning time was chosen because separate experiments showed that the uptake of tritium reached a maximum after this period. The samples were thoroughly washed with dry acetone, dried in an argon flow and immersed in the scintillating liquid. The release of tritium in the scintillating liquid was measured as a function of time until the radiochemical activity reached a constant value.

Films of α-PbO_2 were prepared from 2 M NaOH solutions saturated with lead acetate. Ozone analysis was performed mostly by iodometric titration. In some cases, the so-obtained results were checked by the spectrophotometric method measuring the absorption at 254 nm and using an extinction coefficient of 3024 L cm^{-1} mol^{-1}.

RESULTS AND DISCUSSION

X-Ray characterization

The effect of electrodeposition conditions on the XRD spectra of PbO_2 is shown in Fig. 1. At room temperature, an increase in the constant deposition current does not result in significant changes in the reflection patterns, except for a larger contribution of some higher index planes as the current increased (Fig. 1a). SEM micrographs (Supplementary material) show that at the higher current densities, the films feature crystals without clear crystal edges.

The obtained films consisted of mixture of α- and β-phase PbO_2, with the calculated amount of the former[14] remaining rather constant and less than 10 % of the total PbO_2. The size of the crystallites, calculated from the Scherrer Equation:

$$D = \frac{k\lambda}{\beta\cos\theta} \quad (1)$$

was also relatively insensitive to current.[14] Using the most intensive β (110) peak, the calculations yielded particle dimensions of 27 and 30 nm for 5 and 20 mA cm^{-2}, respectively.

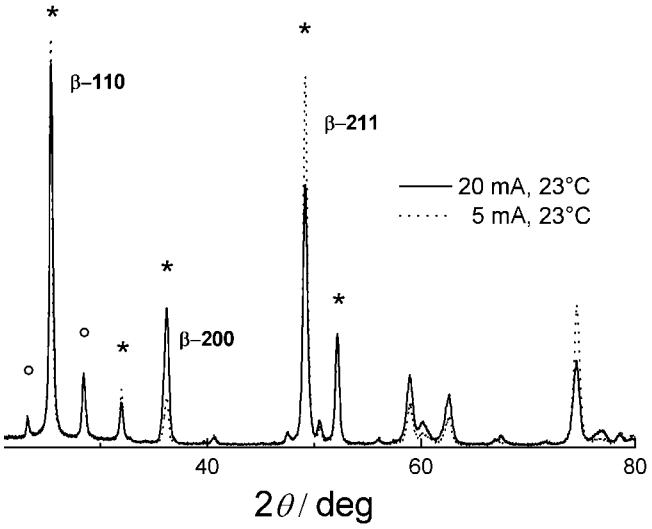

(a)

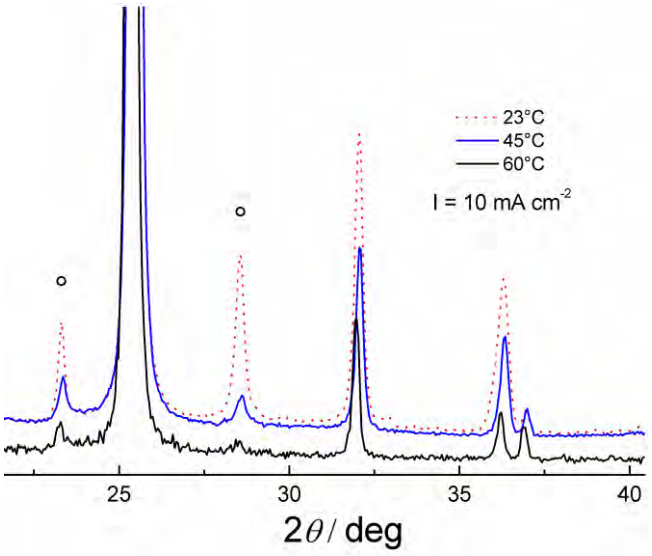

(b)

Fig. 1. a) Effect of the deposition current on the XRD pattern of PbO_2. Peaks marked (*) correspond to β-PbO_2 and those marked (o) to α-PbO_2. Temperature: 23 °C. b) Effect of the deposition bath temperature on the XRD pattern of PbO_2. Peaks marked with (o) correspond to α-PbO_2.

The choice of the deposition temperature had a comparatively more pronounced influence. As shown in Fig. 1b, the contribution of the α-PbO_2 polymorph gradually disappeared as the temperature was increased from 22 to 60 °C. These results are in agreement with those reported by Sirés *et al.* for PbO_2 prepared from methanesulfonic acid.[22]

Tritium exchange

In the study of electrodeposited PbO_2 under different experimental conditions, tritium radiotracer measurements can, in principle, provide a relatively simple method to obtain information on hydrogen incorporation into the oxide and at its surface. In fact, according to the disorder model of electrochemically grown PbO_2, hydrogen ions on interstitial sites together with quasi-free electrons are considered the dominating disorder centers.[23]

The graph displayed in Fig. 2a shows that the total amount of tritium (A_t) incorporated into the whole PbO_2 film was a linear function of thickness. It also showed that the amount of tritium in the more defective α-PbO_2 film was much larger than that observed with β-PbO_2 for the same deposition current and temperature (*cf.* plots 1 and 2). The amount of tritium in the bulk decreased significantly as the deposition temperature was increased to 60 °C, for the same constant current (*cf.* plots 2 and 3). The small amount of the α-polymorph present in the films obtained at room temperature (*vide supra*) does not explain the large decrease in the tritium inclusion brought about by temperature.

In an analogous experiment, the amount of tritium exchanged with the surface (A_s) was determined as described in the experimental section. The results reported in Fig. 2b show the release of tritium as a function of time and temperature from films that had been previously equilibrated in tritiated water for 60 h. It is possible to note that at there is a rapid initial exchange which may be referred to as surface proton exchange, followed by a slower process, which is thought to evidence the presence of less accessible protons.[17]

The effects of the deposition current and temperature on the radiochemical activity are summarized in Table I. In principle, a number of correlations are possible; for example, one may note that both A_t and A_s increase as the current increased, and that the increase was very pronounced only for samples prepared at room temperature.

Since it could reasonably be expected that A_s would depend on the effective surface area, cyclic voltammetry experiments were performed at different scan rates in the double layer region (1.35–1.45 V) and calculated the capacities as reported in the literature.[24] Then the effective areas were estimated by taking the double layer capacity of smooth electrodes (20 μF cm^{-2}) as a reference,[25,26] Examples are given in Table II. It was observed that there is a direct propor-

tionality between the surface radiochemical activity (A_s) and the effective area: both increased with deposition current and decreased with temperature.

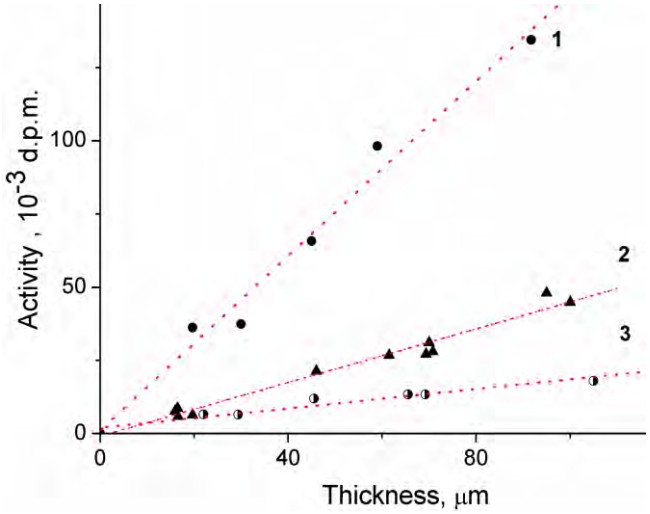

(a)

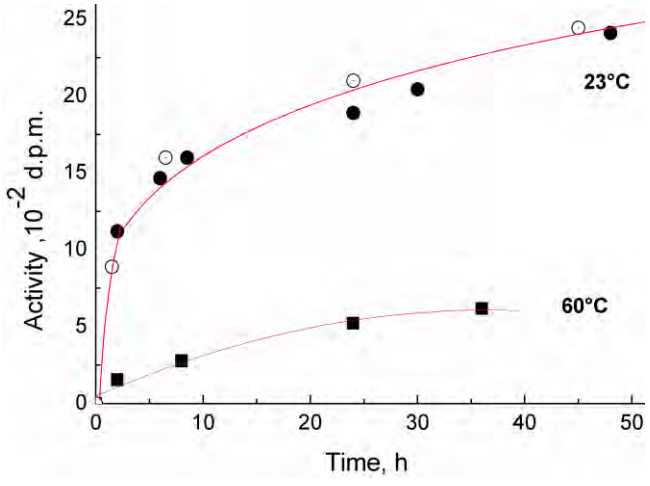

(b)

Fig. 2. a) Overall amount of tritium incorporated into α-PbO_2, t = 23 °C (1), β-PbO_2, t = 23°C (2), and β-PbO_2, t = 60°C (3), as a function of film thickness; b) amount of tritium released by β-PbO_2 in contact with the scintillating medium after a 60-h contact with tritium water. Samples prepared by electrodeposition at a constant current (10 mA cm^{-2}) onto Pt/Ti substrates. See experimental section for details.

It was generally observed that high currents favor the formation of PbO_2 films that are less stoichiometric. Additionally, under these conditions, oxygen

evolution could occur and lead to an increase in the microporosity of the coating, and. as a consequence, the exchange of tritium between the films and the environment occur more easily due to the large number of lattice defects and morphological disorder.[17] Conversely, more compact, less defective surfaces are formed at high temperature,[22,27] which explains why a smaller amount of hydroxyl species was present in the surface region as well as across the film.

TABLE I. Amount of tritium incorporated into α-PbO_2 (t = 23 °C) and β-PbO_2 (t = 23 and 60 °C) electrochemically grown onto platinized Ti substrates (2 cm^2) at a constant current (10 mA cm^{-2})

Deposition current, mA cm^{-2}	t / °C	
	23	60
	Surface activity (A_s/100), d.p.m.	
5	11.04	3.82
10	18.8	5.89
20	30	7.3
30	35.4	8.2
40	38	9.32
	Total activity (A_t/100), d.p.m.	
5	17.8	16.45
10	31.2	30.3
20	47	33.3
30	62	35
40	74.2	33.25

TABLE II. Double layer capacities and roughness factors as a function of PbO_2 deposition current and temperature

Deposition current, mA cm^{-2} (temperature, °C)	Capacity, mF	Roughness factor	Effective area, cm^2
5 (23)	1.75	87.5	15.8
5 (60)	0.685	34.2	6.15
20 (23)	4.6	230	41.4
5 (23), α-PbO_2	30	1500	270

Electrochemical characterization

Electrodeposited PbO_2 is reported to be a narrow band gap semiconductor with high electron conductivity due to non-stoichiometry, which varies with preparative conditions.[7,28] Often the Hall effect is used to determine the number of free charges. However, reasoning that useful information was obtained from Mott–Schottky analysis for conductive materials, such as Sb–SnO_2[29] and boron-doped diamond,[30] the capacities of the prepared PbO_2 films were calculate from their impedance and the data was plotted according to:

$$\frac{A^2}{C^2} = \frac{2}{q\varepsilon\varepsilon_0 N}\left(E - E_{\mathrm{fb}} - \frac{kT}{q}\right) \quad (2)$$

where q is the electron charge, A is the area, ε_0 is the vacuum permittivity, ε is the dielectric constant of PbO_2, taken as 3.91,[7] and E and E_{fb} are the applied and flat-band potentials, respectively. A plot of A^2/C^2 *vs.* E should give a straight line, the slope of which is inversely proportional to the number of carriers N. Straight lines were indeed observed with a positive slope (n-type conductivity) for PbO_2 (5 mA, 23 °C) and PbO_2 (5 mA, 60 °C) from which the calculated values of N were 6×10^{21} and 8×10^{21} cm^{-3}, respectively. The data are the same within experimental error and so there is no apparent correlation with tritium/ /proton incorporation as a function of temperature. The results are not completely unexpected, and in fact, Ruetschi and Giovanoli drew attention to this type of experimental findings several years ago.[4] On the other hand, the effect of current density is more conspicuous as seen in the example of experimental plots of Fig. 3. In the case of PbO_2 (20 mA, 23 °C), The Mott–Schottky plots are non-linear, which could be due, for example, to a high number of defects[31] and/or porosity.[32] It is noteworthy that hydration was also observed to cause non-linearity in Mott–Schottky plots.[33]

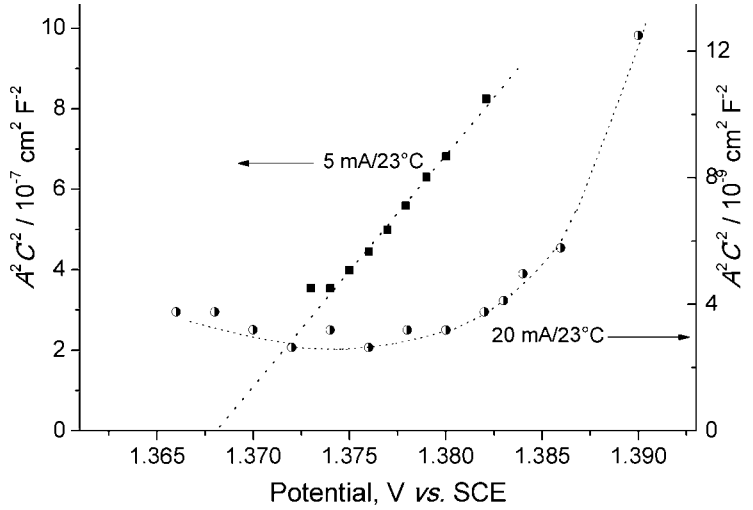

Fig. 3. Mott–Schottky plots for PbO_2 electrodeposited at 5 and 20 mA cm^{-2} at a temperature of 23 °C.

In the literature, reduction of PbO_2 electrodeposited under different conditions has been investigated frequently in order to gain insight into activity related to film morphology. Thus, for example, films with structural characteristics such

as accessibility to species in the electrolyte and fast surface and subsurface exchange of protons are expected to be more easily reduced.[12]

The results reported in Fig. 4a are first scan linear sweep voltammetry curves for the reduction of different PbO_2 samples in $HClO_4$. The scan was started at 1.5 V, where no faradaic process occurs, and $HClO_4$ were chosen in order to avoid effects of strong adsorption of the anions. It appears that reduction occurred at more positive potentials when the films were obtained at relatively high currents;

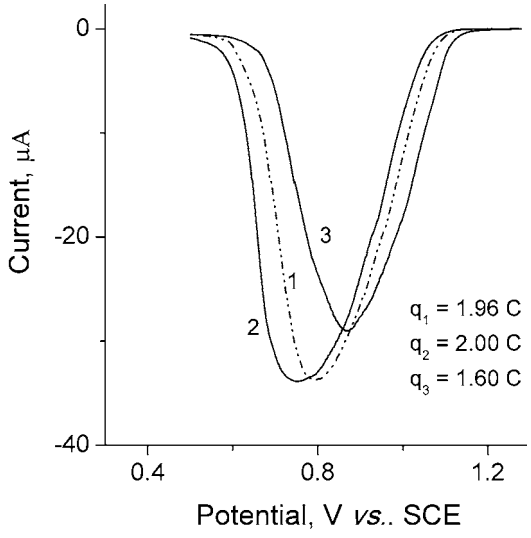

(a)

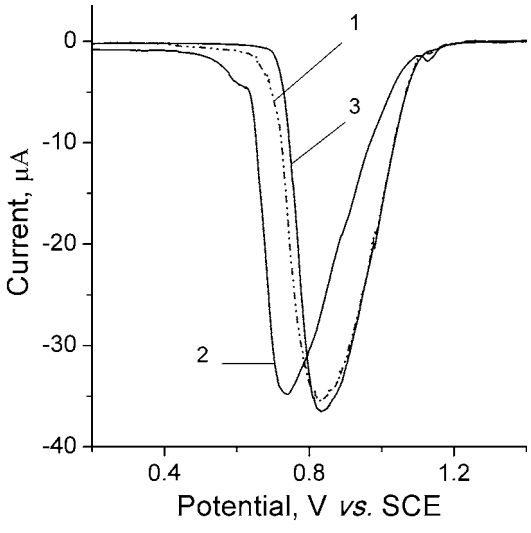

(b)

Fig. 4. Linear sweep voltammetry curves for the reduction of PbO_2 prepared under different experimental conditions: 1) 5 mA cm^{-2}, 23 °C; 2) 5 mA cm^{-2}, 60 °C; 3) 20 mA cm^{-2}, 23 °C; a) first scan experiments after preparation and b) after polarization of the electrodes at 1.95 V for 1200 s. Scan rate: 5 mV s^{-1}. Electrolyte: 1 M $HClO_4$.

conversely, an increase in the deposition temperature shifted the reduction process to more negative potentials. Films of pure α-PbO_2 were more readily reduced, typically at ≈0.95 V. The lower reduction charge q_3 (Fig. 4a) is likely due to a lower electrodeposition efficiency at high currents, because of the occurrence of O_2 evolution.[10] Qualitatively, the described behavior seemingly parallels the defective structure of films, as also shown by the tritium uptake experiments.

Experiments with films that had previously been used as electrodes for O_2 evolution in $HClO_4$ at high potentials showed that the only detectable effect was that of temperature (Fig. 4b). A possible explanation is that a gel layer is rapidly formed on PbO_2 in contact with water,[1] which is involved in the reduction process:[34]

$$\underset{\text{(crystal zone)}}{PbO_2} + H_2O \leftrightarrows \underset{\text{(gel zone)}}{PbO(OH)_2} \quad (3)$$

$$PbO(OH)_2 + 2\,H^+ + 2e^- \rightarrow Pb(OH)_2 + H_2O \quad (4)$$

$$Pb(OH)_2 + 2\,H^+ \rightarrow Pb^{2+} + 2H_2O \quad (5)$$

The influence of gel formation and its involvement in the cyclic voltammetry behavior of PbO_2 electrodes in H_2SO_4 solutions was discussed in a recent EQCM investigation by Pech *et al.*[35]

One may speculate that the contribution of the crystal zones remains more pronounced even after polarization at high positive potentials. According to Pavlov,[36] however, equilibrium (3) is reversible and washing the electrode restores the crystalline zones

$$[PbO(OH)_2]_n \rightarrow nPbO_2 + nH_2O \quad (6)$$

and since the present experiment was *ex situ*, it does not appear likely that gel formation could explain the observed behavior. Alternatively, following electrolysis at high current densities, re-deposition of PbO_2 occurred with the formation of small crystallites on the surface, as proposed by Thanos and Wabner.[37]

Thus, experiments were performed in dilute H_2SO_4, analogous to those described in Fig. 4 (Supplementary material). The obtained results agreed with those reported earlier in this paper and with the conclusion of Devilliers *et al.*[38] that reduction of PbO_2 constituted of larger, more regular crystallites is more difficult.

Electrocatalytic behavior

The results presented so far demonstrated that the preparation method determines the amount of hydrogen incorporated within PbO_2 films and influences the electrochemical behavior. The connection between these experimental aspects is probably the non-stoichiometry of the films.[39]

Continuing with the characterization, again three types of PbO_2 electrodes, prepared at different temperature and constant current, were examined in order to assess the effects of these parameters on the O_2 evolution process.

Oxygen evolution proceeds in the gel-layer (*vide supra*) through the following elementary steps:

$$PbO^*(OH)_2 + H_2O \rightarrow PbO_2(OH)_2\cdots(OH^\circ) + H^+ + e^- \quad (7)$$

$$PbO^*(OH)_2\cdots(OH^\circ) \rightarrow PbO^*(OH)_2 + O_{ads} + H^+ + e^- \quad (8)$$

$$2O_{ads} \rightarrow O_2 \quad (9)$$

where $PbO^*(OH)_2$ is an active center located in the hydrous layer and $OH^\bullet$ is a hydroxyl radical bound to an active center. Thus, it is to be expected that the thickness of this layer would exert an important influence on this electrochemical process and indeed, it was reported that it lowers the potential of O_2 evolution.[40] Unfortunately, there is presently no convincing evidence of an influence of the preparation method on the degree of gel-layer formation; the interesting EQCM study by Pech *et al.*[35] did not explore the effects of varying the electrodeposition conditions of PbO_2.

In the present study, the O_2 evolution was mainly investigated by impedance spectroscopy, and the results obtained by fitting the data according to the equivalent circuit displayed in Fig. 5 are reported in Table III. In this circuit, R_{ct} is the electron transfer faradaic resistance; R_p is the resistance associated to desorption of oxygen radical intermediates; C_{dl} is the known double layer capacity; C_p is related to the pseudo-capacitance, *i.e.*, to the potential dependence of the steady state coverage by reaction intermediates and is hence related in an important way to electrocatalysis. The number "*n*" appearing in the tables refers to the behavior of the constant phase element[18] and has a value of 1 for a pure capacity.

A comparison of the data at a fixed potential shows that electrodeposition at high current or temperature causes a decrease and an increase, respectively, of both R_{ct} and R_p. In all cases $R_p > R_{ct}$, which seemingly indicates to a mechanism in which desorption of intermediates (reaction (8)) is slow. As reported before:[18]

$$\log (R^{-1}) = \log (bi^\circ) + bE \quad (10)$$

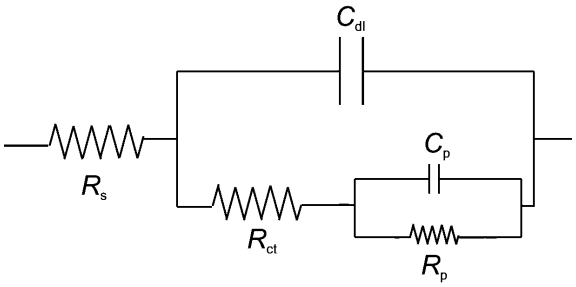

Fig. 5. Scheme of the equivalent circuit used for fitting the impedance data.

and the Tafel slope b can be obtained from plots of log (R^{-1}) *vs.* potential. In effect, Fig. 6 shows that there is quite good agreement between the steady-state polarization plots of E *vs.* log I (Fig. 6a) and log (R_p^{-1}) plots (Fig. 6b), at least at potentials below 1.9 V. At more positive potentials, R_p decreases rapidly and reaction (8) becomes faster. Indeed, according to MNDO calculations[41] based on the hydroxylate cluster model $Pb_3(OH)_{12}(H_2O)$, electron transfer producing OH radicals and their removal from the surface to give (O) species requires almost the same energy: 685.3 and 712.5 kJ mol^{-1}, respectively.

TABLE III. Impedance spectroscopy data for PbO_2 prepared under different experimental conditions. Electrolyte: 1 M $HClO_4$

E / V	R_s / Ω	R_{ct} / Ω	R_p / Ω	C_{dl} / 10^{-3} F (n)	C_p / 10^{-3} F (n)
		5 mA cm^{-2}, 23 °C			
1.65	1.12	11.25	932.8	1.72 (0.92)	1.20 (1.0)
1.70	1.96	10.53	443.7	1.92 (0.96)	1.17 (1.0)
1.75	1.45	8.90	150.2	1.88 (0.94)	1.13 (1.0)
1.80	1.13	8.57	41.3	1.84 (0.93)	1.05 (1.0)
1.85	1.13	6.25	18.4	1.62 (0.94)	1.10 (1.0)
1.90	1.15	3.80	11.4	1.30 (0.96)	1.25 (1.0)
1.95	1.12	2.17	8.0	0.88 (1.0)	1.05 (1.0)
2.00	1.10	1.78	4.31	0.83 (1.0)	1.69 (0.90)
2.05	1.10	1.68	2.24	0.58 (1.0)	1.27 (0.90)
		5 mA cm^{-2}, 60 °C			
1.75	1.07	17.65	206.4	1.45 (0.98)	0.55 (1.00)
1.80	1.20	15.20	91.15	1.38 (0.96)	0.42 (1.00)
1.85	1.18	10.17	47.20	1.24 (0.95)	0.50 (0.92)
1.90	1.14	3.78	33.15	1.03 (0.98)	0.72 (0.85)
1.95	1.00	1.16	15.07	1.36 (0.98)	0.97 (0.85)
2.00	1.00	1.06	4.95	1.10 (1.00)	1.41 (0.84)
2.05	1.18	1.40	2.55	0.77 (1.00)	1.91 (0.84)
		20 mA cm^{-2}, 23 °C			
1.70	0.86	6.05	111.6	3.60 (0.92)	2.02 (0.98)
1.75	0.86	5.6	47.15	3.50 (0.91)	2.00(1.00)
1.80	0.88	4.15	15.25	3.00 (0.92)	2.30 (0.95)
1.85	0.88	2.3	8.92	1.70 (0.98)	2.92 (0.92)
1.90	0.87	1.46	6.10	1.42 (1.00)	2.42 (0.93)
1.95	0.87	2.29	2.89	1.36 (0.97)	3.35 (1.00)
2.00	0.88	1.42	1.36	1.36 (1.00)	6.40 (0.85)
2.05	0.90	1.07	0.85	1.30 (1.00)	9.3 (0.83)

Ozone formation is an important reaction occurring on PbO_2 at relatively high potentials, in parallel with O_2 evolution[42] (reaction (9)):

$$O_2 + O_{ads} \rightarrow O_3 \qquad (11)$$

and the efficiency of O_3 generation evidently depends on the coverage and stability of O_{ads}; the recombination process (reaction (9)) that forms an oxygen

molecule ensures a gain in energy of 891.2 kJ mol^{-1}.[41] In this context, it is noteworthy that the stability of O is reported to be higher on less defective oxide surfaces,[18] which would correspond to the less hydrated PbO_2 (5 mA, 60 °C) samples prepared in the present work.

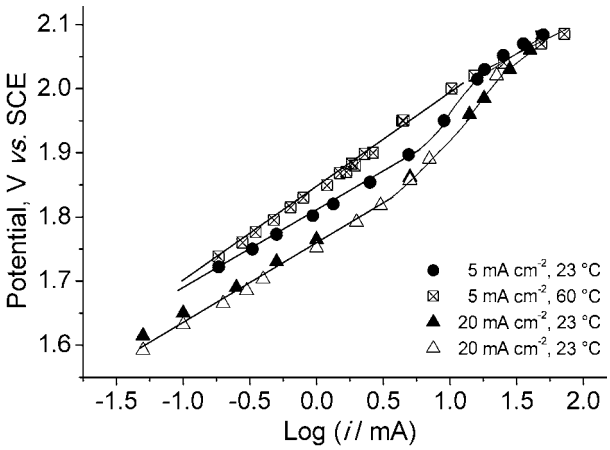

(a)

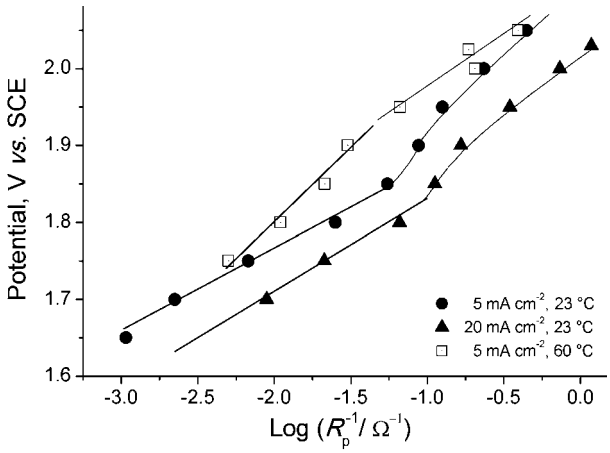

(b)

Fig. 6. Effects of PbO_2 preparation parameters on: a) *E vs.* log *I* from quasi steady-state data; b) *E vs.* log(1/R_p) from impedance data. Electrolyte: 1 M $HClO_4$.

The data on the effect of temperature on O_3 formation shown in Fig. 7 confirmed the above reasoning. In addition, it was shown previously[18] that for $E > 1.95$ V, the current–potential curves reached a stable profile after relatively long polarization times. These results were confirmed in the present work for

samples prepared at room temperature, while those deposited at 60 °C did not exhibit such a time dependence. A tentative explanation might be that in the latter case, corrosion is less pronounced and the equilibrium in reaction (3) is shifted to the left; this conclusion would agree with the results of Fig. 4.

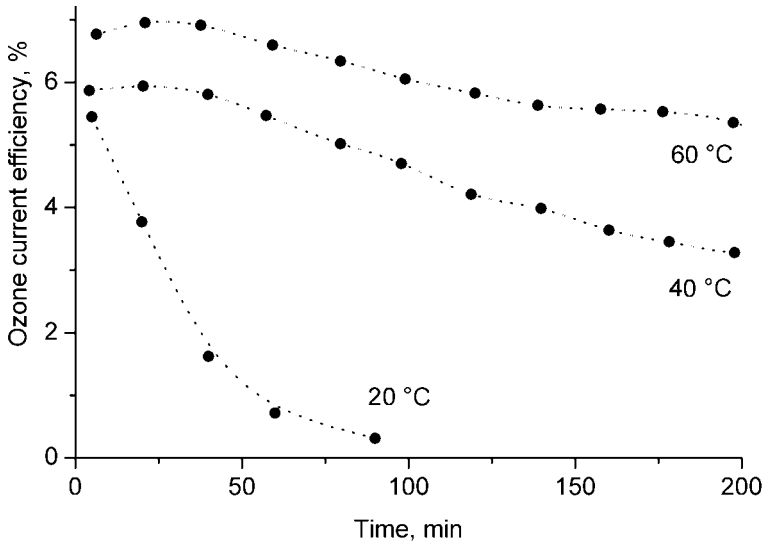

Fig. 7. The effect of the PbO_2 electrodeposition temperature on the current efficiency of ozone electrogeneration in 0.5 M H_2SO_4 as a function of time of operation at 0.5 A cm^{-2}.

CONCLUSIONS

Herein, an investigation into some aspects of the influence of current and temperature on electrodeposited PbO_2 has been presented. In particular, tritium radiochemical studies provide unequivocal evidence for the presence of structural water in the bulk of the oxide film and not only on its surface. In battery studies, the role of the hydrogen content in the PbO_2 lattice has been an issue for years and is still in focus these days.

We find, In accordance with the conclusions of Hill,[21] it was found that the amount of hydrogen in PbO_2 has no direct influence on the electrochemical and electrocatalytic behavior. However, the degree of hydrogen/tritium incorporation provides information on changes in the chemico-physical characteristics. In particular, it is related to PbO_2 morphological defects, which in turn influence electrocatalytic processes, such as O_2 and O_3 generation. In this regard, the hydration degree of the surface seems to be an important parameter, the control of which could affect the efficiency of electrocatalytic oxidation processes. Probably, the question that requires further investigation is a more quantitative analysis of the relationship between degree of bulk hydration and that of the surface.

SUPPLEMENTARY MATERIAL

Figures S1–S3 are available electronically at http://www.shd.org.rs/JSCS/, or from the corresponding author on request.

ИЗВОД

ИСПИТИВАЊЕ ОЛОВО(IV)-ОКСИДА ЕЛЕКТРОХЕМИЈСКИМ МЕТОДАМА И МЕТОДОМ ИЗОТОПСКИХ ОБЕЛЕЖИВАЧА: УТИЦАЈ СТРУЈЕ ТАЛОЖЕЊА И ТЕМПЕРАТУРЕ

ROSSANO AMADELLI[1], LUCA SAMIOLO[1] и ALEKSANDR B. VELICHENKO[2]

[1]CNR-ISOF u.o.s. Ferrara c/o Dipartimento di Scienze Chimiche e Farmaceutiche, via Fossato di Mortara, 17, 44121 Ferrara, Italy u [2]Ukrainian State University of Chemical Technology, Gagarin ave. 8, 49005 Dnipropetrovsk,Ukraine

На својства електродепонованог PbO_2 значајно утичу струја таложења и температура. Мерења са трицијумом као изотопским обележивачем показују да су протони инкорпорирани и у маси оксидног филма и да се налазе на његовој површини. Степен хидратације се повећава са повећањем струје, а опада са температуром, што је повезано са морфолошким карактеристикама оксида као што је храпавост која је одређена преко капацитивности двојног слоја. Супротно, количина водоника занемарљиво утиче на број слободних преносилаца наелектрисања израчунат из Mott–Schottky дијаграма. Изгледа да је степен хидрататације површине важан фактор за електрокаталитичке процесе на високим потенцијалима као што су издвајање O_2 и стварање O_3. На мање хидратисаним, више кристалиничним PbO_2 површинама први процес је инхибиран, а у складу са тиме, други фаворизован.

(Примљено 22. октобра 2013)

REFERENCES

1. D. Pavlov, *A Handbook of Lead-Acid Battery Technology,* Elsevier, Amsterdam, 2011
2. R. G. A. Wills, J. Collins, D. Stratton-Campbell, C. T. J. Low, D. Pletcher, F. C. Walsh, *J. Appl. Electrochem.* **40** (2010) 955
3. X. Li, D. Pletcher, F. C. Walsh, *Chem. Soc. Rev.* **40** (2011) 3879
4. P. Ruetschi, R. Giovanoli, in*: International Power Sources Committee*, Vol. 13, T. Kelly, B. W. Baxter, Eds., Leatherhead, 1991, p. 81 (and refs. therein)
5. S. R. Ellis, N. A. Hampson, M. C. Ball, F. Wilkinson, *J. Appl. Electrochem*. **16** (1986) 159
6. D. J. Payne, R. G. Egdell, W. Hao, J. S. Foord, A. Walsh, G. W. Watson, *Chem. Phys. Lett.* **411** (2005) 181
7. D. J. Payne, G. Paolicelli, F. Offi, G. Panaccione, P. Lacovig, G. Beamson, A. Fondacaro, G. Monaco, G. Vanko, *J. Electron Spectrosc. Relat. Phenom.* **169** (2009) 26
8. D. J. Payne, R. G. Egdell, D. S. L. Law, P. A. Glans, T. Learmonth, K. E. Smith, J. Guo, *J. Mater. Chem.* **17** (2007) 267
9. R. Fitas, L. Zerroual, N. Chelali, B. Djellouli, *J. Power Sources* **64** (1997) 57 (and refs. therein)
10. A. B. Velichenko, R. Amadelli, A. Benedetti, D. V. Girenko, S. V. Kovalyov, F. I. Danilov, *J. Electrochem. Soc.* **149** (2002) C445
11. S. Abaci, K. Pekmez, T. Hokelek, A. Yildiz, *J. Power Sources* **88** (2000) 232
12. D. Zhou, L. Gao, *Electrochim. Acta* **53** (2007) 2060

13. P.-K. Sheng, X. L. Wei, *Electrochim. Acta* **48** (2007) 1743
14. N. Munichandraiah, *J. Appl. Electrochem.* **22** (1992) 825
15. Y. Mohd, D. Pletcher, *J. Electrochem. Soc.* **152** (2005) D102
16. G. Horányi, in *Radiotracer Studies of Interfaces*, G. Horányi, Ed., Elsevier, Oxford, 2004, pp. 39–92
17. G. Lodi, G. L. Zucchini, A. De Battisti, A. Giatti, *Surf. Sci*. **250–252** (1991) 836
18. R. Amadelli, A. Maldotti, A. Molinari, F. I. Danilov, A. B. Velichenko, *J. Electroanal. Chem.* **534** (2002) 1
19. A. B. Velichenko, R. Amadelli, G. L. Zucchini, D. V. Girenko, F. I. Danilov, *Electrochim. Acta* **45** (2000) 4341
20. A. B. Velichenko, R. Amadelli, E. A. Baranova, D. V. Girenko, F. I. Danilov, *J. Electroanal. Chem.* **45** (2000) 4341
21. R. J. Hill, *J. Power Sources* **25** (1989) 313
22. I. Sirés, C. T. J. Low, C. Ponce-de-León, F. C. Walsh, *Electrochim. Acta* **55** (2010) 2163
23. G. L. Schlechtriemen, *Z. Phys. Chem. NF* **130** (1982) 193
24. S. Trasatti, O. A. Petrii, *Pure Appl. Chem*. **63** (1991) 711
25. B. V. Tilak, C. G. Rader, S. K. Rangarajan, *J. Electrochem. Soc.* **124** (1977) 1879
26. U. Casellato, S. Cattarin, M. Musiani, *Electrochim. Acta* **48** (2003) 399
27. Y. Matsumoto, M. Noguchi, T. Matsunaga, *J. Phys. Chem., B* **103** (1999) 7190
28. A. Walsh, A. B. Kehoe, D. J. Temple, G. W. Watson, D. O. Scanlon, *Chem. Commun.* **49** (2013) 448
29. G. Boschloo, D. Fitzmaurice, *J. Phys. Chem., B* **103** (1999) 3093
30. M. Wang, N. Simon, C. Decorse-Pascanut, M. Bouttemy, A. Etcheberry, M. Li, R. Boukherroub, S. Szunerits, *Electrochim. Acta* **54** (2009) 5818
31. G. A. Hope, A. J. Bard, *J. Phys. Chem.* **87** (1983) 1979
32. C. F. Windisch Jr., G. J. Exarhos, *J. Vac. Sci. Technol., A* **18** (2000) 1677
33. L. Kavan, B. O'Regan, A. Kay, M. Grätzel, *J. Electroanal. Chem*. **346** (1993) 291
34. N. Chelali, L. Zerroual, B. Djellouli, *Solid State Ionics* **127** (2000) 49
35. D. Pech, T. Brousse, D. Bélanger, D. Guay, *Electrochim. Acta* **54** (2009) 7382
36. D. Pavlov, *J. Electrochem. Soc.* **139** (1992) 3075
37. J. C. G. Thanos, D. W. Wabner, *J. Electroanal. Chem*. **182** (1985) 37
38. D. Devilliers, M. T. Dinh Thi, E. Mahé, V. Dauriac, N. Lequeux, *J. Electroanal. Chem*. **573** (2004) 227
39. H. P. Fritz, J. C. G. Thanos, D. W. Wabner, *Z. Naturforsch., B* **34** (1979) 1617
40. D. Pavlov, B. Monahov, *J. Electrochem. Soc.* **143** (1996) 3616
41. A. B. Velichenko, D. V. Girenko, N. V. Nikolenko, R. Amadelli, E. A. Baranova, F. I. Danilov, *Russ. J. Electrochem*. **36** (2000) 1373
42. A. A. Babak, R. Amadelli, A. De Battisti, V. N. Fateev, *Electrochim. Acta* **39** (1994) 1597 (and refs. therein).

Journal of the Serbian Chemical Society
JSCS-info@shd.org.rs • www.shd.org.rs/JSCS

J. Serb. Chem. Soc. 78 (12) 2115–2130 (2013)
JSCS–4554

UDC 546.131+544.6.076.32–13:66.094.3:
541.135:544.4
Original scientific paper

The kinetics of hydrogen chloride oxidation•

ISAI GONZALEZ MARTINEZ[1], TANJA VIDAKOVIĆ-KOCH[2]*, RAFAEL KUWERTZ[3], ULRICH KUNZ[3], THOMAS TUREK[3] and KAI SUNDMACHER[1,2]

[1]Otto-von-Guericke University, Process Systems Engineering, Universitätsplatz 2, 39106 Magdeburg, Germany, [2]Max-Planck Institute for Dynamics of Complex Technical Systems, Sandtorstrasse 1, 39106 Magdeburg, Germany, and [3]Institute of Chemical Process Engineering, Clausthal University of Technology, Leibnizstr. 17, 38678 Clausthal-Zellerfeld, Germany

(Received 19 November 2013)

Abstract: Hydrogen chloride (HCl) oxidation was investigated on technical membrane electrode assemblies in a cyclone flow cell. The influences of Nafion loading, temperature and hydrogen chloride mole fraction in the gas phase were studied. The apparent kinetic parameters, such as reaction order with respect to HCl, Tafel slope and activation energy, were determined from the polarization data. The apparent kinetic parameters suggest that the recombination of adsorbed Cl intermediate is the rate-determining step.

Keywords: gas diffusion electrodes, Nafion, electrolysis, HCl gas phase oxidation, kinetics.

INTRODUCTION

Anhydrous gaseous HCl is a by-product of different reactions in the plastics industry, for example during production of isocyanates by treating amines with phosgene.[1] This by-product is commonly absorbed in water or neutralized. A further option for handling gaseous HCl is its recycling back to chlorine. This option is more advantageous since chlorine is a high value product with a number of applications in the chemical industry. HCl can be chemically or electrochemically converted to chlorine.[2] The chemical process follows the so-called Deacon stoichiometry: $4HCl + O_2 \rightarrow 2Cl_2 + 2H_2O$.

This process was initially outperformed by electrochemical processes, but, due to the recent advances in ruthenium-based catalysts, it has been successfully revisited.[3] Still, even with the present progress in heterogeneous chemical catal-

* Corresponding author. E-mail: vidakovic@mpi-magdeburg.mpg.de
• Dedicated to the 70th birthday of Prof. Branislav Nikolić.
doi: 10.2298/JSC131119142G

ysis, electrochemical processes outperform chemical HCl oxidation in terms of the investment costs per ton of chlorine, the possibility of module-based (decentralized) operation[4] and the required process temperature (*ca*. 343 K in the electrochemical compared to 453–773 K for the chemical process[3]). The major electrochemical routes for recycling chlorine back from HCl were summarized in recent publications.[4–6] To recapitulate shortly, the state-of-the-art electrochemical process (DuPont–DeNora) is based on direct splitting of HCl into chlorine and hydrogen: $2HCl \rightarrow Cl_2 + H_2$

Further developments in the electrochemical recycling of HCl were mainly directed towards an increase in energy efficiency. In this respect, the major savings were obtained by influencing the thermodynamics of the process through change in the aggregate state of the reactant or by changing the process stoichiometry. The change in the process stoichiometry by introducing an oxygen-consuming instead of a hydrogen-evolving cathode resulted in *ca*. 30 % energy saving compared to the state-of-the-art process.[6] This so-called Bayer–Hoechst–Uhde process with an overall process stoichiometry corresponding to the Deacon process has already been realized on the technical scale. Aqueous HCl is employed in this process. It was demonstrated recently that utilization of gaseous instead of aqueous HCl resulted in an additional energy saving (up to 50 % compared to that obtained in the state-of-the-art process).[5]

Further development and optimization of this promising process variant requires detailed knowledge of the reaction kinetics. In this respect, especially kinetic information on the electro-oxidation of gaseous HCl are extremely rare.[7] To obtain meaningful information for process development, kinetic measurements have to be performed under technically realistic conditions using membrane electrode assemblies (MEA), and keeping simultaneously the influence of the counter electrode and the membrane negligible. These conditions can be realized in a specially designed electrochemical cell, the so-called cyclone flow cell. The advantages of this special experimental set-up have been exemplified in previous publications.[8–10] Recently, this set-up was employed for an investigation of the influence of structural parameters of MEA on HCl oxidation.[6] The determination of apparent kinetic parameters, such as Tafel slopes, reaction order with respect to HCl and the activation energy for HCl oxidation are the focus of this contribution. The kinetic parameters were determined between room temperature and 60 °C and for MEAs comprising different Nafion loadings. The significance of these apparent parameters was further evaluated with respect to possible mechanisms of HCl oxidation.

EXPERIMENTAL

Membrane electrode assembly (MEA) preparation

The MEA was composed of a gas diffusion layer (GDL) and a catalyst layer (CL) sprayed over a Nafion 117 membrane by a wet-spraying method as described in the lierature.[5] 60 mass

% platinum supported on Vulcan XC72R (BASF) was employed as the catalyst. The catalyst-sprayed membrane was hot-pressed for 3 min at 90 kg cm^{-2}. The total geometrical active MEA area was 2 cm^2.

Electrochemical measurements

All measurements were performed in a cyclone flow cell as described in the literature.[6] Hydrogen chloride was diluted with nitrogen in order to attain the desired concentrations. The cell was kept in a convection oven with integrated temperature control (Mammert UNP500) in order to maintain the system at the desired reaction temperature.

The electrodes were pre-conditioned by cyclic voltammetry in the range from 0.2 to 1.0 V *vs*. Ag/AgCl with a sweep rate of 50 mV s^{-1} for 10 cycles. Polarization curves were obtained under quasi-steady state conditions using linear sweep voltammetry with a Solarton 1286 potentiostat at a sweep rate of 1 mV s^{-1}. Ohmic drop compensation was employed *via* the current interrupt method. Before each temperature change, a linear sweep with N_2 was recorded and employed as a base line correction for all measurements with hydrogen chloride. The baseline corrections never exceeded 7 % of the total current. The results presented in this work are the average of at least three measurements. All potentials are expressed vs. standard hydrogen electrode (SHE).

RESULTS

Origin of limiting current behavior

Polarization curves for the electro-oxidation of gaseous HCl at MEAs comprising different Nafion loadings at constant platinum loading (0.5 mg cm^{-2}) are shown in Fig. 1. As can be seen, all electrodes reach technical current densities (300 to 400 mA cm^{-2}) at relatively low overpotentials. The optimization of the Nafion loading resulted in an increase in catalyst utilization. In addition, the increase in Nafion loading decreases the reaction overpotential (*ca*. 40 mV for the electrodes comprising the highest with respect to lowest Nafion loading at 400 mA cm^{-2}). Although the difference is not strikingly high, it still has importance for energy saving in this process, especially taking into account that technical electrolysis systems operate at high current densities.

The maximal current densities observed in the present study were similar to those reported by Eames and Newman[7] in a solid-polymer electrolyte reactor for electrochemical conversion of anhydrous HCl to Cl_2. However, the overpotentials (expressed relative to the open circuit potentials) of *ca*. 200 mV in the present study are much lower compared to those obtained in the study of Eames and Newman[7] study (*ca*. 1 V). This significant difference might be partly due to an improved MEA structure in the present case. In addition, the data of Eames and Newman[7] accounts not only for the voltage losses related to the anode (as here), but incorporate also the losses on the cathode side and in the membrane. The membrane losses can be significantly high, since the conductivity of Nafion strongly decreases in the presence of HCl.[14]

As can be seen in Fig. 1, all studied the MEAs showed limiting current behavior at more positive overpotentials. The limiting currents were also observed

in the study with gaseous HCl oxidation[7] as well as in studies where chlorine evolution from aqueous HCl[11] or NaCl[12] were investigated. In the study with gaseous HCl,[7] as possible sources of limiting behavior, the limitations caused by the membrane and gas-phase mass transfer were discussed, and it was concluded that the main cause for the experimentally observed limiting behavior was low membrane conductivity due to dehydration. In the study on chlorine evolution from brine solution, Conway and Ping[12] considered limitations by slow diffusion of the product chlorine. They performed their experiments using a rotating disc electrode and observed only a small effect of the electrode rotation on the reaction rate, which led them to the conclusion that the chemical step, *i.e.*, chlorine recombination, and not diffusion effects limited the currents at more positive overpotentials.

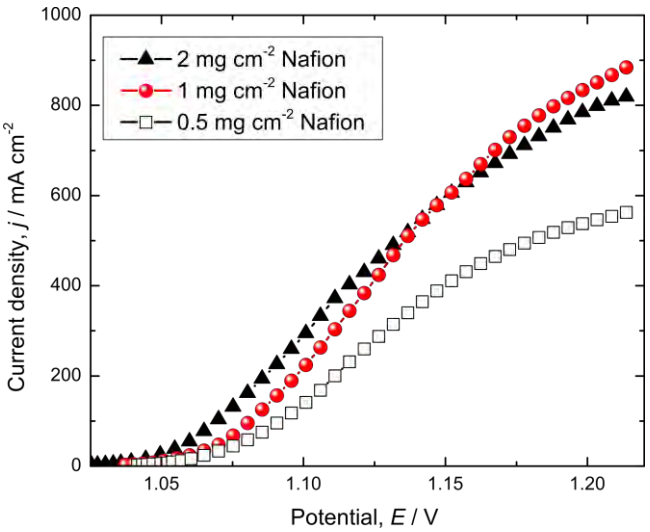

Fig. 1. Influence of Nafion loading at constant platinum loading (0.5 mg cm^{-2}) on HCl oxidation. Conditions: temperature: 60 °C, pressure: 101.3 kPa, HCl flow rate: 500 ml min^{-1} and sweep rate: 1 mV s^{-1}.

In the present study, since the MEA consists of several layers of different thicknesses and porosities, different mass transfer resistances or combinations of them can contribute to the observed limiting behavior. In addition, electrochemical reaction itself can be limiting. To estimate the effects of single resistances, analysis with dimensionless numbers, as is common in chemical reaction engineering and as shown by Vidaković *et al.*[9] using as an example methanol electrooxidation, was employed. Two kinds of dimensionless numbers were considered, the Biot number for the estimation of diffusion resistances in the adherent layers where only the diffusion occurs and the so-called second Damköhler number that is used in reacting systems with diffusion. The second Damköhler number is

defined as the ratio of the resistance of diffusion and resistance of electrochemical reaction as follows:

$$Da_{\mathrm{II}} = \frac{\delta_{\mathrm{CL}}\, j}{nFc_{\mathrm{HCl}} D_{\mathrm{HCl}}^{\mathrm{CL}}} \tag{1}$$

where δ_{CL} is the thickness of the catalyst layer (*ca*. 20 μm), j is the current density (*ca*. 9 kA m^{-2}), c_{HCl} the HCl gas phase concentration (36.6 mol m^{-3} assuming ideal gas behavior at 101.3 kPa and 60 °C) and $D_{\mathrm{HCl}}^{\mathrm{CL}}$ the HCl diffusion coefficient in the CL (2.10×10^{-6} m^2 s^{-1}). The HCl diffusion coefficient in the CL accounts for the porosity of the layer (*ca*. 20 %); furthermore, it has been assumed that the void fraction in the CL is filled with the gas phase. The given data result in a Damköhler number of $Da_{\mathrm{II}} \approx 0.012$. This value indicates that the resistance of the electrochemical reaction is bigger than the resistance of the diffusion.

The relevance of the mass transport resistance in the gas diffusion layer (GDL) was estimated by means of the following Biot number (*Bi*):

$$Bi^{\mathrm{GDL/CL}} = \frac{D_{\mathrm{HCl}}^{\mathrm{CL}} / \delta_{\mathrm{CL}}}{D_{\mathrm{HCl}}^{\mathrm{GDL}} / \delta_{\mathrm{GDL}}} \tag{2}$$

where $D_{\mathrm{HCl}}^{\mathrm{GDL}}$ is the effective HCl diffusion coefficient in the GDL (8.63×10^{-6} m^2 s^{-1}) and δ_{GDL} is the thickness of the GDL (*ca*. 250 μm). The calculated value of this Biot number is *ca*. 3, which means that the mass transfer resistance in the GDL is 3 times higher than in the CL. This reflects the fact that the GDL is *ca*. 12 times thicker than the CL (250 *vs*. 20 μm), while the diffusion coefficient in the GDL is only *ca*. 4 times greater than in the CL (8.63×10^{-6} *vs*. 2.10×10^{-6} m^2 s^{-1}).

The relevance of the external film resistance in relation to the resistance of diffusion exerted by the GDL can be estimated in a similar manner:

$$Bi^{\mathrm{HDL/GDL}} = \frac{D_{\mathrm{HCl}}^{\mathrm{GDL}} / \delta_{\mathrm{GDL}}}{k_{\mathrm{m}}} \tag{3}$$

where k_{m} is the film mass transfer coefficient (1.61×10^{-3} m s^{-1}, calculated based on correlation provided by Schultz and Sundmacher[13]). The calculated value of $Bi^{\mathrm{HDL/GDL}}$ based on the given data is *ca*. 20.

Multiplying Da_{II} with the Biot numbers defined above yields the electrochemical reaction rate (resistance of electrochemical reaction) in relation to the mass transfer rates, i.e., resistance of diffusion in GDL and resistance of external film diffusion, respectively:

$$Da_{\mathrm{II}} Bi^{\mathrm{GDL/CL}} \approx 0.036 \tag{4}$$

$$Da_{\mathrm{II}} Bi^{\mathrm{GDL/CL}} Bi^{\mathrm{HDL/GDL}} \approx 0.72 \tag{5}$$

The last expression gives the ratio between all mass transfer resistances and the resistance of electrochemical reaction and shows that the two resistances are comparable.

Determination of the apparent kinetic parameters

Tafel slope values. For complex electrochemical reactions involving diffusion, electrochemical and chemical steps, it can be shown that in the steady state:[14]

$$\frac{1}{j_{\text{meas}}} = \frac{1}{j_{\text{diff}}} + \frac{1}{j_{\text{react}}} + \frac{1}{j_{\text{kin}}} \tag{6}$$

where on the right hand side only the last term will be dependent on the potential. This equation demonstrates that at more positive overpotentials, the reaction rate can become limited by diffusion (j_{diff}) or chemical reaction (j_{react}). Since the previous analysis showed that, under the present conditions and at more positive overpotentials, the current is probably diffusion–reaction-limited, one can use the Eq. (6) for an estimation of the rate of the electrochemical step (j_{kin}) in accordance to:

$$j_{\text{kin}} = \frac{j_{(\text{diff,react})} j_{\text{meas}}}{j_{(\text{diff,react})} - j_{\text{meas}}} \tag{7}$$

where the values of $j_{(\text{diff,react})}$ can be estimated from the experimental data (Fig. 1) at more positive overpotentials. The calculated values of j_{kin} can be now plotted against the electrode potential in the form of a Tafel plot (Fig. 2). As can be seen in Fig. 2, irrespective of the Nafion loading, two linear regions could be observed with a lower Tafel slope value of *ca*. 30 mV dec^{-1} at low overpotentials, followed by a higher Tafel slope value of *ca*. 60 mV dec^{-1} at high overpotentials.

In a similar way, the experimental data for MEA comprising 0.5 mg cm^{-2} platinum and 1 mg cm^{-2} Nafion at a constant temperature of 60 °C and at varying partial pressures of HCl in the gas phase was analyzed, as shown in Fig. 3. Again, two linear regions are clearly seen but only in the experiments at higher HCl partial pressures, while at lower partial pressures, these two regions merge into one with an effective Tafel slope of *ca*. 40–45 mV dec^{-1}.

The MEA of the same composition was further tested at varying temperatures with the other conditions being kept constant. The results presented in Fig. 4 show two distinct linear regions in the temperature range from 40–60 °C. The Tafel slope values in these two regions were virtually independent of temperature. At room temperature, the transition from low Tafel slope region to high Tafel slope region was more gradual with an intermediate Tafel slope value of *ca*. 40 mV dec^{-1}.

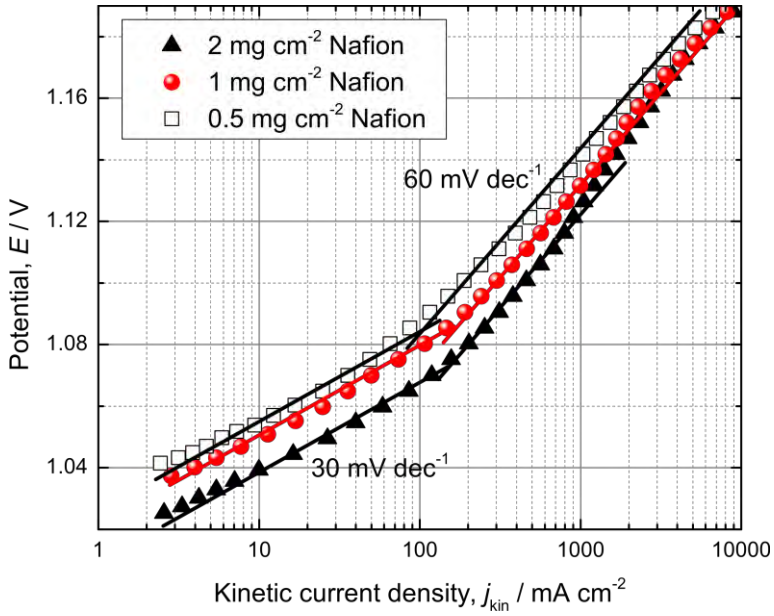

Fig. 2. Tafel plot for the HCl oxidation on an MEA comprising a constant Pt loading (0.5 mg cm^{-2}) and different Nafion loadings. Conditions as in Fig. 1.

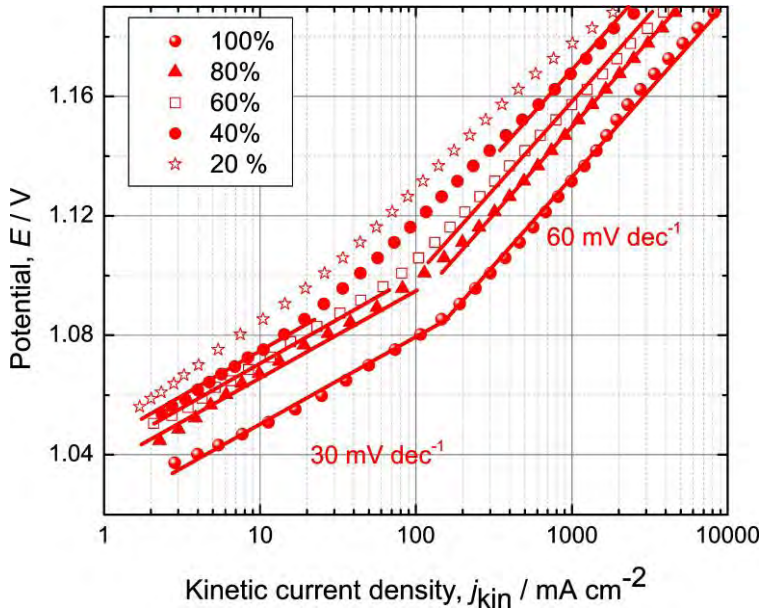

Fig. 3. Influence of HCl partial pressure on HCl oxidation on an MEA comprising 0.5 mg cm^{-2} Pt and 1 mg cm^{-2} Nafion. Conditions: temperature: 60 °C, pressure: 101.3 kPa, HCl flow rate: 500 ml min^{-1} and sweep rate: 1 mV s^{-1}.

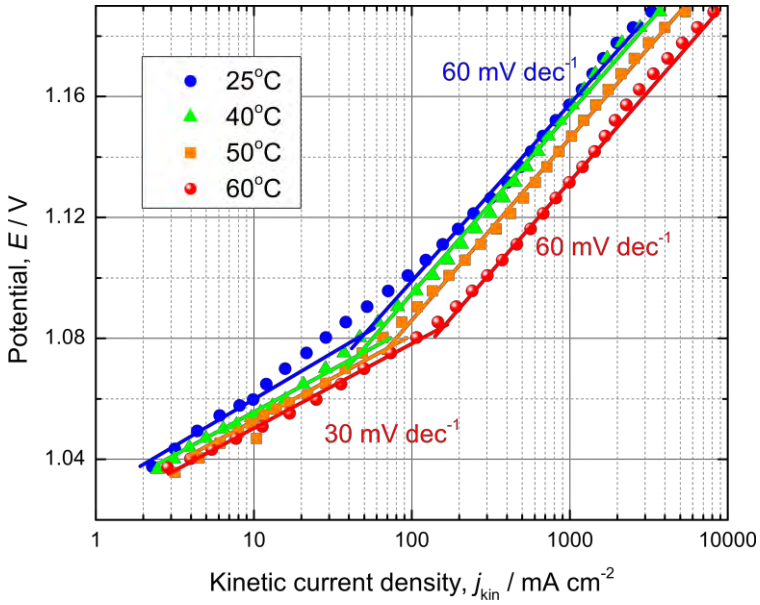

Fig. 4. Influence of temperature on HCl oxidation on an MEA comprising 0.5 mg cm^{-2} Pt and 1 mg cm^{-2} Nafion. Conditions: HCl pressure: 101.3 kPa, HCl flow rate: 500 ml min^{-1} and sweep rate: 1 mV s^{-1}.

Apparent reaction order. In addition to the Tafel slope, the reaction order is an important kinetic parameter for discrimination between different reaction mechanisms. In the present study, the apparent reaction orders were calculated from the slope of ln j_{kin} *vs.* ln y_{HCl} plot at constant electrode potentials (Fig. 5). The calculated values were 0.82±0.07, 1.07±0.09 and 0.97±0.07 at 1.065, 1.095 and 1.155 V, respectively. For the calculations, only the points up to 0.8 mole fraction HCl were considered. As can be seen in Fig. 5, the last points corresponding to pure HCl gas lay out of the trend lines at all potentials.

The apparent activation energies. The apparent activation energies were calculated from Arrhenius plots at constant overpotentials (Fig. 6a). The obtained values changed from *ca*. 16 kJ mol^{-1} at low overpotentials to *ca*. 30 kJ mol^{-1} at intermediate values of the overpotentials. At very positive overpotentials, again values around 16 kJ mol^{-1} were obtained (Fig. 6b).

DISCUSSION

The onset vs. *equilibrium electrode potential, gas or liquid phase HCl oxidation*

In the present experiments, HCl was introduced as a reactant in the gas phase. However, in the employed experimental set-up, the Nafion membrane was from one side equilibrated with acid and therefore fully humidified. Water from the Nafion membrane could also enter the CL, which under some conditions can

lead to flooding of the void fraction of the CL. In this scenario, HCl from the gas phase absorbs in water prior to electrochemical reaction according to:

$$\mathrm{HCl(g)} \rightarrow \mathrm{HCl(aq)} \tag{8}$$

$$\mathrm{HCl(aq)} \rightarrow \mathrm{H^+(aq) + Cl^-(aq)} \tag{9}$$

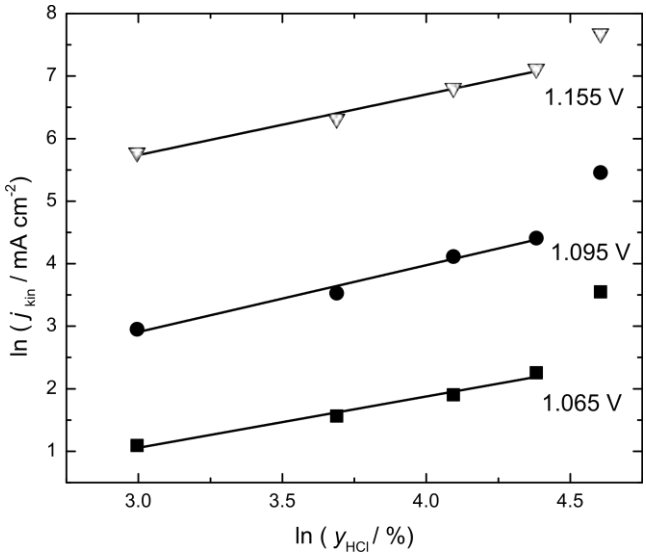

Fig. 5. Apparent reaction order with respect to the HCl concentration expressed in terms of HCl mole fraction (in %) in the gas phase. Data extracted from Fig. 3.

The chlorine ion reacts further electrochemically according to the well-known reaction for chlorine evolution from, *e.g.*, brine solution:

$$\mathrm{2Cl^-(aq) \rightarrow Cl_2(g) + 2e^-} \tag{10}$$

If reactions (8) and (9) are multiplied with 2 and summed with reaction (10), one obtains:

$$\mathrm{2HCl(g) \rightarrow Cl_2(g) + 2H^+(aq) + 2e^-} \tag{11}$$

this corresponds to the case of direct HCl oxidation from the gas phase.

The standard equilibrium potentials of reactions (10) and (11) are significantly different with values of 1.358 and 0.988 V, respectively. The observed open circuit potentials in the present work were around 1.03 V. This value is closer to the standard equilibrium potential of the gas phase reaction (Eq. (11)). Under the present conditions, a deviation from the standard value could be caused by deviations in the proton activity and the chlorine partial pressure from their standard values. The temperature dependence with a temperature coefficient of –0.1 mV K^{-1} (calculated based on literature data[15]) is not strongly expressed (which

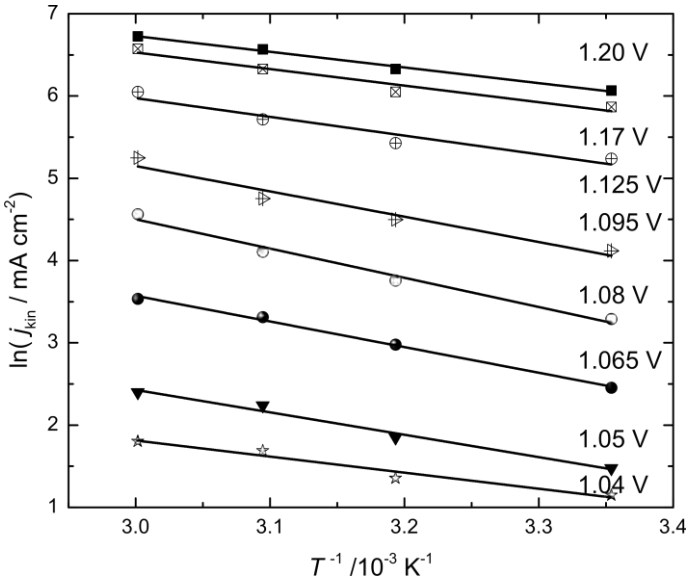

(a)

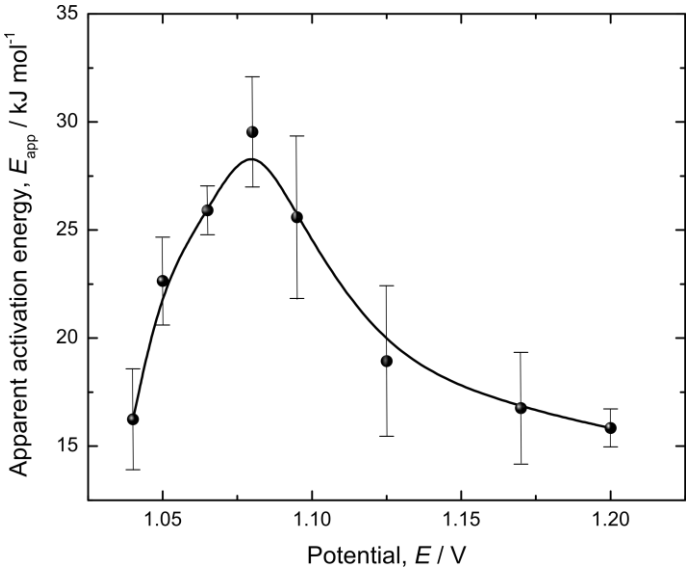

(b)

Fig. 6. a) Arrhenius plots for HCl oxidation on an MEA comprising 0.5 mg cm^{-2} Pt and 1 mg cm^{-2} Nafion (data extracted from Fig. 4) and b) dependence of the apparent activation energies on potential.

also corresponds to the experimental observations in Fig. 4). The proton activity is given by the activity of protons in the Nafion membrane, which at 60 °C is *ca*.

2.[16] This deviation from the standard conditions contributes to a *ca*. 16 mV increase in the equilibrium potential, which would result in a value close to the experimentally observed one. However, it should be mentioned that the chlorine activity was not controlled under the employed conditions, and this effect would decrease the equilibrium potential value.

The standard potential of the liquid phase reaction (Eq. (10)) is much more positive than the observed experimental values. However, assuming the formation of a very concentrated HCl solution (*e.g*., 30 mass %) and taking into account the high non-ideality of such a solution, a reduction of the standard value by *ca*. –140 mV could be obtained. The deviation of the chlorine activity from standard conditions would cause a further lowering compared to the value under standard conditions, which could bring this potential eventually close to the measured values. The temperature dependence for this reaction with a temperature coefficient of *ca*. –1.2 mV K^{-1} is more pronounced than for the reaction (Eq. (11)) resulting in a *ca*. –40 mV difference between the values at room temperature and 60 °C.

The experimentally observed deviation with temperature (Fig. 4) was only *ca*. –3 mV, which could be an argument for the gas phase reaction (Eq. (11)). However, the less explicit dependence of measured open circuit potentials than expected for the liquid phase reaction could be the consequence of the temperature influence on the gas–liquid equilibrium (reactions (8) and (9)). Consequently, the expected molality of chlorine ions in the liquid phase at room temperature would be higher (*ca*. 15.5 mol kg^{-1}) than at 60 °C (*ca*. 12 mol kg^{-1}). Taking into account that the HCl acid deviation from ideality at room temperature was more expressed than at elevated temperatures (molal activity coefficients 37.55 and 9.83 at room temperature and 60 °C, respectively[17]) a value of *ca*. 26 mV could be calculated based on this effect. In addition, the membrane potential would contribute in a similar manner, giving a virtually unchanged potential value, as was observed in the experiments.

In the experiments with varying partial pressures of hydrogen chloride at 60 °C, the experimentally observed difference of the open circuit potentials between the lowest and highest HCl partial pressures was *ca*. 19 mV. Assuming ideal gas behavior for HCl under all conditions, a deviation of *ca*. 46 mV could be expected. If a reaction from the liquid phase is assumed, a deviation of *ca*. 55 mV could be obtained. Both values are significantly different compared to the experimentally observed value.

The measured open circuit potential values are additionally influenced by junction potentials in the present experimental set-up. The most significant one is the membrane potential, the so-called Donnan potential.[15] The Donnan potential is caused by the different activities of protons inside the membrane and in interfacing solutions. In the case of the liquid phase reaction (Eq. (10)), assuming the

activity of protons is the same as that of chlorine ions; a value of *ca*. –140 mV (calculated for 60 °C) could be obtained. This value will be different in the case of the gas phase reaction (Eq. 11), since in this case, the Donnan potential is formed only at the liquid/membrane interface, giving a value of *ca*. –20 mV (calculated for 60 °C). It should also be mentioned that in the experiments with varying temperature or partial pressure of HCl, the Donnan potential would be also influenced through changes in the proton activities.

Finally, the measured values are influenced by the diffusion potential at the interface of the reference electrode and the liquid acid, which is difficult to calculate for the case of concentrated solutions. An estimation based on the Henderson Equation[15] gives a value of *ca*. 3 mV, which is significantly smaller than the Donnan potential.

To summarize, the presence of junction potentials and the uncertainty in the effect of the partial pressure of chlorine on the equilibrium conditions of the reactions (Eqs. (10) and (11)), makes it difficult to conclude which of these two reactions effectively determines the observed open circuit values.

Mechanism of HCl oxidation

The only proposed mechanism for the gaseous HCl oxidation (corresponding to overall reaction Eq. (11)) was presented by Eames and Newman,[7] Eqs. (A-1) and (A-2), with the chemical reaction (A-2) as a rate determining step (r.d.s.). This mechanism will be further denoted as mechanism "A":

$$\mathrm{HCl(g)} + \mathrm{Pt} \square \quad \mathrm{PtCl} + \mathrm{H^+(aq)} + \mathrm{e^-} \qquad \text{(A-1)}$$

$$2\mathrm{PtCl} \rightarrow 2\mathrm{Pt} + \mathrm{Cl_2(g)} \qquad \text{(A-2)}$$

It is also possible to assume that both steps proceed as electrochemical reactions:

$$\mathrm{HCl(g)} + \mathrm{Pt} \square \quad \mathrm{PtCl} + \mathrm{H^+(aq)} + \mathrm{e^-} \qquad \text{(B-1)}$$

$$\mathrm{HCl(g)} + \mathrm{PtCl} \rightarrow \mathrm{Pt} + \mathrm{Cl_2} + \mathrm{H^+(aq)} + \mathrm{e^-} \qquad \text{(B-2)}$$

This mechanism will be further denoted as mechanism "B".

Alternatively, if instead of the overall reaction (Eq. (11)), the overall reaction (Eq. (10)) would be valid, similar reaction mechanisms could be formulated, simply by replacing HCl(g) with Cl^-(aq). Additionally, protons would disappear from the expressions for mechanisms "A" and "B". The presence of protons appears to be an important criterion to differentiate between the overall reactions Eqs. (10) and (11), since for reaction Eq. (10), the protons should not have any influence on the equilibrium conditions. However, Boggio *et al.*[18] determined a reaction order with respect to protons of –1 in the case of chlorine evolution from brine. This could indicate that in addition to previously mentioned chlorine species, also non-dissociated HCl(aq), reaction Eq. (9), could be a potential source

of chlorine. Presently, as was previously discussed, it is not possible to assign which overall reaction occurs, but the following analysis is not affected by this uncertainty.

The mechanisms "A" and "B" with Cl^- as the reacting species were previously introduced by Gileadi.[19] He assumed that in both mechanisms, the second reaction was the rate determining one, which was further assumed to be irreversible. The first step was always assumed to be in quasi-equilibrium. In his analysis, the pre-exponential term in the Frumkin isotherm, assuming effectively the so-called Temkin isotherm, was neglected. With these assumptions, the values of Tafel slopes and the reaction orders for different degrees of coverage at the electrode surface were determined. The data that have been recalculated for the temperature range in the present study are presented in Table I.

TABLE I. Tafel slopes and reaction orders with respect to HCl calculated based on literature data[19]

Coverage	Mechanism "A"		Mechanism "B"	
	Tafel slope mV dec^{-1}	Reaction order	Tafel slope mV dec^{-1}	Reaction order
Low ($\theta \to 0$)	17–19	2	13–14	2
Intermediate ($0.2 < \theta < 0.8$)	26–29	1.5	26–29	1
High ($\theta \to 1$)	51–57	1	∞	–

The Tafel slope values that were observed in the present study are in the range from *ca*. 30 mV dec^{-1} at low overpotentials to *ca*. 60 mV dec^{-1} at high overpotentials. These values were relatively temperature independent. The only exception was the value at room temperature with a slope of *ca*. 40 mV dec^{-1}) at low overpotentials. In the experiments with changing HCl partial pressure, the Tafel slope values also changed from 30 to 60 mV dec^{-1} for low and high overpotentials. These values were concentration dependent with an average Tafel slope of *ca*. 40–45 mV dec^{-1} at low HCl partial pressure. If these values are compared with the theoretical predictions in Table I, good agreement between the calculated values for mechanism "A", with a chemical step as a rate determining step, at intermediate and high degrees of coverage with adsorbed intermediates, and the experimental one could be registered. Mechanism "B" can obviously be disregarded, since at high coverage, it predicts an infinite Tafel slope value. Slightly different Tafel slope values under low temperature conditions and low HCl partial pressures could obviously be the consequence of the influence of temperature and concentration on the degree of coverage with adsorbed intermediates.[6]

The second apparent kinetic parameter that was determined in the present paper was the reaction order with respect to HCl. The determined values were *ca*. 0.82, 1.07 and 0.97 for 1.065, 1.095 and 1.155 V, respectively. The first two

values correspond to the region of the first Tafel slope (intermediate coverage of adsorbed intermediate) and the last value to the region of the second Tafel slope (high coverage of adsorbed intermediate). The theoretical values in Table I are between 1.5 and 1 for mechanism "A". As can seen, the apparent values deviate from calculated ones, which was especially evident in the first Tafel slope region. It should be recalled here that the last points in Fig. 5 corresponding to pure HCl were off trend lines at all potentials. Inclusion of these points obviously resulted in an increase in the apparent reaction orders, but straight lines in that case would have very low linear coefficients, making them unreliable. Since the gas–liquid equilibrium of the HCl(g) – water system exhibited high non-linearities (especially in the range of low and high HCl partial pressures) and taking into account the previous discussion on gas or liquid phase HCl oxidation, the data in Fig. 5 was recalculated with respect to Cl^- activities. It was assumed that the Cl^- activity coefficient was the same as the mean activity coefficient of the acid. The recalculated data are presented in Fig. 7. As can be seen, the data at all potentials in the whole range of studied activities followed the trend lines. The slopes of these trend lines were 1.27±0.06, 1.29±0.07 and 0.98±0.12 for 1.065, 1.095 and 1.155 V, respectively. The new calculated values are in much better agreement with the theoretical values in Table I for the case of mechanism "A" with the chemical step (recombination of adsorbed Pt–Cl) as the rate-determining step.

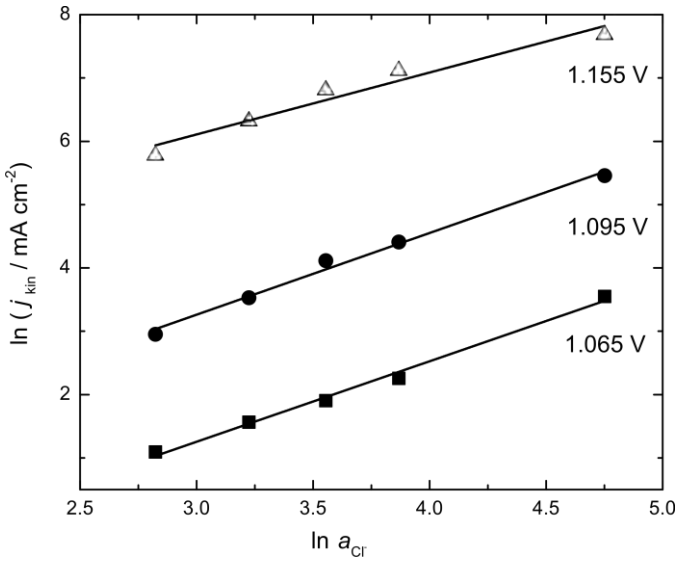

Fig. 7. Apparent reaction order with respect to HCl concentration expressed in terms of Cl^- activity in the liquid phase. Kinetic current densities are extracted from Fig. 3.

Finally, the determined values of the apparent activation energies in the range from 16 to 30 kJ mol^{-1} support further Pt–Cl recombination (Eq. (A-2)) as

the rate determining step.[19] As can be seen in Fig. 6b, the apparent activation energy is potential dependent. This was expected since the apparent values include also the contribution of the electrochemical activation. Additionally, the observed trend indicates the dependence of the activation energies on the surface coverage with Pt–Cl. The increase in the apparent activation energies at more negative overpotentials (first Tafel slope region) was probably caused by an increase of the Pt–Cl surface coverage. At more positive potentials, the overall values decrease due to the higher dominance of electrochemical activation as well as smaller changes in the apparent activation energies because of the very high Pt–Cl coverage.

CONCLUSIONS

The kinetics of HCl oxidation was studied on technical MEAs comprising different Nafion loadings at constant Pt loading. The influence of temperature and HCl partial pressure was studied for a selected MEA comprising 0.5 mg cm^{-2} Pt and 1 mg cm^{-2} Nafion. It was found that the HCl oxidation at industrially relevant current densities was viable on all studied MEAs. The optimization of the Nafion loading resulted in an increase of the catalyst utilization and a reduction in the reaction overpotential. An analysis with dimensionless numbers showed that the current at more negative overpotentials was at mixed reaction–diffusion-limitations.

Analysis of the apparent reaction order and Tafel slopes showed that the most viable mechanism to describe gaseous HCl oxidation is the one assuming dissociative electrochemical adsorption of reacting chlorine species and chemical recombination of the adsorbed Pt–Cl as the rate-determining step. According to this mechanism, the reaction proceeded under conditions of intermediate and high degree of coverage with adsorbed Pt–Cl.

A significant question in the present analysis was the question of whether a gas or liquid HCl oxidation mechanism applies. It was shown that based on the values of the open circuit potentials and their dependences on the operating parameters (temperature and HCl partial pressure), it is not possible to distinguish between these two scenarios. As was discussed, the appearance of different junction potentials in the system, where the membrane potential is probably the most influencing one, makes this analysis even more difficult. However, the dependence of the kinetic currents on the Cl^- activity adds some argument for liquid HCl oxidation.

Acknowledgments. The authors are grateful to the German Research Foundation (Deutsche Forschungsgemeinschaft, DFG) for financial support of this research work under the Project Grants SU 189/4-1 and KU 853/5-1. TVK is grateful to Prof. Mihai Christov (University of Chemical Technology and Metallurgy, Department of Physical Chemistry, 1756 Sofia, Bulgaria) for fruitful discussion on electrode kinetics.

ИЗВОД

КИНЕТИКА ОКСИДАЦИЈЕ ХЛОРОВОДОНИКА

ISAI GONZALEZ MARTINEZ[1], TANJA VIDAKOVIĆ-KOCH[2], RAFAEL KUWERTZ[3], ULRICH KUNZ[3], THOMAS TUREK[3] и KAI SUNDMACHER[1,2]

[1]Otto-von-Guericke University, Process Systems Engineering, Universitätsplatz 2, 39106 Magdeburg, Germany, [2]Max-Planck Institute for Dynamics of Complex Technical Systems, Sandtorstrasse 1, 39106 Magdeburg, Germany и [3]Institute of Chemical Process Engineering, Clausthal University of Technology, Leibnizstr. 17, 38678 Clausthal-Zellerfeld, Germany

Оксидација хлороводоника је проучавана на техничким гасно-дифузионим електродама у циклонској ћелији. Испитиван је утицај количине нафиона у каталитичком слоју, температуре и молског удела хлороводоника у гасовитој фази на кинетику ове реакције. На основу мерења одређени су привидни кинетички параметри, као што су ред реакције по хлороводонику, Тафелов нагиб и енергија активације. Вредности ових параметара указују на то да је рекомбинација адсорбованих атома хлора спори ступањ у реакцији.

(Примљено 19. новембра 2013)

REFERENCES

1. C. Six, F. Richter, in *Ullmann's Encyclopedia of Industrial Chemistry*, Wiley-VCH, 2000
2. P. Schmittinger, T. Florkiewicz, L. C. Curlin, B. Lüke, R. Scannell, T. Navin, E. Zelfel, R. Bartsch, in *Ullmann's Encyclopedia of Industrial Chemistry*, Wiley-VCH, 2000
3. J. Perez-Ramirez, C. Mondelli, T. Schmidt, O. F. K. Schlueter, A. Wolf, L. Mleczko, T. Dreier, Energy Environ. Sci. **4** (2011) 4786
4. T. Vidakovic-Koch, I. Gonzalez Martinez, R. Kuwertz, U. Kunz, T. Turek, K. Sundmacher, *Membranes* **2** (2012) 510
5. R. Kuwertz, I. Gonzalez Martinez, T. Vidakovic-Koch, K. Sundmacher, T. Turek, U. Kunz, *Electrochem. Commun*. **34** (2013) 320
6. I. Gonzalez Martinez, T. Vidaković-Koch, R. Kuwertz, U. Kunz, T. Turek, K. Sundmacher, *Electrochim. Acta* (2013), submitted
7. D. J. Eames, J. Newman, *J. Electrochem. Soc*. **142** (1995) 3619
8. K. Sundmacher, *J. Appl. Electrochem*. **29** (1999) 919
9. T. Vidakovic, M. Christov, K. Sundmacher, *Electrochim. Acta* **49** (2004) 2179
10. T. Vidakovic, M. Christov, K. Sundmacher, *J. Electroanal. Chem*. **580** (2005) 105
11. R. S. Yeo, J. McBreen, A. C. C. Tseung, S. Srinivasan, J. McElroy, *J. Appl. Electrochem*. **10** (1980) 393
12. B. E. Conway, G. Ping, *J. Chem. Soc., Faraday Trans*. **86** (1990) 923
13. K. Sundmacher, T. Schultz, *Chem. Eng. J*. **82** (2001) 117
14. T. Vidaković-Koch, V. K. Mittal, T. Q. N. Do, M. Varničić, K. Sundmacher, *Electrochim. Acta* **110** (2013) 94
15. C. H. Hamann, W. Vielstich, *Elektrochemie*, Wiley-VCH, Weinheim, 2005.
16. M. Umeda, K. Sayama, T. Maruta, M. Inoue, *Ionics* **19** (2013) 623
17. G. Akerlof, J. W. Teare, *J. Am. Chem. Soc.* **59** (1937) 1855
18. R. Boggio, A. Carugati, G. Lodi, S. Trasatti, *J. Appl. Electrochem*. **15** (1985) 335
19. E. Gileadi, *Electrode Kinetics for Chemists*, *Chemical Engineers, and Materials Scientists*, Wiley-VCH, New York, 1993.

Journal of the Serbian Chemical Society
JSCS-info@shd.org.rs • www.shd.org.rs/JSCS

J. Serb. Chem. Soc. *78* (12) 2131–2140 (2013) UDC 541.132.4+547.292–38+544.6.076.32–039.59:543.544.5.068.7
JSCS–4555
Original scientific paper

Determination of clopidogrel using square wave voltammetry at a gold electrode

ALEKSANDAR R. MLADENOVIĆ[1], VLADISLAVA M. JOVANOVIĆ[2#], SLOBODAN D. PETROVIĆ[3#], DUŠAN Ž. MIJIN[3#], SAŠA Ž. DRMANIĆ[3#] and MILKA L. AVRAMOV IVIĆ[2*#]

[1]Hemofarm AD, Beogradski put bb, 26300 Vršac, Serbia, [2]ICTM – Institute of Electrochemistry, University of Belgrade, Njegoševa 12, Belgrade, Serbia and [3]Faculty of Technology and Metallurgy, University of Belgrade, Karnegijeva 4, Belgrade, Serbia

(Received 13 September 2013)

Abstract: The determination of clopidogrel, an antiplatelet agent, was performed at a gold electrode in pH 3.7 acetate buffer using cyclic voltammetry (CV) and square wave voltammetry (SWV). Each voltammogram was characterized by the well defined peak at approximately 1.0 V. The current of anodic stripping peak exhibited a linear dependence on the clopidogrel concentration in the range from 317.89 to 935.16 μg cm^{-3}. The obtained linearity was applied to determine clopidogrel in the tablet form of the pharmaceutical preparation (Plavix®). The results were compared to the UV spectrophotometric and HPLC methods.

Keywords: cyclic voltammetry; acetate buffer; tablet; UV, HPLC.

INTRODUCTION

Clopidogrel (CLP), methyl (+)-(*S*)-α-(*o*-chlorophenyl)-6,7-dihydrothieno-[3,2-*c*]pyridine-5(4*H*)-acetate (Fig. 1), is an antiplatelet agent widely used in the prevention of ischemic stroke, myocardial infarction and stroke.[1,2]

It inhibits platelet aggregation by selectively preventing the binding of adenosine diphosphate (ADP) to its platelet receptor.[3] This drug reduces thrombotic events in a wide range of patients (*e.g.*, recent myocardial infarction, established peripheral arterial disease and acute coronary syndrome). Clopidogrel is an inactive prodrug, and a biotransformation by the liver is necessary to induce expression of its anti-aggregating activity.[4] It is rapidly absorbed and undergoes extensive metabolism after oral administration and its plasma concentration goes down considerably rapidly.[5]

* Corresponding author. E-mail: milka@tmf.bg.ac.rs
# Serbian Chemical Society member.
doi: 10.2298/JSC130913116M

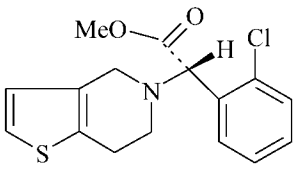

Fig. 1. Structure of clopidogrel.

Analytical methods for the determination of clopidogrel include mostly chromatographic and spectrophotometric techniques: gas chromatography–mass spectrometry (GC–MS),[6] liquid chromatography–mass spectrometry (LC–MS),[7–10] high-performance liquid chromatography (HPLC),[11–13] liquid chromatography,[14] LC–MS/MS,[15] LC–ESI-MS/MS,[16] thin-layer chromatography (TLC),[17] high-performance thin-layer chromatography (HPTLC),[18] UV spectrophotometry.[19–24] Furthermore, the determination of clopidogrel and its impurities by capillary electrophoresis was reported.[25]

Electrochemical determination of clopidogrel in standard form and pharmaceutical preparations using the differential pulse voltammetry (DPV) method with a glassy carbon working electrode was recently published.[26] Hitherto, a detailed voltammetric determination and electrochemical behaviour of clopidogrel at a gold electrode have not been published.

The aim of this study was to investigate the electrochemical behaviour of clopidogrel using cyclic voltammetry and to present its quantitative determination at a gold electrode in pH 3.7 acetate buffer using square wave voltammetry. Clopidogrel was studied as the pure standard or in the pharmaceutical preparation (Plavix®). The square wave voltammetry (SWV) method was applied to determine the amount of clopidogrel in the tablet form of a pharmaceutical preparation (Plavix®) and the results were compared with the UV spectrophotometric and HPLC methods.

EXPERIMENTAL

Materials

Clopidogrel bisulphate (CLB) standard was kindly provided by Hemofarm AD, Vršac, Serbia. Plavix® tablets containing a 75 mg dose of clopidogrel were obtained from local pharmacies. HPLC grade acetonitrile, methanol, ammonium acetate, sodium bicarbonate, sulphuric acid, sucrose, dichloromethane, sodium dihydrogenphosphate ($NaH_2PO_4{\cdot}H_2O$), H_3PO_4 and $NaHCO_3$ (*p.a.* purity), were obtained from Merck. Diethylamine, analytical grade, and ammonium hydroxide 25 % were obtained from J. T. Baker. All solutions were prepared with water obtained from a Millipore system (18 MΩ cm). Acetate buffer was prepared according to the USP pharmacopoeial procedure.

Cyclic voltammetry

The three electrode electrochemical cell used for the cyclic voltammetry measurements was described in detail previously.[27,28] The cyclic voltammetry measurements were performed using an Autolab potentiostat/galvanostat Pgstat128N (Metrohm Autolab B.V., The Netherlands).

Polycrystalline gold served as the working electrode, a gold wire was used as the counter electrode and a saturated calomel electrode as the reference electrode. Polycrystalline gold (Pine rotating disc, used as the stationary electrode, surface area 0.500 cm^2) was polished with diamond paste, cleaned with a mixture of water (18 MΩ cm) and sulphuric acid and further cleaned with deionised water (18 MΩ cm) in an ultrasonic bath. All the potentials are given *vs*. SCE. Prior to the addition of the investigated substance, the electrolyte was deoxygenated by purging with nitrogen. All the experiments were performed at room temperature. The voltammetric examinations of all the substances used were performed in acetate buffer solution. The potential was cycled between 0 and 1.5 V at a sweep rate of 50 mV s^{-1}.

Square wave voltammetry

*S*quare wave voltammetry (SWV) measurements were also performed using the Autolab potentiostat/galvanostat. The operating parameters were: step size 2 mV, pulse size 20 mV, frequency 8 Hz and scan rate 15 mV s^{-1}.

Solution preparation for voltammetry

Working standard solutions were prepared daily by dissolving appropriate amounts of CLB in 10 cm^3 of methanol and diluting to 100 cm^3 with acetate buffer (pH 3.7).

Preparation of the standard solutions for the analysis of clopidogrel bisulphate as a content of a solid dosage form

Twenty Plavix® tablets were weighed and then the average mass per tablet was determined. The tablets were grounded to a fine powder in a mortar. The required amount of the crushed tablets powder was dissolved in 50 cm^3 of methanol. After sonication for 10 min, the mixture was filtered into a 100 cm^3 volumetric flask. The residue was washed three times with acetate buffer (pH 3.7) and the volume was completed to the mark with the same buffer and stored in dark bottle at 4 °C. The obtained concentrations were checked by HPLC.

UV spectrophotometric instrument

The spectrophotometric analysis were performed on an Agilent 8453 UV–Vis spectrophotometer with a photodiode array (PDA) detector for measurement of the complete ultraviolet to visible light spectrum. The UV–Vis spectra were recorded in a quartz cuvette of 1 cm path length. The spectrophotometer was connected to a computer with Agilent ChemStation software that was used for all the spectrophotometric measurements and data processing. The samples were tested using a UV–Vis analytical procedure analogous to the procedure for content uniformity determination given in the US pharmacopeia monograph for clopidogrel tablets (USP 36 NF 31).[29]

Preparation of standard stock solution for spectrophotometric analysis

About 100 mg of clopidogrel bisulphate standard was accurately weighed, transferred to a 50 ml volumetric flask and dissolved in methanol. The flask was shaken and volume was made up to the mark with methanol.

Linearity for clopidogrel bisulphate for spectrophotometric analysis

Appropriate aliquots of standard stock solutions were taken in different volumetric flasks and diluted to obtain final concentrations of 0.04, 0.06, 0.08, 0.1, 0.2, 0.4 and 1.0 mg cm^{-3} of clopidogrel bisulphate in Britton Robinson buffer, pH 3.7. The UV spectra of the solutions were recorded and the determination of clopidogrel was realized employing the absorption at 270 nm, the wavelength of maximum absorption.

High performance liquid chromatography (HPLC) – instrumentation and chromatographic conditions

An Agilent HPLC system equipped with 1100 series high pressure binary gradient pump along with pulse damper, a photodiode array detector with an auto liquid sampler handling system was used for the analysis of the samples. The samples were tested using an HPLC analytical procedure analogous to the analytical procedure given in a US pharmacopeia monograph for the assay of clopidogrel tablets and determination of related substances (USP 36 NF 31).[29] The HPLC system was equipped with a 4.6 mm × 15 cm analytical column Ultron ES-OVM immobilized with ovomucoid as chiral stationary phase of 5 μm particle size (USP packing designation L57). The column eluent was monitored at a detection wavelength 220 nm. The mobile phase consisted of filtered and degassed mixture of phosphate buffer and HPLC grade acetonitrile in 75:25 ratio. Phosphate buffer was prepared by dissolving 1.36 g of monobasic potassium phosphate in 1000 cm^3 of purified water. The chromatography was performed at room temperature at a flow rate of 1.0 cm^3 min^{-1}. Data was recorded using OpenLab CDS, Ezchrom edition, software.

Preparation of standard stock solution for HPLC analysis

About 100 mg of clopidogrel bisulphate standard was weighed accurately and transferred to a 100 cm^3 volumetric flask and dissolved in methanol. The flask was shaken and volume was made up to the mark with methanol.

HPLC linearity for clopidogrel bisulphate

Appropriate aliquots of standard stock solutions were taken in different volumetric flasks and diluted to obtain final concentrations of 0.04, 0.2, 0.4, 0.6, 0.8, 1.0 and 1.2 mg cm^{-3} of clopidogrel bisulphate in Britton Robinson buffer, pH 3.7. Equal volumes of 10 μl of the solutions were injected and chromatograms were recorded.

HPLC analysis of clopidogrel bisulphate as a content of a solid dosage form

Twenty tablets of Plavix were weighed and thoroughly powdered. The average of one tablet was weighed, transferred into a 100 cm^3 volumetric flask, 50 cm^3 of methanol was added and sonicated for 5 min and stirred for 30 min. The solution was diluted with methanol to volume, and mixed. 5 cm^3 of this solution was transferred to a flask and diluted with Britton–Robinson buffer, pH 3.7, to 50 cm^3. A portion of this solution was passed through a 0.45-μm pore size PTFE membrane filter and discatograms were recorded. The pharmaceutical formulation was analyzed by performing six independent determinations.

RESULTS AND DISCUSSION

Electrochemical determination of clopidogrel in standard form and in pharmaceutical preparations by differential pulse voltammetry on a glassy carbon electrode was recently successfully performed[26] and pH 3.7 acetate buffer in mixture with methanol was found to be the optimal electrolyte. The intention was to study the feasibility of the electrochemical determination of clopidogrel as a pure standard and as the content of commercial tablets Plavix® by square wave voltammetry on a gold electrode only in pH 3.7 acetate buffer as electrolyte.

The electrochemical behaviour of the pure standard of clopidogrel on gold electrode was first studied by cyclic voltammetry in pH 3.7 acetate buffer. As is presented in Fig. 2, clopidogrel exhibited an apparent oxidative ability in this

electrolyte on a gold electrode. The cyclic voltammogram shows the beginning of anodic activity of clopidogrel in double layer region from 0.2 to 0.6 V. An apparent anodic current maximum appears at 1.0 V before oxide formation on the gold electrode and second one at 1.17 V in the area of oxide formation. The rapid increase of anodic current on gold oxide at 1.30 V in the presence of clopidogrel was observed as well as its shift by 0.1 V to a more negative potential, compared to a clean gold electrode (dashed line in Fig. 2).

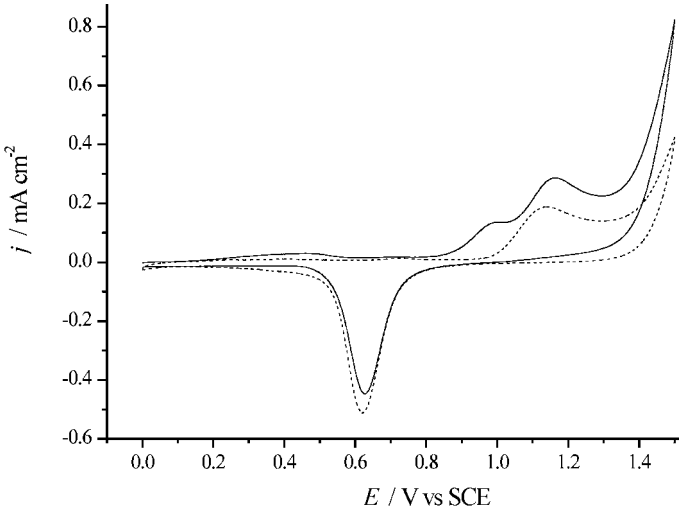

Fig. 2. Cyclic voltammogram of an Au electrode in pH 3.7 acetate buffer, dashed line, and after the addition of clopidogrel (concentration 32.0 μg cm^{-3}), full line; sweep rate: 50 mV s^{-1}. Only the first sweep is presented.

This voltammetric behaviour indicated the possible successful quantitative determination of clopidogrel using square wave voltammetry.

The application of square wave voltammetry for the quantitative determination of clopidogrel on the gold electrode is presented in Fig. 3. The SW voltammograms for different concentrations of clopidogrel were recorded in pH 3.7 acetate buffer in the potential range from 0 to 1.5 V at a scan rate of 15 mV s^{-1}. Before each scan, the compound was accumulated at the electrode surface at 0 V for 180 s. Under these conditions, the oxidation of clopidogrel proceeded before oxide formation on Au and reached maximum currents at the onset potential of Au oxide formation. Each voltammogram was characterized by a well defined peak at approximately 1.0 V. The currents of anodic stripping peak exhibited a linear dependence on the clopidogrel concentration, as shown in the inset of Fig. 3.

As already mentioned, the successful electrochemical determination of clopidogrel in standard form and pharmaceutical preparations described in literature[26] was performed by differential pulse voltammetry on a glassy carbon electrode in

a mixture of pH 3.7 acetate buffer and methanol. In the present study, square wave anodic stripping voltammetry was used to determine clopidogrel at a gold electrode in a similar mixture of acetate buffer (pH 3.7) with methanol in a 50:50 (*V*/*V*) ratio. However, the results obtained showed inhibition of the gold electrode surface by methanol, resulting in more than two-times smaller anodic currents of clopidogrel oxidation, as presented in Fig. 4. This indicates that further analysis of clopidogrel in Plavix ® should be continued in acetate buffer (pH 3.7) alone.

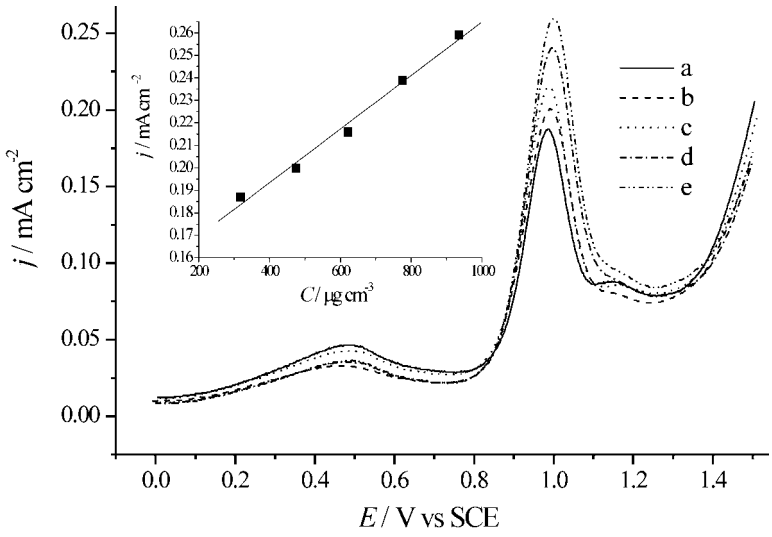

Fig. 3. Square wave anodic stripping voltammograms of clopidogrel at a gold electrode in acetate buffer (pH 3.7). Clopidogrel concentration: a) 317.89, b) 474.49, c) 622.03, d) 775.63 and e) 935.16 μg cm^{-3}. Accumulation time: 180 s at E = 0.0 V; step size 2 mV, pulse size 20 mV, frequency 8 Hz, scan rate 15 mV s^{-1}. Inset: The linear dependency of the anodic peak current *vs*. concentration of clopidogrel.

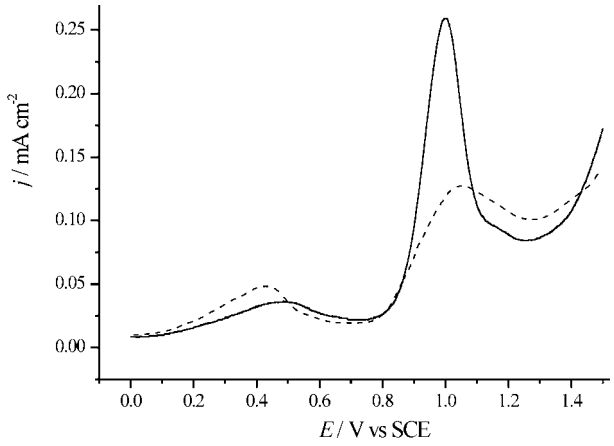

Fig. 4. Square wave anodic stripping voltammograms of 935.16 μg cm^{-3} clopidogrel at a gold electrode in acetate buffer, pH 3.7 (full line), and in acetate buffer (pH 3.7)/methanol, 1:1, *V*/*V* (dashed line), solutions. Accumulation time: 180 s at E = 0.0 V; step size 2 mV, pulse size 20 mV, frequency 8 Hz, scan rate 15 mV s^{-1}.

The voltammetric behaviour of clopidogrel as the content of commercial tablets Plavix® was also in a first stage investigated by cyclic voltammetry. Its voltammetric behaviour even in the presence of the excipients present in Plavix® showed the same anodic activity as the standard substance, presented in Fig. 2, with a negligible reduction in the values of the current maximums.

Similarly as for clopidogrel, the oxidation of Plavix® at a gold electrode using square wave voltammetry proceeded at potentials before the formation of oxide on the Au. The square wave voltammogram was characterized by a well defined peak at approximately 1.0 V.

The obtained linear relationship between current and concentration of clopidogrel in acetate buffer (pH 3.7) by SW voltammetry within the concentration range 0.317–0.935 mg cm^{-3} (Table I) was used for the determination of clopidogrel in tablet form (Plavix®) and the results were compared with those obtained by the UV and HPLC methods. The validation of the SW procedure was carried out by evaluation of the limit of detection (*LOD*), limit of quantification (*LOQ*) and recovery. The *LOD* and *LOQ* were calculated from the calibration curves as kSD/b where $k = 3$ for *LOD* and 10 for *LOQ*, *SD* is the standard deviation of the intercept and b is the slope of the calibration curve.[30,31] The *LOD* and *LOQ* values for the SW voltammetry method were 117.50 and 391.66 μg cm^{-3}, respectively.

TABLE I. Determination of CLP by SW voltammetry (SWV), UV spectrophotometry and HPLC

Parameter	SWV	UV	HPLC
Range / mg cm^{-3}	0.317–0.935	0.030–0.747	0.032–0.962
Regression equation[a]			
Slope	0.00012	1.81	23358783.00
SD of slope	7.09×10^{-6}	0.0003	0.0026
Intercept	0.1457	0.0076	36117.71
SD of intercept	0.0047	0.0001	0.0015
Regression coefficient	0.9947	0.9999	0.9999
Recovery, %	99.6	99.94	99.57
SD / %	1.11	1.65	1.38
LOD / μg cm^{-3}	117.50	8.56	8.24
LOQ / μg cm^{-3}	391.66	30.46	29.28

[a] $Y = a + bc$, where c is the concentration of clopidogrel, mg cm^{-3}; Y is the current per area unit, mA cm^{-2}, absorbance, A, and peak area unit, mAu, for the SWV, UV and HPLC methods, respectively, and *SD* is the standard deviation

Recovery studies were also performed to judge the accuracy of the SW voltammetry method by performing six measurements at low, intermediate and high CLP concentrations (317.89, 622.03 and 935.16 μg cm^{-3}). Mean percentage

recoveries of 99.6 % with relative standard deviation of 1.11 % were found and are presented in Table I.

Tablet solutions of appropriate concentrations were prepared and voltammograms were taken under the same experimental conditions (Fig. 5). The obtained results show that the excipients in the tablet were not electro-active and did not affect the voltammetric analysis. The results of drug analysis by the SW voltammetric technique are compared in Table II with those obtained by the UV-spectrophotometric and high pressure liquid chromatography methods. The analytical results demonstrated that the amount of active substance in the Plavix® tablet was within the limits specified in the pharmacopoeia. This indicates that the proposed method could be an alternative to chromatographic and spectrophotometric methods.

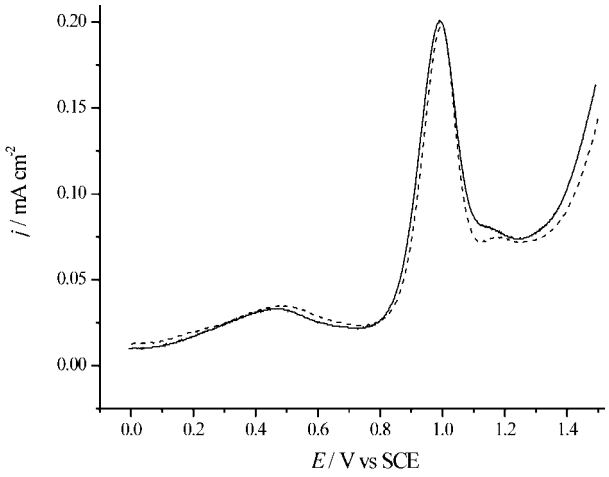

Fig. 5. Square wave anodic stripping voltammograms of clopidogrel standard (full line) and clopidogrel as the content of commercial tablets Plavix® (dashed line) at a gold electrode in acetate buffer (pH 3.7). Clopidogrel concentration: 474.49 μg cm^{-3}. Accumulation time: 180 s at E = 0.0 V; step size 2 mV, pulse size 20 mV, frequency 8 Hz, scan rate 15 mV s^{-1}.

TABLE II. Comparative studies for the determination of clopidogrel in Plavix® tablets (75 mg per tablet)

Parameter	Method		
	SWV	UV	HPLC
Mean coontent[a], mg	74.6	76.1	75.2
SD / %	0.8	1.1	0.3

[a]Each value is the mean of six experiments

The results obtained in this work show that the SW voltammetry method exhibited an accuracy that recommends it for routine and quality control analysis of the drug in pharmaceutical dosage forms.

CONCLUSIONS

The electrochemical determination of clopidogrel, as standard and in commercial tablets, Plavix®, was performed at a gold electrode in pH 3.7 acetate buf-

fer using square wave voltammetry. Prior to the determination, their electrochemical behaviour was studied by cyclic voltammetry. It was shown by both techniques that each voltammogram is characterized by a well defined peak at approximately 1.0 V. The linear dependence of currents of the anodic stripping peak on clopidogrel concentration was used to determine the amount of clopidogrel in Plavix® tablets. The results demonstrated that the SW voltammetric technique could be used directly, easily and rapidly for the determination of clopidogrel in tablet dosage forms. The SW voltammetric technique was compared to the results of drug analysis by UV and HPLC methods. The analytical results demonstrated that the amount of active substance in the Plavix® tablets was within the limits specified in the pharmacopoeia. This indicates that the proposed method could be an alternative to chromatographic and spectrophotometric methods.

*Acknowledgement***.** The work was supported by the Ministry of Education, Science and Technological Development of the Republic of Serbia (Grant No. ON172013).

ИЗВОД

ОДРЕЂИВАЊЕ КЛОПИДОГРЕЛА ВОЛТАМЕТРИЈОМ СА ПРАВОУГЛИМ ИМПУЛСИМА НА ЕЛЕКТРОДИ ОД ЗЛАТА

АЛЕКСАНДАР Р. МЛАДЕНОВИЋ[1], ВЛАДИСЛАВА М. ЈОВАНОВИЋ[2], СЛОБОДАН Д. ПЕТРОВИЋ[3], ДУШАН Ж. МИЈИН[3], САША Ж. ДРМАНИЋ[3] и МИЛКА Л. АВРАМОВ ИВИЋ[2]

[1]Хемофарм АД, Београдски пут бб, 26300 Вршац, [2]ИХТМ – Центар за електрохемију, Универзитет у Београду, Његошева 12, Београд и [3]Технолошко–металуршки факултет Универзитета у Београду, Карнегијева 4, Београд

Клопидогрел је антитромботски агенс из тиенопиридинске класе, који се користи за инхибирање формирања крвних угрушака при лечењу коронарне артеријске болести, периферне васкуларне болести, и цереброваскуларне болести. Електрохемијско понашање клопидогрел стандарда и као састојка таблете Plavix® је дефинисано цикличном волтаметријом. Њихово квантитативно одређивање на електроди од злата у ацетатном пуферу, pH 3,7, урађено је волтаметријом са правоугаоним импулсима (SWV). Показано је обема техникама да је сваки волтамограм окарактерисан добро дефинисаним струјним врхом на 1,0 V. На основу линеарне зависности анодних струја од концентрације клопидогрел стандарда одређена је маса клопидогрела у Plavix® таблети. Добијени резултати показују да SWV техника може бити коришћена директно, брзо и једноставно за одређивање клопидогрела у таблетама. Резултати добијени SWV волтаметријском техником су поређени са резултатима анализе клопидогрела UV спектрофотометријом и течном хроматографијом са високим перформансама. Аналитички резултати показују да је маса активне супстанце у таблетама Plavix® у оквиру лимита специфікованог фармакопејом. То указује да волтаметрија са правоугаоним импулсима може бити успешна алтернатива хроматографским и спектрофотометријским методама.

(Примљено 13. септембра 2013)

REFERENCES

1. S. J. Cutler, G. H. Cocolas, in: *Wilson and Gisvold's Textbook of Organic Medicinal and Pharmaceutical Chemistry*, J. H. Block, J. M. Beale, Eds., Lippincott Williams and Wilkins, Philadelphia, PA, 2004, Chap. 19, pp. 622–675
2. J. A. Coukell, A. Markham, *Drugs* **54** (1997) 745
3. T. L. Lenz, A. F. Wilson, *Clin. Pharmacokinet*. **42** (2003) 909
4. P. Savi, J. M. Herbert, A. M. Pflieger, F. Dol, D. Delebassee, J. Combalbert, G. Defreyn, J. P. Maffrand, *Biochem. Pharmacol*. **44** (1992) 527
5. H. Caplain, F. Donat, C. Gaud, J. Necciari, *Semin. Thromb. Hemost*. **25** (1999) 25
6. P. Lagorce, Y. Perez, J. Ortiz, J. Necciari, F. Bressolle, *J. Chromatogr., B* **720** (1998) 107
7. H. Ksycinska, P. Rudzki, M. B. Kiliszek, *J. Pharm. Biomed. Anal*. **41** (2006) 533
8. A. Mitakos, I. Panderi, *Anal. Chim. Acta* **505** (2004) 107
9. R. V. S. Nirogi, V. N. Kandikere, M. Shukla, K. Mudigonda, S. Maurya, R. Boosi, *Rapid Commun. Mass Spectrom*. **20** (2006) 1695
10. B. S. Shin, S. D. Yoo, *Biomed. Chromatogr*. **21** (2007) 883
11. S. S. Singh, K. Sharma, D. Barot, P. R. Mohan, V. B. Lohray, *J. Chromatogr., B* **821** (2005) 173
12. E. Souri, H. Jalalizadeh, A. Kebriaee-Zadeh, M. Shekarchi, A. Dalvandi, *Biomed. Chromatogr*. **20** (2006) 1309
13. M. Gandhimati, T. K. Ravi, *Indian J. Pharm. Sci.* **69** (2007) 123
14. A. Mitakos, I. Panderi, *J. Pharm. Biomed. Anal*. **28** (2002) 431
15. M. Takahashi, H. Pang, K. Kawabata, N. A. Farid, A. Kurihara, *J. Pharm. Biomed. Anal*. **48** (2008) 1219
16. N. K. Patel, G. Subbaiah, H. Shah, M. Kundlik, P. S. Shrivastav, *J. Chromatogr. Sci*. **46** (2008) 867
17. D. Antić, S. Filipić, D. D. Agbaba, *Acta Chromatogr*. **18** (2007) 199
18. H. Agrawal, N. Kaul, A. R. Paradkar, K. R. Mahadik, *Talanta* **61** (2003) 581
19. P. Mishra, A. Dolly, *Indian J. Pharm. Sci*. **67** (2005) 491
20. *The United States Pharmacopoeia*, Thirtieth Revision, and *The National Formulary*, 25th ed., Rockville, MD, 2007, p. 1802
21. H. E. Zaazaa, S. S. Abbas, M. Abdelkawy, M. M. Abdelrahman, *Talanta* **78** (2009) 874
22. S. Dermiş, E. Aydoğan, *Commun. Fac. Sci. Univ. Ank. Ser. B* **55** (2009) 1
23. S. Gurav, R. Venkatamahesh, *Int. J. ChemTech Res*. **42** (2012) 497
24. P. B. Cholke, R. Ahmed, S. Z. Chemate, K. R. Jadhav, *Arch. Appl. Sci. Res*. **4** (2012) 59
25. A. S. Fayed, S. A. Weshahy, M. A. Shehata, N. Y. Hassan, J. Pauwels, J. Hoogmartens, A. Schepdael, *J. Pharm. Biomed. Anal*. **49** (2009) 193
26. S. Dermis, E. Avdogan, *Pharmazie* **65** (2010) 3
27. K. M. Drljevic-Djurić, V. D. Jović, U. Č. Lačnjevac, M. L. Avramov Ivić, S. D. Petrović, D. Ž. Mijin, S. B. Djordjević, *Electrochim. Acta* **56** (2010) 47
28. M. Nevešćanin, M. L. Avramov Ivić, S. D. Petrović, D. Ž. Mijin, S. N. Banović Stević, V. M. Jovanović, *J. Serb. Chem. Soc.* **78** (2013) 1373
29. *The United States Pharmacopoeia-36* and *National Formulary-31 first supplement*, 2013 ed., http://www.uspnf.com/uspnf/pub/index?usp=36&nf=31&s=1&officialOn=August-%201,%202013 (10.9.2013)
30. J. C. Miller, J. N. Miller, *Statistics for Analytical Chemistry*, 2nd ed., Wiley, New York, 1984, p. 83
31. *The United States Pharmacopoeia*, in: *Validation of Compendial Methods*, 26th ed, Pharmacopoeial Convention Inc., Rockville, MD, 2003, pp. 2439.

Journal of the Serbian Chemical Society
JSCS-info@shd.org.rs • www.shd.org.rs/JSCS

J. Serb. Chem. Soc. *78* (12) 2141–2164 (2013)
JSCS–4556

UDC 546.96–31+546.93–31+
661.666.4.004.17:537.872.004.4:543.42
Authors' Review

AUTHORS' REVIEW

Tailoring the supercapacitive performances of noble metal oxides, porous carbons and their composites

VLADIMIR V. PANIĆ[1*#], ALEKSANDAR B. DEKANSKI[1#] and BRANISLAV Ž. NIKOLIĆ[2#]

[1]*Institute of Chemistry, Technology and Metallurgy, Department of Electrochemistry, University of Belgrade, Njegoševa 12, 11000 Belgrade, Serbia and* [2]*Faculty of Technology and Metallurgy, University of Belgrade, Karnegijeva 4, 11000 Belgrade, Serbia*

(Received 31 October 2013)

Abstract: Porous electrochemical supercapacitive materials, as an important type of new-generation energy storage devices, require detailed analysis and knowledge of their capacitive performances under different charging/discharging regimes. An investigation of the responses to dynamic perturbations of typical representatives, noble metal oxides, carbonaceous materials and RuO_2-impregnated carbon blacks, by electrochemical impedance spectroscopy (EIS) is presented. This presentation follows a brief description of supercapacitive behavior and origin of pseudo-capacitive response of noble metal oxides. For all the investigated materials, the electrical charging/discharging equivalent of the EIS response was found to obey the transmission line model envisaged as a so-called "resistor/capacitor (RC) ladder". The ladder features are correlated to material physicochemical properties, its composition and the composition of the electrolyte. Fitting of the EIS data of different supercapacitive materials to appropriate RC ladders enables in-depth profiling of the capacitance and pore resistance of their porous thin-layers and finally the complete revelation of capacitive energy storage issues.

Keywords: energy storage; pseudo-capacitance; carbon blacks; RuO_2; IrO_2; electrochemical impedance spectroscopy; transmission line model.

CONTENTS

* Corresponding author. E-mail: panic@ihtm.bg.ac.rs
# Serbian Chemical Society member.
doi: 10.2298/JSC131031128P

1. INTRODUCTION

Supercapacitive materials have attracted the most intense attention in contemporary technologies of electrochemical energy conversion and storage since they were found to fit almost completely the rather wide gap in power–energy characteristics between classic electrical capacitors (CEC) and batteries and fuel cells.[1] Table I shows that special constructions of electrochemical capacitors (EC) are able to release energy in times as short as classic capacitors do, and to store the amount of energy that is comparable to that stored by batteries. These extraordinary characteristics of EC lay in the intrinsic origin of their capacitive behavior – the physicochemical properties of the double layer and electrochemical processes at the supercapacitor sheath/electrolyte interphase. In comparison to CEC, whose characteristics are dictated by the dieletric constant and the thickness of the medium between the sheaths as current connectors, the electrode surface and outer Helmholtz plane play the role of the sheaths in EC, whereas the constituents of the double layer (ions and water molecules) determine its behavior as a dieletric medium. The large capacitance of an EC is hence mainly due to the nm size of the Debye length. However, in case of EC, there is an additional possibility to increase the capacitance by increasing the surface area of the sheaths by the application of nano-structured porous materials. Finally, some noble metal oxides, carbons and polymers are known for their ability to exchange considerable quantity of charge due to fast reversible redox transitions. Since there are no net faradaic manifestations, this ability is recognized as pseudo-capacitance.[1] These three specific features enable the overlapping of energy–power characteristics of EC, the so-called supercapacitors and even ultra-capacitors, with CEC and batteries, as presented in Table I. These features form two categories of EC: the double layer- and pseudo-capacitors.

1.1. The types of electrochemical capacitors

Depending on the process for capacitive energy storage in the charging/discharging cycle, two types of EC are recognized: those based on double layer capacitance, which store the energy electrostatically by rearrangement of the

species constituting the double layer upon imposition of an external electric field, and those mainly based on pseudo-capacitance as a consequence of charge exchange across the electrode/electrolyte interphase due to redox transitions. The second group can involve to some extent the contribution of double layer charging/discharging, especially if the active material is of high surface area.

TABLE I. Energy–power characteristics of energy conversion and storage devices, given per unit mass of active material[1]

Device	Active material	Specific energy, kW kg^{-1}	Specific power, W h kg^{-1}
Classic electrical capacitors	Dielectric medium	3–10^4	0.01–0.06
Electrochemical capacitors	Sheath (electrode) material	8×10^{-3}–10^3	0.06–12
Batteries	Electrode material	6×10^{-3}–0.5	8–200
Fuel cells		5×10^{-3}–0.2	100–10^3

The main representatives of the first type of EC are different forms of powdered carbons[1] (carbon blacks,[2–6] their single- and multi-walled nanotube forms[7–9] and graphene sheets[10–12]), although some contribution of carbon functional groups at the surface of activated carbons could cause the pseudocapacitive behavior.[13]

The diverse group of pseudo-capacitors can be subdivided according to the processes from which the pseudo-capacitance originates. Three main processes are involved: redox transitions of the electrode material itself, electrosorption and intercalation.[1] As already mentioned, redox pseudo-capacitors are noble metal oxides (RuO_2 and IrO_2) and some non-noble oxides and hydroxides (MnO_2, Co_3O_4, $NiO/Ni(OH)_2$, V_2O_5, SnO_2, *etc*.),[14,15] as well as electroconductive polymers.

This review focuses on carbon powder materials and noble metal oxides, RuO_2 and IrO_2, as well as on carbon-supported RuO_2 composite materials. The supercapacitive properties of noble metal oxides appear superior in comparison to other types of EC. Depending on the preparation procedure and, consequently, the physicochemical properties, literature reports the specific capacitance of RuO_2 in the range 100–750 F g^{-1}.[16–19] However, the limiting factor for their widespread use is the enormously high cost and relatively hardly-accessible porous structure of nanostructured oxides. For these reasons, these oxides are combined with other cheap materials, such as carbonaceous materials,[11,12,20–24] PbO_2[25] and NiO,[26] of high surface area able to distribute uniformly and preserve the fine distribution of oxide particles, thus increasing their efficiency.

2. PSEUDO-CAPACITANCE OF NOBLE METAL OXIDES

Upon exposure of the noble metal oxide electrode to potentiodynamic changes, an almost symmetric cyclovoltammetric (CV) response is registered, with nearly constant currents in a potential window as wide as 1.4 V in the case of RuO_2.[1] Typical CV responses of RuO_2 and IrO_2, mixed with stabilizing TiO_2,

coatings on titanium are presented in Fig. 1.[27,28] Iridium oxide introduces superior currents at the potentials above 0.40 V_{SCE}, while rather poor response is registered below 0.40 V_{SCE}. Two well-separated peaks for IrO_2 at around 0.70 and 1.0 V_{SCE} are seen, whereas only a weakly-pronounced broad peak around 0.60 V_{SCE} could be resolved for RuO_2. However, the increase in cathodic currents below 0.10 V_{SCE} is reserved for this oxide. These manifestations are believed to be the origin of pseudo-capacitance, since the currents are considerably larger than those corresponding to classic double layer charging/discharging. Apparently, there are some faradaic transitions, but no steady-state currents were registered in the presented potential window. The capacitance, $I\mathrm{d}t/\mathrm{d}E = \mathrm{d}q/\mathrm{d}E$, with q being the charge spent, is nearly constant. Thermodynamics allow for the appearance of pseudo-capacitance if the molar ratio between the reduced (Me_{Red}) and oxidized (Me_{Ox}) state of a metal (Me = Ru or Ir), $x_{Me_{Red}/Me_{Ox}}$, depends on E as follows:[1]

$$\frac{1 - x_{Me_{Red}/Me_{Ox}}}{x_{Me_{Red}/Me_{Ox}}} = K \exp\left(\frac{E}{RT}\right) \quad (1)$$

where K is a proportionality constant and the other thermodynamic quantities have their usual meanings. Accordingly, it is believed that mechanism of pseudocapacitive charging/discharging within an MeO_2 structure involves mixed electron–proton transition across the electrode/electrolyte interphase.[29–31] The metal-like conductivity of non-stoichiometric RuO_x facilitates the transport of electrons within the oxide matrix, whereas that of protons is faster and more pronounced if the oxide is more hydrous.[16] The proton-assisted, solid-state surface redox transitions are usually presented in summary as:

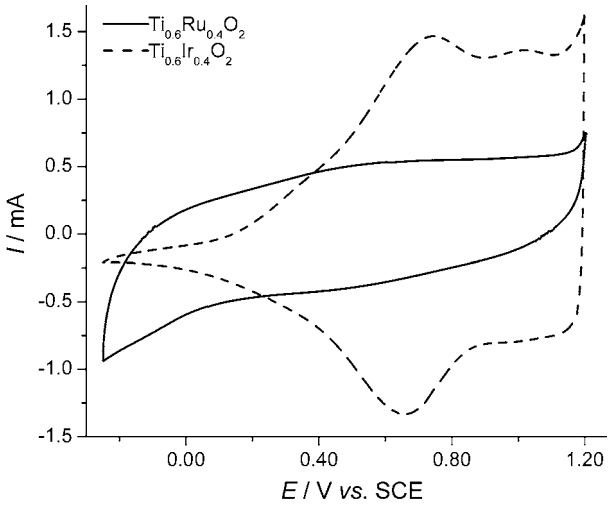

Fig. 1. Typical cyclic voltammograms of binary TiO_2–RuO_2 and TiO_2–IrO_2 coatings on Ti in acid solution.

$$RuO_x(H_2O) \rightleftharpoons RuO_{(x-\delta)}(H_2O)_{(x-\delta)} + 2\delta H^+ + 2\delta e^-, \quad 0 \le \delta \le x \qquad (2)$$

If the redox transitions (2) would be similar in energy demands, the sum of charge spent for charging could be almost constant over a wide potential range.[32] A possible Gaussian deconvolution of the anodic CV part for an RuO_2-based material, with up to six highly overlapped transitions is shown in Fig. 2. Some of them could cause the appearance of the very weak, but distinguishable, peaks at around 0.35 and 0.50 V_{SCE}.

The highest capacitance of RuO_2 was achieved upon optimization of its crystallinity and degree of hydration. In case of hydrous RuO_2,[16] 750 F g^{-1} was registered upon heating at 150 °C, whereas sol–gel processed oxide supported in a low amount on high surface area carbon black reached 700 F g^{-1} with calcinations at 300 °C.[21] It was supposed that the ordering of the RuO_6 octahedra, the content of crystalline water and the particle size were optimally balanced at this temperature, enabling the best pseudocapacitive properties to be obtained.

2.1. Three types of capacitive contributions for RuO_2

Detailed potentiodynamic investigations[33–35] of the capacitive behavior of crystalline RuO_2 revealed at least three types of capacitive processes distinguishable by the potential region over which each of them dominates. The double layer charging is the fastest, and contributes with up to 35 % to the overall capacitance even at a very low discharging rate.[33] The cathodic increase in currents is assigned to diffusion-limited incorporation of protons into the oxide matrix. The release of the appropriate charge spreads over the whole anodic branch with simultaneous redox transitions according to Eq. (2) and Fig. 2. The valuable development of this pseudocapacitive process requires slow discharge in crys-

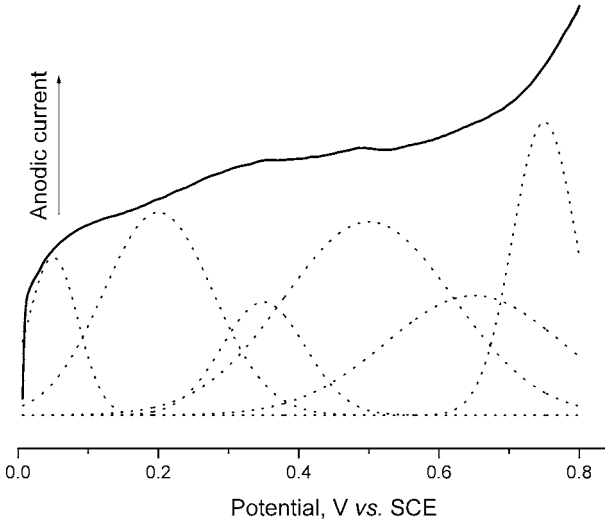

Fig. 2. An illustration of possible overlapping of at least six redox transitions during the charging of RuO_2-based supercapacitors.

talline RuO_2, but it is believed that it is dominant (65 % contribution[36]) and much faster for the hydrous state of the oxide. Finally, the pseudo-capacitance appears additionally increased by a contribution of the third type of capacitive processes – electrosorption of ions from the solution, which can contribute by 20 % to the overall capacitance.

If the considered mechanism of pseudo-capacitive behavior of noble metal oxides would be applied to the IrO_2 response shown in Fig. 1, it follows that either the proton intercalation process is suppressed or it manifests itself at more positive potentials with respect to RuO_2. The later implies its pronounced overlapping with redox transitions of Ir and, consequently, a much harder determination of capacitive performances. On the other hand, the consideration presented in Section 2.1 does not analyze the distribution of the capacitance throughout the porous layer, which depends on the charging/discharging rate.[37] Bearing in mind these particularities, the analysis of an in-depth pore resistance and capacitance profile through the porous layers of oxides, carbon blacks and their composites will be presented in the following sections. This analysis was performed by applying the methodology of a transmission line equivalent to the dynamic response of porous capacitive materials[1,15] to the charging/discharging data gained from electrochemical impedance spectroscopy.

3. DYNAMIC RESPONSE OF POROUS SUPERCAPACITIVE MATERIALS

The electrical equivalent of an idealized uniform porous supercapacitive material exchanging the charge with the electrolyte can be presented by an RC ladder,[37] schematically shown in Fig. 3. The RC ladder is a transmission line electrical circuit consisting of n parallel branches with a resistor and capacitor in series. The parameter n depends on the thickness of the porous layer (pore length) and electrolyte composition.[6,15,23,38] In real systems, the tortuous pores are not ideally cylindrical, their diameter can vary along the length and pore size distribution exists, which should also affect the number of the required branches.

Upon sinusoidal perturbation of the input potential, the charging/discharging current response at the pore orifice is:[37]

$$I(0,t) = \frac{E_\mathrm{a}}{R_{\mathrm{p},0}}(\sin\omega t + \cos\omega t)\sqrt{\frac{1}{2\omega R_{\mathrm{p},0}C_{\Sigma,0}}} \tag{3}$$

where E_a is the input amplitude and ω is the angular frequency. Eq. (3) implies that the output current is phase-shifted with respect to the input by –45° at any ω. The frequency required to reach the bottom of a pore of the length ℓ has to fulfill the condition:[37]

$$\omega = \frac{64}{R_{p,\ell}C_{\Sigma,\ell}\ell^2} \tag{4}$$

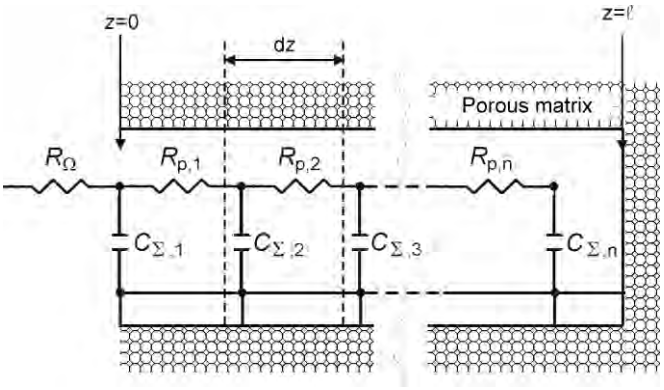

Fig. 3. A schematic diagram of the electrical equivalent of a porous supercapacitive material with uniform size distribution of semi-infinite cylindrical pores of length ℓ. R_Ω presents bulk electrolyte resistance, while $R_{p,n}$ and $C_{\Sigma n}$ is the pore resistance and sum of the capacitances of different origin (see Section 2) at position z, respectively.

The RC ladder model indicates generally (irrespective of whether the system is ideal or not) that the frequency of the output signal does not change through the porous layer, whereas its amplitude weakens, reaching asymptotically zero for given ω at a certain distance z, according to Eq. (4). Consequently, the signal penetration depth, z_p, can be defined as:[37]

$$z_p = \ell \sqrt{\frac{2}{\omega R_{p,z_p} C_{\Sigma,z_p}}} \tag{5}$$

Eq. (5) makes no physical sense if $\omega \leq (2/R_{p,\ell} C_{\Sigma,\ell})$, *i.e.*, the bottom of the pore is already reached at frequencies as low as $2/R_{p,\ell} C_{\Sigma,\ell}$. For thin-layer, porous supercapacitive materials usually having the capacitance of several hundreds of F g^{-1} and pore resistances not above several thousands of Ω, a reliable analysis of the in-depth capacitance profile should be obtained at reasonable frequencies down to the order of mHz. Eqs. (3)–(5) imply that the capacitive response of the most outer parts of a porous layer is obtained at $\omega \to \infty$, since the inner surface defined by pores can hardly follow the fast changes of the periodic input.

3.1. The number of required branches in the RC ladder equivalent electrical circuit

In order to analyze the capacitive response upon sinusoidal perturbation by an input potential using the electrochemical impedance spectroscopy (EIS) method, suitable software, able to fit the measured data into a freely chosen equivalent electrical circuit (EEC), is applied. The EEC that gives the best fitting results, which are evaluated according to the overall relative fitting error, ε_r, calculated as the square root of χ^2 – the error parameter usually used in EIS and directly obtained by the fitting software, defines the required number of RC branches.[39] Additionally, the fitting quality is to be judged with respect to the

values of obtained fitting parameters, which were taken as reliable if the relative dissipation of the gained values was less than 20 %. Finally, the plots of fitting data should agree with those registered experimentally as far as possible.

3.1.1. RC ladders for RuO_2- and IrO_2-based coatings on titanium

Detailed analysis of the in-depth capacitance profile of RuO_2 was investigated in the cases of thick and thin coatings (different pore lengths) on Ti prepared by an alkoxide ink procedure.[38,40] In order to alter the capacitive characteristics, the EIS spectra of the coatings were registered in two different solutions, 1.0 mol dm^{-3} H_2SO_4 and 5.0 mol dm^{-3} NaCl, pH 2. The ε_r values as a function of the required branches in the RC ladder EEC are shown in Fig. 4. The EECs with highest number of branches are those that gave the best fittings of the EIS data (if this number is further increased, the fitting does not return reasonable and reliable values of the EEC parameters). It follows generally that thicker coatings and electrolytes of higher concentrations with less movable ions require more branches. According to Eq. (2), an additional influence of different proton concentrations in the applied electrolytes (pH 0 and 2) on the coating in-depth distribution of the pseudo-capacitance, and consequently, on the number of required branches, is to be expected. It is usual to assume that the fitting quality is satisfactorily good if ε_r is below 3 %. Fig. 4 shows that ε_r steeply decreases in solutions of higher ionic strength, the decrease being more pronounced for thicker coatings. On the other hand, it appears that a good fitting quality in H_2SO_4 solution was already achieved with no branching ($R_\Omega C_{\Sigma,1}$ in Fig. 3). However, the plots of this EEC and the data did not agree well (not shown), unless at least 2 and 4 branches were applied for the data in H_2SO_4 and NaCl solutions, respectively.

The requirement for the introduction of more branches is already indicated at first glance of the measured data shown in Fig. 5, which shows the capacitance complex plane plots of thick coating in the two investigated solutions. Apparently, several overlapping capacitive loops appear in NaCl solution, which is not the case in H_2SO_4 solution. Full development of the branching in NaCl solution required two orders of magnitude lower frequencies (2.5 mHz) in comparison to corresponding features registered in H_2SO_4 solution (0.2 Hz). In the spectrum of thin coating (not shown), two well-separated loops were distinguishable only in NaCl solution, whereas the lowest required frequency appeared insensitive to the coating thickness in both H_2SO_4 and NaCl solution.

The considered differences in the EIS spectra and the EECs for coatings of different thickness in different solutions appear not to be due to the expected differences in pore resistance. Although the ionic strengths of H_2SO_4 and NaCl solution differ considerably, their ohmic resistances as well as pore resistances up to the last branch in H_2SO_4 solution are similar, irrespective of the coating thick-

ness.[38] It follows that the lower ionic strength of the H_2SO_4 solution is compensated for by the much larger ion mobility. On the other hand, well-separated capacitive loops, and consequently the requirement for more branched RC ladders, are the most pronounced in EIS spectra registered at the potential of the appearance of reversible CV peaks related to Eq. (2). A detailed investigation of the EIS behavior along the potential window from Fig. 1, of both RuO_2-[28] and IrO_2-based[41] coatings on Ti, revealed the following. The separation of capacitive loops is clearly visible at 0.74 V_{SCE}, and even more pronounced in H_2SO_4 solution for RuO_2 and IrO_2 mixed with TiO_2 in a binary coating, as TiO_2 is known for its coating stabilizing and surface area-developing influence.[42]

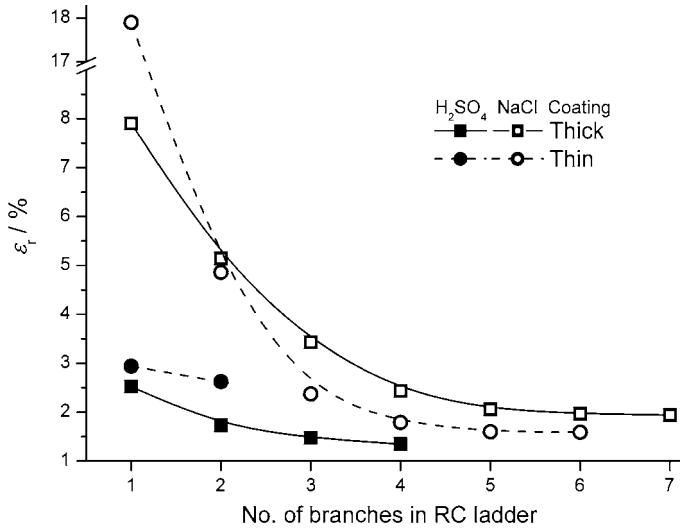

Fig. 4. The relative fitting error, ε_r, of RC ladder type of equivalent circuits with different number of RC branches used to fit the impedance spectra of RuO_2 coatings of different thickness on Ti, registered in H_2SO_4 and NaCl solution.[38]

The mentioned findings indicate that the separation of the capacitive loops is more due to the onset of pseudo-capacitance according to Eq. (2), which is limited by diffusion of protons into and out of the noble metal oxide matrix, than due to the distribution of the pore resistance. In case of pure coatings, the separation is better pronounced in solutions of lower proton concentration (NaCl, pH 2). However, binary MeO_2–TiO_2 coatings require a minimal proton concentration (1 M H_2SO_4) for the development of the separation since the noble metal oxide is finely distributed within the semiconductive TiO_2 matrix (RuO_2/TiO_2 particles diameter ratio ≈8 nm/100 nm[27]). It appears that pH 2 is not enough for the signal of moderate frequencies (down to few mHz) to penetrate the binary coating considerably and evolve full pseudocapacitive behavior. Hence, the separation of capacitive loops, and in-depth capacitance profile, could not be clearly developed.

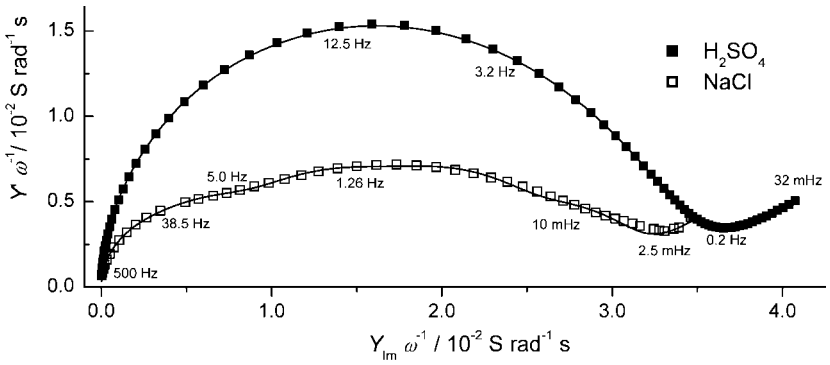

Fig. 5. The capacitance complex plane plots (symbols) for a thick RuO_2 coating on Ti registered in H_2SO_4 and NaCl solution. The data of corresponding RC ladders are presented by the lines.[38]

3.1.2. The RC ladders of carbon blacks and carbon black/RuO_2 composites

Carbon blacks of high surface area are known as double-layer capacitors, although the pseudocapacitive contribution of carbon functional groups (CFGs), which can be created by chemical or electrochemical activation of carbonaceous materials,[13,43–45] can be significant. Electrochemical oxidation of even smooth glassy carbon surfaces (low surface area)[13,45] considerably increases the capacitance due to the formation of CFGs and surface roughening. Abundant creation of CFGs was achieved by modest oxidation, which caused the largest separation of capacitive loops in proton-rich solution, as shown in Fig. 6. Hence, the separation appears to have an origin similar to the case of noble metal oxides – the development of pseudocapacitive behavior. However, thorough oxidation conditions were found to cause a "cutoff" of the CFGs from the surface, and consequently the separation diminished (Fig. 6). Irrespective of the content of CFGs, the capacitance increases from non-oxidized to the thoroughly oxidized state by more than two orders of magnitude.

A thin layer of the two commercial carbon black (CB) supercapacitors of considerably different real surface area, S_{BET} of 1475 (HSC) and 248 m^2 g^{-1} (LSC), were found to obey 5- and 3-branch RC ladder, respectively.[6] These have been fully correlated with the layer morphology (cross section geometry, equivalent pore diameter, pore length and pore tortuosity). The structures of the applied EECs, as well as capacitance and resistance values obtained by fitting the experimental EIS data to the circuits, which are supported by the results obtained by scanning electron microscopy (SEM) and cyclic voltammetry (CV) measurements, enabled an estimation of the capacitance and resistance profile throughout the porous carbon black electrodes.

Capacitance complex plane plots of HSC-supported ruthenium oxide of increasing particle size and low oxide loading are shown in Fig. 7.[23] For com-

parison, a plot for HSC is also shown. The plots consist of capacitive loops of decreasing radius with increasing particle size. Although the capacitance plot of HSC consists of at least two overlapped capacitive loops, only one loop could be clearly seen for the composites, which suggests a decrease in the required number of branches. The lowest capacitance values (both the imaginary and the real part) were registered for HSC at frequencies down to 2.0 Hz. This indicates that a part of the composite surface that was easily accessible to the electrolyte is of larger capacitive ability than corresponding part of the HSC surface, due to the presence oxide particles. However, at the frequencies below 2.0 Hz, the admittance of HSC is much larger than that of composites with larger particles. These results are in accordance with those obtained by cyclic voltammetry.[23]

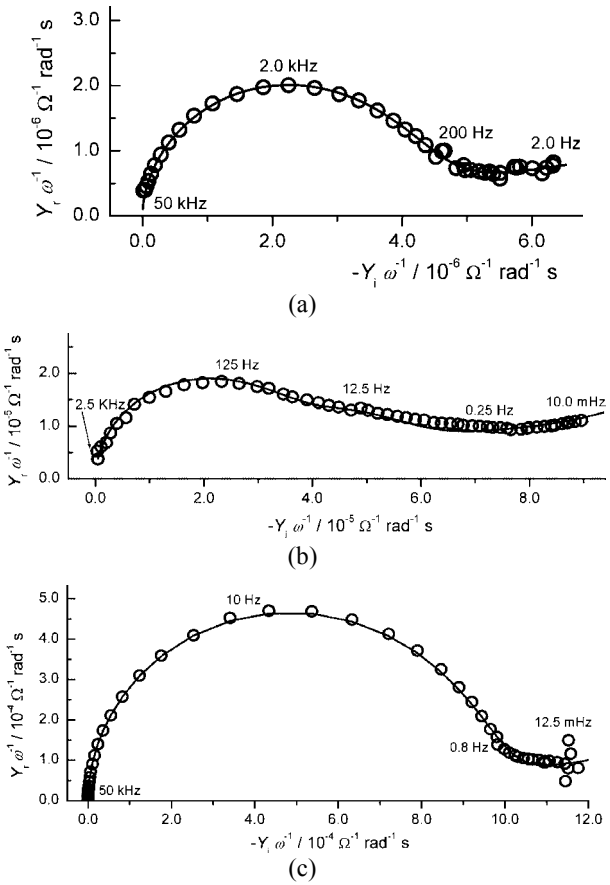

Fig. 6. The development of the capacitance profile of a glassy carbon electrode in the a) non-oxidized, b) moderately oxidized and c) thoroughly oxidized state. The spectra were registered around the potential of the redox transitions of the CFGs in 0.50 mol dm^{-3} H_2SO_4. The lines present the response of a 2-branch RC ladder EEC in each case.[13]

Impregnation of CBs with hydrated ruthenium oxide always causes a decrease in the BET real surface.[46,47] This decrease in real surface becomes more pronounced with increasing oxide mass fraction.[48] However, the decrease

in real surface area is accompanied by an increase in the composite capacitance caused by the pseudo-capacitance of the oxide, which could prevail over the reduction in CB double layer capacitance due to the decrease in the real surface area.[21] These effects of impregnation are more pronounced if the real surface area of the CB substrate is larger. However, if the oxide fraction in the composite is rather small, and if the oxide particles are large enough, the pseudocapacitive contribution of the oxide could not be sufficient to prevail, or at least to compensate, the decrease in the double layer capacitance caused by the decrease in the real surface area of CB substrate (Fig. 7). Hence, under certain impregnation conditions (leading to small oxide fraction and/or large oxide particles) and under rather high charging/discharging rates, the capacitive properties of the composite may be even worse than those of the carbon substrate.[23] These considerations are clearly reflected in the number of required branches in the EEC for the CB/RuO_2 composites. Instead of the five branches required for HSC, only three returned satisfactory good fitting of the EIS data of the HSC/RuO_2 composite. The number of required branches appeared insensitive to oxide loading and particle size.[23] On the other hand, RuO_2 supported on LSC required one branch more than bare LSC, which reflect mostly the capacitive response of the oxide.

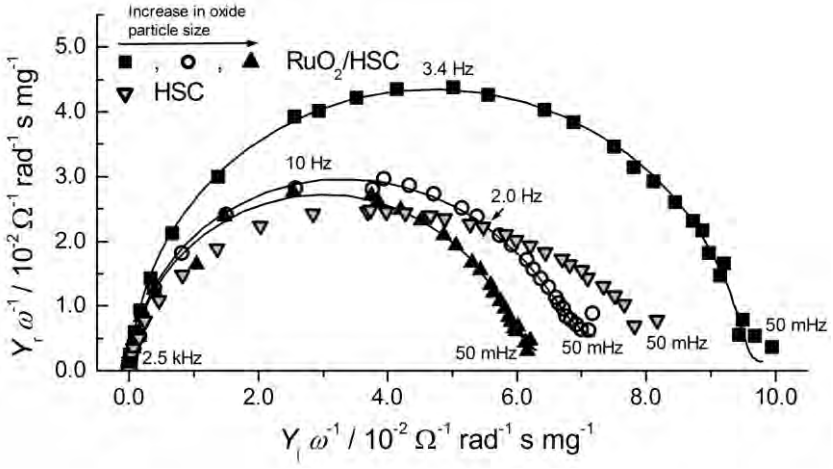

Fig. 7. Capacitance complex plane plots of high surface area carbon and high surface area carbon-supported ruthenium oxide of increasing particle size and low oxide loading.[23] (Reprinted with permission from Elsevier).

3.2. In-depth capacitance profiling of porous supercapacitors

The application of transmission line EEC as presented in Section 3.1 enables a detailed analysis of the capacitance distribution through the thin layers of the mentioned porous supercapacitive materials in correlation to the pore resistance distribution. In the following sections, this analysis is presented.

3.2.1. Ruthenium oxide coatings on titanium

The fitting data obtained according to methodology presented in Section 3.1.1 can be used to calculate the values of the total, C_{tot}, outer, C_{out}, and inner, C_{in}, capacitances of the thick and thin RuO_2 coatings in the two electrolytes. The C_{out} relates to the coating surface directly exposed to the electrolyte, *i.e.*, its capacitive response is not affected by the pore resistance. The C_{in} is the sum of the capacitances each associated to certain signal penetration depth, z_p (Eq. (5)), thus representing the response of coating of the internal surface. Bearing in mind the physical meaning of Eq. (5) and Fig. 3, mentioned capacitances can be calculated using the following equation:

$$C_{tot} = C_{out} + C_{in} = C_{\Sigma,1} + \sum_{i=2}^{n} C_{\Sigma,n} \quad (6)$$

The values calculated according to Eq. (6) are summarized in Fig. 8, in which the values of the so-called electrochemical morphology factor, ε_{ec}, were calculated as the ratio of C_{in} to C_{tot},[49] are also given. The values of total capacitance appear insensitive to the electrolyte composition for both thick and thin coating. This indicates that the applied frequencies were sufficiently low to take into account the diffusion limitations to Eq. (2). On the other hand, the values of the outer and inner capacitance, as well as of morphology factor, differed considerably in the different solutions. The ε_{ec} values were higher for the thick coating in both the H_2SO_4 and NaCl solution, due to the more pronounced contri-

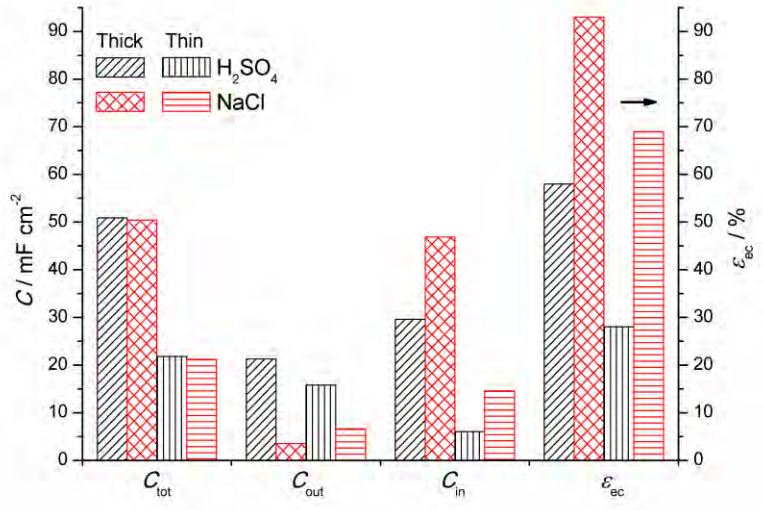

Fig. 8. The total, C_{tot}, outer, C_{out}, and inner, C_{in}, capacitances of the thick and thin RuO_2 coatings on Ti in the two electrolytes; the electrochemical morphology factor, ε_{ec}, is calculated as the ratio of C_{in} to C_{tot}.[38]

bution of the internal surface. The lower values of C_{out} in the NaCl solution for both the thick and thin coating are the consequence of the less pronounced contribution of the pseudo-capacitance to the capacitive characteristics of the coating, since the H^+ concentration was lower in this solution. For the same reason, C_{in} was greater in the NaCl solution, although the higher ion concentration and different mechanism of cation movement in comparison to the H_2SO_4 solution could be also involved in the response of internal surface. Da Silva *et al*.[49] found that the morphology factor was lower in sulfate-containing electrolytes than in those that contained Cl^-. Apparently, the more pronounced contribution of the hardly accessible inner surface to the capacitive characteristics of the thin coating in the NaCl solution considerably exceeded the decreased contribution of the pseudo-capacitance to the value of the outer capacitance with respect to the H_2SO_4 solution.

3.2.2. Poorly conductive and active state of Ir in IrO_2-based coatings on Ti

Since the regions of low CV and high pseudocapacitive currents are clearly separated in the CV response of IrO_2-based coatings (the border is around 0.20 V_{SCE}, Fig. 1), the RC ladder has a slightly different construction with respect to IrO_2-based coatings.[41] It required 2- and 3-branch ladders in parallel, whereas the data at low frequencies were found to be governed by a resistor in parallel to these ladders. The additional resistor was assigned to the poorly conductive state of Ir within the oxide matrix. The data registered above 0.20 V_{SCE} did not require the inclusion of a diffusion element in the EEC, which indicates that mass transport limitations to Eq. (2) were operative at potentials below 0.20 V_{SCE}. It follows that the crucial changes in the Ir oxidation state required for the development of a pronounced pseudocapacitive response above 0.20 V_{SCE} occurred in the potential range below this potential (in the region of the poorly conductive state).

The potential-dependent in-depth capacitance profile of IrO_2-based coating in H_2SO_4 solution is shown in Fig. 9. Generally, the highest values of the capacitances were obtained around 0.75 V_{SCE}, which corresponds to the most pronounced transition currents in Fig. 1. The exception is the value of the last branch at 0.35 V_{SCE}. It follows these values mainly present the pseudo-capacitance caused by the transition of the poorly active state to the more conductive active one. Indeed, if the potential was only slightly shifted anodically to 0.40 V_{SCE}, the mentioned capacitance considerably decreased, while the values in preceding branches increased by an order of magnitude. All these changes concern the capacitors situated "deeper" down the transmission line, which reflect the performances of the internal parts of the coating. However, the corresponding resistances were found negligibly dependent on potential, which suggest their prevailing pore resistance nature.[41] On the other hand, the resistances of outer parts of the coating (the first two branches) decreased considerably, and hence they are to be assigned rather to charge transfer resistance (Eq. (2)). These findings strongly

support the suggestion that the lower, poorly conductive oxidation states of Ir are mainly situated in the internal parts of the coating. The transition from low to high Ir oxidation states, as well as its distribution through the porous coating, appears as crucial for the full development of the capacitive performance of the IrO_2-based coatings.

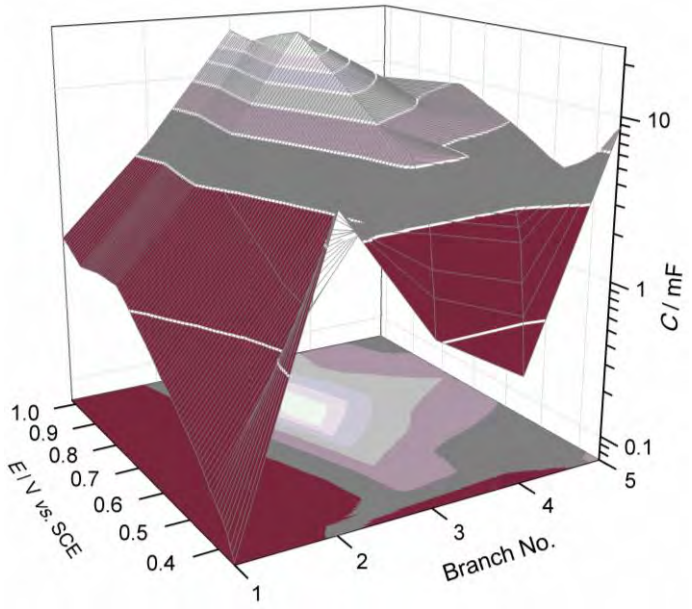

Fig. 9. In-depth capacitance profile at different potentials of IrO_2-based coatings on titanium.[41]

3.2.3. Carbon blacks

The structures of applied EECs used to fit the data of the low and high surface area carbons (LSC and HSC, respectively),[6] as well as the capacitance and resistance values are shown in Fig. 10.

Starting from the external surface, directly exposed to the electrolyte (1st branch, 0.32 F g^{-1}) towards interior of the HSC layer, an increase in the capacitance by two orders of magnitude was registered, which is associated with negligible increase in the pore resistance (down to the 3rd branch, Fig. 10a). Considering the morphology of the HSC layer (Fig. 11), it could be envisaged that the capacitance increases due to the increasing contribution of the parts of the internal surface available to the electrolyte through about 30-μm wide macropores, as the frequency decreases. In a certain frequency range, which corresponds to the time constants of the 3rd and 4th transmission branches (Fig. 10a), the capacitance values are similar, but pore resistance starts to increase noticeably. Since capacitors are connected in parallel, the layer capacitance in this

frequency range can be calculated as the sum of capacitances in all the preceding circuit branches using Eq. (6). This summation down to fourth branch gives a value of 48 F g^{-1}, which agrees with the value for outer capacitance obtained by cyclic voltammetry. It appears that electrolyte easily reaches those parts of the internal surface that are available through macro-pores, *i.e.*, spaces between the large agglomerates observed in Fig. 11. Near five-fold increase in capacitance as well as pore-resistance is registered at sufficiently low frequencies, which correspond to the time constant of the 5th transmission branch. This branch can be associated to the parts of internal surface comprising micro-pores, *i.e.*, the microporous structure of the agglomerates (Fig. 11). Total capacitance of the layer equals 175 F g^{-1}, which is a value nearly two times than that obtained by cyclic voltammetry. Hearing in mind that total CV capacitance is obtained under hypothetical condition at zero CV charging/discharging rate, which is close to the value according to BET surface area of HSC, it follows from CV and EIS analysis that almost half of the HFC thin layer is virtually inaccessible to the electrolyte.

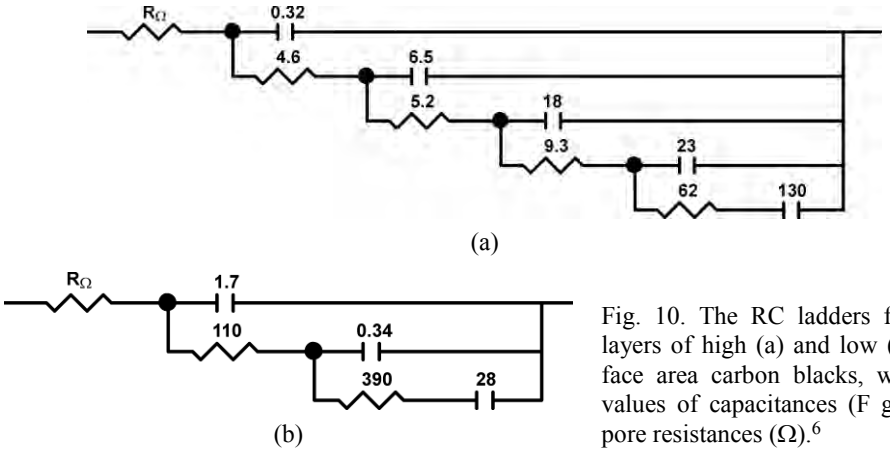

Fig. 10. The RC ladders for thin layers of high (a) and low (b) surface area carbon blacks, with the values of capacitances (F g^{-1}) and pore resistances (Ω).[6]

Contrary to the HSC capacitive in-depth profile, the LSC capacitance was found to decrease at moderate frequencies (down to $n = 2$, Fig. 10b) going from the external surface towards the bulk of the layer, with a corresponding increase in the pore resistance of two orders of magnitude. A remarkable increase in the capacitance was registered at very low frequencies, associated with the relaxed increase in the pore resistance. It appears that the capacitive response of the LSC internal surface, available through constricted and branched pores of a loose LSC layer,[6] is expressed in this low-frequency domain. The remarkably higher pore resistance, as well as the decrease in capacitance, on going from the external towards the interior of the layer (2nd branch) of the LSC in comparison to the HSC could be explained by visually observed poor wetting of the LSC layer by the electrolyte.[24] A similar capacitance distribution of the external and internal

surface was also obtained by CV analysis.[6] The capacitance of external surface is larger than internal, similarly to the EIS data for the 1st and 2nd branch (Fig. 10b). The total capacitance of the LSC, immediately after electrode immersion, was calculated by Eq. (6) to be 32.6 F g^{-1}, a value that is in agreement with that obtained by CV. However, after successive charging/discharging cycles, total capacitance of the layer increases to 39.9 F g^{-1}. This can be explained by the continuous decrease in hydrophobicity of the XC layer,[24] as a consequence of carbon activation by formation of surface oxygen-containing groups during prolonged charging/discharging.[47] The similarity of CV and EIS data for the obtained LSC capacitance profile indicates that this LSC could be nearly completely utilized during slow charging/discharging processes.

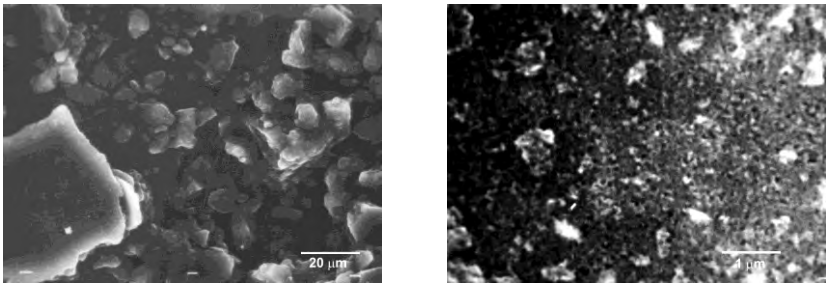

(a) (b)

Fig. 11. Surface appearance of a thin layer of high surface area carbon black. a) Non-uniform microscopic distribution of large agglomerates separated by *ca*. 30 μm-wide pores; b) compact texture of the agglomerates.[6] (Reprinted with permission from Elsevier).

3.2.4. Ruthenium oxide/carbon black composites

As mentioned in Section 3.2.1, the impregnation of carbon blacks with supercapacitive hydrous ruthenium oxide can cause a reduction or extension of the required branches in EEC, depending on the real surface area of the CB. Consequently, this alters the total capacitance, and, in some cases, can even result in its reduction with respect to the CB support.[23,50,51] The alteration of the capacitance profile for thin layer ruthenium oxide/CB composites was also found to be dependent on the particle size and loading of the oxide.[23] Since there is qualitative difference between composite and carbon substrate due to the presence of the oxide phase, a more complex morphology for the composite layer could be expected. From the standpoint of the EIS capacitive characteristics presented in Fig. 7, this is not the case. The specific capacitances and pore resistances, obtained by fitting the BP/R composite impedance data from Fig. 7 to a 3-branch EEC, are presented in Fig. 12.

The outer capacitance of the composites, given as the value of the 1st branch, is by two orders of magnitude larger than the outer capacitance of HSC (0.32 F g^{-1},

Fig. 10a), and decreases with oxide particle size. The much larger outer capacitance of the composite in contrast to the carbon substrate is a consequence of presence of oxide particles impregnated into the outer surface of the carbon grains (Fig. 11), represented by the sum of the pseudo-capacitance and the double layer capacitance at electrolyte/oxide interface. There is also a decrease in the values of inner capacitances (2nd branch) as the particle size increases. However, the value obtained for smallest oxide particle size is comparable to the sum of inner capacitances of the carbon substrate from the 2nd to 4th branch (47 F g^{-1}, Fig. 10a), while the inner capacitance of the composites of larger particle size are lower with respect to HSC. These findings indicate that small oxide particles are distributed over the surface of carbon grains, with the morphology of the composite resembling that of the carbon support and hindering electrolyte access to the bare carbon surface with the porous grains. On the other hand, larger oxide particles tend to form a physical mixture with the carbon grains, causing only a partial sealing of the pores between the carbon grains, and leaving considerable part of the internal surface of carbon grains uncovered.

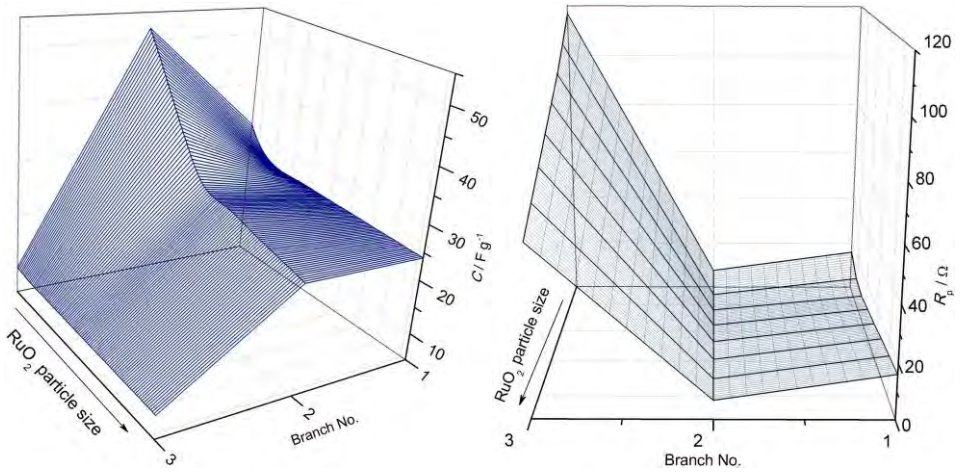

Fig. 12. In-depth capacitance and pore resistance profiles for the composites of RuO_2 supported on high surface area carbon as the functions of the oxide particle size.[23]

Decrease in composite inner capacitances with oxide particle size is accompanied by an increase in the pore resistance (Fig. 12). The resistance in the pores of the composite with smallest oxide particle size corresponds to resistances in the 1st and 2nd branch of the HSC (Fig. 10a), while the resistances in the composite pores with larger oxide particle size are larger than those for the HSC. This is a consequence of volume shrinkage of the micro-pores (interparticle space within the carbon grains), in which the oxide particles accumulated, thus hindering the approach of the electrolyte to the interior of the composite layer.

Inner capacitance of the composite in the third branch (Fig. 12) is much lower than the inner capacitance of the second branch and does not depend considerably on the aging time. This capacitance value is by an order of magnitude lower than corresponding value for the HSC (about 10 and 130 F g^{-1}, respectively). However, the associated pore resistance is similar to the corresponding value for the HSC, which implies that the inner capacitance in the third circuit branch is associated with morphologically similar parts of the porous composite layer and the carbon substrate – to those corresponding to the internal surface of the carbon grains. For these parts of the surface, impregnation failed, since oxide particles on the top closed the pore orifices at the surface of carbon grains (Fig. 13). These oxide particles at the surface of the carbon grains block electrolyte access to the porous interior of the carbon grains, thus leaving it even dry and making it inactive. This should cause the values of inner capacitance of the composites from the third branch to be much smaller than that of the carbon substrate.

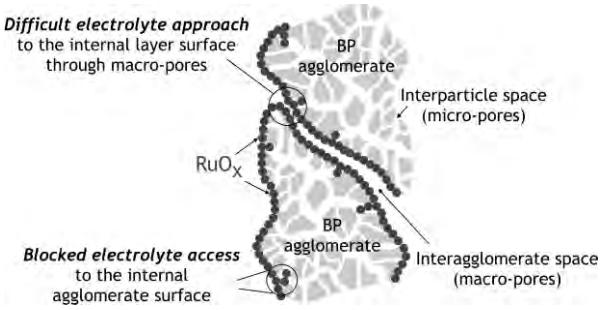

Fig. 13. A sketch of the proposed packing of hydrous ruthenium oxide particles onto the surface of a high surface area carbon substrate.[23] (Reprinted with permission form Elsevier).

With a four-fold increase in the loading of the smallest particles, all capacitances down the RC ladder were found to increase, with the total capacitance of the composite being more than doubled with respect to the HSC.[23]

It follows from above considerations that the combination of a HSC and small oxide particles could hardly lead to superior capacitive performance of RuO_2/HSC composite. Since oxide particles block the pore orifices of the carbon grains, the interior, *i.e.*, most of the extended carbon surface area, is inaccessible, and the HSC support (in a grained form) acts only as a pattern for the distribution and carrier of the active oxide.

RuO_2/LSC Composite. The in-depth capacitance and pore resistance profiles for composites of increasing size of oxide particles supported on the low surface area carbon at an optimal loading[23] are presented in Fig. 14.

The outer composite capacitance (1st branch) increased with particle size, which is opposite to the case of the RuO_2/HSC composites (Fig. 12). Although the outer capacitance of the HSC-based composites was considerably larger than that of the HSC, the outer capacitance of the LSC-based composite with the smallest oxide particles (about 4 F g^{-1}, Fig. 14) was only doubled that of the LSC

(1.7 F g^{-1}, Fig. 10b). However, the outer capacitance of the composite of the largest particle size (about 20 F g^{-1}) was an order of magnitude larger than that of the LSC. These findings clearly indicate that the impregnation of the outer surface of the carbon was weak in the case of the smallest particle size, while it became pronounced only with the XC/R 46 composite. The surface appearance of the small-particle RuO_2/LSC composite was found to be quite similar to the loose structure of an LSC layer,[23,51] while a more compact structure of the grains pasted together was seen from the appearance of the surface of the large-particle RuO_2/LSC composite.[23,51] The inner capacitances of the smallest-particle RuO_2/ /LSC composite (2nd and 3rd branch, Fig. 14) was much larger than the outer, while in the cases of the larger-particle RuO_2/LSC composite, these two capacitances had similar values. The associated pore resistances increased, whereas the values obtained for the RuO_2/LSC composite layers were considerably lower than the corresponding values obtained for the LSC (110 Ω, Fig. 10b), but quite similar to the values obtained for the RuO_2/HSC composites, which was also the case of the values of the inner capacitances (Fig. 12). This suggests that these circuit parameters are to be assigned rather to the oxide than to the carbon substrate. The inner capacitance of small-particle RuO_2/LSC composite is much larger than corresponding capacitances of composites of the larger oxide particles. Therefore, the largest capacitance at rather slow charging/discharging rates is to be expected for the composite of the small oxide particles. Inner capacitance of the small-particle RuO_2/LSC composite in the 4th branch is significantly smaller than the values of the 2nd and 3rd branch. Taking into account the corresponding resistance in the pores of about 170 Ω (Fig. 14), this part of the inner capacitance should be considered to correspond to the capacitive response of hardly accessible parts of the inner oxide surface, located in the intergranular spaces of the carbon substrate.

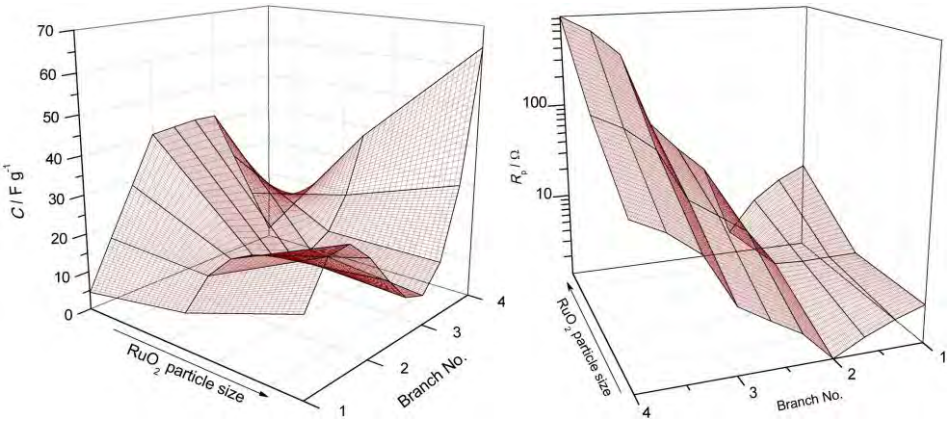

Fig. 14. In-depth capacitance and pore resistance profiles for the composites of RuO_2 supported on the low surface area carbon as the functions of oxide particle size.[23]

4. CONCLUSIONS

An analysis of the capacitive responses to dynamic perturbations of typical supercapacitive materials, *i.e.*, noble metal oxides (RuO_2 and IrO_2), carbonaceous materials and RuO_2-impregnated carbon blacks using the methodology of electrochemical impedance spectroscopy (EIS) and transmission line equivalence led to their comprehension. EIS responses of all the investigated materials in the form of porous thin layer were found to obey RC ladder-type equivalent electrical circuits, requiring different numbers of branches of R and C in series, which depended on the type and composition of the material, as well as on the electrolyte composition. This finding allows the profiling of the capacitance performances through the porous supercapacitive materials.

Owing to pseudocapacitive behavior and characteristic coating texture, the EIS response of RuO_2-based coatings on Ti required more branches, *i.e.*, was caused by a more pronounced coating in-depth capacitance distribution, as the coating thickness increased and the proton concentration in the solution decreased. The former influenced the distribution of the pore resistance of the coatings, whereas the later affects the pseudocapacitive response of the oxide. Similar findings also held for IrO_2-based coatings on Ti. The EIS measurements showed that the transition from the poorly active to the pseudocapacitive active state of IrO_2 was limited by proton diffusion, which negligibly depended on the proton concentration in the electrolyte. This transition, as well as its distribution through the porous coating, appeared cardinal for the full development of the capacitive performance of the coating. The transition occurred much easier in a solution of lower hydrogen ion content. This unexpected behavior is the consequence of much closer potential positions of the transitions reactions.

The number of required branches in RC ladder increased with real surface area of carbon blacks as typical representatives of double layer supercapacitors. The capacitance of a layer of high-surface-area carbon (HSC) increased on going from the external surface towards the bulk of the layer. This increase was associated with a negligible increase in pore resistance of the layer. A considerably larger part of the total capacitance of the HSC originated from its internal surface, a considerable amount of which was inaccessible to the electrolyte. The external capacitance reflected the capacitive characteristics of a macro-scale surface consisting of relatively large agglomerates, while the internal capacitance originated from the micro-porous inner surface. Contrary to HSC, the low-surface-area carbon black (LSC) had a loose structure that produced the opposite distribution of the total capacitance between the external and internal surfaces. In this case, the internal surface was fully available for slow charging/discharging processes.

The impregnation of the HSC by sol–gel processed supercapacitive RuO_2 decreased the number of required branches with respect to carbon support, while

impregnation of the LSC increased the required number. The capacitance of the HSC-supported composites decreased with increasing oxide particle size, while the capacitance of the LSC-supported composites increased. Increasing the oxide loading led to an increase in capacitance of the HSC-supported composites. However, the inner surface of the HSC as substrate became even less accessible to the electrolyte and rather inactive, because of pore blocking by the oxide particles at the top of the carbon grains. The best energy storage performances at low charging/discharging rates are to be expected for composites prepared from small oxide particles and LSC, while composites with HSC would suffer from the loss of the energy storage ability of the carbon double layer capacitor part.

*Acknowledgment*s. VVP and ABD appreciate the valuable contribution of their teacher, Professor Branislav Nikolić, to their knowledge of the electrochemistry of noble metal oxides, on the occasion of his 70th birthday. The Ministry of Education, Science and Technological Development of the Republic of Serbia financially supported this study, Project No. 172060.

ИЗВОД

РАСВЕТЉАВАЊЕ СУПЕРКОНДЕНЗАТОРСКИХ ОДЛИКА ОКСИДА ПЛЕМЕНИТИХ МЕТАЛА, ПОРОЗНИХ УГЉЕНИЧНИХ МАТЕРИЈАЛА И ЊИХОВИХ КОМПОЗИТА

ВЛАДИМИР В. ПАНИЋ[1], АЛЕКСАНДАР Б. ДЕКАНСКИ[1] и БРАНИСЛАВ Ж. НИКОЛИЋ[2]

[1]*ИХТМ – Центар за електрохемију, Универзитет у Београду, Његошева 12, 11000 Београд и*
[2]*Технолошко–металуршки факултет, Универзитет у Београду, Карнегијева 4, 11000 Београд*

Истраживања порозних електрохемијских суперкондензаторских материјала, као важне врсте уређаја за складиштење енергије нове генерације, захтевају детаљну анализу и познавање њихових кондензаторских одлика при различитим режимима пуњење/пражњење. Приказани су резултати ових истраживања, у форми одговора на динамичку побуду, типичних представника ових материјала: оксида племенитих матала, угљеничних материјала и угљеничних прахова импрегнираних оксидом рутенијума, који су добијени спектроскопијом електрохемијске импеданције (СЕИ). Овом приказу предходи сажет опис суперкондензаторског понашања и порекла псеудокондензаторког одговора оксида племенитих метала. Електрични еквивалент при пуњењу/пражњењу свих испитиваних материјала одговара моделу трансмисионе линије представљене тзв. „отпорник/кондезатор (RC) лествицом“. Одлике лествице су корелисане са физичко–хемијским својствима материјала, њиховим саставом, као и са саставом електролита. Усклађивање СЕИ података различитих суперкондензаторских материјала са одговарајућом RC лествицом омогућава анализу расподеле капацитивности и отпорности у порама кроз танки порозни слој материјала и коначно расветљавање одлика суперкондензаторског типа складиштења енергије.

(Примљено 31. октобра 2013)

REFERENCES

1. B. Conway, *Electrochemical Supercapacitors – Scientific Fundamentals and Technological Applications*, Plenum Publishers, New York, 1999
2. E. Frackowiak, F. Béguin, *Carbon* **39** (2001) 937
3. C.-C. Hu, C.-C. Wang, *J. Power Sources* **125** (2004) 299
4. A. B. Fuertes, F. Pico, J. M. Rojo, *J. Power Sources* **133** (2004) 329

5. A. Braun, J. Kohlbrecher, M. Bärtsch, B. Schnyder, R. Kötz, O. Haas, A. Wokaun, *Electrochim. Acta* **49** (2004) 1105
6. V. V. Panić, R. M. Stevanović, V. M. Jovanović, A. B. Dekanski, *J. Power Sources* **181** (2008) 186
7. V. V. N. Obreja, *Physica, E* **40** (2008) 2596
8. C. Du, N. Pan, *J. Power Sources* **160** (2006) 1487
9. C. Peng, S. Zhang, D. Jewell, G. Z. Chen, *Prog. Nat. Sci*. **18** (2008) 777
10. Y. Zhu, S. Murali, M. D. Stoller, K. J. Ganesh, W. Cai, P. J. Ferreira, A. Pirkle, R. M. Wallace, K. A. Cychosz, M. Thommes, D. Su, E. A. Stach, R. S. Ruoff, *Science* **332** (2011) 1537
11. Y. Wang, Z. Shi, Y. Huang, Y. Ma, C. Wang, M. Chen, Y. Chen, *J. Phys. Chem., C* **113** (2009) 13103
12. S. Bose, T. Kuila, A. K. Mishra, R. Rajasekar, N. H. Kim, J. H. Lee, *J. Mater. Chem*. **22** (2012) 767
13. S. I. Stevanović, V. V. Panić, A. B. Dekanski, A. V. Tripković, V. M. Jovanović, *Phys. Chem. Chem. Phys*. **14** (2012) 9475
14. G. Wang, L. Zhang, J. Zhang, *Chem. Soc. Rev*. **41** (2012) 797
15. Yu. M. Vol'fkovich, T. M. Serdyuk, *Russ. J. Electrochem*. **38** (2002) 935
16. J. P. Zheng, P. J. Cygan, T. R. Jow, *J. Electrochem. Soc.* **142** (1995) 2699
17. J. P. Zheng, Y. Xin, *J. Power Sources* **110** (2002) 86
18. D. McKeown, P. Hagans, L. Carette, A. Russell, K. Swider, D. Rolison, *J. Phys. Chem., B* **103** (1999) 4825
19. W. Sugimoto, T. Kizaki, K. Yokoshima, Y. Murakami, Y. Takasu, *Electrochim. Acta* **49** (2004) 313
20. M. Ramani, B. Haran, R. White, B. Popov, *J. Electrochem. Soc*. **148** (2001) A374
21. V. Panić, T. Vidaković, S. Gojković, A. Dekanski, S. Milonjić, B. Nikolić, *Electrochim. Acta* **48** (2003) 3789
22. W.-C. Chen, C.-C. Hu, C.-C. Wang, C.-K. Min, *J. Power Sources* **125** (2004) 292
23. V. V. Panić, A. B. Dekanski, R. M. Stevanović, *J. Power Sources* **195** (2010) 3969
24. V. V. Panić, A. B. Dekanski, V. B. Mišković-Stanković, B. Ž. Nikolić, *Chem. Biochem. Eng. Q.* **23** (2009) 23
25. F. Cao, J. Prakash, *J. Power Sources* **92** (2001) 40
26. X. M. Liu, X. G. Zhang, *Electrochim. Acta* **49** (2004) 229
27. V. V. Panić, A. B. Dekanski, M. Mitrić, S. K. Milonjić, V. B. Mišković-Stanković, B. Ž. Nikolić, *Phys. Chem. Chem. Phys*. **12** (2010) 7521
28. V. V. Panić, A. B. Dekanski, V. B. Mišković-Stanković, S. K. Milonjić, B. Ž. Nikolić, *J. Serb. Chem. Soc*. **75** (2010) 1413
29. T. Arikado, C. Iwakura, H. Tamura, *Electrochim. Acta* **22** (1977) 513
30. S. Ardizzone, S. Trasatti, *Adv. Colloid Interface Sci*. **64** (1996) 173
31. L. D. Burke, M. E. Lyons, E. J. M. O'Sullivan, D. P. Whelan, *J. Electroanal. Chem*. **122** (1981) 403
32. T. Liu, W. G. Pell, B. E. Conway, *Electrochim. Acta* **42** (1997) 3541
33. W. Sugimoto, T. Kizaki, K. Yokoshima, Y. Murakami, Y. Takasu, *Electrochim. Acta* **49** (2004) 313
34. M. Vuković, D. Čukman, *J. Electroanal. Chem*. **474** (1999) 167
35. L. M. Doubova, S. Daolio, A. De Battisti, *J. Electroanal. Chem*. **532** (2002) 25
36. D. Mitchell, D. A. J. Rand, R. Woods, *J. Electroanal. Chem*. **89** (1978) 11

37. R. de Levie, *Electrochim. Acta* **8** (1963) 751
38. V. V. Panić, T. R. Vidaković, A. B. Dekanski, V. B. Mišković-Stanković, B. Ž. Nikolić, *J. Electroanal. Chem*. **609** (2007) 120
39. Derek Johnson, *ZView® Software, Help file*, Schribner Associates Inc., Southern Pines, NC, © 1990–2002
40. V. Panić, A. Dekanski, S. Milonjić, V. B. Mišković-Stanković, B. Nikolić, *J. Serb. Chem. Soc.* **71** (2006) 1173
41. B. Ž. Nikolić, V. V. Panić, A. B. Dekanski, *Electrocatal*ysis **3** (2012) 360
42. V. Panić, A. Dekanski, S. Milonjić, R. Atanasoski, B. Nikolić, *Electrochim. Acta* **46** (2000) 415
43. M. D. Obradović, G. D. Vuković, S. I. Stevanović, V. V. Panić, P. S. Uskoković, A. Kowal, S. Lj. Gojković, *J. Electroanal. Chem*. **634** (2009) 22
44. T. L. McCreery, *Chem. Rev*. **108** (2008) 2646
45. A. Dekanski, J. Stevanović, R. Stevanović, B. Ž. Nikolić, V. M. Jovanović, *Carbon* **39** (2001) 1195
46. Y. Sato, K. Yomogida, T. Nanaumi, K. Kobayakawa, Y. Ohsawa, M. Kawai, *Electrochem. Solid State Lett*. **3** (2000) 113
47. A. Braun, J. Kohlbrecher, M. Bärtsch, B. Schnyder, R. Kötz, O. Haas, A. Wokaun, *Electrochim. Acta* **49** (2004) 1105
48. H. Kim, B. N. Popov, *J. Power Sources* **104** (2002) 52
49. L. M. Da Silva, L. A. De Faria, J. F. C. Boodts, *Electrochim. Acta* **47** (2001) 395
50. V. Panić, A. Dekanski, S. Gojković, V. Mišković-Stanković, B. Nikolić, *Mater. Sci. Forum* **453–454** (2004) 133
51. V. Panić, A. Dekanski, S. Gojković, S. Milonjić, V. B. Mišković-Stanković, B. Nikolić, *Mater. Sci. Forum* **494** (2005) 235.

Journal of the Serbian Chemical Society
JSCS-info@shd.org.rs • www.shd.org.rs/JSCS
J. Serb. Chem. Soc. 78 (12) 2165–2177 (2013)
JSCS–4557
UDC 544.6.001.6+62.001.5:001.38
Essay

ESSAY

The third century of electrochemistry: Lowering the horizon or raising it further?•

SVETOMIR HADŽI JORDANOV*

Faculty of Technology and Metallurgy, UKIM, Skopje

(Received 4 November 2013)

Abstract: A survey is given of the development of electrochemistry with the author's unmasked wish for more advanced development in the future. The survey is based on past achievements of electrochemistry, which is listed concisely herein. As far as the recent state is concerned, author's dissatisfaction is expressed with the acceptance of electrochemistry as both a favorite profession of graduate students and a top priority field in the financing of research. For the sake of honesty, an alternative view is mentioned that takes the recent state of electrochemistry as normal and in accordance with the usual course of development, (*i.e.*, birth, rise, achieving of maximum and then decay, fading, *etc*.) that is common in nature. This statement is based on the belief that today electrochemistry exists on a broader basis than before, and is mainly incurporated into other (new) branches of chemistry and science. Examples are given where recent electrochemistry failed to fulfill its promises (*e.g.*, the production of cheap hydrogen by means of electrocatalysts with high performance for H_2 evolution, economical use of large-scale fuel cells, *etc*.). In summarizing the recent fields of interest that cover electrochemistry, their diversification, specialization, complexness and interdisciplinary nature must be stressed. A list of desirable highlights that could possibly help electrochemistry to improve its rating among other branches of science is composed. In addition, a list of the author's personal preferences is given.

Keywords: electrochemistry; lost priority; recovery; desirable highlights; history; current trends; future prospects.

INTRODUCTION

If we agree that (modern) electrochemistry was born with the invention of the first ever d.c. power source (the so-called *Voltaic pile*, 1800), then nowadays

* Corresponding author. E-mail: shj@tmf.ukim.edu.mk
• Dedicated to Prof. B. Nikolić, on the occasion of his 70th birthday.
doi: 10.2298/JSC131104126H

this science is running the second decade of its 3rd Century**. One must admit that such a long history is not a common phenomenon in the world of science*. Therefore, if we wish electrochemistry to continue its successful story, we should follow its state, continuously evaluate its achievements and push it further up.

Recently, on the occasion of the 3rd Regional South East European Symposium on Electrochemistry, that took place in Bucharest, Romania, I presented the lecture entitled: *Electrochemistry – the Central Science of Tomorrow: Reality or Fantasy?*[1] My intention was to promote my wishes for electrochemistry to regain its leading position in the world of science, as it used to have for a long period in the past. I expressed my dissatisfaction with the recent low ranking of electrochemistry. In order to attract wider attention, herein some more aspects are presented that may aid electrochemistry to take in the future the place it deserves.

A brief history

Let me start with quoting some basic and well-known facts. Electrochemistry is a science that is concerned with two phenomena: changes of the chemical nature of matter caused by the passing of an electrical current and *visa versa*, the generation of an electrical current due to certain chemical reactions. Electrochemistry is part of Physical Chemistry, together with many other branches, such as, *e.g.*, Structural Chemistry, Photochemistry, Chemical Thermodynamics and Kinetics, *etc*. Physical chemistry on its own is part of chemistry, together with parts such as, *e.g.*, General Chemistry, Inorganic Chemistry, Organic chemistry, *etc*.

It is normally to ask oneself: When there are so many branches of chemistry, "why is electrochemistry so important and why does it attract so much attention?"

The answers are simple: modern electrochemistry was founded and commenced its career long before other sciences or their branches existed. Furthermore, electrochemistry is important for a number of merits, such as, *e.g.*, demystification of some basic concepts of chemistry, structure of matter, *etc*. It should be remembered that electrochemistry commenced dealing with the electron one century before it was discovered at the dawn of the 20th Century.[2] Moreover, by means of electrochemistry, some ten chemical elements were in no time isolated or discovered, while the number of useful products was much higher. All this occurred in the early stages of the transition of chemistry from empirical into a modern science. In this way, electrochemistry supported the progress of other

** "Modern" electrochemistry is the one that started with Alessandro Volta and other scientists in 18th and 19th century. This statement is just a precaution in case there is another – "ancient" electrochemistry, judging according the controversy generated with the discovery of so called "Baghdad Candle" – see further in this paper).

* Just a reminder: at the beginning of 19th century, it was hardly known that combustion is a chemical process of combining with oxygen, other sciences were in the early stage of development, and the technology had just started to exploit the fruits of the steam engine and the Industrial Revolution.

sciences. Together, they provided many benefits for people's life and made it healthier, richer, *etc*.[3]

It is well known and widely accepted that electrochemistry started its career with the achievements of two Italian researchers at the end of the 18th century.[4]* Luigi Galvani "discovered" electricity indirectly. Bringing into contact two different metals, electricity was generated that made dead body parts (frog's leg) contract. Yet, Alessandro Volta is credited as the founder of electrochemistry for his 18th century invention of the first d.c. power source (a column of alternatively packed silver and zinc plates) that was able to split water into hydrogen and oxygen.

Despite of this fact, there is another claim (speculation?) that the art of generating d.c. power was known 2 millenniums before Volta's discovery. Artifacts found near Baghdad resemble very much the components of a dry cell, *i.e*., the clay pot could be the body, and the copper mantle and iron rod, the electrodes (see Fig. 1). The exactness of this discovery, the so-called Baghdad candle, is not yet verified.[6]

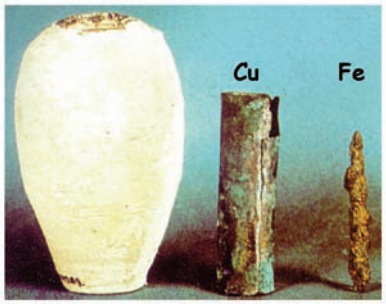

Fig. 1. The Baghdad candle, 2200 BC: artifact parts that could be combined into a battery.

A glance over the highlights of electrochemistry in the 19th century, Table I, and the technical application resulting from them confirm the great value of this science. Important theoretical breakthroughs and advances in industrial electrochemistry were achieved and they continue to be valuable today.

The actual list of the scientist and their achievements is far richer. There are more sources (reference literature) giving a detailed survey of the electrochemical activities in the 1800s.[8–10] The end of century was especially fruitful, with the work of S. Arrhenius on the dissociation of electrolytes and the resulting activity of ions as a function of their concentration. F. W. Ostwald continued the research in the field of electrical conductivity and catalysis. W. H. Nernst defined the dependence of electrode potential on the nature of the electrode reaction, as well as on the concentration/activity and other parameters of the ions participating in the electrode equilibrium, known as the Nernst Equation. E. Weston is

*In previous centuries, experiments connected with electricity were a subject of interest of scientists as well. Some of them were William Gilbert, Otto von Guericke, Benjamin Franklin and Charles Coulomb.[5]

remembered for his cell with constant voltage of 1018 mV, which is used as a standard for measuring voltage. F. Haber, famous for the invention of the nitrogen-fixation process, is also credited with the invention of the glass electrode and some other work on measuring the acidity of solutions. J. Tafel, a pioneer in organic electrochemistry, with his Tafel Equation, explained how the rates of electrode reactions depend on the overpotential. The list does not end with these names only.

TABLE I. Some of the most important discoveries of electrochemistry in the 19th century[7]

Discovery	Author/Year	Significance
Voltaic pile	A. Volta, 1800	First d.c. source
Water splitting by electrolysis	W. Nicholson and A. Carlisle, 1800	H_2 production
Extraction of base metals	H. Davy, 1807	Na, K, Ca, *etc*. isolated
Laws of electrolysis	M. Faraday, 1830	Quantitative aspects of electrolysis
Two-fluid battery	J. F. Daniell, 1836	Long-lasting constant d.c. source
Electroplating	J. Ecklington, 1836	Electroplating of Ag
Fuel cell envisaged	W. R. Grove. 1839	Sophisticated d.c. source
Electrolysis of molten salts	R. W. Bunsen, 1852	Mg, Li isolated
Lead-acid battery	G. Planté, 1859	First portable d.c. source
Primary cell	G. Leclanchè, 1868	Forerunner of the dry cell
Refining of metals	J. Ecklington, 1869	Cu refining by electrolysis
Electrowinning	Balbach & Thum, 1871	Cu extraction by electrolysis
Al molten salts electrolysis	P. L. Heroult and C. M. Hall, 1885	Al extraction from molten salts by electrolysis

Further strengthening, progress and diversification

During the 20th century, electrochemistry continued to advance, to foster the theoretical basis and, consequently, to achieve more and more useful and valuable practical results.

It started with the considerations of ionic transport in solutions, defining the pH as a measure for hydrogen ion concentration, respectively, activity. Experiments in bioelectrochemistry were improved, membranes were introduced in the experiments, the charge of an electron was determined using an oil drop, *etc*.

Application of electrochemistry for analytical purposes started with the invention of polarography, *i.e*., recording and interpreting current-potential curves. The success was recognized some 30 years later by awarding the Nobel Prize to the inventor J. Heyrovsky.[11] The properties of electrolyte solutions were interpreted in terms of their structure, *etc*.

The Russian Electrochemistry School, which was concerned with the fundamentals of electrode reactions, electrochemical interfaces, electron transfer, adsorption, *etc*., matured.

Corrosion became the subject of interest of electrochemists and its nature was explained in terms of coupled electrochemical oxidation, respectively reduction processes. This knowledge was further elaborated and applied to the understanding of corrosion and the design of corrosion protection. Passivity, local cell action, cathodic protection, Pourbaix diagrams, *etc*. followed. Then photochemistry was expanded to fields such as, *e.g*., semiconductors, solid-state ionics, and diffusion aspects of scales growth.

The energetic of electrochemical systems achieved its best in the first practical fuel cell, which was based on an alkaline electrolyte and porous gas-diffusion electrodes. It was employed in early space missions (Apollo) for providing in-flight power, heating and drinking water, Fig. 2.[12] Later on, due to the ultimate progress in innovating cationic selective membranes sustainable under the most severe conditions, such as, *e.g*., in chlorine cells, membrane cells were engineered that operated at almost reversible electrode potentials.[13]

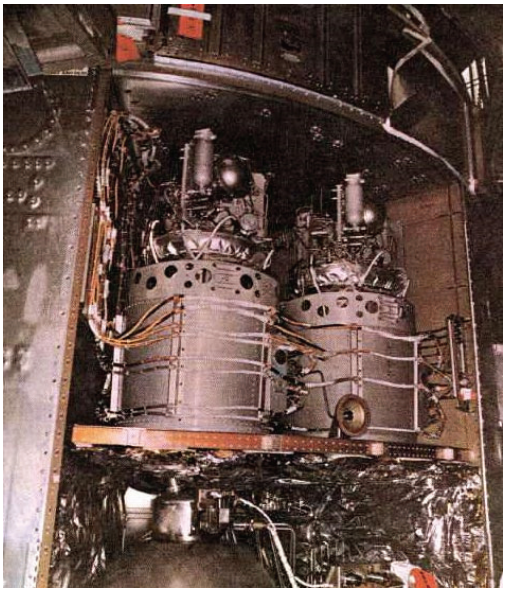

Fig. 2. The Apollo spacecraft fuel cells, 1970s.[12]

The kinetics of electrochemical reactions dominated between the branches of theoretical electrochemistry. The achievements were the Butler–Volmer Equation, the understanding of the existence of exchange current, the order of electrochemical reactions, *etc*. Not only electrocatalysis, batteries and fuel cells, *etc*., but also the broadening of electrochemistry in new fields and the intertwining with existing ones are recent subjects of interest. Advances in materials science and perfection of characterization techniques, miniaturization down to the nano-

scopic and even atomic level, led to the benefits of obtaining knowledge of discrete surfaces.

This short summary is given here in order to stress that over a long period electrochemistry was a nest where the best bachelors were accepted after their graduation as recognition of their success. They were introduced to the secrets of scientific research, further educated and trained to become leaders not only in electrochemistry, but also in many other fields of chemistry. In other words, electrochemistry was a kind of kindergarten from where new generations of top scientists and experts were disseminated throughout traditional and new branches of chemistry.

The present status of electrochemistry

In contrast to the glorious golden ages of electrochemistry, the present state is just fading. Electrochemistry is not anymore the mainstream science or technology. The interest for electrochemistry, in education, research and industry is low. Chemistry and science in general share similar crisis.

According to the reductions in funding research and new equipment purchase, electrochemistry is not a priority for strategic research, no mater that there is disproportion between regions and countries.

The place that used to belong to electrochemistry and its different branches nowadays is occupied by some other sciences or techniques. For example, the NASA's Mars Rover (vehicle) Curiosity is powered by a nuclear generator – not with a fuel cell. Similar substitutions occurred in some other domains that were believed to belong to electrochemistry, such as, *e.g.*, industrial hydrogen generation by thermal decomposition processes instead of electrolysis, *etc*.

The case of hydrogen generation is very illustrative. For more than 50 years, electrochemistry was promising that it is on the best way to produce cheap hydrogen by means of electrolysis and electrocatalysts with high performance for H_2 evolution, thus enabling economic use of large scale fuel cells that would supply cheap electricity for vehicles, heating/cooling and other power needs. Despite of the tremendous advances in the field of electrocatalysis, the situation so far is not that that was promised: the market share of hydrogen produced by electrolysis is rather low (5 %), so that fuel cells are still expensive and rare in application. Electricity produced by fuel cells is expensive too, and the number of electric cars on the streets is symbolic. Recent market figures show only some 5.000 electric cars are sold per annum in Europe (0.07 % of the total sale), because they are many times more expensive than classical cars.

Other exaggerations have frequently been made in presenting the performance of newly prepared electrocatalysts or fuel cells. Statements such as "our non-platinum catalysts are similar (or, in some cases, better) than those based on platinum" are frequently used in scientific papers or lectures. Or "We did prepare

a fuel cell that is very effective in the combustion of biofuel (ethanol or so); our calculations show that with the crop harvested from a relatively small part of the state's agriculture land, enough electricity could be produced to satisfy all the needs of the state (!)".

Normally, such unrealized promises do not improve the image of electrochemistry.

As a conclusion of the recent status of electrochemistry, the following should be stressed:

– subjects of interest of electrochemistry are numerous and diversified*;

– fields where electrochemistry is applied are highly specialized, complex and often interdisciplinary and

– electrochemistry is no longer a top priority in many aspects**.

Actual fields of interest and electrochemistry

The quoted false expectation together with some other disappointments caused contemporary electrochemistry to sink towards the bottom of the science priority ranking. According to a list presented in the EuCheMS' Program document, electrochemistry is ranked 6th out of 8 areas of chemistry that are expected to achieve significant breakthroughs, *i.e.*:[15]

Synthesis,
Analytical Science,
Catalysis,
Chemical Biology,
Computational Chemistry,
Electrochemistry,
Materials Chemistry and
Supramolecular chemistry and nanoscience.
Within electrochemistry, priority is given to the following items:
Energy,
Batteries,

* Here is an example of how rich in different subjects modern electrochemistry is. At the RSE-SEE 3 Symposium in Bucharest, May 14th, 2012, the following fields were included:[14] Biosensors & Biofuel cells (Wolfgang Schumann); Organometallic catalysis (Jutand Anny); Proteins for biomedicine (E. Palaček); Scaning ECh microscopy (Carlos M. Sanchez-Sanchez); CNTs for salicylic acid detection (Adriana-Ileana Remes *et al.*); Monitoring of parameters for the study of nephrolithiasis (Szilveszter Gáspár *et al.*) and an enzymatic O_2 removal system for bioelectrochemical application (Nicolas Plumeré *et al.*).

** The author's concern about the future of electrochemistry is only his personal opinion, not necessarily generally accepted. It is quite possible that electrochemists working in more advanced academic surroundings are more optimistic regarding this subject.
A recent event, "the Dissolution of a Division of Electrochemistry" realized on the EuCheMS General Assembly in October 2013,[16] further justified the author's concern, no matter what reasons caused the quoted decision.

Hydrogen,
Solar cells,
Sensors,
Analytical application and
Synthesis of compounds.

Reasons for giving priority to these issues are understandable. Energy supply has been the permanent concern of human societies long back in history, and will remain so in the future due to: *i*) further increase of the world's population and *ii*) continuous increase in per capita energy consumption, especially in the developing parts of the globe. Nowadays, people are occupied with the idea of harvesting energy from renewable sources. New concepts are developing, such as, *e.g.*, artificial photosynthesis. Batteries, the mobile sources of electricity, are part of human life. Now, the search for batteries for the next generation of electric cars is on. Clean and cheap generation of hydrogen and efficient photovoltaic cells are regular items on the energy-oriented agenda. The challenge of developing fuel cells avoiding the use of rare metal catalysts is permanent. The expectations from electrochemical sensors are wide, and they cover biological systems and healthcare, not only for analysis, but for therapy as well.

The awareness that recent catalysts are based mainly on the use of platinum and similar rare metals and that electrochemistry is not the only consumer of these metals (that approach the end of their availability) dictates the necessity for future catalysts to be based on other, more abundant metals. Even metal-free alternatives are envisaged.

Desirable highlights

It is worth the effort of forecasting highlights that could return the former glory to electrochemistry and eventually return it to mainstream science. The idea of forecasting is attractive, but risky. In such a situation, the sentence of Niels Bohr "*Prediction is very difficult, especially about the future*"[17] seems very appropriate.

So let us compose a list of such achievements.

– Fulfillment of already promised benefits, such as hydrogen generation at a competitive price or fuel cells that will run using such hydrogen and generate a vast amount of cheap electricity.[18] They were expected long time ago. They would solve the crucial global problem of energy supply and would be highly prized. In the case of a lucky event, this could happen by tomorrow, or in case of normal progress – when ongoing research gradually achieves the required level. There are some other promises as well that are on the "waiting list".

– Less certain innovations that would address some of the recent global problems, as, *e.g.*, cold fusion, low-energy nuclear reactions at room temperature, that involves electrolysis of heavy water on the surface of a palladium elec-

trode.[19] In the 1990s, this topic[20] attracted worldwide attention and raised expectations that something colossal was "knocking on the door". Unfortunately, it had to be disclaimed due to errors in the interpretation of the experimental results. Discoveries of similar importance could put electrochemistry again among the front-runner favorites of science.

– Breakthroughs that are currently unknown could be of similar importance as the first two categories in this list. There is no warranty when and whether they will occur, but according to previous experience, continuous progress is achieved as result of advances in fundamental knowledge and performed experimental research. There are also jumps in the progress - they are desirable, but not a regular event.

As can be seen, this list is only of general nature and does not offer any specific achievement. Going into detailed descriptions of future achievements, may, on one hand, become repetition of already known items or, on the other, become a non-serious gambling with such an important subject.

Despite this precaution, I could not resist quoting some of my personal preferences, which are:

– electrochemistry must find a way of *attracting more top quality* young scientists. Without the best scientists, one cannot expect to be part of mainstream science.

This is the first step in the winning spiral:

"Knowledge + infrastructure + funding"'

More ("knowledge + infrastructure + funding")'

High priority ('knowledge + infrastructure + funding');

etc.

(It has to be stressed that the stage of *high priority funding* is of crucial importance in climbing the success hill.)

Simultaneously to officially approved research, which is often a matter of prestige for the related institution, researchers should practice some *curiosity driven research*. This may seem childish, but even if it fails to deliver the expected result, it will somehow refresh and cheer up the researchers (especially the younger ones).

Non-paved approaches, *i.e.*, the use of non-standard ways in selecting the research subject, the method(s) or techniques used in other branches may result in surprising new achievements. Thus, from time to time, it may be amusing, if not useful, to try ones own approach in performing research.

No matter how strange, it has to be born in mind that the occurrence of a *lucky event* is always possible. We should do everything that is required to perform successfully our research, but we should never abandon the idea that, sometimes, unexpected success is possible. Unexpectedly, we could reach the aimed goal in one of the first trials, despite of the established practice that it takes

tens, hundreds or more trials for such a success. There are other lucky events too, such as, *e.g*., when in an attempt to reach a specific goal, some quite different, but nevertheless, valuable one is attained, *etc*. However, in order to recognize the importance and valorize the benefits of such an unexpected gift, one should be prepared. The importance of a *prepared mind* was stressed in many cases. Examples of such events are given elsewhere.[21]

I personally experienced what a lucky event means with a pioneer work on the discovery of supercapacitors. The goal was research of the electrochemical reactions at a Ru metal surface, in an attempt to understand the electrocatalytic phenomena already shown by TiO_2–RuO_2 type DSA.[22,23] Incidentally some voltamograms failed to serve the primary purpose but I somehow resisted to throw them. My professor, with a well-prepared mind, immediately recognized that the registered behavior was of importance, but not for the studied problem. It was tremendously valuable for another field, the field of electrochemical supercapacitors. Thus, by chance, we discovered how to prepare electrode materials with extremely developed surface areas, which later become excellent materials for supercapacitors.[24]

The above examples are far from completing the list of highlights that could push electrochemistry to a higher position among other branches of science, because it is not easy to specify what merits are required for that*.

Alternative view

One should admit that besides the above attitude, other could exist as well that take the “return to a mainstream position” as an ambitious wish.

The alternative view could be based on following reasoning. It is customary for the leading position to be taken by some new science/branch with new and promising possibilities. Electrochemistry was once in that position for a long period, due to its merits in creating exciting and useful achievements. Today, other branches share the leading position, and electrochemistry could join them only with results that offer solutions for the most important needs of humankind. It is quite uncertain when and if ever this will happen.

Such reasoning could continue in the following way:

Electrochemistry was once the most propulsive science.

So what? Does this give us the right to insist on returning to the old glory?

* An impressive event of the newborn science that makes us be proud electrochemists occurred in 1801, as shown on the oil painting (Fig. 1) of ref. 25: Alessandro Volta demonstrates his discovery at the French National Institute. The guest of honor, Napoleon Bonaparte, highly impressed with the possibilities of electrochemistry, expresses a wish to become part of Volta’s team!

Could we imagine such an event today, *e.g*., some of modern electrochemists demonstrating his discovery to the UN General Assembly or at least to the Nobel Committee?

Isn't it normal for sciences to appear, grow, flourish and at the end to decay and fade? The same way as civilizations and many other items do. So, forget the idea of leading science and similar childish ambitions.

Today electrochemistry exists on a broader basis than before, and is mainly incorporated into other (new) branches of chemistry and science. Even if electrochemistry should discover, (innovate or engineer) real colossal achievements, the recognition will probably be given not only to electrochemistry, but to some other branches, such as, *e.g*., material science, biochemistry, etc., as well.

Today electrochemical techniques are part of the general (universal) list of techniques. Thus, polarography, cyclic voltammetry, potentiometry, *etc*. are applied in a number of sciences, and their origin in electrochemistry is forgotten. This does not diminish the value of electrochemistry.

CONCLUSIONS

A brief survey is offered on the birth, progress and recent stagnation in importance ranking of electrochemistry. The main purpose of this analysis was to raise concern for the future of electrochemistry, in the expectation that it will improve its performance and return to a higher position, as it used to have for the greater part of the past two centuries. This assignment will not be easy to fulfill and requires the involvement of a number of scientist and engineers, institutions and industries.

Next to the emotive wishes and ambitions, another attitude (cold minded and probably more realistic) is given that expresses a different opinion, *i.e*., that electrochemistry is running the normal course of development. Contemporary electrochemistry is incorporated into many branches of chemistry and science in general, as well in technologies, *etc*. It is a useful tool, *e.g*., in biochemistry, environmental protection, mechanical engineering, etc.

Despite the differences in the evaluation of the present position of electrochemistry, a wish is expressed that electrochemistry achieve extraordinary highlights, such as, *e.g*., the generation of hydrogen at a competitive price, participation in low energy nuclear reactions (former: cold fusion), photovoltaic conversion of near 100 %, *etc*. In other words, this is repetition of some old and well-known ideals concerned with health, wealth, longevity, *etc*.

ИЗВОД

ТРЕЋИ ВЕК ЕЛЕКТРОХЕМИЈЕ: СУЖАВАЊЕ ВИДИКА ИЛИ ЊИХОВО ДАЉЕ ШИРЕЊЕ?

SVETOMIR HADŽI JORDANOV

Faculty of Technology and Metallurgy, UKIM, Skopje

Дат је преглед развоја електрохемије са нескривеном жељом аутора да ово подручје што више напредује. Преглед садржи кратак опис досадашњих, веома значајних, достигнућа електрохемије. Садашње стање је оцењено као незадовољавајуће, како у погледу недовољне атрактивности електрохемије да привуче квалитетне студенте – младе истра-

живаче врхунског квалитета, тако и у погледу броја пројеката и износа намењених за финансирање електрохемијских пројеката. Истини за вољу, наведено је и другачије мишљење које сматра да је садашње стање електрохемије у складу са нормалним током развоја процеса у природи, т.ј. рађање, раст, достизање максимума, па опадање. Овакав став је највероватније базиран на уверењу да данас електрохемија има ширу основу него раније и да је углавном инкорпорирана у друга (нова) подручја хемије и науке. Наведени су примери где савремена електрохемија није испунила обећања, на пример добијање јефтиног водоника употребом електрокатализатора високе ефикасности за издвајање водоника, развој и производња горивих ћелија до нивоа конкурентности при масовној употреби, итд. Сумирајући подручја која покрива савремена електрохемија, наглашена је њихова разноликост, уска специјализираност, сложеност и интердисциплинарност. Наведен је списак пожељних достигнућа који би помогао да се унапреди положај електрохемије међу осталим наукама. Наведене су и ауторове личне преференце.

(Примљено 4. новембра 2013)

REFERENCES

1. S. Hadzi Jordanov, *Electrochemistry, the central science of tomorrow: reality or fantasy?* Keynote lecture at the 3rd Regional Symposium on Electrochemistry – South East Europe, Bucharest, 2012, Program & Book of Abstracts, p. 14
2. *The discovery of the electron*, AIP Center for history of physics, http://www.aip.org/ /history/electron/ (accessed in Oct, 2013)
3. A. Pavlath and ACS-members, *Technology milestones from the chemist's view*, version of the Gallery "Technological Milestones", Washington DC, 2005
4. http://www.famousscientists.org/alessandro-volta/ (accessed in Oct, 2013)
5. R. P. Olenick, T. M. Apostol, D. L. Goodstein, *Beyond the mechanical universe: from electricity to modern physics*, Cambridge University Press, Cambridge, 1986, p. 160
6. J. A. M. Bleeker, J. Geiss, M. Huber *The century of space science*, Vol. 1, Springer, Berlin, 2001, p. 227
7. *The world of chemistry*, Gallery of the Serbian Academy of Sciences and Arts, Belgrade, 1997, p. 37 (in Serbian)
8. S. Hadzi Jordanov, P. Paunovic, *Electrolysis – theory and technology*, Faculty of Technology and Metallurgy, UKIM, Skopje, 2008, p. 22 (in Macedonian); see also: http://en.wikipedia.org/wiki/ Electrochemistry (accessed in Oct, 2013)
9. A. Bond, *Broadening Electrochemical Horizons: Principles and Illustration of Voltammetric and Related Techniques*, Oxford University Press, Oxford, 2002
10. A. K. Shukla, T. Prem Kumar, *Pillars of modern electrochemistry: A brief history*, Central Electrochemical Research Institute, Karaikudi, India, 2008, http://electrochem.cwru.edu/encycl/art-p05-pillars-of-ec.htm (accessed in Oct, 2013)
11. *Jaroslav Heyrovsky*, in *Nobel Laureates in Chemistry 1901–1992*, L. K. James, Ed., American Chem. Soc. and Chemical Heritage Foundation, 1993, p. 412
12. http://galaxywire.net/2009/05/21/fast-facts-apollo-fuel-cells/
13. M. M. Jaksic, in *Advances in Physical Chemistry*, Editorial introduction, Article ID 180604, 4 pages, Hindawi Publ. Co., Cairo, 2011
14. *Book of Abstracts of the Third Regional Symposium on Electrochemistry South-East Europe*, Bucharest, 2012, pp. XIII–XXIII
15. *Chemistry – Developing Solutions in a Changing World*, Document of European Association for Chemical and Molecular Sciences, EuCheMS aisbl, www.euchems.eu, (accessed in Oct, 2013)

16. EuCheMS General Assembly 2013, Decision 1307/07, resp. 06/GA/2013, Oct. 2013, Budapest, http://www.quotationspage.com/quote/26159.html (accessed in Oct, 2013)
17. http://www. quotationspage.com/quote/26159.html (accessed in Oct, 2013)
18. V. S. Bagotsky, *Fuel Cells: Problems and Solutions*, J. Wiley, Hoboken, NJ, 2009
19. http://en.wikipedia.org/w/index.php?title=File:Cold_fusion_electrolysis.svg&page=1 (accessed in Oct, 2013)
20. M. Fleischmann, S. Pons, *J. Electroanal. Chem.* **261** (1989) 301
21. S. Hadzi Jordanov, *Some Hidden Qualities for Successful Scientific Research*, Lecture presented at the *10th Congress of pure and applied chemistry of students from Macedonia*, Skopje, 2013, Book of Abstracts, p. 1
22. H. B. Beer, *S. African Pat. Act No. 1952*, 59, 1968
23. M. D. Spasojevic, N. V. Krstajic, M. M. Jaksic, *J. Res. Inst. Catalysis, Hokkaido Univ.* **31** (1983) 77
24. B.E. Conway, *Electrochemical Supercapacitors*, Kluwer Academic/Plenum Publishers, New York, 2000, p. 264
25. M.E. Bowden, *Chemistry is Electric*, Chem. Heritage Foundation, Publ. No. 15, 1997.

Journal of the Serbian Chemical Society
JSCS-info@shd.org.rs • www.shd.org.rs/JSCS
J. Serb. Chem. Soc. 78 (12) 2179–2200 (2013) UDC 547.462.3+66.092–977:678.7/.8+577.1
JSCS–4558 *Authors' Review*

AUTHORS' REVIEW

The thermal degradation of some polymeric di-alkyl esters of itaconic acid•

IVANKA POPOVIĆ*# and LYNNE KATSIKAS

Faculty of Technology and Metallurgy, University of Belgrade, Karnegijeva 4, 11000 Belgrade, Serbia

(Received 14 December 2013)

Abstract: One group of polymers that may help relieve the dependence on crude oil is based on itaconic acid, the biotechnological production of which has become feasible. Itaconic acid and its derivatives can easily be incurporated into polymers and may serve as a substitute for petrochemically derived acrylate or methacrylate monomers. The applications of polymers based on itaconic di-esters depend largely on their thermal stability. The thermal stability of poly(di-itaconates) is dependent, not only on the general structure of the monomer repeating unit, but also on the structure of the ester substituent. Depolymerization, initiated by *β*-scission or random main chain scission, is the dominant thermolysis mechanism in most cases. The deploymerization of poly-(di-itaconates) may be accompanied by de-esterification, elimination, cross-linking, random main or side chain scission and carbonization. Comparison of the thermal degradation mechanism of polymeric di-esters of itaconic acid to that of corresponding poly(methacrylates) confirms the viability of substituting poly(methacrylates) by poly(di-itaconates).

Keywords: itaconic acid; polyitaconates; thermal degradation; biosynthetic polymers.

CONTENTS

* Corresponding author. E-mail: ivanka@tmf.bg.ac.rs
# Serbian Chemical Society member.
• This paper is dedicated to our friend and colleague Prof. Dr. Branislav Nikolić on the occasion of his 70th birthday and in recognition of his unselfish work for the Serbian Chemical Society.
doi: 10.2298/JSC131214154P

1. INTRODUCTION

The role of plastics in modern society is being re-examined due to problems related to the persistence of mass polymers in the environment. Plastics, considered as the marvel of modern society, have replaced traditional materials such as wood, cotton, wool, stone, metal, glass or ceramics in many of their former uses and feature in advanced technologies from engineering materials to high tech applications. On the negative side, plastics deteriorate, but do not decompose under ambient conditions. Some plastics can and are being recycled, but mostly they are disposed of in landfills, incinerated or used to produce electricity at waste-to-energy plants, all of which have their downsides, especially concerning environmental pollution.[1] Moreover, plastic debris is found in water bodies, in oceans[2,3] and freshwater lakes,[4] enabling them to enter the human food chain *via* filter feeders.

Nevertheless, life without plastics is hardly imaginable. Plastics consist mainly of synthetic polymers, predominantly based on petrochemicals. As crude oil reserves diminish and oil prices inevitably increase due to ever increasing global needs, as far as polymers are concerned, a more sustainable approach for polymer scientists could be to search for biosynthetic polymers that can match the performance of synthetic ones.

One group of polymers that may help relieve the dependence on crude oil, is based on itaconic acid (methylene succinic acid, 2-methylidenebutanedioic acid (IUPAC)). Itaconic acid (IA) is an unsaturated dicarbonic organic acid. IA and its derivatives can easily be incorporated into polymers and may serve as a substitute for traditional acrylate and methacrylate monomers.

The biosynthesis of itaconic acid by fermentation processes has been known for a long time.[5] The price, however, has not been competitive in comparison to the IA obtained by petrochemical means. This aspect has now changed. More than 80,000 tons of IA are produced worldwide annually and sold at a price of around US$ 2/kg.[6] In time, biosynthetic polymers based on IA could become attractive alternatives to acrylics. The most common representatives of the di-alkyl itaconates, the methyl and ethyl di-esters of IA, can be synthesized by esterifying with biomethanol[7] or bioethanol.[8]

Dibasic IA is a building block that enables the synthesis of monomers for homo-, co- and terpolymers that are structurally more diverse than poly(methacrylates). It is possible to make di-esters, mono-esters and mixed esters with various substituents, as well as di-amides, amino acids and imides.

IA derivatives are widely used or are being investigated as co-components in various formulations in controlled drug release systems,[9,10] for paints and coatings,[11,12] in resist compositions,[13] for contact lenses[14] and ocular lenses[15] and personal care compositions.[16]

The applications of polymers based on itaconic di-esters most commonly depend on their mechanical properties and thermal stability. This review will focus on the thermal degradation behaviour of poly(di-itaconates) and compare it with the thermolysis of polymethacrylates.

2. POLY(DIMETHYL ITACONATE) (PDMI) *vs*. POLY(METHYL METHACRYLATE) (PMMA)

Very early in the study of methacylate polymers, Grassie[17] showed that the thermal degradation of PMMA proceeded almost completely by depolymerization, the yield of monomer being about 99 %. Thermogravimetric (TG) investigations, however, showed that the thermal degradation of PMMA occurred in three stages, as demonstrated by the differential TG (DTG) curves shown in Fig. 1,[18] all of which represented depolymerization of the polymer. PMMA deploymerization was first initiated by the scission of head-to-head bonds in the polymer, followed by β-scission at the vinylidene chain ends and, finally, by random main chain scission. Head-to-head bonds and chain-end unsaturation may be eliminated by changing the conditions of synthesizing PMMA. A thermally more stable PMMA is obtained by radical polymerization in the presence of chain-transfer agents or anionic polymerization.

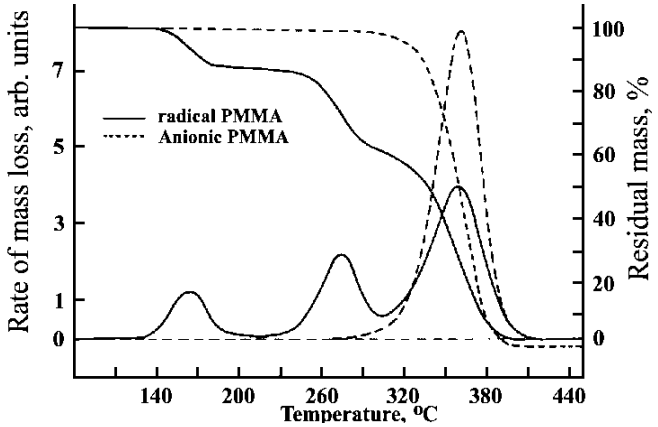

Fig. 1. Effects of the polymerization method on DTG curves for PMMA samples degrading in nitrogen: radically polymerized (——) and anionically polymerized (-----).[18]

The structures of the repeating units of PMMA and PDMI are:

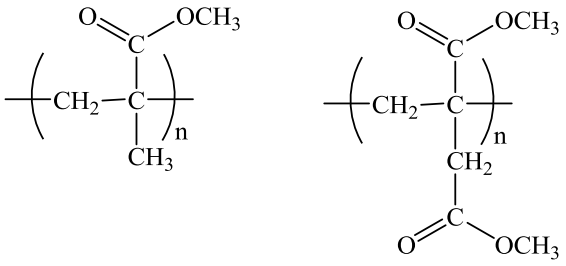

PMMA PDMI

Analysis of the volatile products of PDMI thermal degradation showed that dimethyl itaconate (DMI) monomer was the main product, about 95 %.[19,20] Very small amounts of methane, carbon dioxide and carbon monoxide are evolved during the thermolysis of PDMI, as seen in Fig. 2. The DTG curves are expected to be similar to those of PMMA. However, as seen in Fig. 3, there are only two DTG maxima, corresponding to the second and third peak of the PMMA DTG curve. This difference may be explained by the structure of the itaconate monomer. No head-to-head bonds are formed during di-itaconate bulk radical polymerization because of steric hindrance to the approach of two bulky propagating radicals. Nagai and Yoshida[21] proposed that, due to the allylic structure of the di-itaconate monomers, chain transfer to monomer would be favoured during radical polymerization. This hypothesis was later confirmed by us.[22–24] Thus, PDMI

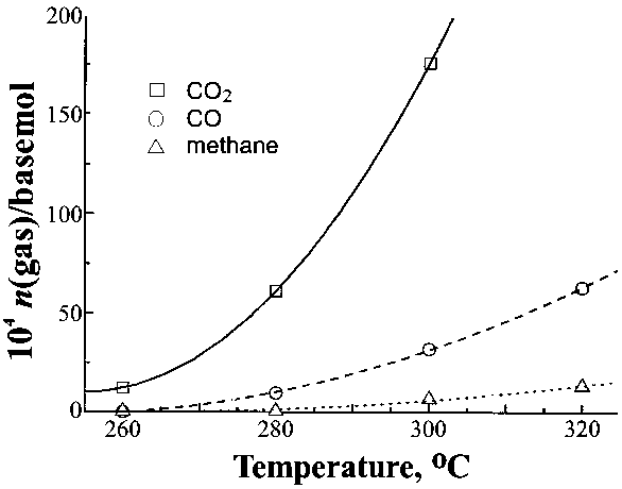

Fig. 2. The amount of CO_2 (□), CO (○) and methane (Δ) formed during the thermal degradation of PDMI as a function of temperature, heating time 30 min.[20]

depolymerization is initiated by β-scission at chain-end unsaturation and, at higher temperatures, by random main chain scission. The double bonds at the chain ends originate not only from termination by disproportionation, but also from considerable chain-transfer to monomer during radical polymerization. As PDMI does not have any β-hydrogens in the ester substituents, no relevant ester decomposition is expected. Very small amounts of methanol were detected in the thermolysis volatiles.[20]

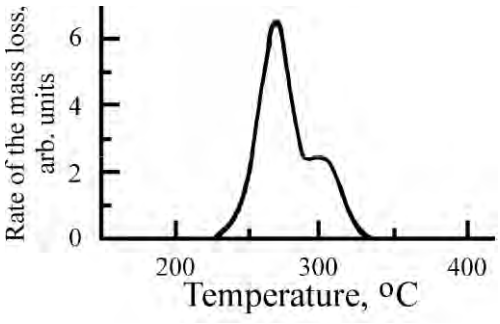

Fig. 3. The DTG curve of PDMI, heating rate: 2.5 °C min^{-1}, nitrogen flow rate: 25 cm^3 min^{-1}.[19]

The depolymerization of PDMI is accompanied by a decrease in polymer molar mass, Fig. 4a. It is useful to analyse the decrease in relative molar mass as a function of conversion, *i.e.*, mass loss, Fig. 4b. The shape of the curve indicates that the kinetic chain length of depolymerization, Z, is low. Z is derived from the following equation:[25]

$$\frac{W}{W_0} = \frac{\bar{P}_n}{\bar{P}_0} \frac{(Z + \bar{P})_0}{(Z + \bar{P}_n)}$$

where W/W_0 is the ratio of the mass of the residue and the mass of the initial polymer and $\bar{P}_0$ and $\bar{P}_n$ are the degrees of polymerization of the initial and degraded polymer, respectively. This calculation does not consider chain transfer reactions, only depropagation. The values of Z for PMMA range between 1000 and 2000 in the temperature range 260–300 °C,[25] while the values of Z for PDMI in the same temperature interval are no greater than 20.[26] The low value of Z implies that chain transfer to polymer occurs during the dezipping process and that, in this case, Z may only be considered as an apparent value.

3. POLY(DI-*n*-ALKYL ITACONATES)

*3.1. Thermal degradation of poly(di-*n*-alkyl itaconates) polymerized in bulk*

The general structures of poly(methacrylates) and poly(di-itaconates) are:

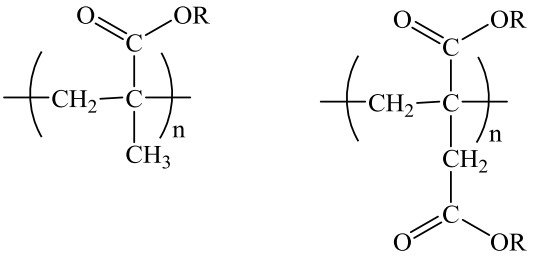

Poly(methacrylate) Poly(di-itaconate)

As the *n*-alkyl substituent in poly(di-itaconates) increases in length, depolymerization remains the dominant thermal degradation mechanism with monomer yields ranging from 85 to 90 %. The appearance of *β*-hydrogens in the ester substituent allows for the occurrence of ester decomposition during thermolysis. Poly(di-*n*-alkyl itaconates) have two *β*-hydrogens, except poly(di-ethyl itaconate)

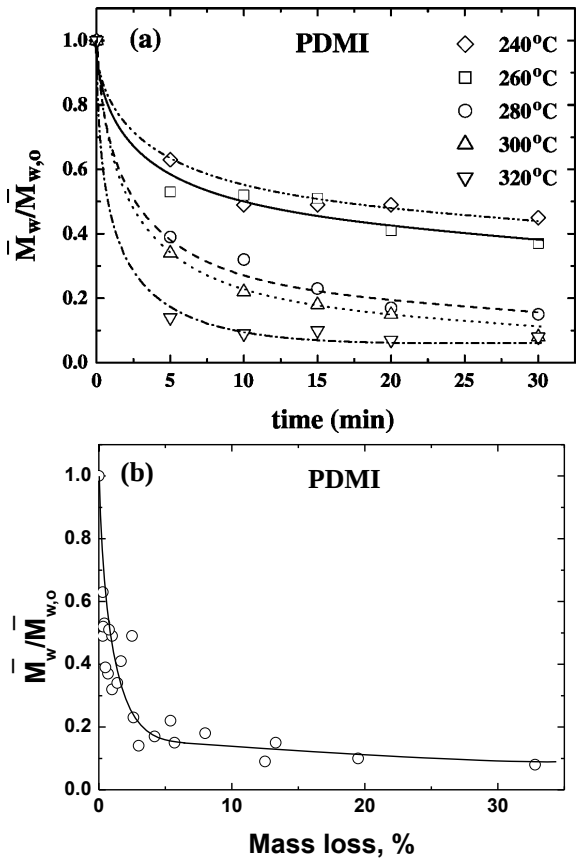

Fig. 4. Changes in the relative molar mass of PDMI as a) a function of time at various degradation temperatures and b) a function of mass loss at various times and temperatures.[19]

(PDEI), which has three. The role of β-hydrogens in the thermal degradation of poly(methacrylates) is well documented.[27] Ester decomposition leads to the evolution of 1-alkenes and to the formation of free acid groups in the polymer chain according to the following mechanism (Scheme 1).

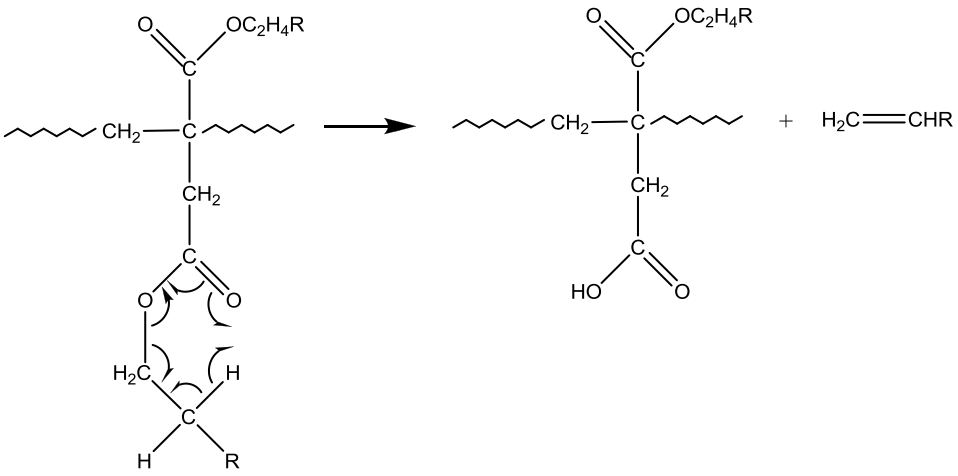

Scheme 1. Ester decomposition.[20]

Most of the other detected degradation products such as the corresponding *n*-alkanols, *n*-alkyl acetates, *n*-alkyl acrylates, *n*-alkyl methacrylates, *n*-alkyl esters of 3-methylene butyric acid, corresponding isomeric mesaconates and citraconates and di-*n*-alkyl esters of 1-methyl succinic acid, may be related to processes initiating depolymerization. The possible scission sites are shown below (Scheme 2).

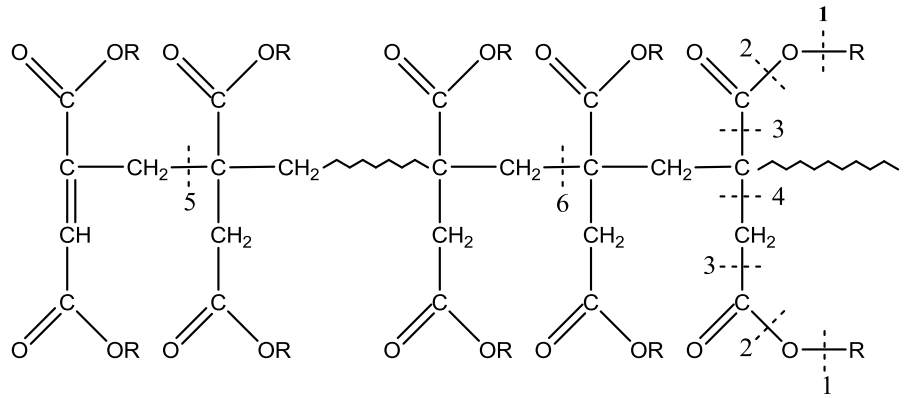

Scheme 2. Possible scission sites.[20]

The amounts of evolved carbon dioxide and carbon monoxide as a function of substituent size do not vary much. In the case of PDEI, ester decomposition is preferred to CO_2 and CO evolution, Fig. 5.

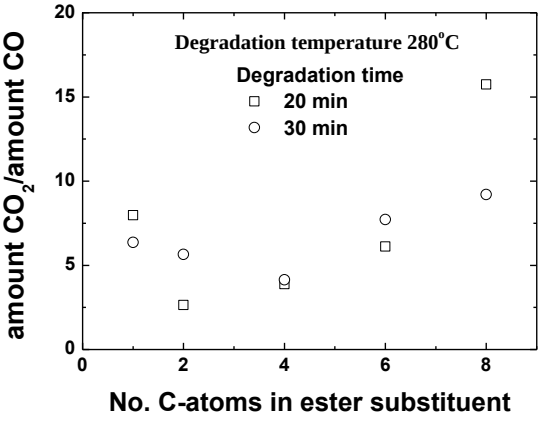

Fig. 5. The ratio of the amount of CO_2 and CO evolved as a function of number of carbon atoms in the ester substituent at various temperatures, degradation time 30 min.[20]

The availability of chain-end double bonds in poly(di-*n*-alkyl itaconates) decreases as the length of the substituent increases. As the substituents become bulkier, chain transfer to monomer is suppressed during polymerization due to steric hindrance. Consequently, depolymerization is still initiated by chain-end *β*-scission and random main chain scission, the chain end structures originating from termination by disproportionation. The DTG curves of some poly(di-*n*-alkyl itaconates) are shown in Fig. 6.[28]

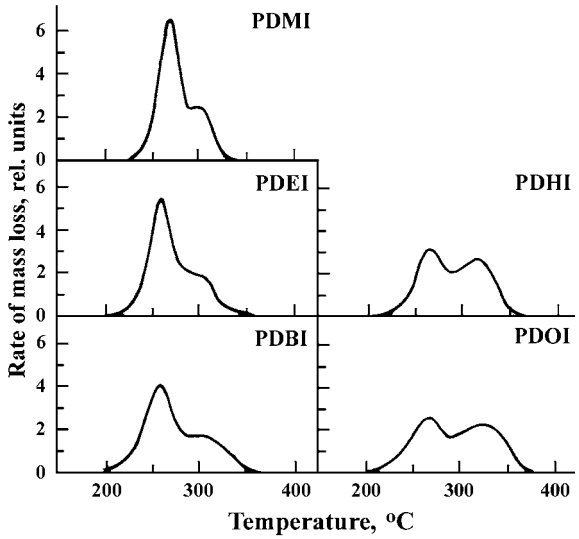

Fig. 6. The DTG curves of PDMI, PDEI, PDBI, PDHI and PDOI, heating rate 2.5 °C min^{-1}, nitrogen flow rate 25 cm^3 min^{-1}.[28]

The higher poly(di-*n*-alkyl itaconates), starting from poly(di-*n*-butyl itaconate) (PDnBI), tend to branch and crosslink at lower degradation temperatures, $t < 280$ °C, Fig. 7. In the case of poly(di-*n*-octyl itaconate) (PDOI), some insoluble swellable gel is formed. The possibility of hydrogen abstraction increases as the *n*-alkyl substituent becomes longer, so radical–radical combination may lead to branching and even crosslinking. As the degradation temperature and time increase, chain scission predominates and the polymer molar mass decreases. The kinetic chain lengths of depropagation are low for all the poly(di-*n*-alkyl itaconates) and the *Z* values are not higher than 20, Fig. 8. The changes in polymer relative molar mass as a function of polymer mass loss are similar to those for PDMI, indicating that chain transfer to polymer occurs during the depolymerization of poly(di-*n*-alkyl itaconates). A mechanism for the chain transfer reaction is given in the scheme below (Scheme 3).[28]

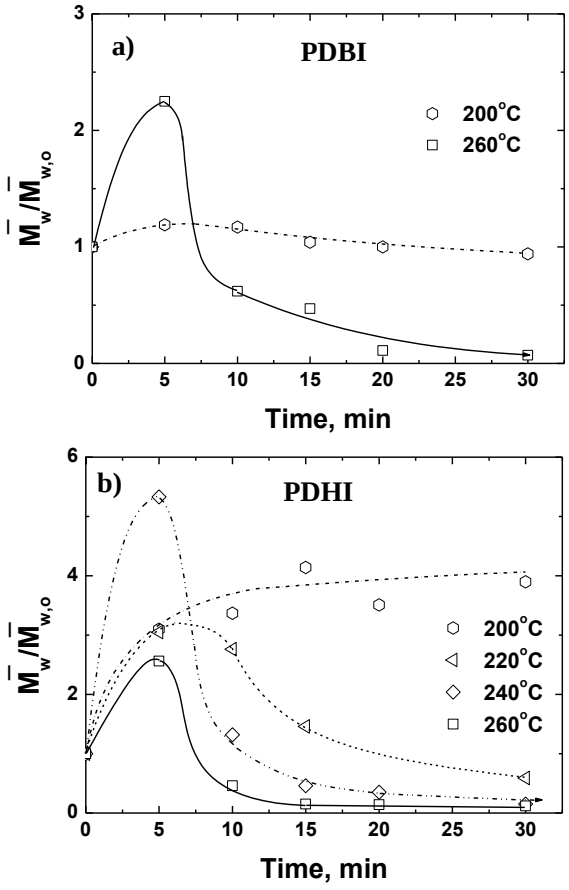

Fig. 7. Changes in the relative molar masses of the degraded polymer residues of a) PDnBI and b) PDHI as a function of degradation temperature and time.[28]

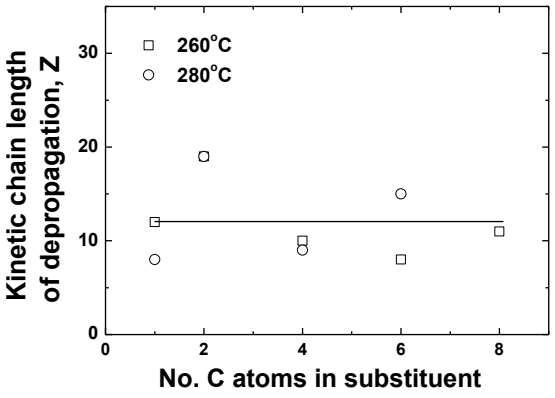

Fig. 8. Kinetic chain length of depropagation for poly(di-n-alkyl itaconates) as a function of the size of the alkyl substituent, degradation temperature 260 (□) and 280 °C (○), degradation time 30 min.[28]

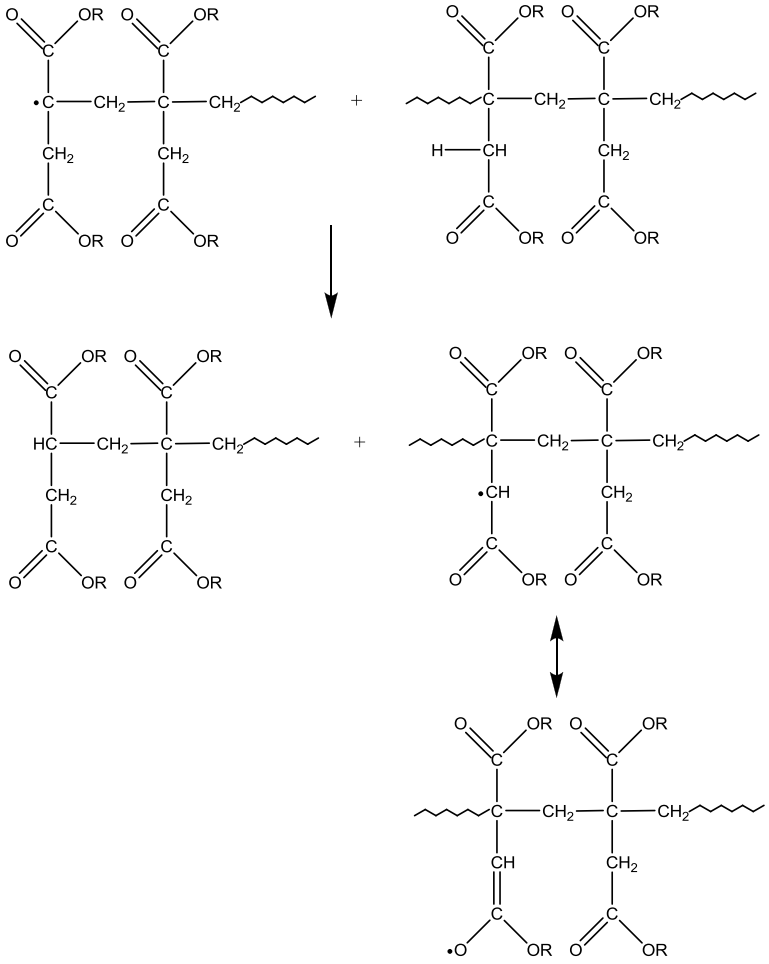

Scheme 3. Chain transfer to polymer.[28]

The number of main chain scissions per monomer unit can serve as a useful measure of polymer thermal stability. The value of s/P_0 may be calculated from the following equation:

$$\frac{s}{P_0} = \frac{1-x}{P_t} - \frac{1}{P_0}$$

where s is the number of scissions and x is the fraction of evaporated thermolysis volatiles. As expected, the values of s/P_0 increase with increasing degradation temperature and exposure time. Poly(di-*n*-hexyl itaconate) (PDHI) was chosen as an example to show this trend, Fig. 9. The thermal stability of poly(di-*n*-alkyl itaconates) decreases with increasing length of the *n*-alkyl substituent, Fig. 10.[28]

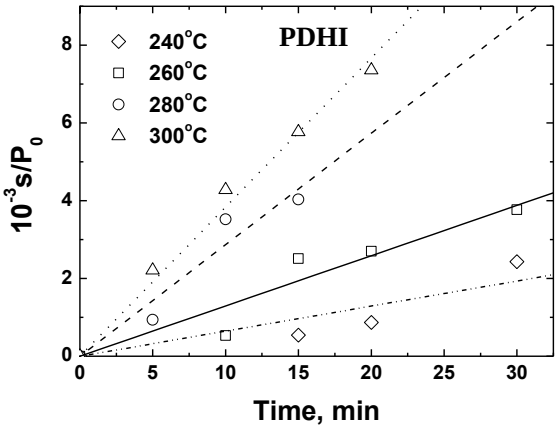

Fig. 9. Number of bonds broken per monomer unit during the thermal degradation of PDHI at various temperatures as a function of time.[28]

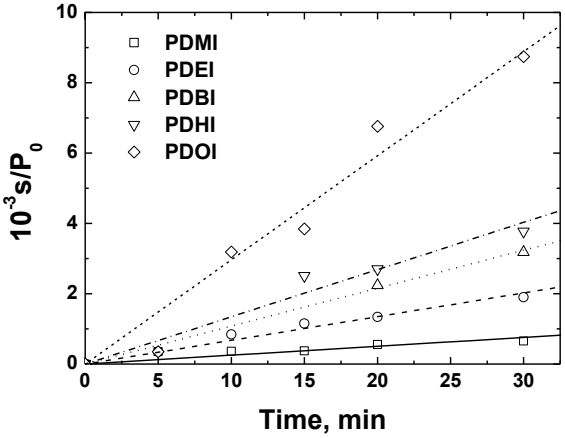

Fig. 10. Number of bonds broken per monomer unit during the thermal degradation of poly(di-*n*-alkyl itaconates) at 260 °C as a function of time.[28]

*3.2. Thermal degradation of poly(di-*n*-alkyl itaconates) polymerized in bulk in the presence of chain transfer agents*

The thermal stability of poly(di-*n*-alkyl itaconates) may be improved by reducing the number of polymer chains with terminal double bonds during polymer synthesis. The thermal degradation of PDHI samples synthesized in the presence of various amounts of *n*-dodecyl mercaptan (DDM) illustrates the phenomenon well.[22] As the growth of polymer chains is terminated by transfer reactions to the thiol, the number of macromolecules with saturated chain-ends increases. The polymer samples are thermally more stable because thermal degradation is initiated predominantly by random main chain scission. The TG and DTG curves of the PDHI samples are shown in Fig. 11.

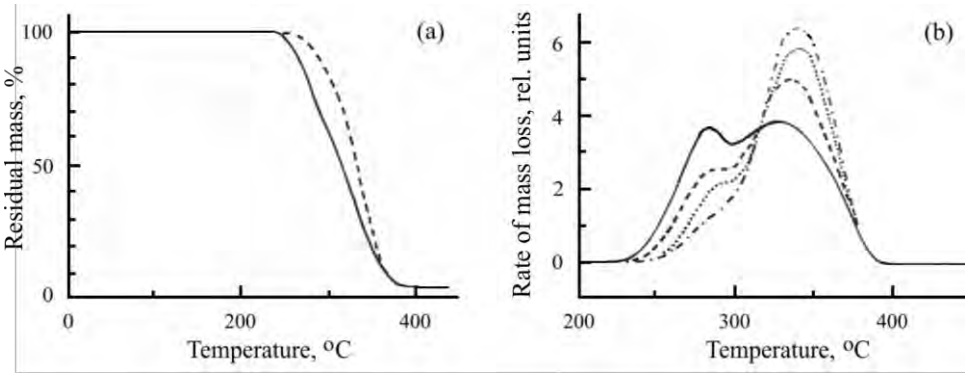

Fig. 11. a) TG curves of PDHI polymerized in the absence (——) and in the presence of 150 mmol L^{-1} of DDM (-----); b) DTG curves of PDHI polymerized in the presence of no (——), 45 (-----), 80 (·····) and 150 (- · - ·) mmol L^{-1} of DDM. Heating rate 10 °C min^{-1}; nitrogen flow rate 25 cm^3 min^{-1}.[22]

*3.3. Thermal degradation of poly(di-*n*-alkyl itaconates) polymerized in solution*

As already stated, the thermal stability of poly(di-*n*-alkyl itaconates) depends on the amount of chain-end double bonds present in the polymer sample. Besides standard termination by disproportionation, terminal double bonds are also formed readily by chain transfer to monomer. It is possible to suppress double bond formation by chain transfer agents other than mercaptans. Polymerizations of di-alkyl itaconates have been carried out in various solvents (toluene, chloroform or dioxane).[23,28] In all cases it was possible to significantly decrease the number of formed chain-end double bonds in the polymer, even in benzene, an "inert" solvent with a low tendency to transfer to solvent. Such effective chain transfer by numerous solvents may be explained in the following way.[24,29] The propagation rate constants, k_p, of itaconates are an order of magnitude lower than those of the corresponding methacrylates.[29] Thus, the values of any constant of chain transfer to solvent, $C_S = k_{tr,S}/k_p$, for itaconates, even though the values of

the transfer rates to solvent, $k_{tr,S}$, may be very low, are unusually high. An example is shown in Fig. 12, indicating effective chain transfer to benzene, yielding thermally more stable PDBI samples. The DTG curves clearly demonstrate that the number of unsaturated polymer chain ends decreases when the radical polymerization is performed at higher benzene concentrations.

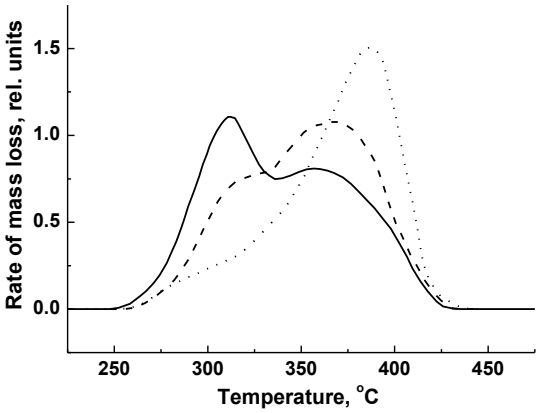

Fig. 12. DTG Curves of PDBI samples synthesized in benzene under nitrogen at 57 °C, 0 (——), 7.78 (-----) and 9.53 (·····) mol dm^{-3} benzene; heating rate: 10 °C min^{-1}; nitrogen flow rate: 25 cm^3 min^{-1}.[23]

4. POLYMERIC DIESTERS OF ISOMERIC DI-ALKYL ITACONATES

The thermal degradation mechanism of poly(di-alkyl itaconates) with isomeric ester substituents becomes more complex. The number of β-hydrogens in the ester substituent determines the susceptibility to ester decomposition. Similar trends have already been observed in the case of poly(methacrylates).[27] Generally, when the number of β-hydrogens is higher than three, de-esterification becomes a major thermolysis pathway. The characteristic TG curves of poly(di-*iso*-propyl itaconate) (PDiPI), poly(di-*sec*-butyl itaconate) (PDsBI) and poly(di-*iso*-butyl itaconate) (PDiBI), having three, five and one β-hydrogen, respectively, are presented in Fig. 13.[30] Characteristic DTG curves of the same polymers are shown in Fig. 14.

The thermal stability of PDiPI and PDsBI differs to that of the poly(di--itaconates) discussed so far. Even though the major thermolysis product in all cases is the respective monomer, the reactions initiating depolymerization differ. The first DTG peak is correlated to monomer being evolved as a consequence of chain-end β-scission. The second DTG peak is assigned to the evolution of monomer initiated by ester decomposition and main chain scission. Carbonaceous residues at 600 °C of about 10 % were found in both cases. The occurrence of ester decomposition during the thermal degradation of PDiPI was confirmed when free acid groups were detected in the degradation residue, Fig. 15, and by the evolution of 1-propene, Fig. 16. The free acid groups are not thermally stable and easily carboxylate leading to the evolution of CO_2, Fig. 16, and the gradual formation of a carbonaceous residue.

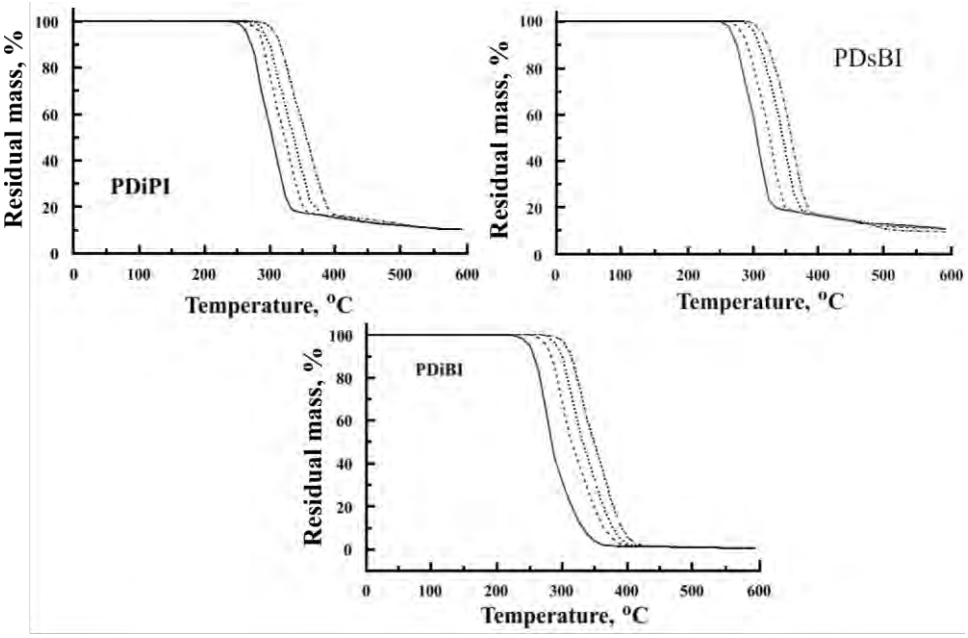

Fig. 13. Non-isothermal TG curves of PDiPI, PDsBI and PDiBI. Heating rates 2.5 (——), 10 (-----), 20 (·····) and 40 °C min^{-1} (- · - ·). Nitrogen flow rate: 26 cm^3 min^{-1}.[30]

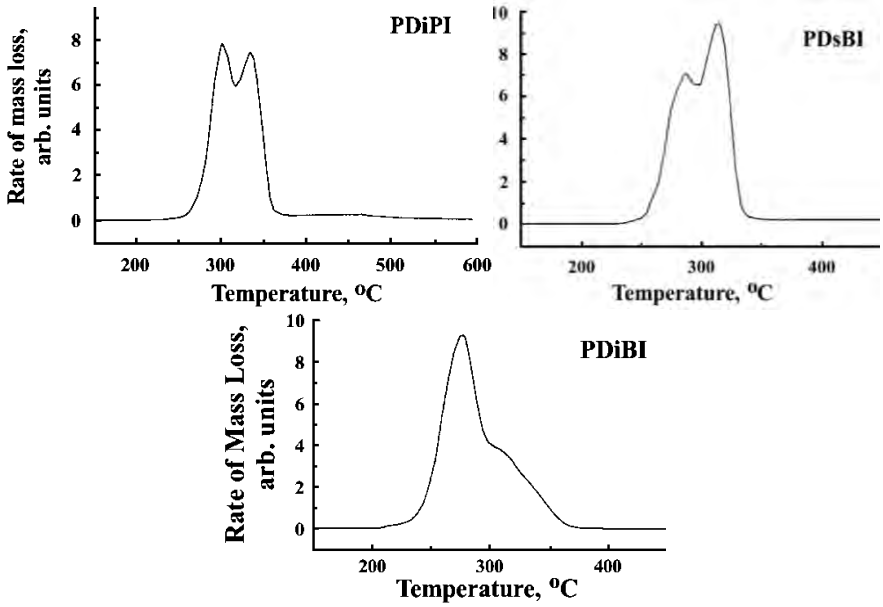

Fig. 14. Non-isothermal DTG curves of PDiPI, PDsBI and PDiBI. Heating rate: 10 °C min^{-1}. Nitrogen flow rate: 26 cm^3 min^{-1}.[30]

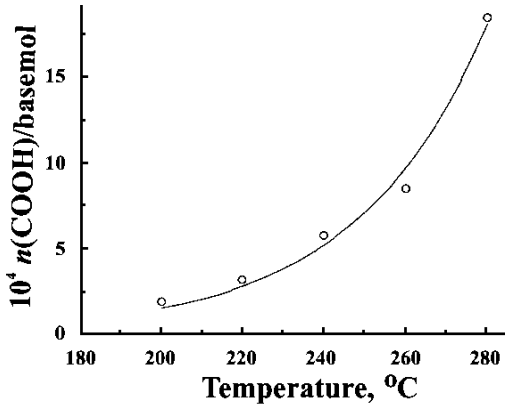

Fig. 15. Moles of COOH groups in PDiPI residue as a function of thermolysis temperature, degradation time 30 min.[31]

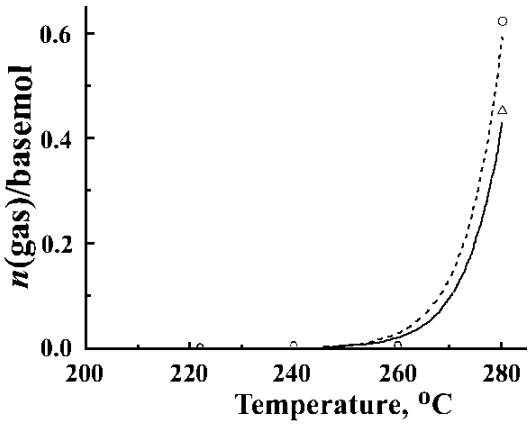

Fig. 16. Moles of evolved CO2 (○) and propene (Δ) per basemol PDiPI as a function of thermolysis temperature, degradation time 30 min.31

A similar trend was found in the case of PDsBI. Ester decomposition is extensive, as may be seen in Fig. 17, expressed as butene evolution. It is interesting to compare the thermolysis of PDsBI and its analogue, poly(*sec*-butyl

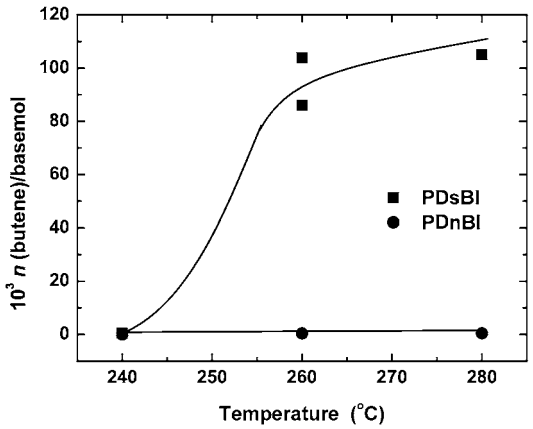

Fig. 17. Amount of butene evolved on heating PDnBI and PDsBI for 30 min at various temperatures.32

methacrylate) (PsBMA).[33] It was established that the thermolysis mechanisms were very similar. Comparable results of free acid group formation in the residue and butene evolution, taking into account the number of ester groups in the monomer unit, were obtained.

PDiBI, with one β-hydrogen in the ester substituent, was found to have similar thermal stability to PDnBI. Depolymerization is the predominant thermolysis mechanism, ester decomposition is almost negligible and there is no carbonization.

5. POLY(DI-ALKOXYETHYL ITACONATES)

The thermal degradation of a series of poly(di-alkoxyethyl itaconates) was investigated: poly(di-methoxyethyl itaconate) (PDMOEI), poly(di-ethoxyethyl itaconate) (PDEOEI), poly(di-propoxyethyl itaconate) (PDPOEI) and poly(di-butoxyethyl itaconate) (PDBOEI). The ester substituents of the four polymers are bulky and they all have two β-hydrogens. Monomer was again the main thermolysis product.[34] The non-isothermal TG curves of these polymers are presented in Fig. 18, while characteristic DTG curves are shown in Fig. 19. The shapes of the DTG curves do not change with substituent size and are similar to those of the lower poly(di-*n*-alkyl itaconates). However, in this series of polymers, a carbon atom has been substituted by a hetero atom in the substituent, making it thermally less stable due to the presence of C–O bonds. Less energy is required to break these bonds and it is assumed that bond scissions in the substituent efficiently initiate depolymerization. Even though side chain scission is extensive, carbonization does not occur.

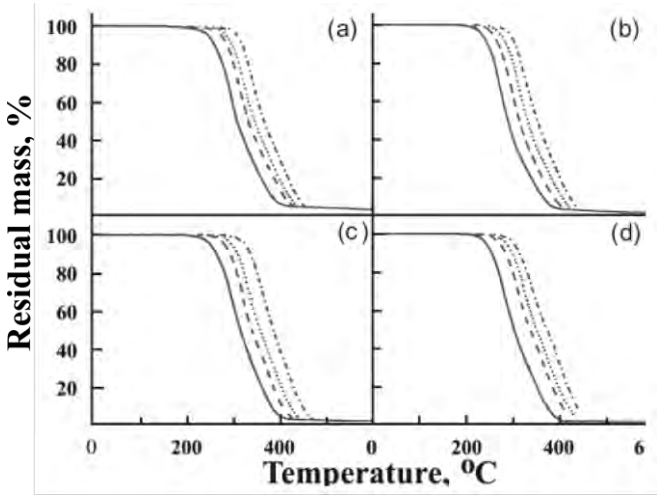

Fig. 18. Non-oxidative TG curves of poly(di-alkoxyethyl itaconates), a) PDMOEI, b) PDEOEI, c) PDPOEI and d) PDBOEI. Heating rates: 2.5 (——), 10 (-----), 20 (·····) and 40 °C min^{-1} (- · - ·). Nitrogen flow rate: 22 cm^3 min^{-1}.[32]

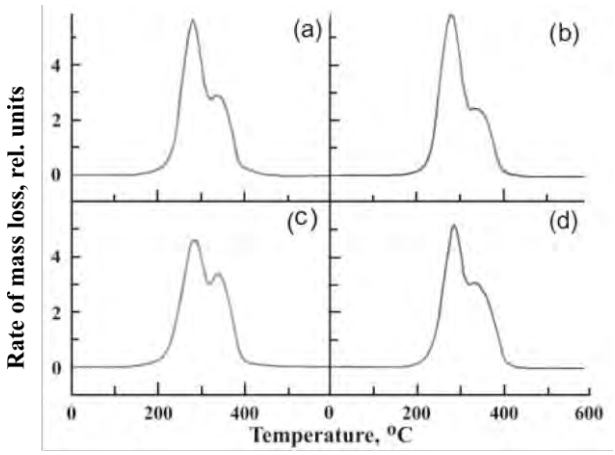

Figure 19. Non-oxidative DTG curves of poly(di-alkoxyethyl itaconates), a) PDMOEI, b) PDEOEI, c) PDPOEI and d) PDBOEI. Heating rate: 10 °C/min (——); nitrogen flow rate: 22 cm^3 min^{-1}.[32]

6. POLY(DI-ALKYLCYCLOHEXYL ITACONATES)

The non-isothermal TG curves of poly(di-cyclohexyl itaconate) (PDCHI), poly(dimethylcyclohexyl itaconate) (PDMCHI) and poly(di-ethylcyclohexyl itaconate) (PDECHI) are presented in Fig. 20, while characteristic DTG curves of these polymers are shown in Fig. 21.[35] There is a clear difference between the TG and DTG curves of PDCHI and the other two polymers. The single, irregularly shaped DTG peak of PDCHI indicates that the thermal degradation of this polymer is initiated by a reaction continuously yielding highly volatile products, probably originating from the substituents, as well as by random main chain scission. Both cyclohexane and cyclohexene have higher vapour pressures than other possible thermolysis products. The evolution of these vapours is to be expected, due to the structure of the monomer unit, *i.e.*, the tertiary hydrogen on the C1 atom of the cyclohexyl ring. This tertiary hydrogen is present in all three polymers, but it has different surroundings. Analysis of the volatiles revealed that depolymerization was the major degradation mechanism with almost 90 % monomer content.[35]

Relative changes in the mean molar mass of PDCHI and PDECHI during thermolysis are similar to those of the higher poly(di-*n*-alkyl itaconates). Increases in the mean molar mass are noticeable at lower degradation temperatures. At higher temperatures there more main chain scissions occur than cross-links, so the overall effect is a mean molar mass decrease. Lateral macroradicals may form during bond scissions in the ester substituents. Such lateral macroradicals may combine, which implies that branching of the polymer is possible in the initial stages of degradation. At higher temperatures, carbonization is favoured.[35]

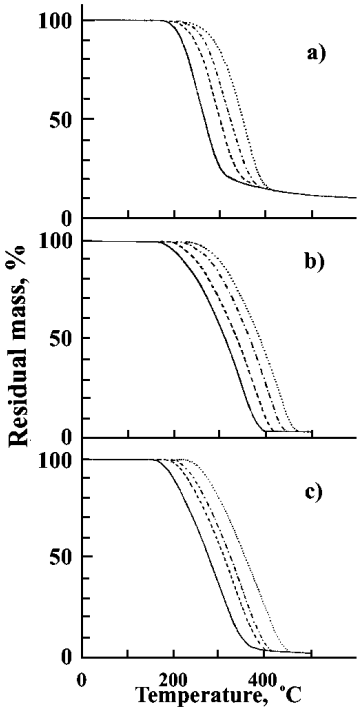

Fig. 20. Non-oxidative TG curves of poly(di-alkylcyclohexyl itaconates), a) PDCHI, b) PDMCHI and c) PDECHI. Heating rates 2.5 (——), 10 (-----), 20 (·····) and 40 °C min^{-1} (- · - ·). Nitrogen flow rate: 25 cm^3 min^{-1}.[35]

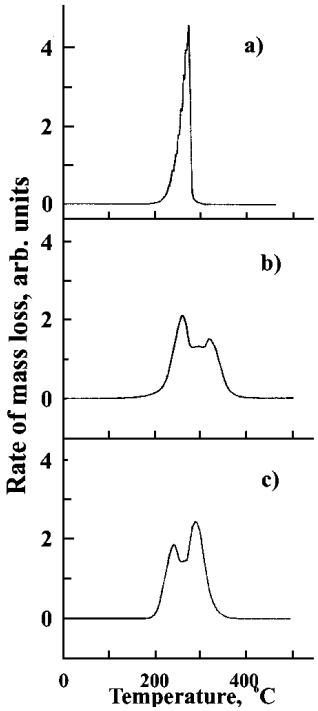

Fig. 21. Non-oxidative DTG curves of poly(di-alkylcyclohexyl itaconates), a) PDCHI, b) PDMCHI, and c) PDECHI. Heating rates 0.625 °C min^{-1} (——). Nitrogen flow rate: 25 cm^3 min^{-1}.[35]

7. POLY(DI-2-CHLOROETHYL ITACONATE)

The introduction of chlorine into the ester substituent of poly(di-itaconates) dramatically changes the thermal degradation mechanism.[36] The TG curves of poly(di-2-chloroethyl itaconate) (PD2CEI) become heating rate-dependent. The slope of the TG curve changes with heating rate, as does the amount of residue. The TG and DTG curves of PDCEI recorded at a very slow heating rate, at which the maximum amount of carbonaceous residue is obtained, are presented in Fig. 22. Even though the major thermolysis product is still monomer, the formation of a carbonaceous residue implies that crosslinking occurs. The DTG curve of PD2CEI is more complex than that of the single peak DTG curve of poly(2-chloroethyl methacrylate) (P2CMA).[37] It is interesting to note that the thermal degradation activation energy, E_a, of P2CMA is constant over mass loss, while the E_a of PDCEI continuously increases, which indicates that carbonization is occurring.[38] Isothermal degradation experiments were carried out in order to determine changes in mean molar mass or degree of crosslinking and to compare the two polymers, Fig. 23.

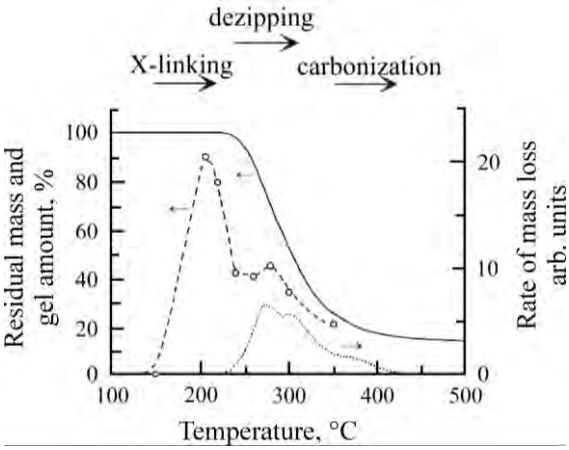

Fig. 22. Overall non-oxidative thermal degradation scheme of PD2CEI, TG (——) and DTG (-----) curves, heating rate 0.625 °C min^{-1}, amount of gel formed (% of initial polymer) (---○---), degradation time 45 min.[36]

During the thermal degradation of PD2CEI several processes occur simultaneously. Depolymerization competes with crosslinking up to 280 °C. At higher temperatures, main chain scission-initiated depolymerization is dominant. At temperatures greater than 280 °C, the residual crosslinked structures start to carbonize. The strong affinity to crosslinking can be related to the two ester substituents in the monomer unit of PD2CEI. Figure 22 explains the course of the degradation. The start of significant mass loss on the TG curve coincides with a decrease in the amount of formed gel. The first DTG peak coincides with the saddle in the gel content curve indicating extensive depolymerization. The second DTG peak or plateau corresponds to the second, smaller maximum of formed insoluble product, which can be related to simultaneous depolymerization and initial carbonization. The dominant process at higher temperatures is carbonization.

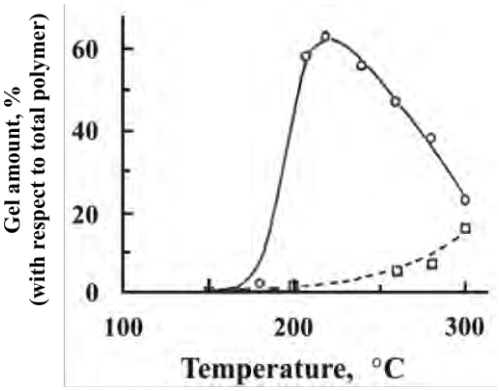

Fig. 23. Dependence of the amount of gel (% of initial polymer) on temperature, degradation time 30 min, PDCEI (○), P2CMA (□).[36]

8. CONCLUSIONS

The thermal degradation of poly(di-alkyl itaconates) was investigated in detail using numerous analytical techniques. Based on these investigations, a

general thermal degradation mechanism was proposed. It was established that the following reactions take place: depolymerization, ester decomposition, elimination, crosslinking, random main and/or side chain scission and carbonization. The susceptibility toward specific reactions depends on the structure of the ester substituent.

The basic and predominant process is depolymerization that may be initiated in several ways by end-chain or side chain scission. Ester decomposition becomes relevant when there are three or more β-hydrogens in the substituent. If crosslinking takes place at lower thermal degradation temperatures, carbonization is likely to occur at higher temperatures. A schematic presentation of the thermal degradation mechanism is presented below (Scheme 4).

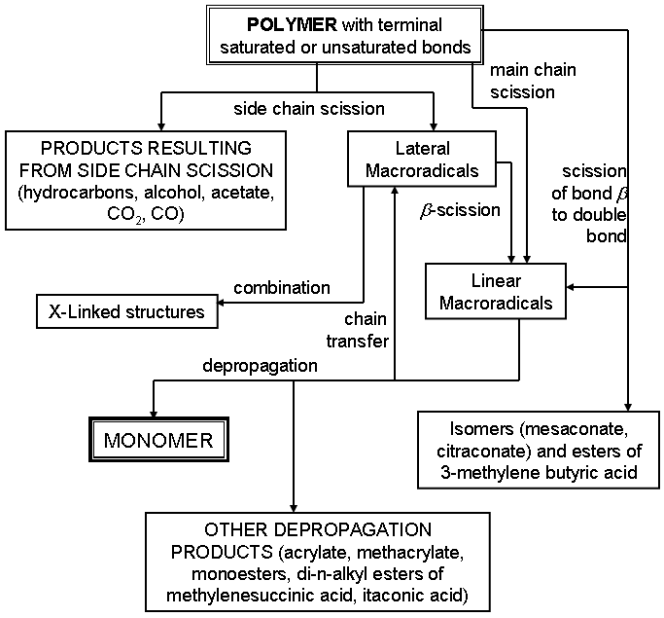

Scheme IV. Overall thermal degradation scheme of poly(di-alkyl itaconates).

Acknowledgement. The authors acknowledge the financial support provided by the Ministry of Education, Science and Technological Development of the Republic of Serbia through project 172062.

ИЗВОД

ТЕРМИЧКА РАЗГРАДЊА НЕКИХ ПОЛИМЕРНИХ ДИАЛКИЛ ЕСТАРА ИТАКОНСКЕ КИСЕЛИНЕ

ИВАНКА. Г. ПОПОВИЋ[1] и LYNNE KATSIKAS

Технолошко–металуршки факултет, Универзитет у Београду, Карнегијева 4, 11000 Београд

Једну групу полимера, који би могли да умање зависност од сирове нафте, чине полимери на бази итаконске киселине, чија биотехнолошка производња постаје исплатива. Итаконска киселина и њени деривати могу лако да се уграде у полимере и

могу да служе као замена за петрохемијски добијене акрилатне и метакрилатне мономере. Примена полимера на бази ди-естара итаконске киселине зависи у великој мери од њихове термичке стабилности. Термичка стабилност поли(ди-итаконата) зависи не само од опште структуре мономерне понављајуће јединице, већ и од структуре естарског супституента. Деполимеризација, иницирана кидањем или насумичним раскидањем везе у основном ланцу, је доминантан механизам термолизе у већини случајева. Деполимеризација поли(ди-итаконата) може да буде праћена де-естерификацијом, елиминацијом, умрежавањем, насумучним раскидањем везе у основном и/или бочном ланцу и карбонизацијом. Поређење механизма термичке разградње полимерних ди-естара итаконске киселине и одговарајућих полиметакрилата потврђује одрживост замене полиметакрилата поли(ди-итаконатима).

(Примљено 14. децембра 2013)

REFERENCES

1. J. Hopewell, R. Dvorak, E. Kosior, *Phil. Trans. R. Soc., B*. **364** (2009) 2115
2. K. L. Law, S. Morét-Ferguson, N. A. Maximenko, G. Proskurowski, E. E. Peacock, J. Hafner, C. M. Redd, *Science* **329** (2010) 1185
3. P. G. Ryan, C. J. Moore, J. A. van Franeker, C. L. Moloney, *Phil. Trans. R. Soc., B* **364** (2009) 1999
4. H. K. Imhof, N. P. Ivleva, *Curr. Biol.* **23** (2013) R867
5. T. Kobayashi, *Process Biochem*. **13** (1978) 15
6. M. Okabe, D. Lies, S. Kanamasa, E. Y. Park, *Appl. Microbiol Biotechnol*. **84** (2009) 597
7. A cleaner route to methanol http://www.rsc.org/chemistryworld/News/2008/November/05110802.asp (accessed Dec, 2013)
8. Y. Sun, J. Cheng, *Bioresour. Technol*. **83** (2002) 1
9. S. K. Bajpai, J. Sonskusley, *React. Funct. Polym*. **35** (2005) 197
10. M. Stanojević, M. T. Kalagasidis Krušić, J. M. Filipović, J. Parojčić, M. Stupar, *Drug Deliv*. **13** (2006) 1
11. M. Nakamura, T. Inoue, US Patent 6,759,473 July 6, 2004
12. ITACONIX®DSP2K™, http://www.itaconix.com/downloads/Tech%20Data% 20Sheet-%20DSP2K-v1.0.5.pdf (accessed Dec, 2013)
13. K. Sato, K. Kodama, US Patent 6,773,862, August 10, 2004
14. E. J. Ellis, A. P. Olson, J. A. Bonafini, Jr., US Patent CA2159327, March 2, 1999
15. T. Watanabe, E. Ito, S. Tanikawa, S. Ichinohe, T. Yamazaki, M. Lamrani, US Patent 6, 770,728, August 3, 2004
16. E. R. Lukenbach, C. Kaminski, S. Pascal-Suisse, M. Tahar, M. Ruggiero, US Patent 6,762,158, July 13, 2004
17. N. Grassie, H. W. Melville, *Proc. Roy. Soc. Ser. A* **199** (1949) 24
18. T. Kashiwagi, A. Inabi, J. E. Brown, K. Hatada, T. Kitayama, E. Masuda, *Macromolecules* **19** (1986) 2160
19. J. S. Veličković, I. G. Popović, *Croat. Chem. Acta* **60** (1987) 173
20. I. G. Popović, L. Katsikas, J. S. Veličković, *Polym. Deg. Stab*. **89** (2005) 153
21. S. Nagai, K. Yoshida, *Kobunshi Kagaku* **17** (1960) 79
22. I. G. Popović, L. Katsikas, K. A. Voloshchuk, S. Schrötter, J. S. Veličković, *Polym. Deg. Stab*. **42** (1993) 345
23. I. G. Popović, L. Katsikas, H. Weller, S. Schrötter, J. S. Veličković, *J. Appl. Polym. Sci*. **50** (1993) 1475

24. S. L. Tomić, J. M. Filipović, J. S. Veličković, L. Katsikas, I. G. Popović, *Macromol. Chem. Phys*. **200** (1999) 2421
25. T. Kashiwagi, T. Hirata, J. E. Brown, *Macromolecules* **18** (1985) 131
26. I. G. Popović, L. Katsikas, J. S. Veličković, *Polym. Deg, Stab*. **89** (2005) 165
27. N. Grassie, *Pure Appl Chem*. **30** (1972) 119
28. I. G. Popović, L. Katsikas, J. S. Veličković, *J. Thermal Anal*. **38** (1992) 953
29. L. Katsikas, M. Milovanović, I. G. Popović, *Eur. Polym. J*. **44** (2008) 3028
30. L. Katsikas, G. Bošković, S. J. Veličković, J. S. Veličković, I. G. Popović, *Eur. Polym. J*. **36** (2000) 1619
31. G. Bošković, L. Katsikas, J. S. Veličković, *Polymer* **41** (2000) 5769
32. S. J. Veličković, L. Katsikas, I. G. Popović, *J. Anal. Appl. Pyrolysis* **49** (1999) 75
33. K. Novaković, L. Katsikas, I. G. Popović, *J. Serb. Chem. Soc*. **65** (2000) 867
34. L. Katsikas, T. A. Djakov, J. M. Filipović, J. S. Veličković, I. G. Popović, *J. Thermal Anal.* **47** (1996) 1093
35. I. G. Popović, L. Katsikas, D. Jovanović, A. Blažić, J. S. Veličković, *J. Serb. Chem. Soc*. **58** (1993) 551
36. D. Živković, L. Katsikas, J. S. Veličković, I. G. Popović, *J. Thermal Anal*. **40** (1993) 767
37. I. G. Popović, L. Katsikas, W. Schnabel, J. S. Veličković, *J. Serb. Chem. Soc*. **60** (1994) 187
38. I. G. Popović, L. Katsikas, K. A. Voloschuk, J. S. Veličković, W. Schnabel, *J. Thermal Anal*. **38** (1992) 267.

Journal of the Serbian Chemical Society
JSCS-info@shd.org.rs • www.shd.org.rs/JSCS

J. Serb. Chem. Soc. 78 (12) 2201–2214 (2013)
JSCS–4559

UDC 537.311.35:536.7.004.12+
53.004.12+54.004.12:536.416
Review

REVIEW

Physical, chemical and structural effects as important factors for the determination of thermodynamic and transport properties and the modelling of non-electrolyte solutions

BOJAN D. DJORDJEVIĆ*#, MIRJANA Lj. KIJEVČANIN#, IVONA R. RADOVIĆ#, SLOBODAN P. ŠERBANOVIĆ# and ALEKSANDAR Ž. TASIĆ

Faculty of Technology and Metallurgy, University of Belgrade, Karnegijeva 4, P. O. Box 35-03, 11120 Belgrade, Serbia

(Received 23 October, revised 8 November 2013)

Abstract: In our previous review, an attempt was made to relate the volumetric effects involved in binary mixtures of normal and branched alcohols. The present paper summarizes some selected research activities related to complex molecular structure of various authors that appeared in leading international journals. The main aim was a better understanding of the complex structure of different non-electrolyte mixtures with no alcohols, which are most frequently present in the chemical, petrochemical and related industries. The influences of the basic physical, chemical and structural effects of the most often chosen types of various binary and ternary mixtures were analyzed. These contributions are of primary importance for the determination and modelling of thermodynamic, transport and other properties.

Keywords: thermophysical properties; transport properties; non-electrolyte systems; structural effect.

CONTENTS

* Corresponding author. E-mail: bojan@tmf.bg.ac.rs
# Serbian Chemical Society member.
doi: 10.2298/JSC131023129D

INTRODUCTION

Increasing use of many non-electrolyte mixtures in various industrial processes, such as in the chemical, petrochemical and related industries, has greatly stimulated need for extensive data on the thermodynamic and transport properties. These properties play an important role in the comprehension of the nature of the complex molecular structures that exists in binary and ternary mixtures.

Knowledge of adequate structures forms the basis for the development of new theoretical and empirical models. Herein, excess molar volumes, V^E, viscosity deviations, $\Delta\eta$, speed of sound deviations, Δu, changes of isentropic compressibility, $\Delta\kappa_S$, molar refraction changes of mixing, ΔR, changes in the refractive indices on mixing, Δn_D, *etc*., are considered, bearing in mind that their values are the consequence of molecular motion, molecular packing and various types of molecular interactions caused by the chemical nature and the size and shape of different molecules.

Thermodynamic and transport properties are attributed to a balance between physical, chemical and structural effects. Physical contributions represent non-specific interactions between the actual species present in the solution. The chemical contributions function as specific intermolecular interactions, which include charge-transfer type forces and other complex forming interactions. The structural contributions arise from several effects, especially from interstitial accommodation and changes in free volume. Namely, geometrical fitting of one component into another might occur due to differences in size and shape of components. More information about these contributions can be found in the literature.[1–7] Additionally, an in detail definition[8,9] and theory[10] of the hydrogen bond are given.

Mixtures that include alcohols are not treated herein, since in previous papers, they were presented and analyzed in detail.[11–23] In addition, a review[17] was particularly devoted to molecular interactions of binary liquid mixtures containing alcohols, *i.e*., *n*-alcohols, branched alcohols and alkanediols in mixtures with aromatics, nitroaromatics, halo-aromatics, amines, *n*-alkanes, ketones and esters.

With the aim of a deeper understanding of molecular liquid structures and intermolecular interactions that occur in diverse types of non-alcohol containing organic mixtures, in this manuscript, non-electrolyte systems containing amines, amides, ethers, esters and chloro-alkanes with different polar or non-polar compounds are treated. Bearing in mind that an analysis of non-ideal behaviour mainly focuses on excess molar volumes, it is desirable to mention the factors that produce positive or negative values of V^E.[1–10]

The magnitude and the positive sign of V^E can arise mainly from the following factors: *i*) absence of strong specific interactions between the components of a mixture; *ii*) the consequence of the rupture of H-bonds in self-associated

alcohol molecules and the physical dipole–dipole interactions between real species, as well as the breaking of chemical and/or non-chemical interactions among molecules in pure components during the mixing process; *iii*) predominant intermolecular H-bond stretching of associated alcohol molecules in the presence of other component; *iv*) steric hindrance of branched substances; *v*) improper interstitial accommodation due to similar molar volumes and free volumes between unlike molecules.

The negative contributions are consequence of the effects: *vi*) a more efficient packing in the mixture than in the pure liquids is considered to be the major contribution to negative V^E values. This could be the consequence of strong intermolecular interactions attributed to charge-transfer complex, dipole–dipole and dipole-induced dipole interactions and H-bonding between unlike molecules; *vii*) structural effects that arise from proper interstitial accommodation and orientation ordering leading to more compact structures and greater packing in mixtures; *viii*) the presence of electron donor–acceptor interactions between different molecules.

Complex behaviour and specific characteristics of different molecules determine the predominance of particular type of interactions in each mixture stipulating which contribution is dominant, as can be seen in the mixtures considered as follows.

The empirical and theoretical models used to correlate or predict corresponding thermodynamic and transport properties in the considered articles are also mentioned here.

INTERACTIONS IN DIFFERENT TYPES OF MIXTURES

Systems containing amines

Aliphatic amines + n-*alkanes*. Kašparek *et al.*[24] measured the V^E values of some aliphatic amines with members of a homologous series of *n*-alkanes. The V^E values were positive over the whole range of concentration for all mixtures and increase with increasing length of the *n*-alkane molecule for mixtures containing *n*-hexylamine and di-*n*-propylamine. Maximum values were obtained for *n*-alkane + diethylamine mixtures. These positive values of V^E are probably due to the dissociation of hydrogen-bonded aggregates of the amines. The similar situation exits in the case[25] of the V^E values of mixtures of *cyclo*-hexylamine with *n*-alkanes, benzene and substituted benzenes.

Aliphatic amine + *benzene or substituted benzene* + n-*alkane compounds*. Letcher[26] determined the V^E values of binary mixtures for primary amines (*n*-propylamine and *n*-butylamine), secondary amines (diethylamine, di-*n*-propylamine and di-*n*-butylamine) and tertiary amines (triethylamine, tri-*n*-propylamine and tri-*n*-butylamine) with benzene, chlorobenzene, nitrobenzene, toluene, hexane, heptane and cyclohexane at 25 °C.

For the mixtures of tertiary amines with cyclohexane, the V^E values were the result of the reduction of predominantly dipole–dipole interactions between the amine molecules. This effect was partly dipole–dipole in nature. The mixtures of tertiary amines with hexane and heptane showed small V^E values, which were more negative when the alkyl chains on the amine were longer. This trend could be attributed to the fitting of alkanes in the lattice of a long-chain amine, giving reductions in volume. However, the negative values of V^E showed that cross interactions dominated. Secondary amines show positive values of V^E in mixtures with cyclohexane due to the decrease in H-bonded self-association of the amines caused by dilution with cyclohexane. Negative changes of V^E increase in mixtures of secondary amines with alkanes with increasing size of the amine molecule. Namely, an alkane molecule fits better into the more open structure of longer chain amines than into shorter chain amines. The explanation for the negative values of V^E for secondary amines with benzene and substituted benzenes is similar to that for the case of mixtures of tertiary amines + aromatics. This is probably due to the size of the alkyl groups which diminish the effect of the amine–aromatic interaction. The V^E values of primary amines + cyclohexane are positive, as in the case of mixtures with secondary amines. The maximum V^E value for mixtures with primary amines is larger. This is probably due to the breakdown of the more compact H-bonded structure of the primary amines. The V^E values for primary amines with alkanes are much larger than their secondary or tertiary counterparts. This could be the consequence of two effects: *i*) the breakdown of the H-bonded structure of primary amines and *ii*) primary amines have more compact structures than secondary and tertiary amines. Namely, an alkane molecule cannot pack into the structure of primary amine as easily as into those of secondary and tertiary amines. In the mixtures of primary amines with benzene and substituted benzenes, it could be concluded that the substituted groups are responsible for the fact that these aromatics do not fit into the primary amine lattice as easily as benzene molecules. For this reason, the V^E values are more negative for the mixtures of primary amines with benzene.

Trialkylamines + n-*alkanes or alkylamines*. Oswal *et al.*[27] determined the isentropic compressibilities, κ_S, and changes of isentropic compressibility, $\Delta\kappa_S$, from measurements of speeds of sound, u, and densities, ρ, for 14 binary mixtures of triethylamine (TEA) and tri-*n*-butylamine (TBA) with *n*-hexane, *n*-octane, *n*-propylamine, *n*-penthylamine, *n*-hexylamine and *n*-octylamine. The values of $\Delta\kappa_S$ for mixtures with alkanes are positive for systems containing TEA and negative for systems containing TBA. The positive values of $\Delta\kappa_S$ are the consequence of the disruption of dipole–dipole association in TEA. On the other hand, the negative values of $\Delta\kappa_S$ arise due to the following contributions: *i*) a positive effect due to the disruption of dipole–dipole association in the TBA molecule and *ii*) the negative effect due to the interstitial accommodation of alkane molecules into

the large free volume of the TBA structure. It is clear that the contribution *ii* is quite large and dominates over the contribution *i*.

In the cases of TEA + primary amines, the $\Delta\kappa_S$ values are less positive and become negative as the chain length of the primary amine increases.

For the TBA + primary amine mixtures, the $\Delta\kappa_S$ values first increase from *n*-propylene to *n*-butylamine and then decrease as the chain length of the alkyl amine increases to *n*-octylamine. Positive values of $\Delta\kappa_S$ for TEA and TBA mixtures with primary amines are connected with destruction of H-bonds in these amines, for TEA + *n*-propylamine and n-pentylamine mixtures and for all mixtures with TBA. For the mixtures of TEA with *n*-hexylamine and *n*-octylamine, positive effect of $\Delta\kappa_S$ associated with the destruction of H-bonds is masked by the negative effect due to interstitial accommodation. The experimental speed of sound, *u*, was analyzed in terms of the collision factor theory, free length theory and Prigogine–Flory–Patterson statistical theory of solutions.

Diethylamine + ethyl acetate + n-*heptane*. Lillo *et al*.[28] calculated excess molar volumes and viscosity deviations for the ternary system diethylamine + ethyl acetate + *n*-heptane at 25 °C and for the corresponding binary systems. The positive values of V^E for all binaries indicate that molecular interactions between different molecules are weaker than interactions between the same molecules in their pure liquid. In addition, repulsive forces were dominant in these mixtures, causing very small excess viscosities for all binary systems.

Aniline + benzene + N,N-*dimethylformamide*. In the work of Kharat and Nikam,[29] the excess molar volumes and viscosity deviations for the ternary system aniline + benzene + *N*,*N*-dimethylformamide at 298.15, 303.15, 308.15 and 313.15 K were determined. At all temperatures, the V^E and $\Delta\eta$ values were negative. The main contribution to the negative values for V^E was the consequence of the interstitial accommodation of non-associated benzene molecules into aggregates of aniline. This also implies that no complex-forming interactions were present in system, leading to the negative values of $\Delta\eta$.

The McAllister three-body interaction model[30] was used to correlate the kinematic viscosities of the investigated systems. The V^E and $\Delta\eta$ values were predicted by the polynomial equations of Radojković *et al*.,[31] Kohler[32] and Scatchand *et al*.[33]

Systems containing esters

Methyl butanoate + n-*heptane + (*n-*octane or cyclooctane or 1-chlorooctane)*. Matos *et al*.[34,35] and Trenzado *et al*.[36] determined the V^E and $\Delta\eta$ values for the ternary systems of (methyl butanoate + *n*-heptane) with *i*) *n*-octane, *ii*) cyclooctane or *iii*) 1-chlorooctane at 283.15, 293.15, 303.15 and 313.15 K at atmospheric pressure over the entire concentration range.

The mixing effects corresponding to each binary system were the consequence of the following specific interactions and net packing effects: *i*) systems of methyl butanoate with *n*-heptane and *n*-octane exhibited positive values of V^E because the net rupture of dipole–dipole interactions in methyl butanoate dominates over the molecular packing and heteromolecular dipole–dipole induced interactions; *ii*) in the system *n*-heptane + *n*-octane, molecular packing was the prevalent factor; *iii*) in the system *n*-heptane + cyclooctane, the negative values of V^E confirmed that the packing effect predominated over physical interactions; *iv*) the positive V^E values for the system methyl butanoate + cyclooctane indicated that the rupture of dipole–dipole interactions between the ester molecules predominated over the effect of molecular packing and volume contraction; *v*) the negative values of V^E at all the investigated temperatures for the system *n*-heptane + 1-chlorooctane showed that the molecular packing effect was the prevalent factor, exhibiting a slightly endothermic effect. Moreover, the effects of the breakage of dipole–dipole interactions in the 1-chlorooctane molecule predominated over those due to molecular packing and heteromolecular dipole–dipole induced interactions, *vi*) the positive values of V^E and endothermic effect for the system methyl butanoate + 1-chlorooctane suggested that net rupture of heteromolecular dipole–dipole interactions prevailed over dipole–dipole heteromolecular interactions. The negative values of $\Delta\eta$ for both binary systems showed that the effect of dispersive forces prevailed.

The viscosity values were used to test the predictive capability of the UNIFAC-VISCO[34–36] and UNIVAC[34,35] group contributions models.

n-*Butyl acetate* + *aromatic hydrocarbons*. The dependences of V^E on temperature for the mixtures *n*-butyl acetate + aromatic hydrocarbons (toluene, ethylbenzene, *p*-xylene, mesitylene, *i*-propylbenzene, *n*-butylbenzene, *i*-butylbenzene and *t*-butylbenzene) were analyzed in the article by Resa *et al*.[37]

n-Butyl acetate is a weakly polar compound while the aromatic hydrocarbons are nearly non-polar. The aromatic hydrocarbon molecules intersperse among the *n*-butyl acetate molecules, affecting decreased interactions among the dipoles of butyl acetate and destruction of the dispersive interactions among the benzene rings. The obtained interaction between unlike molecules was weak, which caused expansion. It is clear that the influence of the intermolecular forces was higher than the packing effect caused by geometrical fitting for some chemicals (mesitylene, butylbenzene, *etc*.). For the mixtures that contained light solvents, the opposite effect would be detected, as aromatic hydrocarbon molecules with small molecules destroy neither π electron dispersive forces nor ester polar attraction.

The experimental data were used to test the Soave–Redlich–Kwong[38] and the Peng–Robinson[39] equations of state, which are of general interest in the calculation of thermodynamic properties of multicomponent complex mixtures.

Methyl ethanoate + 1-chlorooctane + n-*alkane*. Matos *et al*.[40] reported V^E values at 25 °C of four ternary mixtures of methyl ethanoate + 1-chlorooctane + + (*n*-heptane, *n*-octane, *n*-nonane or *n*-decane). The values of V^E for 1-chlorooctane + *n*-alkane showed that the packing effect was significant in the mixture containing *n*-heptane (negative values of V^E), which decreased with increasing number of carbon atoms in the *n*-alkane. As a result, positive values of V^E for the mixtures with *n*-nonane and *n*-decane were obtained. Moreover, the determination of the excess molar enthalpies[41] suggested that the breakage of dipole––dipole interactions in the chloro-alkanes predominates over the dispersive and induced heteromolecular dipole–dipole interactions in these binaries. For methyl ethanoate + *n*-alkane mixtures, the positive values of V^E imply that the effects due to heteromolecular interactions and degree of molecular packing efficiency decrease as the difference in molecule size of the compounds in the mixture increases.

Investigations of mixing enthalpies for these systems[40] confirmed that the dominant factor was breakage of dipole–dipole interactions in the methyl ester molecules. Finally, the small values of V^E of the system methyl ethanoate + + 1-chlorooctane suggest that the effects due to the heteromolecular dipole––dipole interactions are more important than those related to the breakage of dipolar interactions among the 1-chlorooctane molecules.

The V^E values were utilized to test the Nitta–Chao group-contribution model.[42] In addition, several empirical and semi empirical models were used to predict the experimental results of the ternary mixtures.[32,43–46]

Systems containing ethers

1,1-Dimethylethyl methylether with ethyl acrylate/butyl acrylate/methyl methacrylate/styrene. Peralta *et al*.[47] calculated the V^E values of the binary systems of 1,1-dimethylethyl methylether (MTBE) with ethyl acrylate, butyl acrylate, methyl methacrylate and styrene at 298.15 K and atmospheric pressure. The interactions between MTBE as an almost non-polar component and esters as polar components could be considered as complex formation between two species by n–π interaction. For all binary systems, negative values of V^E were obtained as a result of the effect of breaking the dipole–dipole association of the ether and the net packing effect contributed to by structural effects arising from interstitial accommodation. The largest negative values of V^E obtained for the system MTBE + styrene indicate that the disruption of dipolar associations of the MTBE as an ether is remarkably less than the additional specific interactions between its pair of electrons and the π electron of the aromatic ring. It is important to emphasize that the values of V^E increase as an ester chain increases from methyl to butyl, apparently due to pronounced contribution of interstitial accommodation.

The calculated V^E values were correlated with the Redlich–Kister Equation and with a series of Legendre polynomials.

MTBE with allyl methacrylate, n-*butyl methacrylate, methacrylic acid and vinyl acetate*. Wisniak *et al.*[48] calculated V^E of the binary systems 1,1-dimethylethyl methylether (MTBE) with allyl methacrylate, *n*-butyl methacrylate, methacrylic acid and vinyl acetate at 298.15 and 308.15 K and atmospheric pressure. The magnitude and sign of V^E are consequence of the type of interactions present in the mixtures. A double bond and an ester group are simultaneously present in acrylate solutes. In addition, methacrylic acid has a free –COOH group, which can lead to H-bonding. The V^E values are the result of the effect of breakage the dipole–dipole association in the ether; negative values of V^E indicate a net packing effect contributed by structural effects arising from interstitial accommodation. The maximum value of V^E for the system MTBE + methacrylic acid is considerably higher than that for the system MTBE + *n*-butyl methacrylate, reflecting a substantial additional packing by H-bonding between the different molecules. With increasing temperature, the V^E values are more negative, bearing in mind that the kinetic energy of the molecules of both components facilitates interaction of one specie into the other and both H-bonding and interaction between the tertiary ether group and the carbonyl group of the ester.

The calculated V^E values were correlated with the Redlich–Kister Equation and with a series of Legendre polynomials.

MTBE + toluene + isooctane. Morávková *et al.*[49] calculated the excess molar volumes, V^E, and adiabatic compressibility, κ_S, of the ternary system methyl tetrabutylether + toluene + isooctane (2,2,4-trimethylpentane) at temperatures from 298.15 to 328.15 K.

Molecular interactions for investigated binary systems are as follows: *i*) in the binary system toluene + trimethylpentane, small deviations are the consequence of a slightly different packing effect in the mixture compared to those in the pure substances; *ii*) this effect is much stronger in the binary mixture MTBE + trimethylpentane; *iii*) in the binary mixture MTBE + toluene, on the contrary, two effects are dominant, packing effects and specific $n+\pi$ interactions. No special ternary interactions are present.

The V^E and κ_S values for the ternary mixtures and corresponding binaries were fitted to the Redlich–Kister Equation.

Tetrahydrofuran + cyclic ether + hydrocarbon. Pintos *et al.*[50] investigated the effect of alkane chain-length on the V^E values of binary mixtures containing a cyclic ether at 298.15 K and atmospheric pressure. The binary mixtures of tetrahydrofuran (THF) and tetrahydropyran (THP) with *n*-hexane, *n*-heptane, *n*-octane and *n*-nonane were treated. In all cases the positive values of V^E increase with the length of the alkane chain for a given ether. However, the V^E values decrease with increasing length of the hydrocarbon chain of the ether. The positive values

of V^E could be explained by the breakage of interactions among molecules of pure species during the mixing process. Moreover, the spatial arrangement of the molecules of these ethers enables an easier accommodation of molecule of *n*-alkanes in the mixtures with THP than in those with THF.

The Nitta–Chao[42] Equation provides a reasonable correlation of the results.

Ether + chloro-ethylenes. Pal and Singh[51] calculated the V^E values of binary mixtures of trichloro-ethylene and tetrachloro-ethylene with 1,4-dioxane and some *n*-alkoxyethanol components at 298.15 K. The V^E values are positive for the mixture tetrachloro-ethylene + 1,4-dioxane, while an inversion in the sign of V^E values was obtained from positive to negative in the mixture with trichloro-ethylene. The V^E value are the result of several opposing effects: differences in the molecular size and shape of the components, and complex formation between the π-electrons of chloro-ethane and oxygen (–O–) in 1,4-dioxane.

These results were fitted to the Redlich–Kister Equation to estimate the binary coefficients.

Anisole/MTBE + benzene or chlorobenzene or benzonitrile or nitrobenzene. Viswanathan *et al*.[52] calculated V^E and $\Delta\eta$ values for binary systems of anisole or MTBE with benzene, chlorobenzene, benzonitrile and nitrobenzene at 288.15, 293.15 and 298.15 K.

The V^E values of all anisole and MTBE systems were negative, except for the anisole + chlorobenzene system, which showed a change in sign. The deviations in viscosity $\Delta\eta$ were negative for all the investigated temperatures. The MTBE systems gave greater V^E and $\Delta\eta$ values than the anisole systems, showing that the former systems deviated more from ideal behaviour. This fact could also indicate that the attractive interactions of the unlike molecules were stronger in the MTBE systems. Namely, the existence of electron-pair donor–electron pair acceptor type of interactions in all investigated systems is evident, showing that MTBE is a better electron-pair donor than anisole.

All the results are fitted by the Redlich–Kister Equation.

Anisole + 2-chloroethanol or 1,4-dioxane or tetrachloroethylene or tetrachloroethane or DMF or DMSO or diethyl oxalate. Baragi *et al*.[53] calculated V^E, $\Delta\eta$, ΔR, Δu and $\Delta\kappa_S$ values for the binary mixtures of anisole + 1,4-dioxane or tetrachloroethylene or tetrachloroethane or dimethylformamide (DMF) or dimethyl sulphoxide (DMSO) or diethyl oxalate at 298.15, 303.15 and 308.15 K. The V^E data for mixtures anisole + 1,4-dioxane and anisole + tetrachloroethylene are positive. Dispersion forces combined with a low molar volume of 1,4-dioxane led to the small positive values of V^E for the mixture anisole + 1,4-dioxane. Higher positive values of V^E for system anisole + tetrachloroethylene were the consequence of dispersion forces between the electronic charges on the O atom of the anisole molecules and the π electrons of the double bond of the tetrachloro-ethylene molecule, having a higher molar volume. Negative values of V^E were

obtained for the mixtures anisole + tetrachloroethane or dimethyl sulphoxide or diethyl oxalate or dimethylacetamide.

The computed quantities were fitted to the Redlich–Kister Equation to derive the coefficients and to estimate the standard error values.

Systems containing amides

Xylene + N,N-*dimethylformamide*. Chen and Liu[54] calculated the V^E values of binary mixtures of *o*-xylene, or *m*-xylene, or *p*-xylene with *N*,*N*-dimethylformamide (DMF) in the temperature range 293.15 to 353.15 K and at atmospheric pressure. In all cases, the V^E values were negative as result of chemical or specific interactions between DMF and xylene or a structural effect leading to the formation of molecular complexes. These interactions may be classified as electron (donor + acceptor)-type interactions involving the π-electrons of the xylene ring and the carbonyl group of DMF, or interactions through H-bond formation with xylene acting as the H donor and DMF as the acceptor. V^E data increase with rise in temperature for all analysed systems. The kinetic energy of molecules also increases leading to a decrease of interactions between molecules, so the contraction in volume decreases and as the result V^E increases.

The V^E results were correlated using the fourth-order Redlich–Kister polynomial equation with maximum likelihood principle being applied for the determination of the adjustable parameters.

N,N-*Dimethylformamide* + *aniline* + *benzonitrile*. Nikam and Kharat[55] calculated the V^E and $\Delta\eta$ values for the binary systems *N*,*N*-dimethylformamide (DMF) with aniline and benzonitrile at 298.15, 303.15, 308.15 and 313.15 K. The negative values of V^E and $\Delta\eta$ for the system DMF + aniline are caused by interstitial accommodation of the DMF molecules into the clusters of aniline. Namely, molar volumes of aniline and DMF differ considerably and no associated DMF molecules are geometrically fitted into aggregates of aniline. This shows that complex forming interactions are not present in the DMF + aniline system and therefore, the calculated $\Delta\eta$ values are negative. The negative values of V^E and positive values of $\Delta\eta$ for the DMF + benzonitrile system indicate strong specific interactions through dipolar association between the DMF and benzonitrile molecules.

The V^E and $\Delta\eta$ values are fitted by the Redlich–Kister polynomial equation.

DMF + *benzene or toluene or ethylbenzene*. Peng *et al*.[56] calculated the V^E values for the binary systems DMF with benzene or toluene or ethylbenzene in the temperature range 293.15 to 353.15 K and at atmospheric pressure. The negative values of V^E for all binary mixtures are the consequence of molecular interaction between the polar molecules of DMF and the non-polar molecules of the aromatic hydrocarbons. Namely, these mixtures are formed by dipole–dipole interactions of DMF molecules and the interaction of dipole–induced dipole

between DMF and the aromatic hydrocarbon molecules. It is clear that interaction between unlike molecules is stronger than the intra-molecular interactions. In addition, the small size of the DMF molecules and its linear aliphatic configuration could be other factors giving rise to the contraction in the V^E of the mixtures.

The increase in the kinetic energy of molecules with increasing temperature leads to a decrease in the interactions of the molecules. The interaction between DMF molecules is smaller than between aromatic molecules, so the contraction in volume increases and the V^E values decrease.

The V^E were fitted by the fourth-order Redlich–Kister Equation.

Cyclohexanone + N,N-*dimethylacetamide*. Iloukhani and Rakhshi[57] calculated the V^E, $\Delta\eta$ and Δn_D values for the binary system cyclohexanone + *N*,*N*-dimethylacetamide at 298.15, 308.15 and 318.15 K as a part of the ternary system with *N*,*N*-diethylethanolamine as the third component. The positive V^E is due to chemical and structural effects with more positive values on increasing the temperature from 298.15 to 318.15 K. The negative values of $\Delta\eta$ and Δn_D suggest that the forces between the pairs of unlike molecules are weaker than the forces between like molecules due to the difference in shape and size of the component molecules.

The binary results of V^E, $\Delta\eta$ and Δn_D were fitted by Redlich–Kister Equation, while the Cibulka,[58] Jasinski and Malanowski,[59] Singe *et al*., Pintos *et al*. and Calvo *et al*. Equations were used to correlate the ternary properties.[60] The predictions were performed by the Kohler[32] and Jacob–Fitzner Equations.[61] The McAllister three-body interaction model and the Hind *et al*.[62] Equation were used for correlation of kinematic and dynamic viscosities, respectively.

Systems containing chloro-alkanes

Zhang[63] determined the V^E and $\Delta\eta$ values for three binary mixtures of chlorinated alkanes: carbon tetrachloride + chloroform, carbon tetrachloride + dichloromethane and chloroform + dichloromethane, and one ternary mixture of chloroform + 1:1 carbon tetrachloride:dichloromethane at 303.15 K.

Both binary systems with carbon tetrachloride have positive values of V^E. The larger values of V^E for the system with chloroform are the consequence of two factors: *i*) carbon tetrachloride as non-polar component interacts weakly with polar dichloromethane and chloroform, where dichloromethane has a larger polarity than chloroform; *ii*) the present molecules show differences both in size and shape. The values of V^E for chloroform + dichloromethane are negative. The small magnitude is the consequence of very weak specific interactions, most probably due to dipole–dipole interactions between different molecules. The positive values of V^E could be explained from the fact that the most compact packing of spherical carbon tetrachloride is destroyed by mixing with spherical molecules of

the two other components. Negative $\Delta\eta$ could be caused by differences in size, shape and polarity between carbon tetrachloride and dichloromethane or chloroform. In addition, molecular interactions between these species are weaker than those in their pure state.

CONCLUSIONS

It is evident that thermodynamic and transport properties of mixtures could provide more and deeper information on molecular interactions. They show very complex behaviour expressed by three main effects: chemical, physical and geometrical. Which of the contributions is dominant depends on the nature of investigated mixture.

For the investigated mixtures, these contributions are balanced giving the corresponding values of thermodynamic and transport properties and the explained complex behaviour of the mixtures.

Acknowledgements. The authors gratefully acknowledge the financial support received from the Research Fund of the Ministry of Education, Science and Technological Development of the Republic of Serbia and the Faculty of Technology and Metallurgy, University of Belgrade (Project No. 172063).

И З В О Д

ФИЗИЧКИ, ХЕМИЈСКИ И СТРУКТУРНИ ЕФЕКТИ КАО ВАЖНИ ФАКТОРИ ЗА ОДРЕЂИВАЊЕ И МОДЕЛОВАЊЕ ТЕРМОДИНАМИЧКИХ И ТРАНСПОРТНИХ СВОЈСТАВА НЕЕЛЕКТРОЛИТНИХ РАСТВОРА

БОЈАН Д. ЂОРЂЕВИЋ, МИРЈАНА Љ. КИЈЕВЧАНИН, ИВОНА Р. РАДОВИЋ, СЛОБОДАН П. ШЕРБАНОВИЋ и АЛЕКСАНДАР Ж. ТАСИЋ

Технолошко–металуршки факултет, Универзитет у Београду, Карнегијева 4, 11120 Београд

У нашем прегледном раду учињен је покушај да се повежу волуметријски ефекти укључени у бинарне смеше нормалних и разгранатих алкохола. У овом раду су укратко изложене неке изабране истраживачке активности аутора повезаних са сложеним молекулским структурама које су објављене у водећим међународним часописима. Главни циљ је био боље разумевање комплексне структуре различитих смеша неелектролита, без алкохола, које су најчешће присутне у хемијској, петрохемијској и сродним индустријама. Анализиран је утицај основних физичких, хемијских и структурних ефеката више изабраних типова различитих бинарних и тернерних смеша. Оваква истраживања су од примарног значаја за одређивање и моделовање термодинамичких, транспортних и других особина.

(Примљено 23. октобра, ревидирано 8. новембра 2013)

REFERENCES

1. A. Assarsson, F. R. Eirich, *J. Phys. Chem.* **72** (1968) 2710
2. D. Patterson, G. Delmas, *Disc. Faraday Soc*. **49** (1970) 98
3. A. J. Treszczanowicz, O. Kiyohara, G. C. Benson, *J. Chem. Thermodyn.* **13** (1981) 253
4. M. C. S. Subha, K. C. Rao, *J. Phys. Chem. Liq.* **18** (1988) 185
5. E. A. Muller, *J. Chem. Eng. Data* **36** (1991) 214

6. S. L. Oswal, R. P. Phalak, *J. Solution Chem.* **22** (1993) 43
7. J. A. González, I. Garcié de la Fuenta, J. C. Cobos, *Fluid Phase Equilib*. **168** (2000) 31
8. E. Arunan, G. R. Desiraju, R. A. Klein, J. Sadlej, S. Scheiner, I. Alkorta, D. C. Clary, R. H. Crabtree, J. Donnenberg, P. Hobza, H. G. Kjaegaard, A. C. Legon, B. Mennucci, D. J. Nesbitt, *Pure Appl. Chem.* **83** (2011) 1619
9. E. Arunan, G. R. Desiraju, R. A. Klein, J. Sadlej, S. Scheiner, I. Alkorta, D. C. Clary, R. H. Crabtree, J. Donnenberg, P. Hobza, H. G. Kjaegaard, A. C. Legon, B. Mennucci, D. J. Nesbitt, *Pure Appl. Chem.* **83** (2011) 1637
10. P. A. Kollman, L. C. Allen, *Chem. Rev.* **72** (1972) 283
11. S. P. Šerbanović, M. Lj. Kijevčanin, I. R. Radović, B. D. Djordjević, *Fluid Phase Equilib.* **239** (2006) 69
12. M. Lj. Kijevčanin, S. P. Šerbanović, I. R. Radović, B. D. Djordjević, A. Ž. Tasić, *Fluid Phase Equilib.* **251** (2007) 78
13. B. D. Djordjević, S. P. Šerbanović, I. R. Radović, A. Ž. Tasić, M. Lj. Kijevčanin, *J. Serb. Chem. Soc*. **72** (2007) 1437
14. I. R. Radović, M. Lj. Kijevčanin, E. M. Djordjević, B. D. Djordjević, S. P. Šerbanović, *Fluid Phase Equilib.* **263** (2008) 205
15. J. D. Smiljanić, M. Lj. Kijevčanin, B. D. Djordjević, D. K. Grozdanić, S. P. Šerbanović, *Int. J. Thermophys.* **29** (2008) 586
16. M. Lj. Kijevčanin, I. R. Radović, S. P. Šerbanović, A. Ž. Tasić, B. D. Djordjević, *Thermochim. Acta* **496** (2009) 71
17. B. D. Djordjević, I. R. Radović, M. Lj. Kijevčanin, A. Ž. Tasić, S. P. Šerbanović, *J. Serb. Chem. Soc.* **74** (2009) 477
18. I. R. Radović, M. Lj. Kijevčanin, A. Ž. Tasić, B. D. Djordjević, S. P. Šerbanović, *J. Serb. Chem. Soc.* **74** (2009) 1303
19. E. M. Živković, M. Lj. Kijevčanin, I. R. Radović, S. P. Šerbanović, B. D. Djordjević, *Fluid Phase Equilib.* **299** (2010) 191
20. M. Lj. Kijevčanin, I. R. Radović, B. D. Djordjević, A. Ž. Tasić, S. P. Šerbanović, *Thermochim. Acta* **525** (2011) 114
21. A. B. Knežević-Stevanović, S. P. Šerbanović, B. D. Djordjević, D. K. Grozdanić, J. D. Smiljanić, M. Lj. Kijevčanin, *Thermochim. Acta* **533** (2012) 28
22. M. Lj. Kijevčanin, B. D. Djordjević, I. R. Radović, E. M. Živković, A. Ž. Tasić, S. P. Šerbanović, *Modeling of Volumetric Properties of Organic Mixtures Based on Molecular Interactions*, in: *Molecular Interactions*, A. Megha, Ed., Intech, Rijeka, p. 3
23. B. D. Djordjević, M. Lj. Kijevčanin, I. R. Radović, S. P. Šerbanović, A. Ž. Tasić, *J. Serb. Chem. Soc*. **78** (2013) 1079
24. M. Kašparek, I. Cibulka, L. Hnědkovsky, *J. Chem. Thermodyn*. **28** (1996) 595
25. G. Dharma Raju, G. Narayana Swamy, G. K. Raman, *J. Solution Chem*. **10** (1981) 79
26. T. M. Letcher, *J. Chem. Thermodyn*. **4** (1972) 159
27. S. L. Oswal, S. G. Patel, R. L. Gardas, N. Y. Ghael, *Fluid Phase Equilib.* **215** (2004) 61
28. P. Lillo, L. Mussari, M. A. Postigo, *J. Solution Chem*. **29** (2000) 183
29. S. J. Kharat, P. S. Nikam, *J. Mol. Liq.* **131–132** (2007) 81
30. R. A. McAllister, *AIChE J*. **6** (1960) 427
31. N. Radojković, A. Tasić, D. Grozdanić, B. Djordjević, D. Malić, *J. Chem. Thermodyn.* **9** (1977) 349
32. F. Kohler, *Monatsh. Chem.* **91** (1960) 738
33. G. Scatchard, L. B. Ticknor, J. R. Goates, E. R. McCartney, *J. Am. Chem. Soc.* **74** (1952) 3721

34. J. S. Matos, J. L. Trenzado, E. Gonzáles, R. Alcalde, *Fluid Phase Equilib*. **186** (2001) 207
35. J. S. Matos, J. L. Trenzado, E. Gonzales, R. Alcalde, *Fluid Phase Equilib*. **202** (2002) 133
36. J. L. Trenzado, J. S. Matos, R. Alcalde, *Fluid Phase Equilib*. **200** (2002) 295
37. J. M. Resa, C. Gonzalez, R. G. Concha, M. Iglesias, *Phys. Chem. Liquids* **42** (2004) 493
38. G. Soave, *Chem. Eng. Sci.* **27** (1972) 1197
39. D. Y. Peng, D. B. Robinson, *Ind. Eng. Chem. Fundam.* **15** (1976) 59
40. J. S. Matos, J. L. Trenzado, E. Romano, M. N. Caro, M. E. Pérez, *J. Solution Chem*. **30** (2001) 263
41. T. H. Doan-Nguyen, J. H. Vera, A. Ratcliff, *J. Chem. Eng. Data* **23** (1978) 218
42. T. Nitta, E. A. Turek, R. A. Greenkorn, K. C. Chao, *AIChE J*. **23** (1977) 144
43. C. Colinet, *Ph.D. Thesis*, University of Grenoble, Grenoble, 1967
44. C. C. Tsao, J. M. Smith, *Chem. Eng. Prog. Symp. Ser.* **49** (1953) 107
45. G. W. Toop, *Trans. TMS-AIME* **233** (1965) 850
46. R. P. Rastogi, J. Nath, S. S. Das, *J. Chem. Eng. Data* **22** (1977) 249
47. R. D. Peralta, R. Infante, G. Cortez, R. G. López, J. Wisniak, *Int. J. Thermophys*. **24** (2003) 173
48. J. Wisniak, R. D. Peralta, R. Infante, G. Cortez, *J. Chem. Thermodyn*. **37** (2005) 729
49. L. Morávková, Z. Wagner, Z. Sedláková, J. Linek, *J. Chem. Thermodyn*. **42** (2010) 920
50. M. Pintos, A. Amigo, R. Bravo, *J. Chem. Thermodyn*. **25** (1993) 337
51. A. Pal, W. Singh, *J. Chem. Eng. Data* **41** (1996) 428
52. S. Viswanathan, M. A. Rao, D. H. L. Prasad, *J. Chem. Eng. Data* **45** (2000) 764
53. J. G. Baragi, M. I. Aralaguppi, T. M. Aminabhavi, M. Y. Kariduraganavar, A. S. Kittur, *J. Chem. Eng. Data* **50** (2005) 910
54. B. Chen, W. Liu, *J. Chem. Thermodyn*. **39** (2007) 192
55. P. S. Nikam, S. J. Kharat, *J. Chem. Eng. Data* **48** (2003) 972
56. S.-J. Peng, H.-Y. Hou, C.-S. Zhou, T. Yang, *J. Chem. Thermodyn*. **39** (2007) 474
57. H. Iloukhani, M. Rakhshi, *J. Mol. Liq*. **149** (2009) 86
58. I. Cibulka, *Collect. Czech. Chem. Commun.* **47** (1982) 1414
59. B. Jasinski, S. Malanowski, *Chem. Eng. Sci.* **25** (1970) 913
60. M. Dominguez, I. Gascon, A. Valen, F. M. Royo, J. S. Urieta, *J. Chem. Thermodyn*. **32** (2000) 1551
61. K. T. Jacob, K. Fitzner, *Thermochim. Acta* **18** (1977) 197
62. R. K. Hind, E. McLaughlin, A. R. Ubbelohde, *Trans. Faraday Soc.* **56** (1960) 328
63. H.-L. Zhang, *J. Chem. Eng. Data* **48** (2003) 52.

Journal of the Serbian Chemical Society
JSCS@tmf.bg.ac.rs • www.shd.org.rs/JSCS
J. Serb. Chem. Soc. 78 (12) 2215–2227 (2013)

Contents of Volume 78

NUMBER 1

NUMBER 2

NUMBER 5

NUMBER 12

Journal of the Serbian Chemical Society
JSCS-info@shd.org.rs • www.shd.org.rs/JSCS

J. Serb. Chem. Soc. 78 (12) 2229–2236 (2012)

Author Index

Subject Index of Vol. **78** and *List of Referees* in the year *2013* are given in the electronic form at the Internet address of the Journal of the Serbian Chemical Society (http://www.shd.org.rs/JSCS/Vol78/No12.html).

End of Volume 78.